Analysis and mitigation of the factors limiting the efficiency of high power distributed feedback diode lasers

Vorgelegt von Diplom-Physiker

Christoph Matthias Schultz

Von der Fakultät IV - Elektrotechnik und Informatik
der Technischen Universität Berlin
zur Erlangung des akademischen Grades
Doktor der Naturwissenschaften
- Dr. rer. nat -
genehmigte Dissertation

Promotionsausschuss:

Vorsitzender:	Prof. Dr.-Ing. Wolfgang Heinrich
Berichter 1:	Prof. Dr. Günther Tränkle, Technische Universität Berlin
Berichter 2:	Prof. Dr. Klaus Petermann, Technische Universität Berlin
Berichter 3:	Prof. Dr. Hartmut Hillmer, Universität Kassel

Tag der wissenschaftlichen Aussprache: 9. Juli 2013

Berlin, 2013

D 83

Abstract

The subject of this thesis is the analysis of the factors limiting the efficiency of high power broad area (BA) distributed feedback (DFB) lasers, in comparison to conventional BA lasers. During this work it will be shown how high power conversion efficiency in the $\sim 60\,\%$ range can be achieved from 10 W-class wavelength stabilized $\sim 100\,\mu$m stripe DFB-BA lasers – values close to those of state of the art Fabry-Pérot (FP) BA lasers.

The work is structured as follows. Firstly, the factors limiting the efficiency of real DFB-BA lasers are identified. Secondly, these factors are reduced close to their fundamental physical limitations by identifying an appropriate laser design and by the development of an improved fabrication technology. Thirdly, high efficiency, high power DFB-BA lasers are fabricated using the new design and buried overgrowth technology as are reference FP-BA lasers to the same epitaxy design grown in a single stage epitaxy, which will be used for comparison. Subsequently, the properties of the newly developed DFB-BA lasers and reference lasers are experimentally analyzed in terms of threshold current, slope efficiency, optical output power, voltage drop, power conversion efficiency, spectral properties, spatial emission properties and reliability. Selected experimental results are compared to theory.

In order to identify how design limits the efficiency, a coupled-mode-theory-based numerical calculation of the threshold gain and differential quantum efficiency of DFB-BA lasers is presented – with the influence of the facet phases treated by approximation. Based on these calculations it is shown that a low coupling strength ($\kappa \cdot L \leq 1$ for coupling coefficient κ and cavity length L) is required to achieve a high differential quantum efficiency. It is further shown that in this range, the differential quantum efficiency and threshold gain should be comparable for FP-BA lasers and DFB-BA lasers.

In addition, this work reviews previously published studies on DFB-BA lasers, where the power conversion efficiency was typically reduced compared to appropriate reference FP-BA lasers because of an excessive coupling strength of the DFB grating, additional internal optical loss from the grating region, radiation loss from higher-order gratings or due to higher voltage. The

reduction of the power conversion efficiency can be nearly completely eliminated as follows: Firstly, the internal optical loss in the DFB-BA lasers must be reduced to the value of an efficient FP-BA laser by using an optimized DFB grating design and fabrication technology. Secondly, the radiation loss should be negligible. Thirdly, the differential quantum efficiency must be increased by reducing the coupling strength so that the DFB resonator loss equals the mirror loss of an efficiency optimized FP-BA laser. Finally, the DFB grating has to be optimized to enable carrier transport without any excess series resistance.

Two experimental iterations were performed, that made use of successively improved design and technology. During the first iteration, an AlGaAs-based epitaxy design optimized for efficient high power lasers was developed which is suitable for the integration of the DFB grating. A DFB grating design was developed based on two aluminum-free layers and an in-situ etching technique inside the epitaxy reactor was utilized for the fabrication, leading to low losses. The coupling strength was $\kappa \cdot L \sim 1$. It is shown that the developed DFB-BA lasers and reference FP-BA lasers have comparable internal optical loss, internal quantum efficiency and transparency current density. The oxygen contamination in the grating region was reduced to $< 10^{17}\,\mathrm{cm}^{-3}$ for optimized in-situ etching parameters. This is of particular importance because oxygen contamination can lead to the formation of deep level trap states. Optimized DFB gratings, developed in the second iteration of this work, have a floating grating design which allows to eliminate any excess voltage from the buried overgrown DFB grating and enable the fabrication of DFB-BA lasers with exactly the same voltage-current characteristics as obtained from the reference FP-BA lasers. The coupling strength of the DFB grating was reduced to $\kappa \cdot L \approx 0.2$.

These newly developed DFB-BA lasers achieve for the first time worldwide 10 W optical output power ($> 12\,\mathrm{W}$ at 15 A) and both 62 % peak power conversion efficiency and 58 % at 10 W. Compared to reference devices to the same epitaxy design, the power conversion efficiency is now reduced by only $\sim 5\,\%$. Wavelength stabilization is demonstrated with this DFB-BA lasers from threshold to 15 A with a narrow spectral width of $< 0.8\,\mathrm{nm}$ with 95 % power content. For some devices, additional side modes appear in the optical spectrum. These Bragg modes are shown to arise from higher-order vertical modes of the waveguide. The factors limiting the spectral width were also experimentally studied. The spectrum contains many separate lines and spectrally resolved lateral near field and far field measurements show that most arise from a regular series of lateral modes, which dominate the spectral width. These lateral modes are found to be stable and reproducible in their spectral and spatial distribution. One ore more longitudinal modes are

also observed. To confirm comparability with industrial applications, a reliability test was performed with four devices operating over $> 8000\,\mathrm{h}$ at $10\,\mathrm{W}$ optical output power.

In the experimental analysis, the spectral detuning between the Bragg wavelength of the DFB grating and the gain peak wavelength was found to have an important impact on the roll-over of the power-current characteristics, threshold current, slope efficiency, power conversion efficiency and spectral properties of high power DFB-BA lasers. A significant reduction in the suppression of higher-order waveguide modes was observed compared to the reference FP-BA lasers because higher-order modes typically have higher coupling coefficients which lead to comparatively low threshold currents. At high current levels and output powers, lasing on FP-like modes at the gain peak must be suppressed by using a very low front facet reflectivity at the wavelength range of the gain peak, which requires a specific optimization of the reflectivity spectrum.

In conclusion, during this work, the factors limiting the efficiency of DFB-BA lasers compared to state of the art FP-BA lasers have been identified and largely eliminated. DFB-BA lasers and reference FP-BA lasers now differ in power conversion efficiency by just $5\,\%$, with the spectral detuning between the Bragg wavelength of the DFB grating and the gain peak wavelength playing an important role. Possibilities for the further improvement of the spectral properties and power characteristics over a wide $\sim 15\,\mathrm{A}$ current range are discussed.

Kurzfassung

Das Thema dieser Arbeit ist die Analyse der Faktoren, welche die Effizienz von leistungsstarken Breitstreifen (BA) distributed feedback (DFB) Lasern im Vergleich zu konventionellen BA Lasern limitieren. Im Rahmen dieser Arbeit wird gezeigt, wie eine hohe Konversionseffizienz von $\sim 60\,\%$ bei einer Leistung von 10 W mit $\sim 100\,\mu$m breiten wellenlängenstabilisierten DFB-BA-Lasern erzielt werden kann. Dabei handelt es sich um Effizienz- und Leistungswerte wie sie mit aktuellen Fabry-Pérot (FP) BA-Lasern erzielt werden.

Diese Arbeit ist folgendermaßen strukturiert: Zunächst werden die Faktoren identifizieren, welche die Effizienz realer DFB-BA-Laser limitieren. Zweitens werden diese Faktoren bis nah an ihre jeweilige physikalische Grenze verringert, in erster Linie durch eine geeignete Struktur der DFB-Laser und durch die Entwicklung einer verbesserten Technologie zu deren Herstellung. Drittens werden hocheffiziente, leistungsstarke DFB-BA-Laser basierend auf der neuen Struktur und Technologie durch epitaktisches Überwachsen hergestellt, sowie in einer einzigen Epitaxie gewachsene Referenz-FP-BA-Laser mit dem gleichen Epitaxie Design, welche später zu Vergleichszwecken dienen. Anschließend werden die Eigenschaften der neu entwickelten DFB-BA-Laser und Referenz-Laser bezüglich ihres jeweiligen Schwellenstroms, Anstiegs, ihrer Spannung, optischen Leistung, Konversionseffizienz, spektralen Eigenschaften, Abstrahlungscharakteristik und Lebensdauer analysiert. Ausgewählte experimentelle Ergebnisse werden mit theoretischen Resultaten verglichen.

Um untersuchen zu können wie das Design die Effizienz von DFB-BA-Lasern limitiert, wird eine auf der Theorie gekoppelter Moden basierende numerische Berechnung des Schwellengewinns und der differentiellen Quanteneffizienz von DFB-BA-Lasern präsentiert, in welcher der Einfluss der Phasenbeziehung zwischen den Facetten und dem letzten Gitterstreifen näherungsweise berücksichtigt wird. Basierend auf dieser Berechnung wird gezeigt, dass die Verwendung einer geringen Kopplungsstärke ($\kappa \cdot L \leq 1$, mit dem Koppelkoeffizienten κ und der Resonatorlänge L) erforderlich ist um

eine hohe differentiellen Quanteneffizienz erzielen zu können. Weiterhin wird gezeigt, dass mit DFB-BA-Lasern eine vergleichbar hohe differentielle Quanteneffizienz wie mit Referenz-BA-Lasern gleichen Schwellengewinns erreicht werden kann.

In dieser Arbeit wird analysiert, dass die Konversionseffizienz von DFB-BA-Lasern, deren Ergebnisse überwiegend vor Beginn dieser Arbeit publiziert wurden, gegenüber Effizienz-optimierten konventionellen BA-Lasern typischerweise aufgrund einer zu hohen Kopplungsstärke des DFB Gitters, zusätzlicher interner optischer Verluste im Gitterbereich, durch Strahlungsverluste bei Bragg-Gittern höherer Ordnung oder eine erhöhte Flussspannung reduziert war. Auf folgende Weise kann die Reduktion der Konversionseffizienz fast vollständig eliminiert werden: Erstens müssen die internen optischen Verluste in den DFB-BA-Lasern durch die Verwendung verlustarmer DFB-Gitter und Herstellungs-Technologien auf das Niveau effizienter BA-Laser reduziert werden. Zweitens müssen die Strahlungsverluste vernachlässigbar gering sein. Drittens muss die differentielle Quanteneffizienz durch Reduzieren der Kopplungsstärke des DFB-Gitters erhöht werden, so dass die DFB-Resonatorver-luste den Spiegelverlusten eines Effizienz-optimierten FP-BA-Lasers gleichen. Schließlich muss das DFB-Gitter für einen Ladungsträgertransport ohne zusätzlichen Serienwiderstand optimiert werden.

Es wurden zwei experimentelle Iterationen durchgeführt, die auf schrittweisen Verbesserungen des Design der DFB-Gitter und deren Herstellungs-Technologie basieren. Während der ersten Iteration wurde ein auf AlGaAs basierendes, für effiziente, leistungsstarke Laser optimiertes Epitaxie-Design entwickelt, welches zugleich für die Integration des DFB Gitters geeignet ist. Weiterhin wurde ein Design für ein aus zwei Aluminium-freien Halbleiterschichten bestehendes DFB-Gitter entwickelt, dass sich durch geringe Verluste auszeichnet. Für dessen Herstellung wird unter anderem ein in-situ Ätzverfahren innerhalb des Epitaxie-Reaktors verwendet. Die Kopplungsstärke des DFB-Gitters betrug $\kappa \cdot L \sim 1$. Es wurde gezeigt, dass die entwickelten DFB-BA-Laser und Referenz-FP-BA-Laser vergleichbare interne optische Verluste, interne Quanteneffizienz und Transparenzstromdichten besitzen. Die Sauerstoff-Kontamination im Bereich des Gitters konnte für geeignete in-situ Ätzparameter auf $< 10^{17}\,\mathrm{cm}^{-3}$ reduziert werden. Diese Tatsache ist von besonderer Bedeutung, da Sauerstoff zur Bildung tiefer Störstellen führen kann.

Im Rahmen der zweiten Iteration hergestellte DFB-Gitter bestehen aus voneinander isoliert liegenden Gitterstegen, wodurch ein zusätzlicher Spannungsabfall durch das überwachsene Gitter vollständig eliminiert werden konnte. Dies ermöglicht die Herstellung von DFB-BA-Lasern welche die gleichen Strom-Spannungs-Kennlinien wie die Referenz-FP-BA-Lasern besitzen.

Zusätzlich wurde die Kopplungsstärke des DFB-Gitters auf $\kappa \cdot L \approx 0.2$ reduziert.

Die neu entwickelten DFB-BA-Laser erzielen erstmalig optische Leistungen bis zu 12 W und eine maximale Konversionseffizienz von 62 %. Am 10 W-Arbeitspunkt beträgt die Konversionseffizienz bis zu 58 %. Im Vergleich zu Referenzlasern welche auf dem gleichen Epitaxiedesign basieren, ist die Konversionseffizienz um nur noch $\sim 5\,\%$ reduziert. Mit diesen DFB-BA-Lasern wurde eine Wellenlängen-Stabilisierung zwischen dem Schwellenstrom und 15 A mit einer geringen Spektralbreite von < 0.8 nm mit 95 % Leistungsgehalt demonstriert. Einige dieser Laser wiesen zusätzliche Seitenmoden im optischen Spektrum auf, welche auf vertikale Wellenleitermoden höherer Ordnungen zurückgeführt werden konnten. Auch die Faktoren welche die spektrale Breite der DFB-BA Laser bestimmen wurden experimentell untersucht. Die Spektren bestehen aus vielen scharfen spektralen Linien. Messungen der spektral aufgelösten Nah- und Fernfelder haben gezeigt, dass diese spektralen Linien auf Serien lateraler Moden zurückzuführen sind, welche die Breite des Spektrums maßgeblich bestimmen. Diese lateralen Moden zeigten sich bezüglich ihrer spektralen und räumlichen Verteilung als stabil und reproduzierbar. Auch konnte in Abhängig vom injizierten Strom das Auftreten einer einzigen oder mehrerer longitudinaler Moden festgestellt werden. Um die Vereinbarkeit dieser Laser mit industriellen Anwendungsmöglichkeiten zu belegen, wurde ein Lebensdauertest bei einer optischen Ausgangsleistung von 10 W über > 8000 h durchgeführt.

Im Rahmen der experimentellen Analyse der DFB-BA-Laser konnte festgestellt werden, dass die spektrale Verschiebung zwischen der Bragg-Wellenlänge des DFB Gitters und dem Maximum des Gewinnspektrums einen bedeutenden Einfluss auf das Überroll-Verhalten der Strom-Leistungs-Kennlinie, auf den Schwellenstrom, die Steilheit der Leistungskennlinie, Konversionseffizienz und die spektralen Eigenschaften hat. Weiterhin wurde eine signifikant geringere Unterdrückung von vertikalen Wellenleitermoden höherer Ordnungen im Vergleich zu den FP-BA-Referenz Lasern beobachtet, welche sich aus der Tatsache ergibt, dass die Moden höherer Ordnungen typischerweise höhere Koppelkoeffizienten aufweisen, was zu vergleichsweise geringen Schwellenströmen führt. Im Bereich hoher Ströme und Leistungen müssen Laser-Oszillationen auf FP-artigen Moden am Gewinnmaximum durch die Verwendung einer sehr geringen Reflektivität der Frontfacette im Wellenlängenbereich des Gewinnmaximums unterdrückt werden, was eine spezifische Optimierung des Reflektionsspektrums erfordern kann.

Die Faktoren welche die Effizienz von DFB-BA-Lasern im Vergleich zu FP-BA-Lasern vom aktuellen Stand der Technik limitieren, konnten identifiziert und überwiegend eliminiert werden. Nunmehr weisen DFB-BA-Laser

gegenüber Referenz-FP-BA-Lasern eine lediglich um $\sim 5\,\%$ reduzierte Konversionseffizienz auf, wobei die spektrale Verschiebung zwischen der Bragg-Wellenlänge des DFB Gitters und dem Maximum des Gewinnspektrums von besonderer Bedeutung ist. Möglichkeiten für eine weitere Verbesserung der spektralen Eigenschaften und der Leistungs-Charakteristik über einen weiten Strombereich von $\sim 15\,\mathrm{A}$ werden diskutiert.

Contents

List of Figures

List of Tables

Introduction

The subject of this work is the analysis and mitigation of the factors, limiting the performance and especially, the power conversion efficiency in high power distributed feedback (DFB) semiconductor lasers, compared to conventional high power lasers. The work is based on theoretical considerations and the development of a laser structure which is optimized for high power conversion efficiency operation of distributed feedback semiconductor lasers.

Until the beginning of this work, wavelength stabilized DFB lasers are experimentally found to be substantially degraded compared to conventional high power lasers in terms of the achievable optical output power, voltage and power conversion efficiency [Yor92], [Sch09a], [Sch09b]. Some appreciable improvement in the development of high power, high efficiency DFB lasers has been reported by Kanskar *et al.* in 2006 [Kan06]. On the one hand, the reasons for the degradation of the DFB lasers are unclear and very little studied to date. On the other hand, technical progress in the development of high power, high efficiency wavelength stabilized diode lasers is expected to be of a significant industrial importance [Roh09], [Hua11], [Gra12], [Hei12]. This makes it an appropriate subject for a detailed physical and technical study.

The aim of this work is to gain theoretical knowledge about the physical limitations to the power conversion efficiency of DFB lasers, improvement in the development of adequate laser designs and experimental experiences with the operation of highly efficient DFB lasers. Because of the following practical reasons, DFB lasers are not exclusively optimized for a maximum power conversion efficiency in this work: Firstly, high optical output powers in the $\sim 10\,\mathrm{W}$ range are required for many possible applications and can be already achieved with conventional semiconductor diode lasers without spectral stabilization. Secondly, the wavelength stabilization and the spectral width should be significantly improved, compared to conventional semiconductor diode lasers. Thirdly, the spatial emission properties, such as the divergence angle of the laser beam, must be at least comparable to what is achieved with conventional semiconductor diode lasers. Therefore, all these

additional properties must be considered during the development and have to be investigated with the devices. Taking into account additional requirements limits the design options and must also be considered to possibly limit the achievable power conversion efficiency.

A motivation, why it is desirable to improve the power conversion efficiency of DFB lasers, can be derived from the technological requirements to semiconductor lasers for a selection of important industrial applications. DFB lasers and other semiconductor diode lasers with wavelength stabilization and narrow spectral width can be utilized for applications, where a narrow spectral width or a weak dependence of the emission wavelength on changes of the ambient temperature or injection current is required. One kind of such applications is the pumping of narrow absorption bands in the gain media of solid state lasers, fiber lasers and fiber amplifiers. Another example is the need to increase the optical output power of laser systems for the direct application of multiple semiconductor diode lasers, focused into a large mode area optical fiber. In both cases, the output power can be further increased by use of spectral beam combining [Sev08], [And09], [Roh09], [Hua11], [Gra12], [Hei12]. One typical example is the pumping of the $\sim$ 976 nm absorption bands of ytterbium (Yb) doped crystals and germanosilicate glasses (as Yb^{3+}-ion). Paschotta *et al.* [Pas97] discuss the advantages and disadvantages of pumping fiber-amplifiers, based on Yb-doped germanosilicate glass, at the comparatively narrow $\sim$ 976 nm absorption band with a high absorption cross-section, instead of the broad absorption peak between 870 and 950 nm, used conventionally. Semiconductor diode lasers with wavelength stabilization can be used to replace conventional diode lasers, light-emitting diodes (LEDs) or even less efficient lamps as pump sources in kW-class solid state or fiber laser systems [Vai08], [Hu09], [Köh09], [Pat09], [Vai10], [Wol11], [Köh12], [Gal12] or used in direct diode applications [Koe11], [Wol11], [Coh09]. In the context with such applications, increasing the power conversion efficiency of the whole laser system by a more efficient pumping scheme and by an increased efficiency of the pump source can drastically decrease the power consumption.

Wavelength stabilized diode lasers with a narrow spectral width can be obtained by the use of different concepts, such as external wavelength stabilization, by use of a distributed Bragg reflector (DBR) or DFB. For external wavelength stabilization, one facet of the laser is anti-reflection (AR) coated and an externally adjusted mirror is used to obtain optical feedback just over a very narrow spectral range. A grating, for example a volume Bragg grating (VBG) [Sch07], [Cru12c], or a Fabry-Pérot (FP) etalon can be used for this application. Nevertheless, external wavelength stabilization requires a very precise and stable fine-adjustment of the optical elements, a compar-

atively huge amount of space and is therefore cost-intensive. The application of DBR or DFB lasers with monolithic integrated (on-chip) wavelength-selective feedback-elements has many advantages in terms of stability, place requirement and costs. Both concepts which allow monolithic integration – DBR and DFB – have in common, that they function on the basis of Bragg reflection. Indeed, the Bragg reflector in a DBR laser is a passive optical element, which is not pumped electrically. In contrast, a DFB grating in a one-section diode laser is an active optical element because the whole region is electrically pumped. From this reason, DBR and DFB lasers have a different behavior under changes of the injection current I. In opposite to a DFB grating, a DBR is not directly heated by the thermal dissipation loss. As a consequence, the temperature-induced refractive index-change in the DBR region and the wavelength change of the laser wavelength λ, is smaller than for a DFB laser. Thus, DBR and DFB lasers have a comparable dependence of the laser wavelength on the ambient temperature $\mathrm{d}\lambda/\mathrm{d}T \cong 0.07\,\mathrm{nm\,K^{-1}}$ but DFB lasers have a stronger dependence of the laser wavelength on the injection current $\mathrm{d}\lambda/\mathrm{d}I$.

For this work, goals have been defined, which are based on technical requirements for possible applications of such diode lasers. These goals are to achieve a continuous wave optical output power of $\geq 10\,\mathrm{W}$ with a power conversion efficiency of $\geq 60\,\%$, a spectral width of $\leq 0.3\,\mathrm{nm}$ and a vertical beam divergence of $\leq 45\,^\circ$, both with 95 % power content. Furthermore, the following limitations have been made: This work concerns the development and analysis of DFB lasers. DBR lasers and diode lasers with external wavelength-stabilization have not been considered. The limitation was made on the basis of already published experimental results on efficient DFB lasers in the $\leq 5\,\mathrm{W}$ range [Kan06], as well as on the basis of promising experimental results with conventional FP diode lasers [Kan05], [Kni05] and DFB gratings. The targeted power range also requires the use of broad-area (BA) lasers, which typically have a contact stripe width of 50 to 200 μm. A stripe width of $\approx 100\,\mu\mathrm{m}$ is optimum for coupling the emitted power into standard 100 μm core optical fibers. In contrast to narrow stripe ridge-waveguide (RW) lasers with a typical contact stripe width of 2 to 8 μm, BA lasers operate in multiple higher-order optical modes in the transverse in-plane (epitaxy-plane) direction (lateral direction) of the laser cavity. Thus, for high optical output powers, disadvantages in the beam quality have to be accepted. Several industrial applications such as pumping and many material processing applications do not require a high beam quality, which is characterized by a beam parameter product [Ren92], [Sie98], [Eic04], [Hod05] value $M^2 \approx 1$. DBR or DFB tapered diode lasers would be another approach for high power levels and of better beam quality than a BA laser, but with disadvantages for

the power conversion efficiency and have not been considered. Limitations were also made concerning the DFB grating itself. Second-Bragg-order DFB gratings will be used, because this allows one to enlarge the grating period by a factor of two. Furthermore, only refractive index DFB gratings, will be used, which are formed by a modulation of the refractive index with a certain period along the longitudinal direction of the diode laser. In principle, DFB can be also achieved by introducing a modulation of gain or loss with a certain period along the longitudinal direction [Kog71], [Kog72], [Luo90], [SZA00]. Gain or loss gratings are preferred for DFB lasers, if a high side-mode suppression ratio (SMSR) must be achieved [Kam01], for example in telecommunication applications. A high SMSR is not critical for efficient high power DFB-BA lasers and is therefore not considered here.

Using DFB-BA lasers for the development of wavelength stabilized high power lasers with a power conversion efficiency close to the theoretical limits has some advantages and disadvantages and requires to overcome technical difficulties. The following advantages are crucial factors for the decision to use DFB-BA lasers for the approach, mentioned above: Firstly, DFB-BA lasers with a buried overgrown DFB grating (no surface grating) can be soldered and mounted like a conventional high power BA laser, because the grating corrugation is thoroughly embedded inside the laser chip (in contrast to a DBR surface grating, for example). Secondly, the fact that the DFB grating is extended over the whole laser enables a design freedom in terms of a wide range of possible coupling strengths, which can be translated into an effective front facet reflectivity (identical mirror and DFB loss), if the rear facet is high reflection (HR) coated and the front facet AR coated. Thirdly, the demand on wafer area is smaller than for a DBR laser and roughly identical to a FP laser. The stronger dependence of the Bragg wavelength on the injection current is a disadvantage, compared to a DBR laser. Technical difficulties for the fabrication of a DFB-BA laser with a very high power conversion efficiency must be expected in the lithographic structuring and epitaxial overgrowth of the buried DFB grating, for example because of possible contamination with oxygen [Bug11], crystal defects [Bug11], incomplete planarization of the growth surface and self-assembly of structured material hetero-interfaces [And89], [Hof01], [Bug11]. In an ideal case, the monolithic integration of the DFB grating should cause no degradation in the electrical properties and internal loss of the laser, compared to a reference laser design without the DFB grating and grown in a single, un-interrupted epitaxy.

This work is subdivided into three main chapters. In chapter 1 “Theoretical foundation for high power distributed feedback lasers”, the differential quantum efficiency, internal quantum efficiency, internal optical loss and series resistance are figured out to be critical parameters, possibly limiting the

power conversion efficiency of DFB lasers. Experimental results, obtained with DFB-BA lasers, fabricated until the beginning of this work, have shown, that the slope efficiency of DFB-BA lasers is too low and the resistance too high, compared to FP reference devices [Sch09a]. If one assumes that it is possible to integrate a DFB grating into a laser structure without adding significant series resistance, internal loss and without significant reductions in the internal quantum efficiency (which is in fact essential), the coupling coefficient, the cavity length and facet coatings determine the optical output power from the front facet. For a DFB laser of a specific cavity length with a HR coated rear facet and AR coated front facet mirror, the coupling coefficient determines the value of the threshold current and slope efficiency, analogous to the front facet reflectivity of a FP laser. Thus, the coupling coefficient must be chosen to achieve the optimum DFB resonator loss, like the front facet reflectivity of a FP laser can be adjusted for an optimum mirror loss, adequate to achieve the maximum optical output power at a specific injection current. Coupled mode theory [Kog72], [Str75], [Str77], [Kaz85], [Wen06] is used to derive the coupling coefficient and threshold conditions for a DFB laser with a second-order index grating [Kaz85]. Based on these calculations, threshold gain and differential quantum efficiency can be determined. The influence of the phase relation between the last grating stripe and the facet is studied and a simple a-priori approach is motivated which is assumed to solve this problem for BA lasers.

In chapter 2 "DFB-BA laser review", experimental results and theoretical findings on DFB-BA lasers are reviewed which have been published before the beginning of this work. The aim of this chapter is to draw relevant conclusions for the development of high efficiency, high power DFB-BA lasers from the state of the art technology.

Chapter 3 "Experimental and theoretical results from iteration I" describes in detail, how an epitaxy design for a laser waveguide is developed, which offers promising prospects to fabricate high power, high efficiency reference lasers (without a DFB grating) and is, as well, suitable for the integration of a DFB grating. Reference FP-BA lasers are fabricated from this material and the power-voltage-current (PUI) characteristics, spectral properties, spatial emission characteristics are investigated. Indeed, these FP-BA reference lasers were found to reach power conversion efficiencies of $> 60\,\%$ at 10 W output power. Afterwards, the development of a DFB grating, optimized for high power, high efficiency DFB-BA lasers is explained and the manufacturing and optimum coupling strength is discussed. Fabricated DFB-BA lasers have a record high peak power conversion efficiency up to 59 % and $> 50\,\%$ at 10 W. Experiments prove that the internal loss and internal quantum efficiency of the DFB-BA lasers are comparable to the FP reference

lasers. Compared to FP reference lasers, the DFB-BA lasers are still slightly degraded due to a lower slope efficiency and an increased series resistance. Further improvement of the performance of DFB-BA lasers is analyzed to be possible in all likelihood by reducing the coupling strength for a higher slope efficiency and by a DFB grating design which enables a better charge transport through it and thus, reduces the series resistance. Experimental results for the threshold current and slope efficiency are in good agreement with the values which have been obtained with coupled mode theory and BA laser approximation. Results from the first experimental iteration have been published in [Sch10a], [Sch10b], [Cru10] and [Wen11].

A second experimental iteration has been executed, because the results from iteration I have shown, that the power conversion efficiency and spectral properties of DFB-BA lasers can be further optimized. The results are presented in chapter 4 "Experimental and theoretical results from iteration II". Firstly, a concept for the improvement of the electro-optical properties of DFB-BA lasers is discussed. Secondly, a DFB grating, further optimized for a lower series resistance and an even smaller coupling coefficient for a higher slope efficiency is developed. Afterwards, fabricated DFB-BA lasers are investigated and an increase of the peak power conversion efficiency to $> 60\,\%$ and up to $59\,\%$ at $10\,\mathrm{W}$ is observed. A very low reflectivity of the front facet is found to be crucial for a sufficient wavelength stabilization of these low-coupled high efficiency DFB-BA lasers. A high material quality in the re-grown grating region enables reliable operation of DFB-BA lasers over $> 5000\,\mathrm{h}$ at $10\,\mathrm{W}$ output power. Results from the second experimental iteration were reported in [Sch11], [Cru11a] and [Cru11c].

In chapter 5, the gained results are evaluated on the basis of other publications about DFB lasers and one publication about high power DBR-BA lasers. Finally, the results of this work are summarized and conclusions are drawn, how the performance of DFB broad area lasers can be further improved.

Chapter 1

Theoretical foundation for high power distributed feedback lasers

The aim of this chapter is to provide the theoretical background which is required to comprehend how factors, limiting the efficiency of DFB lasers were identified, and how high power, high efficiency DFB lasers can be developed. The chapter begins with definition of the power conversion efficiency and continues with the calculation of the optical output power and electrical power consumption of an in-plane edge emitting diode laser. This calculation is done for a Fabry-Pérot laser with reflecting mirrors at both ends of the cavity. Most of the definitions are also valid for DFB lasers. If this is not the case, it is mentioned and adequate definitions are derived later in this chapter. Based on these calculations, it is shown, how a high peak power conversion efficiency can be achieved in combination with a high optical output power. Afterwards, it is discussed, how in practice parameters can be optimized for a high optical output power and low electric power consumption. The impact of dissipated power on selected laser properties is discussed subsequently.

In the second part of the chapter, the principle of distributed feedback is introduced and the calculation of coupling coefficients for second-order DFB gratings is derived. Afterwards, the threshold condition for DFB lasers is derived in order to calculate the threshold current and slope efficiency. An approximation for broad are lasers is motivated and numerical calculations for broad area lasers are explained. Finally, the threshold gain and differential quantum efficiency is compared between a DFB-BA laser and a FP reference laser and consequences onto the power and efficiency characteristics are discussed.

1.1 Power conversion efficiency

1.1.1 Power conversion efficiency in DFB and FP lasers

The power conversion efficiency describes the fraction of power that has been obtained by a conversion process from an original nature of power into another nature of power. In real physical processes, the conversion efficiency is < 1 and a fraction from the original amount of power is not converted into the wanted nature of power but into further natures of power, which is often – heat. Power conversion and the related achievable conversion efficiency are of an enormous importance for many natural an technical processes. To achieve higher power conversion efficiencies in technical processes is expected to be an essential contribution to decreasing the net energy consumption. In this work, the power conversion efficiency η_{pc} of a semiconductor laser is defined as the amount of optical power P_{opt} that can be generated from an original amount of electric power input into the device P_{el}. The electric power is defined as the product of the diode voltage $U(I)$ and the current I, which is injected into the device.

$$\eta_{\mathrm{pc}}(I) = \frac{P_{\mathrm{opt}}(I)}{P_{\mathrm{el}}(I)} = \frac{P_{\mathrm{opt}}(I)}{U(I) \cdot I} \tag{1.1}$$

The overall amount of electric power that is required to operate a semiconductor laser in an experiment or in an industrial application is higher because of the need of additional power for the electric power supply, temperature stabilization as well as due to the electrical resistance of external electrical connections. Nevertheless, the power conversion efficiency of the diode laser is a convenient measure because it is a physical variable with good comparability and is the ultimate limit in a system.

For the optimization of the power conversion efficiency, the optical power $P_{\mathrm{opt}}(I)$ has to be maximized and the voltage drop $U(I)$ to be minimized. In this work, high optical output power is also targeted. This requires an accordingly high injection current I. Therefore, both, $P_{\mathrm{opt}}(I)$ and $U(I)$ have to be optimized especially in the range of injection currents, where high optical output power can be achieved. In the following subsections the optical output power of an edge emitting in-plane diode laser will be derived, as well as the voltage drop over the diode. With the results gained, the peak power conversion efficiency and the corresponding optical output power is calculated. The calculations allows to study the influence of individual parameters that affect the power conversion efficiency.

1.1.2 Optical output power

Understanding the power conversion efficiency η_{pc} requires to derive the optical output power P_{opt} and the electrical power consumption P_{el} of a diode laser. In this subsection, the optical output power is calculated, based on the derivation presented in [Col95]. The derivation is valid for an edge emitting in-plane diode laser with a waveguide structure and reflecting mirrors, defining the cavity. Thus, it is a derivation for FP lasers. Nevertheless, most of the considerations are always true for DFB lasers where a periodic modulation of the index of refraction along the cavity axis provides the major optical feedback. It will be explicitly denoted, if an equation is not valid for a DFB laser. The corresponding relations for DFB lasers are derived later in this chapter.

Intuitively, the derivation must be based on the definition of rate equations for the generation and recombination of electrons and photons. Firstly, one can define a rate equation for electrons that is valid inside the active region, which will be formed by one or more quantum wells. The time evolution of the electron density N depends on the rate of injected and recombining electrons G_{gen} and R_{rec}, respectively. The density of electrons, injected per second into the active region of volume V is given by $(\eta_{\mathrm{i}} I)/(qV)$. Here, I is the electric current which is injected into the laser diode, η_{i} is the internal quantum efficiency and q the charge of a single electron. It should be noted, that the internal quantum efficiency is defined differently below and above the lasing threshold. Below threshold, it indicates the fraction of electric current that generates carriers inside the active region [Col95]. Therefore, it is sometimes called an injection efficiency. In contrast, the internal quantum efficiency above threshold is the fraction of current, which results in stimulated emission [Col95]. The recombination of electrons is determined by the rates for spontaneous recombination R_{sp}, nonradiative recombination R_{nr}, carrier leakage R_{l} and stimulated recombination R_{st}. Thus one obtains,

$$\frac{\mathrm{d}N}{\mathrm{d}t} = G_{\mathrm{gen}} - R_{\mathrm{rec}} \tag{1.2}$$

$$G_{\mathrm{gen}} = \frac{\eta_{\mathrm{i}} I}{qV} \tag{1.3}$$

$$R_{\mathrm{rec}} = R_{\mathrm{sp}} + R_{\mathrm{nr}} + R_{\mathrm{l}} + R_{\mathrm{st}}. \tag{1.4}$$

In the absence of generation and photons, the carrier recombination represents a natural decay with carrier lifetime τ, $\mathrm{d}N/\mathrm{d}t = N/\tau = R_{\mathrm{sp}} + R_{\mathrm{nr}} + R_{\mathrm{l}}$. One can write

$$R_{\mathrm{rec}} = \frac{N}{\tau} + R_{\mathrm{st}}. \tag{1.5}$$

The confinement factor of the active region is defined as $\Gamma = V/V_\mathrm{p}$, where V_p is the cavity volume which is occupied with photons. The photon rate equation can be written as

$$\frac{\mathrm{d}N_\mathrm{p}}{\mathrm{d}t} = \Gamma R_\mathrm{st} + \Gamma \beta_\mathrm{sp} R_\mathrm{sp} - \frac{N_\mathrm{p}}{\tau_\mathrm{p}}, \tag{1.6}$$

where N_p is the photon density, β_sp the spontaneous emission factor and τ_p the photon lifetime in which the photon density decays in the absence of any photon generation. The stimulated recombination rate R_st represents a gain process for photons because it describes the photon stimulated recombination of electrons and holes which generates more photons. With the gain per unit length g and a cavity length element Δz one can write

$$N_\mathrm{p} + \Delta N_\mathrm{p} = N_\mathrm{p}\, \mathrm{e}^{g\,\Delta z}. \tag{1.7}$$

For sufficiently small Δz one can approximate $\mathrm{e}^{g\,\Delta z} \approx 1 + g\Delta z$. With the group velocity v_g one can write $\Delta z = v_\mathrm{g}\Delta t$ and $\Delta N_\mathrm{p} = N_\mathrm{p}\, g\, v_\mathrm{g}\, \Delta t$, where Δt is the time increment, a photon with group velocity v_g needs to cover the distance Δz. For the photon generation one obtains

$$\left(\frac{\mathrm{d}N_\mathrm{p}}{\mathrm{d}t}\right)_\mathrm{gen} = \Gamma R_\mathrm{st} = g\, v_\mathrm{g}\, N_\mathrm{p}. \tag{1.8}$$

Thus, the new expressions for the carrier and photon density rate equations are:

$$\frac{\mathrm{d}N}{\mathrm{d}t} = \frac{\eta_\mathrm{i} I}{qV} - \frac{N}{\tau} - g\, v_\mathrm{g}\, N_\mathrm{p} \tag{1.9}$$

$$\frac{\mathrm{d}N_\mathrm{p}}{\mathrm{d}t} = \Gamma\, g\, v_\mathrm{g}\, N_\mathrm{p} + \Gamma\, \beta_\mathrm{sp}\, R_\mathrm{sp} - \frac{N_\mathrm{p}}{\tau_\mathrm{p}}. \tag{1.10}$$

The threshold gain in a diode laser can now be derived in the following way. The optical energy propagates in a dielectric waveguide mode. This allows one to make the ansatz to express the electric field $\overrightarrow{E}$ with a transverse field profile $U(x, y)$ and a magnitude E_0 that propagates along the cavity axes z with the complex amplitude propagation constant β and angular frequency ω in transverse electric (TE) polarization, indicated by the unity vector $\overrightarrow{\mathrm{e}}_\mathrm{y}$:

$$\overrightarrow{E}(x, y, z, t) = \overrightarrow{\mathrm{e}}_\mathrm{y}\, E_0\, U(x, y)\, \mathrm{e}^{i(\omega t - \beta z)}. \tag{1.11}$$

The real part of the complex propagation constant β contains the dependency on the effective index of refraction n_eff and wavelength λ, while the imaginary

part contains any transverse modal gain $\Gamma_{xy}\, g$ and loss $\alpha_{\mathrm{i}\,xy}$ (both are related to power).

$$\beta = \Re[\beta] + i\Im[\beta] = \frac{2\pi n_{\mathrm{eff}}}{\lambda} + \frac{i}{2}\left(\Gamma_{xy} g - \alpha_{\mathrm{i}}\right) \tag{1.12}$$

It is now necessary to define the cavity length L and the amplitude reflectivity of the front and rear facet mirror r_{f} and r_{r}. The threshold gain is reached, when the gain in the active region compensates for all loss in the cavity due to absorption and partially transmitting mirrors. After one roundtrip in the cavity (after the field has covered a distance of $2L$), the electric field must replicate itself. From this requirement applied to equation 1.11, one obtains the common threshold condition for a FP in-plane laser as

$$r_{\mathrm{f}} r_{\mathrm{r}}\, \mathrm{e}^{-2i\beta_{\mathrm{th}} L} = 1. \tag{1.13}$$

With respect to equation 1.12, one can transform the complex equation 1.13 into two equations for its magnitude and phase. For the magnitude part one obtains $r_{\mathrm{f}} r_{\mathrm{r}}\, \mathrm{e}^{(\Gamma_{xy}\, g_{\mathrm{th}} - \alpha_{\mathrm{i}})L} = 1$ and

$$\Gamma g_{\mathrm{th}} = \alpha_{\mathrm{i}} + \frac{1}{L} \ln\left(\frac{1}{r_{\mathrm{f}} r_{\mathrm{r}}}\right). \tag{1.14}$$

The second summand in equation 1.14 is the mirror loss α_{m}. With the power reflectivities $R_{\mathrm{f}} = r_{\mathrm{f}}^2$ and $R_{\mathrm{r}} = r_{\mathrm{r}}^2$ one can write

$$\alpha_{\mathrm{m}} = \frac{1}{2L} \ln\left(\frac{1}{R_{\mathrm{f}} R_{\mathrm{r}}}\right). \tag{1.15}$$

For a DFB laser, the equivalent DFB resonator loss α_{DFB} will be derived later in this chapter. It depends on the optical feedback from the DFB grating, as well as on optical feedback from the facet mirrors. Optical feedback in a DFB laser or the DFB resonator loss can be compared to a FP laser by setting $\alpha_{\mathrm{DFB}} = \alpha_{\mathrm{m,eff}}$, where $\alpha_{\mathrm{m,eff}}$ is an effective mirror loss. With a given rear facet reflectivity, this allows to calculate an effective front facet reflectivity.

Above threshold, which is expressed here by the threshold current I_{th}, both, the steady state gain and steady state carrier density clamp at its threshold values.

$$g(I > I_{\mathrm{th}}) = g_{\mathrm{th}} \tag{1.16}$$

$$N(I > I_{\mathrm{th}}) = N_{\mathrm{th}} \tag{1.17}$$

By using the steady-state carrier rate equation 1.3 at threshold (with $R_{\mathrm{st}} = 0$), one obtains

$$\frac{\eta_{\mathrm{i}} I_{\mathrm{th}}}{qV} = \left(R_{\mathrm{sp}} + R_{\mathrm{nr}} + R_{\mathrm{l}}\right)_{\mathrm{th}} = \frac{N_{\mathrm{th}}}{\tau}. \tag{1.18}$$

Above threshold, $R_{sp} + R_{nr} + R_l$ clamps at its threshold value because it depends monotonically on the carrier density N, which clamps at its threshold value (equation 1.17). Substituting equation 1.18 into equation 1.10 gives a new carrier rate equation which is valid only above threshold ($I > I_{th}$) where the carrier density in the active region clamps at ist threshold value $N = N_{th}$, so that $(N - N_{th})/\tau$ vanishes, resulting in:

$$\frac{dN}{dt} = \eta_i \frac{I - I_{th}}{qV} - v_g\, g\, N_p. \tag{1.19}$$

Under steady-state condition above threshold one obtains

$$N_p = \frac{\eta_i (I - I_{th})}{q\, v_g\, g_{th}\, V}. \tag{1.20}$$

The optical output power of a laser can be calculated from the product of the optical energy in the cavity $h\,\nu\,N_p\,V_p$ and the energy loss rate through the mirrors, given by $v_g\,\alpha_m = 1/\tau_m$. Here, h is the Planck constant and $\nu = \omega/2\pi$ is the frequency.

$$P_{opt} = v_g\,\alpha_m\,N_p\,h\,\nu\,V_p. \tag{1.21}$$

With equations 1.14 and 1.20 one obtains the common equation

$$P_{opt} = \eta_d \frac{h\nu}{q}(I - I_{th}). \tag{1.22}$$

The factor $\eta_d = (\eta_i\,\alpha_m)/(\alpha_i + \alpha_m)$ in equation 1.22 is the differential quantum efficiency η_d which determines the slope efficiency $S = ((\eta_i\,\alpha_m)/(\alpha_i + \alpha_m))(h\,\nu/q)$ of a laser at a specific wavelength $\lambda = c/\nu$:

$$\eta_d = \eta_i \left(\frac{\alpha_m}{\alpha_i + \alpha_m}\right) = \frac{q}{h\nu}\frac{dP_{opt}}{dI}. \tag{1.23}$$

A maximum slope efficiency $S = 1.2716\,\mathrm{W\,A^{-1}}$ can be theoretically obtained at a wavelength of $\lambda = 975\,\mathrm{nm}$ for $\alpha_m \to \infty$, $\eta_i \to 1$ and $\alpha_i \to 0$. For a DFB laser, equation 1.22 remains true with the adequate differential quantum efficiency which will be derived later in this chapter.

Now, a formula for the threshold current for a FP diode laser needs to be derived, which is based on variables that can be obtained experimentally. For positive gain $g \geq 0$, the dependency of the gain on the carrier density N can be approximated with a differential gain $\partial g/\partial N = g_0/N$ [Col95] as

$$g = g_0 \ln\left(\frac{N}{N_{tr}}\right). \tag{1.24}$$

The threshold carrier density can be calculated with equations 1.14 and 1.24 as

$$N_{\mathrm{th}} = N_{\mathrm{tr}}\, \mathrm{e}^{(\alpha_{\mathrm{i}}+\alpha_{\mathrm{m}})/(\Gamma g_0)}. \tag{1.25}$$

In principle, this enables to derive a formula for the threshold current, based on equation 1.18 and the polynomial expression for the recombination rates in equation 1.5. For example, [Col95] argues, that in state of the art QW diode lasers, the carrier recombination at threshold would be dominated by spontaneous recombination and thus, with equation 1.18, one would obtain $I_{\mathrm{th}} \cong (B N_{\mathrm{th}}^2\, q\, V)/\eta_{\mathrm{i}}$. This argument is questionable. Instead of doing this, it is common to replace equation 1.24 for the charge carrier density dependence of the gain $g(N)$ by an equation for the current density dependence of the gain $g(j)$, where j is the current density and j_{tr} the transparency current density:

$$g = g_0 \ln\left(\frac{j}{j_{\mathrm{tr}}}\right). \tag{1.26}$$

Note, that the gain coefficient g_0 in equation 1.26 is different to g_0 in equation 1.24. Consequently, one obtains in analogy to equation 1.25:

$$j_{\mathrm{th}} = j_{\mathrm{tr}}\, \mathrm{e}^{(\alpha_{\mathrm{i}}+\alpha_{\mathrm{m}})/(\Gamma g_0)}. \tag{1.27}$$

The threshold current density j_{th} and the threshold current I_{th} are therefore given by the equations

$$j_{\mathrm{th}} \cong j_{\mathrm{tr}}\, \mathrm{e}^{(\alpha_{\mathrm{i}}+\alpha_{\mathrm{m}})/(\Gamma g_0)} \tag{1.28}$$

$$I_{\mathrm{th}} \cong I_{\mathrm{tr}}\, \mathrm{e}^{(\alpha_{\mathrm{i}}+\alpha_{\mathrm{m}})/(\Gamma g_0)}, \tag{1.29}$$

where $I_{\mathrm{tr}} = j_{\mathrm{tr}} W L$. The transparency current or current density can be experimentally obtained from the cavity length dependence of the threshold current and differential quantum efficiency [Col95].

1.1.3 Electrical power consumption

The electric power P_{el} of a diode laser is given by the product of the injection current I and the voltage drop over the device $U(I)$. The voltage characteristics $U(I)$ of a laser diode can be fractionized into a contribution from the energy separation of the quasi-Fermi level which is here called the ideal diode voltage U_{d}, an additional series voltage U_{s} and a contribution from the series resistance R_{s} [Col95]:

$$P_{\mathrm{el}}(I) = U(I) \cdot I = (U_{\mathrm{d}} + U_{\mathrm{s}} + R_{\mathrm{s}} \cdot I) I. \tag{1.30}$$

Because of its dependence on the quasi-Fermi level energy separation, the ideal diode voltage can be approximately calculated from the photon energy, divided by the electron charge, $U_\mathrm{d} \approx (h\nu)/q$. For 975 nm lasers, one obtains $U_\mathrm{d} = 1.272\,\mathrm{V}$. The ideal diode voltage is therefore a lower limit for the turn-on voltage of the laser diode. For typical laser diodes, a small series voltage $U_\mathrm{s} < U_\mathrm{d}$ increases the turn-on voltage. In principle, the turn-on voltage can be increased by a series voltage U_s to the band-gap energy of the highest band-gap material in the epitaxy structure, which is often, a cladding layer on the p-side or n-side of the waveguide. For earlier InGaAs/AlGaAs single quantum well lasers, $U_\mathrm{s} \approx 0.4V$ has been reported [Bou89] but in state of the art AlGaAs-based quantum well lasers, the series voltage is smaller, $U_\mathrm{s} < 0.1V$ [Kni05].

The series resistance R_s determines the slope of the voltage drop $U(I)$ with increasing current I. Its value is determined by the resistivity of the epitaxial layers and substrate, as well as by additional contributions from interfaces. For this reason it must be expected, that the series resistance of a DFB laser can be higher than the series resistance of a FP reference laser, if the DFB grating is integrated into the device with incorporation of additional epitaxial layers and corresponding hetero-interfaces. From a practical point of view, the series resistance of a laser diode with contact stripe width W, cavity length L and a known resistivity ρ_s can be calculated as $R_\mathrm{s} = \rho_\mathrm{s}/(WL)$.

1.1.4 How to achieve a high peak power conversion efficiency

Equations 1.1, 1.22 and 1.30 enable the calculation of the current dependence of the optical output power $P_\mathrm{o}(I)$, voltage $U(I)$ and power conversion efficiency $\eta_\mathrm{PCE}(I)$, abbreviated as PUI characteristics. In the beginning of this section, such characteristics are calculated for variations of the front facet reflectivity R_f, internal optical loss α_i, series resistance R_s and series voltage U_s, in order to demonstrate their impact on the characteristics of the optical power and power conversion efficiency. For this calculation, laser parameters have been chosen according to promising values for a state of the art single quantum well diode laser. The fixed physical variables are denoted in table 1.1.

In Fig. 1.1, calculated PUI characteristics are are depicted for FP-BA lasers with additional fixed parameters $R_\mathrm{s} = 20\,\mathrm{m\Omega}$ and $U_\mathrm{s} = 50\,\mathrm{mV}$. In Fig. 1.1 (a) the influence of the optical feedback onto the optical power and efficiency is demonstrated by increased the front facet reflectivity from 0.1

Table 1.1: The physical variables, their notations and values, used in the computation example.

Variable	Notation	Value
Cavity length	L	$3000\,\mu\mathrm{m}$
Contact stripe width	W	$100\,\mu\mathrm{m}$
Reflectivity, rear facet	R_r	$98.00\,\%$
Internal quantum efficiency	η_i	0.95
Transparency current density	j_tr	$150\,\mathrm{A\,cm^{-2}}$
Gain coefficient	g_0	$2100\,\mathrm{cm^{-1}}$
Confinement factor	Γ	$0.7\,\%$

to 10 %. The increase of the front facet reflectivity causes a decrease of the threshold current and a decrease of the slope efficiency. In the high power range at $\sim 10\,\mathrm{W}$, decreasing the front facet reflectivity enables to achieve higher powers and efficiencies, because the increase in the slope efficiency more than compensates for the increase in threshold current. The peak power conversion efficiency increases with decreasing optical feedback and is also shifted towards higher currents and output powers. Low optical feedback is therefore preferred for high power, high efficiency lasers. The validation of this concept has to be controlled for DFB lasers, were the threshold current and slope efficiency must be calculated in a different way.

The impact of the internal optical loss is shown in Fig. 1.1 (b). Therefore, α_i is increased from 0.5 to $2.0\,\mathrm{cm^{-1}}$. One observes, that the according increase in the threshold current is nearly negligible, compared to the rapid decrease of the slope efficiency. Because of being driven at currents significantly above threshold, high power, high efficiency lasers require low internal optical loss.

Figure 1.2 shows calculated PUI characteristics for FP-BA lasers with additional fixed parameters $R_\mathrm{f} = 2.0\,\%$ and $\alpha_\mathrm{i} = 1.0\,\mathrm{cm^{-1}}$. The influence of the series resistance onto the voltage and efficiency is demonstrated in Fig. 1.2 (a) between 20 and $30\,\mathrm{m\Omega}$. Because the series resistance determines the slope of the voltage characteristics, its impact increases with the injection current and is therefore of exceedingly importance for the efficiency of high power lasers.

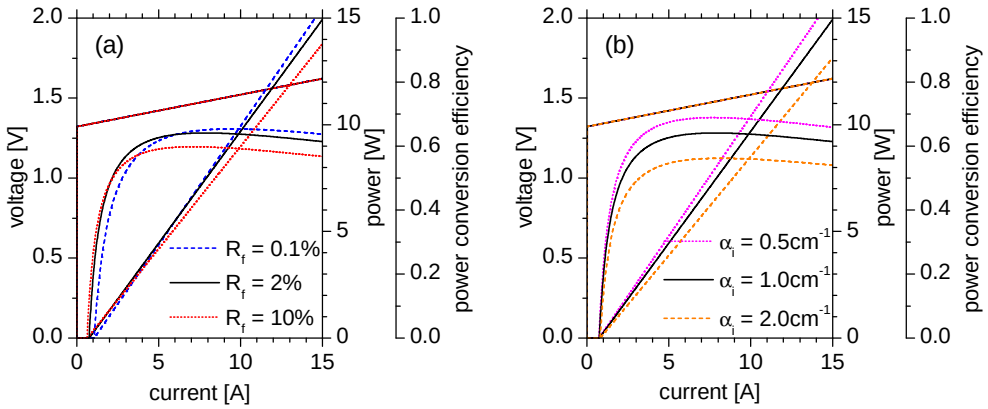

Figure 1.1: Voltage, power and efficiency characteristics, calculated with parameters given in table 1.1 and $R_\mathrm{s} = 20\,\mathrm{m\Omega}$, $U_\mathrm{s} = 50\,\mathrm{mV}$. (a) Variation of the front facet reflectivity $R_\mathrm{f} = 0.1$, 2 and 10 %. (b) Variation of the internal optical loss $\alpha_\mathrm{i} = 0.5$, 1.0 and $2.0\,\mathrm{cm}^{-1}$.

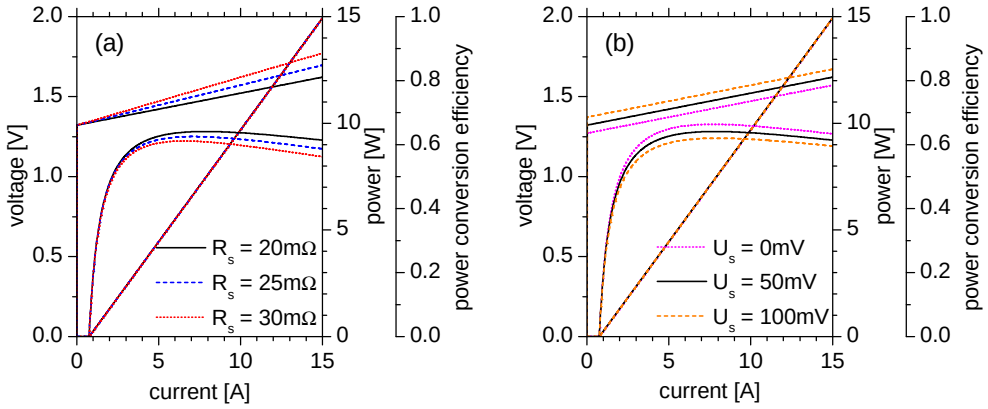

Figure 1.2: Voltage, power and efficiency characteristics, calculated with parameters given in table 1.1 and $R_\mathrm{f} = 2\,\%$, $\alpha_\mathrm{i} = 1.0\,\mathrm{cm}^{-1}$. (a) Variation of the series resistance $R_\mathrm{s} = 20$, 25 and $30\,\mathrm{m\Omega}$. (b) Variation of the series voltage $U_\mathrm{s} = 0$, 50 and 100 mV.

The influence of the series voltage (or turn-on voltage, because the ideal diode voltage has not been changed) onto the efficiency is demonstrated in Fig. 1.2 (b). Naturally, to achieve low series voltage is an aim for the improvement of all high efficiency lasers.

With the results from sections 1.1.2 and 1.1.3, the current dependence of the power conversion efficiency $\eta_\mathrm{pce}(I)$ can be calculated for a simple model

of an edge-emitting in-plane FP diode laser. This enables to analyze the dependence of the power conversion efficiency on important laser parameters, such as the cavity length L, the facet reflectivities R_f and R_r and the internal optical loss α_m. The aim of this work is to analyze the limiting factors to the power conversion efficiency in order to practically achieve a very high power conversion efficiency from $\sim 10\,\mathrm{W}$ high power DFB lasers. This requires the lasers to be optimized to either reach the peak power conversion efficiency at such high power levels or at least to offer a low drop of the power conversion efficiency between the current at the peak power conversion efficiency I_0 and the operation current. It is therefore reasonable to analyze the dependence of the peak power conversion efficiency on the laser parameters, mentioned above.

The power conversion efficiency is defined as $\eta_\mathrm{pce}(I) = P_\mathrm{opt}/P_\mathrm{el}$ and can be expressed as a product of four factors with specific physical relevance [Erb07]:

$$\eta_\mathrm{pce}(I) = \eta_\mathrm{i} \cdot \frac{\alpha_\mathrm{m}}{\alpha_\mathrm{i} + \alpha_\mathrm{m}} \cdot \frac{h\,\nu/q}{U_0 + I R_\mathrm{s}} \cdot \frac{I - I_\mathrm{th}}{I}. \tag{1.31}$$

where the ideal diode voltage and the series voltage have been summed up to the turn-on voltage $U_0 = U_\mathrm{d} + U_\mathrm{s}$. The first factor, which is the internal quantum efficiency, indicates, how efficient the injected current above threshold is used for the generation of stimulated emission. The second factor is the optical efficiency of a FP laser and evaluates, the out-coupling from the facets relative to the total loss of the cavity. Its definition is different for a DFB laser. The third factor represents a drop in the efficiency due to extra voltage which has to be applied because of the series resistance and series voltage which raise the real voltage drop above the quasi-Fermi energy level separation. Finally, the fourth factor describes a drop in the efficiency which occurs due to the fact, that the threshold current has to be exceeded, before stimulated emission dominates.

For the analysis of the peak power conversion efficiency, the current I_0 at which the power conversion efficiency $\eta_\mathrm{pce}(I)$ reaches its maximum has to be calculated from $\mathrm{d}\eta_\mathrm{pce}/\mathrm{d}I = 0$ [Bou89]. One obtains

$$I_0 = I_\mathrm{th}\left(1 + \sqrt{1 + \frac{U_0}{I_\mathrm{th} R_\mathrm{s}}}\right). \tag{1.32}$$

For the peak value of the power conversion efficiency one calculates

$$\eta_\mathrm{pce}^\mathrm{peak} = \eta_\mathrm{pce}(I_0) = \eta_\mathrm{d}\left(\frac{h\nu}{qU_0}\right) \frac{\frac{U_0}{I_\mathrm{th} R_\mathrm{s}}}{\left(1 + \sqrt{1 + \frac{U_0}{I_\mathrm{th} R_\mathrm{s}}}\right)} \tag{1.33}$$

and the optical output power at the peak power conversion efficiency is consequently

$$P_{\text{opt}}^{I_0} = P_{\text{opt}}(I_0) = \eta_{\text{d}} \left(\frac{h\nu}{q} \right) I_{\text{th}} \sqrt{1 + \frac{U_0}{I_{\text{th}} R_{\text{s}}}}. \tag{1.34}$$

To analyze the influence of the optical feedback on the threshold current, slope efficiency, optical output power at the peak power conversion efficiency and the peak power conversion efficiency itself, these physical variables are computed as functions of the cavity length for different values of the front facet reflectivity $R_{\text{f}} = 0.5, 1.0, 2.0$ and $4.0\,\%$. During the computation, the internal optical loss was set to $\alpha_{\text{i}} = 1.0\,\text{cm}^{-1}$. The fixed physical variables are denoted in table 1.2. Their values are selected, according to promising values for a state of the art single quantum well diode laser.

Table 1.2: The physical variables, their notations and values, used in the computation example.

Variable	Notation	Value
Cavity length	L	$500, 600, \ldots, 6000\,\mu\text{m}$
Contact stripe width	W	$100\,\mu\text{m}$
Reflectivity, rear facet	R_{r}	$98.00\,\%$
Internal quantum efficiency	η_{i}	0.95
Transparency current density	j_{tr}	$150\,\text{A}\,\text{cm}^{-2}$
Gain coefficient	g_0	$2100\,\text{cm}^{-1}$
Confinement factor	Γ	$0.7\,\%$
Resistivity	ρ_{s}	$6 \cdot 10^{-5}\,\Omega\,\text{cm}^{-2}$

In Fig. 1.3, the resulting length dependence is depicted for the threshold current (a), the slope efficiency (b), the optical output power at the peak power conversion efficiency (c) and the peak power conversion efficiency itself (d). The threshold current as a function of the cavity length has a characteristic local minimum at $\sim 0.15\,\text{cm}$ and a quasi linear slope towards longer resonator length. The minimum of the threshold current is shifted to longer resonator length with decreasing front facet reflectivity (decreasing optical feedback). The threshold-current increase with increasing cavity

length has been fitted linearly between 0.3 and 0.6 cm, the coefficients are given in Fig. 1.3 (a) for $R_f = 0.5$ and 4.0 %. For a 100 μm stripe BA laser at 10 W optical output power, the relevant cavity length is expected to be in the 0.3 to 0.4 cm range (3000 to 4000 μm), which corresponds to current densities of 3667 and 2750 A cm^2 if one assumes that the laser will have a threshold current of 1 A and a slope efficiency of 1 W A^{-1}. State of the art high power single emitter diode laser can be operated at CW current densities up to 5000 A cm^2 [Kön10], [Bao11]. Thus, the evaluation of the computed results should be focused 0.3 to 0.4 cm cavity length. The changes in the threshold current are relatively low, compared to the absolute currents at the peak power conversion efficiency I_0 of 8.41 A at $R_f = 0.5$ % and 10.32 A at $R_f = 4.0$ %.

The slope efficiency, depicted in Fig. 1.3 (b) decreases nearly linear with increasing cavity length, the linear fitted coefficients (between 0.3 and 0.6 cm) are given in Fig. 1.3 (b) for $R_f = 0.5$ and 4.0 %. An increasing front facet reflectivity (increasing optical feedback) increases the negative slope of the slope efficiency as a function of the cavity length. Figures 1.3 (a) and (b) point out that there is a tradeoff between the aims to achieve a low threshold current and a high slope efficiency by an optimization of the optical feedback. For lasers, driven at a designated working current I_w substantially above threshold ($I_w \geq 10 \cdot I_{th}$), a decrease of the slope efficiency due to an increase in the optical feedback can have a dramatic impact on the optical power $P_o(I_w)$ and efficiency $\eta_{PCE}(I_w)$, overcompensating the effect of the reduced threshold current.

The optical output power at the peak power conversion efficiency is a very important parameter for the optimization of high power, high efficiency lasers. Figure 1.3 (c) shows that the output power at the peak power conversion efficiency increases with increasing cavity length for length above ≈ 0.1 cm for the computed cases. The slope is nearly linear with coefficients given in Fig. 1.3 (c), fitted linear between 0.3 and 0.6 cm for $R_f = 0.5$ and 4.0 %.

Finally, the peak power conversion efficiency is depicted in Fig. 1.3 (d) as a function of the cavity length. The peak power conversion efficiency has a maximum whose position depends on the front facet reflectivity (optical feedback) and whose value is here always the same (0.677), because it is limited by the same internal optical loss of $\alpha_i = 1.0$ cm^{-1}. Above the maximum, the peak power conversion efficiency decreases with increasing cavity length nearly linear with coefficients, given in Fig. 1.3 (d), determined from linear fits between 0.3 and 0.6 cm for $R_f = 0.5$ and 4.0 %. Thus, in the preferred range of cavity lengths (0.3 to 0.4 cm) and with the given parameters, high power conversion efficiencies of > 60 % can be achieved with all the front

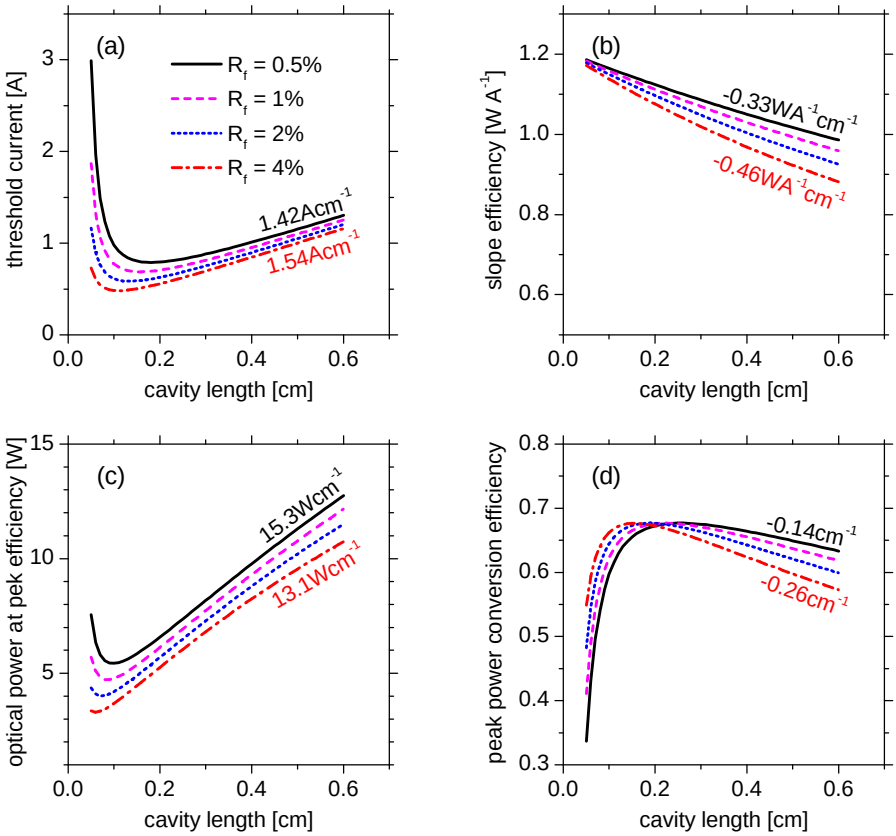

Figure 1.3: Analysis on the influence of the front facet reflectivity R_f on the power and efficiency characteristics, $\alpha_\mathrm{i} = 1.0\,\mathrm{cm}^{-1}$. (a) Threshold current as a function of the cavity length. (b) Slope efficiency as a function of the cavity length. (c) Output power at the peak power conversion efficiency as a function of the cavity length. (d) Peak power conversion efficiency as a function of the cavity length.

facet reflectivities, used for the computation.

A further calculation, varying the internal optical loss $\alpha_\mathrm{i} = 0.5, 1.0, 2.0$ and $4.0\,\mathrm{cm}$, has been carried out with the fixed physical variables, denoted in table 1.2. For this computation, the front facet reflectivity was set to $R_\mathrm{f} = 1.0\,\%$. Figure 1.4 (a) shows the characteristics for the threshold current. In contrast to increasing the front facet reflectivity, increasing the internal optical loss causes higher threshold currents, of course. The threshold increase with cavity length has been fitted linear between 0.3 and 0.6 cm, the coefficients are given in Fig. 1.4 (a) for $\alpha_\mathrm{i} = 0.5$ and $4.0\,\mathrm{cm}^{-1}$.

The slope efficiency characteristics are depicted in Figure 1.4 (b). While

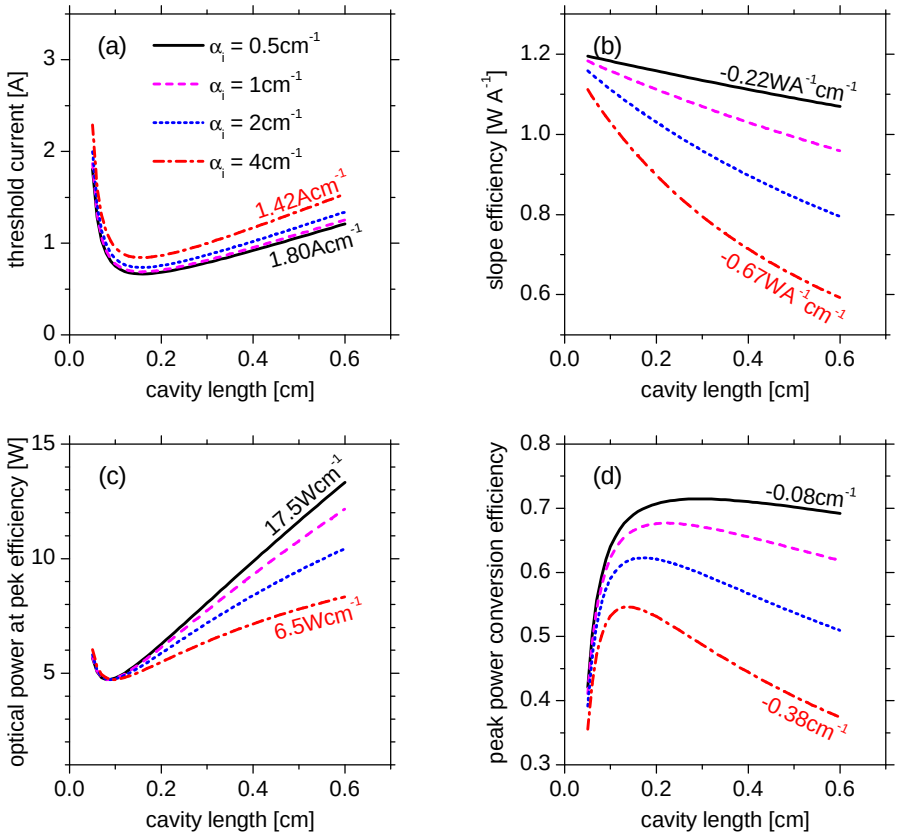

Figure 1.4: Analysis on the influence of the internal optical loss α_i on the power and efficiency characteristics, $R_\mathrm{f} = 1.0\,\%$. (a) Threshold current as a function of the cavity length. (b) Slope efficiency as a function of the cavity length. (c) Output power at the peak power conversion efficiency as a function of the cavity length. (d) Peak power conversion efficiency as a function of the cavity length.

increasing the internal optical loss, the slope efficiency decreases and its decrease with increasing cavity length becomes more pronounced. Thus, internal optical loss $\leq 1\,\mathrm{cm}^{-1}$ is preferred for high power lasers with cavity lengths $\geq 0.3\,\mathrm{cm}$ (with the chosen fixed parameters), in order to achieve slope efficiencies in the $\sim 1\,\mathrm{W\,A}^{-1}$ range or above. The decrease of the slope efficiency with cavity length has been fitted linear between 0.3 and 0.6 cm, the coefficients are given in Fig. 1.4 (b) for $\alpha_\mathrm{i} = 0.5$ and $4.0\,\mathrm{cm}^{-1}$.

Figure 1.4 (c) shows the optical output power at the peak power conversion efficiency as a function of the cavity length. The roughly linear increase with the cavity length strongly depends on the internal optical loss. The

gradients were fitted linear between 0.3 and 0.6 cm, the coefficients are given in Fig. 1.4 (c) for $\alpha_\mathrm{i} = 0.5$ and $4.0\,\mathrm{cm}^{-1}$.

Finally, the peak power conversion efficiency is depicted in Fig. 1.4 (d). Its maximum strongly depends on the internal optical loss. The cavity length at which it is reached increases with decreasing internal optical loss. Based on the fixed parameters, optical loss $\leq 2\,\mathrm{cm}^{-1}$ is required in order to obtain peak power conversion efficiencies ≥ 0.6 in the 0.3 to 0.4 cm cavity length range.

1.1.5 Continuous wave power and efficiency characteristics

Real diode lasers which are driven under continuous wave (CW) current injection have power, voltage and efficiency characteristics, which deviate from what has been derived in the first sections of this chapter. These deviations occur due to the current and temperature dependence of important laser parameters. In some cases, these deviations are small and can be neglected, for example close to threshold, where the diode laser is not significantly heated and current induced effects are of minor importance.

The fraction of the electric power input that is not converted into optical power output is called the dissipated power P_d and appears in form of heat that increases the temperature inside the diode laser and especially, in the active region. The exact temperature distribution depends on the design of the diode laser, as well as on the mounting and cooling scheme. The appearance of power dissipation is a consequence of the fact, that the power conversion efficiency of a real diode laser is limited to a value below one.

$$P_\mathrm{d} = P_\mathrm{el} - P_\mathrm{opt} = (1 - \eta_\mathrm{pc})\, P_\mathrm{el} \tag{1.35}$$

The power dissipation in the diode laser results in heating the device and causes several, mostly unwanted physical effects. The actual temperature increase ΔT in K is determined by the thermal resistance R_th in $\mathrm{K\,W}^{-1}$:

$$\Delta T = R_\mathrm{th} P_\mathrm{d}. \tag{1.36}$$

For free running FP lasers, the most common temperature effects are the temperature-induced increase of the threshold current, the temperature-induced decrease of the slope efficiency and the thermal roll-over at high current and power levels. These changes in the power characteristics occur due to a temperature-driven decrease of the internal quantum efficiency and the increase of the internal loss. For high power DFB lasers, one additional important effect is the wavelength-shift of the gain spectrum ($\approx 0.3\,\mathrm{nm\,K}^{-1}$)

relative to the wavelength-shift of the Bragg-wavelength ($\approx 0.07\,\mathrm{nm\,K^{-1}}$). The voltage characteristics of a diode laser $U(I) = U_\mathrm{d} + U_\mathrm{s} + (W\,L)\rho_\mathrm{s}\,I$ is also effected by a temperature increase which occurs, when the CW drive current is increased. The temperature dependence of the resistivity causes a decrease of the series resistance. Furthermore, the quasi-Fermi level energy separation is decreased with increasing temperature. This causes a decrease of the ideal diode voltage and an increase of the gain peak wavelength.

Both, the decrease of the internal quantum efficiency and the increase of the internal losses are expected to be comparable in DFB and FP lasers, if both lasers have the same efficiency. A fundamental difference between DFB and FP lasers occurs under the impact of the wavelength-shift of the gain spectrum. The DFB laser is assumed to show an increased threshold current and a decreased slope efficiency, if the maximum of the gain-spectrum λ_gain shifts to longer or shorter wavelength than the Bragg-wavelength of the DFB grating λ_Bragg.

DFB lasers, reported until now, have a reduced power conversion efficiency, compared with FP lasers from the same vertical epitaxy design and with an optimized facet coating [Ear98], [Sch09a], [Sch10a]. For this reason, DFB lasers are assumed to be stronger heated at the same current or output power and to underlie increased temperature-driven effects.

Phenomenological, the temperature and carrier density effects on the power characteristics of a FP laser can be expressed by using the dependence of the threshold current and slope efficiency on the quantum well temperature and by using the thermal resistance of the device. The temperature dependence of the threshold current can be empirically described by the threshold current characteristic temperature T_0 [Tho80]

$$I_\mathrm{th}(T_\mathrm{b}) = I_\mathrm{th}(T_\mathrm{a}) \cdot \exp\left(\frac{T_\mathrm{b} - T_\mathrm{a}}{T_0}\right), \tag{1.37}$$

were $T_\mathrm{a} < T_\mathrm{b}$ are the temperatures inside the active region before and after the temperature has been increased. In an experiment, this can be realized by driving the diode laser with short current pulses ($< 1000\,\mathrm{ns}$) and a low repetition rate, so that the temperature in the active region equals the temperature in the rest of the laser chip (the ambient temperature). Similarly, a slope efficiency characteristic temperature T_1 can be defined:

$$S(T_\mathrm{b}) = S(T_\mathrm{a}) \cdot \exp\left(\frac{T_\mathrm{a} - T_\mathrm{b}}{T_1}\right). \tag{1.38}$$

With these definitions, the CW output power characteristics of a FP diode

laser can be approximately calculated as discussed in [Erb00]

$$P_{\mathrm{opt}} = \eta_{\mathrm{d}} \frac{h\,\nu}{q} \cdot \exp\left(\frac{-R_{\mathrm{th}}[I(U_0 + IR_{\mathrm{s}}) - P_{\mathrm{opt}}]}{T_1}\right) \times \left[I - I_{\mathrm{th}} \cdot \exp\left(\frac{R_{\mathrm{th}}[I(U_0 + IR_{\mathrm{s}}) - P_{\mathrm{opt}}]}{T_0}\right)\right]. \quad (1.39)$$

Power characteristics, numerically calculated from equation 1.39 asymptotically approach to linear power characteristics, calculated with equations 1.22 and 1.28 / 1.29 for $T_0 \to \infty$ and $T_1 \to \infty$. Figure 1.5 shows power characteristics, computed with equation 1.39 for different values of R_{th} and T_1, together with calculated voltage and efficiency characteristics. The computation is based on the parameters, given in table 1.2 and $W = 100\,\mu\mathrm{m}$, $L = 3000\,\mu\mathrm{m}$, $R_{\mathrm{f}} = 2.0\%$, $\alpha_{\mathrm{i}} = 1.0\,\mathrm{cm}^{-1}$, $U_{\mathrm{s}} = 50\,\mathrm{mV}$ and $T_0 = 150\,\mathrm{K}$. In Fig. 1.5 (a), the dependence of the power and efficiency characteristics on the slope efficiency characteristic temperature is depicted for $T_1 = 800$, 400 and 200 K with fixed value $R_{\mathrm{th}} = 4\,\mathrm{K\,W}^{-1}$. The characteristics, plotted in black and labeled "linear" are calculated based on equations 1.22 and 1.29 and are identical to the black characteristics in Fig. 1.3 and 1.4. The reduction of T_1 causes a decrease of the local slope efficiency which is marginal below 5 A but causes a significant decrease of the optical power above 10 A and leads to the beginning of a thermal roll-over. Consequently, the power conversion efficiency cannot reach its former peak value and its decrease beyond the peak is now also driven by the decrease of the slope efficiency, in addition to the quadratic dependence of the series resistance term on the injection current.

The influence of the thermal resistance R_{th} on the power and efficiency characteristics is demonstrated in Fig. 1.5 (b), computed with equation 1.39 for $T_1 = 150\,\mathrm{K}$. Here the thermal resistance has been increased from $R_{\mathrm{th}} = 4$ to $12\,\mathrm{K\,W}^{-1}$. This causes the local slope efficiency to decrease with increasing current, comparable to decreasing the parameter T_1, shown in Fig. 1.5 (a). For $R_{\mathrm{th}} = 12\,\mathrm{K\,W}^{-1}$, power saturation is observed at 10 A. Further increasing the injection current would in this case lead to a reduction in output power and a considerable increase in device heating.

The temperature dependence of the threshold current and slope efficiency, presented above, is approximately valid for FP diode lasers. For DFB lasers, the temperature dependence will be different due to differences in the wavelength-shift of the gain spectrum ($\approx 0.3\,\mathrm{nm\,K}^{-1}$) and the wavelength-shift of the Bragg-wavelength ($\approx 0.07\,\mathrm{nm\,K}^{-1}$) with temperature. The different behavior of FP and DFB lasers is illustrated schematically in Fig. 1.6. Figure 1.6 (a) shows a scheme of a parabolic shaped gain curve and a lasing mode at the specific Bragg wavelength at three different temperatures

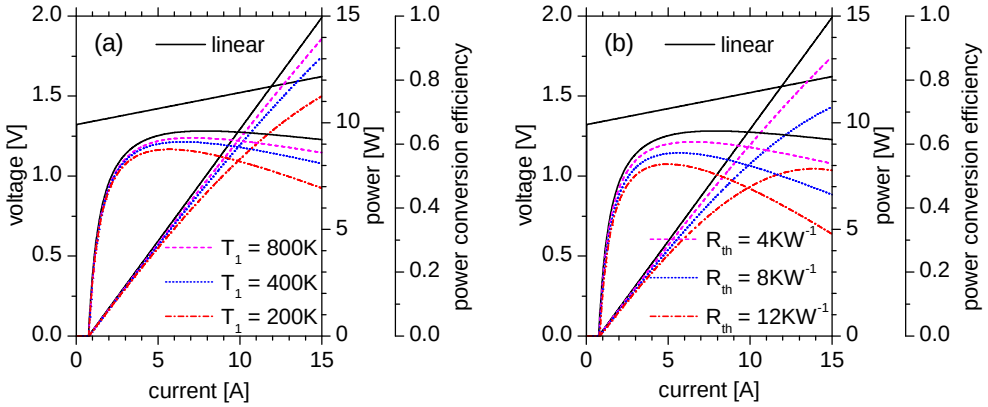

Figure 1.5: Voltage, power and efficiency characteristics of a 100 μm wide and 3000 μm long FP-BA laser, calculated with parameters, given in table 1.2 and $R_f = 2.0\%$, $\alpha_i = 1.0\,\mathrm{cm}^{-1}$, $T_0 = 150\,\mathrm{K}$. (a) Variation of the slope efficiency characteristic temperature $T_1 = 800$, 400 and 200 K with $R_{th} = 4\,\mathrm{K\,W}^{-1}$. (b) Variation of the thermal resistance $R_{th} = 4$, 8 and $12\,\mathrm{K\,W}^{-1}$ with $T_1 = 400\,\mathrm{K}$.

$T_1 < T_2 < T_1$ (not to be confused with threshold-current and slope efficiency characteristic temperatures T_0 and T_1). The required threshold gain is indicated with a horizontal line. While at T_2, the Bragg wavelength of the DFB grating is centered on the peak of the gain curve, the Bragg wavelength is shifted to positions beyond the gain peak for T_1 and T_3. This suggests the assumption, that at T_1 and T_3, the threshold current will be higher than for T_2, because higher carrier density must be achieved. Degradation of the slope efficiency occurs at T_3 , compared to T_2 due to the temperature-induced decrease of the internal quantum efficiency and increase of the internal optical loss. At T_1, the slope efficiency might be also degraded but this is quantitatively not clear. On the one hand, the higher carrier density which is required to reach threshold at T_1 has a decreasing effect onto the internal quantum efficiency. On the other hand, the internal optical loss decreases and the internal quantum efficiency increases at lower temperatures.

For the operation of DFB lasers it is of particular importance that the gain spectrum of an InGaAs quantum well in AlGaAs is typically several tens of nanometers broad [Bos96], [Bef00]. This allows the Bragg wavelength of the DFB grating to be significantly shifted away from the gain peak wavelength. For example, Morgott *et al.* report that they can tune the laser emission from a tapered external cavity laser between 1030 and 1085 nm, using wavelength-tunable optical feedback from an grating-turned external cavity [Mor98].

In contrast to the DFB laser example, the lasing modes of a free running

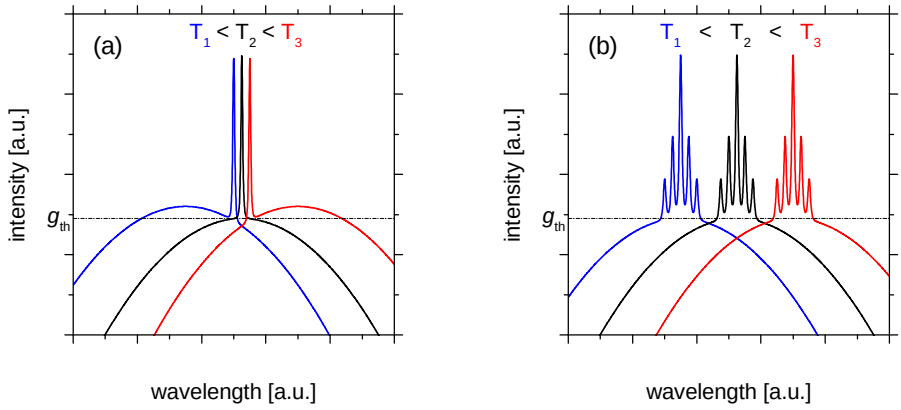

Figure 1.6: Scheme of the gain spectrum and lasing modes relations at three different temperatures for (a) DFB lasers and (b) FP lasers.

FP laser can remain at the specific gain peak for all three temperatures, as schematically depicted in Fig. 1.6 (b).

Thus, if values for the threshold characteristic temperature T_0 and slope efficiency characteristic temperature T_1 are experimentally determined for a DFB laser, deviations must be expected even compared to a reference FP laser from the same epitaxy design. On the one hand, if the gain-peak is detuned to a wavelength much lower as the Bragg wavelength of the DFB grating and then stepwise increased towards the Bragg wavelength, even negative values might occur for T_0 and T_1. On the other hand, T_0 and T_1 values of a DFB laser are expected to be comparable to a reference FP laser, if the spectral detuning between the gain-peak and the Bragg wavelength is sufficiently small.

Figure 1.7 (a) shows CW voltage, power and power conversion efficiency characteristics, calculated with parameters given in table 1.2, as well as $\alpha_\mathrm{i} = 1.0\,\mathrm{cm}^{-1}$, $R_\mathrm{f} = 2.0\,\%$ and $U_\mathrm{s} = 50\,\mathrm{m\Omega}$. The thermal resistance was set to $R_\mathrm{th} = 4\,\mathrm{K\,W}^{-1}$, the threshold current and slope efficiency characteristic temperatures are $T_0 = 150\,\mathrm{K}$ and $T_1 = 400\,\mathrm{K}$. The dissipated power $P_\mathrm{diss}(I)$ and the optical power $P_\mathrm{opt}(I)$ are calculated plotted in Fig. 1.7 (b) to the left axis.

Additionally, the center wavelength of a DFB and FP laser has been calculated from $\lambda(I) = \lambda_0 + P_\mathrm{d}(I) \cdot R_\mathrm{th} \cdot \mathrm{d}\lambda/\mathrm{d}T$. The temperature dependence of the laser wavelength has been assumed as $\mathrm{d}\lambda_\mathrm{DFB}/\mathrm{d}T = 0.07\,\mathrm{nm\,K}^{-1}$ for the DFB laser and $\mathrm{d}\lambda_\mathrm{FP}/\mathrm{d}T = 0.3\,\mathrm{nm\,K}^{-1}$ for the FP laser. The temperature coefficient for the gain shift $\mathrm{d}\lambda_\mathrm{gain}/\mathrm{d}T$ has a value of $\approx 0.3\,\mathrm{nm\,K}^{-1}$. The tem-

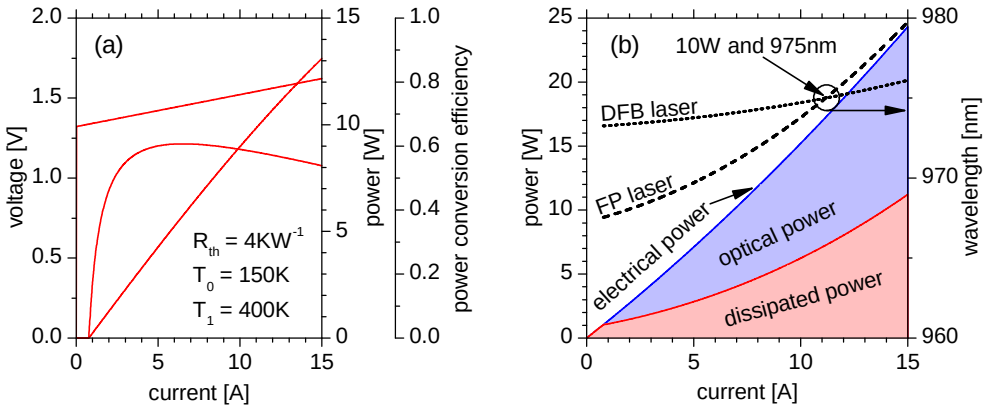

Figure 1.7: (a) Voltage, power and power conversion efficiency characteristics, calculated with parameters given in table 1.2 and $\alpha_\mathrm{i} = 1.0\,\mathrm{cm}^{-1}$, $R_\mathrm{f} = 2.0\,\%$ and $U_\mathrm{s} = 50\,\mathrm{m\Omega}$. (b) Dissipated power (light red area), optical output power (light blue area) and overall electrical power (upper blue line). Wavelength shift for a DFB laser ($0.07\,\mathrm{nm\,K}^{-1}$) and a FP laser ($0.30\,\mathrm{nm\,K}^{-1}$) is calculated and shown to the right axis.

perature dependence of the gain-peak wavelength is dominated by the temperature dependence of the band-gap in the active region. For $In_{13}Ga_{0.87}As$ at $T = 300\,\mathrm{K}$, one obtains $\approx 0.34\,\mathrm{nm\,K}^{-1}$ with the formula $E_\mathrm{g} = 0.42 + 0.625x - (5.8/(T+300) - 4.19/(T+271)) \cdot 10^{-4} T^2 \cdot x - 4.19 \cdot 10^{-4} \cdot T^2/(T+271) + 0.475x^2$, given in [PTI11] and $x = 0.87$.

The temperature coefficient for the Bragg wavelength of the DFB grating $\mathrm{d}\lambda_\mathrm{Bragg}/\mathrm{d}T$ can be derived in the following way. For example, a DFB laser with a second-order grating is assumed to have an effective index of refraction of $n_\mathrm{eff} = 3.42$ and a grating period of $\Lambda = 285.088\,\mathrm{nm}$ at $T = 25\,^\circ\mathrm{C}$. The Bragg condition can be written as $m(\lambda/2) = \Lambda n_\mathrm{eff}$ where m is the order of the Bragg grating and λ is the wavelength. The temperature dependence of the effective refractive index is $\mathrm{d}n_\mathrm{eff}/\mathrm{d}T \approx 2.5 \cdot 10^{-4}\,\mathrm{K}^{-1}$ [Wen12] and the thermal expansion coefficient of GaAs at $25\,^\circ\mathrm{C}$ is $\alpha \approx 6.0 \cdot 10^{-6}\,\mathrm{K}^{-1}$ [Bro96]. With these values, one achieves a wavelength increase of $0.071\,\mathrm{nm\,K}^{-1}$ due to the temperature dependence of the effective index of refraction. In contrast, the thermal expansion causes an wavelength shift of only $0.006\,\mathrm{nm\,K}^{-1}$. The resulting temperature coefficient for the Bragg wavelength of the DFB grating is $\mathrm{d}\lambda_\mathrm{Bragg}/\mathrm{d}T = 0.077\,\mathrm{nm\,K}^{-1}$.

The non-linear increase of the dissipated power with the injection current causes the wavelength also to be increased faster than linear. The different temperature coefficients for the wavelength shift require DFB and FP lasers

to be differently optimized to achieve a requested wavelength (here: 975 nm) at a specific current or output power (here: 10 W). In the shown example this requires, that the FP laser has a wavelength of 967.5 nm at threshold and the DFB laser 973.3 nm. This example can be also understood in an other way, which is very important for the optimization of high power DFB lasers. If a wavelength of 975.0 nm shall be achieved at an optical power of 10 W, the gain peak wavelength must be designed to a shorter wavelength at threshold, in order to coincide at 10 W.

1.2 Distributed feedback in semiconductor lasers

1.2.1 The principle of distributed feedback

In this section, distributed feedback is introduced as a principle, enabling longitudinal optical mode selection in edge emitting in-plane diode lasers due to wavelength selective longitudinal optical feedback. This allows to discriminate unwanted longitudinal optical modes. Mode selection will be discussed in a geometrically one dimensional laser model for the longitudinal direction (along the cavity axis). The optimization of transverse mode profiles is also large topic but is not discussed here.

In general, one must presume a laser to emit in a number of different optical modes. It depends on the particular gain and loss relations of each mode, if it can exceed threshold, or not. Single longitudinal mode emission is preferred for laser applications where a narrow spectral width of the stimulated emission is required. In a Fabry-Pérot laser cavity, multiple longitudinal modes can exceed threshold, because of two reasons. Firstly longitudinal FP modes have equal losses $\alpha_\mathrm{i} + \alpha_\mathrm{m}$ with the internal loss α_i and the mirror loss $\alpha_\mathrm{m} = (1/2L)\ln(1/(R_\mathrm{f}R_\mathrm{r}))$. Secondly, a typical gain spectrum of a quantum well $g(\lambda)$ has a finite width and close to its peak value, it is relatively flat and approximately parabolic shaped over some nanometers. The gain of a quantum well diode laser calculated and discussed in detail in [Chi88]. Figure shows a scheme of the modal gain spectrum in a QW diode laser. Multiple longitudinal modes can exceed threshold, if the gain does not exactly clamps, after the first mode exceeded threshold. In the case of multi modal lasing from a FP laser, the overall width of the lasing spectrum is determined by the shape of the gain spectrum, which determines the number of optical modes exceeding threshold.

For a diode laser with a DFB grating it will be derived, that longitudinal modes does not have equal losses $\alpha_\mathrm{i}+\alpha_\mathrm{DFB}$, because the DFB resonator losses α_DFB have a wavelength dependence due to the wavelength selective optical feedback. In Fig. 1.9 (a) and (b), the longitudinal optical modes and their specific threshold gain, a gain spectrum and the resulting laser spectrum is depicted schematically for a FP laser.

Accordingly, one longitudinal mode could be selected by increasing the particular gain or by decreasing their losses. In edge emitting quantum well semiconductor lasers, gain driven mode selection is not a suitable method because of the typically $> 10\,\mathrm{nm}$ wide quantum well gain spectrum and the narrow spectral distance of longitudinal modes $< 1\,\mathrm{nm}$. In contrast, a strong

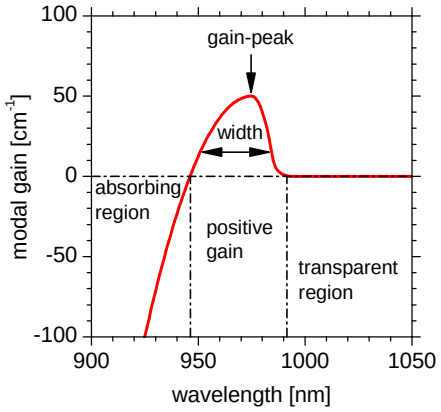

Figure 1.8: Scheme of a gain spectrum for a QW in a diode laser. The gain-peak and width is indicated, as well as the absorbing region, regions with positive gain and the transparent region.

differentiation of the cavity losses for neighboring longitudinal modes is possible due to the principle of Bragg scattering in periodic structures. The term Bragg scattering and the Bragg-condition traces back to W. H. Bragg and W. L. Bragg who found, that they can calculate crystallographic lattice plane distances in solid state crystals form the measurement of the glancing angles with monochrome X-radiation. Constructive interference appears, if the optical path difference between two waves is an integer multiple n of the wavelength $\lambda^{'}$ (in the material) for a fixed value of the angle θ between the incident wave and the lattice planes and the distance between two lattice planes Λ: $\mathrm{n}\lambda^{'} = 2\Lambda sin(\theta)$. This is illustrated in Fig. 1.10 (a). For wave propagation along the refractive index variation in a laser waveguide structure, $\theta = 0$ and the Bragg-condition reduces to $\mathrm{n}\lambda^{'} = 2\Lambda$ as visualized in Fig. 1.10 (b). With the effective refractive index n_{eff} and the vacuum wavelength λ, the Bragg-condition in a laser structure with a Bragg index grating of the order m writes:

$$\Lambda = \lambda m / 2 n_{\mathrm{eff}} \tag{1.40}$$

Modal selection by use of Bragg scattering can be achieved with distributed Bragg reflector (DBR) cavity mirrors [Cho77], [Dup78], [Fri09], [Pas10], [Red11] or by the principle of distributed feedback (DFB) along the cavity axis [Kog71], [Kog72], [Luo90], [Ear98], [Cha00], [Sch10a]. Both physical principles, the distributed Bragg reflection and the distributed feedback lead to strongly increased optical feedback an thus, decreased cavity losses for modes with an emission wavelength very close to the Bragg wavelength

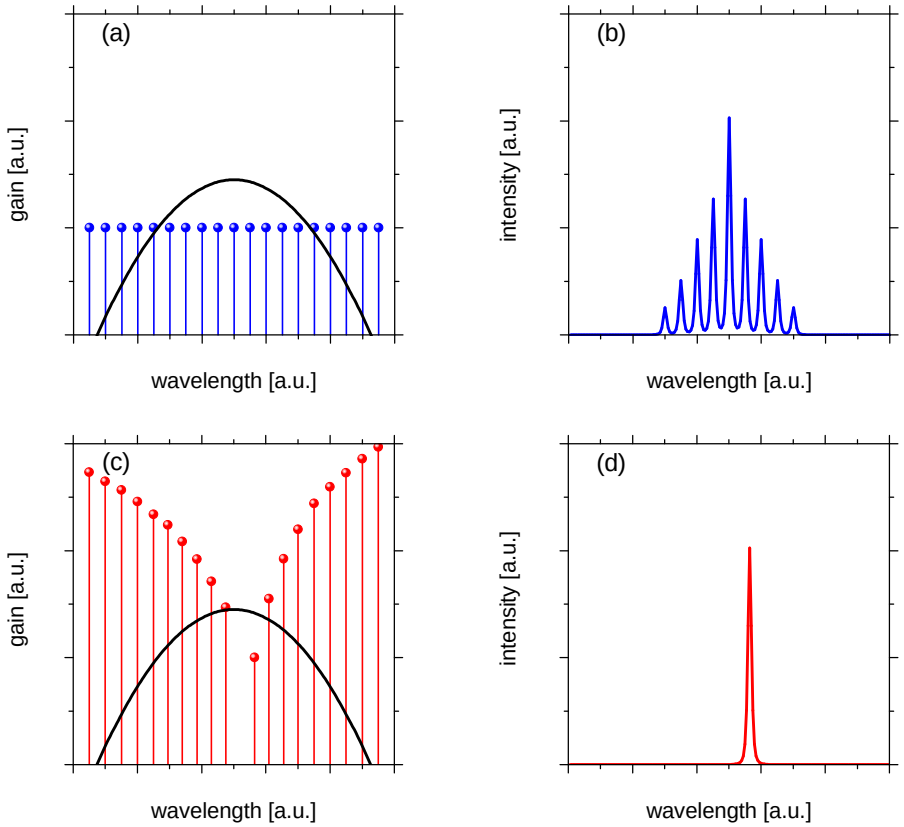

Figure 1.9: Schematic construction of the gain spectrum and threshold gain of optical modes for a FP laser (a) and a DFB laser (c) and the resulting lasing spectrum above threshold for a FP laser (b) and a DFB laser (d).

of the periodic structure. The periodic structure, providing Bragg scattering, is typically a periodic array of refractive index variations, henceforth denominated as DBR or DFB grating respectively. Periodic variations of optical gain or loss can be also used to provide distributed feedback [Kog71], [Rob97] but are not considered in this work. Gain or loss DFB gratings can be beneficial for achieving a high side mode suppression ratio (SMSR).

In Fig. 1.11, the propagation and reflection of waves in an periodic index structure is depicted. Figure 1.11 (a) and (b) demonstrates the relation of a standing wave period at the Bragg-wavelength in a first-order grating with 50 % duty cycle and a second-order grating with 25 % duty cycle respectively. Each grating stripe can be understood as two weak mirrors with reflectivity $\pm r$. The minus sign stands for the $\lambda'/2$ phase shift at reflections with an index

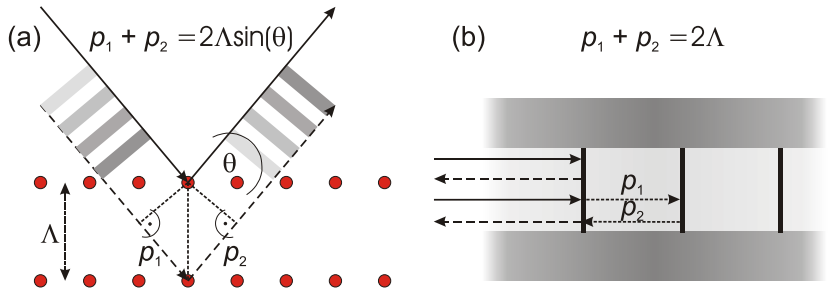

Figure 1.10: Scheme of Bragg reflection. (a) At lattice planes under an angle θ. (b) Perpendicular, as it appears in a DBR or DFB laser.

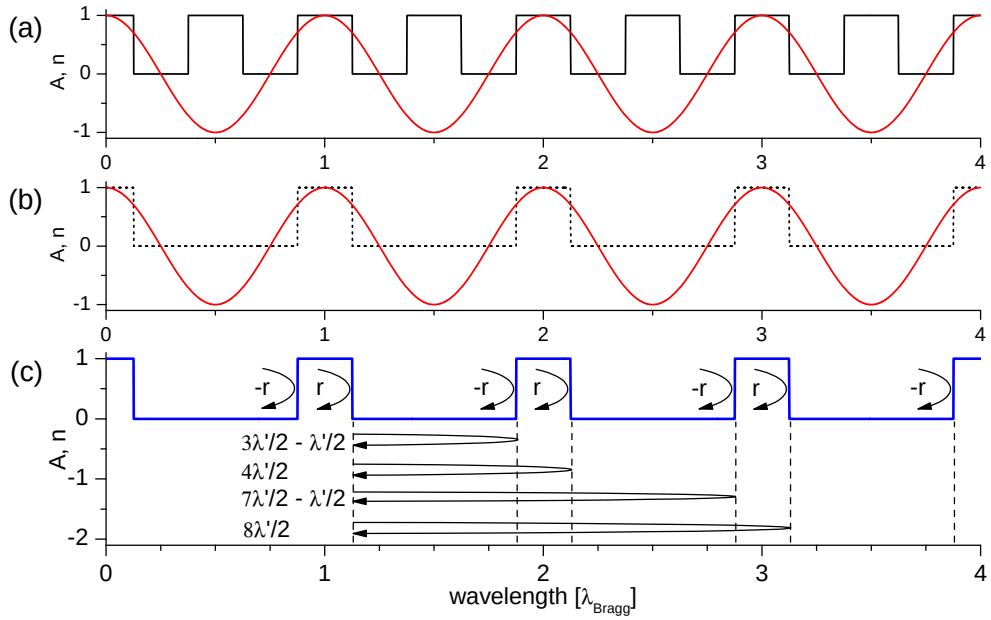

Figure 1.11: Amplitude of an optical wave at the Bragg-wavelength in first and second-order gratings. (a) First-order grating with 50 % duty cycle. (b) Second-order grating with 25 % duty cycle. (c) Second-order grating with 25 % duty cycle. The reflections at index discontinuities with reflectivities r and $-r$ ($\lambda'/2$ phase shift) add in phase and lead to constructive interference of the reflected wave parts.

step from low to high. For a DBR reflector, a number of small reflections sums up to a high net reflection because the reflected parts of the incident wave add up in phase (Fig. 1.11 (c)) if the wavelength of the incident wave fulfills the Bragg-condition. In a DFB laser waveguide structure, waves are assumed to propagate forward and backward. At the Bragg wavelength, each

part of the forward propagating wave that is reflected at one of the index discontinuities couples constructively to the backward propagating wave and vice versa. Accordingly, for DFB laser operation, no reflectivity is required at the ends of the laser cavity, because forward and backward propagating waves interchange and superpose due to weak mirrors (the index discontinuities) that are distributed over the whole cavity length. During the propagation, energy is coherently transferred between the forward and backward traveling waves which form a standing wave laser mode at the Bragg wavelength. The strength of the coupling between the counterpropagating waves is determined by the coupling coefficient κ of the DFB grating which will be derived in the following section.

The possibility to utilize higher-order Bragg gratings $m = 2, 3, \ldots$ is of importance for the fabrication because it allows to use lattice constants that are $m/2$-times larger than the wavelength in the medium (For $\lambda = 976\text{nm}$, $n_{\text{eff}} = 3.4$, $\Lambda_{m=1} \cong 143.5\text{nm}$, $\Lambda_{m=2} \cong 287.1\text{nm}$, $\Lambda_{m=3} \cong 430.6\text{nm}$, $\ldots$).

In a DFB laser, the DFB grating provides a distributed optical feedback with spectral selectivity. This is different from using a Bragg index grating as a passive back-reflector. Nevertheless, plotting the power reflectivity $R_{\text{g}}(\lambda)$ of the grating as a function of the vacuum wavelength λ can be helpful to demonstrate the impact of parameters such as the coupling coefficient κ and the length of the grating L. The reflectivity can be calculated from the ratio of the reflected wave to the incident wave with an ansatz for coupled mode theory as explained in [Col95]. For a rectangular grating without any optical loss one obtains:

$$R_{\text{g}} = \left| -i \frac{\kappa \tanh(\sqrt{\kappa^2 - \Delta\beta^2}\, L)}{\sqrt{\kappa^2 - \Delta\beta^2} + i\Delta\beta \tanh(\sqrt{\kappa^2 - \Delta\beta^2}\, L)} \right|^2 \tag{1.41}$$

In this formula, $\Delta\beta = \beta - \beta_0 = 2\pi n_{\text{eff}}/\lambda - 2\pi/\Lambda$ is the real part of the propagation constant, Λ is the grating period and L the length of the DFB grating. Figure 1.12 shows calculated reflection spectra of Bragg index gratings with variation of the coupling coefficient and grating length. No optical loss has been considered. The Bragg wavelength is set to $\lambda_0 = 975\,\text{nm}$ and the reflectivity is always scaled from 0 to 1.

In Fig. 1.12 (a), the reflectivity spectra of a grating with fixed real coupling coefficient $\kappa = 25\,\text{cm}^{-1}$ are depicted for a variation of the grating length from $L = 0, \ldots, 2\,\text{mm}$. The reflectivity at λ_0 increases with L and approaches 1 at $L \approx 1\,\text{mm}$. While the width of the reflection band is unchanged, the form of the reflection band becomes more and more rectangular. Note, that the width of the reflection band approximately corresponds to the width of the so called stopband in a DFB laser. With increasing grating length, the

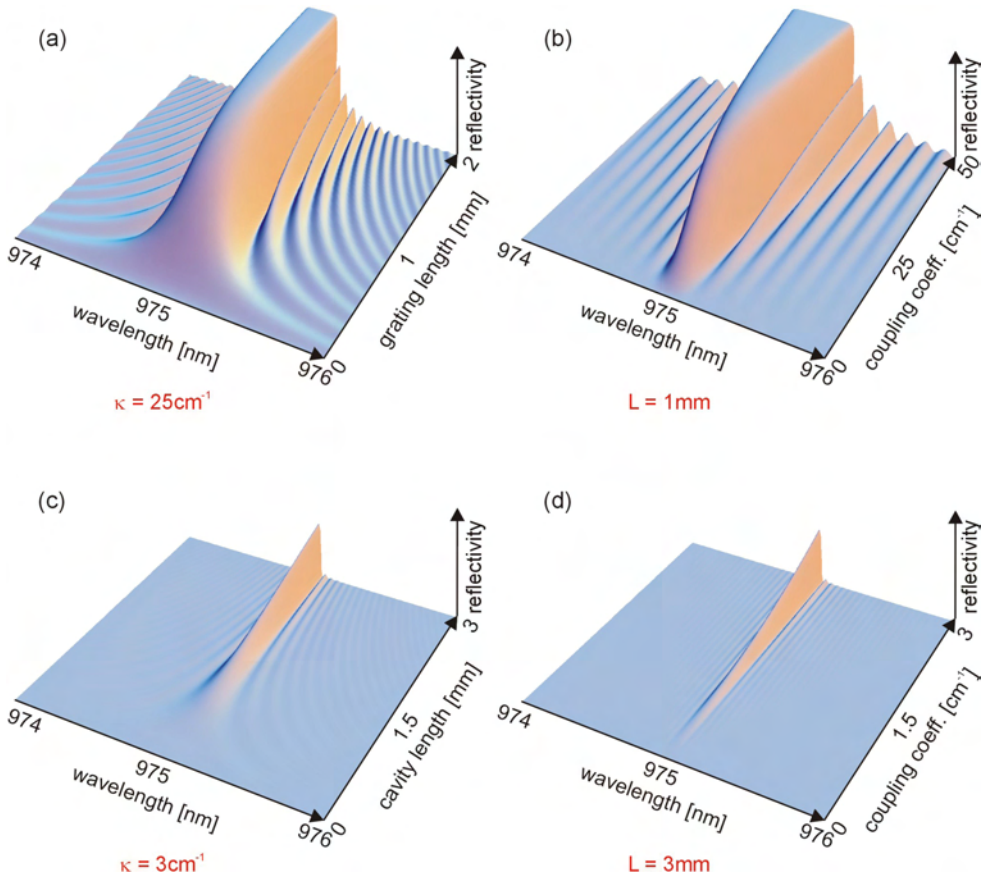

Figure 1.12: Calculated reflection spectra (always scaled from 0 to 1) with variations in the coupling coefficient and grating length. (a) Variation of the grating length with fixed $\kappa = 25\,\mathrm{cm}^{-1}$. (b) Variation of the coupling coefficient with fixed $L = 1\,\mathrm{mm}$. (c) Variation of the grating length with fixed $\kappa = 3\,\mathrm{cm}^{-1}$. (d) Variation of the coupling coefficient with fixed $L = 3\,\mathrm{mm}$.

number of side maxima in the plotted spectral range also increases analogous to the decrease of the free spectral range in a FP cavity with increasing cavity length $\Delta\lambda = \lambda^2/(2n_g L)$ [Col95], where n_g is the group index. With $\lambda = 975.0\,\mathrm{nm}$, $L = 1\,\mathrm{mm}$ and $n_g = 4.0$, one obtains $\Delta\lambda = 0.12\,\mathrm{nm}$ which corresponds to 8.4 FP modes per nanometer. For comparison, in Fig. 1.12 (b), 7 local maxima can be observed per nanometer. Figure 1.12 (b) shows the reflectivity spectra of a grating with fixed $L = 1\,\mathrm{mm}$ for a variation of the real coupling coefficient from $\kappa = 0, \ldots, 50\,\mathrm{cm}^{-1}$. The reflectivity at λ_0 is comparable to (a), but in contrast, the width of the reflection band increases with the grating length. The peak reflectivity approaches 1 at $\kappa \approx 25\,\mathrm{cm}^{-1}$

and thus, at the same κL value as observed in Fig. 1.12 (a). The width of the reflection band depends on the value of the coupling coefficient, while the grating length determines, how sharp a band is formed. The absolute reflectivity at λ_0 depends on the product $\kappa \cdot L$, because at the Bragg wavelength $\lambda = \lambda_0$, equation 1.41 reduces to $R_g^{max} = |i \tanh(\kappa L)|^2$. Instead of the behavior observed in (a), the number of side maxima in the plotted spectral range is unchanged and identical to the $L = 1\,\text{mm}$ case in Fig. 1.12 (a). Reflectivity spectra with a peak reflectivity in the range between 0.8 and 1.0 are suitable for the application as a wavelength selective back reflector in a DBR laser.

In Fig. 1.12 (c) and (d), reflectivity spectra as discussed in (a) and (b) are plotted for values of the grating length and coupling coefficient, as they will appear in DFB lasers, developed during this work. The last spectrum shows the identical case in both diagrams (c) and (d) with $L = 3\,\text{mm}$ and $\kappa \approx 3\,\text{cm}^{-1}$. It es representative for the DFB gratings, prepared during iteration I (see chapter 3). At this specific combination of κ and L, the reflectivity has a maximum of 51.3 %. A further relevant example, representative for the DFB gratings, prepared during iteration II (see chapter 4), can be found in Fig. 1.12 (d) at $\kappa \approx 0.5\,\text{cm}^{-1}$. At this low coupling coefficient, the reflectivity has a maximum of only 2.2 %. One might tend to suppose, that a 3 mm long index grating with a reflectivity of only 2.2 % will not be adequate for DFB lasers with a sufficient suppression of side modes in the optical spectrum. For a DBR laser, a DBR rear mirror reflectivity $\geq 80\,\%$ is typically necessary for good electro-optic properties. The crucial difference between DBR and DFB lasers is, that the grating is used to achieve spectral selectivity and a high differential quantum efficiency from a DBR laser. A front facet reflectivity, comparable to a FP laser with the same cavity length is therefore used. In contrast, the grating in a DFB laser enables a wavelength depending feedback but significantly reduces the differential quantum efficiency at high coupling regime. Consequently, the strength of the DFB grating κL should be as low as possible if high efficiency is required. The front facet reflectivity of a DFB laser must be chosen low enough to avoid lasing on FP-like modes at the maximum of the gain spectrum and to enable a high differential quantum efficiency, because it also influences the total optical feedback for the lasing modes. Note that in the following, FP-like modes which appear in a DFB laser at the maximum of the gain spectrum will be also called FP modes or FP-like modes, even though they are influenced by the DFB grating but this influence decreases with increasing spectral separation from the Bragg wavelength.

1.2.2 Coupled mode theory and coupling coefficients for second-order DFB gratings

Calculating the threshold gain and differential quantum efficiency for optical modes in DFB lasers is essential for a deep understanding that allows to optimize this type of diode lasers for high power and high efficiency operation. One possible mathematical description of the DFB problem is the coupled mode theory (CMT). In this section, CMT is applied to a model for a DFB laser with a DFB grating, which is a thin layer in the y-z-plane (x: vertical, y: lateral, z: longitudinal) and provides a periodic perturbation of the index of refraction or dielectric constant along the z-direction. No perturbation of gain or loss is considered in the following calculations. In accordance to the DFB gratings which have been experimentally realized during this work, coupled mode theory will be derived for a second-order DFB grating. The aim of this section is to find a mathematical description for the coupling coefficient and to derive a set of two coupled differential equations which describe the wave propagation and energy exchange between counterpropagating waves in a second-order DFB laser.

The electric field in the waveguide of a diode laser is supposed to consist of eigenmodes which can be expressed as

$$\mathbf{E}(x,y,z,t) = \mathbf{e}_\mathrm{y} E(x,y,z)\,\mathrm{e}^{i\omega t}, \tag{1.42}$$

where $\mathbf{e}_\mathrm{y}$ indicates linear transverse electric (TE) polarization, $E(x,y,z)$ is the time-independent field intensity distribution and $\mathrm{e}^{i\omega t}$ indicates the time dependence. By plugging this ansatz for the electric field of an eigenmode into the Maxwell equations, one obtains the following time-independent wave equation for the field intensity distribution:

$$\left[\nabla^2 + \frac{\omega^2}{c^2}\varepsilon(x,y,z)\right] E(x,y,z) = 0, \tag{1.43}$$

with the angular frequency ω, the vacuum speed of light c and the dielectric function $\varepsilon(x,y,z)$. The time-independent field intensity distribution can be expressed by two counterpropagating modes $\Phi(x,y)[A(z)\cdot\exp(iK_0 z) + B(z)\cdot\exp(-iK_0 z)]$, where $\Phi(x,y)$ is the transversal mode profile, and a radiated wave $\Delta E(x,z)$ which alters the coefficients $A(z)$ and $B(z)$. In the following, the problem is reduced to two dimensions by neglecting the lateral y-dependence. Thus, the field intensity distribution can be written as:

$$E(x,z) = \Phi(x)\left[A(z)\mathrm{e}^{iK_0 z} + B(z)\mathrm{e}^{-iK_0 z}\right] + \Delta E(x,z). \tag{1.44}$$

Note that for a second-order DFB grating $m = 2$ and from the Bragg condition (equation 1.40) one finds that $\Lambda = m\lambda_0/2n_\mathrm{eff}$. The second-order

periodic index grating ($m = 2$) with wave vector $K_0 = 2\pi/\Lambda$ couples two oppositely propagating waves with propagation vectors $\pm K_0$.

The transverse (vertical) field $\Phi(x)$ fulfills the equation

$$\left[\frac{\partial^2}{\partial x^2} + \frac{\omega^2}{c^2}\varepsilon_0 - \beta^2\right]\Phi(x) = 0, \tag{1.45}$$

where ε_0 is the dielectric function of the unperturbed waveguide and β is the complex propagation constant.

Considering second-order DFB gratings requires to discuss the different role of first-order and second-order Bragg scattering in the grating structure. The following explanations in this subsection are based on the derivations of R.F. Kazarinov and C.H. Henry [Kaz85], as well as on [Col95]. In the case of a second-order DFB grating ($m = 2$), second-order Bragg scattering is what leads to coherent phasing in the coupling between the counterpropagating waves. Additionally, two first-order Bragg scattering events lead to additional radiated waves at $\cong 90\,^\circ$ and thus, perpendicular to the grating plane. The radiated waves $\Delta E(x, z)$ imply a loss mechanism in coupling between the oppositely propagating waves. The effect of the additional radiated waves is, that they alter the coupling between the coefficients $A(z)$ and $B(z)$, which are slowly varying functions of z. A part of the $90\,^\circ$ waves is refracted back into the fundamental propagating mode. The remaining part of it leads to an additional radiation loss term for second-order DFB gratings which will be later shown to depend on the duty cycle of the grating.

From this ansatz, coupled wave equations can be derived by using equation 1.44 in the wave equation 1.43. Firstly, the periodic dielectric perturbation will be discussed. Secondly, the ansatz for the propagating modes will be introduced into the wave equation. This will be used to derive expressions for the coupled mode equations and coupling coefficients.

The perturbation of the dielectric constant which is expected to lead to distributed feedback coupling between the counterpropagating modes is introduced by a z-dependence of the dielectric constant

$$\varepsilon(x, z) = \varepsilon_0(x) + \Delta\varepsilon(x, z). \tag{1.46}$$

In this expression, $\Delta\varepsilon(x, z) = \varepsilon_1 - \varepsilon_2$ is the periodic dielectric perturbation along the z-direction which exists only in the grating layer (at a small, specific range in x), with local dielectric constants ε_1 and ε_2. In Fig. 1.13 (a), a scheme of a rectangular DFB grating is depicted that is composed of a material with dielectric function ε_2, embedded into material with dielectric function ε_1. The duty cycle is $c_\mathrm{d} = (\Lambda - b)/\Lambda$. Note, that the x-direction is defined perpendicular to the grating plane. The resulting periodic dielectric function is shown in Fig. 1.13 (b).

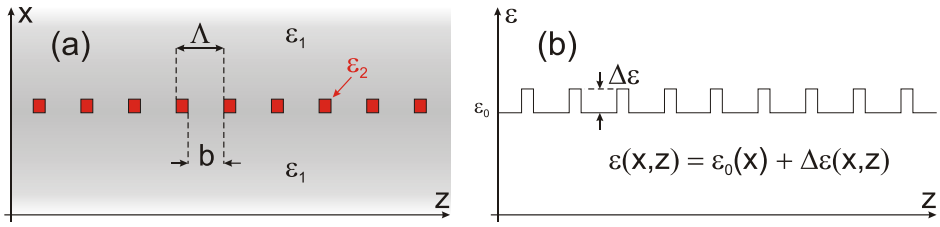

Figure 1.13: Scheme of a rectangular DFB grating that is composed of a material with dielectric function ε_2, embedded into material with dielectric function ε_1. The resulting longitudinal dielectric function can be expressed as $\varepsilon(x,z) = \varepsilon_0(x) + \Delta\varepsilon(x,z)$.

Fourier analysis of $\Delta\varepsilon(x,z)$ leads to

$$\Delta\varepsilon(x,z) = -\Delta\varepsilon \sum_{l\neq 0} \xi_l(x)\, \mathrm{e}^{-il(2\pi/\Lambda)z}, \tag{1.47}$$

with the perturbation amplitude $\Delta\varepsilon$, Fourier coefficients $\xi_l(x)$, perturbation period Λ and the space harmonics $2\pi l/\Lambda$. For a symmetric second-order grating, $\Delta\varepsilon(x,z) = \Delta\varepsilon(x,-z)$ and $\xi_l = \xi_{-l}$ can be derived. Application of equation 1.47 to a rectangular grating with grating period Λ and length b between the grating stripes, results in Fourier coefficients of the form

$$\xi_l(x) = \frac{\sin\left(\pi l b(x)/\Lambda\right)}{\pi l}. \tag{1.48}$$

For a desired laser wavelength at the Bragg condition of 975 nm and for $n_{\mathrm{eff}} = 3.42$ one calculates that the grating period is $\Lambda_{m=2} \cong 285.1\,\mathrm{nm}$ for a second-order DFB grating instead of $\Lambda_{m=1} \cong 142.5\,\mathrm{nm}$ for a first-order DFB grating.

With the wave equation 1.43, the expression for the dielectric function 1.47 and considering that $K_0 = 2\pi/\Lambda$, the wave equation that has to be solved can be written as

$$\left[\frac{\partial^2}{\partial x^2} + \frac{\partial^2}{\partial z^2} + \frac{\omega^2}{c^2}\varepsilon_0(x) - \frac{\omega^2}{c^2}\Delta\varepsilon \sum_{l} \xi_l(x)\cdot e^{iK_0 l z}\right] E(x,z) = 0. \tag{1.49}$$

One substitutes the expression for $E(x,z)$ from equation 1.44 into 1.49 and drops terms with $\partial^2 A/\partial z^2$ and $\partial^2 B/\partial z^2$. By setting the sum of terms with the same exponential factors to zero, one obtains the following three expres-

sions:

$$\left[\frac{\partial^2}{\partial x^2}+\frac{\omega^2}{c^2}\varepsilon_0(x)\right]\Delta E(x,z) = \frac{\omega^2}{c^2}\Delta\varepsilon\left[\left(\xi_{-1}(x)A(z)+\xi_1(x)B(z)\right)\Phi(x)\right] \tag{1.50}$$

$$\left[\frac{\partial^2}{\partial x^2}+\frac{\omega^2}{c^2}\varepsilon_0(x)-K_0^2+2iK_0\frac{\partial}{\partial z}\right]A(z)\Phi(x) = \frac{\omega^2}{c^2}\Delta\varepsilon\left[\left(\xi_1(x)\Delta E(x,z)+\xi_2(x)B(z)\Phi(x)\right)\right] \tag{1.51}$$

$$\left[\frac{\partial^2}{\partial x^2}+\frac{\omega^2}{c^2}\varepsilon_0(x)-K_0^2-2iK_0\frac{\partial}{\partial z}\right]B(z)\Phi(x) = \frac{\omega^2}{c^2}\Delta\varepsilon\left[\left(\xi_{-1}(x)\Delta E(x,z)+\xi_{-2}(x)A(z)\Phi(x)\right)\right]. \tag{1.52}$$

Equation 1.50 can be solved with a Greens function $G(x,y)$ that satisfies

$$\left[\frac{\partial^2}{\partial x^2}+\frac{\omega^2}{c^2}\varepsilon_0(x)\right]G(x,y)=\delta(x-y). \tag{1.53}$$

Thus, an expression for $\Delta E(x,z)$ is given due to the definition of the Greens function by

$$\Delta E(x,z)=\frac{\omega^2\Delta\varepsilon}{c^2}\int \mathrm{d}y \quad G(x,y)\xi_1(y)\left(A(z)+B(z)\right)\Phi(y). \tag{1.54}$$

Two coupled differential equations for $A(z)$ and $B(z)$ can be obtained by multiplying equations 1.51 and 1.52 with $\Phi(x)$, integrate and use equation 1.45. For simplicity, only symmetric gratings with $\xi_{-l}=\xi_{+l}$ have been considered and the following approximation has been used:

$$\beta^2-K_0^2=\underbrace{(\beta+K_0)}_{\cong 2K_0}\cdot(\beta-K_0)\cong 2K_0\cdot(\beta-K_0). \tag{1.55}$$

Furthermore, the complex propagation constant β was expressed as

$$\beta=\Re[\beta]+i\Im[\beta]=K_0+\frac{\Delta\omega}{v_\mathrm{g}}+i\frac{(\alpha-g)}{2}, \tag{1.56}$$

where v_g stands for the group velocity, α for optical loss and g for optical gain and $\Delta\beta$ was defined as

$$\Delta\beta = \frac{\Delta\omega}{v_g} + i\frac{(\alpha - g)}{2}. \tag{1.57}$$

For the two coupled differential equations for $A(z)$ and $B(z)$ one obtains:

$$\begin{aligned} & \left[\frac{\Delta\omega}{v_g} + i\frac{\alpha - g}{2} + i\frac{\mathrm{d}}{\mathrm{d}z}\right] A(z) \\ + \quad & h_2 B(z) + ih_1[A(z) + B(z)] = 0 \end{aligned} \tag{1.58}$$

$$\begin{aligned} & \left[\frac{\Delta\omega}{v_g} + i\frac{\alpha - g}{2} - i\frac{\mathrm{d}}{\mathrm{d}z}\right] B(z) \\ + \quad & h_2 A(z) + ih_1[A(z) + B(z)] = 0. \end{aligned} \tag{1.59}$$

The coupling coefficients for second-order diffractions h_2 and for two first-order diffractions h_1 which appear in equations 1.58 and 1.59 are defined as:

$$h_2 = \frac{-\omega^2\Delta\varepsilon}{2K_0c^2}\int \mathrm{d}x \quad \Phi^2(x)\xi_2(x) \tag{1.60}$$

$$h_1 = \frac{i\omega^4\Delta\varepsilon^2}{2K_0c^4}\int \mathrm{d}x \int \mathrm{d}y \quad \xi_1(x)\xi_1(y)\Phi(x)\Phi(y)G(x,y). \tag{1.61}$$

A set of two coupled differential equations for $A(z)$ and $B(z)$ has been found and coupling coefficients h_2 and h_1 determine how energy is transferred between the counterpropagating modes. The radiation loss which is associated with h_1 cancels for $A(z) = -B(z)$. To understand the meaning of the second-order coupling efficient h_2 which will be most important for second-order DFB gratings optimized for in-plane coupling, the coupled differential equations shall be discussed at the Bragg wavelength ($\Delta\omega = 0$), for $\alpha = g$ and for $h_1 = 0$. Under this circumstances, equations 1.58 and 1.59 can be reduced to:

$$\frac{\mathrm{d}A(z)}{\mathrm{d}z} = ih_2 B(z) \tag{1.62}$$

$$\frac{\mathrm{d}B(z)}{\mathrm{d}z} = -ih_2 A(z). \tag{1.63}$$

Thus, at the Bragg wavelength and under absence of radiation loss, the coupling coefficient h_2 clearly determines the coherent energy transfer.

For completeness, a mathematical description for the first-order coupling coefficient h_1 is required. As already mentioned above, it causes radiating

waves, perpendicular to the grating plane. On the one hand, the radiating waves cause an increase of the optical loss of the DFB laser cavity [Str76], [Hen85], [Kaz85], [SZA00], [Wen04], [Wen06]. On the other hand, this can be also functionalized for out-coupling of a laser beam perpendicular to the grating plane and epitaxy plane [Sci75], [Lop99], [Li03]. Furthermore, it must be investigated, if part of the radiated wave can be coupled back into the propagating wave and therefore, alter the second-order coupling coefficient h_2. To calculate h_1 one needs to find the Greens function $G(x, y)$ that satisfies equation 1.53. It is given by:

$$G(x,y) = \frac{1}{\mathcal{W}} \begin{cases} \Phi_+(x)\Phi_-(y) & \text{for } x > y \\ \Phi_-(x)\Phi_+(y) & \text{for } x < y \end{cases} \tag{1.64}$$

$\Phi_\pm(x)$ are radiating waves into $\pm x$-direction and satisfying equation 1.53. The Wronskian associated $\mathcal{W}$ with equation 1.53 is given by:

$$\mathcal{W} = \frac{\mathrm{d}\Phi_+}{\mathrm{d}x}\Phi_- - \Phi_+\frac{\mathrm{d}\Phi_-}{\mathrm{d}x}. \tag{1.65}$$

If $\Phi_\pm(x)$ are approximated as plane waves $\Phi_\pm \sim \mathrm{e}^{\pm iK_x x}$, equation 1.64 becomes

$$\begin{aligned} G(x,y) &= \frac{1}{2iK_x} \begin{cases} \mathrm{e}^{iK_x(x-y)} \\ \mathrm{e}^{iK_x(y-x)} \end{cases} \\ &= \frac{1}{2iK_x} \begin{cases} \cos\left[K_x(x-y)\right] + i\sin\left[K_x(x-y)\right] & \text{for } x > y \\ \cos\left[K_x(y-x)\right] + i\sin\left[K_x(y-x)\right] & \text{for } x < y \end{cases} \end{aligned} \tag{1.66}$$

For the coupling coefficient of two first-order diffractions one finds the fol-

lowing complex expression:

$$
\begin{aligned}
& h_1 \underbrace{\left(\frac{\omega^4 \Delta\epsilon^2}{4K_0 K_x c^4}\right)^{-1}}_{1/F} = \\
= & \int \mathrm{d}x \int \mathrm{d}y \quad \xi_1(x)\Phi(x) G(x,y) \xi_1(y)\Phi(y) \\
= & \int\limits_{x>y} \mathrm{d}x \int \mathrm{d}y \quad \xi_1(x)\Phi(x) \left\{\cos\left[K_x(x-y)\right] + i \sin\left[K_x(x-y)\right]\right\} \xi_1(y)\Phi(y) \\
+ & \int\limits_{x<y} \mathrm{d}x \int \mathrm{d}y \quad \xi_1(x)\Phi(x) \left\{\cos\left[K_x(y-x)\right] + i \sin\left[K_x(y-x)\right]\right\} \xi_1(y)\Phi(y) \\
= & \int\limits_{x>y} \mathrm{d}x \int \mathrm{d}y \quad \xi_1(x)\Phi(x) \left\{\cos\left[K_x(x-y)\right] + i \sin\left[K_x(x-y)\right]\right\} \xi_1(y)\Phi(y) \\
+ & \int\limits_{x<y} \mathrm{d}x \int \mathrm{d}y \quad \xi_1(x)\Phi(x) \left\{\cos\left[K_x(y-x)\right] + i \sin\left[K_x(y-x)\right]\right\} \xi_1(y)\Phi(y) \\
+ & \int\limits_{x<y} \mathrm{d}x \int \mathrm{d}y \quad \xi_1(x)\Phi(x) \underbrace{\left\{i \sin\left[K_x(x-y)\right] - i \sin\left[K_x(x-y)\right]\right\}}_{=0} \xi_1(y)\Phi(y) \\
= & \underbrace{\left| \int \mathrm{d}x \quad \xi_1(x)\Phi(x) e^{iK_x x} \right|^2}_{\Re[h_1]/F} \\
+ & \underbrace{i\,2 \int\limits_{y>x} \mathrm{d}x \int \mathrm{d}y \quad \xi_1(x)\Phi(x) \sin\left[K_x(y-x)\right] \xi_1(y)\Phi(y)}_{\Im[h_1]/F} . \qquad (1.67)
\end{aligned}
$$

Thus, h_1 has an dominating real part (equation 1.68) which stands for radiation loss. An additional imaginary part (equation 1.69) can be also derived for h_1 [Wen06] in contrast to what is stated in [Kaz85]. The real part of h_1 can be understood as a small correction to h_2. In cases when the duty cycle of a second-order DFB grating is close to $c_\mathrm{d} = 1/2$, it becomes of a not negligible magnitude compared to h_2.

$$
\Re[h_1] = \frac{\omega^4 \Delta\varepsilon^2}{2K_0 c^4} \left| \int \mathrm{d}x \quad \xi_1(x)\Phi(x) e^{iK_x x} \right|^2 \qquad (1.68)
$$

$$
\Im[h_1] = \frac{\omega^4 \Delta\varepsilon^2}{K_0 c^4} \int\limits_{y>x} \mathrm{d}x \int \mathrm{d}y \;\; \xi_1(x)\Phi(x) \sin\left[K_x(y-x)\right] \xi_1(y)\Phi(y) \qquad (1.69)
$$

Accordingly one can write the coupling coefficient κ in the common way as a complex value κ that is defined by the coupling coefficients h_1 and h_2.

$$\begin{aligned} \kappa &= \Re[\kappa] + i\ \Im[\kappa] \\ &= (h_2 - \Im[h_1]) + i\ \Re[h_1] \end{aligned} \tag{1.70}$$

In this work, second-order DFB gratings have an optimized duty cycle of $c_\mathrm{d} = 1/4$ in-order to achieve a high coupling coefficient h_2 and a comparatively low radiation loss. The coupling coefficient κ will be dominated by h_2 so that it can be approximated to be real with $\kappa \cong h_2$. The relation between the real and imaginary part of the coupling coefficient is depicted in Fig. 1.14 (a) as a function of the duty cycle c_d for a second-order and a first-order DFB index grating.

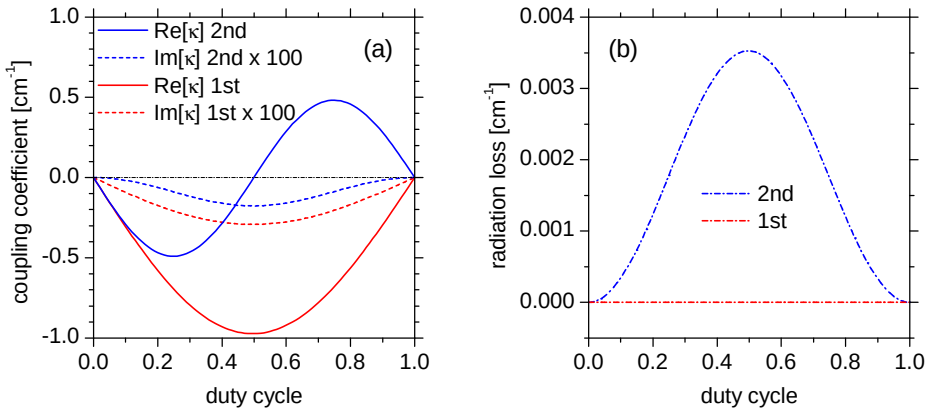

Figure 1.14: Complex coupling coefficients and radiation loss for second- and first-order DFB gratings. (a) Real and imaginary part ($\times 100$ for better visibility) of the coupling coefficient as a function of the duty cycle. (b) Radiation loss as a function of the duty cycle.

The real part of the coupling coefficient for the second-order grating has a local minimum at $c_\mathrm{d} = 0.25$ (maximum in-plane optical feedback.) and crosses zero at $c_\mathrm{d} = 0.50$ (no in-plane optical feedback). From the used definition, $\Re[\kappa]$ is negative for $c_\mathrm{d} < 0.50$, because $\Delta\varepsilon$ is < 0 in this calculation example. Positive values for $\Re[\kappa]$ occur for $c_\mathrm{d} > 0.50$ because the fourier coefficient (equation 1.47) changes its algebraic sign at $c_\mathrm{d} = (\Lambda - b)/\Lambda = 0.50$. Nevertheless, the in-plane optical feedback at $c_\mathrm{d} = 0.75$ equals the in-plane optical feedback at $c_\mathrm{d} = 0.25$. For the second-order grating, $\Im[\kappa]$ reaches its minimum at $c_\mathrm{d} \approx 0.33$ and crosses zero at $c_\mathrm{d} \approx 0.67$.

The resulting radiation loss $\alpha_{\mathrm{rad}} = 2\Re[h_1]$ (factor 2 appears because it shall be related to power) from first-order Bragg scattering in the second-order DFB grating, is shown in Fig. 1.14 (b). As mentioned above, it is maximal at $c_{\mathrm{d}} = 0.50$. Note that the radiation loss for a second-order grating is > 0 for all $0 < c_{\mathrm{d}} < 1$. With $\alpha_{\mathrm{rad}}^{\mathrm{max}} < 0.004\,\mathrm{cm}^{-1}$ in the shown example, it is two-orders of magnitude smaller than the typical internal optical loss of a state of the art broad area laser, $\alpha_{\mathrm{i}} \sim 1\,\mathrm{cm}^{-1}$.

In contrast to the second-order DFB grating, the coupling coefficients for a first-order grating $\Re[\kappa]$ and $\Im[\kappa]$ have a single local minimum at $c_{\mathrm{d}} = 0.50$ and radiation loss does not appear.

1.2.3 Threshold condition for DFB lasers

The next step towards calculating the threshold properties of longitudinal modes in a DFB laser is to derive a threshold condition. The coupled homogenous differential equations 1.58 and 1.59 can be solved, substituting $A(z) \sim B(z) \sim \mathrm{e}^{ikz}$. One obtains a dispersion relation of the form:

$$\frac{\Delta\omega}{v_g} = i\left(\frac{g-\alpha}{2}\right) - ih_1 \pm \left[(h_2 + ih_1)^2 + k^2\right]^{1/2} \tag{1.71}$$

Equation 1.71 has to be solved for k. It is clear that each longitudinal mode of a DFB laser will have its own wavelength an thus, $\Delta\omega$. An ansatz for general solutions of $A(z)$ and $B(z)$ can be defined as

$$A(z) = \alpha \mathrm{e}^{ikz} + \beta R \mathrm{e}^{-ikz} \tag{1.72}$$

$$B(z) = \alpha R \mathrm{e}^{ikz} + \beta \mathrm{e}^{-ikz}, \tag{1.73}$$

where the coefficient R provides the coupling between $A(z)$ and $B(z)$. Substituting equation 1.71 into equation 1.59 results in

$$R(k) = \frac{-(h_2 + ih_1)}{\pm\left[(h_2 + ih_1)^2 + k^2\right]^{1/2} + k}. \tag{1.74}$$

The physical properties of the modes of a DFB laser at threshold can be calculated as follows. At each end of the laser, the field (equations 1.72 and 1.73) and its derivative must be continuously matched with an outgoing wave. Writing the field $E(z)$ as the sum of an incident and reflected wave with expressions 1.72 and 1.73 leads to:

$$E(z) = \left[\alpha \mathrm{e}^{ikz} + \beta R \mathrm{e}^{-ikz}\right] \mathrm{e}^{iK_0 z} + \left[\alpha R \mathrm{e}^{ikz} + \beta \mathrm{e}^{-ikz}\right] \mathrm{e}^{-iK_0 z}. \tag{1.75}$$

The cavity length L shall be defined as an integer multiple of the grating period Λ, which is completed by so called facet phase sections at the rear

and front facet d_a and d_b. The definition of the facet phase sections enables a precise choice of the facet mirrors relative to the last grating stripe of the DFB grating. In most cases it will be adequate to let $d_\mathrm{a} \leq \Lambda$ and $d_\mathrm{b} \leq \Lambda$. This is a suitable definition for all DFB lasers with $L \gg \Lambda$. Thus, one cane write $L = L_\mathrm{nom} + d_\mathrm{a} + d_\mathrm{b}$ with $L_\mathrm{nom} = l \cdot \Lambda$, and a real integer l. The boundary conditions are applied at positions $z = -d_\mathrm{a}$ (rear facet) and $z = L_\mathrm{nom} + d_\mathrm{b}$ (front facet). The amplitude facet reflectivities are given by r_a (at $z = -d_\mathrm{a}$) and r_b (at $z = L_\mathrm{nom} + d_\mathrm{b}$). With the boundary conditions and equation 1.74 one obtains:

$$\alpha R \mathrm{e}^{ikL} + \beta \mathrm{e}^{-ikL} = r_\mathrm{b} \mathrm{e}^{2iK_0 d_\mathrm{b}} \left[\alpha \mathrm{e}^{ikL} + \beta R \mathrm{e}^{-ikL}\right] \quad (1.76)$$

$$\alpha + \beta R = r_\mathrm{a} \mathrm{e}^{2iK_0 d_\mathrm{a}} \left[\alpha R + \beta\right]. \quad (1.77)$$

Exponents ikd_a and ikd_b have been neglected because of $k \ll K_0$. Equations 1.76 and 1.77 results in the following equation, whose solutions for complex values of k describe the threshold properties of longitudinal modes of a DFB laser with nonzero reflecting facets:

$$\left[R - r_\mathrm{a} \mathrm{e}^{2iK_0 d_\mathrm{a}}\right] \left[R - r_\mathrm{b} \mathrm{e}^{2iK_0 d_\mathrm{b}}\right] \mathrm{e}^{2ikL} = \left[1 - R r_\mathrm{a} \mathrm{e}^{2iK_0 d_\mathrm{a}}\right] \left[1 - R r_\mathrm{b} \mathrm{e}^{2iK_0 d_\mathrm{b}}\right]. \quad (1.78)$$

In order to calculate the threshold gain for optical modes, equation 1.78 must be solved for k. This will be discussed in the following section. Furthermore, equation 1.78 has got two familiar border solutions. For $R(k) = 0$ or for $r_\mathrm{a} = r_\mathrm{b} = 0$ one obtains respectively:

$$r_\mathrm{a} r_\mathrm{b} \mathrm{e}^{2i(K_0+k)(L_\mathrm{nom}+d_\mathrm{a}+d_\mathrm{b})} = 1 \quad (1.79)$$

$$R^2 \mathrm{e}^{2ikL} = 1. \quad (1.80)$$

Equation 1.79 describes the modes of a Fabry-Pérot laser with cavity length $L = L_\mathrm{nom} + d_\mathrm{a} + d_\mathrm{b}$ and amplitude facet reflectivities r_a and r_b, because any distributed feedback effects have been neglected. In contrast, equation 1.80 describes a DFB laser with non reflecting facets (for example anti-reflection coated), which is sometimes called the ideal DFB laser.

1.2.4 Approximations and numerical solutions for DFB-BA lasers

To calculate the threshold conditions of the modes of a DFB laser, equation 1.78 has to be solved for a complex value of k. The calculations have been carried out with the computational software program “Mathematica”.

In most cases it turned out to be advantageous to start with the k values for a Fabry-Pérot laser with the facet reflectivities, the DFB laser later should have; for example with power reflectivity $R_\mathrm{f} = r_\mathrm{b}^2 = 0.05\%$ at the front facet and $R_\mathrm{r} = r_\mathrm{a}^2 = 96\%$ at the rear facet. These k starting values can be simply calculated analytically as

$$k_n^{\mathrm{start}} = n\pi/L + i\ln(r_\mathrm{a} r_\mathrm{b})/L, \tag{1.81}$$

for real integers $n = (0, \pm1, \pm2, \ldots)$, where n = 0 is chosen to indicate the Bragg-condition. Note that based on this definition, the longitudinal mode index is $n > 0$ for longitudinal modes with a wavelength $\lambda < \lambda_0$ and $n < 0$ for longitudinal modes with a wavelength $\lambda > \lambda_0$. The absolute value of the coupling coefficient h_2 is afterwards gradually increased from $0\,\mathrm{cm}^{-1}$ to the value of interest $h_{2\mathrm{max}}$ as $h_2 = (0.0, -0.1, -0.2, \ldots, -h_{2\,\mathrm{max}})\mathrm{cm}^{-1}$ (from the used definition, $h_2 \leq 0$). The step size has to be chosen very carefully, because the result for k of the previous calculation has been used as starting value for the following numerical calculation. The step size of h_2 has to be so small, that the change in k is much smaller than the difference between k and the k value of the neighboring longitudinal modes. When the imaginary coupling coefficient h_1 was considered as well, it has been gradually increased simultaneously, for example $h_1 = (0.00, 0.01, 0.02, \ldots, h_{1\,\mathrm{max}})\mathrm{cm}^{-1}$. To ensure that the DFB mode with the lowest threshold gain (at one of the two possible sides of the stopband) has definitely been found, typically five longitudinal modes that are located close to the Bragg wavelength have been calculated (for example $n = -2, -1, 0, 1, 2$).

The steady-state threshold condition for a specific mode is fulfilled, if $\Im[\Delta\beta] = 0$. Accordingly, if the complex value k has been found for this mode, the DFB resonator losses α, the threshold gain g_th and the wavelength λ can be calculated from equation 1.71, here replicated as equation 1.82. The DFB resonator loss α is caused by the DFB grating and facet mirrors. It can be compared to the mirror loss of a FP laser α_m, which is caused only by facet mirrors. To point out this comparability, the DFB resonator loss α will be written in the following as α_DFB.

$$\frac{\Delta\omega}{v_g} + i\left(\frac{\alpha - g}{2}\right) = -ih_1 \pm \left[(h_2 + ih_1)^2 + k^2\right]^{1/2} = \Delta\beta \tag{1.82}$$

$$\alpha_\mathrm{DFB} = 2\Im[\Delta\beta] \tag{1.83}$$

$$g_\mathrm{th} = 2\left(\alpha_\mathrm{i} + \Im[\Delta\beta]\right) \tag{1.84}$$

$$\lambda = \frac{2n_\mathrm{eff}\pi}{K_0 + \Re[\Delta\beta]}. \tag{1.85}$$

An overview of input parameters, used for an simulation example is given in table 1.3. In Fig. 1.15 (a), the results of the threshold gain are depicted for

Table 1.3: The fixed physical variables, their notations and values, used in the numerical simulation example. The effective index of refraction n_{eff} and the grating period Λ are chosen for a Bragg wavelength of $\lambda_0 = 975.000\,\text{nm}$.

Variable	Notation	Value
Cavity length	L	$3000\,\mu\text{m}$
Contact stripe width	W	$90\,\mu\text{m}$
Rear facet Reflectivity	R_r	$96.00\,\%$
Front facet Reflectivity	R_f	$0.09\,\%$
Rear facet phase section	d_a	$(0.00, 0.02, ..., 0.48)\Lambda$
Front facet phase section	d_b	0.00
Effective index of refraction	n_{eff}	3.434308
Grating period	Λ	283.9 nm
Second-order coupling coefficient	$h_{2\,\text{max}}$	$10.0\,\text{cm}^{-1}$
First-order coupling coefficient	$h_{1\,\text{max}}$	$0.0\,\text{cm}^{-1}$
Internal optical loss	α_i	$0.80\,\text{cm}^{-1}$
Internal quantum efficiency	η_i	0.90
Transparency current density	j_tr	$151\,\text{Acm}^{-2}$

the modes with the longitudinal mode indices $n = (0, \pm1, \pm2)$. The coupling coefficient has been varied from $0\,\text{cm}^{-1}$ to $10\,\text{cm}^{-1}$ with a step size of $0.1\,\text{cm}^{-1}$. The fixed physical variables that have been used in the simulation example are denoted in table 1.3. With increasing coupling coefficient $\kappa = |h_2|$, the threshold gain decreases. The strongest decrease is observed for the mode with the lowest threshold gain (black arrow), which will be the only lasing mode.

Besides the threshold gain, the differential quantum efficiency η_d is important for the analysis of the maximum achievable power conversion efficiency. It determines the slope efficiency of the power characteristics $P(I)$ for $I > I_\text{th}$. The differential quantum efficiency of one specific facet is defined as the product of the internal quantum efficiency η_i and the power transmitted through this facet, divided through the integrated stimulated emission in the cavity. The power transmitted through one of the facets is given by the product of the incident field and the facet transmittancy $1 - |r_{\text{f/r}}|^2$. For the

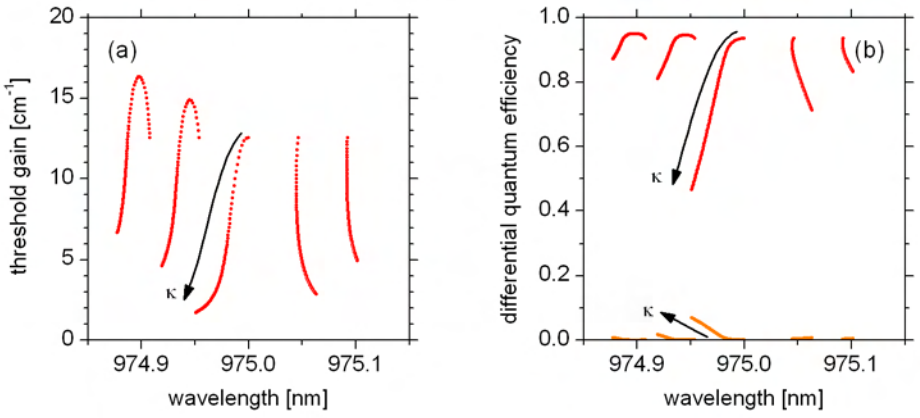

Figure 1.15: Threshold gain and differential quantum efficiency of five modes around the stopband for a 3 mm long DFB laser with zero facet phase sections. (a) Threshold gain. (b) Differential quantum efficiency with $\eta_\mathrm{i} = 1$ at the front facet (curves above $\eta_\mathrm{d} = 0.4$) and at the rear facet (curves below $\eta_\mathrm{d} = 0.2$). The evolution with $\kappa = (0.0, 0.1, \ldots, 10.0)\,\mathrm{cm}^{-1}$ is marked with arrows.

rear facet at $z = -d_\mathrm{a}$, the incident field is given by $\alpha R \mathrm{e}^{ik(-d_\mathrm{a})} + \beta \mathrm{e}^{-ik(-d_\mathrm{a})}$, while for the front facet at $z = L_\mathrm{nom} + d_\mathrm{b}$, the incident field is given by $\alpha \mathrm{e}^{ik(L_\mathrm{nom}+d_\mathrm{b})} + \beta R \mathrm{e}^{-ik(L_\mathrm{nom}+d_\mathrm{b})}$. The integrated stimulated emission in the cavity is defined as the integral of $|E(z)|^2$, multiplied with the threshold gain. Thus, one obtains for the differential quantum efficiency:

$$\eta_{\mathrm{d\ f/r}} = \eta_\mathrm{i} \frac{\left[\alpha \mathrm{e}^{ikz} + \beta R \mathrm{e}^{-ikz}\right]\left(1 - |r_\mathrm{f/r}|^2\right)}{g_\mathrm{th} \int_0^L \mathrm{d}z \quad |E(z)|^2} \tag{1.86}$$

In Fig. 1.15 (b), the results of the differential quantum efficiency are shown for the front and rear facet. Note that in Fig. 1.15 (b), the internal quantum efficiency was set to $\eta_\mathrm{i} = 1$, for simplicity. With increasing coupling coefficient $\kappa = |h_2| = (0.0, 0.1, \ldots, 10.0)\,\mathrm{cm}^{-1}$, the differential quantum efficiency at the front facet decreases. The strongest decrease of the differential quantum efficiency with κ is observed for the mode with the lowest threshold gain (black arrow). Simultaneously with the decrease of the differential quantum efficiency at the front facet, an increase of the differential quantum efficiency at the rear facet is observed.

This kind of calculation was performed for different values of the so called facet phase, expressed here by the facet phase sections $d_\mathrm{a} \leq \Lambda$ and $d_\mathrm{b} \leq \Lambda$. By adding a phase section of the length $\Lambda/2$ to the cavity length L_nom for a second-order DFB grating, the mode with the longitudinal mode index

$n+1$ overtakes the role of the mode withe the index n and the value of the threshold gain is replicated. Fig. 1.16 (a) and (b) show the results of the threshold gain and differential quantum efficiency for the same parameters as in Fig. 1.15 (a) and (b) but now for different rear-facet phase sections $d_\mathrm{a} = (0.00, 0.02, ..., 0.48)\Lambda$, respectively. The increase of the rear-facet phase-section d_a is indicated with a red arrow.

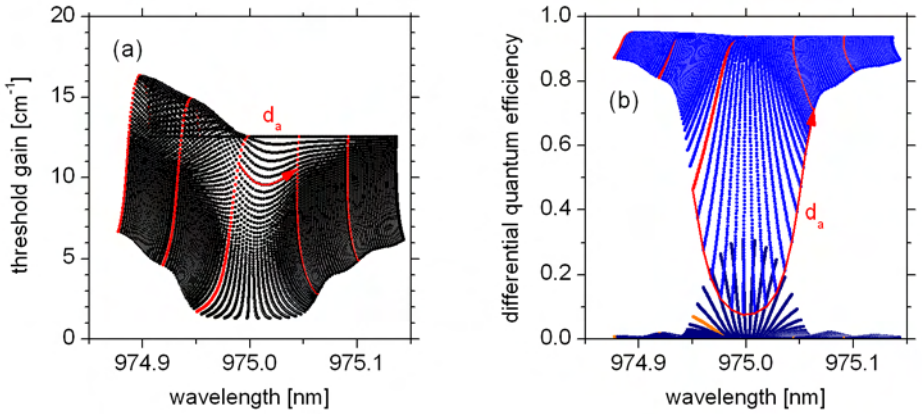

Figure 1.16: Threshold gain and differential quantum efficiency with $\eta_\mathrm{i} = 1$ of five modes around the stopband for a 3 mm long DFB laser with facet phase sections $d_\mathrm{a} = (0.00, 0.02, ..., 0.48)$. (a) Threshold gain. (b) Differential quantum efficiency at the front facet (upper series of curves) and at the rear facet (lower series of curves).

As predicted above, by tracing the threshold gain or differential quantum efficiency of a specific mode and specific value for the coupling coefficient for increasing d_a (for example along the red arrow), the longitudinal mode index $n-1$ overtakes the role of the mode with the index n. Especially the differential quantum efficiency is found to show a very strong dependence on the rear facet phase section d_a. This dependence increases with increasing coupling coefficient κ or coupling strength κL.

The assumption that the counter propagating waves in DFB laser see a fixed phase condition between the facet position and the grating corrugation is valid either in a one dimensional model or if the grating stripes in a real laser with a lateral elongation are aligned to the facet plane with infinite accuracy. In the case of a ridge waveguide laser, a fixed phase condition (a constant value of the phase sections d_a and d_b) can be achieved easily. Assuming that the angular misalignment or tilting between the facet plane and the grating stripes of a second-order DFB grating for 975nm ($\Lambda = 284$nm,

$n_{\text{eff}} \cong 3.433$) is $\leq 0.5\,^\circ$ for a $3\,\mu$m wide ridge waveguide laser, one finds that the phase section varies by less than 0.1 grating periods Λ.

In contradiction to a ridge waveguide laser, a constant value of the phase sections is an implausible assumption for a broad area laser. For $\Lambda = 284\,$nm and a stripe width of $90\,\mu$m one finds that the phase sections vary by Λ, if the grating stripes are tilted to the facet plane by only $0.18\,^\circ$.

Practically, the interference pattern of a laser holography tool, used to define the grating, are manually aligned to the flat of a three inch GaAs wafer. The direction of the flat is parallel to the (100) direction of the GaAs crystal with an accuracy better than $0.5\,^\circ$. If one assumes an accuracy for the manual alignment better than $0.5\,^\circ$, the over all misalignment of up to $1.0\,^\circ$ leads to a phase section variation of 5.53Λ. In Fig. 1.17, a scheme of the facet and the resonator end section is depicted for a DFB-BA laser with a grating, tilted by $0.5\,^\circ$. The scheme is not true to scale, so that the facet phase modulation along the facet is clearly visible.

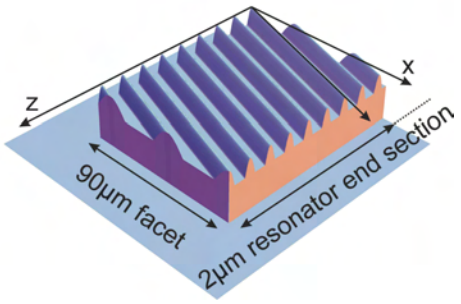

Figure 1.17: Facet and resonator end section of a DFB-BA laser with a grating, tilted by $0.5\,^\circ$. The scheme is not true to scale.

It has been assumed that the properties of a DFB-BA laser with a varying phase between the grating and the facets, can be approximated by calculating the threshold gain and differential quantum efficiency for a number of different phases and finally, utilize the arithmetic mean of the threshold gain and differential quantum efficiency as a broad area laser approximation. If the reflectivity of the rear facet is very high ($R_{\text{r}} > 95\,\%$) and the reflectivity of the front facet very low ($R_{\text{f}} < 0.5\,\%$), it should be sufficient to apply this averaging the rear facet phase section and choose any front facet phase section. Different lateral modes are expected to "see" an effective facet phase which depends on the phase modulation and on the lateral field profile. Thus, a large number of different lateral modes with different field profiles could

indeed lead approximately to an averaging over the facet phase. Lateral field profiles of different lateral modes have been measured and are shown later in the following chapter of this work.

As already mentioned above, the properties of the longitudinal modes are "periodic" in $d_a = 1/2\,\Lambda$. This means, that the threshold gain and differential quantum efficiency of the longitudinal mode m at $d_a = 0\,\Lambda$ and mode $m-1$ at $d_a = 1/2\,\Lambda$ must be identical. To prove this, the properties of 11 longitudinal modes around the stopband have been calculated for $d_a = (0.00, 0.01 \ldots 1.00)\Lambda$. The other parameters are the same as given in table 1.3. Figure 1.18 (a) shows the rear facet phase section versus the wavelength for the 11 modes. The Bragg wavelength is set to 975 nm and one can see the stopband at this position as a slightly broadened spectral gap between the longitudinal modes. At $d_a = 0.13\,\Lambda$, mode 0 crosses the 975 nm line and at $d_a = 0.63\,\Lambda$, mode -1 crosses it again. Thus, the difference between these crossings is $\Delta d_a = 1/2\,\Lambda$. At $d_a = 1/2\,\Lambda$, the wavelength of mode -1 equals the wavelength of mode 0 at $d_a = 0\,\Lambda$.

In Fig. 1.18 (b) 11 specific numbered curves represent the threshold gain for the 11 longitudinal modes at $d_a = (0.00, 0.01, \ldots 0.50)\Lambda$. The black arrows indicate the direction in which the rear-facet phase section d_a increases. As expected, the curves pass into each other without any steps in the threshold gain and form a minimum at the Bragg wavelength. A similar behavior is found for the differential quantum efficiency ($\eta_i = 1$) and is shown in Fig. 1.18 (c). Finally, in Fig. 1.18 (d), the rear facet phase section versus the wavelength wavelength is depicted like in Fig. 1.18 (a), but with an additional false-color scale, indicating the threshold gain for each mode at a specific value of d_a. One can clearly see that the lowest threshold gain occurs, when a longitudinal mode crosses the Bragg wavelength, and that the lasing mode jumps to the next shorter wavelength mode if the rear facet phase section is more and more increased. Thus, with the help of the calculations presented in Fig. 1.18 it has been shown, that the numerical calculation treats the impact of the facet phase sections quite well.

After showing that the numerical calculation treats the impact of the facet phase sections correctly, the threshold gain and differential quantum efficiency has been calculated for five modes ($n = 0, \pm 1, \pm 2$) around the stopband. For each longitudinal mode, the threshold gain and differential quantum efficiency was averaged over the rear-facet phases ($d_a = (0.00, 0.02, \ldots, 0.48)\Lambda$). Fig. 1.19, 1.20, 1.21 and 1.22 show the resulting phase-averaged curves for the threshold gain and differential quantum efficiency of five modes around the stopband as a function of the coupling coefficient ($\kappa = h_2$), for cavity length of $L_{\text{nominal}} = 1500, 3000, 4000$ and $6000\,\mu$m.

At first, similarities of the diagrams for the DFB-BA lasers with different

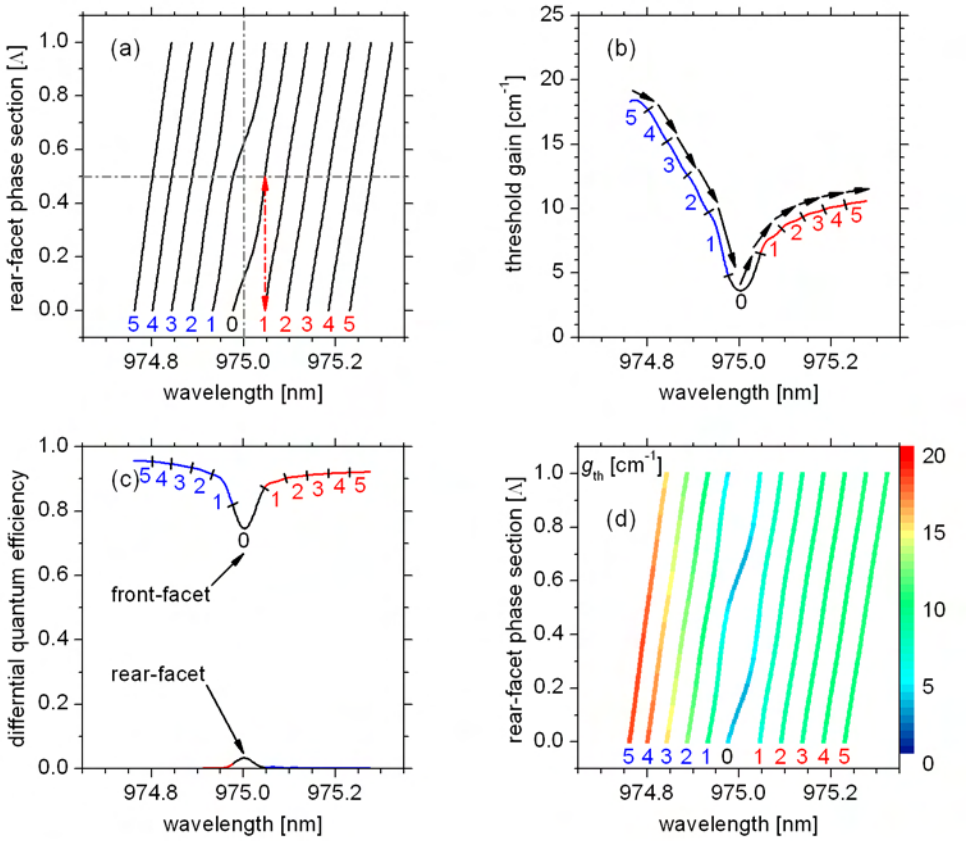

Figure 1.18: Properties of 11 modes around the stopband at 975 nm under variations of the rear-facet phase section d_a by one grating period Λ: $d_a = (0.00, 0.01 \ldots 1.00)\Lambda$. (a) Phase section versus wavelength. The modes are numbered with relative longitudinal mode numbers 0, 1, 2, ... where red stands for the long-wavelength side and blue for the short-wavelength side of the stopband. (b) Threshold gain versus wavelength for each mode from $d_a = 0.00\,\Lambda$ to $d_a = 0.50\,\Lambda$. Arrows indicate the increase of d_a. (c) Differential quantum efficiency versus wavelength. (d) Phase section versus wavelength with additionally false-color intensity indicating the threshold gain (the scale is depicted at the right hand side).

cavity length shall be discussed. For $\kappa = 0\,\mathrm{cm}^{-1}$, all the five longitudinal modes have the same threshold gain and differential quantum efficiency. This is comprehensible, because at $\kappa = 0\,\mathrm{cm}^{-1}$, these lasers are FP lasers with a front-facet reflectivity of $R_f = 0.09\,\%$, a rear-facet reflectivity of $R_r = 96\,\%$ and its specific cavity length. With increasing κ, mode 0 turns out to be the lowest threshold gain mode, the lasing mode. In comparison with the other modes, its threshold gain decreases stronger with the increasing coupling

coefficient. Simultaneously, mode 0 is the mode with the strongest decrease of the differential quantum efficiency for the front-facet with increasing coupling coefficient. For mode 0, the differential quantum efficiency for the rear-facet increases with κ faster, than for the other modes.

With increasing cavity length, the coupling strength $\kappa \cdot L$ increases for the same value of the coupling coefficient κ. This causes the differential quantum efficiency for the front-facet to decrease faster with κ while the differential quantum efficiency for the rear–facet increases faster. For $L = 6000\,\mu$m, and $\kappa = 10\,\mathrm{cm}^{-1}$, the differential quantum efficiency for the front- and rear-facet becomes equal. Further increasing the coupling coefficient would lead both to decrease towards zero, because in resonators with very low loss through the facets, the stimulated emission is stored and absorbed inside the cavity.

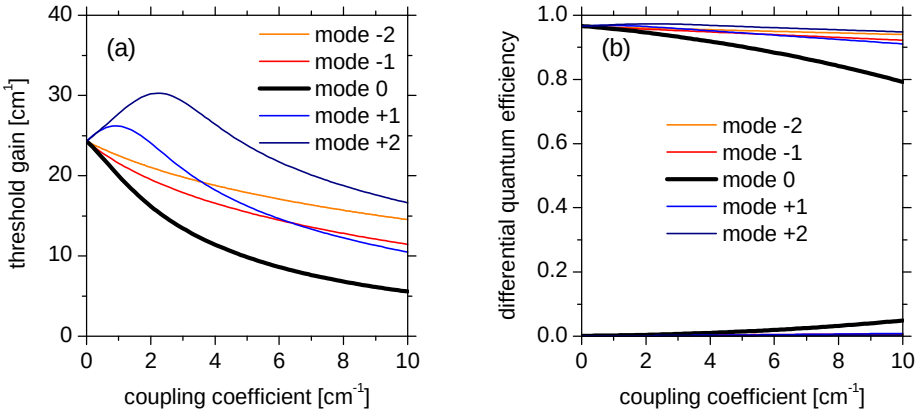

Figure 1.19: Facet phase-averaged threshold gain and differential quantum efficiency of five modes around the stopband for a 1500 μm long DFB laser as a function of the coupling coefficient. (a) Threshold gain. (b) Differential quantum efficiency at the front facet (upper curves) and at the rear facet (lower curves).

For a better comparison, the threshold gain and differential quantum efficiency ($\eta_\mathrm{i} = 1$) of the lasing mode is plotted together for all cavity length in Fig. 1.23 (a) and (b), respectively. At $\kappa = 0\,\mathrm{cm}^{-1}$, the threshold gain is the same as for a FP laser with the specific facet reflectivities, cavity length and internal optical loss. Due to the low optical feedback in this case and even at low $\kappa > 1\,\mathrm{cm}^{-1}$, the threshold gain is dominated by the resonator loss. For high values of the coupling strength, for example at $L = 0.60\,$cm and $\kappa \geq 5\,\mathrm{cm}^{-1}$, the threshold gain converges towards the value of the internal optical loss, because the contribution from the resonator loss decreases. This will in principle allow to adjust the coupling coefficient in order to obtain

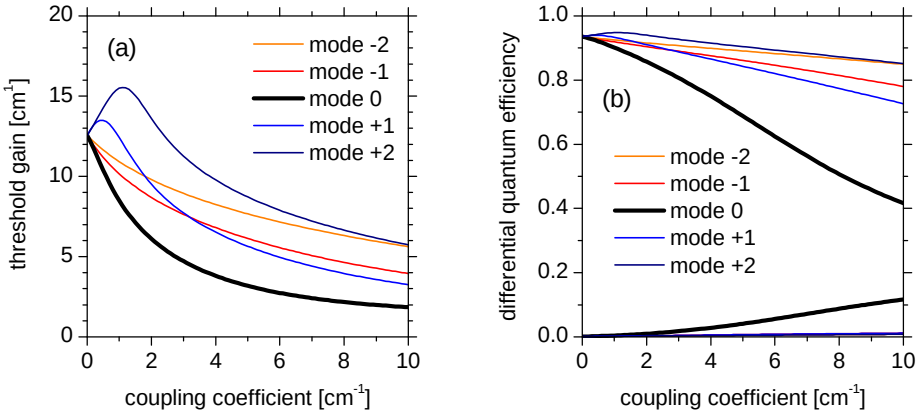

Figure 1.20: Facet phase-averaged threshold gain and differential quantum efficiency of five modes around the stopband for a 3000 μm long DFB laser as a function of the coupling coefficient. (a) Threshold gain. (b) Differential quantum efficiency at the front facet (upper curves) and at the rear facet (lower curves).

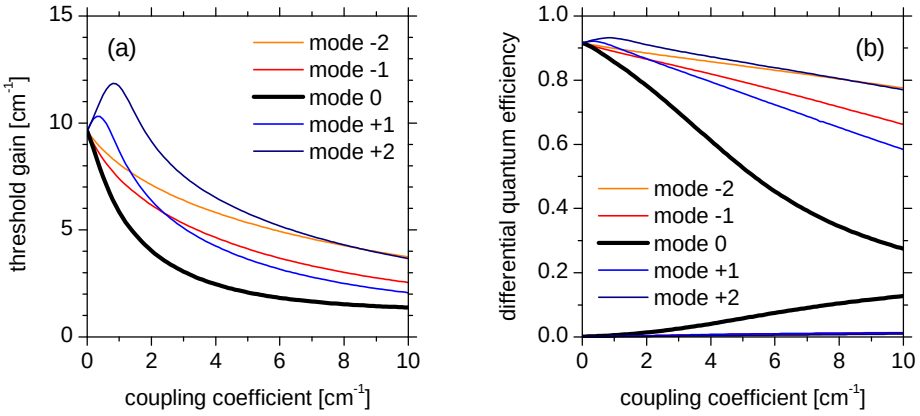

Figure 1.21: Facet phase-averaged threshold gain and differential quantum efficiency of five modes around the stopband for a 4000 μm long DFB laser as a function of the coupling coefficient. (a) Threshold gain. (b) Differential quantum efficiency at the front facet (upper curves) and at the rear facet (lower curves).

the same threshold gain as it would be obtained from a FP laser with an optimized front facet reflectivity ($R_{\mathrm{f}}^{\mathrm{FP}} > R_{\mathrm{f}}^{\mathrm{DFB}} = 0.09\,\%$). The differential quantum efficiency, plotted in Fig. 1.23 (b) decreases with increasing κ. In the cavity length range of special interest between $L = 0.30$ and $0.40\,\mathrm{cm}$, $\kappa \leq 3.2\,\mathrm{cm}^{-1}$ must be chosen to achieve a differential quantum efficiency

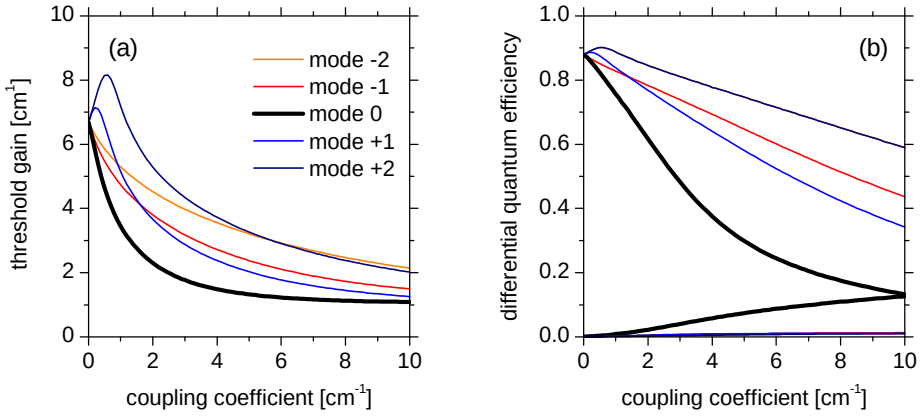

Figure 1.22: Facet phase-averaged threshold gain and differential quantum efficiency of five modes around the stopband for a 6000 μm long DFB laser as a function of the coupling coefficient. (a) Threshold gain. (b) Differential quantum efficiency at the front facet (upper curves) and at the rear facet (lower curves).

from the front facet of ≥ 0.80, which is approximately required for efficient high power lasers.

Sometimes it is advantageous to plot the threshold gain or differential quantum efficiency as a function of $\kappa \cdot L$ instead of plotting it as a function of κ. This is especially the case for the threshold gain minus the internal optical loss, multiplied with the cavity length, because $(\Gamma g_{\mathrm{th}} - \alpha_{\mathrm{i}})/L$ is a universal function for DFB lasers with different internal loss, cavity length and coupling coefficient. This can be clearly seen from Fig. 1.23 (c), where the calculated $(\Gamma g_{\mathrm{th}} - \alpha_{\mathrm{i}})/L$ for $L = 0.15$, 0.30, 0.40 and 0.60 cm overlay on the same curve but cover different ranges of $\kappa \cdot L$. In Fig. 1.23 (d), the differential quantum efficiency is also plotted as a function of $\kappa \cdot L$.

Chen *et al.* [Che98] have already performed calculations of the differential quantum efficiency as a function of the coupling coefficient or as a function of the cavity length. Because they were interested in narrow linewidth diode lasers for telecommunication applications, they performed their computations for specific phase relations between the facets and the grating stripes. In detail, they state that they have set both phases to 0 – a random choice. Nevertheless, the authors draw important conclusions for the optimization of high power DFB laser. Firstly, they recognize the importance to achieve $\kappa \cdot L \leq 1$. Secondly, they discuss that low distributed feedback may arouse the onset of lasing on FP-like modes. Thirdly, they show that it is necessary to obtain a low internal optical loss. Finally, reducing the coupling coefficient while increasing the cavity length is discussed as a strategy for high power

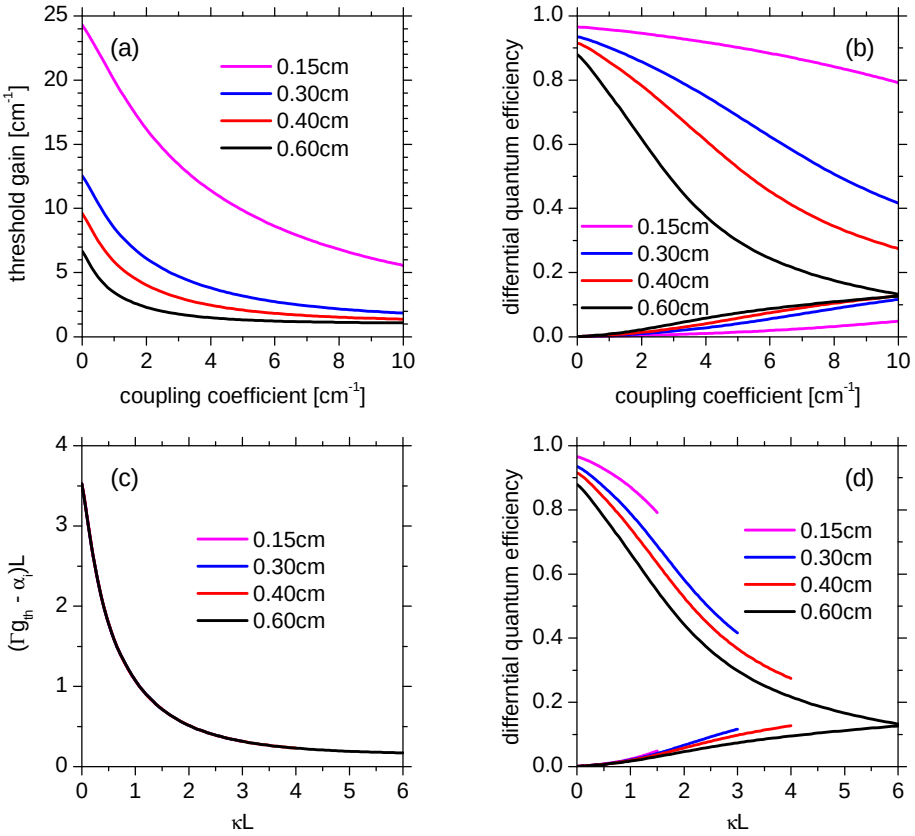

Figure 1.23: Facet phase-averaged threshold gain and differential quantum efficiency ($\eta_i = 1$) of the lasing mode for 0.15, 0.30, 0.40 and 0.60 cm long DFB lasers. (a) Threshold gain as a function of the coupling coefficient κ. (b) Differential quantum efficiency at the front facet (upper curves) and at the rear facet (lower curves) as a function of the coupling coefficient κ. (c) Threshold gain as a function of $\kappa \cdot L$. (d) Differential quantum efficiency at the front facet (upper curves) and at the rear facet (lower curves) as a function of $\kappa \cdot L$.

DFB lasers.

Finally, the influence of the coupling strength $\kappa \cdot L$ on the longitudinal field profile shall be discussed briefly. As mentioned above, $\kappa \cdot L = 1$ is often stated in literature to arouse a uniform longitudinal field profile [Ear98]. Also promising slope efficiency has been achieved with $\kappa \cdot L \approx 1$ [Kan06], [He09]. Uniform longitudinal field profiles are expected to reduce the effect of longitudinal spatial hole burning, which occurs under the presence of longitudinal inhomogeneities of the photon density due to the interactions

between photons and electrons. Longitudinal spatial hole burning stands for a reduction in the gain at specific longitudinal positions and therefore may alter the slope efficiency of high power diode lasers. Basically two questions arises which shall be answered in the following by plotting longitudinal profiles of the squared optical field, based on derivations, presented in section 1.2.3. Firstly, what does "uniform longitudinal field profile at $\kappa \cdot L = 1$" means under the consideration of the facet phase conditions between the last grating stripe and the facet mirror for an asymmetrically facet coated DFB laser? Secondly, how does the longitudinal field profile and the impact of the facet phases change under variations of $\kappa \cdot L$?

To answer these questions, the square of the electric field $|E(z)|^2$ has been computed following equation 1.75 during numerical DFB calculations, based on parameters, given in table 1.3. Deviating from parameters, given in table 1.3, the rear-facet phase section d_a has been increased with a larger step size of $\Delta d_\mathrm{a} = 0.05\,\Lambda$. The fast oscillating mixed term of the square and fast oscillations $\exp[iK_0 z]$ have been neglected. In Fig. 1.24, longitudinal profiles of the squared electric field are depicted for rear-facet phase section values of $d_\mathrm{a} = (0.00, 0.05, ..., 0.45)\Lambda$ (grey lines) and the averaged profile (red line) for three different values of the coupling strength $\kappa \cdot L$, all applied to the same cavity length $L = 0.3\,\mathrm{cm}$. The computed profiles are normalized at the front-facet position at $z = 0.3\,\mathrm{cm}$. Figure 1.24 (a) shows the $\kappa \cdot L \approx 1$ case. The depicted squared field profiles deviate strongly, depending of the rear-facet phase between increasing and decreasing from $z = 0.0\,\mathrm{cm}$ to $z = 0.3\,\mathrm{cm}$. However, approximately uniform longitudinal profiles can be observed for specific values of the rear-facet phase section, such as $d_\mathrm{a} = 0.00\Lambda$. Interestingly, the averaged longitudinal profile (red) is also approximately uniform.

Figure 1.24 (b) shows profiles for $\kappa \cdot L = 0.30$. The squared field profiles show a much lower deviation with the rear-facet phase and always, increase from $z = 0.0\,\mathrm{cm}$ to $z = 0.3\,\mathrm{cm}$. Such behavior will be also observed for a FP laser with strongly asymmetric facet coatings. Consequently, the averaged longitudinal profile (red) increase from $z = 0.0\,\mathrm{cm}$ to $z = 0.3\,\mathrm{cm}$. Further reduction of the coupling strength to $\kappa \cdot L = 0.15$ as shown in Figure 1.24 (c) results in squared field profiles with vanishing deviation with the rear-facet phase. Such behavior might have been expected because for $\kappa \cdot L \to 0$, the DFB-BA laser converges to a FP-BA laser with the defined facet reflectivities.

To conclude, $\kappa \cdot L \approx 1$ only results in uniform longitudinal squared field profiles, for specific configurations of the facet phases – and results in a uniform phase-averaged profile. The dependence of the profiles on the facet phases is rapidly reduced for $\kappa \cdot L < 1$ and the profiles converge to what is well known for FP lasers with HR coated rear-facets and AR coated front-facets

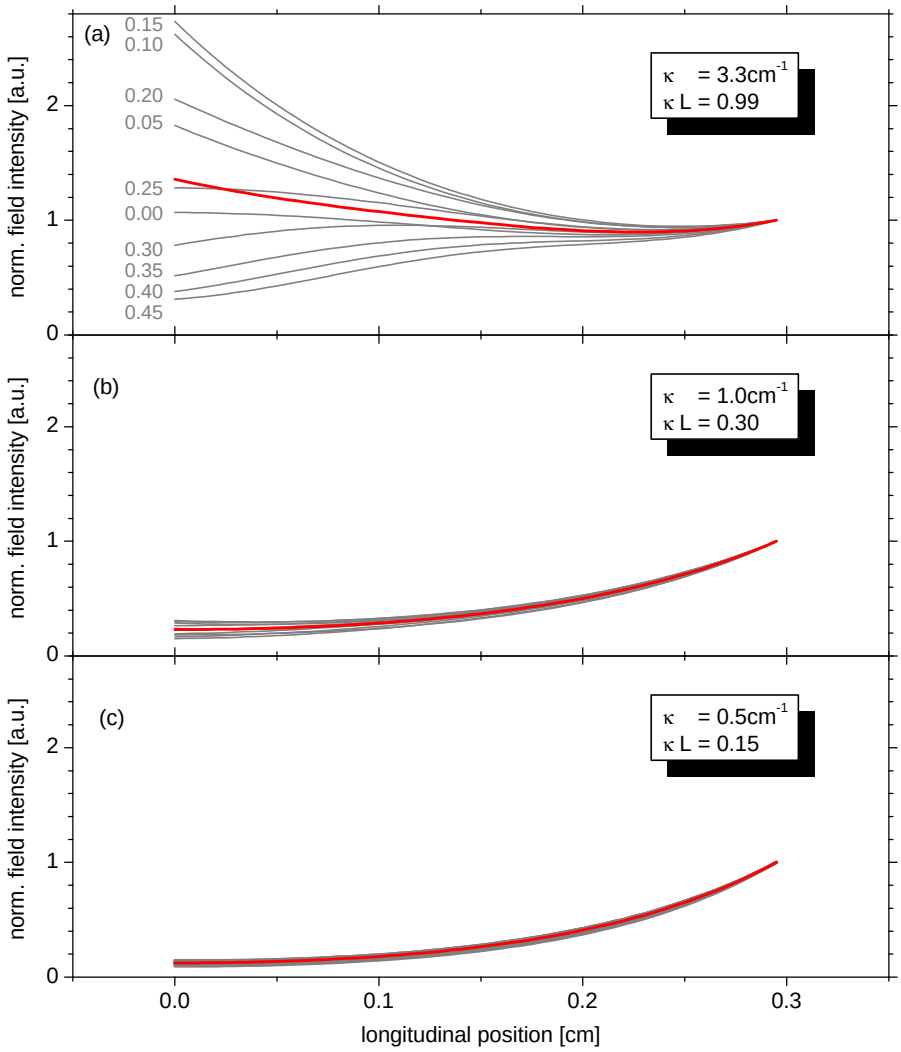

Figure 1.24: Calculated (normalized) longitudinal profiles of the squared electric field for DFB lasers with different coupling coefficients. Fixed parameters are: $L = 3\,\mathrm{mm}$, $R_\mathrm{f} = 0.09\,\%$, $R_\mathrm{r} = 96\,\%$ and $\alpha_\mathrm{i} = 0.8\,\mathrm{cm}^{-1}$. The calculation was performed for various phases of the rear-facet (at 0 cm) with phase sections of $(0.00, 0.05, ..., 0.45)\Lambda$. (a) $\kappa = 3.3\,\mathrm{cm}^{-1}$, $\kappa \cdot L \cong 1$. (b) $\kappa = 1.0\,\mathrm{cm}^{-1}$, $\kappa \cdot L = 0.3$. (c) $\kappa = 0.5\,\mathrm{cm}^{-1}$, $\kappa \cdot L = 0.15$.

– they increase towards the front-facet. For efficient high power DFB-BA lasers with $\kappa \cdot L \leq 1$, uniform or increasing (towards the front-facet) profiles must be therefore expected. On the other hand, a DFB grating might be used in diode lasers with very long cavity length $L \geq 6\,\mathrm{mm}$ in order to keep

the longitudinal field uniform. This could possibly enable very high current densities and power levels due to avoiding longitudinal spatial hole burning.

1.2.5 Power and efficiency characteristics of DFB-BA lasers

It has been already mentioned, that the coupling coefficient of a DFB laser can be used to achieve the same threshold gain as for a FP laser, used as a reference device. In this section, it will be analyzed, how a comparable threshold gain can be achieved for a DFB-BA laser and what this means for the differential quantum efficiency. The gained results are then used to calculate the threshold current and slope efficiency, in order to transfer the consequences to the optical output power and power conversion efficiency.

At first, some parameters shall be fixed. The DFB and FP laser shall be comparable in all aspects, besides the principles, how optical feedback is achieved. Therefore, parameters given in table 1.3 have been used for both, the DFB and FP laser with the following exception: The front facet of the FP laser was set to values of $R_\mathrm{f} = 0.5$, 1.0, 2.0, 4.0, 8.0, 16.0 and 32.0 %. Based on equation 1.15, this results in FP mirror loss, given in table 1.4. As a next step, the coupling coefficient $\kappa = |h_2|$ for which the DFB-BA laser has the same DFB resonator loss (with averaging over the rear-facet phase section) has been determined from the numerical DFB calculation. Considering the internal optical loss of $0.80\,\mathrm{cm}^{-1}$, this leads to the same threshold gain for both, the DFB and FP laser. Now, the differential quantum efficiency has been determined. For the DFB laser, the values for the front- and rear-facet have been obtained from the numerical calculation and $\eta_\mathrm{i} = 0.9$ has been considered. In order to ensure comparability, the differential quantum efficiency has been calculated also with respect to the fact, that less than 100 % of the optical power will be emitted from the front facet. In former calculations for FP lasers, this has been considered, for example in equation 1.23, no differentiation for the facets is used. A factor $F_\mathrm{f/r}$ which describes the fraction of the optical power which is emitted through the front- and rear-facet can be calculated based on the reflectivity and transmissivity of the facets as explained in [Col95]:

$$F_\mathrm{f/r} = \frac{\sqrt{1 - r_\mathrm{f/r}^2}}{(1 - r_\mathrm{f/r}^2) + \frac{r_\mathrm{f/r}}{r_\mathrm{r/f}}(1 - r_\mathrm{r/f}^2)}. \tag{1.87}$$

The differential quantum efficiency of the FP laser was therefore calculated

with the following equation:

$$\eta_{\mathrm{d\,f/r}} = F_{\mathrm{f/r}}\,\eta_{\mathrm{i}}\left(\frac{\alpha_{\mathrm{m}}}{\alpha_{\mathrm{i}}+\alpha_{\mathrm{m}}}\right). \tag{1.88}$$

The results for the coupling coefficient κ, the threshold gain Γg_{th}, and the differential quantum efficiencies $\eta_{\mathrm{d\,FP}}^{\mathrm{f/r}}$ and $\eta_{\mathrm{d\,DFB}}^{\mathrm{f/r}}$ are given in table 1.4.

Table 1.4: Input parameters and results of a comparison of the threshold gain and differential quantum efficiency of a DFB-BA laser and a reference FP laser, both with $L = 3000\,\mu$m.

R_{f} [%]	$\alpha_{\mathrm{m/DFB}}$ [cm^{-1}]	κ [cm^{-1}]	Γg_{th} [cm^{-1}]	$\eta_{\mathrm{d\,FP}}^{\mathrm{f/r}}$	$\eta_{\mathrm{d\,DFB}}^{\mathrm{f/r}}$
0.5	8.899	0.668	9.698	0.823/0.003	0.823/0.002
1.0	7.743	0.986	8.542	0.812/0.004	0.812/0.003
2.0	6.588	1.389	7.388	0.798/0.005	0.797/0.006
4.0	5.433	1.929	6.233	0.778/0.007	0.774/0.010
8.0	4.278	2.689	5.078	0.749/0.010	0.741/0.015
16.0	3.112	3.860	3.912	0.703/0.014	0.682/0.027
32.0	1.967	5.922	2.767	0.619/0.021	0.567/0.056

Figure 1.25 (a) shows the front-facet reflectivity of the FP reference laser and the corresponding coupling coefficients of the DFB-BA laser over the resonator loss. In Fig. 1.25 (b), the threshold gain is plotted for both, the FP reference laser and the DFB-BA laser is depicted. The threshold gain values are identical for both laser types, because identical internal optical loss has been considered and the coupling coefficient of the DFB-BA laser was chosen to achieve the same resonator loss as obtained for the FP laser. Figure 1.25 (c) shows the differential quantum efficiencies from the front- and rear facets ($\eta_{\mathrm{i}} = 0.9$). For high resonator loss (low optical feedback), both lasers have nearly identical differential quantum efficiencies, but at low resonator loss (high optical feedback), the curves diverge. By increasing the coupling coefficient (from the right to the left in Fig 1.25 (c)), the differential quantum efficiency from the front-facet shows a stronger decrease for

the DFB-BA laser than for the FP-BA laser. In addition, the differential quantum efficiency form the rear-facet increases stronger for the DFB-BA laser than for the FP-BA laser.

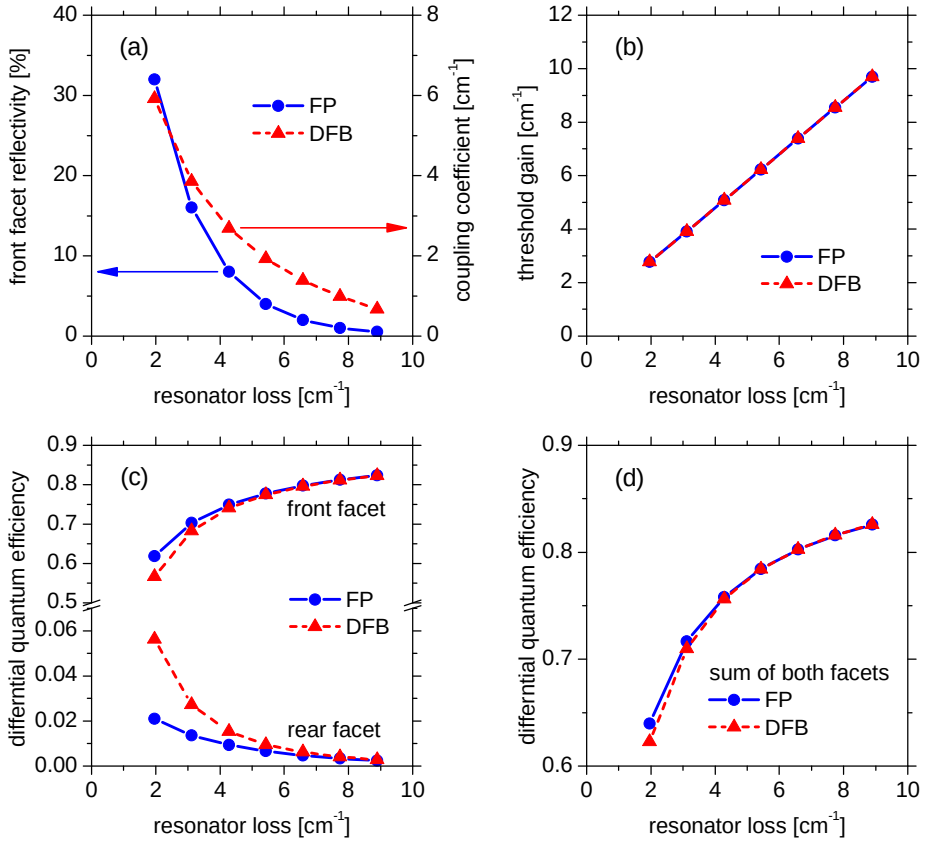

Figure 1.25: Comparison of the differential quantum efficiency between a FP reference laser and a DFB-BA laser with identical threshold gain. (a) Front facet reflectivities of the FP laser and coupling coefficients of the DFB laser. (b) Resulting threshold gain with $\alpha_\mathrm{i} = 0.8\,\mathrm{cm}^{-1}$. (c) Comparison of the differential quantum efficiency from the front- and rear-facet. (d) Comparison of the sum of the differential quantum efficiency from the front- and rear-facet.

Thus, a fundamental difference is observed between the FP laser and the DFB-BA laser in terms of the differential quantum efficiency at identical threshold gain. Note, that for the DFB-BA laser, averaging over the possible facet phase section has been applied. The different relation between the threshold gain and differential quantum efficiency from the front-facet is a drawback for the DFB-BA laser in order to achieve high power, high

efficiency operation, even if all other parameters are identically. The question arises, if the differences between the differential quantum efficiency from the front-facet occur only due to the differences in the differential quantum efficiency from the rear-facet, or if other effects are important. Therefore, the sum of the differential quantum efficiency from the front- and rear-facet was plotted as a function of the resonator loss, shown in Fig 1.25 (d). One can clearly see, that there is a small difference between the curves for the DFB-BA and FP laser at low resonator loss (high optical feedback). Thus, differences between the differential quantum efficiency from the front-facet occur not only due to the differences in the differential quantum efficiency from the rear-facet. It should be also noted that for the calculations presented here, the rear-facet reflectivity R_r is only 96 %. A lower fraction of the differential quantum efficiency for the rear-facet can be achieved by increasing the rear-facet reflectivity to $R_\mathrm{r} \geq 98\,\%$, which accessible with high quality facet coatings. By decreasing the differential quantum efficiency for the rear-facet due to a better HR-coating of the rear-facet, the drawback for DFB lasers is expected to increase as well.

Finally, voltage, power and efficiency characteristics have been calculated for a FP reference laser and a DFB-BA laser. To achieve comparability, identical voltage characteristics, wavelength and transparency current density were considered. For the voltage, $U(I) = U_\mathrm{d} + U_\mathrm{s} + \rho_\mathrm{s} \cdot W \cdot L \cdot I$ has been chosen with $U_\mathrm{d} = h\nu/q$, $U_\mathrm{s} = 50\,\mathrm{m\Omega}$, $\rho_\mathrm{s} = 6.0 \cdot 10^{-5}\,\Omega\,\mathrm{cm}^{-2}$, $W = 0.009\,\mathrm{cm}$. The wavelength of both, the FP reference laser and the DFB-BA laser is 975 nm. The transparency current density was set to $j_\mathrm{tr} = 151\,\mathrm{A\,cm}^{-2}$. The power characteristics $P(I)$ was calculated with equation 1.22 and 1.29. The influence of heat onto the power characteristics as introduced with equation 1.39 has not been considered, because the heat-dependence of the threshold current and slope efficiency is unclear for the DFB-BA laser. Voltage, power and efficiency characteristics have been calculated for parameters, given in table 1.4 and shown in Fig. 1.25, and are depicted in Fig. 1.26 (a). The voltage characteristics is always the same as defined above. The slope efficiency depends strongly on the resonator loss $\alpha_\mathrm{m/DFB}$. For low values of the FP laser front facet $R_\mathrm{f} < 8\,\%$ and the equivalent DFB coupling coefficient $\kappa < 2.689\,\mathrm{cm}^{-1}$, the differences between the slope efficiency of the FP reference laser and the DFB-BA laser are small and roughly negligible. For $R_\mathrm{f} > 8\,\%$ and $\kappa > 2.689\,\mathrm{cm}^{-1}$, the differences become important and lead to a substantial reduction of the output power at $I = 15\,\mathrm{A}$, as well as to a substantial reduction in the power conversion efficiency.

The values of the threshold current and slope efficiency are depicted in Fig. 1.26 (b). The drawback in differential quantum efficiency or slope efficiency for a DFB-BA laser is very low for low DFB coupling strength. In the

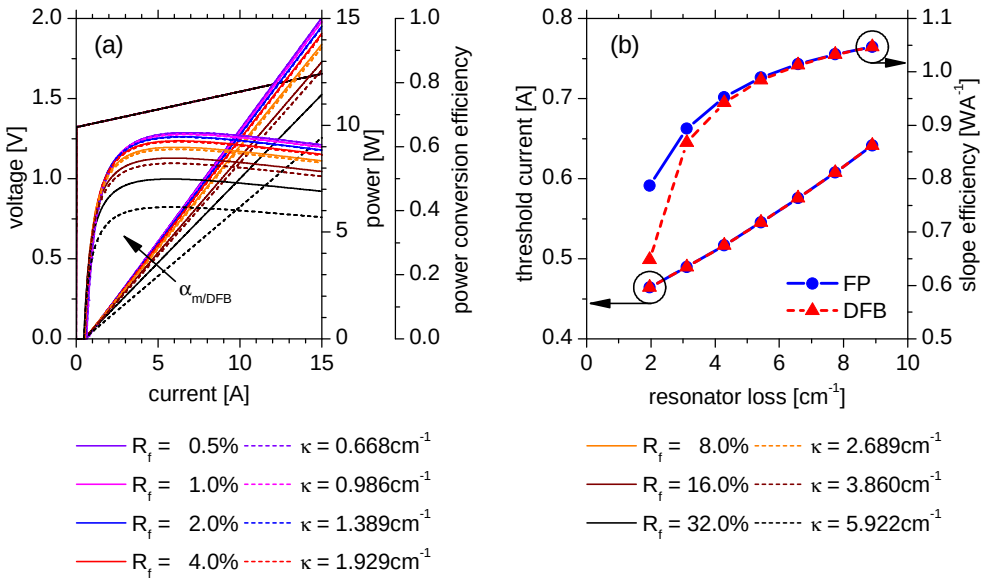

Figure 1.26: Calculated voltage, power and efficiency characteristics for a FP reference laser and a DFB-BA laser with identical threshold gain. (a) Calculated voltage, power and efficiency characteristics based on parameters, given in the text. (b) Threshold currents and slope efficiencies.

calculated example ($L = 0.3\,\mathrm{cm}$, $\alpha_\mathrm{i} = 0.8\,\mathrm{cm}^{-1}$, $R_{\mathrm{f\,DFB}} = 0.09\,\%$, $R_\mathrm{r} = 96\,\%$), the reduction in the differential quantum efficiency from the front-facet is negligible for $\kappa \cdot L \leq 1$

For the optimization of DFB-BA lasers for high output powers and high power conversion efficiency, the following conclusions can be drawn:

- Threshold currents and slope efficiencies comparable to high power, high efficiency FP-BA lasers can be achieved, provided that the coupling strength is low (approximately $\kappa \cdot L \leq 1$) and the front facet is sufficiently anti-reflection coated.

- To achieve comparable threshold currents and slope efficiencies also requires the DFB-BA laser to have the same internal optical loss, transparency current density and internal quantum efficiency.

- Comparable high power conversion efficiency in addition requires the DFB-BA laser to have the same voltage characteristics.

1.2.6 Important aspects for the design of efficient high power DFB-BA lasers

Low optical feedback

High power DFB-BA lasers will be operated significantly above threshold current. In order to achieve high optical output power of 10 W at minimal injection current, there is a tradeoff between the aim to achieve a low threshold current and the aim to achieve a high slope efficiency by optimization of the optical feedback. It has been derived, that there is a principle drawback in terms of this tradeoff for a DFB-BA laser, compared to a FP-BA laser with the same threshold gain. This drawback was shown to vanish when the optical feedback from the DFB grating and from the front facet is sufficiently low. In contrast to the DFB grating and front-facet which should provide low optical feedback, the rear-facet should have a facet coating with the highest possible reflectivity. As already discussed in section 1.1.2, low optical feedback is preferred for high optical output power because the increase in threshold current is more than compensated by the increase in slope efficiency. This is valid for FP and DFB lasers. Low optical feedback results in a low DFB coupling strength $\kappa \cdot L$ and presumably limits the spectral locking on DFB modes. Conventionally, $\kappa \cdot L = 1$ is preferred for DFB lasers in order to achieve stable DFB operation and prevent spatial hole burning [Ear98]. DFB laser operation is limited to currents I and temperatures T, at which the threshold gain of FP-like modes (close the peak of the gain spectrum) is not reached. To achieve high power conversion efficiency, comparable to a efficiency optimized FP-BA laser, the resonator loss of a DFB-BA laser should be approximately the same as for the FP-BA laser.

Low internal optical loss

As already shown in section 1.1.2, low internal optical loss is required for efficient high power diode lasers. This can be achieved by an optimized design of the waveguide structure, which should have a low doping profile and has to prevent coupling to the substrate and contact layers. Firstly, the introduction of a buried DFB grating can have a strong influence onto the internal optical loss [Yor92], because DFB gratings are conventionally highly p-doped (integrated into the p-side waveguide) and must be located within the intensity profile of the transverse optical field. High p-doping levels are required to improve the charge carrier transport through the epitaxy layers. Secondly, semiconductor layers and material interfaces are added to the epitaxy design. As a consequence, DFB gratings for highly efficient DFB-BA lasers should be as thin as possible, consist of a low number of semiconductor layers. Low loss DFB gratings should be placed at a position in the transverse mode

profile with low intensity, for example in the waveguide close to a cladding layer. The introduction of additional impurities and crystal defects due to the fabrication of the DFB grating must be prevented. Finally, radiation loss from higher-order DFB gratings [Str76] [Hen85], [Kaz85] has to be minimized by optimizing the duty cycle [Wen04], [Wen06]. To achieve high power conversion efficiency, comparable to a efficiency optimized FP-BA laser, the internal loss of a DFB-BA laser should be the same as for the FP-BA laser.

High internal quantum efficiency
Basically, an epitaxy design should be optimized for a high internal quantum efficiency. This requires sufficiently high barriers to the quantum wells in the active region, in order to minimize current leakage effects. Furthermore, the DFB grating should be optimized to prevent carrier recombination which would reduce the stimulated emission in the quantum well active region. To achieve high power conversion efficiency, comparable to a efficiency optimized FP-BA laser, the internal quantum efficiency of a DFB-BA laser should be the same as for the FP-BA laser.

Low voltage
A low voltage drop over the laser diode must be achieved at high power operation currents for a high efficiency. The usage of semiconductor materials with a low band-gap in the waveguide structure and a sufficient doping profile helps to reduce the series voltage and series resistance. The resistivity of the epitaxial layer system also depends on its thickness. Clearly, there is a tradeoff between the aim to achieve a ow internal optical loss (requires a low doping profile) and the aim to achieve a low voltage (requires a high doping profile). Additional semiconductor layers and material interfaces should be reduced as much as possible in order to achieve a low series voltage and series resistance. Finally, the n-substrate, p-contact layer and the ohmic contacts to the n- and p-metallization have to be considered. To achieve high power conversion efficiency, comparable to a efficiency optimized FP-BA laser at the same wavelength, the defect voltage $U_{\mathrm{def}}(I) = U(I) - h\nu/q$ of a DFB-BA laser should be the same as for the FP-BA laser.

Spectral properties
A CW driven DFB laser is spectrally locked to the Bragg wavelength of the DFB grating over a certain range in injection current and temperature. This requires, that the gain spectrum is spectrally optimized to the Bragg wavelength of the DFB grating. As already discussed in section 1.1.5, the peak of the gain spectrum and the Bragg wavelength should be optimized to coincide at the required optical output power and at a given temperature for

a high efficiency. This requires that the grating period, the effective index of refraction and the gain spectrum has to be optimized. Because the main aspect of this work is to achieve high power conversion efficiencies, the optical feedback from the DFB grating will be chosen in order to achieve a high slope efficiency, instead of choosing it for a maximum suppression of lasing on FP-like modes. Therefore, the reflectivity of the front facet must be very low and is the key parameter for the suppression of FP-like modes.

Limited operation range
From the discussion of the spectral properties of a CW driven DFB laser it turns out, that its operation will be limited to a specific range in temperature and current, in order to achieve the required high optical output power, high power conversion efficiency, wavelength stabilization and narrow spectral width. This range in temperature and current presumably becomes smaller, if the coupling strength is decreased and broader, if the front facet reflectivity is decreased.

To conclude, the development of high power and high efficiency DFB-BA lasers can be done by approximately adapting the properties of the DFB-BA laser to the properties of a power and efficiency-optimized FP-BA laser. Firstly, the DFB resonator loss should be comparable or slightly smaller than the FP mirror loss $\alpha_{\mathrm{DFB}} \leq \alpha_{\mathrm{m}}$. Secondly, the internal loss and internal quantum efficiency and transparency current density should be comparable. As derived above, this will lead to the same threshold current and slope efficiency for the DFB-BA and FP-BA laser. Based on this requirements, comparable power conversion efficiency will be obtained, if the voltage drop $U(I)$ is approximately identical. Finally, the wavelength of the gain-peak must be optimized to coincide with the Bragg wavelength of the DFB grating at the desired output-power. The qualifications, specified above, imply high requirements to the laser and grating design, fabrication technology and material quality.

Chapter 2

DFB-BA laser review

In this chapter, physical properties and technology of previously published work on typically high power DFB-BA lasers before the beginning of this work are presented. These lasers were usually developed to achieve a narrow spectral width, highly suppression of side modes in the optical spectrum and wavelength stabilization over a wide range in temperature. Additionally, the achievable optical output power was higher than what could be obtained from a DFB-RW laser in transversal and longitudinal single mode emission. The possibility to achieve high optical output power $\geq 4\,\mathrm{W}$ and power conversion efficiency $\geq 50\,\%$ from DFB-BA lasers has not been a major matter of research and development, since first promising results in this field have been reported by Kanskar *et al.* [Kan06]. Good understanding of the best previously published DFB-BA lasers, their design and fabrication technology is essential for further successful development. This chapter summarizes which power and efficiency levels were previously achievable and reviews promising fabrication technologies for DFB gratings to be used in wavelength stabilized BA lasers. Thus, findings from the review concerning the efficiency, optical output power and wavelength stabilization can be used as as a design guidance in this work.

After distributed feedback has been initiated as a principle for optical feedback in a gelatine film dye laser by Kogelnik *et al.* [Kog71] in 1971, this has been rapidly transferred to semiconductor diode lasers [Nak73], [Sci74]. Early DFB diode lasers were typically fabricated using a narrow ridge waveguide design in order to obtain transversal single mode emission, in addition to longitudinal single mode behavior [Nak89], [Wen04]. Other fabrication approaches, such as buried or diffused waveguides have been reported as well [Sin93], [Lam98]. Later, DFB-RW lasers have been used and developed for telecommunications technology [Ber02], [Fun04] and spectroscopy

applications [Sum12], for example. These lasers were typically optimized for lateral and longitudinal single mode lasing, a high side mode suppression ratio (SMSR) and spectral stabilization over a wide range in temperature. Achieving high optical output power was no main focus of the development and typical values in the $< 1\,\mathrm{W}$ range have been achieved [Wen04]. Even the possibility to achieve high power conversion efficiency has not been considered very seriously. Such narrow stripe width DFB lasers must be considered as a basis for the development of DFB-BA lasers but they are rather not the main aspect of this chapter.

In parallel to the development of narrow stripe DFB lasers for transversal single mode emission, the question arises how the optical output power can be increased to $> 1\,\mathrm{W}$. Distributed feedback BA lasers were fabricated based on the obvious assumption, that the achievable optical output power can be increased by increasing the width of the laser stripe. This first types of DFB-BA lasers were primarily developed to achieve a narrow spectral width, good suppression of side modes in the optical spectrum (for example $> 30\,\mathrm{dB}$ SMSR) and wavelength stabilization over a wide range in temperature at optical output powers above 1 W.

The first gain coupled 923 nm DFB-BA lasers were demonstrated by Robadey *et al.* [Rob97]. These lasers consist of a GaAs waveguide with InGaAs quantum wires and AlGaAs cladding layers and were fabricated, based on a two-step epitaxy process. The molecular beam epitaxy (MBE) growth process is interrupted within the GaAs waveguide and a V-groove second-order grating is etched into it with lithographic techniques. After being returned into the MBE reactor, oxide desorption is applied at $\sim 600\,^{\circ}\mathrm{C}$ and the surface is regrown with a thin GaAs layer and InGaAs is grown into the V-grooves to form quantum wires (periodicity of 264 nm), which provide periodic gain and function as a second-order DFB gain grating. From this material, DFB-BA lasers with a stripe width up to $100\,\mu\mathrm{m}$ were fabricated. The authors present spectra with good side mode suppression and a spectral width of $\ll 1\,\mathrm{nm}$. From the width of the stopband, they determine a coupling coefficient of $\sim 30\,\mathrm{cm}^{-1}$. However, measurements had to be performed at liquid nitrogen temperature of 77 K under pulsed current injection and values of the optical output power have not been reported. These lasers could not exceed threshold at room temperature (even on FP modes), presumably because of too high optical loss and too low gain, provided by the quantum wires and regrowth technology.

Earles *et al.* [Ear98] successfully increased the optical output power of DFB-BA lasers at 893 nm above 1 W. The epitaxy design is based on an InGaP waveguide, an InGaAs DQW and InGaAlP cladding layers. A second-order DFB index grating is etched 50 nm deep into the *p*-type waveguide

with lithographic techniques outside the metal-organic chemical vapor deposition (MOCVD) reactor, then overgrown with the InGaP p-type cladding layer. Thus, the authors also apply a two-step epitaxy process, but use the difference of index of refraction between the waveguide and cladding layer material to provide periodic optical feedback, instead of structuring the active region. Compared to the design and technique used by Robadey *et al.* [Rob97], this method has the advantage that the DQW active region can be grown with high quality and is unaffected by the etching and two-step epitaxy process. The grating is etched into aluminum-free material which is reported to prevent problems with the formation of stable aluminum oxide and oxygen contamination at the grating interface. The authors fabricated DFB-BA lasers from the material with 100 μm stripe width and 1 mm cavity length. A coating with a front-facet reflectivity of $R_\mathrm{f} = 5\,\%$ and rear-facet reflectivity of $R_\mathrm{r} = 95\,\%$ has been applied to the cleaved facets. Continuous wave optical output power of $\approx 1.1\,\mathrm{W}$ is obtained at $\approx 1.9\,\mathrm{A}$ with a power conversion efficiency of 32 %. The authors also report on the optical spectrum, which consists of several lateral modes that originate from a single longitudinal mode. They propose that lasing in a single longitudinal mode has been obtained due to using $\kappa \approx 7\,\mathrm{cm}^{-1}$ which leads to a low coupling strength $\kappa \cdot L \approx 0.7\,\mathrm{cm}^{-1}$. Coupling strength between 0.5 and 1.0 is stated to lead to relatively uniform longitudinal field profiles and therefore avoids longitudinal spectral hole burning. The authors further recognize that low coupling strength and an asymmetric facet coating will lead to high differential quantum efficiency.

Further advancement in the technology of BA diode lasers with DFB index gratings has been reported by Chang *et al.* [Cha00], where some of the authors from [Ear98] are also involved. The epitaxy design has been changed towards a completely aluminum-free waveguide structure that consists of InGaP cladding layers, an InGaAsP waveguide and an InGaAs DQW active region. Again, the second-order DFB grating is structured into p-type waveguide region outside the MOCVD reactor, then overgrown with aluminum-free cladding compound. This aluminum-free epitaxy design was developed for $> 10\,\mathrm{W}$ (CW) high power FP-BA diode lasers as reported in [Maw96] and [AM98] and is originally based on the aluminum-free large optical cavity (LOC) design, published in [Bot96]. DFB-BA lasers with 100 μm stripe width, 2 mm cavity length and facet coatings for $R_\mathrm{f} = 5\,\%$, $R_\mathrm{r} = 95\,\%$ achieve optical output power of 1 W with a power conversion efficiency of 33 % and a narrow spectrum ($< 1\,\mathrm{nm}$) at 976 nm. The authors determine a coupling coefficient of $\kappa \approx 1.5\,\mathrm{cm}^{-1}$ and thus, $\kappa \cdot L \approx 0.3$ is quite low. Finally, the authors also determine the internal optical loss under DFB operation ($6\,\mathrm{cm}^{-1}$) and under FP operation ($4\,\mathrm{cm}^{-1}$). Even $4\,\mathrm{cm}^{-1}$ is higher than

the internal optical loss of the same device structure without the grating, reported in [Maw96] and [AM98]. Presumably, the difference occurs due to significant radiation loss from the second-order DFB grating (non-ideal duty cycle) or increased internal optical loss.

In the publications, mentioned above, DFB-BA diode lasers, wavelength stabilized at three different wavelength have been reported. Robadey *et al.* [Rob97] report on 923 nm DFB-BA lasers but the do not explicitly point out possible applications of this wavelength. Earles *et al.* [Ear98] fabricate 893 nm DFB-BA lasers for polarization of Cs which is used for the generation of spin-polarized Xe gas. Furthermore, Chang *et al.* [Cha00] report on 976 nm DFB-BA lasers which could be promising pump sources for Yb-doped solid state lasers or fiber lasers.

Klehr *et al.* [Kle06] have developed DFB-BA lasers emitting at 808 nm, which can be used for pumping Nd:YAG solid state lasers. Besides introducing a new wavelength for DFB-BA lasers, the authors used $Al_xGa_{1-x}As$-based designs with aluminum-free grating layers.

Meanwhile, epitaxy designs with aluminum-free waveguide [Ear98] and even completely aluminum-free designs [Cha00] have been developed and were stated to be favorable for the monolithic integration of the DFB grating with a two-step epitaxy process, because exposing aluminum to air during the grating fabrication would lead to the formation of stable oxides and could cause oxygen contamination in the regrown material. Note, that in contrast to oxides on InGaAsP, aluminum oxides cannot be desorbed by a temperature increase to $\sim$ 700 °C in the epitaxy reactor. In parallel to aluminum-free designs for high power FP-BA lasers, (In)AlGaAs-based epitaxy designs have been developed, showing promising results in power and efficiency [Sak92b], [Sak92a]. Advantages and disadvantages of both material systems are for example discussed in [Tre00].

Klehr *et al.* have implemented a multiple layer DFB grating into the *p*-side of the 2000 nm broad $Al_{0.45}Ga_{0.55}As$ waveguide, 600 nm above the single quantum well active region, located in the center of the waveguide. The wafers were grown using low-pressure metal-organic vapor phase epitaxy (MOVPE). The cladding layers consist of $Al_{0.70}Ga_{0.30}As$. The first epitaxy is finished with a aluminum-free layer system from $In_{0.48}Ga_{0.52}P$, $GaAs_{0.85}P_{0.15}$ and $In_{0.48}Ga_{0.52}P$. The second-order DFB grating is etched into the upper two layers of this aluminum-free layer system with lithographic techniques. The three-layer approach allows the usage of selective etching techniques, so that the last $In_{0.48}Ga_{0.52}P$ layer can stop etching and uncovering of the underlying $Al_{0.45}Ga_{0.55}As$ is avoided. After the ex-situ etching, the surface is regrown with the second part of the *p*-side waveguide and cladding layer to complete the structure. Thus, the authors combine the benefit of aluminum-

free grating material (avoid formation of stable aluminum oxide and oxygen contamination in the regrown compound) with the benefit of $Al_xGa_{1-x}As$-based waveguide and cladding layers. Klehr *et al.* experimentally determine a coupling coefficient of $\sim 1\,cm^{-1}$. DFB-BA lasers with a stripe width of $100\,\mu m$ and a cavity length of 3 mm from this material have therefore a low coupling strength $\kappa \cdot L \approx 0.3$. Facet coating has been applied to achieve a front-facet reflectivity of $R_f < 0.1\,\%$ and rear-facet reflectivity of $R_f = 95\,\%$. Single emitter DFB-BA lasers were investigated at 20 °C under CW current injection and found to have threshold current of 0.58 A and a very high slope efficiency of $1.06\,W\,A^{-1}$. A peak output power of 4.7 W has been obtained at ≈ 5.8 A with 34 % power conversion efficiency, until power saturation and roll-over is observed. Wavelength stabilization is reported for the whole investigated current range (0 - 6 A) with a spectral width < 0.3 nm.

The epitaxy design and grating technology for 808 nm DFB-BA lasers, reported in [Kle06], has later been transferred to 975 nm DFB-BA lasers in [Sch09a]. These lasers were optimized to achieve a narrow vertical far field and for wavelength stabilization over a wide temperature range. The idea behind the development of narrow, far field DFB-BA lasers was to enhance the possible coupling efficiency of the laser emission to lenses or optical fibers. For narrow far field emission, an asymmetrical LOC design has been used for the $4.8\,\mu m$ wide $Al_{0.35}Ga_{0.65}As$ waveguide, embedded between *n*- and *p*-cladding layers from $Al_{0.45}Ga_{0.55}As$ and $Al_{0.85}Ga_{0.15}As$, respectively. The $Al_{0.35}Ga_{0.65}As$ waveguide consists of a $3.9\,\mu m$ thick *n*-type region and a $0.9\,\mu m$ thick *p*-type region with an InGaAs DQW active region located in between. The second-order DFB grating (295 nm period, duty cycle optimized to $c_d \approx 1/4$) is integrated with a two-step epitaxy process into the *p*-type waveguide, $0.8\,\mu m$ above the DQW and $0.2\,\mu m$ under the *p*-cladding layer. As reported in [Kle06], it consists of a three layer system, here using InGaP/GaAs/InGaP, grown at the end of the first epitaxy. The grating is structured with lithographic techniques and selective etching is applied to stop on the lower InGaP layer. Afterwards, the wafer is transferred back to the MOVPE reactor and the surface is regrown with $Al_xGa_{1-x}As$ to complete the structure. The coupling coefficient has been experimentally determined as $\approx 9\,cm^{-1}$. DFB-BA lasers with a stripe width of $100\,\mu m$ and a cavity length of 2 mm have high $\kappa \cdot L \approx 1.8$ and were facet coated to achieve $R_f < 0.1\,\%$ and $R_r = 95\,\%$. Mounted *p*-side down, these lasers achieve an optical output power of 2.4 W at 4 A CW and 25°C. From the voltage and power characteristics, a threshold current of 0.34 A, a slope efficiency of $0.69\,W\,A^{-1}$ and a peak power conversion efficiency of 35 % has been determined. From the length dependence of the differential quantum efficiency and threshold current density, the internal optical loss α_i and internal quantum efficiency

η_i was determined both – for DFB-BA lasers (spectrally detuned to achieve lasing on FP modes) and FP-BA reference devices, grown in a single stage epitaxy without the grating layers. While $\eta_i = 0.85$ was found for the DFB-BA and FP-BA lasers, $\alpha_i^{DFB} = 2.0\,cm^{-1}$ for the DFB-BA lasers is increased, compared to $\alpha_i^{FP} = 1.2\,cm^{-1}$, found for the FP-BA lasers. The asymmetric LOC waveguide design results in a narrow vertical far field emission angle of 14 ° FWHM and 38.5 ° with 95 % power content, which is significantly lower than what has been reported earlier for other DFB-BA lasers. The high coupling strength of $\kappa \cdot L \approx 1.8$ is a compromise which on the one hand, leads to a compromised slope efficiency, but on the other hand, enables wavelength stabilization between 15 and 100°C via a low threshold current and good suppression of FP-like modes [Sch09a], [Sch09b].

From about 2006 onwards, DFB-BA lasers began to be optimized primarily for optical power ($\geq 4\,W$) and power conversion efficiency ($\geq 50\,\%$) to make them suitable for high power pumping applications. This type of DFB-BA lasers was developed to obtain comparable optical output power and power conversion efficiency as already achieved with FP-BA lasers [Sak92b], [Sak92a], [Bot96], [Maw96], [AM98], [Tre00], [Kan05], [Kni05]. In order to maximize the optical output power and power conversion efficiency, some degradations in the temperature range with sufficient wavelength stabilization and side mode suppression must be accepted.

In 2006, Kanskar *et al.* [Kan06] published experimental results which have been obtained with 975 nm DFB-BA lasers (suitable for pumping Yb doped gain media). Even though the authors conceal the material system in use, one may assume that the lasers have been developed, based on the aluminum-free epitaxy design they have published in earlier work [Cha00]. The second-order DFB grating is again placed between the *p*-type waveguide and the *p*-type cladding layer and structured by use of a two-step epitaxy, lithographic techniques and 100 nm deep reactive ion etching. Cleaved into cavity length of 1 and 2 mm, 100 μm broad DFB lasers were facet coated to achieve $R_f \approx 4\,\%$ and $R_r \approx 95\,\%$ and mounted *p*-side down. The authors note that $\kappa \cdot L \sim 1$ (presumably for 1 mm cavity length). DFB-BA lasers with 1 mm cavity length have a slope efficiency of $0.9\,W\,A^{-1}$ and achieve $\approx 4\,W$ CW peak power and a peak power conversion efficiency of 53 % at 2 W at 25°C heatsink temperature. Furthermore, 2 mm long DFB-BA lasers were driven up to 8 A and achieve 5.5 W optical output power. Finally, spectra at 2 A are shown for heatsink temperatures of 10, 20, ... 50°C and provide locking over 40°C. The spectra are structured due to the appearance of multiple lateral and maybe even multiple longitudinal modes and the spectral width remains $< 0.5\,nm$.

Furthermore, part of the authors from [Kan06] report on 808 nm DFB-

BA lasers in He *et al.* [He09]. Presumably, the authors have adapted the epitaxy design from [Kan06] to be suitable for 808 nm DFB-BA lasers (now suitable for pumping Nd:YAG). In fact, the authors again conceal the material system in use. The grating technology is also comparable to what has been published in [Kan06]. DFB-BA lasers ($100\,\mu\text{m} \times 2\,\text{mm}$ were again facet coated to achieve $R_\text{f} \approx 4\,\%$ and $R_\text{r} \approx 95\,\%$ and mounted p-side down, the coupling strength is $\kappa \cdot L \sim 1$. At 25°C, these lasers have a threshold current of 0.45 A, a slope efficiency of $> 1\,\text{W}\,\text{A}^{-1}$ and achieve 4 W optical output power with a power conversion efficiency, close to the peak efficiency of 57 % (at 3 W). The spectral width is shown to be $\sim 0.5\,\text{nm}$ when it is evaluated at approximately 95 % power content. The authors finish their report with a diagram, showing sporadic measurements of the spectral locking range over heatsink temperature (between 10 and 50 °C) and CW drive current (between 0 and 4.5 A). Interestingly, it is limited at high temperatures and currents, as well as for low temperatures. The locking range in heatsink temperature is indeed, lower than for a DFB-BA laser with $\kappa \cdot L > 1$, as for example, reported in [Sch09a].

Finally, the question arises what can be learned from the publications about DFB-BA lasers mentioned above, which have been reported before or at the beginning of this work, with respect to the development targets in this work. The most important findings are itemized below.

- The two-step epitaxy is a successful concept for the monolithic integration of DFB gratings, although it requires a sophisticated fabrication technology.

- Usage of second-order DFB gratings is a proved concept for ease of fabrication and the corresponding radiation loss from first-order Bragg scattering in this gratings can be small if the duty cycle is adjusted precisely.

- The epitaxy design of the waveguide structure can be based either on an aluminum-free material system or on an AlGaAs-based material system, both have achieved promising power and efficiency results in FP-BA lasers and laser bars.

- For high power, high efficiency DFB-BA lasers, long cavity length and low coupling strength $\kappa \cdot L \leq 1$ is preferred in order to achieve a high differential quantum efficiency.

- The front facets of DFB-BA lasers must be AR coated for a sufficient suppression of lasing on FP-like modes at the gain peak wavelength

which is essential to achieve a narrow wavelength stabilized spectrum in a broad range of injection current and heatsink temperature.

Chapter 3

Experimental and theoretical results from iteration I

In this chapter, conclusions drawn in chapter 1 will be applied to the development of high power and efficiency DFB-BA lasers. Firstly, a design for FP-BA reference lasers is presented. These lasers have been optimized for high optical output powers and high power conversion efficiency, as well as for the monolithic integration of a DFB grating. Based on the design specifications, lasers were grown, processed, facet coated and mounted, in order to enable extensive device characterization. Voltage and power characteristics were then investigated, as well as the spectral properties and the temperature dependence of the wavelength, threshold current and slope efficiency. The characterization is completed with investigation of the spatial emission properties. The experimental results show, that these lasers are promising for state of the art FP-BA diode lasers and potentially enable the further development of DFB-BA lasers in the $\sim 10\,\mathrm{W}$ output power, $\sim 60\,\%$ power conversion efficiency range.

In the second part of this chapter, the development of a DFB grating for efficient high power DFB-BA lasers is described. DFB-BA lasers with such gratings are then fabricated and characterized, comparable to the FP-BA reference lasers. DFB-BA lasers are investigated in order to analyze similarities and differences, compared to the reference devices. Finally, the power, voltage and efficiency characteristics of the best DFB-BA lasers from iteration I are compared to results, obtained with the numerical calculations. Conclusions are drawn, how the power conversion efficiency of the DFB-BA lasers can be further optimized in order to approach to the properties of the highly efficient FP-BA reference lasers.

3.1 Design of a low loss laser waveguide

The goal of this work package was the development of an epitaxy design for high-power and high-efficiency edge emitting semiconductor lasers. FP-BA lasers, processed from wafers of this epitaxy design will later on be used as reference devices for the comparison and benchmarking of DFB-BA lasers from the same epitaxy design but with an integrated DFB grating. For this reason, the possibility for the monolithic integration of a DFB index grating had to be considered in addition to general design-requirements in order to achieve low internal optical loss, high internal quantum efficiency, low voltage and series resistance.

Some design parameters were restricted in advance from requirements for the practical usage of high power semiconductor lasers. These restrictions were made on the basis of findings, derived in sections 1.1.4, 1.2.4, 1.2.5, 1.2.6, as well as in chapter 2. The vertical far field distribution that contains 95 % of the emitted optical power was limited to a divergence angle of $\leq 45\,^{\circ}$. The cavity length was limited to 3 - 4 mm and the stripe width determined to 90 - 100 μm.

The decision between the possibilities to use either aluminum-free epitaxy designs for the waveguide structure or $Al_xGa_{1-x}As$-based designs, was made in favor of the $Al_xGa_{1-x}As$-based designs, because of promising experimental results [Kni05] and experience with the related technology at the FBH. The following material systems were taken as a basis:

- $Al_xGa_{1-x}As$ waveguide with $x \leq 0.3$
- $Al_xGa_{1-x}As$ cladding layers
- $In_yGa_{1-y}As$ double quantum well with $GaAs_zP_{1-z}$ barriers

The aluminum content in the waveguide has been limited to $x \leq 0.3$, because the integration of the DFB grating via a two-step epitaxy process is expected to cause less regrowth problems in low-aluminum content $Al_xGa_{1-x}As$. This arises from experimental results, reported in publications such as [Yor92], [Bia99] and [Hof01].

For the design optimization, the semiconductor laser simulation program QIP, developed by H. Wenzel and H.-J. Wünsche has been used. QIP is originally based on a model for the calculation of the threshold current of diode lasers, published in [Wen90]. The design optimization targets are basically to achieve low internal optical loss $\alpha_i \leq 1\,cm^{-1}$ and a high internal quantum efficiency $\eta_i \geq 0.9$. In combination with a low voltage, this will potentially enable efficient high power diode lasers as discussed in section 1.1.4.

In state of the art high quality MOVPE grown InAlGaAs-based QW laser designs, internal optical loss is dominated by doping level dependent free carrier absorption [Bul07] and absorption in the quantum wells. For the free carrier intra-band absorption which depends on the carrier density (n for electrons, p for holes) and wavelength, various values have been reported in literature (often studied at higher energies than equivalent to $\sim 975\,\mathrm{nm}$), for example in [Cas75]. Here, the coefficient of intra conduction band (free electron) absorption has been set to $\sigma_n = 4\,\mathrm{cm}^{-1}$, the coefficient of intra valence band (free hole) absorption was assumed to be $\sigma_p = 12\,\mathrm{cm}^{-1}$ as given in [Pet07] for carrier densities of $1 \cdot 10^{18}\,\mathrm{cm}^{-3}$ (typical at threshold) and at a wavelength of 940 nm. Internal optical loss calculated with these values is in good agreement with internal optical loss, experimentally determined in AlGaAs-based $\sim 950\,\mathrm{nm}$ laser structures at the FBH.

The following parameters have been varied during the optimization of the epitaxy layers:

- the width and aluminum content of the waveguide
- the position of the double quantum well
- the width and aluminum content of the cladding layers
- the graded refractive index change-over regions
- the doping profile

The vertical far field distribution which contains 95 % of the emitted optical power has been limited to a divergence angle of $\leq 45\,^\circ$. As discussed earlier, a narrow vertical far field is an important development target for diode lasers because it enables efficient coupling of the emitted power into lenses or optical fibers for further applications. Broad waveguide designs as reported in [Maw96], [Bot96], [Bot99] and [Kni05] are suitable to achieve a narrow vertical far field. Such designs are often called large optical cavity (LOC) waveguides. In addition to the narrow vertical far field, LOC designs have the advantage that the broad near field results in a low optical power density at the facets. Consequently, the power level at which catastrophical optical mirror damage (COMD) occurs, can be very high, provided that the facet passivation and facet coating is robust. Because of the advantages mentioned above, an LOC waveguide design will be used in this work.

To achieve a high power conversion efficiency, the following qualitative concepts have been taken into account. A high power conversion efficiency requires a high slope efficiency of the power-current characteristic, a moderate threshold current as well as a low diode voltage. High slope efficiency can

be obtained with a laser epitaxy structure with a high internal quantum efficiency and low internal optical loss. While a high internal quantum efficiency can be achieved with a quantum well structure with high electronic barriers that prevent carrier leakage, the internal optical loss can be minimized with a low doping level in regions with non vanishing modal intensity and a low aluminum-concentration x in the $Al_xGa_{1-x}As$ waveguide. The threshold current can be lowered with an epitaxy structure with low loss and a high internal quantum efficiency. In order to reach threshold, the carrier density in the active region must be increased towards $\sim 1 \cdot 10^{18}\,\mathrm{cm}^{-3}$ to generate population inversion and quasi Fermi level energy separation. To achieve this, an external voltage is required to deliver sufficient current through highly (cladding) and in particular through weakly doped layers (waveguide) to support n, p. Effectively, a p-i-n diode is turned on. The diode voltage mostly depends on the quasi Fermi level separation of electrons and holes at threshold and on the series resistance. The quasi-Fermi level separation of a laser epitaxy structure is a monotone rising function of the aluminum concentration x in $Al_xGa_{1-x}As$ because the band gap increases with x. The series resistance is partway produced by the conductivity of the semiconductor bulk material and the quality of the epitaxial grown material hetero-interfaces, which can also lead to steps in series voltage. The carrier mobility is predominantly limited by phonon scattering and alloy scattering [Ada93].

The iterative epitaxy design optimization lead to a laser structure with a $2.1\,\mu$m thick $Al_{0.15}Ga_{0.85}As$ waveguide. A double quantum well (DQW) active region with two $In_yGa_{1-y}As$ quantum wells (7 nm) and $GaAs_zP_{1-z}$ barriers (7.5 nm between the quantum wells and 5 nm outside) is asymmetrically placed within the waveguide (1180 nm n-type waveguide (57 %), 920 nm p-type waveguide(43 %)). The $Al_{0.30}Ga_{0.70}As$ n-cladding layer has a thickness of $1.2\,\mu$m, while the $Al_{0.85}Ga_{0.15}As$ p-cladding layer is $0.3\,\mu$m thin. The transition from the waveguide to the cladding layers is realized with 30 nm thin graded refractive index (GRIN) regions. The doping levels are $1 \cdot 10^{18}\,\mathrm{cm}^{-3}$ in the n-cladding layer, $5 \cdot 10^{16}\,\mathrm{cm}^{-3}$ in the n- and p-waveguide and $2 \cdot 10^{18}\,\mathrm{cm}^{-3}$ in the p-cladding layer respectively.

In Fig. 3.1 (a), the resulting electronic band-structure is depicted for an un-doped case. The red solid line is given by the minimum of the conduction band edges at the Γ- and X-point of the Brillouin zone. At all positions, where the semiconductor crystal has a direct band-gap ($x \leq 0.45$ in $Al_xGa_{1-x}As$), the red curve is defined by the Γ-point conduction band edge. The red dashed-dotted line indicates the position of the first electron energy level which is the fundamental solution of the Schrödinger equation in the quantum well. The heavy hole valence band edge is depicted as a blue solid line and the corresponding first heavy hole energy level as a blue

dashed-dotted line. Fig. 3.1 (b) shows the magnified quantum-well region from Fig. 3.1 (a), so that the two quantum wells and the surrounding barriers are clearly visible.

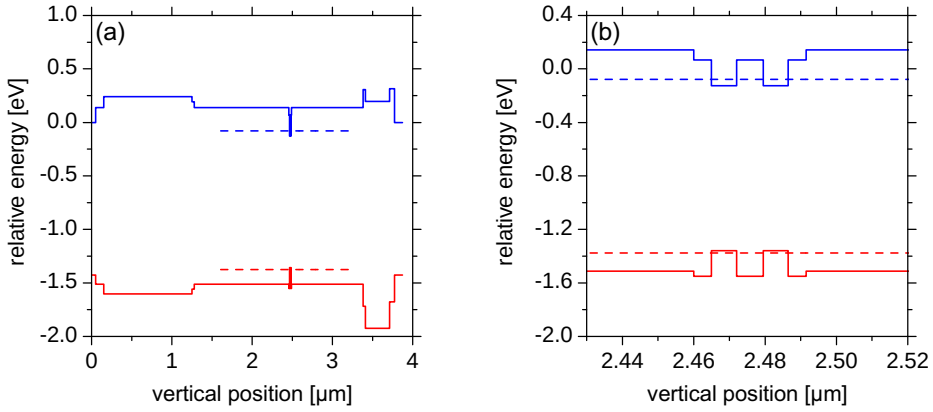

Figure 3.1: Electronic band-structure of the epitaxy design, selected for for high-efficiency, high-power lasers. (a) Minimum of the conduction band edges at the Γ- and X-point (blue solid line) and the heavy hole valence band edge (red solid line). The corresponding first electron energy level and first heavy hole energy level are depicted as blue and red dashed lines, respectively. (b) Magnified section of (a) in the quantum-well region.

The profile of the refractive index, the profiles of the waveguide modes and the resulting far field distributions are depicted in Fig. 3.2. In Fig. 3.2 (a), the refractive index profile is shown in the background as a grey area. The near field profiles of the four different guided modes ($v = 0, 1, 2, 3$) are depicted on top as colored lines. depending on their overlap with the highly absorbing cladding layers, their internal loss α_m ranges from $0.47\,\mathrm{cm}^{-1}$ for the fundamental mode to $24\,\mathrm{cm}^{-1}$ for the highest-order mode. With the vertical field profile $\Phi(x)$, the doping profile $n(x)$ and $p(x)$ and the free carrier absorption coefficients $\sigma_n = 4\,\mathrm{cm}^{-1}$ and $\sigma_p = 12\,\mathrm{cm}^{-1}$, the internal loss is calculated in QIP, following

$$\alpha_\mathrm{i} = \frac{1}{n_\mathrm{eff}} \int |\Phi(x)|^2 \cdot \overline{n}(x) \cdot [\sigma_\mathrm{n} n(x) + \sigma_\mathrm{p} p(x)]\,\mathrm{d}x, \tag{3.1}$$

where n_eff is the effective index of refraction and $\overline{n}(x)$ is the index of refraction.

In Fig. 3.2 (b), the calculated far field profiles of the waveguide modes are depicted as a function of the divergence angle. As required in the ex-

perimental targets of this work, the fundamental mode contains 95 % of the emitted optical power within an angle of $44.3\,° < 45\,°$.

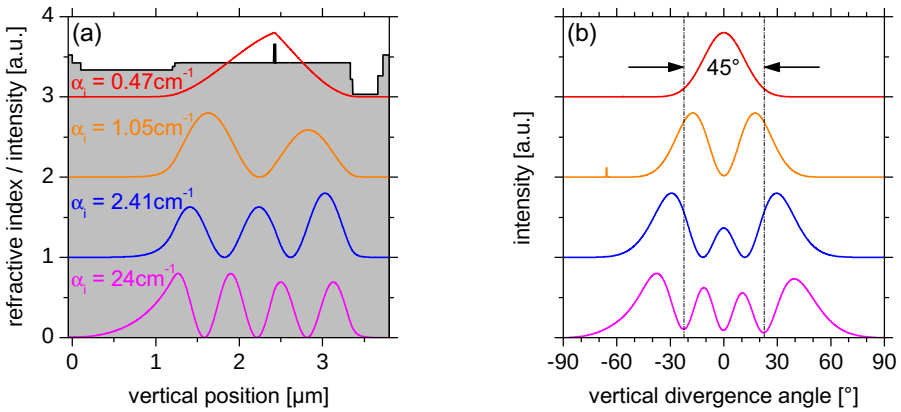

Figure 3.2: (a) Refractive index profile of the epitaxy design for high-efficiency, high-power lasers and the simulated near field profiles of the waveguide modes with the corresponding internal losses indicated. (b) Simulated far field angular distribution of the waveguide modes.

The calculation of the optical modes and their properties, results in four different vertical modes as solution of the waveguide problem. Thus, in addition to the desired fundamental mode ($v = 0$), three higher-order modes with different near field and far field profiles (shown in Fig. 3.2) occur. The question arises, if lasing only on the fundamental mode can be obtained. Lasing on higher-order vertical modes could potentially prevent that the desired vertical far field angle of $\leq 45\,°$ can be achieved, because the width of the vertical far field significantly increases with the vertical mode order v. Therefore, the modal discrimination must be evaluated. As already indicated in Fig. 3.2 (a), these modes have different internal optical loss α_i. From the individual field profiles at the position of the DQW, also different confinement factors with the active region Γ can be estimated from the diagram. Before starting to discuss the modal discrimination, an analysis of the cavity length dependence of the differential quantum efficiency and threshold current density will be carried out. This will allow to experimentally determine the transparency current density j_tr and modal gain coefficient Γg_0. Subsequently, the discussion will return to the modal discrimination and it will be evaluated by calculating the threshold current.

The following characterization is used to determine important parameters for the grown laser material and often used as a quality control in

order to verify, if the experimentally obtained material parameters are in appropriate agreement with the results from the simulation (QIP). To determine important optoelectronic parameters of the laser waveguide design, power-voltage-current characteristics have been measured on un-mounted lasers with a stripe width of 100 and 200 μm and different cavity lengths ($L = 400, 600, \ldots, 2000\,\mu$m). No facet coating has been applied for these measurements, so that both, the reflectivity at the front and rear facet, are approximately 32 %, and 50 % of the optical power is assumed to be emitted through each facet. The measurement-procedure is explained in chapter B.2.2, while the theoretical background is given in [Col95]. In Fig. 3.3 (a) and (c), the inverse value of the differential quantum efficiency η_d^{-1} is depicted as a function of the cavity length L. The linear relation for FP lasers

$$\eta_\mathrm{d}^{-1} = 1/\eta_\mathrm{i} + [\alpha_\mathrm{i}/(\eta_\mathrm{i} \ln(1/R))] \cdot L \tag{3.2}$$

allows to determine the internal optical loss and the internal quantum efficiency. For the linear fit, shown in the graph, the measurement result from devices with a cavity length of 400 μm have been excluded. From the linear fits for 100 and 200 μm stripe width, one obtains internal optical loss of approximately 1.0 cm^{-1} and an internal quantum efficiency of 0.92. Both values are within the desired parameter range, defined above, which is required for high efficiency lasers.

Based on the natural logarithm of the threshold current density j_th, plotted as a function of the inverse cavity length, one can derive the modal gain coefficient Γg_0 and the transparency current density j_tr from the linear relation:

$$\begin{aligned} \ln\left(j_\mathrm{th}\right) &\cong \ln\left(j_\mathrm{tr} \mathrm{e}^{\left(\alpha_\mathrm{i} + \frac{1}{L}\ln\left(\frac{1}{R}\right)\right)/\Gamma g_0}\right) \\ &= \left[\ln(j_\mathrm{tr}) + \frac{\alpha_\mathrm{i}}{\Gamma g_0}\right] + \frac{1}{L}\left[\frac{\ln\left(1/R\right)}{\Gamma g_0}\right], \end{aligned} \tag{3.3}$$

where $R = R_\mathrm{f} = R_\mathrm{r} = 32\,\%$. The measured values and a linear fit curve for this method are depicted in Fig. 3.3 (b) and (d). Again, the measurement results for a cavity length of 400 μm have been excluded. For the modal gain coefficient, one approximately obtains 20.0 cm^{-1} and for the transparency current density 138 A cm^{-2}.

The values, experimentally obtained for α_i and η_i, are promising and represent an improvement compared to values, reported in earlier work [Sch09a]. In [Sch09a], a much wider waveguide design has been used (4.8 μm instead of 2.1 μm), the aluminum-content in the waveguide was higher ($\mathrm{Al_{0.35}Ga_{0.65}As}$ instead of $\mathrm{Al_{0.15}Ga_{0.85}As}$) and also the p- and n-doping level was higher

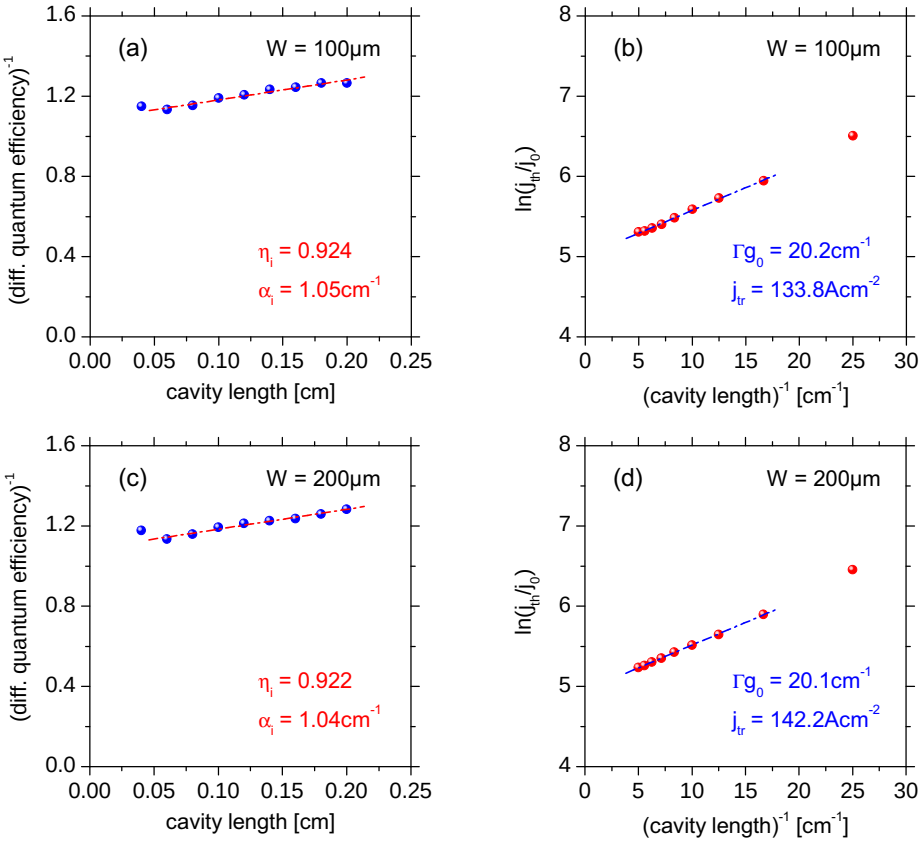

Figure 3.3: Cavity length dependence of the differential quantum efficiency and threshold current density. (a) The inverse value of the differential quantum efficiency over the cavity length allows to determine the internal quantum efficiency η_i and the internal loss α_i (for 100 μm stripe width). (b) $\ln(j_\mathrm{th}/j_0)$ over the inverse cavity length allows to determine the confinement factor of the double quantum well Γg_0 and the transparency current density j_tr (for 100 μm stripe width). (c) Equivalent to (a) but for 200 μm stripe width. (d) Equivalent to (b) but for 200 μm stripe width. j_0 is here always set to one.

$(1 \cdot 10^{17}\,\mathrm{cm}^{-1}$ instead of $5 \cdot 10^{16}\,\mathrm{cm}^{-1})$. Changes in the waveguide design and doping level results in a reduction in the internal optical loss and increase of the internal quantum efficiency, which were $\alpha_i = 1.2\,\mathrm{cm}^{-2}$ and $\eta_i = 0.85$ in [Sch09a]. Compared to [Sch09a], j_tr is nearly unchanged.

Finally, the discussion of modal discrimination will be continued. The cavity length dependence of the differential quantum efficiency and threshold current density gave experimental results for the transparency current density j_tr and modal gain coefficient Γg_0. With these values, threshold currents

have been calculated for a DFB-BA laser with a stripe width of $W = 90\,\mu$m, cavity length of $L = 3000\,\mu$m, front and rear facet reflectivity $R_\mathrm{f} = 2\,\%$ and $R_\mathrm{f} = 98\,\%$ on the basis of equation 1.29. Table 3.1 summarizes the simulated internal optical loss α_i, the simulated confinement factor of the optical field profile with the DQW, Γ, and the calculated threshold currents I_th.

Table 3.1: Discrimination of higher-order vertical modes in the FP laser structure, based on the simulation results. The threshold current has been calculated with $L = 3000\,\mu$m, $W = 90\,\mu$m, $R_\mathrm{f} = 2\,\%$, $R_\mathrm{f} = 98\,\%$ and $j_\mathrm{tr} = 138\,\mathrm{A\,cm^{-2}}$.

mode v	α_i [$\mathrm{cm^{-1}}$]	Γ [%]	I_th [A]
0	0.473	1.400	0.519
1	1.051	0.256	2.662
2	2.411	0.566	1.063
3	24.02	0.760	5.342

Firstly, modal discrimination is obtained because of significant increase of the internal optical loss with increasing mode number v. This leads to higher threshold currents for the higher-order modes. Secondly, the fundamental mode $v = 0$ has the highest confinement factor of the optical field profile with the DQW, which also contributes to the lowest threshold gain. Admittedly, the confinement factor increases from $v = 1$ to $v = 3$ as can be also qualitatively derived from Fig. 3.2 (a). For the calculation of the threshold current it has been assumed, that the reflectivity of the facet mirrors is identical for all vertical modes. This is an approximation. In fact, the reflectivity slightly increases for the higher-order modes and will cause a small reduction in the threshold current. The resulting values for the threshold current of the vertical modes are shown in the last column of table 3.1. The threshold current of the fundamental mode is only half as high ($\sim 0.5\,\mathrm{A}$) as the threshold of mode $v = 2$ ($\sim 1\,\mathrm{A}$, which is the one with the second lowest threshold). This modal discrimination is expected to be sufficient in order to obtain lasing exclusively on the fundamental mode.

3.2 Characterization of FP-BA reference lasers

3.2.1 Facet coating for FP-BA reference lasers

Wafers for FP-BA lasers with 3000 μm cavity length and 90 μm stripe width were grown by low-pressure MOVPE as briefly described in section A.1 and a standard processing has been applied as specified in section A.2. The epitaxy design is detailed in section 3.1. For the further characterization, a facet passivation and facet coating was applied to laser bars with single emitters of 3 mm cavity length and 90 μm stripe widths (adequate for optical coupling into 100 μm-core diameter optical fibers). In order to achieve a maximum front facet slope efficiency, a very high rear facet reflectivity $R_r = 98\,\%$ was targeted. To optimize the slope efficiency and threshold current for a maximum power conversion efficiency, a front facet reflectivity $R_f = 2\,\%$ has been chosen. Much lower front facet reflectivity typically do not lead to an increased slope efficiency at $L = 3000\,\mu$m, but increases the threshold current and makes the lasers sensitive to unwanted external feedback during experiments. With the applied facet coating, $R_f = 2.75\,\%$ and $R_r = 98.06\,\%$ was achieved at 976 nm. In Fig. 3.4, the reflectivity is depicted as a function of the wavelength for both facets. The reflectivity was measured on GaAs-dummies. Afterwards, the reflectivity on the laser facet has been calculated with respect to the effective index of the fundamental waveguide mode.

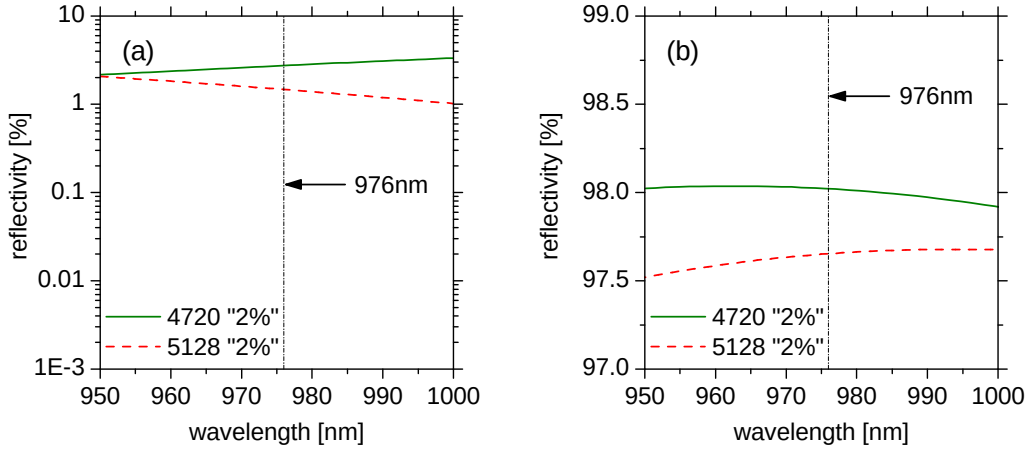

Figure 3.4: Reflectivity of the anti-reflection coated front facet (a) and the high-reflection coated rear facet (b) for FP-BA reference lasers.

3.2.2 P-U-I characteristics of FP-BA lasers

After the facet passivation and coating, single emitters with 3000 μm cavity length and 90 μm stripe width were mounted on 4 mm × 6 mm CuW sub-mounts as explained in chapter A.4. The P-U-I characteristics and the spectrum map were then measured with the setup, explained in chapter B.1.1. Temperature stabilization of the sub-mount at 25.0 °C ± 0.1 °C was also realized as explained in chapter B.1.1. Figure 3.5 (a) shows the P-U-I characteristics of three devices from Wafer F1850-4, measured at 25.0 °C heatsink temperature between 0 and 12 A (for one device also up to 15 A) with a step size of 100 mA. The threshold currents vary between 600 and 621 mA. The slope efficiency, determined from a linear fit over 2.0 A directly above threshold, is in the range between 1.067 and 1.104 W A^{-1}. From a linear fit of the voltage in the flat region above threshold between 1 and 5 A, an average turn-on voltage U_0 = 1.305 V (at 0 A) and an average series resistance of R_s = 23.2 mΩ has been determined for the three devices.

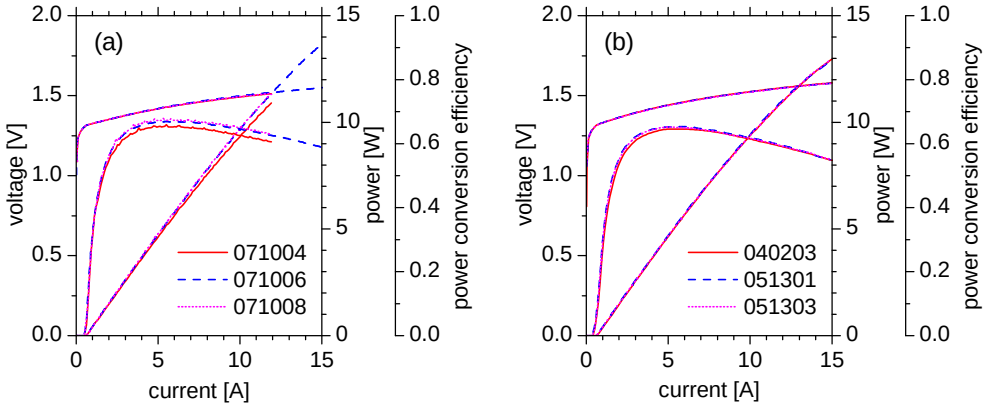

Figure 3.5: P-U-I characteristics from FP-BA lasers from wafers F1850-4 and D1423-1, measured at 25.0 °C heatsink temperature. (a) Lasers F1850-4 071004, 071006 and 071008. (b) Lasers D1423-1 040203, 051301 and 051303.

The electro-optical results of FP-BA lasers from Wafer F1850-4 (MOVPE reactor F), shown in Fig. 3.5 (a) are promising, because the lasers achieve 10 W optical output power at a power conversion efficiency of more than 60 %. Subsequently, wafers for FP-BA lasers were grown in a second MOVPE epitaxy reactor (D), which has been selected for the growth of the DFB-BA lasers in a two step epitaxy process. Of course, the question arises, if the electro-optical properties of FP-BA lasers from reactor D are identical with lasers from reactor F. Figure 3.5 (b) shows P-U-I characteristics of

three devices from Wafer D1423-1 which have been measured in the same way as it has been done for the devices from wafer F1850-4, presented in Fig. 3.5 (a). At a first glance, the threshold current and slope efficiencies are comparable to the devices from Wafer F1850-4. Differences in the P-U-I characteristics occur in the series resistance. This leads to lower power conversion efficiency and consequently, to a slightly increased thermal roll-over of the power characteristics, compared to devices from Wafer F1850-4. This effect is demonstrated in Fig. 3.6, where the P-U-I characteristics of FP-BA laser F1850-4 071006 are compared to the characteristics from D1423-1 051301. An average turn-on voltage of $U_0 = 1.308\,\mathrm{V}$ and an average series resistance of $R_\mathrm{s} = 27.3\,\mathrm{m\Omega}$ was determined for the three devices from Wafer D1423-1.

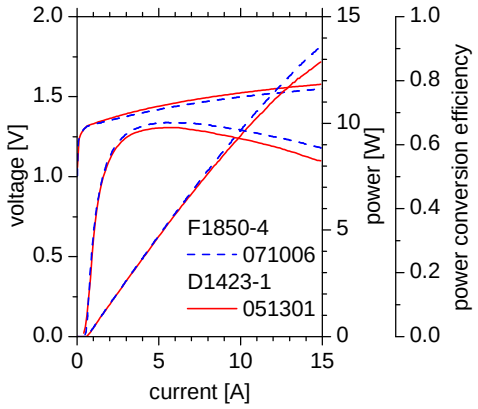

Figure 3.6: P-U-I characteristics from FP-BA laser F1850-4 071006 compared to FP-BA laser D1423-1 051301, measured at 25.0 °C heatsink temperature.

Finally, the threshold current I_th, slope efficiency $S_{2\,\mathrm{A}}$, peak power conversion efficiency $\eta_\mathrm{PCE}^\mathrm{max}$, and power conversion efficiency at 7 and 10 W, $\eta_\mathrm{PCE}^\mathrm{7\,W}$ and $\eta_\mathrm{PCE}^\mathrm{10\,W}$, respectively, are summarized in table 3.2. A comparison of the threshold current and slope efficiency values for Wafers F1850-4 and D1423-1 shows, that occurring differences are of minor importance. This indicates, that important parameters such as the internal optical loss, internal quantum efficiency, threshold current density and facet coatings are comparable for devices from both wafers.

Nevertheless, the increase of the series resistance from Wafer F1850-4 to D1423-1 by only $\approx 4\,\mathrm{m\Omega}$ causes significant differences in the voltage drop $U(I)$. Because the threshold currents and slope efficiencies are nearly identical for devices from wafers F1850-4 and D1423-1, the increase of the thermal roll-over, observed for devices from D1423-1, is presumably a consequence

Table 3.2: Overview of the threshold gain, slope efficiency and power conversion efficiency from FP-BA lasers.

wafer	laser	I_{th} [mA]	$S_{2\,\mathrm{A}}$ [WA^{-1}]	$\eta_{\mathrm{PCE}}^{\mathrm{max}}$	$\eta_{\mathrm{PCE}}^{7\,\mathrm{W}}$	$\eta_{\mathrm{PCE}}^{10\,\mathrm{W}}$
F1850-4	071004	619	1.071	0.659	0.647	0.617
	071006	603	1.092	0.670	0.666	0.642
	071008	624	1.107	0.679	0.671	0.647
D1423-1	040203	657	1.091	0.646	0.640	0.606
	051301	614	1.093	0.654	0.645	0.611
	051303	625	1.092	0.651	0.642	0.609

of the reduction in power conversion efficiency and thus, a consequence of the higher voltage drop. The power conversion efficiency $\eta_{\mathrm{PCE}}^{10\,\mathrm{W}}$ drops from $\approx 64\,\%$ for devices from wafer F1850-4 to $\eta_{\mathrm{PCE}}^{10\,\mathrm{W}} \approx 61\,\%$ for devices from wafer D1423-1. This means, that, if $\eta_{\mathrm{PCE}}^{10\,\mathrm{W}} = 60\,\%$ is a target for the DFB-BA lasers, the reduction in the power conversion efficiency due to the monolithic integration of the DFB grating, must be reduced to $\leq 4\,\%$ and $\leq 1\,\%$, respectively. With respect to earlier results for the P-U-I characteristics of DFB-BA lasers and reference FP-BA lasers [Sch09b], this seems to be very challenging.

The reason for the differences in the series resistance is not clear. Nominal, both wafers were grown identically but this was done in different MOVPE reactors. Basically, minor differences in the laser properties might occur from epitaxy to epitaxy even in the same reactor. Presumably, using reactor D can cause a small penalty but this is the reactor, most suitable for the two-step epitaxy which is required for the growth of buried DFB gratings. Certainly, an increase of the series resistance could be also caused during the processing of the wafer.

3.2.3 Spectral properties of FP-BA lasers

In order to analyze the spectral properties of the FP-BA lasers, spectra were measured under CW current injection between 0 and 15 A with an experimental setup, described in section B.1.2. Afterwards, the spectra were plotted

as a linear scaled spectrum map. In Fig. 3.7, two sample spectral maps are depicted for lasers from wafers F1850-4 and D1423-1, respectively.

At threshold, the spectrum of laser F1850-4 071006 starts with a center wavelength of 968.7 nm and shifts to 980.3 nm at 15 A. An approximately linear shift of the center wavelength with the current of $\approx 0.643\,\mathrm{nm\,A^{-1}}$ is observed. The wavelength shift slightly increases at about 11 A. The spectral width with 95 % power content develops from 1.9 nm close to the threshold to 5.5 nm at 15 A. The spectrum is typical for FP-BA lasers. Note, that the spectrometer in use is not able to resolve the longitudinal and lateral modes. Hence, the measured spectrum appears as a broad, approximately gaussian shaped curve.

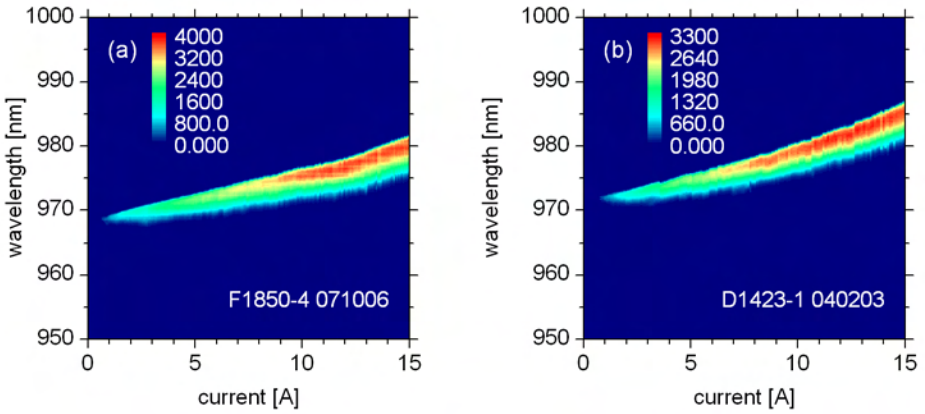

Figure 3.7: Linear intensity-scaled false-color maps oft the spectra from FP-BA lasers from wafers F1850-4 and D1423-1, measured at 25.0 °C heat sink temperature. (a) Laser F1850-4 071006. (b) D1423-1 040203.

Deviations in the lasing wavelength occur for laser D1423-1 040203, compared to F1850-4 071006. At threshold, the center wavelength is shifted to 972.0 nm (+3.3 nm) and shifts to 986.4 nm at 15 A (+5.1 nm). The spectral width with 95 % power content is comparable for the two devices with 2.2 nm at threshold and 5.6 nm at 15 A for D1423-1 040203.

The center wavelength at an optical output power of 10 W is of practical importance for possible applications of such diode lasers for pumping absorption bands in gain media of solid state lasers, fiber lasers and amplifiers. As already mentioned in the introduction (chapter), this work targets a wavelength of 976 nm for the diode lasers, for pumping the narrow absorption line ($\approx 976\,\mathrm{nm} \pm 4\,\mathrm{nm}$) in Yb doped glass or crystals [Pas97]. FP-BA lasers F1850-4 071006 and D1423-1 040203 achieve center wavelengths at 10 W of

975.9 and 981.3 nm, respectively. The spectral width with 95 % power content is 4.7 nm for both lasers. Thus, the wavelength requirements are complied for F1850-4 071006 but not for D1423-1 040203. Further optimization of the DQW active region (width and composition of the quantum wells) would be necessary to adjust the gain spectrum to enable lasing close to 976 nm at the current, at which 10 W output power is obtained.

3.2.4 Thermal properties of FP-BA lasers

For high power performance, the thermal resistance R_{therm} of the mounted diode laser plays an important role. It can be determined experimentally from the shift of the wavelength as a function of the thermal dissipation loss $\mathrm{d}\lambda/\mathrm{d}P_{\mathrm{d}}$, and the wavelength shift with the ambient temperature $\mathrm{d}\lambda/\mathrm{d}T$. The knowledge of the accurate $\mathrm{d}\lambda/\mathrm{d}T$ is important for the adjustment of the wavelength in order to achieve the targeted value of 976 nm at 10 W optical output power. Therefore, three experiments have been carried out: firstly, the measurement of the CW P-U-I characteristics, secondly, the measurement of the spectrum as a function of the CW current and finally, a measurement of the spectrum as a function of the ambient temperature without heating in the active region (for example under short pulsed current injection with a pulse duration of 500 ns and a duty cycle of $5 \cdot 10^{-4}$, which leads to a current heating of 0.015 K with $P_{\mathrm{peak}} = 10\,\mathrm{W}$, $\eta_{\mathrm{pce}} = 60\,\%$ and $R_{\mathrm{th}} = 4.5\,\mathrm{K\,W^{-1}}$). The thermal resistance can be calculated with the temperature coefficient of the emission wavelength $\mathrm{d}\lambda/\mathrm{d}T$ as:

$$R_{\mathrm{th}} = \frac{\mathrm{d}\lambda_{\mathrm{c}}}{\mathrm{d}P_{\mathrm{d}}} \left(\frac{\mathrm{d}\lambda}{\mathrm{d}T} \right)^{-1} . \tag{3.4}$$

The temperature dependence of the emission wavelength $\mathrm{d}\lambda/\mathrm{d}T$ is based on the temperature dependence of the band-gap in the active region, which has been calculated in section 1.1.5 as $\approx 0.34\,\mathrm{nm\,K^{-1}}$, as well as on the temperature dependence of the threshold current. The temperature coefficient of the emission wavelength was determined from several spectra, measured under short pulsed current injection with a pulse duration of 500 ns and a repetition rate of 1 kHz. The resulting duty cycle is $\cong 5 \cdot 10^{-4}$. It has been assumed, that these short-pulse current-injection conditions cause so few heating in the active region, that the temperature in the active region approximately equals the temperature on the sub-mount. This can be also derived from [Vos96] and [Puc00]. The sub-mount was temperature-stabilized at 15, 20, 25, ..., 135 °C. Fig. 3.8 (a) shows the center wavelength of the spectrum as a function of the sub-mount temperature under short pulse current injection as described above. The obtained value for $\mathrm{d}\lambda/\mathrm{d}T$ equals the

calculated temperature dependence of the band-gap in the active region. In Fig. 3.8 (b), the construction of the center wavelength λ_c as a function of the thermal dissipation loss $P_{\text{therm}} = I \cdot U - P_{\text{opt}}(I)$ is depicted. A thermal resistance of $3.35\,\text{KW}^{-1}$ has been determined. The same procedure was applied to 40 comparable devices from the same waver. An average value of $3.58\,\text{K W}^{-1}$ was determined for the thermal resistance.

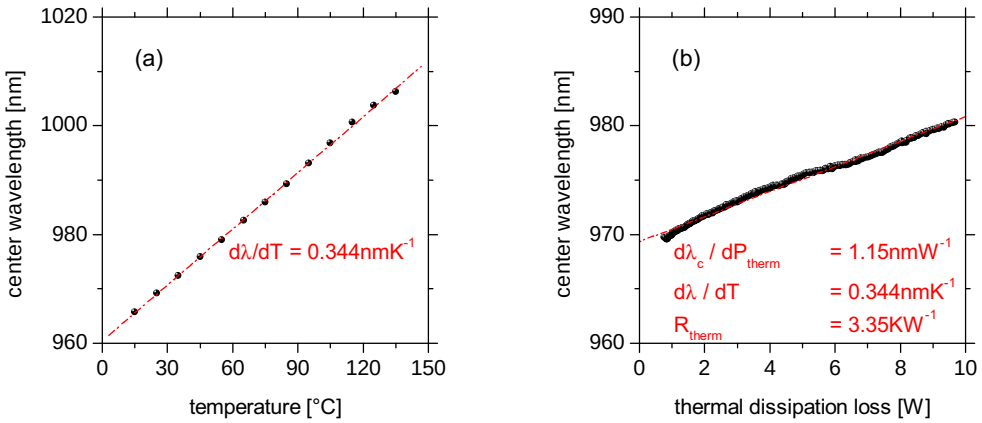

Figure 3.8: Determination of the thermal resistance R_{th}. (a) Temperature dependence of the emission wavelength, measured under short pulse current injection with a pulse duration of 500 ns and a repetition rate of 1 kHz. (b) Shift of the center wavelength as a function of the thermal dissipation loss under CW current injection. The values have been extracted from CW P-U-I characteristics and CW spectrum measurements.

The influence of temperature onto the threshold current and slope efficiency and hence, the high power properties of the diode laser can be expressed quantitatively by the threshold current characteristic temperature T_0 and the slope efficiency characteristic temperature T_1. This analysis is often applied for high power broad area laser and allows for a comparison between different devices.

To determine T_0 and T_1, P-U-I characteristics have been measured under the same short pulse current injection as used for the determination of the temperature coefficient of the emission wavelength. The sub-mount temperature was increased from 15 to 135 °C with a step size of 10 K. Again, it has been assumed that nearly no extra heat was generated in the active region, so that the device temperature could be approximated by the sub-mount temperature. The emission wavelength of the diode laser was measured as well. That allows to correct the wavelength-dependency of the

responsiveness of the InGaAs photo diode, used as a power detector. Note, that the wavelength-dependency of the responsiveness of the photo diode can be larger than the variation of the slope efficiency in the device. The measurement-setup used, is described in chapter B.2.1. In Fig. 3.9 (a), the P-U-I characteristics are depicted. The optical power was determined from the photo current of the photo diode by a calibration with a thermoelectric detector. Fig. 3.9 (b)and (c) depicts the temperature dependence of the threshold current and slope efficiency, respectively, determined from the P-U-I characteristics shown in (a).

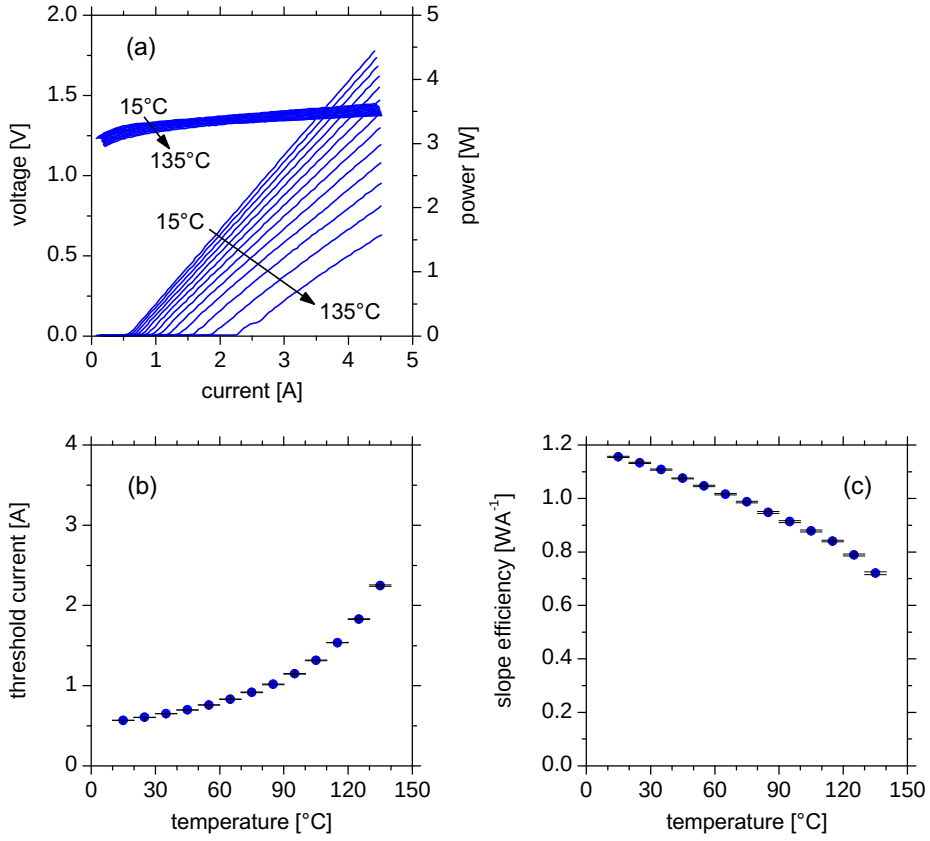

Figure 3.9: Temperature dependence of the threshold current and slope efficiency between 15 C and 135 C (10 C step size) under short pulse current injection with a pulse duration of 500 ns and a repetition rate of 1 kHz. (a) P-U-I characteristics. (b) Threshold current as a function of the temperature. (c) Slope efficiency as a function of the temperature. Threshold current and slope efficiency were determined from linear fits of the P-I characteristics, errors are indicated.

As a consequence of the exponential model for the temperature dependence of the threshold current and slope efficiency, T_0 and T_1 can be determined from a linear fit of $\ln(I_{\mathrm{th}}/I_0)$ and $\ln(S/S_0)$ as a function of T, respectively. These diagrams are shown in Fig. 3.10.

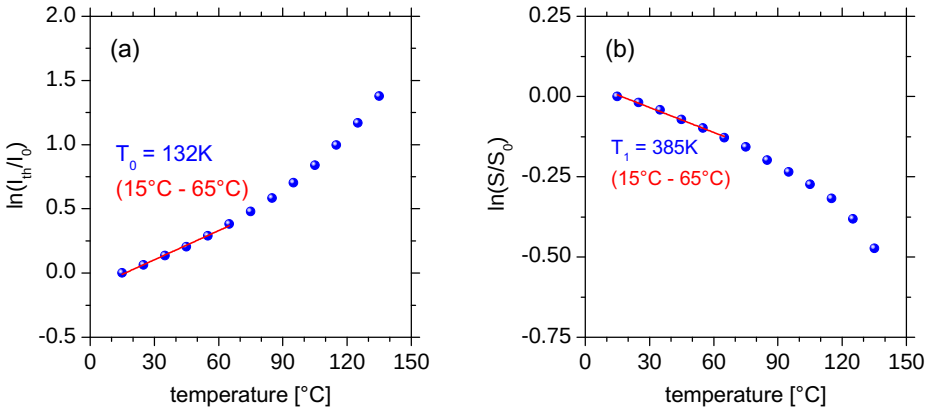

Figure 3.10: Logarithmic diagrams of (I_{th}/I_0) and (S/S_0) for the determination of T_0 and T_1. (a) $\ln(I_{\mathrm{th}}/I_0)$ as a function of T, T_0 has been determined from a linear fit between 15 and 65° C. (b) $\ln(S/S_0)$ as a function of T, T_1 has been determined from a linear fit between 15 and 65 °C.

A threshold current characteristic temperature $T_0 = 132\,\mathrm{K}$ and a slope efficiency characteristic temperature $T_1 = 385\,\mathrm{K}$ have been determined from a linear fit between 15 °C and 65 °C, which expected to be the relevant temperature range for CW applications ($T_0 = 145\,\mathrm{K}$, $T_1 = 422\,\mathrm{K}$ between 15 °C and 65 °C). T_0 and T_1 are the inverse values of the gradients, respectively. It is suitable to determine the characteristic temperatures at temperatures, the active region will have under CW current injection at 25 °C heatsink temperature and at output powers up to 10, W. Assuming an average thermal resistance $R_{\mathrm{th}} = 3.58\,\mathrm{W\,A^{-1}}$ and a power conversion efficiency at 10 W of $\eta_{\mathrm{pc}} = 0.64$, one obtains a temperature rise in the active region by $\approx 20\,\mathrm{K}$ from 25 to $\approx 45\,^{\circ}\mathrm{C}$. The temperature range between 75 °C and 135 °C has not been taken into account. Substantial deviations from linearity in $\ln(I_{\mathrm{th}}/I_0)$ and $\ln(S/S_0)$ can be attributed to a decrease in the internal quantum efficiency at higher temperatures due to increasing current leakage. Generally, the low aluminum content in the waveguide of only 15 % is expected to degrade T_0 and T_1 because the carrier confinement depends on the barrier hight of the quantum wells, which on its part, depends on the barriers and the aluminum content of the surrounding waveguide. A comparison with $T_0 = 140\,\mathrm{K}$ and $T_1 = 620\,\mathrm{K}$, reported for a waveguide design with 35 % aluminum-content

([Sch09a]), shows, that the degradation is moderate, especially for the threshold characteristic temperature.

3.2.5 Spatial emission properties of FP-BA lasers

In the following section, experimental results for the spatial emission properties of FP-BA reference lasers are presented. A verification, that the developed lasers have a vertical beam divergence angle of $\leq 45\,^\circ$ is necessary in order to confirm, that the experimental realization of the developed epitaxy design was successful. The investigation of the lateral near field profile allows to determine, if the electrically pumped stripe width is indeed, 90 μm, as targeted per design.

A narrow vertical and lateral divergence angle is important for many kinds of possible applications of BA diode lasers. One typical application example is to focus the emitted power into an optical fiber. In contrast to narrow stripe RW lasers, BA lasers discussed in this work emit their optical power in multiple lateral optical modes. In stead of analyzing the beam parameter product, which is usually performed for RW lasers [Ren92], [Eic04], [Hod05], the vertical and lateral divergence angle will be determined, in which 95 % of the optical power is emitted, as well as the FWHM value.

The BA LOC design laser beam has characteristic differences for the vertical direction (epitaxy growth direction) and the lateral direction (along the epitaxy surface). While the far field is usually single-modal and approximately gaussian shaped in vertical direction, the lateral far field is multimodal and structured, often top-hat like in the lateral direction. Because of the differences in the geometric extensions and the optical confinement strength in vertical and lateral direction, the vertical and lateral modes can be considered as separable by approximation. The lateral far field, as well as the vertical near field and far field have been measured with the setup, described in section B.1.3.

The vertical far field profiles of the FP-BA lasers show only marginal differences between different devices, even if they are from different wafers with the same epitaxy design. Example vertical far fields of laser 071002 from wafer F1850-4 are depicted in Fig. 3.11.

Figure 3.11 (a) shows the normalized vertical far field profiles at 2.5, 5, 7 and 10 W optical output power in a linear intensity scale. No changes of the field-profile can be seen in dependence on the output power (or on the related drive currents). Weak fluctuations at divergence angles of $0\,^\circ \pm 5\,^\circ$ must be attributed to feedback-effects from the plane of the detector of the measurement setup. From the logarithmic scaled far field profiles in Fig. 3.11 (b), a reduction of the background can be found between 2.5, and 5 W.

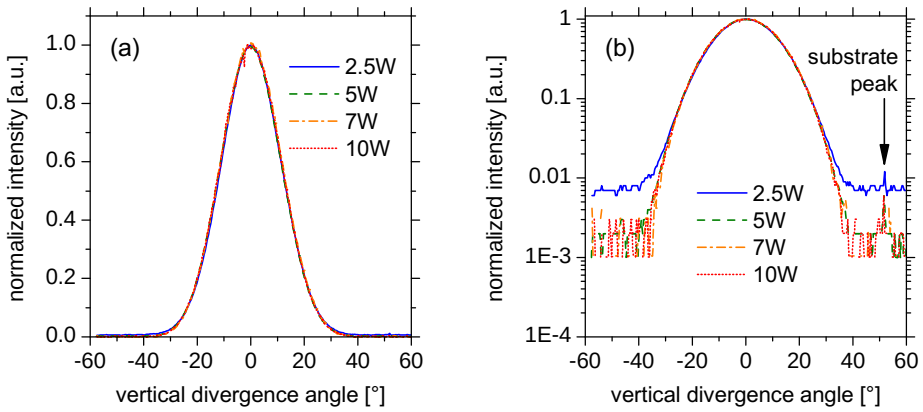

Figure 3.11: Vertical far field profile of FP-BA laser F1850-4 071002 at 25 °C heatsink temperature for optical output powers of 2.5, 5, 7 and 10 W. (a) Linear scaled intensities. (b) Logarithmic scaled intensities, a substrate peak at ≈ 51.5 ° is visible.

Additionally, a peak at ≈ 51.5 ° is visible in all profiles. A comparison with the simulated vertical far field profiles in Fig. 3.2 (b) makes it obvious to suppose, that it is related to coupling into the substrate. No measurements of the vertical near field are shown because the narrow geometric extension of the near field profile in the scale of the width of the waveguide (2.1 μm) does not allow a sufficient resolution. The available system resolution is $\sim 1\,\mu$m.

The lateral near field profiles of FP-BA lasers F1850-4 071006 and D1423-1 040203 at 25 °C heatsink temperature are shown in Fig. 3.12 (a) - (d) for optical output powers of 2.5, 5, 7 and 10 W. The near field profiles have an overall top-hat structure with additional modulations due to the superposition of multiple lateral modes. The width of the profiles with 95 % power content varies in the range between 89.1 and 100.0 μm. thus, it is clearly dominated by the 90 μm stripe width of the p-contact.

In Fig. 3.13 (a) - (d), the lateral far field profiles of FP-BA lasers F1850-4 071006 and D1423-1 040203 at 25 °C heatsink temperature are depicted for optical output powers of 2.5, 5, 7 and 10 W. In contrast to the near field profiles, a dependency on the drive current or output power is visible. The width of the profiles with 95 % power content increases from 10.4 (14.0) to 13.6 ° (16.3 °) for laser F1850-4 071006 (D1423-1 040203). The key reason for the increase of the lateral far field divergence angle of BA lasers with increasing current or power is the thermal lensing [Koe70], [Wen08], which is discussed in [Cru11a], [Cru12a].

An overview on the widths of the vertical far field profiles and the lateral

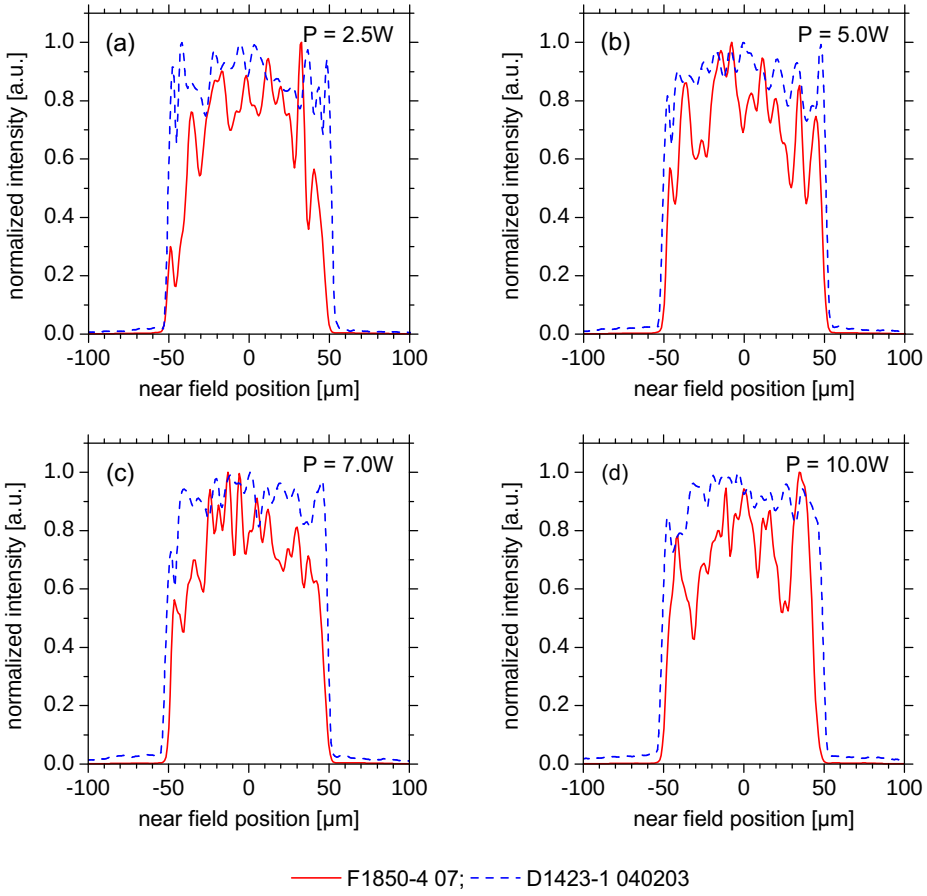

Figure 3.12: Lateral near field profile of FP-BA lasers F1850-4 071006 and D1423-1 040203 at 25 °C heatsink temperature for optical output powers of: (a) 2.5 W, (b) 5 W, (c) 7 W and (d) 10 W.

near field and far field profiles is given in table 3.3. Two major differences between the two lasers, whose spatial emission characteristics are summarized in table 3.3 are conspicuous. Firstly, the lateral near field of FP-BA laser F1850-4 071006 is close to 90 μm for both, the FWHM value and with 95 % power content. In contrast, the lateral near field of FP-BA laser D1423-1 040203 is about 10 μm broader, even though the intended design and processing is identical and a width of $\approx$ 90 μm should be expected for both devices. Secondly, the lateral far field of FP-BA laser D1423-1 040203 is $\sim$ 3 ° wider than the lateral far field of device F1850-4 071006. This could possibly be explained with the lower power conversion efficiency (see table 3.2), which leads to stronger thermal lensing and might broaden the lateral far

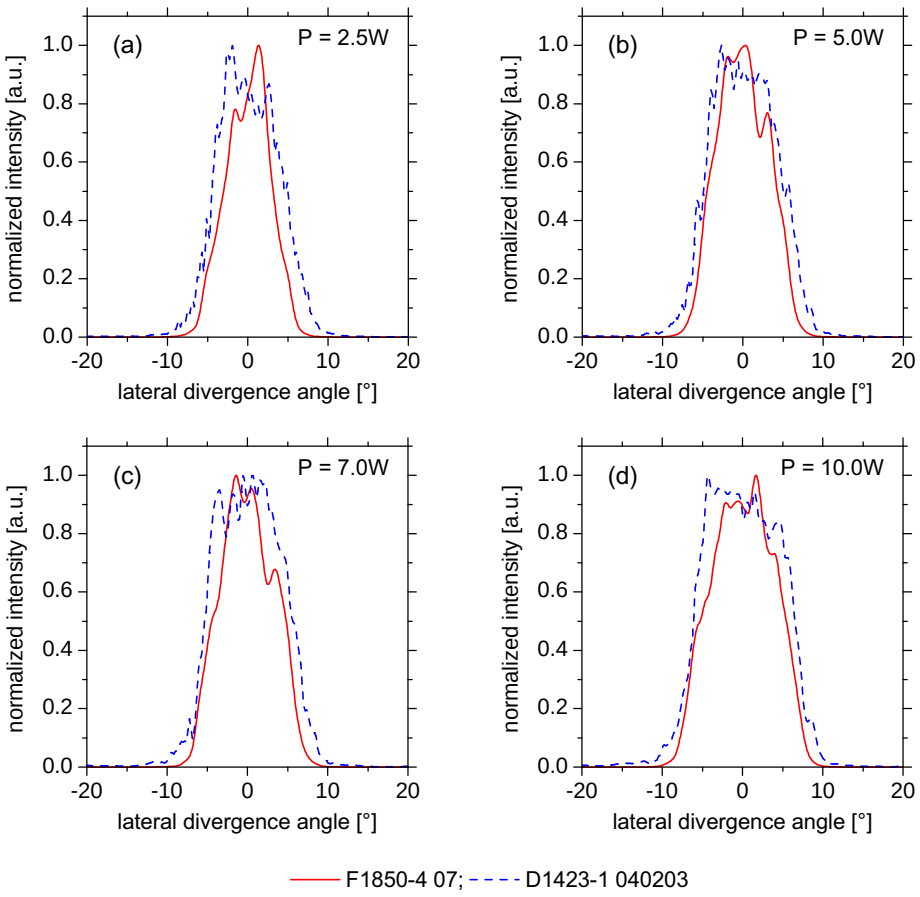

Figure 3.13: Lateral far field profile of FP-BA lasers F1850-4 071006 and D1423-1 040203 at 25 °C heatsink temperature for optical output powers of: (a) 2.5 W, (b) 5 W, (c) 7 W and (d) 10 W.

field divergence. Nevertheless, stronger thermal lensing is expected to cause a narrowing of the lateral near field, which is in antagonism to the widths of the lateral near field, measured for device D1423-1 040203, compared to F1850-4 071006.

3.3 Development of the DFB grating

3.3.1 Properties of the DFB grating

The presence of a periodic structure that couples forward and backward propagating waves is the distinctive feature between a conventional edge

Table 3.3: Overview of the divergence angles of the vertical far field (VFF) as well as the lateral near field (LNF) and far field (LFF) from FP-BA reference lasers.

P_{opt} [W]	VFF [°] FWHM	VFF [°] W95%	LNF [μm] FWHM	LNF [μm] W95%	LFF [°] FWHM	LFF [°] W95%
F1850-4	071006					
2.5	25.5	43.2	80.8	89.1	6.1	10.4
5.0	26.3	43.4	93.7	93.2	8.7	11.3
7.0	26.3	43.8	92.0	91.4	9.2	11.8
10.0	26.3	43.6	88.6	88.4	11.7	13.6
D1423-1	040203					
2.5	–	–	102.0	99.5	9.3	14.0
5.0	–	–	101.0	100.0	10.4	14.5
7.0	–	–	99.0	99.8	10.8	14.8
10.0	–	–	99.0	100.0	12.5	16.3

emitting semiconductor FP laser and a DFB laser. Various different possibilities for the implementation of a DFB grating have been published, such as index-coupling, gain or loss-coupling (for example [Kog71], [Kog72], [Luo90], [Rob97], [SZA00]), buried gratings (for example [Yor92], [Ear98], [Cha00], [Kan06], [Kle06], [He09], [Sch09a]), surface gratings (for example [Kan09], surface gratings are more commonly used for DBR lasers, for example [Fri05]) and side-coupled gratings (for example [Kam01]).

In this work, minimal loss and very high power and power conversion efficiency is targeted. Therefore, several of the possibilities for the realization of a DFB grating must be excluded. With respect to the aim of this work and promising technical experiences at the FBH, the design options for the DFB grating that have been considered were restricted to the following fundamentals:

- Index coupling
- Buried gratings
- Second-order gratings

- Aluminum-free epitaxial layers

The decision for index-coupling and against gain or loss-coupling was made because gain or loss DFB gratings are expected to introduce crucial extra loss mechanisms and to decrease the efficiency of a DFB laser. Gain-coupling can be realized by structuring the grating into the quantum well region, so that distributed feedback is provided by a spatial-periodic gain-modulation. For the construction this means, that it is necessary, to etch through the quantum wells. This has been successfully reported for AlInGaAsP/InP lasers, [Nak89], [Luo90], [Hon99] which have been principally developed to be suitable for telecommunication applications, where it is critical to achieve a high SMSR but power conversion efficiency is not critical. Because of etching through the active region, one can anticipate a serious introduction of defects and the oxidation of the surrounding waveguide, especially if it contains aluminum. A common design option for loss-coupled DFB-RW lasers is the implementation of highly absorbing metal stripes (side-coupling), perpendicular to the etched ridge, which defines the laser stripe in lateral direction. Nevertheless, this is not adequate for broad-area lasers, because coupling would be undefined due to the appearance of multiple lateral modes. On the one hand, differential overlap of lateral modes with the metal stripes would cause a graduation in coupling-strength for different lateral modes. On the other hand, the internal loss is increased.

The DFB grating can be positioned either enclosed within the epitaxy layers (buried gratings) or etched into the epitaxy layers after finishing the epitaxial growth (surface gratings). The technical requirements for low loss buried gratings are of a very high level, because the epitaxial growth must be interrupted for lithographic structuring and continued afterwards. Surface gratings have the advantage that they can be structured when the epitaxial growth is finished. Their disadvantages are that a large etch depth is required what makes it difficult to achieve a targeted duty-cycle and low coupling coefficient. They also make soldering p-side down more complicated, especially for low Bragg orders where a significant fraction of the p-side is disturbed by etched grooves. Otherwise, mounting the lasers p-down with a low thermal and electrical resistance is required for high power, high efficiency DFB-BA lasers. Although the technical requirements for low loss buried gratings are very high as mentioned above, the decision was made for this type of DFB gratings. Buried DFB gratings allow for a precise adjustment of the coupling coefficient via the refractive index contrast and the position within the waveguide. The challenge is to etch the grating into the surface after the first epitaxy with a minimum degradation of the semiconductor material and to overgrow the patterned surface with a very low defect density.

First-order Bragg gratings would have the advantage that they do not lead to extra radiation loss what can be mathematically expressed with a real coupling coefficient. The usage of higher-order Bragg gratings allows to enlarge the dimension of the grating structure, which is often used to make their lithographic preparation more precise and better reproducible as for example discussed in [Cru12b]. A precise preparation is of exceptional importance for second- and higher-order gratings, where the duty cycle defines not only the real part of the coupling coefficient, but also the imaginary part, which causes extra radiation loss (see chapter 1.2.2). For example, considering a 975 nm laser and an effective refractive index of 3.42, one obtains a grating period of 143.5 nm for a first-order DFB grating and 285.1 nm for a second-order DFB grating, respectively. One has to consider that first-order DFB gratings reach their maximum coupling coefficient at a duty cycle of 1/2, while a duty cycle of 1/4 and 3/4 corresponds to the maximum coupling coefficient for a second-order DFB grating and simultaneously, to (see chapter 1.2.2). In both cases, the resulting grating stripe width that has to be precisely adjusted is 71.3 nm. In order to obtain $\geq 80\,\%$ of the maximum possible real coupling coefficient $|\Re[\kappa]|$ for a second-order grating, a deviation of the stripe width of approximately ± 29 nm ($\approx 40\,\%$ of 71.3 nm) is tolerable, due to the sinusoidal shape of $\Re[\kappa](c_\mathrm{d})$.

In general, two methods can be used for exposure of the photo-resist during the lithographic structuring - laser holography and electron beam scribing. With respect to the fact that electron beam scribing is much more time-consuming, feasibility with laser holography has been considered in this work. If the duty-cycle is successfully adjusted to 1/4 or 3/4 ($\pm$ 1/10), the imaginary part of the coupling coefficient is at least two orders of magnitude lower than the real part, which can be, for example, extracted from the diagram in Fig. 1.14. For such a DFB grating and considering that with $\kappa \cdot L \leq 1$, the contribution to the loss in the laser should therefore be negligible in good approximation.

Now the question arises, whether a duty-cycle of 1/4 or 3/4 should be targeted. Therefore it has to be clarified, how the duty cycle c_d is defined with respect to the etching and the proportion of the lower / higher index of refraction part within one period. From the fabrication point of view it is intuitive to define the duty cycle as the fraction of the remaining grating stripes, relative to the grating period, which consists of one grating stripe and one etched groove. In the derivations in section 1.2.2 which are based on [Kaz85], the duty cycle has been defined as $c_\mathrm{d} = (\Lambda - b)/\Lambda$, where b is the width of the etched grooves and Λ is the grating period. Thus, $\Lambda - b$ is the width of the remaining grating stripes. This is in agreement with the definition of the duty cycle which defines the x-axis in Fig. 1.14. With respect

to the real coupling coefficient and radiation loss, the choice of $c_\mathrm{d} = 1/4$ or $c_\mathrm{d} = 3/4$ will lead to the same results. Minor differences occur due to the fact, that the effective wave guide changes with c_d.

There is still another aspect which has to be considered in order to find the best choice for the duty cycle. Depending on the properties of the semiconductor materials in the grating region and its hetero-interfaces, the choice of $c_\mathrm{d} = 1/4$ or $c_\mathrm{d} = 3/4$ may also have a relevant impact on the carrier (hole) transport through the grating region. This insight has to be considered after the semiconductor layer system in which the grating will be etched and overgrown subsequently, is chosen.

Buried DFB gratings require to use two step epitaxy process. This means that the surface of the first epitaxy will be exposed to air, directly after the epitaxy and also after the ex-situ lithographic structuring of the DFB grating. Therefore, no aluminum should be contained in the epitaxy layers of the grating which are exposed to air, because aluminum atoms would otherwise provoke the formation of aluminum oxides. These aluminum oxides are very stable and difficult to remove, because they cannot be desorbed in the MOVPE reactor at temperatures of $\sim 680\,^\circ\mathrm{C}$ like this is possible with oxides on GaAs and InGaP.

Furthermore, a target for the coupling coefficient of the DFB grating must be defined. Two assumptions can help to determine the adequate magnitude of the coupling coefficient for a high power and efficiency DFB laser. On the one hand, the resonator loss α_DFB of the lowest threshold gain mode of the DFB-BA laser should be approximately in the same range as the mirror loss α_m of an efficiency optimized high power FP-BA laser. This has been derived in section 1.2.5 under the assumption, that both, the DFB-BA and FP-BA laser have the same internal optical loss and internal quantum efficiency. High power and efficiency FP-BA lasers, which were developed during this work and are characterized in section 3.2, shall be used for reference, as mentioned above. On the other hand, the resonator loss α_DFB of the lowest threshold gain mode must be smaller than the mirror loss $\alpha_\mathrm{m}^\mathrm{DFB} = (1/2L) \cdot \ln[1/(R_\mathrm{f}^\mathrm{DFB} \cdot R_\mathrm{r}^\mathrm{DFB})]$ of FP modes in the DFB laser, for example $\alpha_\mathrm{DFB} \leq 0.8\,\alpha_\mathrm{m}^\mathrm{DFB}$. Otherwise, FP-like modes might reach threshold in some distance to the Bragg wavelength and disturb the spectral stabilization of the DFB-BA laser.

If one assumes a FP-BA laser with $L = 3\,\mathrm{mm}$ cavity length and facet reflectivities of $R_\mathrm{f}^\mathrm{FP} = 2\,\%$ and $R_\mathrm{r}^\mathrm{FP} = 96\,\%$ and a DFB-BA laser with the same cavity length, and facet reflectivities of $R_\mathrm{f}^\mathrm{DFB} = 0.09\,\%$ and $R_\mathrm{r}^\mathrm{DFB} =$

98 %, one obtains:

$$\alpha_{\mathrm{m}}^{\mathrm{FP}} = \frac{1}{2L} \ln\left(\frac{1}{R_{\mathrm{f}}^{\mathrm{FP}} R_{\mathrm{r}}^{\mathrm{FP}}}\right) \approx 6.6\,\mathrm{cm}^{-1} \tag{3.5}$$

$$\alpha_{\mathrm{m}}^{\mathrm{DFB}} = \frac{1}{2L} \ln\left(\frac{1}{R_{\mathrm{f}}^{\mathrm{DFB}} R_{\mathrm{r}}^{\mathrm{DFB}}}\right) \approx 11.8\,\mathrm{cm}^{-1}. \tag{3.6}$$

From the estimate mentioned above, one finds an approximate magnitude for the DFB loss of $\alpha_{\mathrm{DFB}} \approx 6.6\,\mathrm{cm}^{-1}$. Additionally, one obtains an upper bound for the DFB loss of $\alpha_{\mathrm{DFB}} \leq 0.8 \cdot 11.8\,\mathrm{cm}^{-1} \approx 9.4\,\mathrm{cm}^{-1}$.

Now, one needs to determine the values of the coupling coefficient, that correspond to $\alpha_{\mathrm{DFB}} = 6.6\,\mathrm{cm}^{-1}$ and $\alpha_{\mathrm{DFB}} = 9.4\,\mathrm{cm}^{-1}$. Using the numerical calculations, presented in section 1.2.4, one obtains that a coupling coefficient of $\kappa \approx 1.4\,\mathrm{cm}^{-1}$ corresponds to $\alpha_{\mathrm{DFB}} = 6.6\,\mathrm{cm}^{-1}$ and $\kappa \approx 0.5\,\mathrm{cm}^{-1}$ corresponds to $\alpha_{\mathrm{DFB}} = 9.4\,\mathrm{cm}^{-1}$. A third estimate can be derived from the requirement for a uniform field profile along the cavity axis, $\kappa \cdot L = 1$, that avoids multiple longitudinal mode lasing, caused by longitudinal gain spatial hole burning. This results in $\kappa \approx 3.3\,\mathrm{cm}^{-1}$.

One finally obtains the following values of orientation for the magnitude of the coupling coefficient for high power and efficiency DFB BA lasers:

$$\begin{aligned}
\kappa &\geq 0.5\,\mathrm{cm}^{-1}\,(\text{avoid lasing on FP} - \text{like modes}) \\
\kappa &\approx 1.4\,\mathrm{cm}^{-1}\,(\text{high performance FP laser}) \\
\kappa &\approx 3.3\,\mathrm{cm}^{-1}\,(\kappa L = 1).
\end{aligned}$$

For the first iteration, the aim is to realize 3 mm long DFB-BA lasers, containing a second-order DFB grating with a coupling coefficient of approximately $3\,\mathrm{cm}^{-1}$ (corresponding to $\alpha_{\mathrm{DFB}} \approx 3.9\,\mathrm{cm}^{-1}$). Thus, the coupling strength will be reduced to $\kappa \cdot L \approx 1$, compared to earlier work [Sch09a], where $\kappa \cdot L \approx 1.9$ was found to be much too strong to achieve high differential quantum efficiency. Based on the calculations, presented in section 1.2.5, the differential quantum efficiency should reduced by only $\sim 2\,\%$, compared to the value for a comparable high performance FP-BA laser. This would be a clear benefit, compared to what has been found in [Sch09a] and [Sch09b]. A coupling strength of $\kappa \cdot L \approx 1$ is proposed in literature to provide the best conditions for single longitudinal mode operation (at least close to threshold). Furthermore, a very good suppression of lasing on FP-like modes is expected, because a front facet reflectivity of $R_{\mathrm{f}} \approx 10\,\%$ would be required to achieve $\alpha_{\mathrm{m}} = 3.9\,\mathrm{cm}^{-1}$ with the same $R_{\mathrm{r}} \approx 96\,\%$.

The question arises, which semiconductor materials are applicable for the monolithic integration of such DFB gratings into the $Al_{0.15}Ga_{0.85}As$ waveguide. The following requirements have to be fulfilled: (1) The material must

have a refractive index contrast to $Al_{0.15}Ga_{0.85}As$. (2) The lattice constant of the semiconductor crystal must be close to the one of $Al_{0.15}Ga_{0.85}As$ to avoid strain. (3) The band-structure in the grating region should not form quantum confined regions or barriers for the majority-carriers, so that carrier transport is not too much degraded with adequate doping. (4) Structuring with lithographic techniques, as selective etching, must be possible. (5) The semiconductor material must be free of aluminum.

By avoiding aluminum in the semiconductor material of the grating region, the elements indium (In) and phosphor (P) can be combined with gallium (Ga) and arsenic (As) to binary, ternary or even quaternary III/V semiconductors. Possible binary materials are the arsenides GaAs and InAs as well as the phosphites GaP and InP. These binary III/V semiconductors are the vertexes of material compositions, shown in Fig. 3.14, were the lattice constants a, energy gaps E_g and refractive indices n (at 975 nm) of ternary semiconductors are depicted. The band gap energy and lattice constants were calculated as functions of the material compositions, following the approximate polynomial equations from [PTI11]. The refractive indices at 975 nm were calculated, following [Afr74], [Buu79], [Cam85] and [Pie11]. The calculation is based on the modified single oscillator for the refractive index, described by Buus *et al.* [Buu79] and is valid for photon energies close to the band gap energy. As a guide-line, the curves for $Al_{0.15}Ga_{0.85}As$ are shown as well.

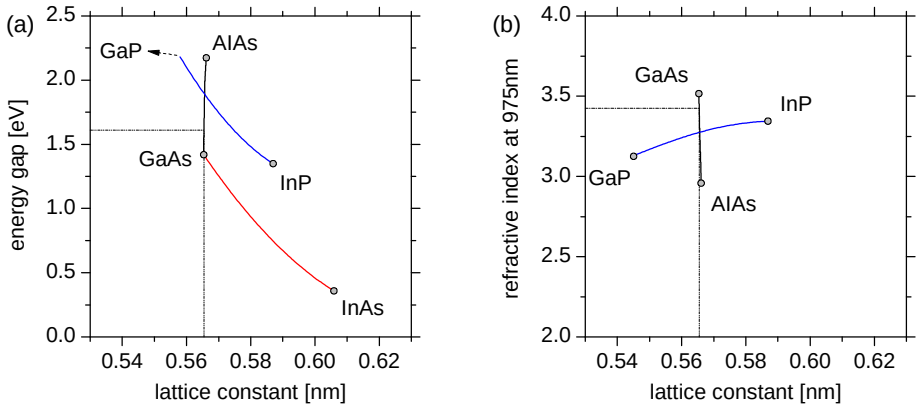

Figure 3.14: Band-gap energies (a) and refractive indices at 975 nm (b) of ternary III/V semiconductor material compositions versus lattice constant [PTI11], [Afr74], [Buu79], [Cam85], [Pie11]. The values for the waveguide material $Al_{0.15}Ga_{0.85}As$ are shown as a guide-line.

One can directly derive from Fig. 3.14, that $In_yGa_{1-y}P$, lattice-matched

to $Al_{0.15}Ga_{0.85}As$, would be a possible choice for a grating material with a negative refractive-index contrast to the surrounding waveguide material. The material choice of $In_{0.49}Ga_{0.51}P$ as effective grating component means, that the band-gap is increased in the grating region from $E_g\,(Al_{0.15}Ga_{0.85}As) = 1.611\,eV$ to $E_g\,(In_{0.49}Ga_{0.51}P) = 1.894\,eV$. In dependence on the relative band-offset in the valence- and conduction band, this leads to the formation of a barrier for electrons and holes (see chapter 3.3.3). Carrier transport through this barrier can be enhanced via a higher doping level, compared to the waveguide. While a doping of $0.5 \cdot 10^{16}\,cm^{-3}$ is sufficient for the waveguide, the doping level will be increased in the grating region to $1.0 \cdot 10^{18}\,cm^{-3}$, in order to prevent an increase of the voltage drop via an increase in series resistance or series voltage.

At a wavelength of 975 nm, the refractive index of $Al_{0.15}Ga_{0.85}As$ is 3.425 and the one of $In_{0.49}Ga_{0.51}P$ is 3.275, respectively. Thus, the refractive index contrast is 0.150. Because of requirements from processing, a buried DFB-grating will usually consist of multiple semiconductor layers. Thereby, the refractive index contrast might be considerably reduced.

To ensure a very secure and reproducible lithographic processing, DFB gratings often consist of a triple layer system [Sch09a], [Sch09b], [Kle06]. A thin cap layer on top serves as a lithography-mask, structured with selective etching. The middle layer is the effective grating component, it is as well structured with selective etching through the lithography-mask, formed by the cap-layer. A bottom layer is used as an etch-stop for the selective etching of the middle layer, so that the aluminum-containing waveguide under the grating layer is not exposed to the atmosphere. Using $Al_xGa_{1-x}As$ for the surrounding waveguide with $x > 0.25$, lattice matched $In_yGa_{1-y}P$ can be used for the cap- and bottom layer, while the middle layer is from GaAs [Sch09a].

In contrast to earlier reported triple layer systems [Sch09a], [Sch09b], [Kle06], thin double layer gratings will be used in this work. Firstly, these thin double layer gratings are assumed to be advantageous in terms of internal optical loss, electrical series resistance and material quality. Secondly, they ar assumed to be more appropriate to obtain low coupling coefficients, which are required for efficient high power DFB-BA lasers as discussed in section 1.2.5. For example in [Sch09a], [Sch09b], the grating consists of a sequence of 20 nm InGaP, 60 nm GaAs, 10 nm InGaP and a 10 nm GaAs cap layer (in the order of growth). After the whole structuring of the grating and before it is overgrown, the 10 nm GaAs cap layer is removed and the corrugation is etched selectively into the 10 nm InGaP and 60 nm GaAs. The lowest 20 nm InGaP remains a s an etch stop for the selective etching. Thus, the corrugation has a depth of 70 m. During the overgrowth of such gratings, various self-

assembly effects can lead to the formation of aluminum-rich and aluminum-poor regions[Bug11] and also crystal defects occur [Bug11]. Furthermore, the material interfaces which are introduced into the current path, potentially add electrical resistance [Lee97]. Earlier reported, deep etched DFB gratings have also been reported to cause additional internal optical loss [Yor92], [Cha00], [Sch09a], [Sch09b], [Cru11a], [Bug11]. The usage of only two layers for the DFB grating will be enabled by a new concept for the etching process. The lithographic structuring of the new DFB gratings is explained in detail in the following section 3.3.2.

The increased series resistance which has been observed for DFB-BA lasers, compared to reference FP-BA lasers in [Sch09a], [Sch09b], is assumed to be dominated by the interfaces in the grating region. Furthermore it is assumed, that the grating interfaces of earlier reported triple layer systems also dominate the additional internal optical loss. Consequently, thin double layer gratings are expected to allow for lower series resistances and lower internal optical loss. A 20 nm thin $In_{0.49}Ga_{0.51}P$ layer will be etched partly without an edge stop layer and serve as the effective grating component. In order to achieve well defined grating stripes, a cap-layer of 25 nm GaAs will be used on top of the $In_{0.49}Ga_{0.51}P$ and will be pre-structured selectively, in order to serve as an etch mask.

After the material system and basic design properties for the DFB grating have been chosen, the best choice of the duty cycle can be discussed. Figure 3.15 (a) shows a scheme of the DFB grating afterv the structuring process with the underlying AlGaAs waveguide, the InGaP layer and the GaAs cap layer. In this illustration, broad, shallow grooves are etched into the InGaP layer, so that narrow grating stripes are left. The resulting shape of the InGaP layer can be described as thin grating stripes (here, 50 % of the thickness), lying on a thin residual InGaP layer (here, 50 % of the thickness). GaAs cap stripes are left over on top of the InGaP grating stripes.

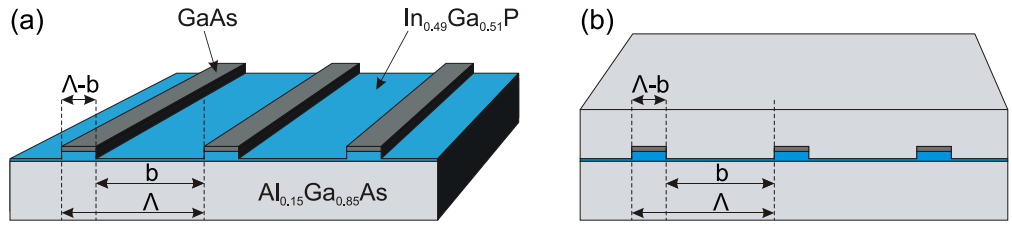

Figure 3.15: Scheme of a double layer InGaP/GaAs DFB grating with a thin residual InGaP layer. (a) After the structuring process. (b) After the overgrowth with AlGaAs.

The duty cycle has been defined in section 1.2.2 as $c_d = (\Lambda - b)/\Lambda$, where Λ is the grating period and b the width of the etched grooves. In Fig. 3.15 (a), the duty cycle is $c_d = 1/4$. Fig. 3.15 (b) shows the DFB grating after overgrowth with AlGaAs.

It has been already mentioned, that the duty cycle of a second-order DFB grating must be $c_d = 1/4$ or $c_d = 3/4$ in order to achieve the maximum coupling coefficient from the structure. The final choice between this two possibilities can be therefore made with respect to the specific duty cycle, which will potentially enable a better charge carrier transport through the grating. From Fig. 3.15 (b) one can derive, that there are two regions with different numbers of hetero-interfaces and different layer thicknesses. Firstly, charge carriers can flow through the regions of the grooves of the grating. In this case, carriers have to cross only two interfaces (AlGaAs/InGaP and InGaP/AlGaAs) and one thin layer of InGaP. Secondly, charge carriers can also flow through the grating ridges. In contrast to the first possibility, they would have to cross three hetero-interfaces (AlGaAs/GaAs, GaAs/InGaP and InGaP/AlGaAs) and two layers, one from GaAs and one from InGaP. From the number of hetero-interfaces and from the thickness of the layers which have to be crossed by the carriers in addition to the unperturbed AlGaAs waveguide, it is assumed, that series resistance and series voltage might be lower, if the area of the grooves predominates the area of the grating ridges. In terms of the duty cycle, this means that $c_d = 1/4$ is expected to be the best choice and this case is in fact shown in Fig. 3.15.

3.3.2 Manufacturing of the DFB grating

The DFB index grating is fabricated into the laser structure by using a two step epitaxy process and lithographic techniques. The etching of the grating is performed in two different steps. The first of it is a standard selective etching of the GaAs cap layer, which is carried out outside the epitaxy reactor (ex-situ) in order to form GaAs stripes. In contrast, the second etching is performed inside the epitaxy reactor (in-situ) which means, that on the one hand, the pre-structured grating corrugation can be molded into the underlying InGaP layer with a considerable material removal and on the other hand, this can be done in the absence of atmospheric oxygen. Etching the last nanometers of the grating corrugation under the clean conditions inside the epitaxy chamber is expected to significantly reduce the amount of incorporated oxygen atoms, which are known to lead to deep level trap states [Goo91] and act as fast carrier recombination centers [Kan97]. Previously, it has been reported that in-situ etching with carbontetrabromide (CBr_4) can be used to transfer nanostructures into an InP semiconductor surface

[Ebe07]. We implement this in AlGaAs-based designs [Maa08] and in the GaAs/$In_{0.49}Ga_{0.51}P$-based grating design. The ≈ 290 nm-period photoresist line pattern which is required for the lithographic structuring of the DFB grating is generated by exposure with an ultraviolet line pattern from a krypton ion gas laser. In the following, the fabrication of the DFB grating is explained in detail and advantages and disadvantages of the used method are discussed.

After finishing the first epitaxy with the 25 nm GaAs cap layer of the grating, the wafers are taken out of the reactor. A positive photoresist is spin coated on top of the wafer. In the following process step, the photoresist is exposed with a ultraviolet light line-pattern with a period of ≈ 290 nm. The line pattern is generated by the heterodyne of the split-of beam of a krypton ion gas laser at 351 nm. Afterwards, the photoresist is developed, so that a photoresist mask remains on the wafer surface as shown in Fig. 3.16 (a). Now, the GaAs cap layer is patterned by selective etching with a solution of $C_4H_6O_6$ and H_2O_2, that stops on the $In_{0.49}Ga_{0.51}P$ layer. When the photoresist is removed, a GaAs line pattern remains on the surface and is used as an etch mask or protection cap layer for the $In_{0.49}Ga_{0.51}P$ as depicted in Fig. 3.16 (b). The photoresist is removed with a suitable photoresist remover (solvent). Afterwards, the wafers are rinsed with water to complete the cleaning process.

Subsequently, the wafers are inserted back into the MOVPE reactor. Within the reactor, the last etching step is applied with an in-situ etching technique. At first, the process temperature in the MOVPE reactor is increased to 600 °C. During the in-situ etching, the process temperature is kept at this value in order to prevent that the $In_{0.49}Ga_{0.51}P$ grating stripes, which are formed gradually during the etching process, can diffluence (indium atoms have a low binding energy) before they are overgrown with $Al_{0.15}Ga_{0.85}As$ and their shape is fixed. In-situ etching is accomplished with carbontetrabromide (CBr_4), which is conventionally used for *p*-doping with carbon. During the in-situ etching, the partial pressure of CBr_4 is 0.5 Pa, group-V-partial pressures are 5 and 25 Pa for arsine (AsH_3) and phosphine (PH_3), respectively [Maa08]. The etching rates of GaAs, $Al_{0.15}Ga_{0.85}As$ [Maa08] and $In_{0.49}Ga_{0.51}P$ were experimentally determined as ≈ 200, ≈ 190 and ≈ 360 nm h^{-1}, respectively. The observed selectivity in the etching rates enables GaAs to act as an etch mask for the $In_{0.49}Ga_{0.51}P$. However, this is not a strict selectivity like the selectivity for etching *GaAs* with a solution of $C_4H_6O_6$ and H_2O_2, which does not affect $In_{0.49}Ga_{0.51}P$ at all. The shape of the DFB grating after the in-situ etching is depicted in Fig. 3.16 (c). In the scheme it can be seen that the corrugation is transferred or molded into the $In_{0.49}Ga_{0.51}P$ layer (≈ 360 nm h^{-1}). Simultaneously, the thickness of the GaAs cap stripes is reduced as well (≈ 200 nm h^{-1}). Three different in-situ etching times (t_{is} = 90

, 120 and 150 s) have been applied to different wafers in order to achieve different etching depths into the $In_{0.49}Ga_{0.51}P$ layer. The expected changes in the shape of the resulting DFB grating will be discussed later in this section in more detail.

After finishing the ex-situ and in-situ structuring, a second epitaxy is applied on top of the grating surface. This epitaxial overgrowth starts with $Al_{0.15}Ga_{0.85}As$ in order to finish the *p*-type waveguide. Subsequently, the epitaxial growth is finish with the cladding and contact layer. The re-growth on top of the patterned surface is a critical process during the manufacturing of buried gratings. In the beginning of the re-growth, the growth temperature must be chosen low enough to ensure that especially indium atoms are not able to migrate too much. Otherwise, the grating ridges would diffluence during the overgrowth. This requirement is fulfilled by starting the re-growth at $\approx 600\,°C$, then, the process temperature is increased to the final growth temperature during the first 50 nm above the grating interface. At this low process temperatures, the growth rate must be very low to achieve a defect-free semiconductor crystal. Figure 3.16 (d) shows a scheme of the overgrown double layer GaAs / $In_{0.49}Ga_{0.51}P$ DFB grating with a duty cycle of 1/4, embedded in the $Al_{0.15}Ga_{0.85}As$ waveguide.

As already mentioned above, three different in-situ etching times $t_{is} = 90$, 120 an 150 s have been chosen. This variation will lead to wafers with three different DFB gratings. The differences of these gratings are the thickness of the GaAs cap stripes d_{GaAs}, the etch depth into the $In_{0.49}Ga_{0.51}P$ layer d_{InGaP} and the thickness of the residual $In_{0.49}Ga_{0.51}P$ layer r_{InGaP}. With increasing etching-time, the etching depth into the $In_{0.49}Ga_{0.51}P$ layer increases, while the thickness of the residual $In_{0.49}Ga_{0.51}P$ layer decreases. The sum of both values remains constant: $d_{InGaP} + r_{InGaP} = 20\,nm$. Also thickness of the GaAs cap stripes decreased with increasing etching time. From the specific indices of refraction for this materials at 975 nm it follows, that the index contrast between the ridges of the grating and the grooves and thus, the coupling coefficient of the DFB grating, increases with the etching time.

Schemes for DFB gratings, fabricated with the three different in-situ etching times $t_{is} = 90$, 120 an 150 s, mentioned above, are depicted in Fig. 3.17. In Fig. 3.17 (a), (b) and (c) the upper scheme shows the pre-structured and cleaned surface before the in-situ etching. In the lower scheme, the shape of the grating after the in-situ etching is depicted. In the small boxes below, the specific values for the thickness of the GaAs cap stripes d_{GaAs}, the etch depth into the $In_{0.49}Ga_{0.51}P$ layer d_{InGaP} and the thickness of the residual $In_{0.49}Ga_{0.51}P$ layer r_{InGaP} is given, simply calculated on the basis of the experimentally determined etching rates.

Additionally, higher material removal with increasing in-situ etching time

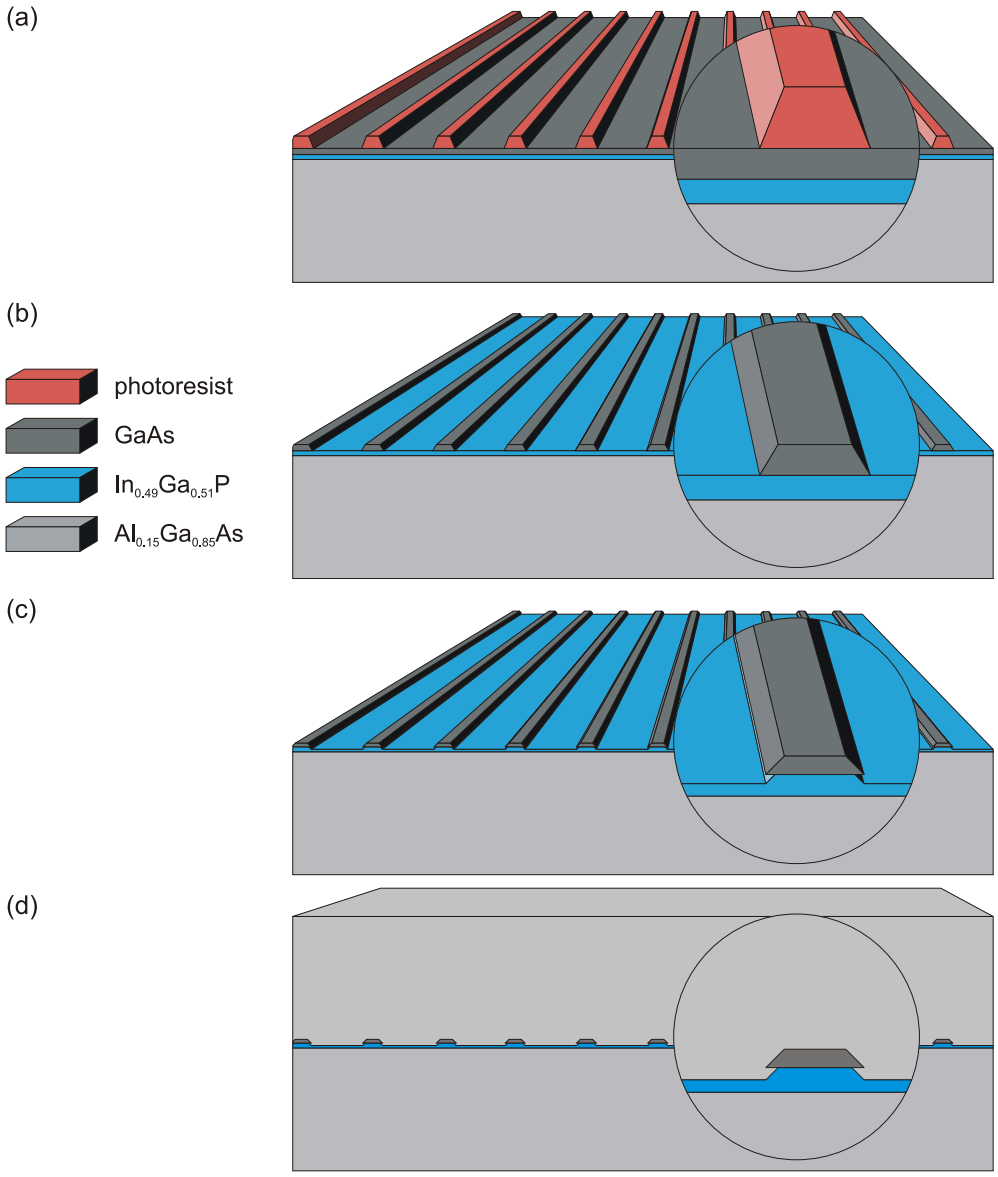

Figure 3.16: Schematic illustration of the processing of the DFB grating. (a) A mask of photoresist is structured on top of the grating layers. (b) The mask is transferred via selective etching into the GaAs cap-layer. (c) The GaAs grating is transferred with a non-selective in-situ etching into the $In_{0.49}Ga_{0.51}P$ layer. (d) The waveguide structure is finished with a second epitaxy step.

will presumably lead to a re-growth interface with a lower impurity density. Note that with increasing in-situ etching time, the duty-cycle of the grating

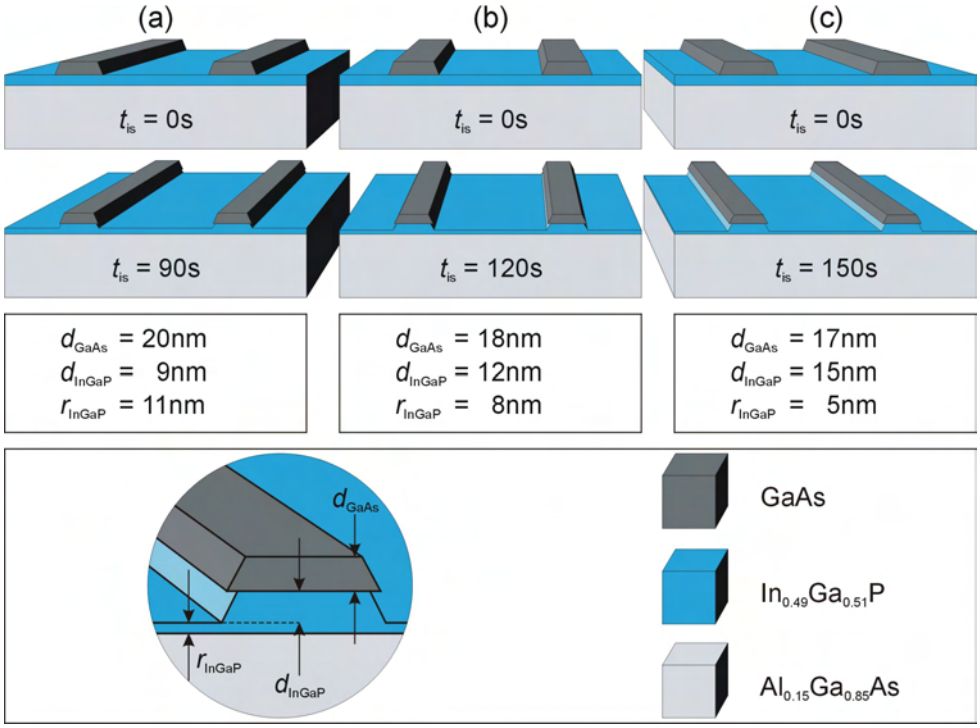

Figure 3.17: Scheme of the DFB grating before and after the in-situ etching for three different in-situ etching times t_{is}. (a) $t_{is} = 90\,s$. (b) $t_{is} = 120\,s$. (c) $t_{is} = 150\,s$. In the small boxes below, the thickness of the GaAs cap stripes d_{GaAs}, the etch depth into the $In_{0.49}Ga_{0.51}P$ layer d_{InGaP} and the thickness of the residual $In_{0.49}Ga_{0.51}P$ layer r_{InGaP} is given.

decreases as well. This occurs, because the etching does not only occur perpendicular to the wafer surface. With respect to the in-plane etching, the width of the photoresist stripes must be chosen specifically for every in-situ etching time in order to achieve a duty-cycle of 1/4 in the final re-grown DFB grating. This is also suggested in the upper schemes of Fig. 3.17 (a), (b) and (c), where the width of the GaAs cap stripes, which depends on the width of the photoresist stripes, increases with increasing target value for the in-situ etching time.

Fig. 3.18 shows a scanning tunneling electron microscope (STEM) micrograph of a buried DFB grating, which has been structured and overgrown as explained above, using an in-situ etching time of $t_{is} = 120\,s$. Four grating stripes are visible in the shown region, which extends over $\approx 1150\,nm$ along the grating interface and $\approx 100\,nm$ below and above the grating in growth direction, respectively. The structured $In_{0.49}Ga_{0.51}P$ layer (white) has a thick-

ness of ≈ 20 nm at the grating stripes and a etching is ≈ 13 nm deep in the grooves. A ≈ 7 nm thin residual layer of $In_{0.49}Ga_{0.51}P$ is left over between the grating stripes. GaAs cap layer (dark gray) is found to have a thickness of ≈ 15 nm. The layer thicknesses and the angled edge of the grating are depicted in the inset.

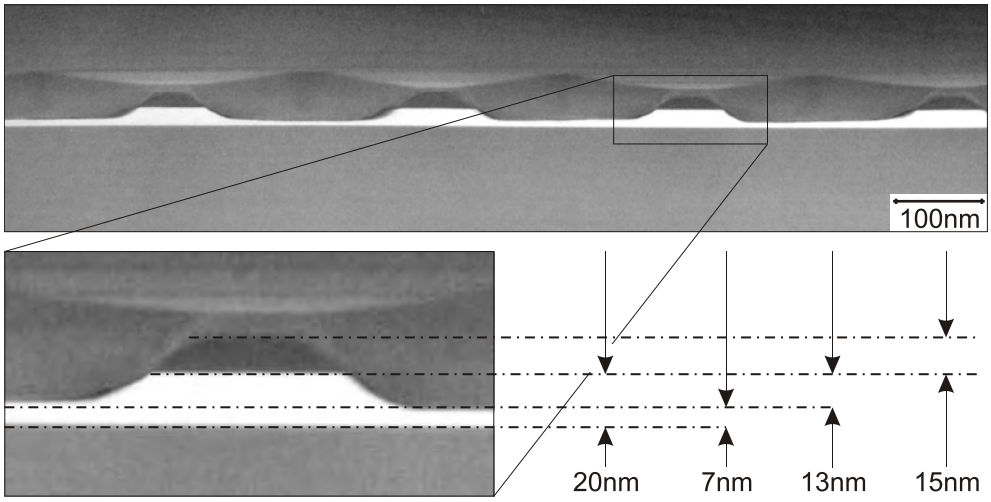

Figure 3.18: SSTEM micrograph of a buried DFB grating with ≈ 15 nm GaAs cap-layer, ≈ 20 nm $In_{0.49}Ga_{0.51}P$ layer and 120 s in-situ etching time. The edge of one grating filament and the corresponding layer thicknesses are depicted in the inset. Variations in the aluminum concentration are visible on top of the grating corrugations as slightly contrasts.

The duty cycle of the shown DFB grating is slightly larger than the targeted value of $c_d = 0.25$. With respect to the fact, that the side faces of the DFB grating are angled and the width of the grating stripe is broader at the basis and narrower on top, an average duty cycle of $c_d \approx 0.32$ can be estimated from the STEM measurements.

In the waveguide directly above the grating, a weak contrast structure provides an indication of variations in the aluminum concentration. Such formation of aluminum-rich and aluminum-poor regions which is observed in the regrown $Al_{0.15}Ga_{0.85}As$ has been already reported in [Hof01] and [Bug11]. Self organized changes in the semiconductor material composition during overgrowth of patterned surfaces have been also reported for regrown InGaAs(P) [Koo00]. The self-organized variations in the aluminum concentration result in an additional $Al_xGa_{1-x}As$ grating [Bug11] and therefor alter the overall refractive index contrast of the grating region and hence, they alter the coupling coefficient. Therefore, this effect will be discussed in more detail in the

following section 3.3.3.

The reason, why in-situ etching is applied to the DFB grating is, that this technique is expected to enable the lowest possible contamination with oxygen and other impurities in the grating region after epitaxial overgrowth. When the ex-situ pre-structured wafers are transferred back into the MOVPE reactor, a thin layer of surface oxides covers the surface which have developed under the presence of atmospheric oxygen. Depending on the used in-situ etching time, the first ≈ 5 - 15 nm (for GaAs and $In_{0.49}Ga_{0.51}P$ with $t_{is} = 90$ - 150 s) of the semiconductor surface (containing the surface oxides), are removed by in-situ etching under conditions, where nearly no new oxygen atoms are available to be incorporated into the semiconductor crystal. This is done before regrowth begins.

As already mentioned above, wafers with three different in-situ etching times $t_{is} = 90$, 120 and 150 s were fabricated for the fabrication of diode lasers, which will be characterized subsequently. A further series of wafers, fabricated with different in-situ etching times $t_{is} = 90$, 120, 150 and 180 s has been used to investigate possible differences in the material properties in the grating region. Secondary ion mass spectroscopy (SIMS) has been used for material-analysis, which allows to detect the material composition of a semiconductor layer system and also the existence and percentage of impurities like oxygen. Therefore, a hole is sputtered into the surface of the probe with a focused primary ion beam and secondary ions are then collected and analyzed with a mass spectrometer. The information about the etch depth can be used to scale the vertical position in the epitaxy structure. In Fig. 3.19, the oxygen concentration (calibrated) and the aluminum concentration (un-calibrated, shown to visualize the vertical position in the epitaxy structure) are depicted as functions of the etch depth. For orientation, the p-type cladding layer ends at $\approx 0.60\,\mu$m ($\approx 1 \cdot 10^5$ counts s^{-1} of aluminum), were the p-type waveguide begins. The p-type waveguide ($\approx 6 \cdot 10^3$ counts s^{-1} of aluminum) extends from $\approx 0.60\,\mu$m till $\approx 1.35\,\mu$m, were the DQW active region can be observed as a sharp dip in the aluminum concentration. The DFB grating is visible in the aluminum concentration as a weak variation at $\approx 0.80\,\mu$m. Please note, that the etch depth, used as x-axis is not very precise (~ 100 nm resolution).

The oxygen concentration reaches its background level in the p-type cladding layer and waveguide at. Note, that the background level of the SIMS for oxygen is calibrated only for the waveguide region and depends on the aluminum concentration in $Al_xGa_{1-x}As$. With a background level of $\approx 5 \cdot 10^{15}$ cm^{-3}, the detection limit is better than one oxygen atom per four million atoms in the $Al_{0.15}Ga_{0.85}As$ crystal.

In the grating region at $\approx 0.80\,\mu$m, the peak hight of the oxygen signal is

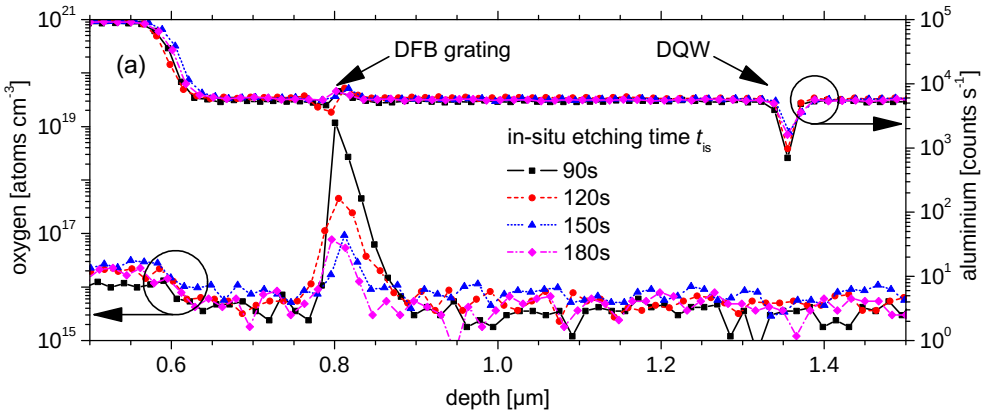

Figure 3.19: SIMS depth profiles of oxygen volume impurity density (calibrated) and aluminum content (un-calibrated) after different in-situ etching times $t_{is} = 90$, 120, 150 and 180 s.

found to be a function of the in-situ etching time t_{is}. At $t_{is} = 90\,s$, the peak oxygen contamination is $\approx 1.17 \cdot 10^{19}\,cm^{-3}$. For an increasing in-situ etching time, the peak oxygen signal decreases to $\approx 4.48 \cdot 10^{17}\,cm^{-3}$ at $t_{is} = 120\,s$, $\approx 9 \cdot 10^{16}\,cm^{-3}$ at $t_{is} = 150\,s$ and finally $\approx 8 \cdot 10^{16}\,cm^{-3}$ at $t_{is} = 180\,s$.

Admittedly, the SIMS resolution is too low to determine if the oxygen is distributed over a range along the growth direction or whether it is located at a sharp interface. Therefore it is favorable to quote both the peak volume impurity density ρ_{peak} and the calculated areal impurity density ρ_{areal}, which has been obtained by integrating over the SIMS profiles in the grating region. Both values are summarized in table 3.4. The areal impurity density must be understood as lower limits.

An in-situ etching time of $t_{is} = 120\,s$ enables to reduce the peak volume impurity density (or areal impurity density) significantly, compared to the values at $t_{is} = 90\,s$. In-situ etching times $t_{is} \geq 150\,s$ are sufficient to reduce the oxygen contamination to $\rho_{peak} \leq 1 \cdot 10^{17}\,cm^{-3}$ or $\rho_{areal} \leq 3 \cdot 10^{11}\,cm^{-2}$. This should be preferred for the fabrication of DFB gratings for DFB-BA lasers in later work. If the oxygen contaminations sufficiently reduced to achieve the same internal optical loss as it has been found for the reference FP-BA lasers in section 3.1, must be investigated subsequently. Further answers to the question, if the oxygen contaminations sufficiently reduced, will be obtained by the measurement of P-I characteristics and comparison to the P-I characteristics from reference FP-BA lasers. Certainly, using in-situ etching techniques enabled a remarkable reduction of the oxygen impurity contamination compared to buried DFB gratings, which were fabricated only

Table 3.4: Peak volume impurity density ρ_{peak} from the oxygen signal of the SIMS and calculated areal impurity density ρ_{areal} for different in-situ etching times t_{is}.

t_{is} [s]	ρ_{peak} [cm^{-3}]	ρ_{areal} [cm^{-2}]
90	$1.2 \cdot 10^{19}$	$2.4 \cdot 10^{13}$
120	$4.5 \cdot 10^{17}$	$1.6 \cdot 10^{12}$
150	$9.2 \cdot 10^{16}$	$3.0 \cdot 10^{11}$
180	$7.7 \cdot 10^{16}$	$2.6 \cdot 10^{11}$

with ex-situ etching and have for example, peak volume impurity density of $\rho_{\text{peak}} \approx 4 \cdot 10^{18}\,\text{cm}^{-3}$ [Bug11].

3.3.3 Coupling coefficient of the DFB grating

In the previous section it has been discussed, how a buried DFB grating can be fabricated on the basis of a double layer system, a two step epitaxy and in-situ etching techniques. Furthermore it has been shown that such gratings have a much lower oxygen impurity density than earlier designs, fabricated without in-situ etching [Bug11]. In this section it will be discussed how sufficient optical feedback can be achieved with the newly developed DFB gratings. It will be discussed, where in the waveguide design, the grating should be located and how the targeted coupling coefficient of $\kappa = 3\,\text{cm}^{-1}$ (see section 3.3.1) can be achieved. Considering the targeted cavity length of $L = 3\,\text{mm}$, this would lead to a coupling strength $\kappa \cdot L$ slightly below one.

If one has got the ability to achieve a buried DFB index grating by a process as explained above, the question arises, at which position in the vertical sectional plane of the waveguide structure, the grating should be positioned. On the one hand, the position of the waveguide determines, together with the refractive index contrast and duty cycle, the magnitude of the coupling coefficient. On the other hand, the grating cannot be positioned at any point in the waveguide structure, if one seeks simultaneously for minimal internal optical loss, low series resistance, a targeted coupling coefficient and good reproducibility in fabrication. In equation 1.60, the real part of the coupling

coefficient for a rectangular index grating has been expressed as:

$$h_2 = \frac{-\omega^2 \Delta\varepsilon}{2K_0 c^2} \int \mathrm{d}x \quad \Phi^2(x)\xi_2(x).$$

In the following, it is assumed that the grating has a duty-cycle very close to 1/4, so that $h_2 \cong \Re[\kappa]$, $\Re[\kappa] \gg \Im[\kappa]$ and $\Im[\kappa]$ vanishes. Thus, the magnitude of the (real) coupling coefficient depends on the contrast in the dielectric function $\Delta\varepsilon$, the vertical field profile in the waveguide $\Phi(x)$ and the fourier coefficient of the grating $\xi_2(x)$ (which contains the duty cycle). For thin, weak DFB gratings with $\Delta\varepsilon \ll \varepsilon$, the field profile $\Phi(x)$ can be approximated to be independent of the presence and position of the grating. Because of the linear dependence on $\Delta\varepsilon$, the coupling coefficient can be adjusted by placing the grating at a vertical position x with an adequate field power $\Phi^2(x)$. If the value of the coupling coefficient κ differs from the target value κ_{tar}, it can be iterative adjusted by finding a position $x^{'}$, so that $\Phi^2(x^{'}) = \Phi^2(x) \cdot (\kappa_{\mathrm{tar}}/\kappa)$.

For the position of the grating, four possibilities can be considered. The grating could either be positioned in the p-side waveguide (between the DQW and the p-cladding layer) or in the n-side waveguide (between the n-cladding layer and the DQW). Furthermore, although positions at the interfaces between the waveguide and the cladding layers and positions inside the cladding layers are possible.

The possibility to place the grating inside the cladding layers has not been considered in this work. In $\mathrm{Al}_x\mathrm{Ga}_{1-x}\mathrm{As}$-based waveguide designs, the cladding layers have a relatively high aluminum content (in this work: n-cladding layer: $x = 0.30$, p-cladding layer: $x = 0.85$). Self-organized formation of an additional grating from aluminum-rich and aluminum-poor regions could in this case lead to difficulties in adjusting the coupling coefficient. High aluminum content is also presumed to possibly degrade the crystal quality of the regrown $\mathrm{Al}_x\mathrm{Ga}_{1-x}\mathrm{As}$ material.

The possibility to place the grating inside the n-waveguide could be advantageous to achieve a low series resistance from the DFB-BA lasers, because the electrons, which were in this case the charge carriers that have to flow through the grating, have a much higher mobility than holes. In the beginning of this work, series of experiments was accomplished to integrate the grating into the n-side waveguide. This method is technically complicated because it requires to grow part of the waveguide and especially the DQW active region on top of the grating layer with its epitaxy interruption and surface corrugation. Because of a too high defect density in the quantum wells and a non-ideal planarization of the growth surface, this has not been continued.

Now, two possibilities are left to find an ideal place for the DFB grating: the interface between the p-type waveguide and the p-cladding layer and a position inside the p-type waveguide. The first of this possibilities was refused because this would require to grow the p-cladding layer with its high 85 % aluminum content on top of the grating. Nevertheless, such position for the DFB grating has been reported for aluminum-free epitaxy designs [Ear98], [Kan06], [He09]. Finally, the grating was positioned within the p-side waveguide, 630 nm above the DQW and 230 nm below the p-cladding layer. In the following, the influence of this choice for the waveguide modes will be discussed. Afterwards it is shown, that this position will potentially lead to the targeted coupling coefficient $\kappa = 3\,\mathrm{cm}^{-1}$.

Figure 3.20 (a), shows the electronic band-structure of the DFB-BA laser (un-doped case), in comparison to the band-structure of of the reference FP-BA laser. The blue solid line is given by the minimum of the conduction band edges at the Γ- and X-point of the Brillouin zone (FP-BA laser: magenta line). The blue dashed line indicates the position of the first electron energy level (FP-BA laser: magenta line). The heavy hole valence band edge is depicted as a red solid line (BA laser: orange line) and the corresponding first heavy hole energy level as a red dashed line (BA laser: orange line). From the band-structures, depicted in Figure 3.20 (a), one can derive that differences between the DFB-BA lasers and FP-BA lasers occur exclusively in the grating region, indicated in the diagram.

Fig. 3.20 (b) shows the magnified region of the DFB grating from Fig. 3.20 (a), so that the band discontinuities are clearly visible (un-doped case). In order to achieve an unresisted carrier (hole) transport, the layers of the DFB grating have a p-doping level of $2 \cdot 10^{18}\,\mathrm{cm}^{-3}$ and the regrown 230 nm-part of the p-waveguide on top of the grating has a p-doping level of $1 \cdot 10^{18}\,\mathrm{cm}^{-3}$ – in contrast the reference FP-BA lasers, whose waveguide is continuously doped with $5 \cdot 10^{16}\,\mathrm{cm}^{-3}$.

In Fig. 3.20 (c), the refractive index profile is shown in the background as a grey area. The calculated near field profiles of the four different guided modes (v = 0, 1, 2, 3) are depicted on top as solid lines. In addition, the mode profiles of the reference FP-BA laser are depicted as dotted lines. Compared to the mode profiles of the reference FP-BA laser, significant changes occur only for the second higher-order mode (v = 2, blue lines). This higher-order mode has substantial intensity at the vertical position of the grating. Especially for the fundamental mode, the assumption, that the near field profile is not changed due to the presence of the DFB grating, as mentioned above, is a good approximation.

Depending on the overlap with the highly absorbing cladding layers and the highly doped DFB grating, the internal loss α_i ranges from $0.59\,\mathrm{cm}^{-1}$ for

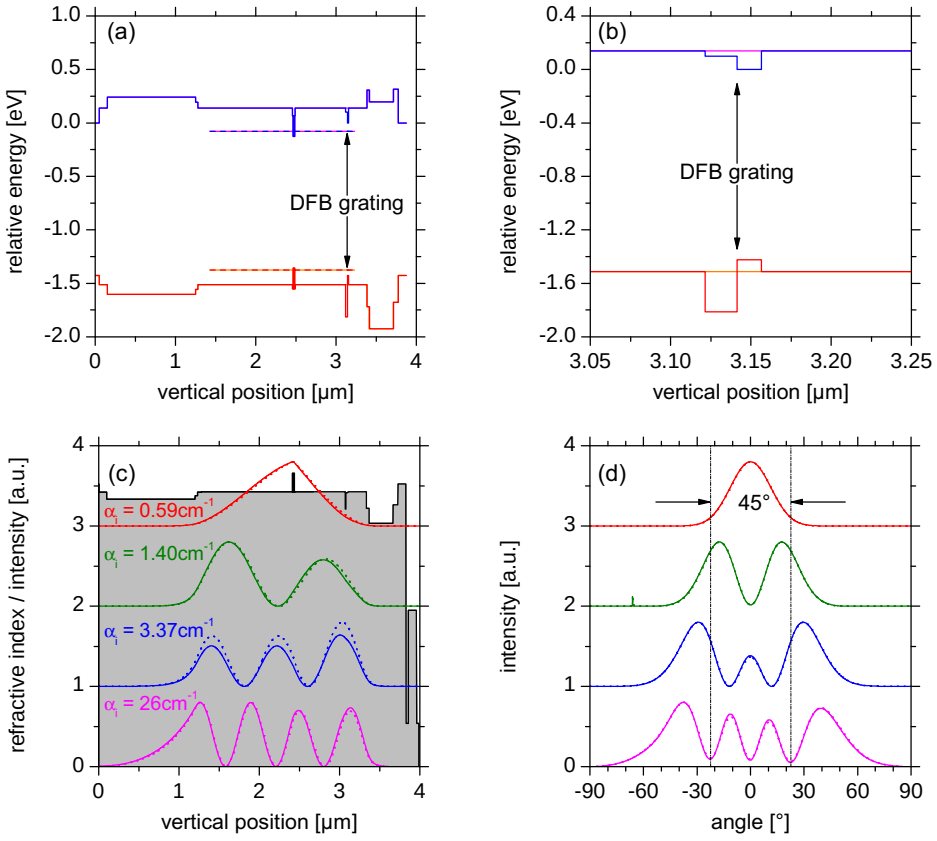

Figure 3.20: Electronic band-structure of the epitaxy design for high-efficiency, high-power DFB lasers. (a) Minimum of the conduction band edges at the Γ- and X-point (blue solid line, BA laser: magenta line) and the heavy hole valence band edge (red solid line, BA laser: orange line). The corresponding first electron energy level and first heavy hole energy level are depicted as blue and red dashed lines respectively (BA laser: magenta and orange line). (b) Magnified section of (a) in the DFB grating region. (c) Refractive index profile and the simulated near field amplitude profiles of the waveguide modes with the corresponding internal losses indicated (modes of BA laser: dotted lines). (b) Simulated far field angular distribution of the waveguide modes (modes of BA laser: dotted lines).

the fundamental mode to $26\,\mathrm{cm}^{-1}$ for the highest-order mode. The simulated internal optical loss is increased, compared to the epitaxy design for the reference FP-BA lasers, indicated in Fig. 3.2. For the fundamental mode ($v = 0$), the internal optical loss is increased by $\Delta\alpha_\mathrm{i}^{\mathrm{DFB-FP}} = 0.12\,\mathrm{cm}^{-1}$. This is roughly in the range of the precision for the determination of α_i, discussed in section 3.1. Note, that the internal optical loss for the FP-BA lasers has

been experimentally determined as $\alpha_\mathrm{i} \approx 1.0\,\mathrm{cm}^{-1}$ instead of the simulated value, which was $\alpha_\mathrm{i} = 0.47\,\mathrm{cm}^{-1}$. With increasing vertical mode order v, the increase of the internal optical loss grows monotonically, $\Delta\alpha_\mathrm{i}^{\mathrm{DFB-FP}} = 0.12$, 0.35, 0.96 and $2\,\mathrm{cm}^{-1}$ for $v = 0$, 1, 2, 3. Thus, the contribution from the internal optical loss to the discrimination of higher-order waveguide modes should be comparable for the DFB-BA and FP-BA lasers.

In Fig. 3.20 (d), the calculated far field profiles of the waveguide modes are depicted as a function of the vertical divergence angle. Again, the mode profiles for the FP-BA lasers are depicted additionally as dotted lines. As targeted, the fundamental mode contains 95 % of the emitted optical power within an divergence angle of $44.6\,^\circ \leq 45\,^\circ$. The deviations of far field profiles for the DFB-BA and FP-BA reference lasers in the far field are negligible.

The characteristics of the refractive index and the valence band edge (un-doped case) for the region of the DFB grating are shown in Fig. 3.21 (a). For a better understanding, the grating is subdivided in to three different regions in vertical direction, as illustrated in Fig. 3.21 (b). Region I is the residual $In_{0.49}Ga_{0.51}P$ layer, which exists at every longitudinal position z. Region II is the part of the grating stripes that also consists of $In_{0.49}Ga_{0.51}P$. It is responsible for the active refractive index contrast. The GaAs cap layer is labeled as region III. The cap layer reduces the active refractive index contrast of Region II, but it is required from technical reasons in the fabrication of the grating as mentioned in section 3.3.2. In Fig. 3.21 (a), the characteristics of the refractive index and valence band edge are depicted for a transversal sections through a grating ridge (red solid curves) and through a longitudinal position between two grating ridges (blue dashed curves). For the refractive index, an averaged curve for a duty cycle of 1/4 is depicted as well as a black dotted line. Note, that the refractive index is averaged over the grating ridges (regions II and III). The curve of the valence band edge forms (in the un-doped case) a quantum barrier in $In_{0.49}Ga_{0.51}P$ and in addition, a weak quantum well in the GaAs cap layer. An increased p-type doping level of $2 \cdot 10^{18}\,\mathrm{cm}^{-3}$ is used to enhance the transport of holes through the grating region. Nevertheless, one must expect that the carrier transport is more hindered through the grating ridges than through the region in between them. Thus, a low duty-cycle as 1/4 should decrease the series resistance of the lasers compared to a duty-cycle of 3/4.

As explained above, the coupling coefficient of the DFB grating can be regulated by the vertical position of the grating in the waveguide structure. A translational displacement of the grating from a distance of only 130 nm from the DQW (blue curve) to 730 nm, close to the p-cladding layer (red curve), is depicted in Fig. 3.21 (c). The field profile of the fundamental waveguide mode is pushed towards the n-type waveguide because of the low

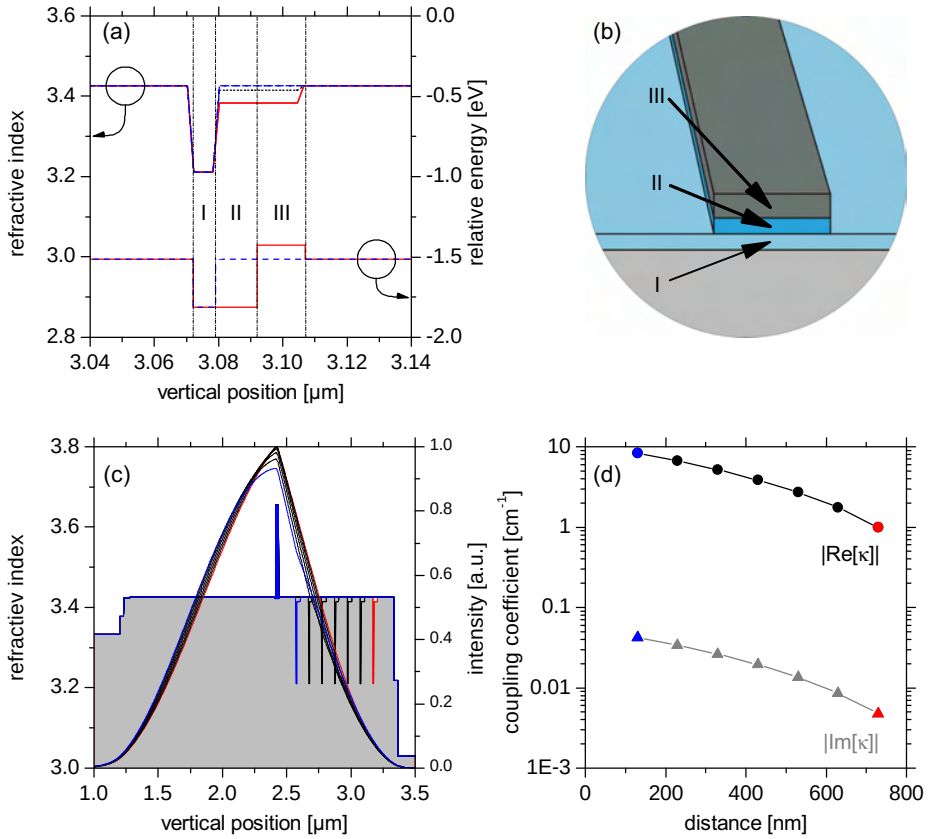

Figure 3.21: Characteristics of the refractive index and conduction band edge (un-doped case) in the grating region and variation of the position of the DFB grating and its influence on the coupling coefficient. (a) Characteristics of the refractive index and valence band edge (un-doped case) in the grating region within a grating ridge (blue dashed lines), between two grating ridges (red solid lines) and the averaged characteristics for a duty-cycle of 1/4 (black dotted line). (b) Magnified scheme of a grating ridge before overgrowth, showing the residual $In_{0.49}Ga_{0.51}P$ layer I, the etched $In_{0.49}Ga_{0.51}P$ grating ridge II and the GaAs cap layer III. (c) Refractive index profile and the simulated near field profiles of the fundamental waveguide mode for (130 (blue), 230, ..., 730 (red))nm distance between the DFB grating and the active region. (d) Real and imaginary part of the coupling coefficient as a function of the distance between the DFB grating and the active region.

average refractive index of the grating layers. This effect reduces, when the grating is positioned stepwise closer to the p-cladding layer. The confinement with the DQW increases coincidental. Fig. 3.21 (d) shows the dependence of

the absolute values of the real and imaginary part of the coupling coefficient ($|\Re[\kappa]|$ and $|\Im[\kappa]|$) on the distance between the grating and the DQW. Because of the negative contrast between the refractive index of the DFB index grating and the waveguide, both, the real and imaginary part of the coupling coefficient have negative values. While the real part decreases from $8.26\,\mathrm{cm}^{-1}$ to $1.00\,\mathrm{cm}^{-1}$, the imaginary part decreases from $0.04\,\mathrm{cm}^{-1}$ to $< 0.01\,\mathrm{cm}^{-1}$. The absolute value of the imaginary part is more than two orders of magnitude smaller than the real part. At a distance of 730 nm from the DQW (the later position of the grating in iteration I), the coupling coefficient is $-1.76\,\mathrm{cm}^{-1} - \mathrm{i}\,0.01\,\mathrm{cm}^{-1}$. As explained above, fluctuations in the aluminum content in the first ~ 20 nm above the residual $In_{0.49}Ga_{0.51}P$ layer further alter the coupling coefficient. This will be discussed in the following paragraph.

In Fig. 3.22 (a), a STEM micrograph of the grating layer is depicted [Mar09]. Within the $Al_xGa_{1-x}As$ of the second epitaxy, areas of aluminum accumulation (light) and depletion (dark) are visible as slightly contrasts [Mar09]. The process of an inhomogeneous aluminum distribution is based on two effects. Firstly, aluminum atoms have a lower mobility (diffusion length) on the growth surface than gallium atoms. Secondly, crystal growth occurs along different crystalline growth directions. Multiple facets are provided by the angled side surfaces of the grating ridges and in the plain grooves between two grating ridges. Fig. 3.22 (b) illustrates an observed {113} side surface at the interface between the $In_{0.49}Ga_{0.51}P$ grating ridge and the $Al_xGa_{1-x}As$, that is filled into the groove [Mar09]. Different crystalline growth direction may have their characteristic aluminum content for a given ratio of provided aluminum and gallium atoms via the vapor phase. Even though areas of multiple specific crystalline growth directions merge over short geometric distances, the inhomogeneous aluminum distribution results basically in two areas A1 and A2 which are characterized by an aluminum-concentrations x of $x(A1) = 0.22 \pm 0.06$ and $x(A2) = 0.12 \pm 0.04$ as determined by [Mar09] with scanning energy dispersive X-ray spectroscopy (EDXS) and indicated in Fig. 3.22 (c). For a theoretical analysis of the influence of the inhomogeneous aluminum distribution on the coupling coefficient of the DFB grating, a rectangular simplification as depicted in Fig. 3.22 (d) has been applied.

In the simulation of the coupling coefficient it has been assumed, that area A1 has a thickness in growth direction of 24 nm, as estimated from the experimental results. One finds that the contrast in the index of refraction within the grating layer increases from 0.042236 to 0.061783. In combination with a change of the confinement of the mode profile with the effective grating area from 0.36 % to 0.66 %, this results in an increase of the coupling coefficient from $\kappa = -1.76\,\mathrm{cm}^{-1} - \mathrm{i}\,0.01\,\mathrm{cm}^{-1}$ to $\kappa = -4.41\,\mathrm{cm}^{-1} - \mathrm{i}\,0.03\,\mathrm{cm}^{-1}$

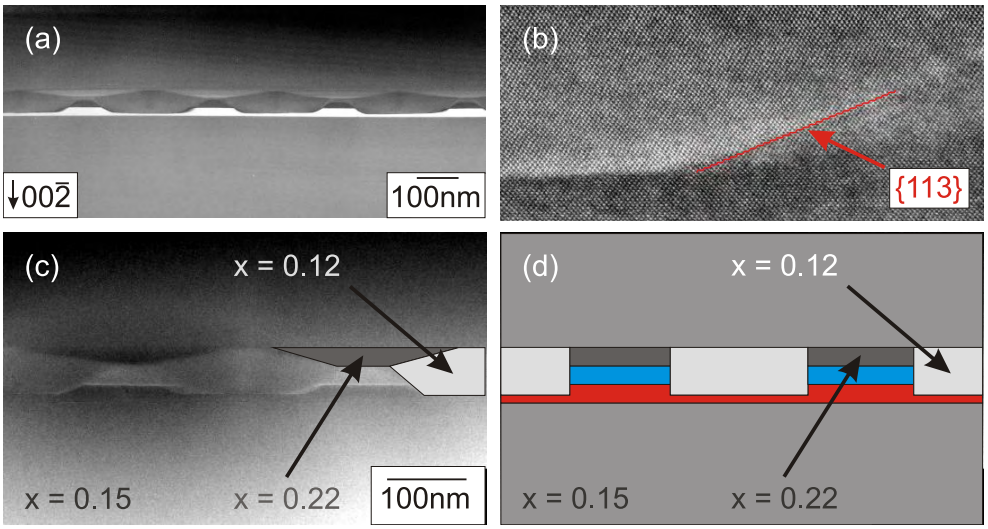

Figure 3.22: DFB gratings with inhomogeneous aluminum distribution in the overlying waveguide and a rectangular approximation. (a) STEM micrograph of the DFB grating region with inhomogeneous aluminum distribution visible as slightly contrasts. (b) STEM micrograph with atomic resolution of the angled, dominant {113} side surface of a grating ridge. (c) Magnified section of the DFB grating region with areas of aluminum accumulation and depletion, that have been identified with EDXS. (c) Rectangular approximation of (c) as used for simulations with QIP.

in the simulation. Changes in the characteristics of the refractive index in the grating region are depicted in Fig. 3.23 (a). The averaged refractive index in the trenches of the DFB grating is enhanced (red dashed line), while the averaged refractive index in the grating ridges (red solid line) is slightly reduced but not visible in the figure. It becomes clear, that the thickness of the effective grating rises because of the 24 nm of area A1 (respectively region IV in Fig. 3.23 (a)).

By comparing the spatial distribution of the aluminum-rich and aluminum-poor regions shown in Fig. 3.22 (d) used in the simulation, with the real distribution, visible in Fig. 3.22 (c), it can be derived that the influence on the coupling coefficient is overestimated in the simulation. This overestimation has tow basic reasons. On the one hand, the real duty cycle of the aluminum-variation induced additional index grating is not 1/4 approximated in the simulation. In fact, the duty cycle is closer to 1/2. On the other hand, the real shape of the aluminum-variation induced grating is not rectangular shaped and the real trapezoidal shape would decrease the coupling coefficient. Thus, from the results of the theoretical analysis of the influence

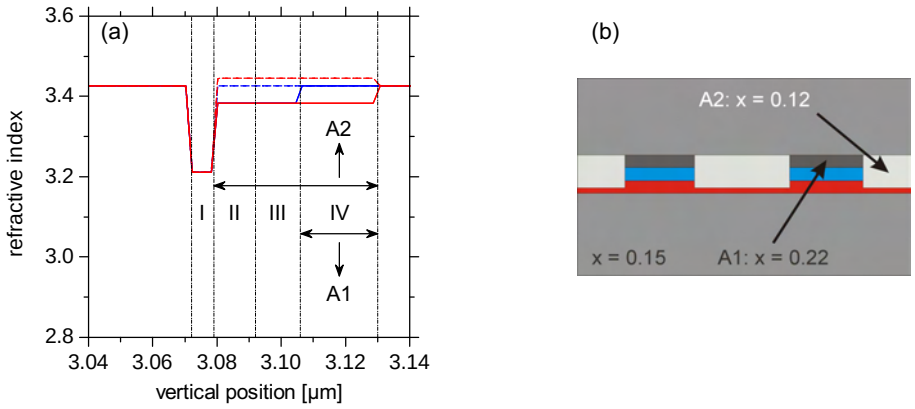

Figure 3.23: Refractive index of the ideal DFB grating and rectangular approximation for the grating with inhomogeneous aluminum distribution. (a) Characteristics of the averaged refractive index profile of the grating as depicted in Fig. 3.22 (a) (red lines) and an rectangular approximation for the DFB grating with inhomogeneous aluminum distribution (blue lines) in the grating filaments (dashed) and in the trenches (solid). (b) Scheme of the rectangular approximation with inhomogeneous aluminum distribution as used in the simulation.

of the inhomogeneous aluminum distribution on the coupling coefficient, one must assume that the absolute value of the coupling coefficient is between $|\Re[\kappa]| = 1.76\,\mathrm{cm}^{-1}$ and $|\Re[\kappa]| \approx 4\,\mathrm{cm}^{-1}$. In the following, it is assumed as $|\Re[\kappa]| \approx 3\,\mathrm{cm}^{-1}$.

3.4 Characterization of DFB-BA lasers

3.4.1 Material parameters of DFB-BA wafers

As a first task in the characterization of the DFB-BA lasers, the material quality of the grown wafers with buried DFB grating will be analyzed. The aim of this analysis must be to compare the results to reference FP-BA laser material. To determine the internal quantum efficiency η_i, internal loss α_i, the modal gain coefficient Γg_0 and the transparency current density j_tr of the DFB-BA laser waveguide design, power-voltage-current characteristics have been measured analogous to the analysis of FP-BA reference material, presented in section 3.1. Running exclusively on FP modes is obligatory for the application of the method for the determination of parameters, mentioned above, because the calculation is based on the cavity length dependence of the mirror loss. This has been realized by shifting the period of the

DFB grating from 284.9 nm to 292.2 nm. Accordingly, the wavelength of distributed feedback is shifted from ≈ 975 nm to ≈ 1000 nm (considering an effective refractive index of 3.4225). Therefore, the lasers oscillates on FP modes at the gain maximum between 958 and 970 nm. In Fig. 3.24 (a) and (c), the inverse value of the differential quantum efficiency η_{d}^{-1} is depicted as a function of the cavity length for contact stripe widths of 100 and 200 μm, respectively. The natural logarithm of the threshold current density j_{th} as a function of the inverse cavity length is depicted in Fig. 3.24 (b) and (d). Measurement results for a cavity length of 400 μm have not been considered for linear fits.

From the linear fit parameters for 100 and 200 μm stripe width, one obtains internal optical loss of $\alpha_{\mathrm{i}} \approx 0.85\,\mathrm{cm}^{-1}$ and an internal quantum efficiency of $\eta_{\mathrm{i}} \approx 0.96$. The modal gain coefficient is determined as $\Gamma g_0 \approx 20.6\,\mathrm{cm}^{-1}$ and for the transparency current density one finds $j_{\mathrm{tr}} \approx 143\,\mathrm{A\,cm}^{-2}$, (The results for $W = 100\,\mu$m stripe width have not been considered because of deviations at $L = 800\,\mu$m cavity length.). The results for the DFB-BA laser material is compared to the results for the FP-BA lasers in tab. 3.5.

Table 3.5: Summary of the results for the internal quantum efficiency, internal loss, confinement factor and transparency current density from cavity-length depending P-U-I measurements and spectra.

	η_{i}	α_{i}	Γg_0	j_{tr}
FP ($W = 100\,\mu$m)	0.924	$1.05\,\mathrm{cm}^{-1}$	$20.2\,\mathrm{cm}^{-1}$	$133.8\,\mathrm{Acm}^{-2}$
FP ($W = 200\,\mu$m)	0.922	$1.04\,\mathrm{cm}^{-1}$	$20.1\,\mathrm{cm}^{-1}$	$142.2\,\mathrm{Acm}^{-2}$
DFB ($W = 100\,\mu$m)	0.960	$0.85\,\mathrm{cm}^{-1}$	$22.3\,\mathrm{cm}^{-1}$	$152.8\,\mathrm{Acm}^{-2}$
DFB ($W = 200\,\mu$m)	0.961	$0.84\,\mathrm{cm}^{-1}$	$20.6\,\mathrm{cm}^{-1}$	$142.8\,\mathrm{Acm}^{-2}$

First of all, there is a good agreement between the results for the DFB-BA laser material and the reference FP-BA laser material. This is an excellent result for the fabrication of the buried grating DFB laser material and very important in order to achieve high power and high efficiency CW operation comparable to the FP-BA lasers as for example mentioned in section 1.2.6. The experimentally determined results for the internal optical loss are comparable the results for high performance FP-BA lasers and much better than

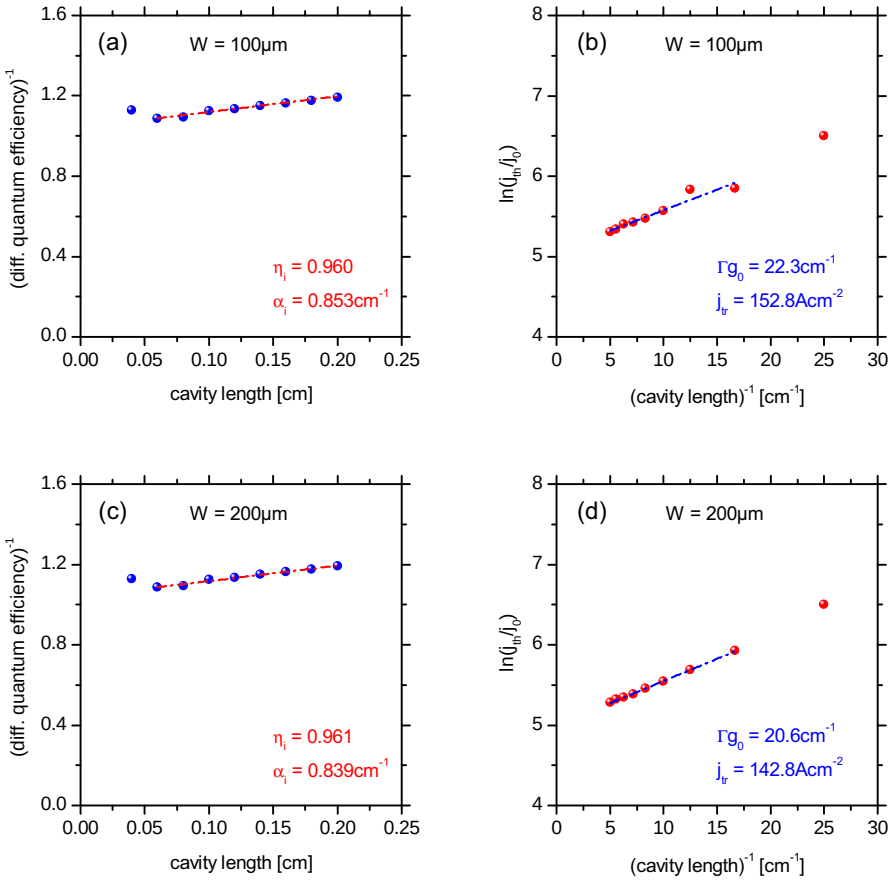

Figure 3.24: Measured cavity length dependence of the inverse differential quantum efficiency and logarithm of the threshold current density. The DFB grating is detuned to 1000 nm, relative to the gain maximum ($\sim$ 970 nm), so that the lasers are running on FP modes. (a) Inverse value of the differential quantum efficiency over the cavity length for $W = 100\,\mu$m. (b) $\ln(j_{\mathrm{th}}/j_0)$ over the inverse cavity length for $W = 100\,\mu$m. (c) Equivalent to (a) but for $W = 200\,\mu$m stripe width. (d) Equivalent to (b) but for $W = 200\,\mu$m stripe width.

reported in all previous publications.

Because of the newly developed design, the DFB grating is only a weak perturbation of the waveguide in the refractive index and optical loss. As a result, the internal optical loss and internal quantum efficiency of both laser structures is theoretically and experimentally found to be nearly identical. In the simulation it has been found, that the internal optical loss should be slightly increased for the DFB lasers by 0.12 cm^{-1}, mostly due to the

higher doping level in the grating region. Astonishingly, the experimentally determined internal optical loss is marginal smaller and the internal quantum efficiency is marginal higher for the DFB-BA lasers than for the FP-BA lasers. It is adequate to assume, that the differences occur due to the limits in the accuracy of measurements. Basically, the measurements indicate that the internal optical loss and internal quantum efficiency are comparable. Under DFB operation, the internal optical loss of the DFB-BA lasers with a second-order DFB grating will be slightly increased relative to the value which has been determined from the cavity length dependence of the differential quantum efficiency due to the appearance of radiation loss. For weak second-order DFB gratings ($\kappa \cdot L \leq 1$) with an optimized duty cycle ($c_\mathrm{d} \approx 0.25$), this effect will be negligible as discussed in section 1.2.2.

3.4.2 Facet coating for DFB-BA lasers

For the characterization, a facet passivation and facet coating was applied to DFB-BA laser bars with single emitters of $L = 3\,\mathrm{mm}$ cavity length and $W = 90\,\mu\mathrm{m}$ contact stripe widths. For a maximum slope efficiency of the optical power, emitted from the front facet, a very high rear facet reflectivity $R_\mathrm{r} = 98\,\%$ was targeted, similar to the reference FP-BA lasers. For an optimal slope efficiency and threshold current and hence, for a maximum power conversion efficiency, a front facet reflectivity of $R_\mathrm{f} < 0.5\,\%$ was targeted in contrast to the FP-BA lasers.

As already discussed in section 1.2.6, a low front facet reflectivity is required for DFB-BA lasers with a low DFB coupling strength ($\kappa \cdot L \leq 1$), in order to suppress lasing on FP-like modes. Basically, the mirror loss of FP modes α_m must be higher than the DFB resonator loss of DFB modes α_DFB. With the applied facet coatings (5128, 4959, 5055), $R_\mathrm{f} = 0.02\,\%$ - $0.04\,\%$ and $R_\mathrm{r} = 97.6\,\%$ was achieved. In Fig. 3.25, the reflectivity is depicted as a function of the wavelength for both facets. The reflectivity was again measured on GaAs-dummies. Afterwards, the reflectivity on the laser facet is calculated with respect to the effective index of the waveguide mode.

3.4.3 Overview of DFB wafers

Within iteration I, four wavers have been fabricated in two process runs, respectively. All these wafers have the same epitaxy structure and surface processing. Differences exist in the targeted DFB wavelength at threshold $\lambda_\mathrm{tar}^\mathrm{DFB}$ and in the in-situ etching time t_is.

Two different values of $\lambda_\mathrm{DFB}^\mathrm{tar}$ have been chosen to find an ideal option for the DFB wavelength $\lambda_\mathrm{DFB}(I)$ and the gain peak wavelength $\lambda_\mathrm{gain}(I)$ to co-

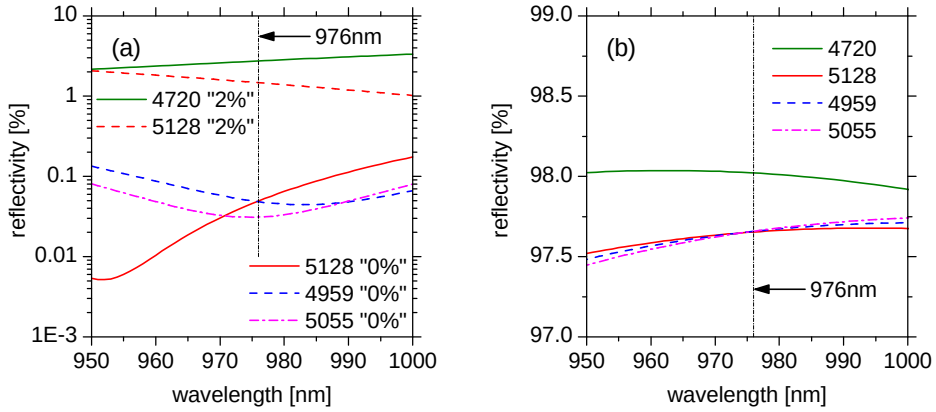

Figure 3.25: Reflectivity of the anti-reflection coated front facet (a) and the high-reflection coated rear facet (b) of the DFB lasers.

incide at $\sim 10\,\mathrm{W}$ optical output power. From the theoretical point of view, it might have been preferred to keep the DFB wavelength $\lambda_{\mathrm{DFB}}^{\mathrm{tar}}$ constant and hence, to keep $\lambda_{\mathrm{DFB}}(P = 10\,\mathrm{W}) \approx 976.0\,\mathrm{nm}$ at the ideal wavelength for pumping applications of ytterbium doped gain media. However, this would require to adjust the gain peak wavelength $\lambda_{\mathrm{gain}}^{\mathrm{tar}}$ for the different wafers. From the practical point of view, it seems to be appropriate to keep $\lambda_{\mathrm{gain}}^{\mathrm{tar}}$ unchanged, because small changes in the epitaxy parameters of the DQW might be hazardous as they provoke the risk of changes in the internal quantum efficiency, for example. For a study of the DFB-BA lasers, most stable epitaxy properties are essential and small changes in the lasing wavelength between lasers from different wafers must be accepted.

As mentioned above, two different values of $\lambda_{\mathrm{DFB}}^{\mathrm{tar}}(I = 0)$ have been chosen. The gain peak wavelength was set to $\lambda_{\mathrm{gain}}(I = 0) = 968.0\,\mathrm{nm}$. For the determination of suitable values for $\lambda_{\mathrm{tar}}^{\mathrm{DFB}}(I = 0\,\mathrm{A})$, the following calculation was made. Firstly, it has been assumed that the power, voltage and current characteristics of the DFB-BA lasers will be roughly comparable to the characteristics of the reference FP-BA lasers. This is acceptable because it has been already shown that the internal optical loss and internal quantum efficiency are comparable, and the resonator loss will be roughly comparable as well. Uncertainties occur with the voltage characteristics. Therefore, the power, voltage current characteristics of FP-BA reference laser D1423-1 051301 have been used, whose wafer was grown in the same epitaxy reactor as the wafers for the FP-BA lasers. Secondly, the heating in the laser chip was calculated form the dissipated power $P_{\mathrm{d}}(I) = U(I) \cdot I - P_{\mathrm{opt}}(I)$

(where spontaneous emission has been neglected) and from the average thermal resistance $R_{\mathrm{th}} \approx 3.58\,\mathrm{K\,W^{-1}}$ (see section 3.2.4). Thirdly, the wavelength of the DFB-BA laser and the gain peak wavelength have been calculated as $\lambda_{\mathrm{DFB}}(I) = \lambda_{\mathrm{DFB}}^{\mathrm{tar}}(I = 0) + (\mathrm{d}\lambda_{\mathrm{Bragg}}/\mathrm{d}T) \cdot R_{\mathrm{th}}$ and $\lambda_{\mathrm{gain}}(I) = \lambda_{\mathrm{gain}}^{\mathrm{tar}}(I = 0) + (\mathrm{d}\lambda_{\mathrm{gain}}/\mathrm{d}T) \cdot R_{\mathrm{th}}$, respectively. The temperature coefficients of the Bragg wavelength and gain peak wavelength were estimated in section 1.1.5 as $\mathrm{d}\lambda_{\mathrm{Bragg}}/\mathrm{d}T = 0.077\,\mathrm{nm\,K^{-1}}$ and $\mathrm{d}\lambda_{\mathrm{gain}}/\mathrm{d}T = 0.34\,\mathrm{nm\,K^{-1}}$.

For the finally chosen values of $\lambda_{\mathrm{DFB}}^{\mathrm{tar}}(I = 0) = 973.7\,\mathrm{nm}$, $\lambda_{\mathrm{DFB}}^{\mathrm{tar}}(I = 0) = 974.6\,\mathrm{nm}$ and $\lambda_{\mathrm{gain}}^{\mathrm{tar}}(I = 0) = 968.0\,\mathrm{nm}$, $\lambda^{\mathrm{Bragg}}(I)$ and $\lambda^{\mathrm{gain}}(I)$ coincide at $I = 9.5\,\mathrm{A}$ and $I = 10.6\,\mathrm{A}$, respectively. Note, that the spectral detuning between the Bragg wavelength of the DFB grating $\lambda_{\mathrm{Bragg}}(I)$ and the gain peak wavelength $\lambda_{\mathrm{gain}}(I)$ has been chosen relatively broad with respect to the possibility that the slope efficiency or voltage of the DFB-BA lasers might be degraded. A DFB lasing wavelength of 976 nm is obtained at 11.9 A and 8.3 A, respectively.

The in-situ etching time t_{is} has been varied to enable different values of the DFB coupling coefficient. Primary experiments and their control with STEM images [Mar09] have shown, that basically the etching depth of the grating corrugations can be increased by increasing t_{is}. Based on simulations with QIP, an increase of the etching depth can be shown to increase the DFB coupling coefficient. Furthermore, an increase of t_{is} also reduces the duty cycle of the DFB grating, if the width of the photoresist stripes and the width of the GaAs cap stripes is not adapted respectively. For very long in-situ etching times $t_{\mathrm{is}} \geq 180\,\mathrm{s}$ it has been observed, that some of the grating stripes vanish due to variations in the in-plane etching, if the width of the GaAs cap stripes was optimized for $t_{\mathrm{is}} \approx 120\,\mathrm{s}$ [Mar09]. Approximately, for $t_{\mathrm{is}} = 90$, 87 and 150 s, the width of the GaAs cap stripes should be ~ 90, ~ 105 and $\sim 110\,\mathrm{nm}$ or slightly broader after oxygen plasma cleaning and oxide removal with sulfuric acid, respectively. This is significantly more than the width of the buried grating stripes which should be about 71 nm (with $\lambda = 976\,\mathrm{nm}$, $n_{\mathrm{eff}} = 3.421$, $\Lambda = 285\,\mathrm{nm}$ and $c_{\mathrm{d}} = 0.25$).

For example, if one simulates the given laser structure with QIP, assuming that DFB gratings have been etched with in-situ etching times of $t_{\mathrm{is}} = 90$, 120 and 150 s and the duty cycle always optimized to $c_{\mathrm{d}} = 0.25$, on obtains $|\kappa_{90\,\mathrm{s}}| \approx 1.5\,\mathrm{cm^{-1}}$, $|\kappa_{120\,\mathrm{s}}| \approx 2.6\,\mathrm{cm^{-1}}$ and $|\kappa_{150\,\mathrm{s}}| \approx 3.8\,\mathrm{cm^{-1}}$. For this simulation, it has been taken into account, that the coupling coefficient is increased do to the formation of aluminum-poor and aluminum-rich regions by $\sim 1.2\,\mathrm{cm^{-1}}$. Furthermore, the given layer thicknesses of 20 nm for $In_{0.49}Ga_{0.51}P$ and 25 nm for GaAs (-3 nm which are approximately removed after oxygen plasma cleaning and oxide removal with sulfuric acid) were considered, as well as the experimentally determined etching rates of 360 and

$200\,\mathrm{nm\,h^{-1}}$, respectively.

An overview of the different DFB wafers from iteration I with the targeted DFB wavelengths $\lambda_{\mathrm{DFB}}^{\mathrm{tar}}$, gain peak wavelength $\lambda_{\mathrm{gain}}^{\mathrm{tar}}$ (both at $I = 0$) and in-situ etching times t_{is} is given in table 3.6.

Table 3.6: Overview of the different DFB wafers from iteration I with the targeted DFB wavelengths $\lambda_{\mathrm{DFB}}^{\mathrm{tar}}$, gain peak wavelength $\lambda_{\mathrm{gain}}^{\mathrm{tar}}$ (both at $I = 0$) and in-situ etching times t_{is}

process	wafer	$\lambda_{\mathrm{DFB}}^{\mathrm{tar}}$ [nm]	$\lambda_{\mathrm{gain}}^{\mathrm{tar}}$ [nm]	in-situ etching [s]
4827	D1365-1	973.7	968.0	90
	D1365-2	974.6	968.0	90
	D1366-4	973.7	968.0	120
	D1366-5	974.6	968.0	120
4955	D1425-1	973.7	968.0	120
	D1425-2	974.6	968.0	120
	D1425-4	973.3	968.0	150
	D1425-5	974.6	968.0	150

3.4.4 Power-voltage-current characteristics of DFB-BA lasers

The analysis of the electro-optical properties of DFB-BA lasers from iteration I follows the steps from chapter 3.2 for the FP-BA lasers, which are here used as reference devices. Figure 3.26 shows the power-voltage-current characteristics of DFB-BA lasers from eight different wafers as specified in Tab. 3.6. The wafers D1365-1, D1365-2, D1366-4 and D1366-5 from wafer process run 4827 have a facet coating from facet process run 4959. The facet coatings of wafer D1425-1 and the wafers D1425-2, D1425-4 and D1425-5 from wafer process run 4955 are from facet process runs 5128 and 5055, respectively.

A number of parameters has been extracted from the measured power-voltage-current characteristics. The threshold current and slope efficiency were determined from a linear fit of the power-current curve over 2 A, starting

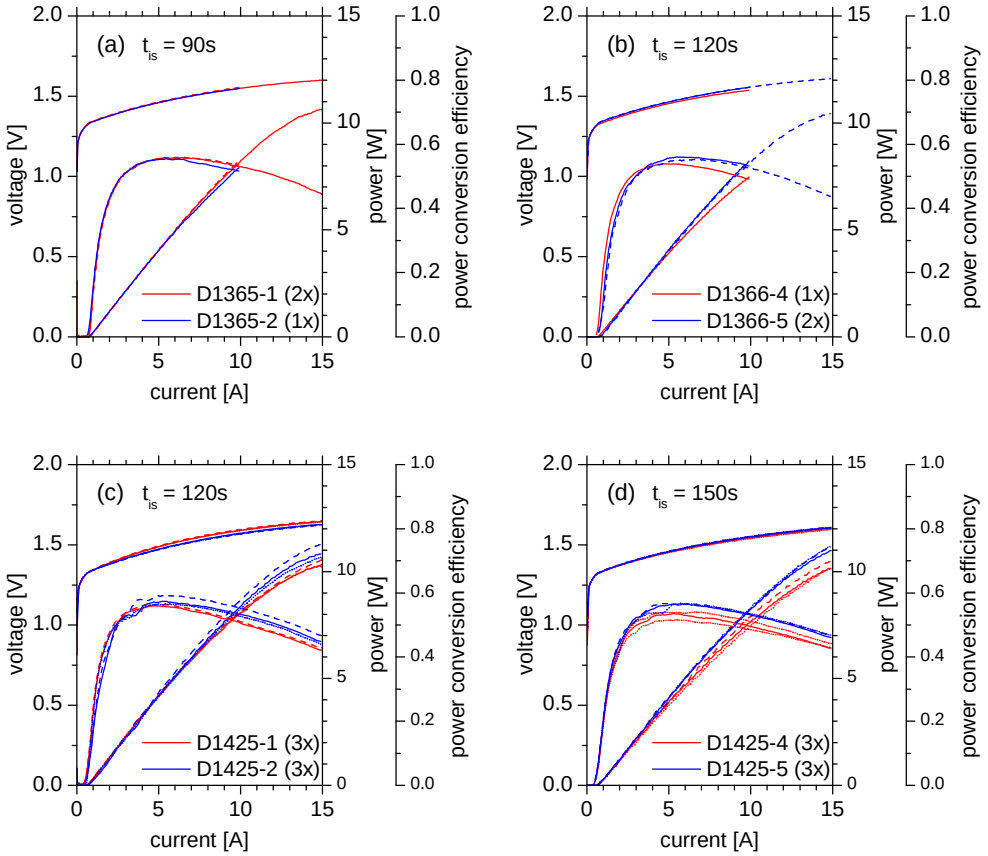

Figure 3.26: P-U-I characteristics of lasers from eight different wafers in iteration I. If more than one laser was measured from a specific wafer, the characteristics are differentiated as solid, dashed and dotted lines. (a) Wafers D1365-1 (red) and D1365-2 (blue) from process 4828, $t_{\mathrm{is}} = 90\,\mathrm{s}$. (b) Wafers D1366-4 (red) and D1366-5 (blue) from process 4828, $t_{\mathrm{is}} = 120\,\mathrm{s}$. (c) Wafers D1425-1 (red) and D1425-2 (blue) from process 4955, $t_{\mathrm{is}} = 120\,\mathrm{s}$. (d) Wafers D1425-4 (red) and D1425-5 (blue) from process 4955, $t_{\mathrm{is}} = 150\,\mathrm{s}$.

from the first discrete measurement point above threshold. In addition, the power conversion efficiency has been determined at its maximum and at an optical power output of 7 W and 10 W, respectively. In table 3.7, the results from the individual lasers are summarized.

In Fig. 3.26 (a), the current characteristics of power voltage, power and power conversion efficiency are depicted for the wafers 1365-1 (red lines) and D1365-2 (blue lines), where the DFB grating was processed with an in-situ etching time of $t_{\mathrm{is}} = 90\,\mathrm{s}$. The characteristics of the two lasers agree very well

Table 3.7: Overview of the threshold gain, slope efficiency and power conversion efficiency from DFB lasers from iteration I.

wafer	laser	I_{th} [mA]	$S_{2\,\mathrm{A}}$ [$\mathrm{W\,A^{-1}}$]	$\eta_{\mathrm{PCE}}^{\mathrm{max}}$	$\eta_{\mathrm{PCE}}^{7\,\mathrm{W}}$	$\eta_{\mathrm{PCE}}^{10\,\mathrm{W}}$
D1365-1	020416	800	0.985	0.558	0.546	0.487
	020417	821	0.997	0.559	0.549	–
D1365-2	020508	778	0.977	0.555	0.530	–
D1366-4	091002	689	0.936	0.540	0.503	–
D1366-5	020618	831	0.985	0.561	0.549	–
	020619	880	0.997	0.553	0.541	0.471
D1425-1	020410	672	0.980	0.560	0.526	0.443
	020411	649	0.987	0.564	0.532	0.456
	020412	645	0.997	0.570	0.532	0.444
D1425-2	040101	805	1.026	0.574	0.554	0.497
	040102	759	0.993	0.591	0.578	0.523
	040103	674	0.967	0.567	0.549	0.483
D1425-4	051301	697	0.906	0.536	0.507	0.435
	051302	682	0.920	0.541	0.524	0.460
	051303	689	0.879	0.516	0.492	0.434
D1425-5	020102	684	0.932	0.565	0.547	0.496
	020104	681	0.942	0.567	0.551	0.501
	020105	707	0.925	0.568	0.552	0.505

below a current of 6 A. Above 6 A, the power-current curve of the laser from D1365-2 bends down, with a resulting reduction in the power conversion efficiency. The voltage-current characteristics are identical. Even though both wafers are designed to have a difference in the Bragg wavelength of the DFB grating, the threshold currents (810 mA / 778 mA) and slope efficiencies ($0.991\,\mathrm{WA^{-1}}$ / $0.977\,\mathrm{W\,A^{-1}}$) have only small differences.

In the case of wafers D1366-4 and D1366-5 ($t_{\mathrm{is}} = 120\,\mathrm{s}$) in Fig. 3.26 (b), one finds another behavior. As one might have expected because of the smaller spectral detuning between the Bragg wavelength of the DFB grating and the gain peak wavelength, the laser from D1366-4 has a smaller threshold current (689 mA / 855 mA) and a lower slope efficiency as well ($0.936\,\mathrm{WA^{-1}}$

/ 0.991 WA^{-1}). As a consequence, the power conversion efficiency at 7 W is increased for D1366-5 (0.503 / 0.545). The minor difference in the diode voltage can be attributed to the temperature depending decrease of the voltage for the laser with the lower power conversion efficiency.

In Fig. 3.26 (c), the power-voltage-current characteristics for three lasers each from wafers D1425-1 and D1425-2 ($t_{\mathrm{is}} = 120\,\mathrm{s}$) are depicted. The differences in the characteristics of the lasers from D1425-1 are smaller than for D1425-2. One also observes some noticeable kinks in the power and power conversion efficiency curves of D1425-2 at currents around 3.5 A. For the threshold current, one finds an average value of (655 mA / 746 mA). The average slope efficiency is (0.988 WA^{-1} / 0.995 WA^{-1}). The diode voltage of D1425-1 is slightly higher than for D1425-2. Again, the threshold current and slope efficiency are reduced for the wafer with the smaller spectral detuning between the Bragg wavelength of the DFB grating and the gain peak wavelength. The most efficient and most powerful DFB-BA laser from iteration I is chip 040102 from wafer D1425-2 ($I_{\mathrm{th}} = 759\,\mathrm{mA}$, $S_{2\,\mathrm{A}} = 0.993\,\mathrm{WA}^{-1}$, $\eta_{\mathrm{PCE}}^{\mathrm{max}} = 0.591$, $\eta_{\mathrm{PCE}}^{7\,\mathrm{W}} = 0.578$, $\eta_{\mathrm{PCE}}^{10\,\mathrm{W}} = 0.523$).

The power-voltage-current characteristics for the wafers D1425-4 and D1425-5 with $t_{\mathrm{is}} = 150\,\mathrm{s}$ are shown in Fig. 3.26 (d). It is clearly visible, that the slope efficiency of the wafer with smaller spectral detuning between the Bragg wavelength of the DFB grating and the gain peak wavelength, D1425-4, is reduced. A threshold current average value of (689 mA / 691 mA) has been determined. The averaged slope efficiency is (0.902 WA^{-1} / 0.933 WA^{-1}). The voltage characteristics of the lasers from both wafers are nearly identical.

To enable a deeper understanding for possible reasons of the different properties of the DFB-BA lasers, the threshold current, slope efficiency and power conversion efficiency, as well as the diode voltage shall be investigated regarding their dependence on the in-situ etching time. Two general effects that are associated with the in-situ etching time must be considered to have an important influence on the performance of the DFB-BA lasers. On the one hand, the coupling coefficient increases with the in-situ etching time t_{is} as estimated above. On the other hand, longer in-situ etching times result in lower peak volume and areal density of oxygen impurity concentration as shown in Fig. 3.19, as well as in a thinner residual $\mathrm{In_{0.49}Ga_{0.51}P}$. This will possibly cause a reduction in the internal optical loss and a reduction in the series resistance or series voltage, respectively.

Fig. 3.27 shows the threshold current, slope efficiency and power conversion efficiency at 7 and 10 W as a function of the in-situ etching time t_{is}. Note, that Fig. 3.27 (a) and (a'), (b) and (b') et cetera show the results for DFB-BA lasers with $\lambda_{\mathrm{DFB}}^{\mathrm{tar}} = 973.7\,\mathrm{nm}$ and $\lambda_{\mathrm{DFB}}^{\mathrm{tar}} = 974.6\,\mathrm{nm}$, respectively.

Even though the values of the threshold current show strong deviations at $t_{is} = 120\,s$ in Fig. 3.27 (a'), a decreasing with increasing etching time can be derived from Fig. 3.27 (a) and (a'). No clear difference in the threshold current is observed between $\lambda_{DFB}^{tar} = 973.7\,nm$ and $\lambda_{DFB}^{tar} = 974.6\,nm$.

Also for the dependence of the slope efficiency on t_{is}, one finds a decline as depicted in Fig. 3.27 (b) and (b'). Both effects can be attributed to an increase of the DFB coupling coefficient with increasing t_{is}, as mentioned above. By comparing the slope efficiencies for $\lambda_{DFB}^{tar} = 973.7\,nm$ and $\lambda_{DFB}^{tar} = 974.6\,nm$, also no clear difference is observed.

The power conversion efficiency at 7 and 10 W is depicted in Fig. 3.27 (c), (c') and (d), (d'), respectively. A very weak decrease with t_{is} is observed. In contrast to the threshold current and slope efficiency, significant differences occur for $\lambda_{DFB}^{tar} = 973.7\,nm$ and $\lambda_{DFB}^{tar} = 974.6\,nm$. The power conversion efficiency has the clear tendency to be higher for the wafers with the longer targeted Bragg wavelength. This is a consequence of the fact that roll-over of the power-current characteristics which here typically occurs at currents above $I \sim 4 - 7\,A$, is significantly stronger for the lasers with $\lambda_{DFB}^{tar} = 973.7\,nm$.

Stronger roll-over of the power-current characteristics leads to lower output powers and therefore results in a lower power conversion efficiency. For $\lambda_{DFB}^{tar} = 973.7\,nm$, the gain peak wavelength $\lambda_{gain}(I)$ is shifted towards longer wavelengths than the Bragg wavelength of the DFB grating $\lambda_{DFB}(I)$ at lower current levels than for $\lambda_{DFB}^{tar} = 974.6\,nm$. Thus, a sufficient spectral detuning between the Bragg wavelength of the DFB grating $\lambda_{DFB}(I = 0)$ and the gain peak wavelength $\lambda_{gain}(I = 0)$ is experimentally confirmed to be an important design requirement for high power and efficiency DFB-BA lasers!

The dependence of voltage drop on the in-situ etching time is shown in Fig. 3.28. In Fig. 3.28 (a), the voltage characteristics of all lasers, presented in Fig. 3.26, are depicted. Fig. 3.28 (b) shows the voltage at 3 A for every laser. Such a low current has been chosen for this comparison in order to keep the heat induced voltage reduction (because of different power conversion efficiencies) to be negligible. In the voltage characteristics and in the voltage at 3 A, one finds a weak decrease for the voltage with increasing in-situ etching time. However, the lasers from wafers with D1425-1 and D1425-2 (both $t_{is} = 120\,s$) deviate from this trend by having a higher voltage. STEM investigations [Mar09] show that even at $t_{is} = 150\,s$, a residual $In_{0.49}Ga_{0.51}P$ layer is left over in the grating region. From a reduction in the voltage with increasing etching time one might speculate that the voltage will significantly decrease if the residual $In_{0.49}Ga_{0.51}P$ layer is completely removed.

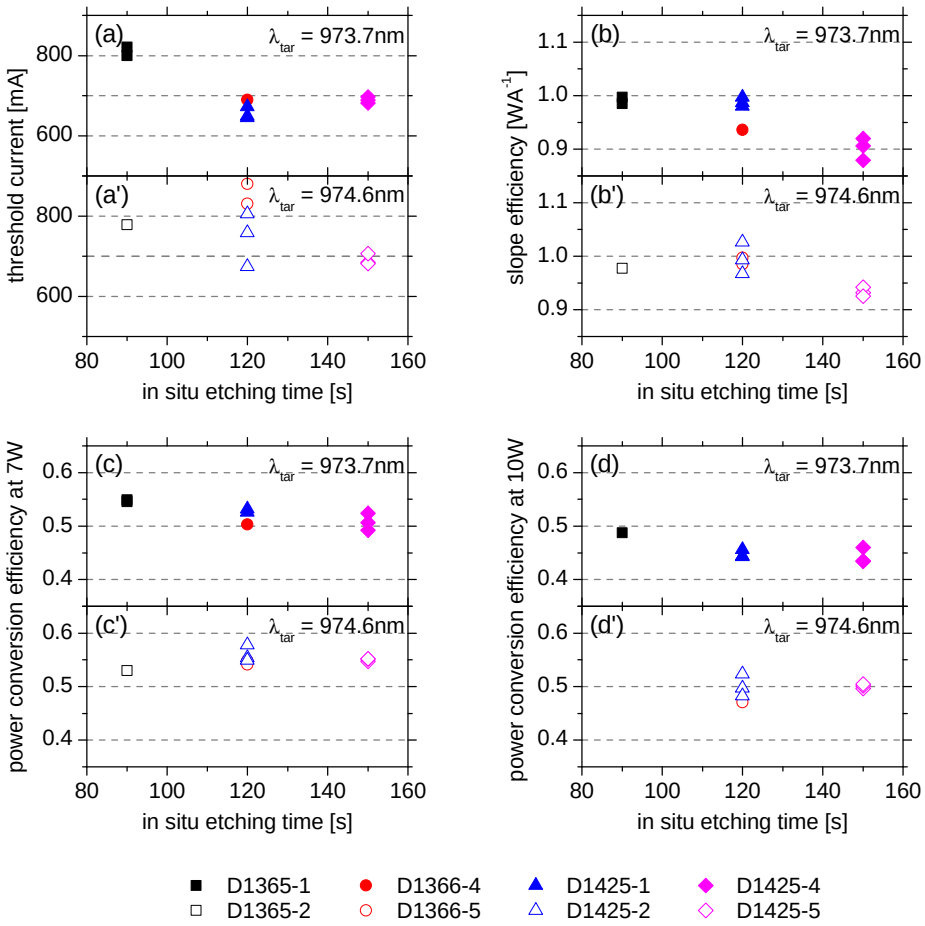

Figure 3.27: Threshold current, slope efficiency (from a linear fit over 2 A above threshold) and power conversion efficiency at 7 and 10 W of DFB-BA lasers from iteration I. (a) Threshold current ($\lambda_{\mathrm{DFB}}^{\mathrm{tar}} = 973.7\,\mathrm{nm}$). (a') ($\lambda_{\mathrm{DFB}}^{\mathrm{tar}} = 974.6\,\mathrm{nm}$). (b) Slope efficiency ($\lambda_{\mathrm{DFB}}^{\mathrm{tar}} = 973.7\,\mathrm{nm}$). (b') ($\lambda_{\mathrm{DFB}}^{\mathrm{tar}} = 974.6\,\mathrm{nm}$). (c) Power conversion efficiency at 7 W ($\lambda_{\mathrm{DFB}}^{\mathrm{tar}} = 973.7\,\mathrm{nm}$). (c') ($\lambda_{\mathrm{DFB}}^{\mathrm{tar}} = 974.6\,\mathrm{nm}$). (d) Power conversion efficiency at 10 W ($\lambda_{\mathrm{DFB}}^{\mathrm{tar}} = 973.7\,\mathrm{nm}$). (d') ($\lambda_{\mathrm{DFB}}^{\mathrm{tar}} = 974.6\,\mathrm{nm}$)

3.4.5 Comparison of the power-voltage-current characteristics with FP-BA reference lasers

The aim of this section is to compare the power-voltage-current characteristics of DFB-BA lasers with the characteristics of FP-BA reference lasers, to clarify differences and similarities. The results will serve as reference point for the trial of a further enhancement of power and power conversion efficiency in iteration II.

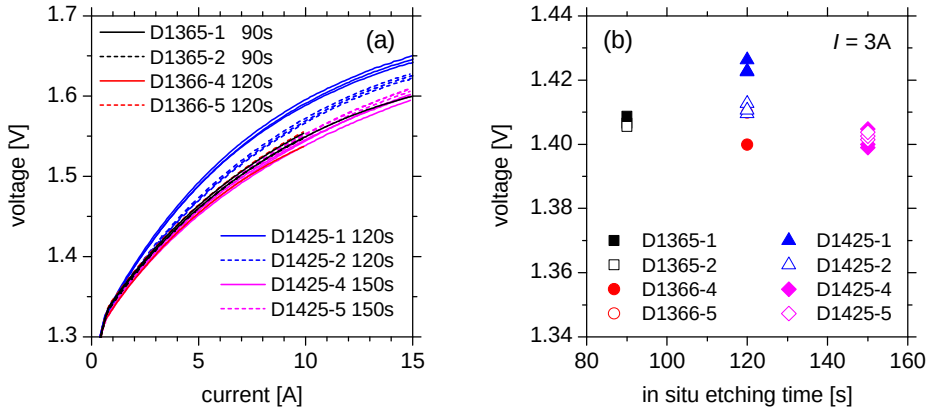

Figure 3.28: Voltage-current characteristics of DFB-BA lasers from iteration I. (a) Voltage-current characteristics. (b) Voltage at 3 A as a function of the in-situ etching time.

In Fig. 3.29, the power-voltage-current characteristics of the best DFB-BA laser of each wafer from Fig. 3.26, is compared to sample power-voltage-current characteristics of FP-BA reference lasers F1850-4 071006 and D1423-1 051301 from Fig. 3.5. In detail, the DFB-BA lasers, chosen for the comparison are: D1365-1 020416, D1365-2 020508, D1366-4 091002, D1366-5 020618, D1425-1 020411, D1425-2 040102, D1425-4 051302 and D1425-5 020104.

In a first overview, one can clearly see that the voltage of the DFB-BA lasers is increased in comparison to the FP-BA lasers. The increase is not due to a higher turn-on voltage, but due to an increased series resistance. Both, the voltage characteristics of the DFB-BA lasers and reference FP-BA lasers converge to the same turn-on voltage $U_0(I = 0) \approx 1.32\,\mathrm{V}$. In contrast, the slope of the voltage characteristics is increased for the DFB-BA lasers. Note, that the voltage decreases (because the series resistance decreases) with an increasing temperature of the laser chip. Accordingly, the increase of the voltage for the DFB-BA lasers is reduced because of their lower power conversion efficiency. The supplementary series resistance is in the order of $5\,\mathrm{m\Omega}$.

The threshold current of the DFB-BA lasers is slightly increased, compared to the FP-BA reference lasers. The FP-BA reference lasers, summarized in Table 3.2, have an average threshold current of 624 mA. For the DFB-BA lasers with $\lambda_{\mathrm{DFB}}^{\mathrm{tar}} = 973.7\,\mathrm{nm}$, summarized in table 3.7, the average threshold current is increased by 87 mA. A higher increase in the average threshold current of 144 mA is observed for the DFB-BA lasers with $\lambda_{\mathrm{DFB}}^{\mathrm{tar}} = 974.6\,\mathrm{nm}$ (also summarized in table 3.7), again compared to the av-

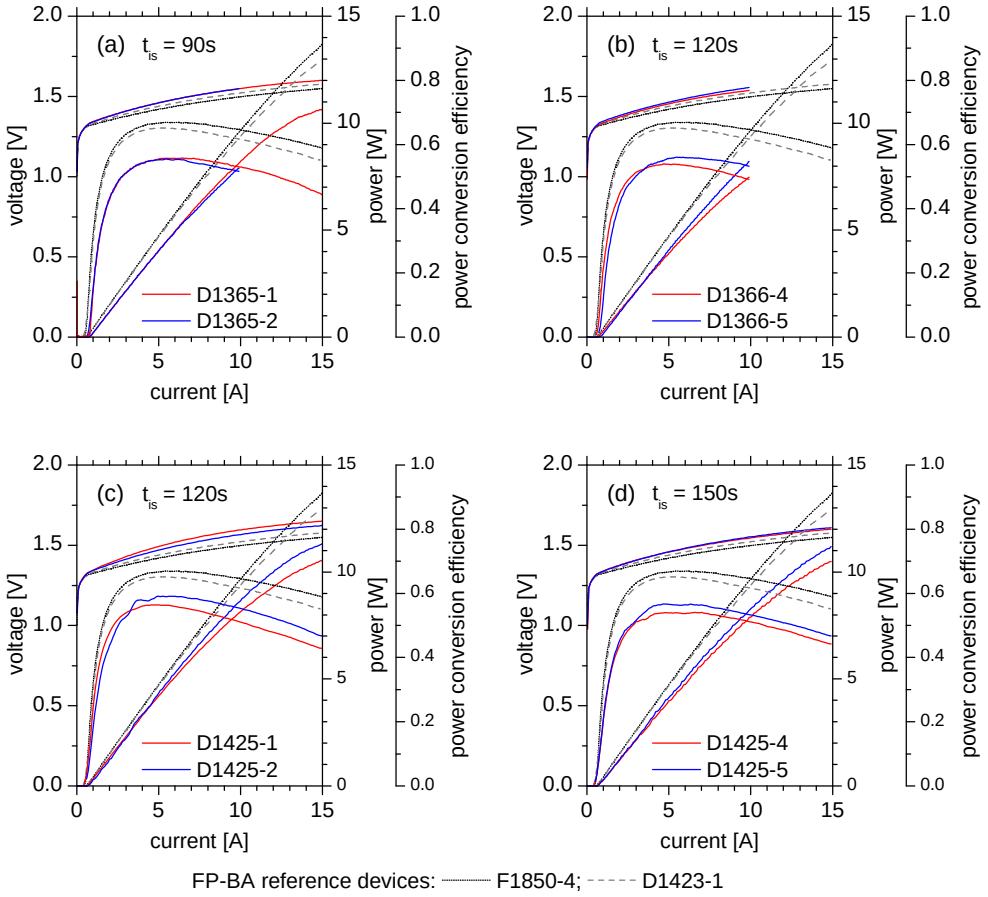

Figure 3.29: Comparison of the P-U-I characteristics of DFB-BA lasers with sample P-U-I characteristics of FP-BA reference lasers F1850-4 071006 and D1423-1 051303.

erage value for the FP-BA reference lasers. Nevertheless, compared to the currents of $\geq 10\,\mathrm{A}$ which are required to drive either the DFB-BA lasers or FP-BA lasers in the 10 W range, the increase of the threshold current is of minor importance.

The slope efficiency of the DFB-BA lasers is significantly reduced in comparison to the FP-BA reference lasers. This is valid for the slope efficiency in the $\leq 7\,\mathrm{A}$ region, as well as for the region above 7 A, were the roll-over of the DFB-BA lasers is stronger than the thermal roll-over of the FP-BA lasers. The reduction in slope efficiency is in the order of $0.14\,\mathrm{W\,A^{-1}}$ for the DFB-BA lasers with $\lambda_{\mathrm{DFB}}^{\mathrm{tar}} = 973.7\,\mathrm{nm}$ and $0.11\,\mathrm{W\,A^{-1}}$ for the DFB-BA lasers with $\lambda_{\mathrm{DFB}}^{\mathrm{tar}} = 974.6\,\mathrm{nm}$. As visible in the power-current character-

istics depicted in Fig. 3.29, the reduction in slope efficiency causes a remarkable reduction in the optical output power in the $\geq 10\,\mathrm{A}$ current range ($0.14\,\mathrm{W\,A^{-1}} \cdot 10\,\mathrm{A} = 1.4\,\mathrm{W}$). The reduction of the optical output power in the $\geq 10\,\mathrm{A}$ current range is further amplified due to the stronger roll-over behavior which is observed for the DFB-BA lasers. This stronger roll-over of the power-current characteristics must be attributed to the fact, that the optical gain decreases significantly, after the gain peak wavelength $\lambda_{\mathrm{gain}}(I)$ is shifted to the long wavelength side of the Bragg wavelength of the DFB grating $\lambda_{\mathrm{DFB}}(I)$.

The power conversion efficiency of the DFB-BA lasers is reduced in comparison to the FP-BA lasers as a consequence of the increased voltage, increased threshold current, decreased slope efficiency and stronger roll-over. The reduction in power conversion efficiency is in the order of 6 - 15 %. These are the smallest differences in power conversion efficiency, that have been published for a DFB laser and a reference laser without a grating [Sch10a], [Sch10b] until 2010.

In order to further increase the power conversion efficiency and optical power of DFB-BA lasers, the following requirements can be derived from the comparison of the power-voltage-current characteristics of DFB-BA lasers and reference FP-BA laser from iteration I. The power-voltage-current characteristics of the DFB-BA lasers could approach the characteristics of the reference FP-BA lasers, if the increase in series resistance and decrease in slope efficiency can be further reduced. The impact of these two degradations on the power conversion efficiency and output power is growing with the injected current and is therefore of particular importance. In contrast, the small increase of the threshold current might be accepted and neglected in an optimization process. The stronger roll-over of the power-current characteristics for the DFB-BA lasers cannot be completely eliminated but reduced by an optimal spectral detuning between the gain peak wavelength and the Bragg wavelength of the DFB grating.

A reduction of the series resistance could be achieved with further improvement of the grating technology, for example with a reduction of the material hetero-interfaces in the grating region.

An enhancement of the slope efficiency is possible due to a reduction of the coupling coefficient of the DFB grating. This can be derived from a comparison of the DFB resonator loss with the mirror loss of the FP-BA lasers, characterized in section 3.2. It has been theoretically derived in section 1.2.5 and was reported in [Sch10a]. While the DFB resonator loss with a coupling coefficient of $\kappa \approx 3\,\mathrm{cm^{-1}}$ ($R_{\mathrm{f}} = 0.09\,\%$, $R_{\mathrm{r}} = 96\,\%$) is only $\alpha_{\mathrm{DFB}} = 3.91\,\mathrm{cm^{-1}}$, the FP mirror loss ($R_{\mathrm{f}} = 2\,\%$, $R_{\mathrm{r}} = 96\,\%$) is $\alpha_{\mathrm{m}} = 6.55\,\mathrm{cm^{-1}}$. Thus, the optical feedback for the DFB-BA lasers from

the DFB grating and the coated facets is larger than optimal. The coupling strength can be expressed by an effective front facet reflectivity for the DFB-BA lasers of $R_{\mathrm{f,eff}} \approx 10\,\%$. The effective front facet reflectivity is defined by the reflectivity which leads to a mirror loss, identical to the DFB resonator loss. A front facet reflectivity of $R_{\mathrm{f,eff}} \approx 10\,\%$ is too high for a 3 mm long high efficiency FP-BA laser (with $R_{\mathrm{r}} = 96\,\%$), as can be for example derived from the calculations, presented in Fig. 1.1 (a).

3.4.6 Spectral properties of DFB-BA lasers

In the following section, the spectral properties of the DFB BA lasers will be analyzed and discussed. The analysis focuses on the impact of the DFB grating on the spectrum, the spectral width and consequences for possible applications. Firstly, representative spectral maps are presented for lasers from each of the eight wafers. Secondly, the spectral width and modal content are discussed.

The motivation to integrate a DFB grating into broad area lasers was to achieve optical spectra with a narrow spectral width, containing 95 % of the emitted optical power. For example $\Delta\lambda \leq 1\,\mathrm{nm}$ would be preferred for pumping ytterbium doped gain media such as Yb:YAG crystals at the narrow $\approx 976\,\mathrm{nm}$ absorption peak. For spectral beam combining (dense wavelength division multiplexing DWDM) of high power lasers, even smaller spectral width in the $\Delta\lambda \leq 0.3\,\mathrm{nm}$ range would be advantageous. In the best case, narrow spectral width emission should be obtained over the whole current range between threshold and the current which is required to achieve the desired optical output power, for example $P_{\mathrm{opt}} = 10\,\mathrm{W}$.

Here, the heatsink of the DFB-BA lasers was temperature -stabilized at $T = 25\,^{\circ}\mathrm{C}$ and spectra were measured in broad spectral range between 950 and 1000 nm between 0 and 15 A injection current. The spectra have been measured with a low resolution spectrometer ($\geq 0.15\,\mathrm{nm}$) with a dynamic range of $\sim 10^3$, relative to the background signal. The measurement setup is explained in section B.1.2. The measured single spectra are then combined to a matrix and plotted as a false color map. The intensity is logarithmic scaled as illustrated in the intensity scale for each spectral map. This spectral maps will be used to analyze the spectral properties of the DFB-BA lasers over the relevant range in current and wavelength.

Spectrum maps over a wide spectral range from 950 - 1000 nm are presented in Fig. 3.30 and 3.31. Fig. 3.30 (a) shows the spectrum map of laser 020416 from wafer D1365-1 ($t_{\mathrm{is}} = 90\,\mathrm{s}$, $\lambda_{\mathrm{DFB}}^{\mathrm{tar}} = 973.7\,\mathrm{nm}$). With respect to the logarithmic scaled intensity, the spectrum is dominated by the DFB spectrum (intense red line). The DFB wavelength close to threshold is 972.6 nm

and shifts to 977.3 nm at 15 A. The wavelength shift of the DFB spectrum is mostly caused by the temperature dependence of the effective refractive index with an additional contribution from the thermal expansion coefficient of the semiconductor crystal as derived in 1.1.5. One additionally finds a spectrally broad lasing background with an evolution from $\approx$ 968 nm at threshold to $\approx$ 985 nm at 15 A. The appearance of this lasing background can be predominantly attributed to lasing on FP-like modes, which are accordingly, not sufficiently suppressed. In an ideal case, FP-like modes should not exceed threshold and would then not be detected by the used setup. Note that in the range between $I = 1.0 - 5.5$ A and $\lambda = 967.5 - 972.0$ nm, the lasing background is considerably structured in contrast to the lasing background at high currents above $I = 9$ A. The spectral shift of the FP lasing background approximately follows the shift of the gain spectrum. This allows to roughly estimate the crossing of the DFB wavelength and the gain maximum at $\approx$ 9 A. In section 3.4.3, the target for the crossing has been defined as $\approx$ 9.5 A for the DFB-BA lasers with $\lambda^{\mathrm{tar}}_{\mathrm{DFB}}(I = 0) = 973.7$ nm and $\approx$ 10.6 A for $\lambda^{\mathrm{tar}}_{\mathrm{DFB}}(I = 0) = 974.6$ nm, considering $\lambda^{\mathrm{tar}}_{\mathrm{gain}}(I = 0) = 968.0$ nm. Thus, in the experiment, the crossing appears at lower currents than estimated, mostly due to the fact that the wavelength at threshold (972.6 nm) is lower than targeted ($>$ 973.7 nm). Thus, the spectral detuning is too low for efficient 10 W operation.

The spectrum map of laser 020508 from wafer D1365-2 ($t_{\mathrm{is}} = 90$ s, $\lambda^{\mathrm{tar}}_{\mathrm{DFB}} =$ 974.6 nm) is depicted in Fig. 3.30 (b). In contrast to laser 020416 from wafer D1365-1, only the DFB spectrum is visible in the spectrum map. This is a typical spectrum for a DFB-BA laser with a sufficient suppression of FP-like modes. The width of the optical spectrum, containing 95 % of the optical power is in the $\sim$ 1 nm range. A more detailed analyzes of the spectral with, measured with a high resolution spectrometer, is presented in the second part of this section. At threshold, the DFB wavelength is 974.1 nm (this is lower than targeted $>$ 974.6 nm) and shifts to 976.2 nm at 10 A. The difference in the wavelength at threshold between laser 020416 from D1365-1 and laser 020508 from D1365-2 is 1.4 nm, a difference of 0.9 nm has been targeted.

In Fig. 3.30 (c), the spectral map of laser 091002 from wafer D1366-4 ($t_{\mathrm{is}} = 120$ s, $\lambda^{\mathrm{tar}}_{\mathrm{DFB}} = 973.7$ nm) is depicted. Lasing on FP-like modes is sufficiently suppressed. The wavelength at threshold is 973.5 nm and shifts to 975.9 nm at 10 A. At $\approx$ 14.6 A, a weak increase of the intensity at $\approx$ 983.8 nm indicates, that FP-like modes begin to exceed threshold ($<$ 5 % power content).

An additional effect is visible in Fig. 3.30 (d), where the spectral map of laser 020619 from wafer D1366-5 ($t_{\mathrm{is}} = 120$ s, $\lambda^{\mathrm{tar}}_{\mathrm{DFB}} = 974.6$ nm) is depicted. In addition to the clearly dominating DFB spectrum above 973.9 nm,

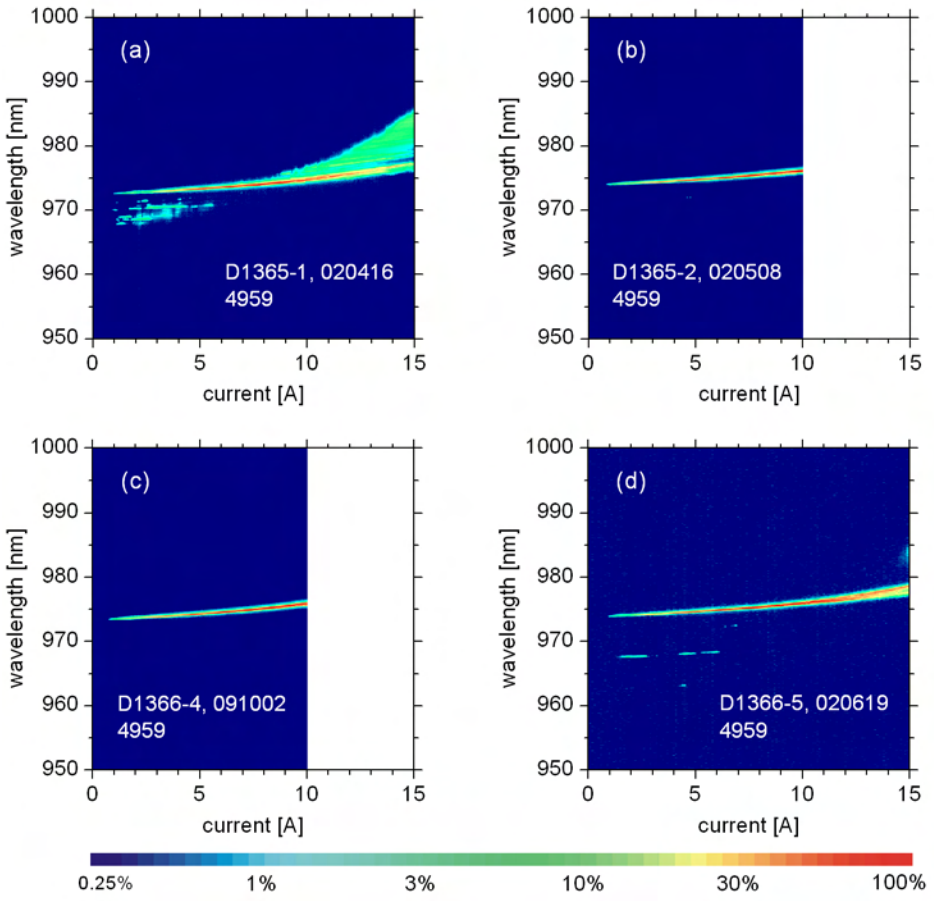

Figure 3.30: Spectrum maps over a wide spectral range for lasers from the following wafers: (a) D1365-1 ($t_{\mathrm{is}} = 90\,\mathrm{s}$, $\lambda_{\mathrm{DFB}}^{\mathrm{tar}} = 973.7\,\mathrm{nm}$), (b) D1365-2 ($t_{\mathrm{is}} = 90\,\mathrm{s}$, $\lambda_{\mathrm{DFB}}^{\mathrm{tar}} = 974.6\,\mathrm{nm}$), (c) D1366-4 ($t_{\mathrm{is}} = 120\,\mathrm{s}$, $\lambda_{\mathrm{DFB}}^{\mathrm{tar}} = 973.7\,\mathrm{nm}$), (d) D1366-5 ($t_{\mathrm{is}} = 120\,\mathrm{s}$, $\lambda_{\mathrm{DFB}}^{\mathrm{tar}} = 974.6\,\mathrm{nm}$).

three further spectrally stabilized lines are visible at shorter wavelength at $\approx 972.3\,\mathrm{nm}$, $\approx 967.2\,\mathrm{nm}$ and $\approx 963.1\,\mathrm{nm}$. Regarding the spectral distance between this further spectrally stabilized lines relative to the dominating DFB spectrum above 973.9 nm, the a priori assumption is made that these lines correspond to DFB lasing on higher-order vertical modes of the waveguide. The hypothesis, that these spectrally stabilized lines at shorter wavelengths correspond to DFB lasing on higher-order vertical modes of the waveguide, will be confirmed in section 3.4.9.

Figure 3.31 (a) shows the spectral map of laser 020412 from wafer D1425-1 ($t_{\mathrm{is}} = 120\,\mathrm{s}$, $\lambda_{\mathrm{DFB}}^{\mathrm{tar}} = 973.7\,\mathrm{nm}$). The spectrum of the DFB-BA laser is well

stabilized with a sufficient suppression of FP-like modes. No intensity from higher-order vertical modes can be found. At threshold, the DFB wavelength is 974.1 nm and shifts to 979.0 nm at 15 A.

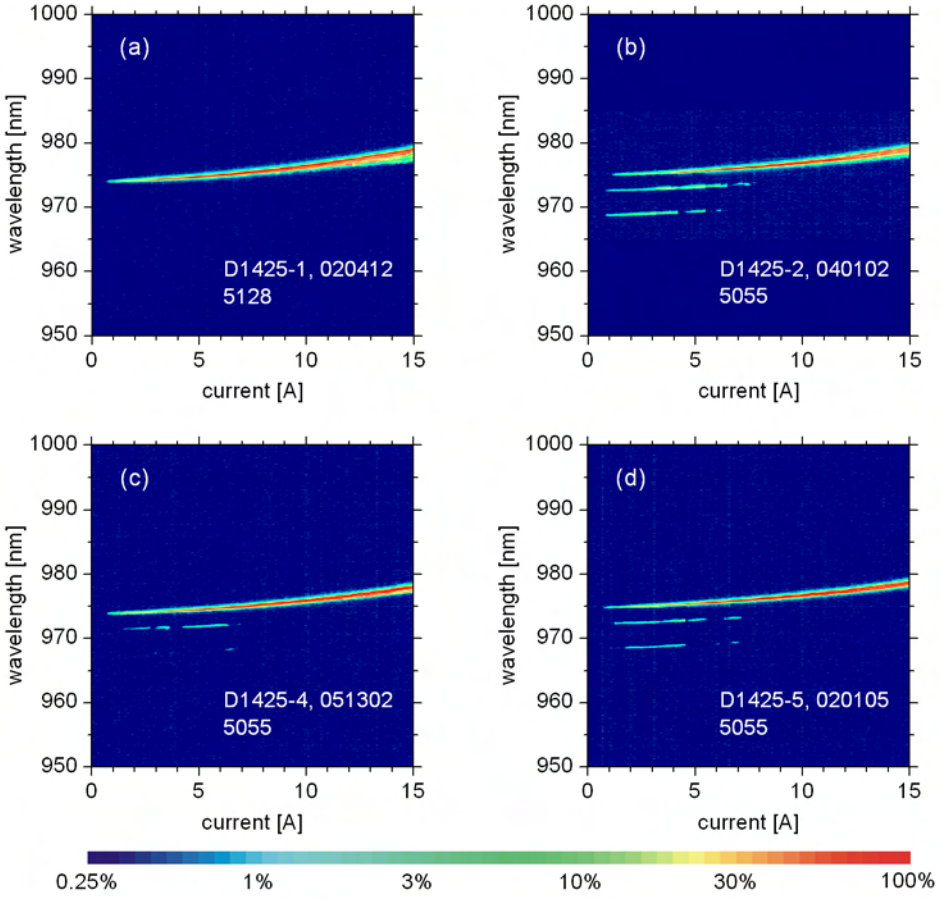

Figure 3.31: Spectrum maps over a wide spectral range for lasers from the following wafers: (a) D1425-1 ($t_{\mathrm{is}} = 120\,\mathrm{s}$, $\lambda_{\mathrm{DFB}}^{\mathrm{tar}} = 973.7\,\mathrm{nm}$), (b) D1425-2 ($t_{\mathrm{is}} = 120\,\mathrm{s}$, $\lambda_{\mathrm{DFB}}^{\mathrm{tar}} = 974.6\,\mathrm{nm}$), (c) D1425-4 ($t_{\mathrm{is}} = 150\,\mathrm{s}$, $\lambda_{\mathrm{DFB}}^{\mathrm{tar}} = 973.7\,\mathrm{nm}$), (d) D1425-5 ($t_{\mathrm{is}} = 150\,\mathrm{s}$, $\lambda_{\mathrm{DFB}}^{\mathrm{tar}} = 974.6\,\mathrm{nm}$).

In Fig. 3.31 (b), the spectral map of laser 040102 from wafer D1425-2 ($t_{\mathrm{is}} = 120\,\mathrm{s}$, $\lambda_{\mathrm{DFB}}^{\mathrm{tar}} = 974.6\,\mathrm{nm}$) is depicted. The spectrum has some similarities with the spectrum of laser 020619 from wafer D1366-5. In addition to the dominating DFB spectrum above 975.5 nm, two side peaks (higher-order vertical modes) are visible at shorter wavelength at $\approx 973.5\,\mathrm{nm}$, and $\approx 969.5\,\mathrm{nm}$. In fact, the threshold current is exceed at first for the second higher-order vertical mode at $\approx 750\,\mathrm{mA}$. The threshold current for the first

higher-order vertical mode is ≈ 850 mA. The fundamental vertical mode exceeds its threshold at ≈ 1150 mA. At its threshold, the fundamental DFB wavelength is 975.9 nm and shifts to 980.6 nm at 15 A. The lasers from wafer D1425-2 have the longest wavelength for the fundamental DFB mode, compared with the lasers from the other wafers in iteration I. Simultaneously, they have the highest slope efficiency and power conversion efficiency. If one considers, that the gain spectrum is equal for all lasers from iteration I (at least this was targeted), it can be assumed, that the highest efficiency is a consequence of the largest spectral detuning between the gain maximum and the DFB Bragg wavelength of the fundamental mode (see table 3.8). The difference in the wavelength at threshold between laser 020412 from D1425-1 and laser 040102 from D1425-2 is ≈ 1.8 nm, a difference of 0.9 nm had been targeted.

The spectrum map of laser 051302 from wafer D1425-4 ($t_{\mathrm{is}} = 150\,\mathrm{s}$, $\lambda_{\mathrm{DFB}}^{\mathrm{tar}} = 973.7\,\mathrm{nm}$) is shown in Fig. 3.31 (c). Again, two side modes are visible at shorter wavelength at ≈ 971.5 nm, and ≈ 968.3 nm. The wavelength of the fundamental DFB mode shifts from 973.9 nm at threshold to 978.0 nm at 15 A. Lasing on FP-like modes is sufficiently suppressed.

Finally, in Fig. 3.31 (d), the spectrum map of laser 020105 from wafer D1425-5 ($t_{\mathrm{is}} = 150\,\mathrm{s}$, $\lambda_{\mathrm{DFB}}^{\mathrm{tar}} = 974.6\,\mathrm{nm}$) is depicted. The fundamental DFB wavelength shifts from 974.75 nm at threshold to 978.73 nm at 15 A. Two side modes appear at shorter wavelength at ≈ 972.3 nm, and ≈ 968.5 nm. The wavelengths at threshold differ between laser 051302 from D1425-4 and laser 020105 from D1425-5 by ≈ 0.9 nm, as it had been targeted.

An overview on the DFB wavelength at threshold $\lambda_{\mathrm{th}}^{\mathrm{m0}}$, at the maximum applied drive current $\lambda_{\mathrm{max}}^{\mathrm{m0}}$, as well as the wavelengths of the characteristic spectral side modes (higher-order vertical modes) at its individual threshold $\lambda_{\mathrm{th}}^{\mathrm{m1\,...\,m3}}$ is given in table 3.8.

In summary, the DFB-BA lasers, fabricated in iteration I, achieve for the first time an optical output power in the 10 W range with a power conversion efficiency in the range of $43 - 58\,\%$ and have a narrow, wavelength stabilized optical spectrum. The spectra maps of the DFB-BA lasers show a sufficient suppression of FP-like modes ($< 5\,\%$ power content, except lasers from wafer D1365-1). Significant lasing on FP-like modes with $> 5\,\%$ power content is only observed for a wafer D1365-1 with the lowest used in-situ etching time of $t_{\mathrm{is}} = 90\,\mathrm{s}$ which corresponds to the lowest DFB coupling coefficient. A high coupling coefficient and a low front facet reflectivity are suitable design options to suppress lasing on FP-like modes.

At low currents $< 7\,\mathrm{A}$, lasing on side modes (higher order vertical modes) affects the spectrum on the short wavelength side of the fundamental DFB spectrum for some lasers, but with a low power content ($< 20\,\%$ power con-

Table 3.8: Overview of the wavelength of the fundamental DFB mode $\lambda_{\mathrm{th/max}}^{\mathrm{m0}}$ at its threshold and at the highest applied current and the wavelength of side modes (higher-order vertical modes) $\lambda_{\mathrm{th}}^{\mathrm{m1\,...\,m3}}$ for DFB-BA lasers from iteration I. Values are shown in brackets, if the suppression of FP-like modes was not sufficient. This means, that they exceed threshold (above the background signal of the used spectrometer) and contain $\geq 5\,\%$ of the optical power. If the highest applied current was 10 A instead of 15 A, the values are marked with *.

wafer	laser	$\lambda_{\mathrm{th}}^{\mathrm{m0}}$ [nm]	$\lambda_{\mathrm{max}}^{\mathrm{m0}}$ [nm]	$\lambda_{\mathrm{th}}^{\mathrm{m1}}$ [nm]	$\lambda_{\mathrm{th}}^{\mathrm{m2}}$ [nm]	$\lambda_{\mathrm{th}}^{\mathrm{m3}}$ [nm]
D1365-1	020416	(972.6)	(977.3)	–	–	–
D1365-2	020508	974.1	976.2*	–	–	–
D1366-4	091002	973.5	975.9*	–	–	–
D1366-5	020619	974.0	978.6	972.3	967.2	963.1
D1425-1	020412	974.1	979.0	–	–	–
D1425-2	040102	975.9	980.6	973.5	969.5	–
D1425-4	051302	973.9	978.0	971.5	968.3	–
D1425-5	020105	974.8	978.7	972.3	968.5	–

tent) in the additional modes. These side modes are observed for lasers from the wafers with $\lambda_{\mathrm{DFB}}^{\mathrm{tar}} = 974.3\,\mathrm{nm}$ but not for lasers from wafers with $\lambda_{\mathrm{DFB}}^{\mathrm{tar}} = 973.7\,\mathrm{nm}$ (one exception: D1425-4 051302). Thus, there is a tradeoff between the requirement to achieve a maximum power conversion efficiency at high power levels (needs high spectral detuning) and the requirement to achieve a spectrum without any side modes (needs low spectral detuning).

A selection of high resolution single spectra at 2.5, 5, 7 and 10 W is depicted in Fig. 3.32 for DFB-BA lasers D1366-5 020619 and D1425-2 040102. For both lasers, the spectral width with 95 % power content increases with the output power from $< 0.3\,\mathrm{nm}$ to $\approx 1\,\mathrm{nm}$ at 10 W.

The spectral width $\Delta\lambda_{\mathrm{W95}}$ of the DFB-BA lasers is significantly lower than the spectral width of typical FP-BA lasers. For example, the spectral width of two reference FP-BA lasers whose spectral maps are depicted in Fig. 3.7, is compared to the spectral width of two DFB-BA lasers in table 3.9. The values for $\Delta\lambda_{\mathrm{W95}}$ have been obtained by integrating over the measured spectrum with respect to the background signal from the spectrometer. Nev-

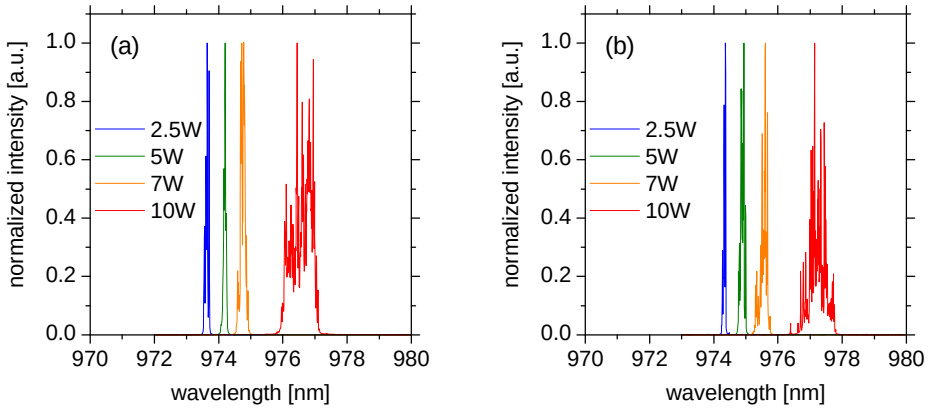

Figure 3.32: Single spectra of DFB-BA lasers at 2.5, 5, 7 and 10 W, measured with ≈ 10 pm spectral resolution and a dynamic range of 10^4. (a) DFB-BA laser D1366-5 020619. (b) DFB-BA laser D1425-2 040102.

ertheless, above ~ 7 W, the spectral width of the DFB-BA lasers with 95 % power content is broader than the targeted value of $\Delta\lambda_{W95} \leq 0.3$ nm. Therefore, an analysis of the reasons for the spectral broadening is required, which will potentially point out solutions, how the spectral width of high power DFB-BA lasers can be further reduced.

Table 3.9: Comparison of the spectral width with 95 % power content $\Delta\lambda_{W95}$ for two FP-BA lasers and two DFB-BA lasers from iteration I.

laser	$\Delta\lambda_{W95}^{2.5\,W}$ [nm]	$\Delta\lambda_{W95}^{5\,W}$ [nm]	$\Delta\lambda_{W95}^{7\,W}$ [nm]	$\Delta\lambda_{W95}^{10\,W}$ [nm]
F1850-4 071006	2.9	3.4	4.1	4.6
D1423-1 040302	2.9	3.7	4.2	4.7
D1366-5 020619	0.17	0.17	0.32	1.01
D1425-2 040102	0.12	0.23	0.40	1.01

The shape of the spectra is characterized by a number of sharp spectral lines, visible at 10 W with best clarity. This indicates, that a large number of different optical modes is involved. Knowledge of the nature of the

observed modes could be helpful for a reduction of the spectral width in further design optimizations. Lasing on a large number of different lateral modes must be assumed for a typical BA laser. It is presumed that lasing on lateral modes broadens the spectral width of the DFB spectrum because of the reasonable presumption that every lateral mode has its specific effective index of refraction (increases with increasing lateral mode order) and therefore, its specific DFB stopband and lasing wavelength. Consequently, the spectral width would depend on the number of different lateral modes (within one longitudinal mode) and the lateral spectral mode spacings. The important question, if more than one longitudinal mode is involved, cannot be answered from this type of measurements but will be later discussed, as well as the problem of the lateral modes in section 3.4.12 on the basis of adequate measurements.

In Fig. 3.33, the spectral width of seven different DFB-BA lasers is plotted as a function of the injection current, optical output power and dissipated power (heat, if the spontaneous emission es neglected), in order to study the dependence of the spectral width on these parameters. For these diagrams, the width with 95 % power content was determined from spectra, measured with a spectrometer with 15 pm resolution. The lasers used for this study are D1365-1 020417, D1365-2 020508, D1366-4 091002 and D1366-5 020619 in Fig. 3.33 (a, c, e) (left column) and D1425-2 040102, D1425-4 051302 and D1425-5 020104 in Fig. 3.33 (b, d, f) (right column). Note that in case of laser D1365-1 020417, the spectral width is affected by simultaneous lasing on FP-like modes as for example, shown for D1365-1 050416 in the spectral map in Fig. 3.30 (a). For all other devices, the spectrum is well stabilized and increases from ≈ 0.1 nm at threshold up to ≈ 1.4 nm at 15 A. The increase of the spectral width is moderate below ≈ 10 A and ≈ 8 W but more drastically above these values. The typical spectral width with 95 % power content at 7 and 10 W is $\approx 0.3 - 0.5$ and $\approx 0.8 - 1.0$ nm, respectively.

Now the question arises, if the spectral width is a function of the coupling coefficient, spectral detuning or heat. If such a dependence were found, this could be recognized for optimizing the design of the DFB-BA lasers. Firstly, a dependence of the coupling coefficient could be derived from the different in-situ etching times t_{is} which were used for the different wafers and are indicated in table 3.6. The dependence of the coupling coefficient on t_{is} has been estimated in section 3.3.3, the coupling coefficient increases with increasing in-situ etching time. However, no clear difference between the spectral width of lasers from wafers with $t_{is} = 90$ s (D1365-1, D1365-2), $t_{is} = 120$ s (D1366-4, D1366-5, D1412-2) and $t_{is} = 150$ s (D1425-4, D1425-5) can be observed in Fig. 3.33. At least, there is one conspicuous feature: The spectral width of the lasers from wafers D1425-4 and D1425-5 (both

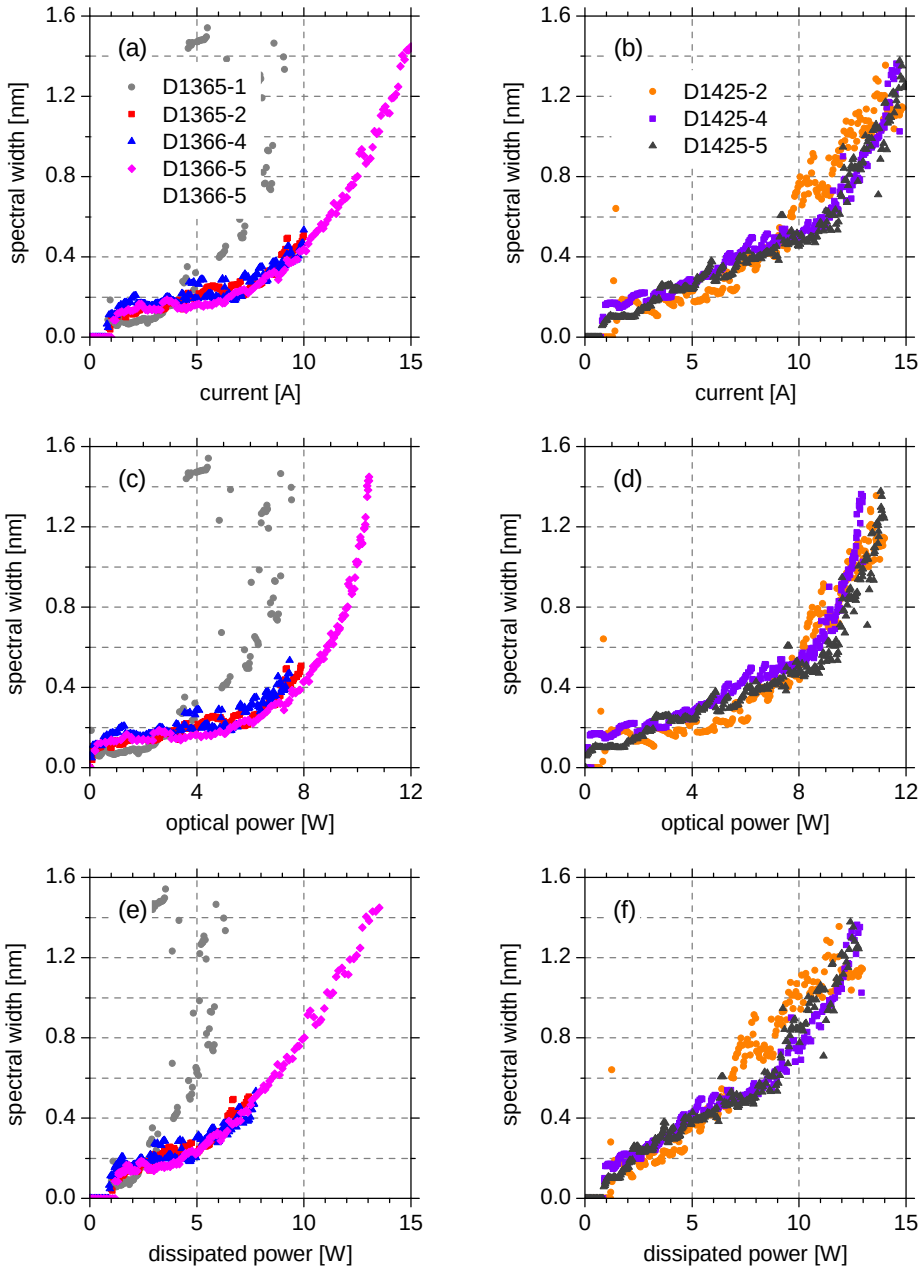

Figure 3.33: Spectral width with 95 % power content of DFB-BA lasers from iteration I. (a, b) As a function of current. (c, d) As a function of optical power. (e, f) As a function of dissipated power.

$t_{\mathrm{is}} = 150\,\mathrm{s}$) decreases more linearly with current and optical power than the

spectral width of the other lasers (t_{is} = 90 and 120 s), which starts at lower values and increases hyper-linearly. Secondly, also no clear dependence of the spectral width on the spectral detuning between the gain peak wavelength and the Bragg wavelength of the DFB grating (also indicated in table 3.6) is observed.

Finally, the dependence of the spectral width $\Delta\lambda_{W95}$ on the dissipated power P_d is depicted in Fig. 3.33 (e, f). Compared to the spectral width as a function of the current and optical power, the spectral width as a function of the dissipated power is more linear and the values for the individual lasers coincide even better. Even though this is not a proof, it might be an indication that $\Delta\lambda_{W95}(P_d)$ is a universal function for DFB-BA lasers with the same stripe widths and cavity lengths. This would mean, that the heat which is generated in the lasers is basically responsible for the increase of the spectral width. A reduction of the spectral width at high power levels should be therefore achieved with better cooling (lower thermal resistance) or higher power conversion efficiency.

To conclude, the spectra of DFB-BA lasers, developed in iteration I of this work are predominantly wavelength stabilized at the Bragg wavelength of the DFB grating. Thus, the shift of the center wavelength relative to the wavelength at threshold depends on the heat which is generated in the devices at a specific injection current. The spectral width is in part, affected by lasing on FP-like modes with a broad spectrum and lasing on additional wavelength stabilized lines on the short wavelength side of the fundamental DFB spectrum, which were supposed to be higher-order vertical modes of the waveguide. For lasers from Wafer D1365-1 (t_{is} = 90 s), lasing on FP-like modes around the gain peak is observed. This is an evidence, that either, the coupling coefficient is too low (t_{is} is too low) or the front facet reflectivity is too high (cannot be confirmed from the reflectivity spectrum , shown in Fig. 3.25 (a)).

The spectral width was also identified to possibly have a universal linear dependence on the heat which is generated in the laser chip. To reduce the spectral width of the DFB-BA lasers, developed in iteration I of this work, lasing on FP-like modes and additional side modes must be suppressed. A further reduction of the intrinsic spectral width can be possibly achieved with a higher power conversion efficiency or a lower thermal resistance.

3.4.7 Thermal properties of DFB-BA lasers

In the following section, the thermal properties of the DFB-BA lasers from iteration I will be determined in the same way, as it has been carried out for the FP-BA lasers in chapter 3.2.4. These experiments were performed on DFB-

BA laser D1425-2 040102. At first, the thermal resistance R_{th} was determined from the measurement data of the CW power-voltage-current characteristics, the spectrum as a function of the CW current and from a measurement of the spectrum as a function of the ambient temperature without heating in the active region. The temperature coefficient of the emission wavelength was determined from spectra, measured under short pulsed current injection with a pulse duration of 500 ns and a repetition rate of 1 kHz ($\cong 5 \cdot 10^{-4}$ duty cycle). The sub-mount was temperature-stabilized at 15, 20, 25, ..., 135 °C. In Fig. 3.34 (a), the center wavelength of the spectrum is depicted as a function of the sub-mount temperature under short pulse current injection. Between 35 and 135 °C, the wavelength shift is linear with 0.0776 nm K^{-1}. This value is in good agreement with the temperature-induced wavelength shift of DFB modes, reported in [Kle06], [Wen04], [Sch09a] (AlGaAs-based designs), [Ear98], [Cha00], [Kan06], [He09] (aluminum-free designs) and in good agreement with the estimation in section 1.1.5. At 15 and 25 °C, the laser runs dominantly on spectral side modes at shorter wavelengths as visible in the spectral map, shown in Fig. 3.31 (b) for $T = 25\,^{\circ}\mathrm{C}$. Fig. 3.34 (b) shows the construction of the CW center wavelength λ_{c} as a function of the CW thermal dissipation loss. A thermal resistance of $R_{\mathrm{th}} = 4.45\,\mathrm{K\,W^{-1}}$ has been determined.

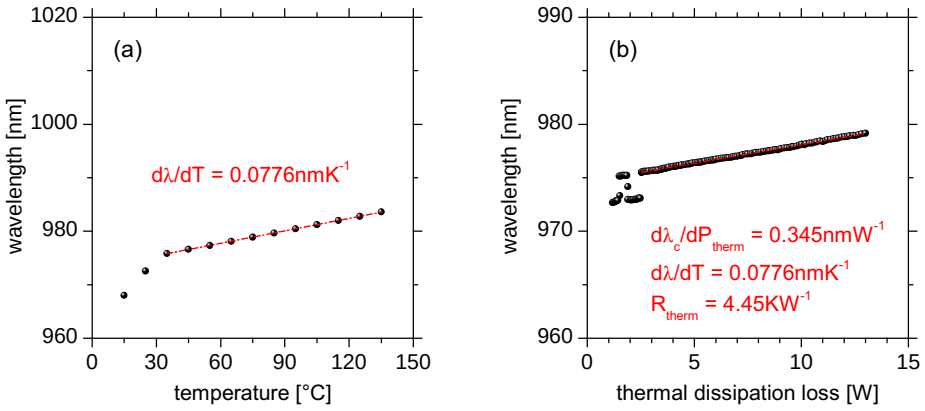

Figure 3.34: Experimental determination of the thermal resistance R_{th}. (a) Temperature dependence of the emission wavelength, measured under short pulse current injection with a pulse duration of 500 ns and a repetition rate of 1 kHz. (b) Shift of the center wavelength as a function of the thermal dissipation loss. The values have been extracted from CW power-voltage-current characteristics and CW spectrum measurements.

The result for the thermal resistance is not the same as the one, ob-

tained for the reference FP-BA lasers in chapter 3.2.4. From 20 DFB-BA lasers from iteration I with the same epitaxy design and mounting, an average value of $R_{\mathrm{th}}^{\mathrm{DFB}} = 4.79\,\mathrm{K\,W^{-1}}$ was determined. From a technical point of view it is implausible, that the FP-BA and DFB-BA lasers, reported here, have different thermal resistances, because they have the same epitaxy design and mounting scheme. Therefore it must be assumed, that the differences $R_{\mathrm{th}}^{\mathrm{DFB}} - R_{\mathrm{th}}^{\mathrm{FP}} = 4.79\,\mathrm{K\,W^{-1}} - 3.58\,\mathrm{K\,W^{-1}} = 1.21\,\mathrm{K\,W^{-1}}$ in the average thermal resistances are a consequence of the methods which were used for their determination. In the case of the reference FP-BA lasers, $\mathrm{d}\lambda_{\mathrm{gain}}/\mathrm{d}T$ is sensitive to the temperature in the active region. The accuracy of R_{th} depends on the determination of the center wavelength of the FP spectrum. In contrast, $\mathrm{d}\lambda_{\mathrm{DFB}}/\mathrm{d}T$ is sensitive to the effective refractive index n_{eff} and hence, sensitive to the vertical temperature profile in the whole waveguide. Furthermore, the thermal dissipation loss has been simply calculated from $P_{\mathrm{d}} = U(I) \cdot I - P_{\mathrm{opt}}(I)$, where $P_{\mathrm{opt}}(I)$ is the optical power, measured at the front facet. This means, that the optical output power from the rear facet has not been considered (it is expected to be higher for the DFB-BA lasers as derived in section 1.2.5) and the spontaneous emission is neglected. An analysis how the thermal resistance of high power DFB-BA lasers and reference FP-BA lasers can be experimentally determined with high precision and which effects have to be therefore considered could be the purpose of a future investigation.

To compare the thermal behavior of the threshold current and slope efficiency with the reference FP-BA laser, power-voltage-current characteristics have been measured under the same short pulse current injection as used for the determination of the temperature coefficient of the emission wavelength. The characteristics of the DFB-BA laser are depicted in Fig. 3.35 (b) and compared to the characteristics of the FP-BA laser, shown in Fig. 3.35 (a). While one finds a strictly monotonic increase of the threshold current and a strictly monotonic decrease of the slope efficiency for the FP-BA laser, the behavior is more complicated for the DFB-BA laser.

Fig. 3.35 (c) and (d) shows temperature dependence of the threshold current and slope efficiency of both, the DFB-BA laser (red triangles) and the FP-BA laser (blue circles), respectively. Here, the more complicated behavior for the DFB-BA laser is confirmed. The threshold current of the DFB-BA laser increases faster with the temperature. Above 55 °C, the gradient increases abruptly. In the range between 15 and 45 °C, the gradient is only slightly higher than for the FP-BA laser. The slope efficiency rapidly increases with the temperature between 15 and 35 °C, then it tangents the curve for the FP-BA laser and shows a faster reduction with the temperature from 75 to 135 °C.

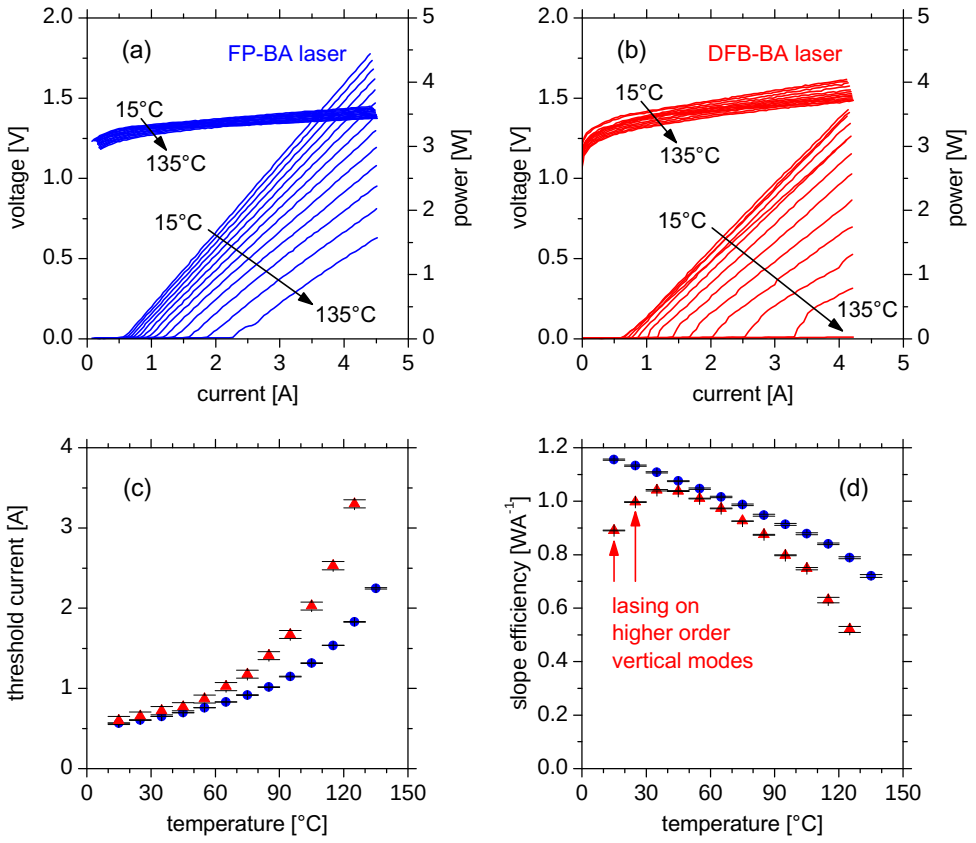

Figure 3.35: Temperature dependence of the threshold current and slope efficiency between 15 °C and 135 °C (10 K step size) under short pulse current injection with a pulse duration of 500 ns and a repetition rate of 1 kHz. (a) Power-voltage-current characteristics of the FP-BA laser. (b) Power-voltage-current characteristics of the DFB-BA laser D1425-2 040102. (c) Threshold current of the DFB-BA laser (red triangles) and the FP-BA laser (blue circles) as a function of the temperature. (d) Slope efficiency of the DFB-BA laser (red triangles) and the FP-BA laser (blue circles) as a function of the temperature.

This, behavior of the DFB-BA laser D1425-2 040102 can be understood by considering the appearance of low wavelength side modes in the optical spectrum which is shown in the spectral map in Fig. 3.31 (b) for $T = 25\,°C$. At low temperatures (15 - 25 °C), the maximum of the gain profile is in the spectral region of the wavelength stabilized side modes and several nanometers apart from the fundamental DFB mode. Lasing on the short wavelength side modes is the reason, why at 15 - 25 °C, the wavelength does not follow

the wavelength trend above 25 °C in Fig. 3.34 (a) and why the slope efficiency increases with increasing temperature in Fig. 3.35 (d) (here, the short wavelength side modes are indicated as higher-order vertical modes of the waveguide). For illustration, such spectral relation between the gain spectrum, fundamental DFB mode and two side modes is shown as a scheme in Fig. 3.36 (a). This results in a low slope efficiency and in a moderate threshold current, which is slightly increased in comparison with the FP-BA laser. Between 35 and 65 °C, the DFB-BA laser runs dominantly on the fundamental DFB mode, because its Bragg-wavelength of the DFB grating is close to the maximum of the gain profile. Such spectral relation between the gain spectrum, the fundamental DFB mode and two side modes is depicted schematically in Fig. 3.36 (b). Hence, the slope efficiency is close to the values for the FP-BA laser. Even the threshold current is only $\sim 20\,\%$ higher. Above 65 °C, the DFB-BA laser still runs on the fundamental DFB mode, but a strong spectral detuning between the Bragg-wavelength and the maximum of the gain profile degrades the threshold current and slope efficiency, compared to the FP-BA laser. Finally, a spectral relation were the peak of the gain spectrum is on the long wavelength side of the fundamental DFB mode is depicted schematically in Fig. 3.36 (c). On the one hand, the two short side modes at the short wavelength side of the fundamental DFB mode are now strongly suppressed. On the other hand, the gain at the fundamental DFB wavelength is now lower than the peak gain and further increasing the temperature leads to a strong increase of the threshold current and to a strong decrease in slope efficiency.

The diagrams of $\ln(I_{\mathrm{th}}/I_0)$ and $\ln(S/S_0)$ as a function of T, are depicted in Fig. 3.37 (a) and (b), respectively. The results for the DFB-BA laser (red triangles) are shown in comparison with the results for the FP-BA laser (blue circles). The DFB-BA laser has a different dependence of the threshold current and slope efficiency on the temperature, than the FP-BA laser. The threshold current increases faster with the temperature. Especially between 45 and 55 °C, the gradient increases abruptly. In the range between 15 and 45 °C, the gradient is only slightly higher than for the FP-BA laser.

A threshold current characteristic temperature $T_0 = 98\,\mathrm{K}$ can be in principle determined from a linear fit between 15 °C and 65 °C for the DFB-BA laser. Nevertheless, the specification of threshold current and slope efficiency characteristic temperatures T_0 and T_1 is not recommendable for DFB lasers because of the spectral detuning between the gain peak wavelength and the Bragg wavelength of the DFB grating. It has been shown in this section that the spectral detuning can lead to fundamental differences in the temperature dependence of the slope efficiency, compared to a free running FP reference device. A good agreement between the temperature dependence of the slope

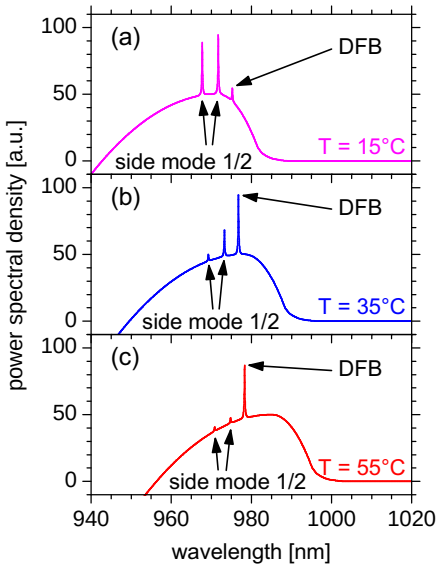

Figure 3.36: Scheme of the optical gain spectrum, the fundamental DFB mode and two also wavelength stabilized side modes at different ambient temperatures. (a) At $T = 15\,°\mathrm{C}$. (b) At $T = 35\,°\mathrm{C}$. (c) At $T = 55\,°\mathrm{C}$.

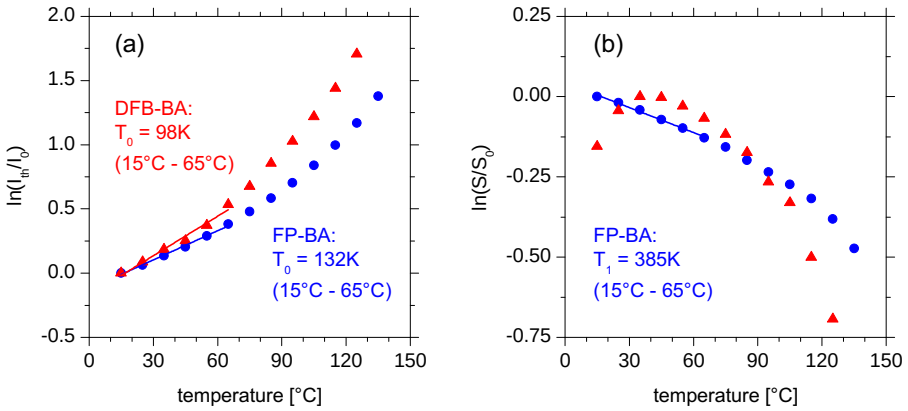

Figure 3.37: Diagrams of $\ln(I_{\mathrm{th}}/I_0)$ and $\ln(S/S_0)$ for the DFB-BA laser D1425-2 040102 in comparison with a FP-BA laser. (a) $\ln(I_{\mathrm{th}}/I_0)$ as a function of T, T_0 has been determined from a linear fit between 15 °C and 45 °C. (b) $\ln(S/S_0)$ as a function of T.

efficiency for the DFB-BA laser and the FP-BA reference laser can be found over a limited temperature range between > 35 and $< 75\,°\mathrm{C}$. This is ap-

proximately the temperature range (under short pulsed current injection) in which the Bragg wavelength of the DFB grating is in the flat peak region of the gain spectrum. However, the temperature dependence of the threshold current is already significantly increased in this temperature range.

3.4.8 Spatial emission properties of DFB-BA lasers

This chapter focuses on the spatial emission properties of the DFB-BA lasers from iteration I. Firstly, it is necessary to show, that the monolithic integration of the DFB grating does not significantly degrades the vertical and lateral far field properties. Secondly, experimental results for the vertical and lateral far field profiles can be useful to analyze the vertical and lateral modes, respectively. In section 3.4.6 it has been discussed that the side modes in the optical spectrum at the short wavelength side of the fundamental DFB mode are supposed to be higher-order vertical modes of the waveguide. Therefore, indications should be found in measured vertical far field profiles. Furthermore, the spectral width of the spectrally stabilized fundamental DFB mode is expected to be limited by the appearance of many different lateral modes like for a typical BA laser. This is based on the reasonable presumption that every lateral mode has its specific effective index of refraction and therefore, its specific DFB stopband and lasing wavelength. This has also been discussed in section 3.4.6.

The vertical far field profiles have been measured with the setup, described in section B.1.3. Note, that the vertical far field profiles were not measured under cw conditions. To keep the exposure of the detector below its damage threshold, quasi-continuous wave (QCW) conditions (500 μs pulse duration, 20 kHz repetition rate) have been applied. The heat sink temperature was stabilized at 25 °C.

Fig. 3.38 shows the vertical far field profiles of DFB-BA lasers D1365-2 020508 and D1425-2 040102. In Fig. 3.38 (a), the linear scaled far field profiles of DFB-BA lasers D1365-1 020508 are depicted for output powers of 2.5, 5 and 7 W. The profiles are Gaussian shaped and very similar for the different output powers. The FWHM value is in the range of 28 ° and the divergence angle with 95 % power content is about 46 °. Thus, the vertical far field profile with 95 % power content is approximately 1 ° broader than it has been targeted. Even in the logarithmic scaled diagram in Fig. 3.38 (b), one finds no significant differences in the measured profiles. Note, that in the spectral map of the identical device, shown in Fig. 3.30 (b), no side modes occur in addition to the fundamental DFB mode. Thus, it has been expected that no indications for the occurrence of higher-order vertical waveguide modes will be observed.

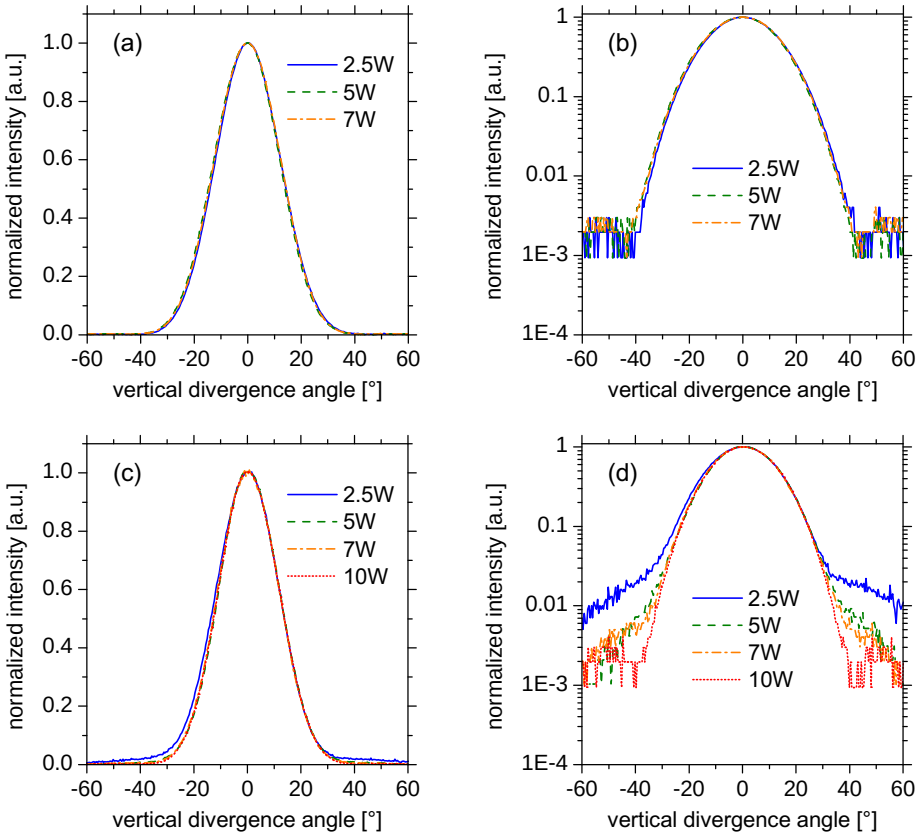

Figure 3.38: Vertical far field profiles of the DFB-BA lasers D1365-2 020508 and D1425-2 040102. (a) Linear scaled vertical far field profiles of the DFB-BA laser D1365-2 020508 for 2.5, 5 and 7 W. (b) Logarithmic scaled vertical far field profiles from (a). (c) Linear scaled vertical far field profiles of the DFB-BA laser D1425-2 040102 for 2.5, 5, 7 and 10 W. (d) Logarithmic scaled vertical far field profiles from (c).

The linear scaled vertical far field profiles of DFB-BA laser D1425-2 040102 are depicted in Fig. 3.38 (c), for output powers of 2.5, 5, 7 and 10 W. For this device, one finds a weak decreasing of the vertical divergence with increasing output power. Especially at 2.5 W, the profile is broadened at negative angles, corresponding to the *p*-side of the waveguide. The FWHM value is in the range of 26 ° and the divergence angle with 95 % power content is about 45 °. In the logarithmic scaled diagram in Fig. 3.38 (d), one finds significant differences in the profiles. Firstly, the broadening at negative angles is visible again. Secondly, a kind of shoulders appears two-sided for angles

with an absolute value above 30 °. These shoulders vanish at 10 W. For DFB-BA laser D1365-2 020508, the width of the measured vertical far field profiles is comparable the results for the reference FP-BA laser, presented in section 3.2.5 and summarized in table 3.3. In contrast, the vertical far field width of DFB-BA laser D1425-2 040102 is in good agreement with the FP-BA laser results only at an output power of 10, W, where the shoulders in the profile have vanished.

It seems to be plausible to attribute these shoulders in the vertical far field profiles of laser D1425-2 040102 to the onset of additional higher-order waveguide modes, which have been found in the corresponding spectral map (Fig. 3.38 (b) and were denoted as spectrally stabilized short wavelength side modes. Thus, the occurrence of higher-order waveguide modes is observed to broaden the vertical far field of DFB-BA lasers, a characteristic behavior which is not observed for the reference FP-BA lasers. The question, why higher-order waveguide modes are sufficiently suppressed for the reference FP-BA lasers but not for the DFB-BA lasers will be discussed in the following section 3.4.9. A better suppression of such higher-order waveguide modes turns out to be important factor for the further optimization of the spectral properties, as well as the spatial emission properties of DFB-BA lasers.

Indeed, one has to take into account, that the profiles have been measured under QCW conditions. Thus, the modal content at 25 °C heat sink temperature is not necessarily identical to the operation under CW conditions. The exact values for the FWHM and the divergence with 95 % power content are given in tables 3.10 and 3.11.

For the measurement of the lateral near field and far field profiles, the setup described in section B.1.3 has been used. The measurements were proceeded under CW conditions, the heat sink temperature was stabilized at 25 °C. For possible applications where the output beam of DFB-BA lasers must be collimated with lenses, it is important to achieve a narrow lateral divergence angle, for example $\leq 7°$ with 95 % power content, in order to minimize the system loss. Furthermore, the shape of lateral near field and far field profiles contains information about the lateral modes in the DfB-BA lasers. Finally, the width of lateral near field profiles allows to investigate, if the targeted contact stripe width of $W = 90\,\mu$m really leads to the targeted near field width of also 90 μm (with 95 % power content).

Figure 3.39 shows the linear scaled lateral near field profiles of DFB-BA lasers D1365-1 020417, D1365-2 020508, D1366-4 091002 and D1366-5 020618 at output powers of (a) 2.5 W, (b) 5 W, and (c) 7 W. The near field profiles are extended over approximately 100 μm, which is at a first glance in good agreement with the contact stripe width of 90 μm. Collectively, the profiles are periodically structured. This periodic intensity modulation is an

indication, that the near field profiles constitute as a sum of multiple higher-order lateral modes. Neglecting the roughly periodic intensity modulation, the near field profiles have a top hat shape. The values for the width with 95 % power content are given in table 3.10.

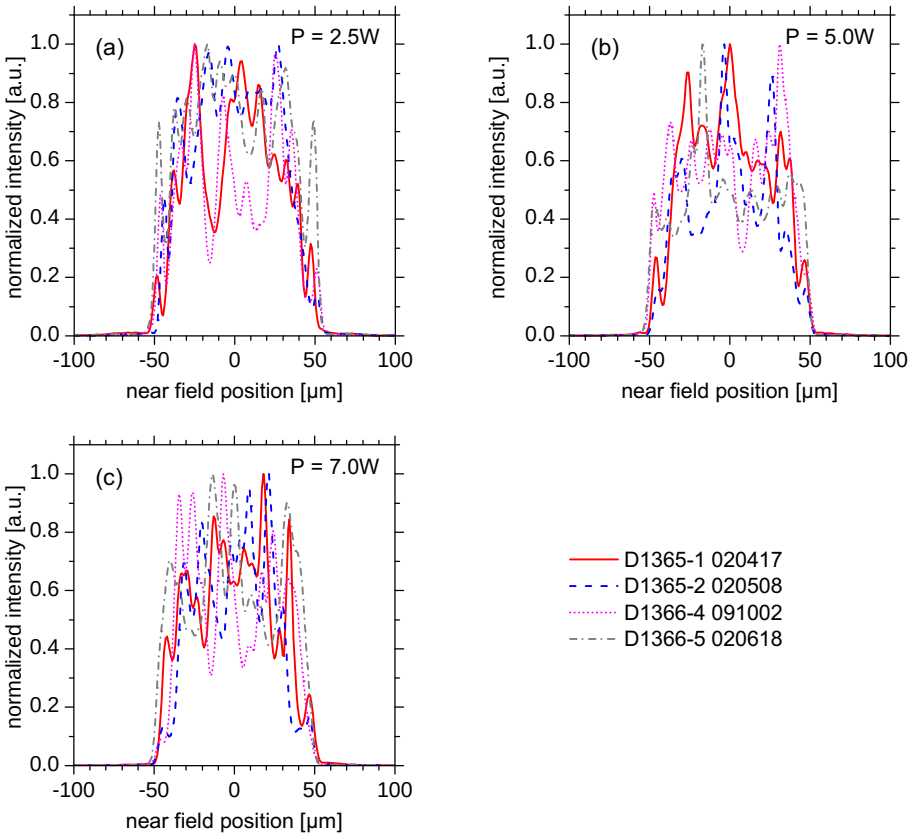

Figure 3.39: Lateral near field profiles of DFB-BA lasers from wafers D1365-1, D1365-2, D1366-4 and D1366-5 for (a) 2.5 W. (b) 5 W and (c) 7 W.

In Fig. 3.40, the linear scaled lateral near field profiles of DFB-BA lasers D1425-1 020410, D1425-2 040102, D1425-4 051301 and D1425-5 020104 are depicted at output powers of (a) 2.5 W, (b) 5 W, (c) 7 W and (d) 10 W. Again, the near field profiles are extended over approximately 100 μm, in good agreement with the contact stripe width. The profiles are roughly periodically structured. The envelope of the near field profiles for output powers $\leq$ 7 W has a top hat shape. In contrast, at 10 W, the profiles tend to a concentration of the intensity in the center part of the electrically pumped area. This intensity concentration is a consequence of the so called thermal lens-

ing [Koe70], [Wen08] in the lateral direction. The phenomenological impact of thermal lensing is consistent with experimental and theoretical results, recently published in [Cru12a]. The values for the width with 95 % power content are given in table 3.11.

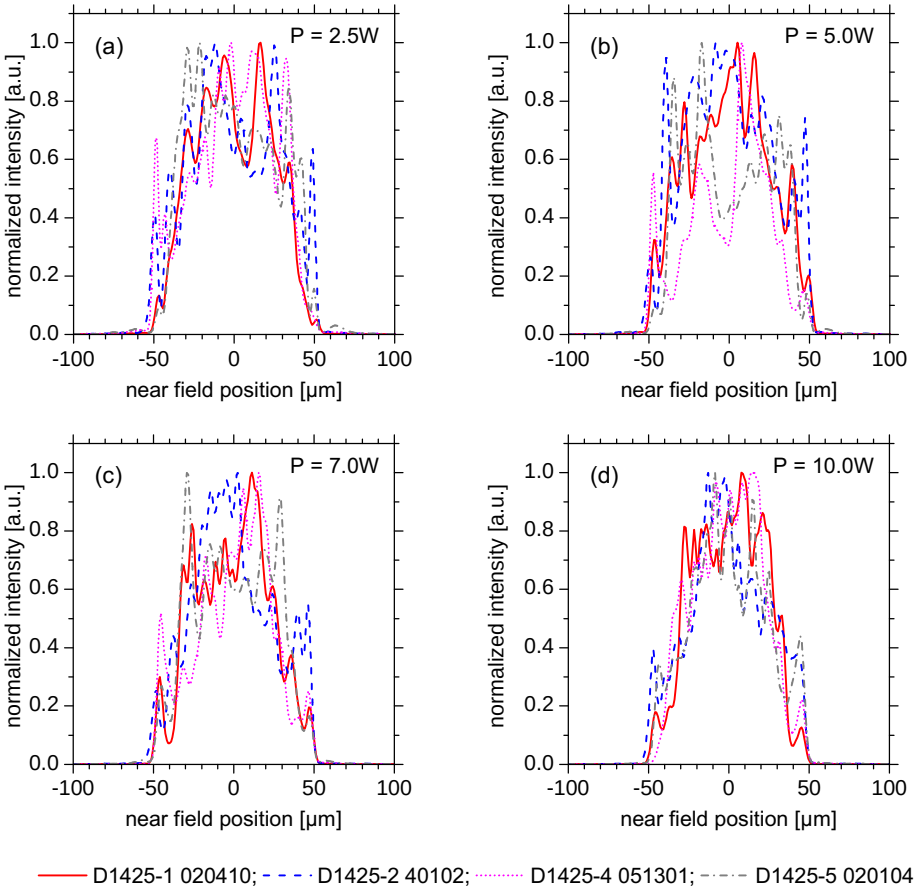

Figure 3.40: Lateral near field profiles of DFB-BA lasers from wafers D1425-1, D1425-2, D1425-4 and D1425-5 for (a) 2.5 W. (b) 5 W, (c) 7 W and (d) 10 W.

The values for the width of the lateral near field with 95 % power content, summarized in table 3.10 and 3.11 show, that the lateral near field extends over a width of $\approx 90\,\mu$m as targeted from the design. With increasing output power, the lateral near field width with 95 % power content and especially, the FWHM value, decreases due to thermal lensing. Both, the near field width and the measured profiles are in good agreement with what has been observed for the reference FP-BA lasers, discussed in section 3.2.5 and summarized in table 3.3. The experimental investigation of comparable lateral near field

profiles for DFB-BA lasers and reference FP-BA lasers is exactly what has been expected because no changes in the lateral design of this lasers have been made and distributed feedback is used as a longitudinal effect which should not alter the lateral near field profile.

Fig. 3.41 shows the linear scaled lateral far field profiles of DFB-BA lasers D1365-1 020417, D1365-2 020508, D1366-4 091002 and D1366-5 020618 at output powers of (a) 2.5 W, (b) 5 W, and (c) 7 W. The far field profiles are also considerably structured, but they have a more gaussian shaped envelope. The divergence angle with 95 % power content is in the range of about 10 ° at 2.5 W and broadens to about 15 ° at 7 W. The values for the divergence angle with 95 % power content and the FWHM are given in table 3.10.

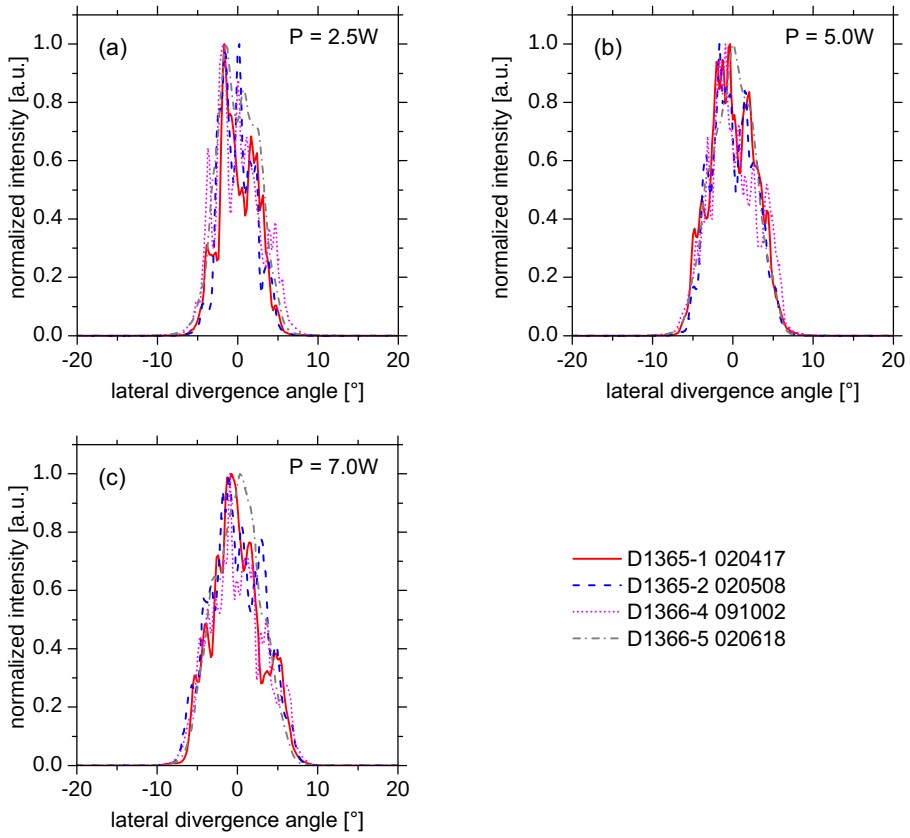

Figure 3.41: Lateral far field profiles of DFB-BA lasers from wafers D1365-1, D1365-2, D1366-4 and D1366-5 for (a) 2.5 W. (b) 5 W and (c) 7 W.

The linear scaled lateral far field profiles of DFB-BA lasers D1425-1 020410, D1425-2 040102, D1425-4 051301 and D1425-5 020104 at output

powers of (a) 2.5 W, (b) 5 W, (c) 7 W and (d) 10 W, are finally shown in Fig. 3.42. The far field profiles broadens strongly with the increasing output power. Especially at 10 W, the far field divergence is very broad with up to 17.8 ° with 95 % power content.

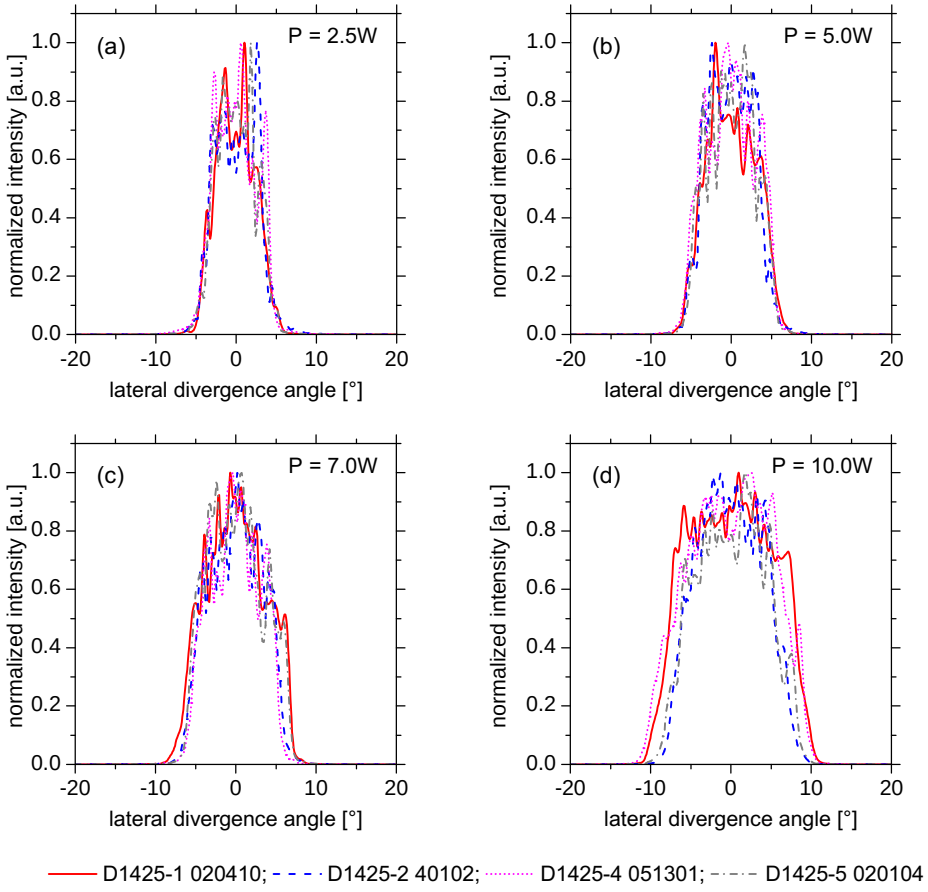

Figure 3.42: Lateral far field profiles of DFB-BA lasers from wafers D1425-1, D1425-2, D1425-4 and D1425-5 for (a) 2.5 W. (b) 5 W, (c) 7 W and (d) 10 W.

Interestingly, the far field profiles have the biggest differences in the divergence angle (with 95 % power content) at 10 W as can bee seen from the values which are summarized in tables 3.10 and 3.11. If one compares the divergence angle with 95 % power content at 10 W with the power conversion efficiency, given in table 3.7, one finds that the lasers with the highest power conversion efficiency (D1425-2 040102: $\eta_{PCE}^{10W} = 0.523$, D1425-5 020104: $\eta_{PCE}^{10W} = 0.501$) have the smallest far field divergence, and the lasers with the lower power conversion efficiency (D1425-1 020410: $\eta_{PCE}^{10W} = 0.443$, D1425-4

051301: $\eta_{PCE}^{10W} = 0.435$) have the highest far field divergence. This correlation is a consequence of thermal lensing, because the impact of the thermal induced change in the lateral refractive index profile on the near field and far field profiles increases with an increasing thermal dissipation loss.

Table 3.10: Overview of the divergence angles of the vertical far field as well as the lateral near field and far field from DFB-BA lasers of the first four wafers.

P_{opt} [W]	VFF [°] FWHM	VFF [°] W95%	LNF [μm] FWHM	LNF [μm] W95%	LFF [°] FWHM	LFF [°] W95%
D1365-1	020417					
2.5	–	–	79.5	90.0	4.8	8.6
5.0	–	–	74.8	88.8	6.4	10.2
7.0	–	–	72.4	88.2	5.4	11.5
D1365-2	020508					
2.5	28.3	43.2	74.6	86.8	5.3	8.2
5.0	28.8	43.4	66.8	84.6	7.2	9.8
7.0	28.3	43.8	65.3	80.3	8.2	12.2
D1366-4	091002					
2.5	–	–	76.1	94.6	6.0	10.4
5.0	–	–	81.3	92.3	7.7	11.2
7.0	–	–	77.7	81.6	7.6	12.5
D1366-5	020618					
2.5	–	–	100.1	97.6	6.5	9.4
5.0	–	–	71.2	94.8	6.8	10.2
7.0	–	–	88.6	90.0	7.2	10.8

The width of the lateral near field and far field profiles with 95 % power content is depicted in Fig. 3.43 as function of the optical output power P_{opt} and dissipation loss $P_d = U(I) \cdot I - P_{opt}$. A weak decrease of the near field width is observed with increasing output power in Fig. 3.43(a) as a consequence of thermal lensing. The width of the lateral far field shown in Fig. 3.43(b) increases with the output power from $\approx 9\,^\circ$ at 2.5 W towards

Table 3.11: Overview of the divergence angles of the vertical far field as well as the lateral near field and far field from DFB-BA lasers of the second four wafers.

P_{opt} [W]	VFF [°] FWHM	VFF [°] W95%	LNF [μm] FWHM	LNF [μm] W95%	LFF [°] FWHM	LFF [°] W95%
D1425-1	020410					
2.5	–	–	70.2	80.0	5.8	8.5
5.0	–	–	78.9	89.3	8.3	10.6
7.0	–	–	60.9	87.4	11.8	12.7
10.0	–	–	63.8	76.2	15.6	17.0
D1425-2	040102					
2.5	27.0	48.2	91.4	97.8	6.6	9.0
5.0	25.6	47.7	91.0	93.2	7.7	10.0
7.0	25.6	45.3	75.9	92.7	9.8	11.2
10.0	26.1	43.8	53.4	90.9	11.5	13.9
D1425-4	051301					
2.5	–	–	86.8	89.2	7.3	8.8
5.0	–	–	73.7	92.3	9.1	10.5
7.0	–	–	69.7	91.1	10.1	12.1
10.0	–	–	60.4	79.3	14.1	17.8
D1425-5	020104					
2.5	–	–	81.6	84.3	6.7	8.5
5.0	–	–	77.5	81.2	8.9	9.9
7.0	–	–	66.9	86.2	10.0	11.8
10.0	–	–	51.6	88.3	11.8	15.1

$\approx 15\,^{\circ}$ at 10 W. Especially the nonlinear increase of the far field width above 7 W, is assumed to be a consequence of thermal lensing. As already mentioned, the power conversion efficiency at the specific optical output power seems to play an important role for the width of the far field, which is important for many possible applications of BA diode lasers. Thus, the width of the lateral near field and far field profiles has been plotted as function of the

dissipation loss in Fig. 3.43(c) and (d) in order to analyze the impact of the generated heat. In contrast to the diagrams as functions of the optical output power (Fig. 3.43(a) and (b)), the measurement results form quasi universal lines. This is especially the case for the divergence angle of the lateral far field.

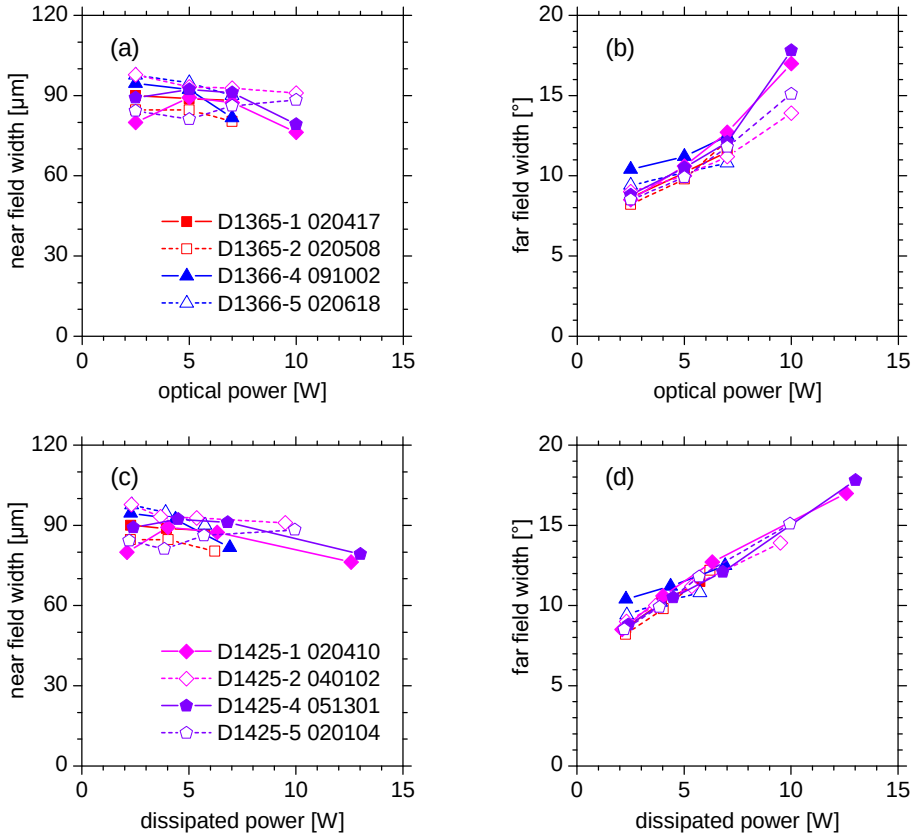

Figure 3.43: Width of the lateral near field and far field profiles of DFB-BA lasers from wafers D1365-1, D1365-2, D1366-4, D1366-5, D1425-1, D1425-2, D1425-4 and D1425-5 with 95 % power content as functions of the optical output power and dissipated power. (a) Lateral near field width as a function of the optical output power. (b) Lateral far field width as a function of the optical output power. (c) Lateral near field width as a function of the dissipated power. (d) Lateral far field width as a function of the dissipated power.

From the quasi universal linear behavior of the lateral divergence angle as a function of the dissipated power ($\sim 0.9\,^\circ\,\mathrm{W}^{-1}$) it can be derived, that reductions in the lateral far field width can be particularly achieved by in-

creasing the power conversion efficiency of the BA lasers. Possibly, the value of the gradient and the crossing with the y-axis can be improved by using optimized lateral design in the wafer processing.

3.4.9 Properties of higher-order vertical waveguide modes

In the CW spectral maps for DFB-BA lasers shown in Fig. 3.30 and 3.31, up to three wavelength stabilized side modes have been observed in the optical spectrum at the short wavelength side of the fundamental DFB mode. These modes were supposed to be higher-order vertical modes of the waveguide. Furthermore, a broadening of the vertical far field profiles was observed at low currents (QCW) and low powers which vanishes at high injection currents $I \geq 10\,\mathrm{A}$. Also the broadening of the vertical far field profiles was attributed to lasing on higher-order vertical modes of the waveguide with low power content. Already the simulations of the waveguide design with QIP have shown that higher-order modes can be found but the strong increase of the internal optical loss with increasing vertical mode order has been expected to result in a sufficient suppression of the higher-order modes. Note that for the reference FP-BA lasers, no indication for lasing on higher-order waveguide modes was found in the optical spectra and vertical far field profiles. The suppression of higher-order modes can be sufficient related to the goals defined for this work, if higher-order modes do not affect the spectral width and vertical far field width by containing more than 5 % of the power content.

In this section, the origin of the side modes in the optical spectrum will be identified. Several measurements were performed in order to confirm that these side modes are higher-order vertical modes of the waveguide. In addition, the theoretical threshold current of the different vertical mode orders is calculated and a comparison of the results for DFB-BA lasers and reference FP-BA lasers shows that indeed, the suppression of higher-order modes is much lower for the DFB-BA lasers than for the FP-BA lasers. Finally, conclusions are derived how sufficient suppression of higher-order waveguide modes can be achieved with optimized DFB-BA laser designs.

The onset of higher-order vertical waveguide modes in the DFB-BA lasers affects the spectrum as well as the vertical near field and far field profiles, threshold current and slope efficiency. Indications for lasing on higher-order vertical waveguide modes can be therefore observed in the measured spectral maps (Fig. 3.30 and 3.31), in the vertical far field profiles (Fig.3.38), and marginally in the threshold current and slope efficiency (table 3.7). However,

to provide clear experimental evidence by measurements of vertical far field profiles turned out to be difficult with the 3 mm long DFB-BA lasers.

Fig. 3.38 (c), (d) shows measured vertical far field profiles of DFB-BA laser D1425-2 040102 with significant intensities in higher-order waveguide modes, as can be seen from the spectrum map in Fig. 3.31 (b). Note, that the vertical far field measurements have been carried out under QCW conditions (500 μs current pulse width and 20 kHz repetition rate) in contrast to the spectral maps which were measured at CW current injection, thus the heating is not exactly the same. At output powers below 10 W, the vertical far field profiles are broadened and show background intensities that vanish at 10 W. Typical multiple peak far fields with hermite-gaussian shaped mode profiles as shown in Fig. 3.20 (d), could not be measured for the 3 mm long DFB-BA lasers because the measured far fields are the sum of multiple vertical modes with high intensity of the fundamental mode (typically $\geq 80\,\%$ power content with CW current injection) only low intensities in the higher-order modes. Therefore, the far field profiles are dominated by the gaussian shaped profile of the fundamental mode.

Evidence of the nature of the higher-order vertical waveguide modes has been successfully provided with DFB-BA lasers with a short cavity length of $L = 1\,\text{mm}$ ($R_\text{f} = 10\,\%$, $R_\text{r} = 96\,\%$). These lasers run predominantly on the second and third higher-order vertical waveguide mode (two and three vertical intensity maxima, respectively) due to a short wavelength of the gain maximum under the used measurement conditions. The emitted vertical far field has a very wide, multiple peak profile. Fig. 3.44 shows some measurement results at this type of short cavity DFB-BA lasers, concerning the vertical modes and their far field profiles.

In Fig. 3.44 (a), a linear scaled spectral map of laser D1366-4 000602 is depicted. The laser runs on two vertical modes, visible as two sharp spectral lines. Fig. 3.44 (b) shows two far field profiles of the same laser, measured at 0.9 A and 2.0 A. From the corresponding linear scaled spectral map shown in Fig. 3.44 (a) one can derive that at $I = 0.9\,\text{A}$, the longer wavelength mode ($\sim 962\,\text{nm}$) clearly dominates while at $I = 2.0\,\text{A}$ the shorter wavelength mode ($\sim 952\,\text{nm}$) has the higher intensity. From the shape of the intensity profiles, especially from the number of local maxima, it has been reasoned that Fig. 3.44 (b) shows the experimental verification of a dominating second higher-order mode (bottom, $I = 0.9\,\text{A}$) and a third higher-order mode (top, $I = 2.0\,\text{A}$) (fundamental mode: zeroth-order).

A mapping of the vertical far field distribution of laser D1366-4 000609 (from the same laser bar as chip 000602, same layout) as a function of the injection current is depicted in Fig. 3.44 (c). By analyzing the number of the vertical intensity maxima between 1.0 and 2.4 A, one finds a transition from

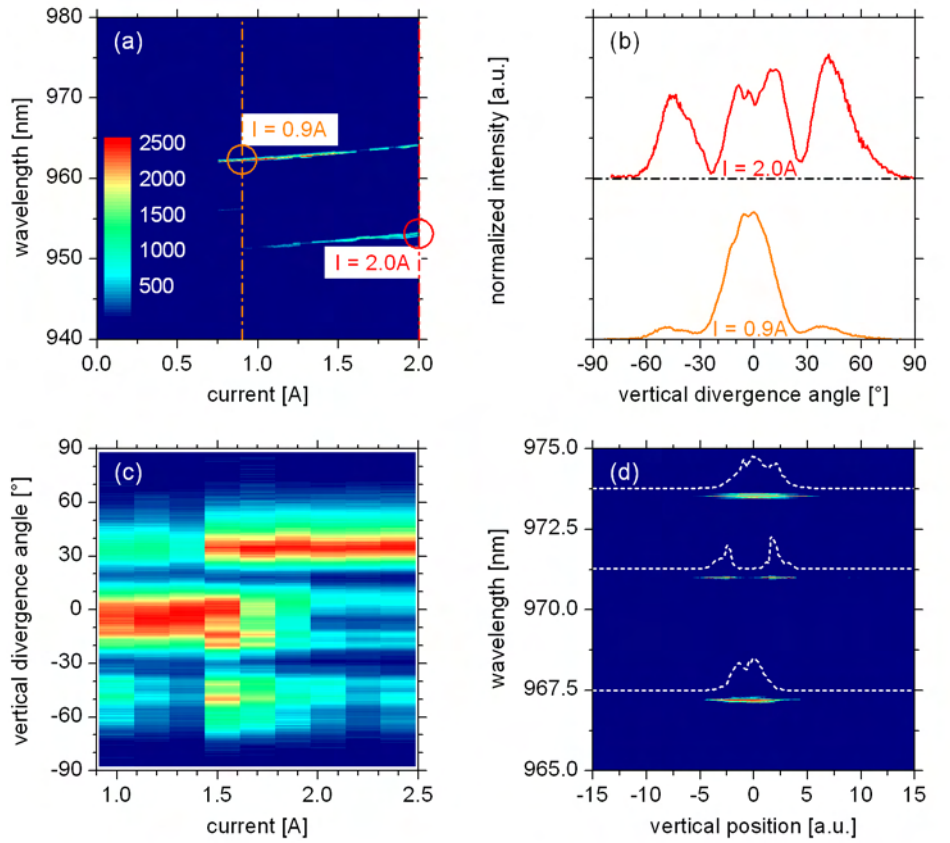

Figure 3.44: Evidence of higher-order waveguide modes in 1 mm long DFB-BA lasers with $W = 50\,\mu$m contact stripe width. (a) Linear scaled spectrum map of laser D1366-4 000602 with two vertical modes, visible as sharp spectral lines. (b) Far field profiles of laser D1366-4 000602, at 0.9 A (bottom) and 2.0 A (top), the positions are indicated (a). (c) Mapping of the far field distribution of laser D1366-4 000609 as a function of the drive current. (d) Spectrally resolved vertical near field scan of the front facet of a laser from wafer D1366-5.

the second-order mode (three maxima, dominating) to the third-order mode (four maxima, dominating).

Finally, Fig. 3.44 (d) shows a false color map of a spectrally resolved vertical near field scan of the front facet of a laser from D1366-5 which has been measured with the same setup as used for the measurement of the lateral near field, but with an optical fiber which was connected to a spectrometer replacing the photodetector. The laser runs on three different modes at 973.54 nm, 971.02 nm and 967.20 nm. These modes have different vertical intensity profiles, additionally drawn on top of the false color map as dashed lines. The

fundamental mode at 973.54 nm is roughly gaussian shaped with some minor substructures. In contrast, the mode at 971.02 nm has a profile with two separated maxima, that reminds on a first higher-order hermite-gaussian mode. The mode at 967.20 nm is more similar to the fundamental mode, with a weak sub-structure visible. Presumably, it is a second-order mode with three intensity maxima which cannot be resolved with the setup. The theoretical resolution limit d_{lim} of the used setup can be estimated with the Rayleigh criterion $d_{\mathrm{lim}} = 1.22\lambda/2NA$. Considering a wavelength $\lambda = 975\,\mathrm{nm}$ and a numerical aperture $NA \approx 0.55$, one obtains $d_{\mathrm{lim}} \approx 1081\,\mathrm{nm}$. Compared to the width of the waveguide ($2.1\,\mu\mathrm{m}$) which approximately defines the width of the vertical modes, the resolution is quite low. Thus, it is critical to resolve the near field profile of a mode with two maxima and almost improbable to resolve the near field profile of modes with more than two vertical maxima.

The question arises how the experimental results for the higher-order vertical modes of the waveguide can be confirmed from a theoretical point of view. Firstly, the measured vertical far field profiles, shown in Fig. 3.44 (b) and (c), will be compared to the simulated far field profiles which have been already depicted in Fig. 3.20 (b). Secondly, the threshold currents for the higher-order vertical modes will be calculated (without consideration of the spectral properties of gain and Bragg wavelengths) and compared to threshold currents which can be derived from the spectral maps, shown in Fig. 3.30 and 3.31.

Fig. 3.45 shows the comparison of the simulated vertical far field profiles (black dotted lines) and measured vertical far field profiles (colored solid lines) from DFB-BA lasers with a cavity length of 1 mm. The measured vertical far field profiles have been chosen from measurement conditions, where one vertical mode dominates the spectrum as can be confirmed with spectral maps.

The agreement of the simulated and measured vertical far field profile for the fundamental mode is nearly perfect. For the first higher-order vertical mode, no experimental evidence was obtained. For the second higher-order vertical mode, considerable differences occur between the simulated and measured vertical far field profiles in terms of the intensity distribution and position of the local intensity maxima (both, in Fig. 3.45 (a) and (b)). Nevertheless, the pronounced central lobe of the second higher-order vertical mode seems to be a real deviation from the simulation result. Finally, for the third higher-order vertical mode, the measured and simulated vertical far field profiles coincide quite well, especially for the angular position of the intensity maxima, (both, for Fig. 3.45 (a) and (b)).

As a second ansatz, the threshold current of the individual vertical waveg-

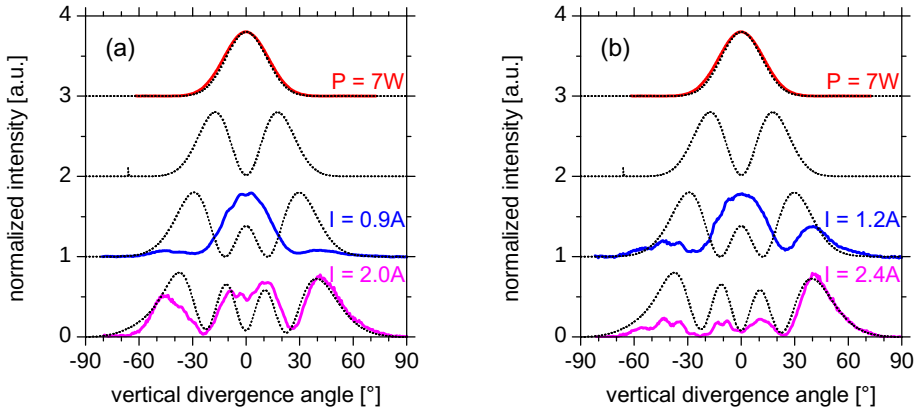

Figure 3.45: Comparison of calculated and measured vertical far field profiles for different mode orders. (a) Predominantly second (blue solid line) and third (magenta solid line) higher-order vertical waveguide mode of laser D1366-4 000602, measured at 0.9 A and 2.0 A, respectively. (b) Predominantly second (blue solid line) and third (magenta solid line) higher-order vertical waveguide mode of laser D1366-4 000609, measured at 1.2 A and 2.4 A, respectively. The vertical far field profile of laser D1365-2 020508 at 7 W is estimated to be single fundamental moded and is shown additionally in (a) and (b) (red solid line).

uide modes has been calculated based on the equation

$$I_{\mathrm{th}} = j_{\mathrm{tr}} \mathrm{e}^{\left[(\alpha_{\mathrm{i}}^{\mathrm{m}} + \alpha_{\mathrm{m/DFB}}^{\mathrm{m}})/\Gamma^{\mathrm{m}} g_0\right]} L \cdot W, \tag{3.7}$$

where the index m for the vertical mode order $\mathrm{m} = 0, 1, 2, \ldots$ indicates that the internal loss $\alpha_{\mathrm{i}}^{\mathrm{m}}$, resonator loss $\alpha_{\mathrm{m/DFB}}^{\mathrm{m}}$ and the confinement factor Γ^{m} wer determined individually for each vertical mode with QIP simulations.

The cavity length was set to $L = 3\,\mathrm{mm}$, the stripe widths to $W = 90\,\mu\mathrm{m}$, the transparency current density to $j_{\mathrm{tr}} = 151\,\mathrm{A\,cm^{-2}}$ and the modal gain of the fundamental mode to $\Gamma g_0^{(0)} = 21.4\,\mathrm{cm^{-1}}$. The modal gain of the higher-order modes has been calculated with their individual confinement factors with the active region Γ^{m} as $\Gamma^{\mathrm{m}} g_0 = \Gamma g_0^{(0)} \cdot \left(\Gamma^{(\mathrm{m})}/\Gamma^{(0)}\right)$. The calculation does not consider the increase of the facet reflectivity with increasing vertical mode order. Thus, the resonator loss of the higher-order modes is slightly overestimated. Also the fact, that the maximum of the gain spectrum and the Bragg wavelength of a certain vertical mode can be separated by a spectral distance of several nanometers, is not considered.

Fig. 3.46 shows the threshold currents for a DFB-BA laser and a FP-BA reference laser, calculated with parameters typical for the lasers in iteration I of this work. The DFB coupling coefficient of the fundamental mode was

assumed to be $3\,\mathrm{cm}^{-1}$ and the front facet reflectivity of the FP-BA laser was set to 2 %.

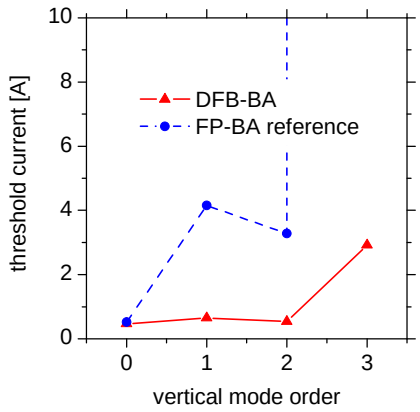

Figure 3.46: Calculated threshold current for the vertical waveguide modes in a FP-BA reference laser and in a DFB-BA laser.

A considerable difference in the increase of the threshold current for higher-order vertical modes is observed in Fig. 3.46. The threshold current for higher-order vertical modes increases much slower for the DFB-BA laser than for the FP-BA reference laser with increasing vertical mode order m. This behavior is mostly caused by the fact that the coupling coefficient κ increases significantly for the higher-order modes (because the confinement factor of the grating with the vertical mode profile increases) and causes a reduction of the DFB resonator loss $\alpha_{\mathrm{DFB}}^{(\mathrm{m})}$. In comparison, the FP mirror loss $\alpha_{\mathrm{m}}^{(\mathrm{m})}$ is approximately constant (The increasing of front facet reflectivity with m has been neglected.).

The parameters, used for the calculation and the resulting threshold currents are detailed in table 3.12. The calculated threshold currents of the higher-order modes of the DFB-BA laser are only slightly higher than the threshold current of the fundamental mode. For example, the threshold current of the first higher-order mode is 138 % of the threshold for the fundamental mode and 115 % for the second higher-order mode. This is a good explanation why higher-order modes start lasing at threshold currents in the $\sim 1\,\mathrm{A}$ range as can be derived from the spectral maps, depicted in Fig. 3.30 and 3.31. From the simulated DFB coupling coefficients it becomes clear, why the higher-order vertical waveguide modes of the DFB-BA lasers are wavelength stabilized. This occurs because of the high coupling strength $\kappa \cdot L > 1$.

Table 3.12: Parameters, used for the calculation of the threshold current for the vertical waveguide modes in a FP-BA reference laser and in a DFB-BA laser.

mode	R_f [%]	κ [cm^{-1}]	Γ [%]	α_i [cm^{-1}]	$\alpha_{m/DFB}$ [cm^{-1}]	I_{th} [A]	$\lambda_0 - \lambda_m$ [nm]
FP							
0	2	–	1.40	0.80	6.55	0.52	–
1	2	–	0.26	1.38	6.55	4.15	5.7
2	2	–	0.57	2.38	6.55	3.28	13.7
3	2	–	0.76	24.35	6.55	$4.0 \cdot 10^5$	24.3
DFB							
0	0.09	3.00	1.40	0.80	3.91	0.47	–
1	0.09	8.05	0.32	1.61	1.37	0.65	5.8 / 2.6*
2	0.09	17.81	0.49	3.58	0.58	0.54	14.0 / 6.5*
3	0.09	12.19	0.77	26.71	0.87	2.92	24.4 / 11.6*

Furthermore, the measured difference in wavelength of the higher-order modes, relative to the fundamental mode $\lambda_0 - \lambda_m$ can be compared to the simulated wavelengths. Therefore, the wavelengths of the waveguide modes has been calculated from the effective index of refraction ($\lambda_m \propto n_{eff,m}$) which was obtained in the QIP simulations. In the last column of table 3.12, the calculated differences in wavelength are compared to the experimentally determined differences, marked with *. The experimentally determined wavelength differences, indicated in table 3.12, are average values from the spectral maps, shown in Fig. 3.30 and 3.31. The measured wavelength differences $\lambda_0 - \lambda_m$ are slightly less than 50 % of the results which have been obtained from the QIP simulations. Thus, although a good overall agreement has been found for the measured and simulated profiles of the vertical far fields as shown in Fig. 3.45, serious deviations in the wavelengths or effective refractive indices show that the actual properties of the measured modes are not thoroughly consistent with the properties of higher-order vertical modes of the waveguide in QIP simulations.

In order to improve the spectral width of DFB-BA lasers over a wide current range from threshold to a designated working point, lasing on higher-order modes of the waveguide should be avoided. To avoid lasing on higher-order vertical waveguide modes in a high power DFB-BA laser with a typical

spectral distance between the gain maximum and the Bragg wavelength of the fundamental mode of several nanometers at threshold, two principal options are available. On the one hand, the waveguide can be designed in a way that only one fundamental mode can be found as a solution. This is challenging for laser designs with a very broad vertical waveguide thickness $\geq 1.6\,\mu$m, as necessary for a narrow vertical divergence angle of $\leq 45\,^\circ$ with 95 % power content. On the other hand, one could accept higher-order vertical waveguide modes as a solution of the mathematical waveguide problem, if they have a low sufficiently low DFB coupling coefficient (high resonator loss) or a very low confinement factor with the active region, (low gain), which results in much higher threshold current than for the fundamental mode ($\sim$ factor 5). However, the DFB coupling coefficient typically increases with the vertical mode order because of increasing confinement of the optical field with the grating layer, if they are positioned in the outer part of the waveguide, close to a cladding layer. A design optimization for pure fundamental vertical mode lasing from high power, high efficiency DFB-BA lasers, will primarily require considerable changes in the epitaxy structure. An additional improvement (minor) could be achieved with a facet coating which provides lower optical feedback for higher-order vertical modes [Cru09].

3.4.10 Experimental determination of the coupling coefficient

For an evaluation of the optical feedback from the DFB grating, knowledge of the value of the coupling coefficient is essential. In section 3.3.3, the coupling coefficient has been estimated with QIP simulations. When the inhomogeneous distribution of aluminum in the regrown $Al_xGa_{1-x}As$ in the grating region is neglected, a coupling coefficient of $|\kappa| = 1.76\,\mathrm{cm}^{-1}$ was obtained (κ underestimated). Consideration of the inhomogeneous aluminum distribution in a rectangular model lead to $|\kappa| = 4.41\,\mathrm{cm}^{-1}$ (κ overestimated). A further possibility to determine the coupling coefficient bases on the measurement of sub-threshold spectra of the DFB stopband. From this spectra, the coupling coefficient can be evaluated with methods, described in [Wen03]. For the evaluation, parameters such as the cavity length, facet reflectivities, center wavelength of the stopband and group index must be provided. The program FIT whose basic principles are described in [Wen03], varies a given number of parameters in a defined parameter range in order to minimize the differences between the calculated and measured spectrum for parameter extraction.

For the experimental determination of the DFB coupling coefficient, spec-

tra of ridge waveguide DFB lasers were measured below threshold with fiber coupling and using a high spectral resolution (10 pm), high dynamic range spectrometer. The used setup is described in section B.1.4. This method enables to obtain DFB stopband spectra in single transversal mode operation. Single transversal mode operation is important for the analysis of the coupling coefficient, because every higher-order mode (for example a higher lateral mode) would lead to a superposition of the stopband spectra of both modes and complicate the determination of the coupling coefficient.

The DFB-RW lasers were fabricated from an additional wafer D1399-2. The DFB grating in this wafer is structured with an in-situ etching time of 120 s. The $W = 10\,\mu$m wide DFB-RW lasers have a lateral index guiding via etched trenches, causing a step in the effective refractive index of $\sim 1 \cdot 10^{-3}$. Two different cavity lengths of 2.0 and 3.0 mm have been used. From the wafer, laser bars were cleaved and an anti reflection coating was applied on one facet in order to suppress lasing on FP-like modes. The resulting laser bars have facet reflectivities of $R_\mathrm{f} \leq 2\,\%$ (AR coated) and $R_\mathrm{r} \simeq 32\,\%$ (uncoated).

Laser bars were fixed on a copper heat sink by vacuum with the n-side down and single emitters were connected with contact needles from the p-side. A CW current was applied with a low noise current source. The intensity was collected by coupling the emission of a single DFB-RW emitter into a tapered single mode fibre. An optical spectrum analyzer was used for the measurement of overview spectra (500 pm resolution over ≤ 50 nm spectral range) and stopband spectra (10 pm resolution over ≤ 10 nm spectral range). The heat sink has been stabilized to a temperature, which allows to shift the maximum of the gain spectrum to the Bragg wavelength of the DFB grating.

In Fig. 3.47, four overview spectra above threshold are depicted. Fig. 3.47 (a), (b) and (c) show spectra over 50 nm from three diffebent devices with 2 and 3 mm cavity length. In Fig. 3.47 (a) and (b), the DFB spectrum is visible as a single sharp peak in the spectrum. Within the broad spectrum of the amplified spontaneous emission (ASE), a further sub-structure is found. At dedicated spectral positions in (a) and (c), one finds additional small dips. In (c), sharp peaks indicate even lasing modes at the same positions. These dips and peaks correspond to the DFB stopbands of higher-order vertical modes of the waveguide which have been already discussed in section 3.4.9. Their spectral distance is determined by the effective index of refraction, which decreases with an increasing mode order. In the spectrum maps in Fig. 3.30 and 3.31, these modes can be found as raised intensities at comparable spectral positions as in Fig. 3.47. A slightly ripple structure, visible in Fig. 3.47 (a), (b) and (c), is caused by feedback from the tip of the tapered fiber into the DFB-RW laser. The waviness or corrugation depth changes,

depending on the adjustment of the tapered fiber. Unfortunately, the optical feedback from the tapered fiber turned out to problematic especially for the measurement of the detailed stopband spectra in combination with the low coupling coefficient of the DFB grating in iteration I of this work.

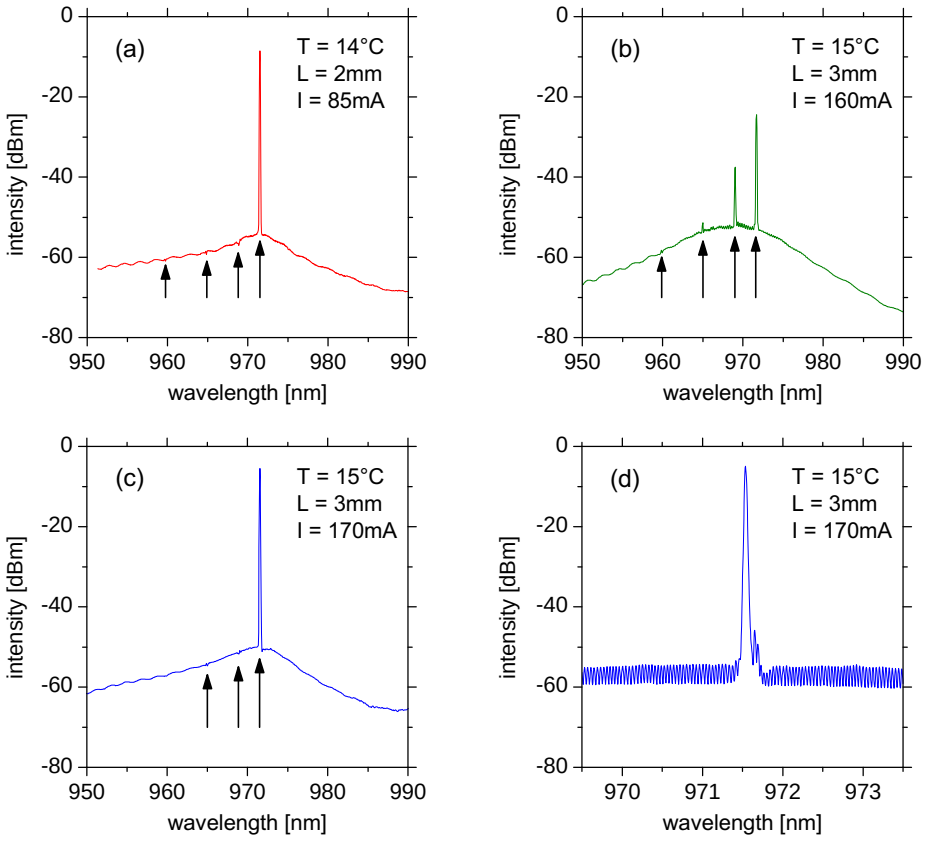

Figure 3.47: Overview spectra of three lasers from wafer D1399-2 above threshold with a broad ASE background. The temperature, cavity length and current are each identified. (a) Spectrum with the fundamental vertical DFB mode at $\approx 972\,\text{nm}$ and three further stopband dips at shorter wavelengths. (b) Spectrum with the fundamental vertical DFB mode at $\approx 972\,\text{nm}$ and three higher-order vertical modes at shorter wavelengths. (c) Spectrum with the fundamental vertical DFB mode at $\approx 972\,\text{nm}$ and two further stopband dips at shorter wavelengths. (d) High resolution spectrum with lasing DFB mode at $\approx 971.6\,\text{nm}$ and longitudinal mode comb below threshold.

A spectrum over 4 nm is depicted in Fig. 3.47 (d) from the same device as shown in Fig. 3.47 (c). Besides the lasing DFB mode, one finds competing

modes on the long wavelength side at $\approx -45\,\mathrm{dB}$ ($\approx 40\,\mathrm{dB}$ SMSR) and an intensity modulation by Fabry-Pérot like modes at $\approx -55\,\mathrm{dB}$.

Figure 3.48 illustrates, how an adequate current for the measurement of the stopband spectrum has been found, provided, that the gain maximum was successfully shifted to the required spectral range by tuning the temperature at the copper heatsink. Firstly, the Bragg wavelength of the DFB grating was identified by searching for the sharp spectral line at $\approx 972\,\mathrm{nm}$ above threshold. Secondly, the injection current was decreased below threshold, which requires spatial readjustment of the fiber coupling. In Fig. 3.48 (a), a logarithmic scaled spectral map is depicted. By increasing the current with small steps, the intensity of the modes around the stopband is observed until one mode is close to threshold. Thereby, an adequate current value is selected to record a high resolution spectrum. Fig. 3.48 (a) also illustrates a typical problem which occurred with these lasers. Even though the stopband seems to be located between the two heightened modes ($\approx 972.0\,\mathrm{nm}$ at $105\,\mathrm{mA}$), the lowest intensity is found at at the short wavelength side of these two modes ($\approx 971.5\,\mathrm{nm}$ at $105\,\mathrm{mA}$) and not in the central region where the stopband is expected. These facts result in a stopband spectrum as shown in Fig. 3.48 (b). One plausible explanation for this finding is, that the resolution of the spectrometer is not high enough, to trace the deep intensity modulation in the actual stopband between the modes. Another possible explanation is, that a second stopband is superimposed, which consists to another lateral mode order, slightly shifted in wavelength. Especially at high currents, a sequence of multiple stopband-like modulations of the spectrum over $\approx 0.5\,\mathrm{nm}$ was measured for many lasers.

The magnitude of the coupling coefficients mostly depends on the width of the stopband, the modulation depth in the stopband and on the intensity relation between the modes directly next to the stopband and the more FP-like modes adjacent to the stopband. A shape of a stopband as shown in Fig. 3.48 (b) must lead to errors, when the coupling coefficient is determined from parameter extraction by fitting a simulated stopband to the measured one. Typical stopband spectra are for example shown in [Wen03] for $\kappa \approx 75\,\mathrm{cm}^{-1}$, facets with $R_\mathrm{f} = 1\,\%$, $R_\mathrm{r} = 30\,\%$ and a cavity length of $L = 365\,\mu\mathrm{m}$ (high coupling coefficient) as well as for $\kappa \approx 1.4\,\mathrm{cm}^{-1}$, $R_\mathrm{f} = 0.01\,\%$, $R_\mathrm{r} = 95\,\%$ and $L = 1500\,\mu\mathrm{m}$ (low coupling coefficient). A measured stopband spectrum for a DFB laser with $\kappa \approx 7\,\mathrm{cm}^{-1}$, $R_\mathrm{f} = 5\,\%$, $R_\mathrm{r} = 95\,\%$ and $L = 1000\,\mu\mathrm{m}$, is shown in [Ear98] and compared to a calculated ASE spectrum which is fitted to a model, described in [Sch94].

Tens of DFB-RW lasers were investigated with the aim, to measure sub-threshold ASE spectra which can be fitted with the program FIT, based on [Wen03]. Unfortunately, typical stopband spectra were only found for a few

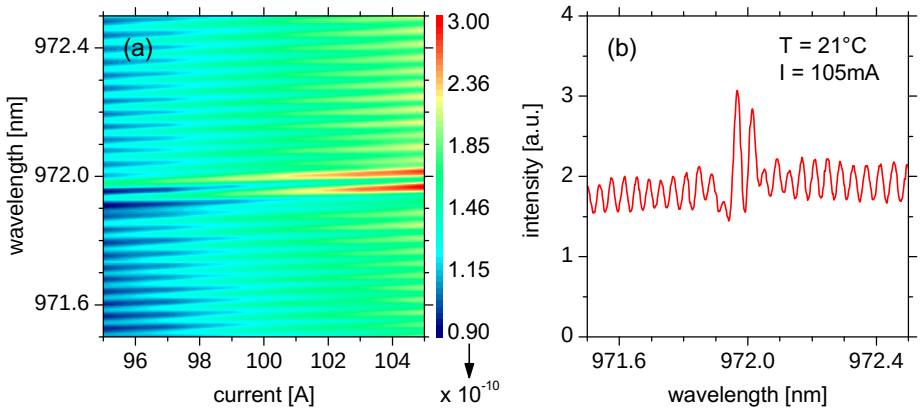

Figure 3.48: A typical but not ideal measured stopband of a $10\,\mu\text{m} \times 3000\,\mu\text{m}$ DFB-RW laser. (a) Logarithmic scaled spectral map below threshold. (b) Linear intensity scaled stopband spectrum at 105 mA.

of these devices. During the measurement it turned out that optical feedback from the tip of the tapered fibre significantly influenced the measured spectra and was an important reason why the reproducibility of the shape of the spectra for an individual DFB-RW laser was quite low. Additionally, it was challenging to couple enough optical power into the optical fiber and the spectrometer, sufficient to obtain a not too noisy ASE spectrum. This has been the case especially for DFB-RW lasers with AR coating on both facets which were also investigated in order to clarify if a better suppression of the FP mode modulation helps to measure well defined stopband spectra, but are not analyzed here. On the one hand, the measurements of the 3 mm long DFB-RW lasers tends in the result, that the resolution of the spectrometer was too low in order to completely resolve the intensity modulation between neighboring longitudinal modes. On the other hand, the stopband structure was very weak for the DFB-RW lasers with $L = 2\,\text{mm}$.

Figure 3.49 shows the measured stopband spectra, the simulated stopband spectra and the results for the coupling coefficient for the best four measurement results. In the simulation, the coupling coefficient was assumed to have only a negligible imaginary part. Besides the coupling coefficient, the facet reflectivities, its phase relations with the grating ridges, the intensity of the spontaneous emission and the gain spectrum have been varied in the simulation with FIT. Values of $\kappa = 1.1$, 0.8, 1.4 and $1.3\,\text{cm}^{-1}$ have been obtained.

The results for the coupling coefficients (average $\kappa = 1.15\,\text{cm}^{-1}$) are lower than expected ($1.76\,\text{cm}^{-1}$ without aluminum accumulation and depletion,

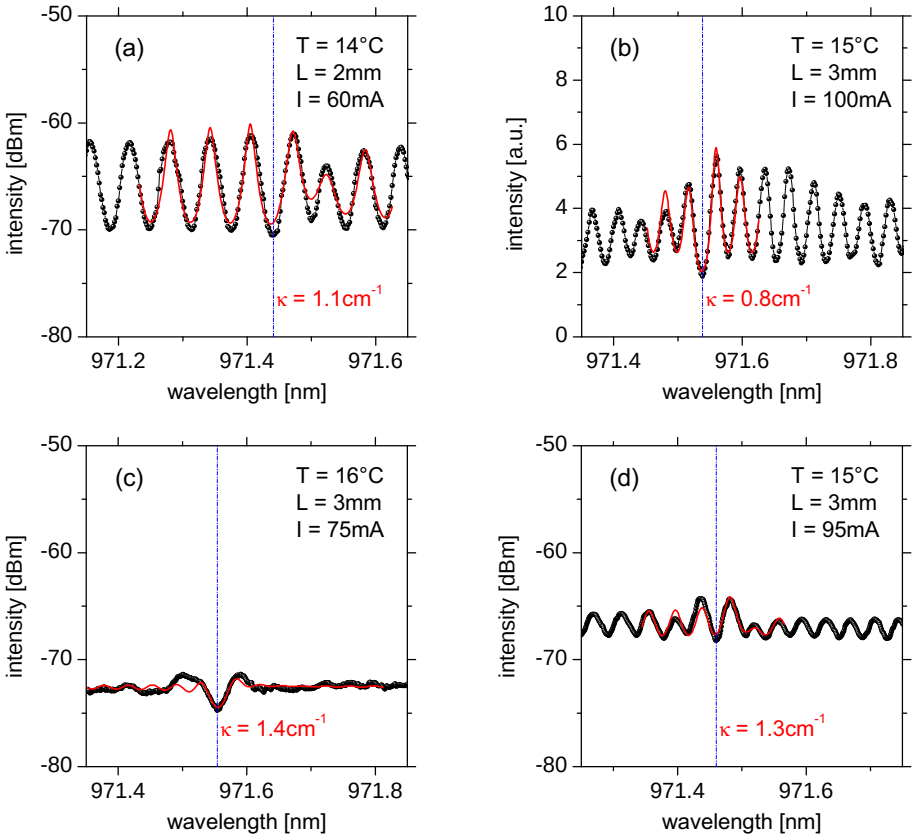

Figure 3.49: Stopband spectra of four DFB lasers from wafer D1399-2 (black dots). The temperature, cavity length and current are each identified. The centrum of the stopband is indicated with a blue dashed dotted line. The simulated stopband spectra are shown as red solid lines, the derived results for the coupling coefficients are given beneath.

4.41 cm^{-1} with aluminum accumulation and depletion). The determination of the coupling coefficient by fitting simulated ASE spectra to the measured spectra with the program FIT has several uncertainties if the measured spectra are significantly affected by the measurement process. Because of the problems with optical feedback and the limited spectral resolution it is presumed, that the coupling coefficient is systematically undervalued in the process. Of course, an unexpected deviation of the coupling coefficient of the DFB grating in the wafer which has been used for the analysis is also possible.

To conclude, because of measurement problems discussed above, the real

value of the coupling coefficient of the DFB-BA lasers from iteration I is presumed to be in the $\sim 3\,\mathrm{cm}^{-1}$ range for an in-situ etching time of $t_{\mathrm{is}} = 120\,\mathrm{s}$. However, the error must be assumed to be as high as $\pm 1\,\mathrm{cm}^{-1}$. For $t_{\mathrm{is}} = 90\,\mathrm{s}$ and $t_{\mathrm{is}} = 150\,\mathrm{s}$, a moderate decrease or increase of the coupling coefficient in the $\sim 1\,\mathrm{cm}^{-1}$ range must be considered, respectively.

For the further optimization of DFB-BA lasers for high power conversion efficiency, better knowledge of the coupling coefficient is required. Therefore, an improvement of the measurement technique which is used to measure ASE spectra is mandatory. A wafer processing, optimized for index guided RW lasers with a smaller stripe width $W \leq 7\mu\mathrm{m}$ and an optimized index guiding of $\Delta n_{\mathrm{eff}} \geq 3{\cdot}10^{-3}$ should be used to ensure single transversal mode operation. Feedback from the tip of the tapered fibre must be reduced drastically, for example by using a setup with anti reflection coated optics. Furthermore, a better AR coating of the front facet can be used to reduce the modulation depth of the FP-like modes and make the stopband better visible (also requires a reduction of the optical feedback).

Nevertheless, the determination of the coupling coefficient of efficiency optimized DFB-BA lasers is experimentally challenging because the requirement of $\kappa \cdot L \leq 1$ and the usage of long cavities $L \geq 3\,\mathrm{mm}$ results in low coupling coefficients in the range of $\kappa \leq 3.3\,\mathrm{cm}^{-1}$. This is significantly lower than the coupling coefficients of other DFB-BA lasers, for example [Ear98] ($\kappa \approx 7\,\mathrm{cm}^{-1}$), [Kan06] ($\kappa \approx 10\,\mathrm{cm}^{-1}$), [Sch09a] ($\kappa \approx 9\,\mathrm{cm}^{-1}$), [He09] ($\kappa \approx 5\,\mathrm{cm}^{-1}$). The coupling coefficient of $\kappa \approx 9\,\mathrm{cm}^{-1}$ reported in [Sch09a] has been measured with the same setup on 21 AR/HR coated DFB lasers with deviations in the range of $\pm 1\,\mathrm{cm}^{-1}$. This measurements lead to typical ASE spectra with a well defined and deep modulated stopband and only minor intensity modulations due to optical feedback from the tapered fiber. Chang *et al.* have presented results from 2 mm long DFB-BA lasers with $\kappa \approx 1.5\,\mathrm{cm}^{-1}$ in [Cha00]. Nevertheless, they do not show ASE spectra of the DFB stopband and lasing on FP modes is visible in the spectra above threshold – presumably due to too low DFB coupling strength ($\kappa \cdot L \approx 0.3$), compared to the feedback from the facet mirrors ($R_{\mathrm{f}} = 5\,\%$, $R_{\mathrm{r}} = 95\,\%$).

Another possibility for the experimental determination of low coupling coefficients could be to place the DFB grating at another vertical position in the waveguide in an additional test wafer. Thereby, the overlap of the DFB grating with the optical field and thus, the coupling coefficient could be considerably enhanced. From the gained value for κ, the coupling coefficient of the DFB lasers with the grating at the primary position can be calculated with respect to the confinement factor, following equation 1.60. This method requires that the influence of the position of the DFB grating on the shape of the vertical optical field profile can be neglected (for example if the grating

is very thin and the index contrast is not too high).

3.4.11 Determination of the DFB locking range

For several possible applications of high power DFB-BA lasers, such as pumping fiber and solid state lasers, a spectrum with a stable wavelength (for example 976 nm ± 2 nm) and a narrow spectral width (for example $\Delta\lambda \leq 1$ nm with 95 % power content) is necessary. The requirement for the stable emission wavelength typically arises from the spectral properties of the absorption cross-section of the gain medium to be pumped optically, while the requirement for a narrow spectral width may arise from the absorption spectrum as well as from needs for dense spectral beam combining. If scalability of the optical output power from the DFB-BA lasers and insensibility against changes in temperature is required as well, it is of importance to analyze the range in CW current I and heatsink temperature T, within the laser is spectrally locked on the fundamental DFB mode. This is what is sometimes called the locking range of a DFB laser.

From a practical point of view, the locking range defines an area in the current-temperature matrix $(I_\mathrm{i}, T_\mathrm{j})$ for which the DFB-BA laser is neither running on FP-like modes nor on higher-order vertical modes – so that the spectrum is dominated (95 % power content) by the fundamental DFB mode with a narrow spectral width $\Delta\lambda$ and the center wavelength of the spectrum λ_c which is given by the Bragg wavelength of the DFB grating. Note, that the locking range does not have to be a simply connected area.

If a very broad locking range in current and temperature could be achieved, this would allow to scale the optical output power via the injection current and would also make changes in heatsink temperature acceptable – without unwanted changes in the spectral properties. To achieve a broad locking range is expected to be challenging especially for efficiency optimized high power DFB-BA lasers because of the following reasons. Firstly, a high coupling strength $\kappa \cdot L > 1$ is advantageous for a wide locking range because it helps to reduce lasing on FP-like modes. This was confirmed in [Sch09a], [Sch09b]. However it has been shown in this work theoretically and experimentally, that a low coupling strength $\kappa \cdot L \leq 1$ is preferred for a high differential quantum efficiency and therefore for a high power conversion efficiency. Secondly, to obtain high power conversion efficiency hat high power levels requires the peak of the gain spectrum at threshold to be shifted several nanometers to the short wavelength side of the Bragg wavelength of the fundamental DFB mode. On the one hand, this enables the gain peak and the Bragg wavelength of the fundamental modes to coincide at the desired working point. On the other hand, the spectral detuning shifts the gain peak

wavelength to the Bragg wavelength of higher-order vertical modes of the waveguide in the current range between threshold and the desired working point. Lasing on these higher-order modes may then degrade the spectral width with 95 % power content.

For the experimental determination of the DFB locking range, power-voltage-current characteristics and spectral maps of laser D1425-2 040102 with a current step size of 0.5 A have been measured under CW conditions at heatsink temperatures of $T = (15, 25, \ldots, 50)$°C. The characteristics of the output power and power conversion efficiency are depicted in Fig. 3.50 (a). Sample spectra from the spectral maps, each at an output power of 7 W, are shown in Fig. 3.50 (b). At 7 W, the laser is spectrally locked on the fundamental DFB mode over the whole investigated temperature range with a spectral width $\Delta\lambda \leq 1.5$ nm with 95 % power content.

The measurement data allow to determine the spectral width (here always with 95 % power content) and the optical output power at every position $(I_\mathrm{i}, T_\mathrm{j})$ in the current-temperature matrix. The criterion $\Delta\lambda \leq 1.5$ nm with 95 % power content has been chosen because this is the highest spectral width which has been observed for the fundamental DFB mode without broadening due to lasing on FP-like modes or higher-order waveguide modes (see Fig. 3.33). Presumably, the width of the fundamental DFB mode is induced by lasing on many different lateral modes and may be even multiple longitudinal modes close to the stopband. Figure 3.50 (c) shows a construction of the DFB locking range. In the diagram, unlocked current-temperature areas, defined by the criteria that either $\Delta\lambda > 1.5$ nm and or by the fact that the laser has not exceeded threshold, are left in white. Unlocked regions appear at the left margin of the diagram (region 1), where the laser is below threshold, in the lower left region (region 2), where lasing on additional higher-order waveguide modes increases the spectral above 1.5 nm (> 5 % power content) and in the upper right region, where lasing on FP-like modes (> 5 % power content) broadens the spectral width. Locked current-temperature areas, defined by $\Delta\lambda \leq 1.5$ nm, are filled with a linear false color scale, which indicates the optical output power $P(I, T)$. Additionally, the center wavelength of the DFB spectrum has been analyzed and its evolution is plotted as black dashed lines for 976, 977, 978 and 979 nm.

The obtained mapping of the DFB locking range has noticeable similarities with the locking range published in [He09], which is apparently as well limited due to lasing on FP-like modes at high currents and heatsink temperatures. One might speculate that the limitation at low currents and low temperatures in [He09] is also caused by higher-order waveguide modes.

From the resulting locking range, one can derive that the spectrum is predominantly well stabilized over a ~ 30 K broad band in heatsink temper-

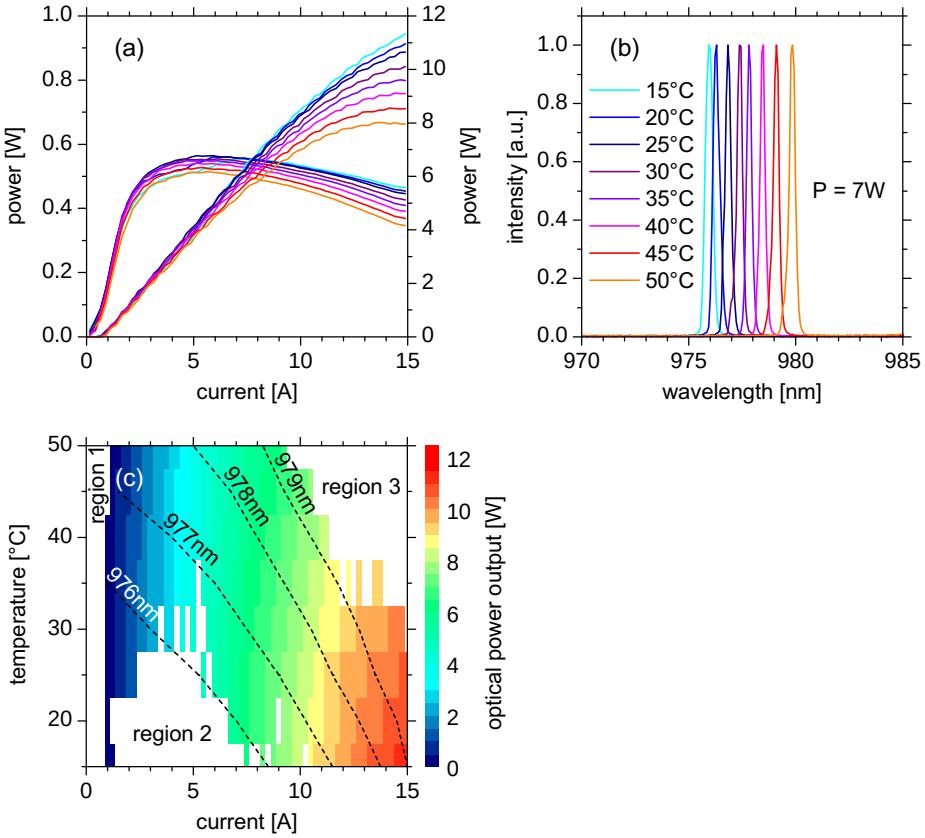

Figure 3.50: Locking range of DFB-BA laser D1425-2 040102 between between 0 and 15 A and 15 and 50 °C. (a) (Power and efficiency characteristics at $15, 20, \ldots, 50\,^{\circ}\mathrm{C}$). (b) Single spectra at 7 W output power at $15, 20, \ldots, 50\,^{\circ}\mathrm{C}$. (c) Diagram of the locking range. Spectrally locked areas with a spectral width (95 % power content) of ≤ 1.2 nm are colored in a false-color scale which indicates the optical output power. The center wavelength is shown with black dash-dotted lines.

ature. This temperature band shifts to lower temperatures with increasing injection current (approximately $-2.7\,\mathrm{K\,A^{-1}}$) and this is an expression of the fact, that the peak wavelength of the gain spectrum must be approximately aligned to the Bragg wavelength of the DFB grating. the appearance of an analogous band in injection current of with a width of ~ 10 A can be also estimated from Fig. 3.50 (c).

Unfortunately, the DFB-BA laser for which the analysis has been carried out, does not provide locking at a fixed heatsink temperature from threshold current to 15 A. In such a power characteristics at a fixed heatsink tem-

perature, either lasing on higher-order waveguide modes (region 2) or lasing on FP-like modes (region 3) will occur with $> 5\,\%$ power content. For an improvement of the spectral locking behavior, unlocked regions 2 and 3 must be eliminated, preferentially without degradation in the output power and efficiency. Region 3 (lasing on FP-like modes) can be reduced by using a front facet coating which provides a lower reflectivity, especially in the spectral region above 979 nm. The reduction of region 2 (lasing on higher-order vertical waveguide modes) can be achieved with a waveguide design, which either completely frustrates higher-order modes or enables lower DFB coupling coefficients for the higher-order modes, in order to increase their threshold currents significantly.

3.4.12 Spectrally resolved lateral near fields and far fields

Although spatial integrated spectra and spectral integrated near field and far field profiles of DFB-BA lasers have been measured and analyzed, several questions, concerning the properties of optical modes in DFB-BA laser, are still unanswered. Firstly, the question arises, if the optical modes which constitute the spectrum are spectrally and spatially stable. Secondly, the number and spectral distance of different lateral modes is unknown. Thirdly, the question if one ore more longitudinal modes are involved with increasing current and output power, needs to be answered. Knowledge of these optical properties will potentially help to understand the width of the optical spectrum and disclose how the spectral width can be further reduced. Finally, the exact shape of individual lateral modes is of a broad interest for finding possibilities to improve the lateral beam quality of BA lasers. Answers to all these questions can possibly be found by applying an additional spectral resolution to measurements of lateral near fields and far fields.

The requirements to the spectral resolution of a spectrometer which will be used in this investigation can be derived from the spectral distance of the concerning optical modes which must be resolved. The spectral distance of longitudinal modes $\Delta\lambda_{\mathrm{DFB}}^{\mathrm{long}}$ can be estimated by calculating the spectral distance of neighboring longitudinal modes in an equivalent FP cavity $\Delta\lambda_{\mathrm{FP}}^{\mathrm{long}}$, because the low coupling coefficient does not influence the spectral distance significantly. With other words, the width of the DFB stopband approaches the distance of neighboring FP modes. With a Bragg wavelength $\lambda_0 = 976\,\mathrm{nm}$, a cavity length of $L = 3000\,\mu\mathrm{m}$ and a group index chosen as $n_{\mathrm{g}} = 3.6$, one obtains $\Delta\lambda_{\mathrm{FP}}^{\mathrm{long}} = \lambda_0^2/2Ln_{\mathrm{g}} \cong 0.044\,\mathrm{nm} \approx \Delta\lambda_{\mathrm{DFB}}^{\mathrm{long}}$ (the formula for $\Delta\lambda_{\mathrm{FP}}^{\mathrm{long}}$ is for example derived in [Kre77]).

Waveguiding in lateral direction arises from several different mechanisms. Firstly, the lasers reported in this work have a weak lateral index guiding due to the presence of trenches, which are etched into the wafer surface from the p-side, 5 μm separated from the 90 μm wide contact stripe. These trenches are designed to cause a decrease in the effective index of refraction of $\Delta n_{\mathrm{eff}} = 1 \cdot 10^{-1}$ (for the fundamental mode, simulated with QIP) and provide therefore waveguiding between the trenches, separated by 100 μm in lateral direction. Secondly, current injection trough the contact stripe geometry causes lateral gain guiding. The contact stripes have a width of 90 μm and are defined by He-implantation of the surrounding wafer surface in order to make the highly doped GaAs contact layer isolating outside the contact windows. Furthermore, under CW current injection, heat generation in the active region and waveguide under the contact stripe leads to a local increase of the refractive index and causes thermal lensing. A discussion of the individual lateral waveguiding mechanisms, based on measurements of FP-BA lasers from the same epitaxy structure as used in this work, can be found in [Cru12a]

For the lateral modes, the absolute mode order typically starts with the fundamental mode $l = 1$ and is much smaller than for the longitudinal modes. While the spectral distance of neighboring longitudinal modes can be assumed to be approximately equidistant over a small range in wavelength of some nanometers, the spectral distance of neighboring lateral modes will strongly depend on the lateral confinement due to their low mode orders l. In a very simple approximation as a box with a width W with perfect electric walls, the spectral distance of neighboring lateral modes behaves like bound states in a quantum mechanical rectangular quantum well with infinite barrier hight – the spectral distance $\Delta\lambda^{\mathrm{lat}}_{l/l+1}$ between neighboring modes l and $l+1$ increases linearly with l and the distance between a certain mode l and the fundamental mode $l = 1$ increases parabolically. On can derive that

$$\Delta\lambda^{\mathrm{lat}}_{l/l+1} \approx \frac{\lambda_0^3}{8 n_{\mathrm{eff}} n_{\mathrm{g}} W^2} (2l+1)\,, \tag{3.8}$$

which coincides with the formula given in [Som73]. For $m = 1, 2$, $\Delta\lambda^{\mathrm{lat}}_{1/2} \approx 0.003\,\mathrm{nm}$ and for $m = 5, 6$, $\Delta\lambda^{\mathrm{lat}}_{19/20} \approx 0.045\,\mathrm{nm}$, approximately equal to the spectral distance of neighboring longitudinal modes.

Accordingly, for the spectral separation of lateral and longitudinal modes, a spectrometer with a spectral resolution limit $\Delta\lambda_{\mathrm{spec}} < 3\,\mathrm{pm}$ is required. At a wavelength of 976 nm, the spectrometer in use has in double pass configuration a resolution limit better than 0.5 pm and a detection bandwidth of $\approx 174\,\mathrm{pm}$ (2046 pixels with a pixel dispersion of $\approx 85\,\mathrm{fm}$). The spatial axes

(lateral near field position or lateral far field divergence angle) was scanned with 500 steps (500 single spectra) using the same setup which has been already used for the measurement of lateral near fields and far fields (without spectral resolution), discussed in section 3.4.8. Therefore, the detector has been replaced by an optical fiber adjusted behind an entrance slit. The spatial resolution of the near field is $d_{\mathrm{lim}} \approx 1000\,\mathrm{nm}$ as estimated in section 3.4.9. More details to the measurement setup ar given in section B.3. The measurements of spectrally resolved near fields and far fields were carried out in collaboration with the master student Hossein Ekhteraei, to whom thanks is given for his extensive assistance. Selected experimental results from these measurements have been reported in [Wen11] and [Cru11a].

In the following, measurements of the spectrally resolved lateral near field and far field will be presented as linearly scaled false color plots. Note, that after measuring the spectrally resolved lateral near field, a further lens was introduced into the setup and a new fine adjustment was necessary. Depending on the absolute width of the spectrum, each plot is composed from a certain number of measurements (matrix with 500×2046 pixels). The first DFB-BA laser which has been analyzed was device 040201 from wafer D1425-2. This laser has a weak lateral index guiding due to etched index trenches with $\Delta n_{\mathrm{eff}} \approx 1 \cdot 10^{-}3$). Figure 3.51 (a) and (b), shows the spectrally resolved lateral near field and far field at $T = 25\,^{\circ}\mathrm{C}$ heatsink temperature, $I = 3.4\,\mathrm{A}$, $P = 2.7\,\mathrm{W}$. Both, in the lateral near field and far field distribution, one observes a system of optical modes with a very narrow spectral width (FWHM $< 10\,\mathrm{pm}$). These modes are spectrally stable over a long time, because the time demand for the measurement of one $\approx 174\,\mathrm{pm}$ wide matrix from 500 single spectra is $\approx 900\,\mathrm{s}$. Furthermore, the spectrally resolved near fields and far fields were observed to be well reproducible even after months in terms of their spectral and spatial properties. Note that Figure 3.51 is composed from two of these matrices with a spectral bandwidth of $\approx 174\,\mathrm{pm}$.

The spatial intensity distribution of the modes approximately reminds on hermite-gaussian modes, which are the eigenfunctions for the eigenmodes of an optical cavity with a negative parabolic shaped profile of the refractive index. Eight different lateral modes with lateral mode indices $l = 1, 2, 3, \ldots 8$ are indicated in Fig. 3.51 (a) and (b). These modes have an increasing number of $1, 2, 3, \ldots 8$ dominant local maxima. Intensity reductions towards the left hand side in the near field (a) are presumably a consequence of non ideal adjustment for the intensity detection in vertical direction. Even though the vertical field is focused in the imaging plane, the scanning fiber selects only a part of the vertical intensity profile. For mode $l = 1$, one minor local maximum is observed on the left and right hand side of the central major local

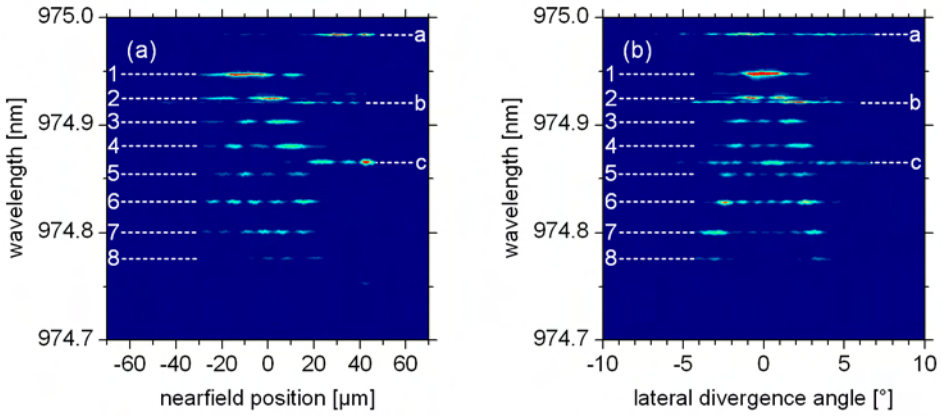

Figure 3.51: Spectrally resolved near field (a) and far field (b) of laser D1425-2 040102 at $I = 3.4\,\mathrm{A}$, $P = 2.7\,\mathrm{W}$.

maximum. This is a clear deviation from hermite-gaussian shaped modes. In the lateral near field (Fig. 3.51 (a)), The modal intensity extends over $\approx 60\,\mu\mathrm{m}$, which is 2/3 of the contact stripe width of $W = 90\,\mu\mathrm{m}$. Mode $l = 1$ has the most narrow spatial distribution of $\approx 45\,\mu\mathrm{m}$ and mode $l = 8$ is the broadest one with $\approx 60\,\mu\mathrm{m}$. In the lateral far field, mode $l = 1$ is extended over a divergence angle of $\approx 3\,^\circ$ and mode $l = 8$ over $\approx 8\,^\circ$. In Fig. 3.52, integrated profiles of single lateral modes from Fig. 3.51 with mode orders $m = 1, 2, 3, \ldots, 8$ are depicted. The integration along the spectral direction was performed over 75 pixels ($\approx 6.4\,\mathrm{pm}$) on the charge-coupled device (CCD) sensor of the spectrometer. In Fig. 3.52 (a) and (b), the profiles are shown normalized on a linear intensity scale. In the near field (Fig. 3.52 (a)), the mode profiles show significant deviations from hermite-gaussian like modes. Besides the intensity decrease towards the left hand side, especially higher-order modes ($l \geq 6$) have their highest intensity in the center part, while hermite-gaussian modes have the highest intensity in the outer, local maxima. Nevertheless, in the far field (Fig. 3.52 (b)), mode profiles are very good comparable to hermite-gaussian like mode profiles.

Three further optical modes with a different spatial distribution are observed, indicated with 'a', 'b' and 'c' in Fig. 3.51. In the near field, these modes are predominantly located asymmetrically between 10 and $50\,\mu\mathrm{m}$. Modes 'a' and 'c' consist of two and three clearly visible local intensity maxima in the near field, respectively. For mode 'b', the number of local intensity maxima cannot be determined precisely. In the far field, all these three modes are widely extended over up to $\approx 12\,^\circ$ (mode 'a'), because of their narrow

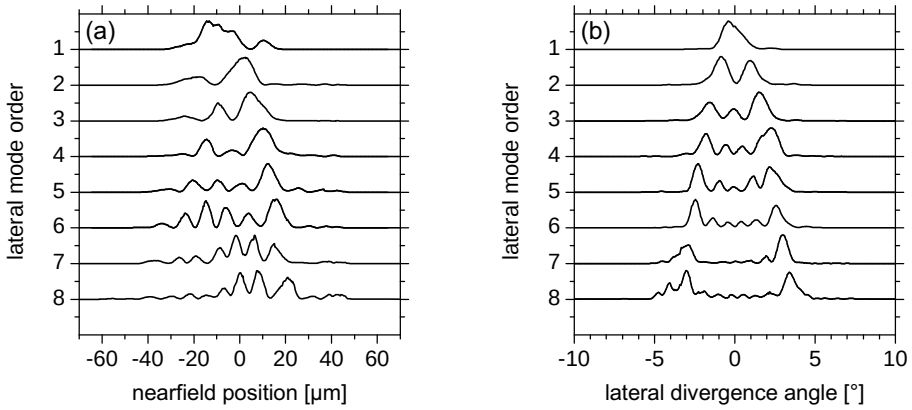

Figure 3.52: Integrated intensity profiles (normalized, linear scaled) of single lateral modes with mode orders $l = 1, 2, 3, \ldots, 8$ from laser D1425-2 040102 at $I = 3.4\,\mathrm{A}$, $P = 2.7\,\mathrm{W}$. (a) Near field profiles. (b) Far field profiles.

lateral near field distribution. Optical modes $l = 1, 2, 3, \ldots 8$ are assumed to be confined in lateral direction due to index guiding from thermal lensing and etched index trenches, as well as due to gain guiding because of the lateral gain-loss profile. Experimental and simulation results on the dominant lateral waveguiding mechanism in 975 nm high power BA diode lasers from the same epitaxy design as used for the reference FP-BA lasers in this work, have been reported in [Cru12a]. In contrast to modes $l = 1, 2, 3, \ldots 8$, modes 'a', 'b' and 'c' are presumably confined into a limited lateral region due to arbitrary changes in the refractive index or photon-carrier interactions. Thus, the appearance of modes 'a', 'b' and 'c' could be called filamentation.

In contrast to the box-model-based estimation of spectral distance between neighboring lateral modes in equation 3.8, the measured mode spacing is approximately equidistant and reaches from $\Delta\lambda_{1/2}^{\mathrm{lat}} \approx 0.023\,\mathrm{nm}$ for $l = 1$ and 2 to $\Delta\lambda_{1/2}^{\mathrm{lat}} \approx 0.025\,\mathrm{nm}$ for $l = 7$ and 8. This is presumably a consequence of the fact, that thermal lensing influences the actual lateral refractive index profile dominantly. The shape of the thermal lens refractive index profile in a BA laser is roughly gaussian shaped as can be derived from [Baw09]. Therefore, the refractive index profile could be approximated with a parabolic function and the resulting lateral modes have a wavelength separation, approximately comparable to the equidistant spectral mode separation of hermite-gaussian modes, for example derived in [Kre77].

The fact, that every mode order l is found only once in Fig. 3.51 and in an increasing order with decreasing wavelength clearly indicates, that only one

longitudinal mode has exceeded threshold at $I = 3.4\,\mathrm{A}$, $P = 2.7\,\mathrm{W}$. Single longitudinal mode lasing is expected for a DFB laser with $\kappa \cdot L \approx 1$ [Ear98], because the resulting homogenous longitudinal intensity profile ([Ear98] and Fig.1.24) should sustain the longitudinal mode suppression which can be obtained from calculations of the threshold conditions, as presented in section 1.2.3, to injection currents considerably above threshold. Nevertheless, significantly above threshold, additional effects such as non perfect gain saturation, longitudinal spatial and spectral hole burning may cause lasing on multiple longitudinal modes.

Figure 3.53 shows the spectrally resolved near field and far field distribution at $T = 25\,^{\circ}\mathrm{C}$, $I = 5.8\,\mathrm{A}$, $P = 5.2\,\mathrm{W}$. Compared to the near field and far field distribution at $I = 3.4\,\mathrm{A}$, $P = 2.7\,\mathrm{W}$, additional modes are observed, although the spectral width is not significantly increased. By analyzing the number of local maxima and the relative spectral position for each mode in detail, on finds, that a second longitudinal mode has exceeded threshold. In Fig. 3.53 (a) and (b), the lateral mode numbers, corresponding to the first longitudinal mode are indicated at the left hand side, while the lateral mode numbers, corresponding to the second longitudinal mode (shorter wavelength) are indicated at the right hand side of the false color plot. For each longitudinal mode, eight lateral modes, beginning with the fundamental mode $l = 1$ are observed.

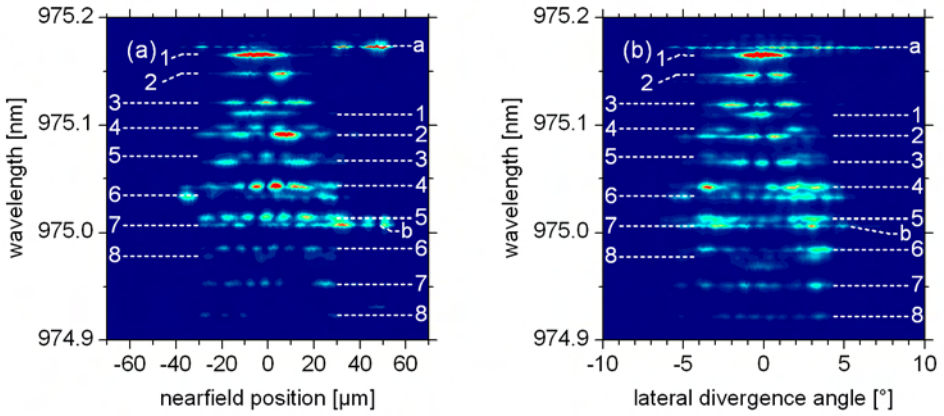

Figure 3.53: Spectrally resolved near field(a) and far field (b) of laser D1425-2 040102 at $I = 5.8\,\mathrm{A}$, $P = 5.2\,\mathrm{W}$.

The fundamental modes of the two different longitudinal modes have a spectral separation of 0.055 nm, slightly more than the estimated spectral distance of neighboring FP modes, calculated as $\Delta\lambda_{\mathrm{FP}}^{\mathrm{long}} \cong 0.044\,\mathrm{nm}$. The

magnitude of the measured spectral separation does not allow to decide, if the second longitudinal mode is the mode at the other side of the stopband or another neighboring mode at the same side of the stopband, because the width of the stopband approaches the spectral separation of neighboring longitudinal modes for the DFB-BA lasers in this work (low coupling coefficient). In addition to the hermite-gaussian like modes, two further modes, indicated with 'a' and 'b' in Fig. 3.53 (a) and (b), have been found. These modes are predominantly located on the right hand side of the near filed and have presumably the same origin as modes 'a', 'b' and 'c' in Fig. 3.51.

In Fig. 3.54, the spectrally resolved near field and far field distribution at $T = 25\,°\mathrm{C}$, $I = 7.9\,\mathrm{A}$, $P = 7.0\,\mathrm{W}$, are depicted. In comparison to the spectrally resolved near fields and far fields at 2.7 and 5.2 W, the spectral width is significantly broadened and has a characteristic region between $\approx$ 975.35 and $\approx$ 975.45 nm with vanishing modal intensity. The classification of lateral mode orders with the help of the number of local maxima is now much more difficult, because of the increasing number, mode order and density of modes, as well as because of the altered shape of the profiles. Lateral modes $l = 1, 2, 3, \ldots, 6$, belonging to one specific longitudinal mode are indicated at the left hand side of Fig. 3.54 (a) and (b).

The question, if one or more longitudinal modes are involved, cannot be answered securely. On the one hand, from the measurement at 5.2 W one must assume, that at least two longitudinal modes are lasing. On the other hand, only one fundamental lateral mode can be clearly observed. Indeed, a further longitudinal mode could appear only with higher lateral mode orders $l > 1$. The lateral near field is extended over $\approx 100\,\mu\mathrm{m}$, in good agreement with the contact stripe width of $W = 90\,\mu\mathrm{m}$. The lateral far field distribution of many modes at wavelength $\leq$ 975.55 nm, with presumably different lateral mode orders l, is extended over the same lateral divergence angle of $10\,°$. Especially on mode at $\approx$ 975.54 nm combines much intensity and a broad divergence angle in the far field distribution. Lateral modes of this kind must be expected to cause an unwanted broadening of the lateral far field. In the near field, this mode shows on the one hand, a constriction of its major intensity to the central part ($\pm 15\,\mu\mathrm{m}$) but on the other hand, a widely extended minor intensity to the outer part of the near field ($\pm 50\,\mu\mathrm{m}$). A systematically suppression of these modes due to increased optical loss induced at $\pm 50\,\mu\mathrm{m}$ could be a design option for a reduction of the lateral far field divergence.

Finally, in Fig. 3.55, the spectrally resolved near field and far field distribution is shown for $T = 25\,°\mathrm{C}$, $I = 12.0\,\mathrm{A}$, $P = 10.0\,\mathrm{W}$. At such high powers, the total number of optical modes is increased drastically and spectral overlap of many modes is observed. At $I = 12.0\,\mathrm{A}$, $P = 10.0\,\mathrm{W}$, the

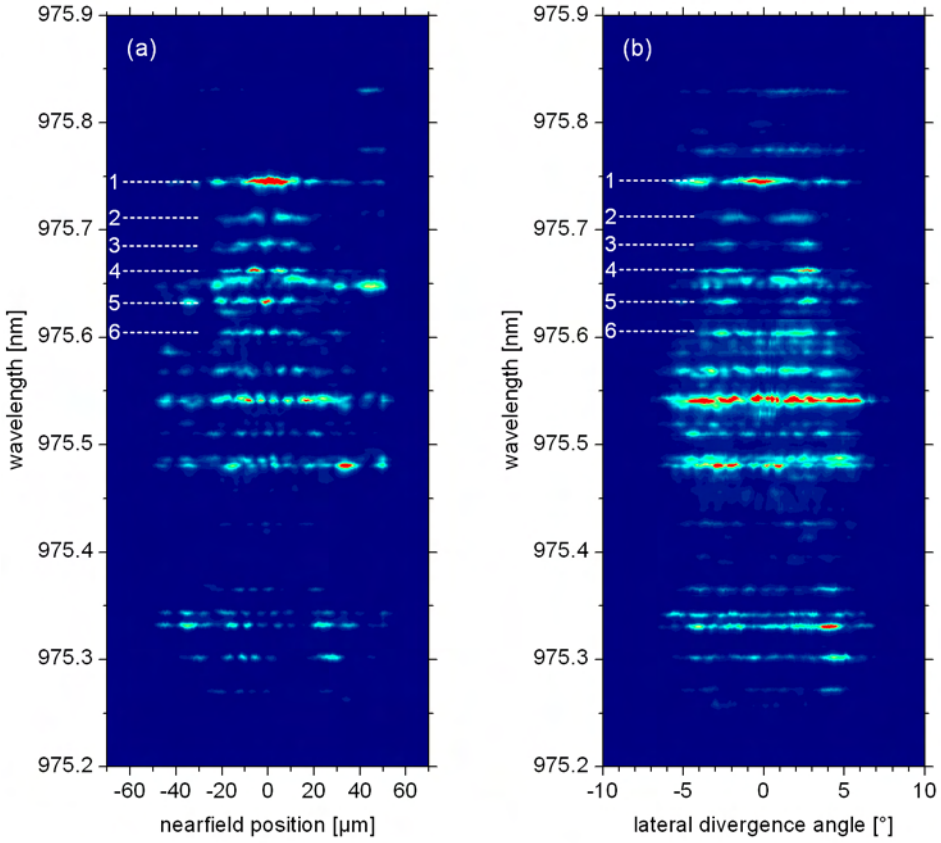

Figure 3.54: Spectrally resolved near field (a) and far field (b) of laser D1425-2 040102 at $I = 7.9\,\mathrm{A}$, $P = 7.0\,\mathrm{W}$.

power conversion efficiency has already exceeded its peak value. The total width of the spectrum is increased drastically to $\approx 1.4\,\mathrm{nm}$, compared to the spectral width at $I = 7.9\,\mathrm{A}$, $P = 7.0\,\mathrm{W}$ which is $\approx 0.6\,\mathrm{nm}$. Like at $I = 7.9\,\mathrm{A}$, $P = 7.0\,\mathrm{W}$, regions with vanishing intensity can be observed in the spectrum. Unfortunately, the spectrally resolved mode pattern in the near field and far field do not match very well in terms of their spectral intensity distribution. In contrast to the measurements at lower output powers (which are well reproducible), the measurements took a measurement time of several hours, required adjustment of the setup in the meantime and were performed at different days. The measurement of the spectrally resolved near field alone took two days because 14 mappings with a spectral width of $\approx 174\,\mathrm{pm}$ and a spectral overlap of $\approx 50\,\mathrm{pm}$ were measured. This required new fine-adjustment and hence, a careful superposition of the mappings along the spatial and

spectral axes. By slightly varying the injection current at the current source, also a weak hysteresis was observed for the appearance and disappearance of single optical modes. The measurement of the spectrally resolved far field has been performed within one day and with one fine-adjustment. Therefore, the spectral and spatial superposition of the 14 single mappings is more reliable than for the near field.

In the spectrally resolved near field, a system of lateral modes which belongs to a specific longitudinal mode is found between ≈ 977.30 and $\approx 977.47\,\mathrm{nm}$. Even though the intensity in the measured far field is relatively low for these modes, they can be found at analogue spectral positions. Many lateral modes of high mode orders $l \geq 10$ seems to dominate the near field and far field, although it is difficult to determine the exact lateral mode order from the number of local maxima. The near field is extended over $\approx 100\,\mu\mathrm{m}$ and the far field is extended over $\approx 14\,^\circ$, in good agreement with the widths of the near field and far field (95 % power content), measured without spectral resolution (see table 3.11).

Until now, DFB-BA laser D1425-2 040102 has been used for the analysis of the spectrally resolved near fields and far fields. This laser has a lateral mode confinement which is defined by the contact stripe width of $90\,\mu\mathrm{m}$ and by etched index trenches which cause a decrease of the effective refractive index of $1 \cdot 10^{-3}$, $5\,\mu\mathrm{m}$ separated from the contact stripe. Thus, it must be considered that the spectral and spatial properties of the optical modes discussed above, are valid for DFB-BA lasers with these lateral design properties.

In section 3.4.8, Fig. 3.43 it has been shown, that for the used lateral design, the lateral divergence angle behaves like a uniform function of the generated heat. Thus, increasing the power conversion efficiency will basically help to reduce the far field width. Further improvement of the lateral far field divergence angle (95 % power content) could be achieved with adequate changes in the lateral design of the DFB-BA lasers. One simple possibility to change the lateral design is to omit etching index trenches. This would eliminate the contribution of designed index guiding to the overall lateral mode guiding mechanisms, with the thermal lens remaining as a probably dominating guiding mechanism. Spectrally resolved lateral near field and far fields of a DFB-BA with $90\,\mu\mathrm{m}$ contact stripe but without index trenches have been investigated on device D1425-2 030919. Selected results are presented in this section and compared to the lateral near fields and far fields of laser D1425-2 040102 (with index trenches).

A spectrally resolved near field and far field of DFB-BA laser D1425-2 030919 is depicted in Fig. 3.56 as an example for lasers without designed index guiding. The measurement was performed at an injection current of $I =$

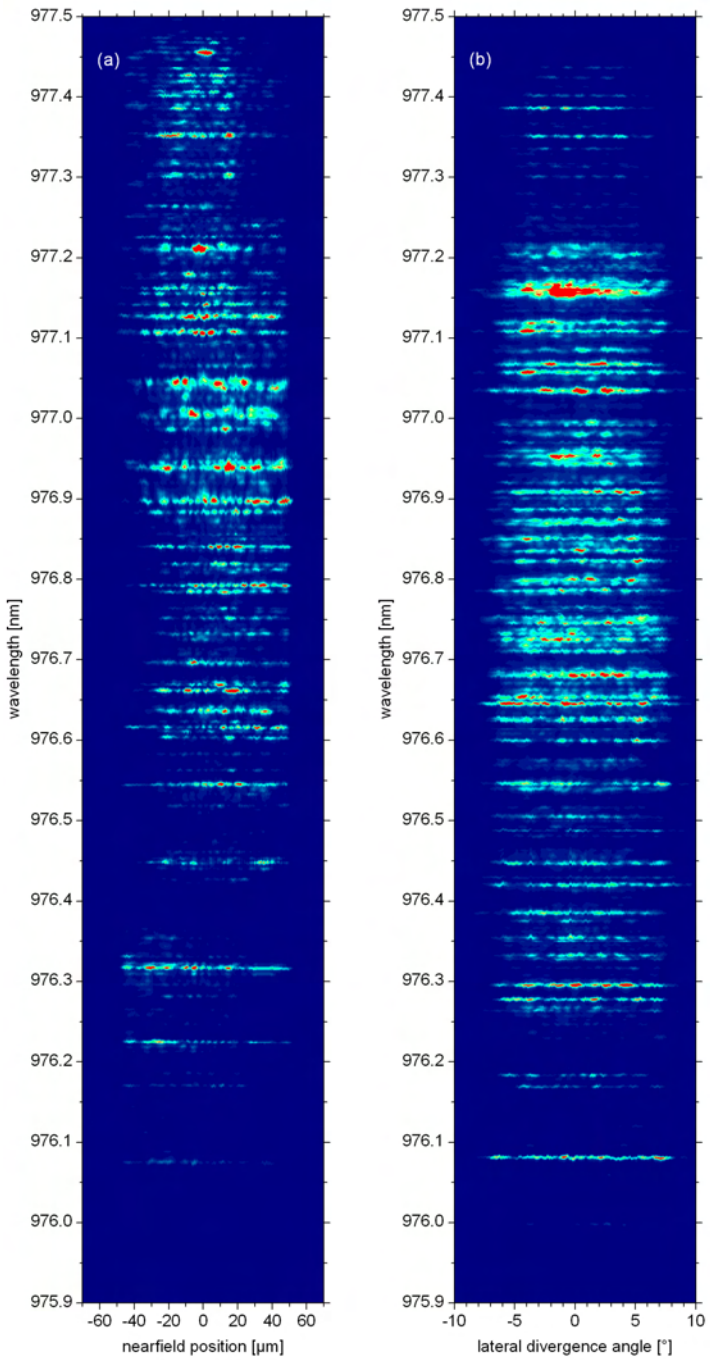

Figure 3.55: Spectrally resolved near field (a) and far field (b) of laser D1425-2 040102 at $I = 12.0\,\mathrm{A}$, $P = 10.0\,\mathrm{W}$.

6.2 A. The corresponding output power is $P = 5.0\,\mathrm{W}$, the power conversion efficiency is 52.1 %. Note that DFB-BA laser D1425-2 030919 less efficient due to a higher voltage and lower slope efficiency, presumably because of local deviations of the DFB grating (etching) in this area of the wafer. The measurement result has been selected in order to illustrate, that the lateral spectral and spatial properties of optical modes in a DFB-BA laser can be changed significantly by modifications in the lateral waveguiding. Several significant differences between the mode pattern in the near field and far field can be observed by comparing Fig. 3.56 to Fig. 3.54, 3.53 and 3.51.

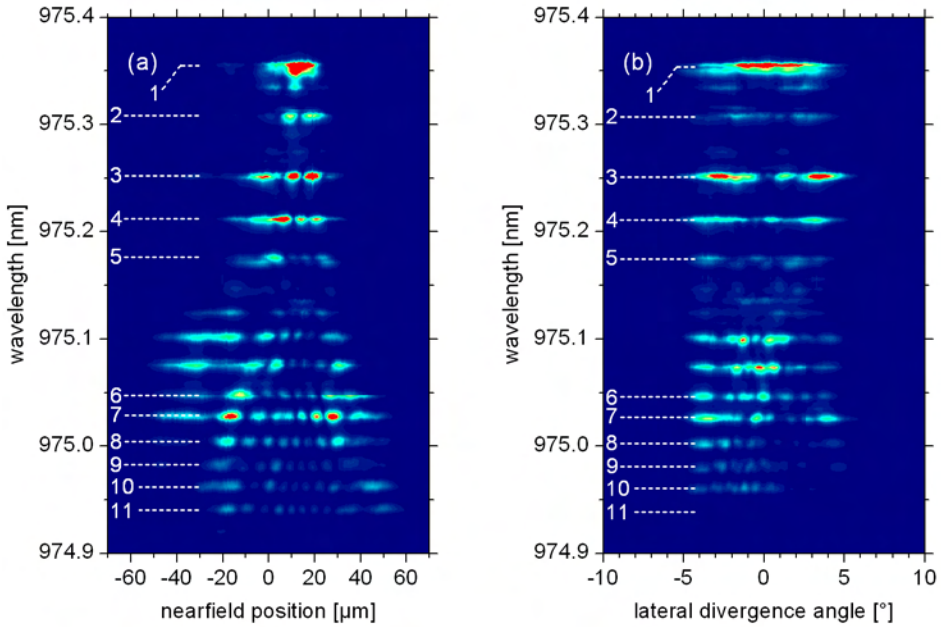

Figure 3.56: Spectrally resolved near field (a) and far field (b) of laser D1425-2 030919 at $I = 6.2\,\mathrm{A}$, $P = 5.0\,\mathrm{W}$.

While the spectral distance between neighboring lateral modes is roughly equidistant for DFB-BA laser D1425-2 040102, two spectral ranges with different mode spacings are observed for laser D1425-2 030919. The first of these spectral ranges begins at $\approx 975.15\,\mathrm{nm}$ and ends at $\approx 975.40\,\mathrm{nm}$. The spectral mode spacing in this range is $\approx 41\,\mathrm{pm}$. It contains lateral modes with mode orders $l = 1, 2 \ldots, 5$, as indicated in Fig. 3.56. In the lateral near field, these modes are considerably constricted, they extend over a lateral range $< 40\mu\mathrm{m}$. Therefore even these lower-order lateral modes are extended in the far field over a wide divergence angle of $\approx 10\,°$. The second spectral range with a more narrow spectral mode spacing ($\approx 24\,\mathrm{pm}$) begins at $\approx 974.90\,\mathrm{nm}$ and

ends at $\approx 975.15\,\mathrm{nm}$. In the second range, lateral mode orders $l = 6, 7 \ldots, 1$ were determined from the number of local intensity maxima.

For explanation, Fig. 3.57 (a) shows the power-voltage-curent characteristics of the DFB-BA laser without index trenches D1425-2 030919 (B), compared to the DFB-BA laser with index trenches D1425-2 040102 (A). The wavelength of identified lateral modes from both lasers have been plotted in Figure 3.57 (b). Firstly, the wavelengths of lateral modes $l = 1cdot8$ from laser A are depicted at $P = 2.7\,\mathrm{W}$ (blue dots) and at $P = 5.2\,\mathrm{W}$ (blue circles for the first longitudinal mode $m1$, half filled blue dots for longitudinal mode $m2$). These lateral modes show an approximately linear spectral separation, which does not changes significantly between the two output powers and different longitudinal modes. Secondly, the wavelengths of lateral modes $l = 1cdot5$ (red squares) and $l = 6cdot11$ (red diamonds) from laser B are depicted for $P = 5.0\,\mathrm{W}$. For the laser without index trenches (B), the lateral modes $l = 1cdot5$ have a much higher spectral mode spacing than the lateral modes of the laser with index trenches (A). In contrast, the second identified group of lateral modes ($l = 6cdot11$) has approximately the same mode spacing than the lateral modes of the laser with index trenches (A). The second group of lateral modes might belong to a second longitudinal mode, but this is not clear. Even the reason for the differences in the spectral mode separation of lateral modes is not understood. Further experimental and theoretical investigation is required in future work in order to improve the understanding of the impact of the lateral design on the spectral and spatial properties of lateral modes in high power BA lasers.

The spectral width (95 % power content) is depicted in Fig. 3.57 (c) as a function of the dissipated power $P_\mathrm{d} = U(I) \cdot I - P_\mathrm{opt}$ which results in heating the device (intensity from higher-order waveguide modes for D1425-2040102 neglected). Even though the lateral design is changed for DFB-BA laser D1425-2 040102 (with index trenches "A") and D1425-2 030919 (without index trenches "B"), the spectral width at the same heat is identical. In contrast, the lateral far field width (also 95 % power content) shows a very different behavior for both lasers. By omitting the index trenches, the far field width starts at a lower value but increases much more drastically with increased dissipated power. Note that for identical lateral design with index trenches, the lateral far field width has been shown (Fig. 3.43 (d)) to behave like a universal function of the dissipated power.

Lateral modes $l = 6$ and 7 in Fig. 3.56 have characteristic extra intensity at the left hand side of the near field. Taking into account the extra intensity at the left hand side, the near field extends over $\approx 100\mu\mathrm{m}$. However, the intensity distribution of lateral mode $l = 8$ for example, is also constricted to $\approx 57\mu\mathrm{m}$. With all its intensity distribution, the lateral near field is slightly

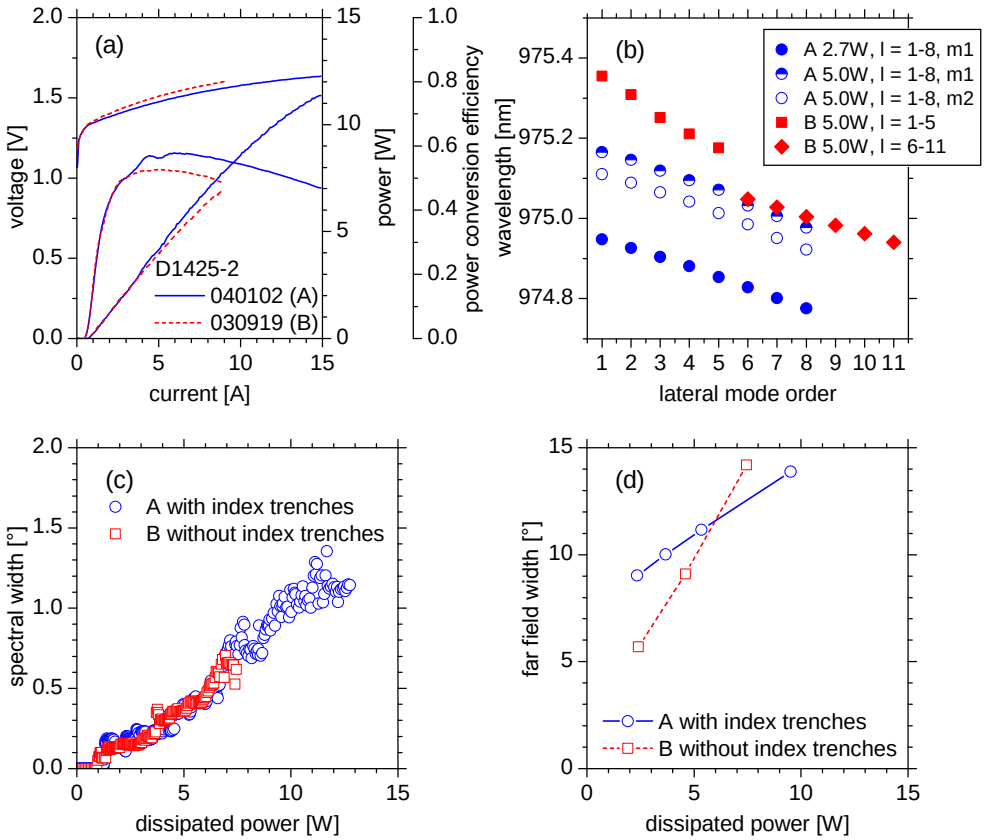

Figure 3.57: Comparison of DFB-BA lasers with (D1425-2 040102 "A") and without index trenches (D1425-2 030919 "B"). (a) Power-voltage-current characteristics. (b) Wavelengths of lateral modes. (c) Spectral width (95 % power content) as a function of the dissipated power (heat). (d) Width of the lateral far field (95 % power content) as a function of the dissipated power (heat).

asymmetric. The angular intensity distribution from the second spectral range is the same as for the lower-order lateral modes in the first range. As a consequence, the lateral far field is not broadening with increasing lateral mode orders (decreasing wavelength), as observed for the DFB-BA laser with index trenches, visible in Fig. 3.51 and 3.53. One possible explanation for the observed near field constriction for laser D1425-2 030919 is, that without index trenches, the lateral mode guiding is even stronger influenced by thermal lensing.

In conclusion, it has been observed that the optical modes in DFB-BA lasers are spectrally and spatially stable, when integration over time scales

$> 100\,\mathrm{ms}$ is applied. Furthermore, it has been verified, that at lower currents and powers ($I = 3.4\,\mathrm{A}$, $P = 2.7\,\mathrm{W}$, $P_\mathrm{d} = 2.3\,\mathrm{W}$) only one longitudinal mode is involved but at higher currents and powers ($I = 5.8\,\mathrm{A}$, $P = 5.2\,\mathrm{W}$, $P_\mathrm{d} = 3.7\,\mathrm{W}$), at least two longitudinal modes are lasing. Thus, the overall width of the spectrum is affected by the number of lateral modes, which occurs within one longitudinal mode and affected by the number of longitudinal modes. At high power levels ($P \geq 7\,\mathrm{W}$), very high lateral mode orders (cannot be clearly identified) are lasing and this presumably determines the overall spectral width. The spectral mode separation of the lateral modes (with index trenches) is approximately equidistant and the spectral width grows linear with the dissipated power (with and without index trenches). Increasing the power conversion efficiency is therefore on possibility to reduce the spectral width.

In addition, the lateral intensity distribution of optical modes is shown and discussed. The majority of all measured modes has roughly hermite-gaussian like intensity profiles. Deviations from hermite-gaussian mode profiles occur in form of extra intensity at the outside of the near fields and as broad asymmetric modes in the far fields. Also indications for the formation of filaments were observed. Finally, by measuring a second DFB-BA laser without index-trenches, it has been shown that the spatial and spectral properties of longitudinal modes depend on the exact lateral waveguiding.

3.5 Comparison of experimental and theoretical results for threshold current and slope efficiency

In the following section, the measured threshold currents, slope efficiencies and power-voltage-current characteristics will be compared to values, determined from the numerical calculation of the threshold gain and differential quantum efficiency as described in chapter 1.2.4. This comparison will indicate, if the experimental findings can be well described by the results from the coupled-mode-theory-based numerical calculations where the effect of the phase relations between the facet and the last grating stripe is approximated for DFB-BA lasers by averaging over the phases. Furthermore, a guideline for the optimization of the coupling coefficient in order to achieve a higher power conversion efficiency might be derived from the results. Certainly, this requires a reliable knowledge of the actual coupling coefficient of the fabricated DFB-BA lasers. Unfortunately, the determination of the DFB coupling coefficient – both by simulations and experimentally – turned out to have re-

markable uncertainties. For the numerical calculation, parameters listed in table 3.13 have been used.

Table 3.13: The fixed physical variables, their notations and values, used in the numerical simulation.

Variable	Notation	Value
Cavity length	L	$3000\,\mu$m
Contact stripe width	W	$90\,\mu$m
Reflectivity, rear facet	R_r	$96.00\,\%$
Reflectivity, front facet	R_f	$0.09\,\%$
Effective index	n_eff	3.434308
Grating period	Λ	283.9 nm
Coupling coefficient	κ	$(0.0, -0.1, ..., -10.0)\,\mathrm{cm}^{-1}$
Rear facet phase sections	d_a	$(0.00, 0.02, ..., 0.48)\Lambda$
Internal loss	α_i	$0.80\,\mathrm{cm}^{-1}$
Internal quantum efficiency	η_i	0.90
Transparency current density	j_th	$151\,\mathrm{Acm}^{-2}$

Five longitudinal modes around the stopband with longitudinal indices $m = -2, -1, 0, 1, 2$ have been considered. For $\kappa = 0\,\mathrm{cm}^{-1}$, and $d_\mathrm{a} = 0$, $m = 0$ corresponds to a wavelength of $\lambda = 975\,\mathrm{nm}$. As described in chapter 1.2.4 in detail, the values of the threshold gain g_th and differential quantum efficiency $\widetilde{\eta}_\mathrm{d}$ for the DFB-BA laser were obtained by averaging over all possible phase relationships between the last grating filament and the high reflection coated rear facet. The longitudinal mode $m = 0$ is the relevant lasing mode with the lowest threshold gain. The threshold current and slope efficiency have been calculated with equations 3.9 and 3.10 for coupling coefficients $\kappa = (0.0, -0.1, ..., -10.0)\,\mathrm{cm}^{-1}$.

$$I_\mathrm{th} \cong j_\mathrm{tr} \mathrm{e}^{(\alpha_\mathrm{i}+\alpha_\mathrm{m})/\Gamma g_0} L \cdot W \tag{3.9}$$

$$S = \widetilde{\eta}_\mathrm{d}\eta_\mathrm{i}\frac{hc}{q\lambda}(I - I_\mathrm{th}) \tag{3.10}$$

Now the question arises, which values shall be supposed for the DFB coupling coefficient of DFB-BA lasers from iteration I with in-situ etching times

of $t_{is} = 90$, 120 and 150 s. In section 3.3.3, the coupling coefficient of the DFB grating has been estimated from design properties and findings from STEM investigations. There it has been shown that under the approximation, that the DFB grating is perfectly rectangular and has the optimal duty cycle of $c_d = 1/4$ at $t_{is} = 120$ s, $|\kappa| \approx 1.78\,\mathrm{cm}^{-1}$ is obtained with QIP simulations. STEM investigations further indicate that the regrown $Al_xGa_{1-x}As$ is subdivided into aluminum rich regions ($x = 0.22$) on top of the grating stripes and aluminum poor regions ($x = 0.11$) between the grating stripes over < 100 nm on top of the grating, instead of being uniform with $x = 0.15$. By implementing this inhomogeneous aluminum distribution into the QIP simulation in form of a simplified rectangular model (which overestimates the effect), one obtains $|\kappa| \approx 4.41\,\mathrm{cm}^{-1}$. Therefore it has been reasoned that the actual coupling coefficient is approximately the average of this two values, which is $|\kappa| \sim 3\,\mathrm{cm}^{-1}$.

In section 3.4.10, it has been tried to determine the coupling coefficient based on measured sub-threshold spectra of the DFB stopband. Therefore, ASE spectra have been measured and parameter extraction was done by fitting calculated ASE spectra to the measured ones. Unfortunately, the measured ASE spectra were significantly affected by optical feedback from the tapered optical fiber and the modulation of the stopband was also limited due to the spectral resolution of the spectrometer. The resulting experimentally determined coupling coefficients were presumably underestimated with an average value of $|\kappa| \approx 1.15\,\mathrm{cm}^{-1}$.

In this section, the different coupling coefficients for $t_{is} = 90$, 120 and 150 s have been estimated in the following way, based on the experiences, mentioned above. Firstly, the increase of the coupling coefficient due to the inhomogeneous distribution of aluminum in the regrown part of the p-side waveguide has been estimated. In section 3.3.3, $\kappa \approx -1.78\,\mathrm{cm}^{-1}$ was obtained without the inhomogeneous aluminum distribution and $\kappa \approx -4.41\,\mathrm{cm}^{-1}$ with considering the inhomogeneous aluminum distribution at $t_{is} = 120$ s. The difference between the average value $\kappa = -3.01\,\mathrm{cm}^{-1}$ (probably a good approximation) and $\kappa \approx -1.78\,\mathrm{cm}^{-1}$ (underestimated) is $\Delta\kappa_{Al} = -1.24\,\mathrm{cm}^{-1} \sim -1\,\mathrm{cm}^{-1}$. The increase of the coupling coefficient $|\Delta\kappa_{Al}|$ is expected to be roughly the same for the different etching times $t_{is} = 90$, 120 and 150 s, because the additional index grating which is induced by the inhomogeneous aluminum distribution is expected to depend on the depth of the corrugation before overgrowth. The depth of the corrugation of the DFB grating before overgrowth can be simply approximated by adding the hight of the remaining GaAs cap ("cap GaAs [nm]") to the etch depth into the InGaP ("etched InGaP [nm]"), calculated on the basis of the experimentally determined etching rates of $\approx 360\mathrm{nm\,h}^{-1}$ for InGaP and $\approx 200\mathrm{nm\,h}^{-1}$ for GaAs.

The resulting values, rounded to integer nanometers, are given in table 3.14. For $t_{is} = 90$, 120 and 150 s, the corrugation depth is 26, 27 and 29 nm, respectively. Because of the slow increase with t_{is}, $\Delta\kappa_{Al} \sim -1\,cm^{-1}$ will be used for all of the three in-situ etching times.

Table 3.14: Layer thickness in the grating region, calculated based on experimentally determined etching rates for different in-situ etching times and resulting coupling coefficients from QIP simulations.

t_{is} [s]	residual InGaP [nm]	etched InGaP [nm]	cap GaAs [nm]	κ [cm^{-1}]	$\Re[\kappa]$ $+\Delta\kappa_{Al}$ [cm^{-1}]
90	11	9	17	$-0.325 - i0.004$	-1.3
120	8	12	15	$-1.439 - i0.007$	-2.4
150	5	15	14	$-2.560 - i0.014$	-3.6

Secondly, the coupling coefficients have been calculated for rectangular DFB gratings with $c_d = 1/4$ and the layer thicknesses given in table 3.14, without considering the inhomogeneous aluminum distribution. The results are shown in the second to last column of table 3.14. Afterwards, $\Delta\kappa_{Al} \sim -1\,cm^{-1}$ can be added to this values as a correction for the inhomogeneous aluminum distribution which forms an additional index grating and increases the coupling coefficient (last column of table 3.14). The coupling coefficients estimated as mentioned above, corresponding to in-situ etching times $t_{is} = 90$, 120 and 150 s, can be now allocated to the average threshold currents and slope efficiencies for the individual wafers which have been determined based on the experimentally determined values, given in table 3.7.

The calculated threshold currents and slope efficiencies are shown in Fig. 3.58 for coupling coefficients in the range of interest between 0 and $6\,cm^{-1}$ as black solid lines. In addition, the values for the devices from table 3.7 are depicted at the estimated coupling coefficients as colored symbols, respectively. In detail, Fig. 3.58 (a) shows the experimentally determined threshold currents at the simulated coupling coefficients without consideration of the inhomogeneous aluminum distribution, while in Fig. 3.58 (b), the corresponding coupling coefficients for the threshold currents are increased

by $|\Delta\kappa_{\mathrm{Al}}| = 1\,\mathrm{cm}^{-1}$. The same comparison is depicted for the experimentally determined slope efficiencies in Fig. 3.58 (c) (inhomogeneous aluminum distribution neglected) and Fig. 3.58 (d) (inhomogeneous aluminum distribution approximated by increasing the coupling coefficient by $|\Delta\kappa_{\mathrm{Al}}| = 1\,\mathrm{cm}^{-1}$).

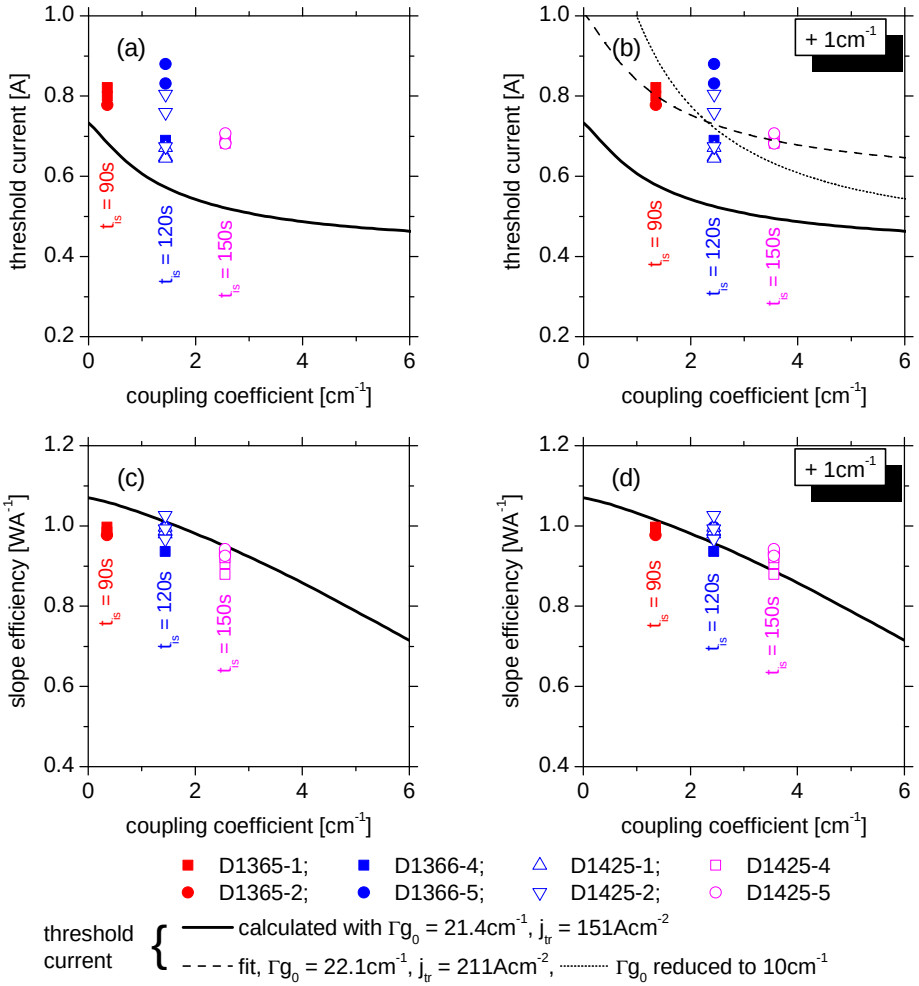

Figure 3.58: Calculated and measured threshold current and slope efficiency. (a) Calculated threshold current (black solid line) and measured values (symbols) from table 3.7. Coupling coefficients correspond to the second to last column in table 3.14. (c) Calculated slope efficiency (black solid line) and measured values (symbols) from table 3.7. Coupling coefficients correspond to the second to last column in table 3.14. (b) Like (a), coupling coefficients correspond to the last column in table 3.14. (d) Like (c), coupling coefficients correspond to the last column in table 3.14.

A comparison of the calculated and measured threshold currents shows that especially in Fig. 3.58 (b) (better estimation of $|\kappa|$ than in (a)), the measured threshold currents are remarkable increased by a value of $\delta I_{\mathrm{th}} \sim 250\,\mathrm{mA}$. This is supposed to be a result of the spectral detuning between the gain peak wavelength and the Bragg wavelength of the DFB grating in the fundamental vertical mode close to threshold. One might presume that the spectral detuning decreases the gain at the Bragg wavelength of the fundamental mode and increases the threshold current.

Two approaches have been chosen in order to analyze the origin of the additional threshold current which is observed, compared to the calculated threshold current.It should be noted that the threshold current (black solid line) has been calculated on the basis of the transparency current density $j_{\mathrm{tr}} \approx 151\,\mathrm{A\,cm^{-2}}$ and modal gain $\Gamma g_0 \approx 21.4\,\mathrm{cm^{-1}}$ which has been determined from the length dependency of the threshold current, presented in section 3.4.1. Both, j_{tr} and Γg_0 have been found to be approximately the same for the DFB-BA lasers and reference FP-BA lasers. Firstly, the threshold current has been fitted to the measurement data by varying j_{tr} and Γg_0. This lead to the black dashed curve shown in Fig. 3.58 (b), which matches well to the measured values. However, the fit leads to $j_{\mathrm{tr}} \approx 211\,\mathrm{A\,cm^{-2}}$ and $\Gamma g_0 \approx 22.1\,\mathrm{cm^{-1}}$. This means, that Γg_0 is nearly unchanged but the transparency current density is significantly increased by $\approx 60\,\mathrm{A\,cm^{-2}}$. In contrast to this finding, it has been expected that Γg_0 would be decreased and j_{tr} approximately unaffected. As a second approach, the modal gain coefficient has been reduced to $\Gamma g_0 = 10\,\mathrm{cm^{-1}}$ and the threshold current density is left as $j_{\mathrm{tr}} \approx 151\,\mathrm{A\,cm^{-2}}$. The resulting threshold current is shown as a black dotted line, which does not coincide with the measurement results. From the findings mentioned above one could reason that the detuning between the Bragg wavelength of the DFB grating and the gain peak wavelength leads to an increase of the threshold current because of both, an increase in j_{tr} and a decrease in Γg_0. Nevertheless, the position of the measurement data on the x-axis is uncertain because of the difficulties with the determination of the coupling coefficient. This should be considered when conclusions are drawn.

A better agreement between the calculated curve and the measured values than for the threshold current is found for the slope efficiency. The good agreement is especially the case for the slope efficiencies with corrections of the corresponding coupling coefficients due to the inhomogeneous distribution of aluminum in the regrown part of the p-waveguide, shown in Fig. 3.58 (d). Here, the measured values vary around the calculated curve.

In Fig. 3.59, power-current characteristics which have been calculated from the threshold gain and differential quantum efficiency obtained by numerical calculations (for $|\kappa| = 2.0$, 3.0 and $4.0\,\mathrm{cm^{-1}}$, compare to estimated

coupling coefficients given in table 3.14) and the characteristics of the power conversion efficiency (calculated with the measured voltage) are compared to the characteristics of the most efficient DFB-BA laser from iteration I (D1425-2 040102, $t_{is} = 120\,s$). The values for the threshold current and slope efficiency are indicated alongside.

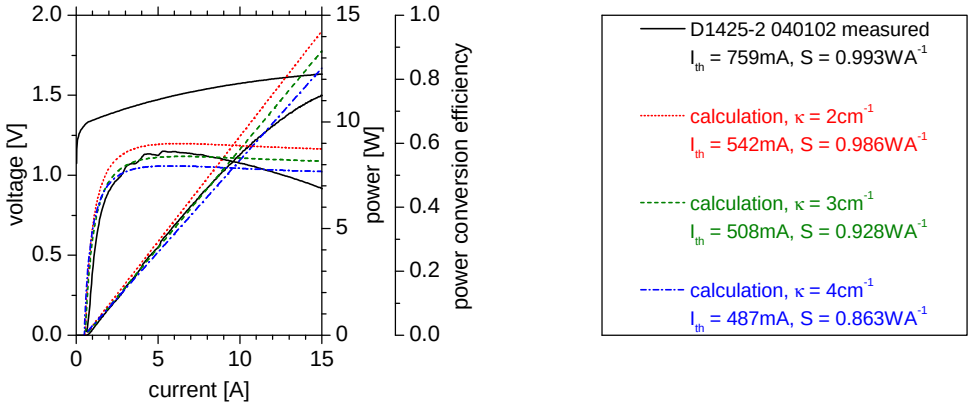

Figure 3.59: Comparison of the power-voltage-current characteristics for the numerical calculation and the measured characteristics for the laser D1425-2 040102 ($t_{is} = 120\,s$). For the calculated characteristics, the threshold current and slope efficiency, gained for $|\kappa| = 2.0$, 3.0 and $4.0\,cm^{-1}$, have been used.

Compared to the calculated power-current characteristics, the measured characteristics have the highest threshold current and also the highest slope efficiency, determined from a linear fit over 2A close above threshold. The reason for the experimentally observed increase in threshold current is as mentioned above, presumably the spectral detuning between the gain peak wavelength and the Bragg wavelength of the DFB grating. The fact that the measured slope efficiency is even higher than the calculated slope efficiency for $|\kappa| = 2.0\,cm^{-1}$ can be explained as follows. Firstly, the accuracy of the experimental determination of the slope efficiency is limited by the accuracy of the measured optical power and current. Secondly, DFB-BA laser D1425-2 040102 is lasing for $I \leq 7.5\,A$ on two higher-order vertical modes in addition to the fundamental mode (see Fig. 3.31 (b)). The variation of the power content in these higher-order modes may alter the power-current characteristics.

A comparison of the calculated and measured power-current characteristics, as well as the power conversion efficiency in Fig. 3.59 leads to the conclusion, that the actual coupling coefficient is in the range between for $|\kappa| = 2.0$ and $3.0\,cm^{-1}$. This is in good agreement with the estimated cou-

pling coefficients for $t_{is} = 120\,s$ ($|\kappa| = 3\,cm^{-1}$ from STEM investigation and average between neglecting aluminum distribution and overestimating model of the aluminum distribution, $|\kappa| = 2.4\,cm^{-1}$ based on etching rates and $\sim 1\,cm^{-1}$ correction for aluminum distribution).

The numerical calculation has the ability to make an approximate forecast for the power-current characteristics of a DFB-BA laser with a given set of known parameters as mentioned above. This fact supports the a priori assumption, that the problem of the non-constant facet phase relationship for a typical DFB-BA laser can be overcome by using the phase averaged values of the lowest threshold mode to calculate the threshold current and differential quantum efficiency. A precise knowledge of the coupling coefficient is critical because of its strong influence on the slope efficiency and threshold current, but experimentally difficult to achieve. Nevertheless, experimentally determined slope efficiencies $S < 1.0\,W\,A^{-1}$ which can be confirmed by numerical calculations indicate that the coupling coefficient κ should be further reduced (to $\kappa < 3\,cm^{-1}$, $\kappa \cdot L < 1$) in order to increase the slope efficiency to values above $1.0\,W\,A^{-1}$, like obtained for the reference FP-BA lasers. Of course, this will lead to even higher threshold currents but the power increase due to the increased slope efficiency is expected to more than compensate the drawback in threshold current. Furthermore, the suppression of FP-like modes will become more critical and require to achieve a very low reflectivity from the front facet in the desired wavelength region.

Of course, the slope efficiency, obtained from this numerical calculation is only valid at threshold (no roll-over) and can be used as a good approximation in a limited current interval above threshold. At higher currents, roll-over processes limit the maximum output power of a DFB-BA laser. In Fig. 3.59, considerable differences emerge for output powers above 10 W between the measured power-current characteristics and for $\kappa = 3.0\,cm^{-1}$. Roll-over of the power-current characteristics can be divided into thermal induced roll-over (like for a FP-BA laser) and spectral detuning induced roll over (depends on gain spectrum and Bragg wavelength).

Under CW current injection at 25 °C heatsink temperature, no significant decrease in the slope efficiency was measured at low powers, were the wavelength of the gain maximum is several nanometers shorter than the Bragg wavelength of the DFB grating, so that the effectively available gain should be lower than at the operation point where they coincide. This determination applies to DFB-BA lasers running only on the fundamental vertical mode as well as for such devices that start lasing on higher-order vertical modes. Only the measurements under short pulsed current injection, shown in section 3.4.7, provides indications that the slope efficiency may decrease if the gain peak is detuned to much shorter wavelengths than the Bragg

wavelength of the grating in the fundamental vertical mode.

3.6 Conclusions from iteration I

In this final section of chapter 3, conclusions will be derived from the results and findings that have been achieved during this part of the work, which will be of importance fur the further improvement of DFB-BA lasers in the second part of this work, presented in chapter 4. For selected topics it will be therefore summarized, what has been already done, what can be learned from this and how this findings can be implemented in iteration II.

Epitaxy design and FB-BA reference lasers

First of all, an epitaxy design has been developed which is potentially suitable for the integration of a DFB index grating via epitaxial overgrowth of a structured wafer surface, obtained after the first epitaxy step and lithographic structuring. In addition, the epitaxy design is optimized to achieve high power and high power conversion efficiency from BA lasers due to low internal optical loss, high internal quantum efficiency and a low voltage. The most important characteristics of this epitaxy design is the usage of a low aluminum content $x = 0.15$ in the $2.1\,\mu$m thick $Al_xGa_{1-x}As$ waveguide and the relatively thick p-type waveguide of $0.89\,\mu$m which allows for a tuning of the coupling coefficient by adjusting the position of the grating in the p-type waveguide.

Wafers without any grating layers in the p-type waveguide were grown in a single stage epitaxy to obtain reference material for the characterization of BA lasers. From the cavity length dependence of the threshold current and slope efficiency of un-coated BA test devices, in internal optical loss of $\alpha_\mathrm{i} \approx 1.0\,\mathrm{cm}^{-1}$ and an internal quantum efficiency $\eta_\mathrm{i} \approx 0.92$ has been determined.

Reference FP-BA lasers with a cavity length of $L = 3000\,\mu$m and a contact stripe width $W = 90\,\mu$m were fabricated from this material, facets passivated and coated to $R_\mathrm{f} \approx 2\,\%$, $R_\mathrm{f} \approx 98\,\%$ and mounted on CuW heatsinks, having a thermal resistance of $R_\mathrm{th} \approx 3.6\,\mathrm{K\,W}^{-1}$. Investigations under CW current injection at 25 °C heatsink temperature have shown that the FP-BA lasers have typical threshold currents of $I_\mathrm{th} = 620\,\mathrm{mA}$, a slope efficiency (over 2 A above threshold) of $S = 1.09\,\mathrm{W\,A}^{-1}$, achieve a power conversion efficiency of $\eta_\mathrm{PCE} \approx 66\,\%$ (peak), $\approx 65\,\%$ at $P_\mathrm{opt} = 7\,\mathrm{W}$ and even $> 60\,\%$ at $P_\mathrm{opt} = 10\,\mathrm{W}$ as targeted. The emission wavelength is in the 975 nm range as desired. Also

the vertical far field fulfills the requirements, is has a divergence angle of 45 ° with 95 % power content.

Broad area reference lasers from the developed epitaxy design fulfill the requirements to optical power, power conversion efficiency, wavelength and vertical far field. Thus, they are promising reference devices as a basis for the development of DFB-BA lasers with the same epitaxy design (except for thin grating layers). Certainly, it would have been preferred that the efficiency at 10 W is several percent higher than 60 % (maximum measured efficiency at 10 W was 64.7 %) in order to leave some more space for the degradation in DFB-BA lasers. Even the vertical far field with ≈ 43.5 ° is very close to the targeted maximum value of 45 °. Because of their high power conversion efficiency at optical output powers in the 10 W-class, their robustness and reliability (> 7000 h at 7 and 10 W output power) which has been reported in [Cru11c], FP-BA lasers from the mentioned design serve as "workhorse" for the further development of high power, high efficiency BA lasers in other projects.

Development of a DFB grating design and technology

A new design for second-order DFB gratings has been developed which bases on just two aluminum-free grating layers (20 nm $In_{0.49}Ga_{0.51}P$ grating layer, 25 nm GaAs cap layer), in contrast to earlier designs which often used four layers with one of them being a sacrificial layer [Kle06], [Kle07], [Sch09a]. Additionally, an improved fabrication technology was developed which uses in-situ etching with CBr_4 inside the epitaxy reactor after the grating is ex-situ pre-structure with lithographic techniques. The resulting gratings are thin (< 40 nm), have a shallow corrugation depth (∼ 30 nm), compared to other reported DFB grating designs [Ear98], [Kan06], [Kle06], [Kle07], [Sch09a] and provide a weak modulation of the effective index of refraction ($\Delta n_{\mathrm{eff}} \sim 1.5 \cdot 10^{-4}$) along the cavity axis, optimized for low coupling coefficients as required for efficient high power DFB-BA lasers. Material analysis with SIMS shows that the contamination of the grating region with oxygen can be reduced to $\rho_{\mathrm{peak}} < 1 \cdot 10^{17}\,\mathrm{cm}^{-3}$ / $\rho_{\mathrm{areal}} \leq 3 \cdot 10^{11}\,\mathrm{cm}^{-2}$.

The coupling coefficient of the DFB grating has been calculated as $|\kappa| = 1.78\,\mathrm{cm}^{-1}$ considering that the grating is positioned 230 nm below the p-cladding layer and assuming a rectangular grating shape and an optimal duty cycle of $c_{\mathrm{d}} = 1/4$. Investigations with STEM show that in the first < 100 nm of the regrown $Al_xGa_{1-x}As$ ($x = 0.15$ nominal), aluminum rich regions ($x = 0.22$ on top of the grating ridges) and aluminum poor regions

($x = 0.11$ in the grooves) are formed which will increase the coupling coefficient of the DFB grating. Considering the effect of this inhomogeneous aluminum distribution in a rectangular model (which potentially overestimates the effect) results in $|\kappa| = 4.41\,\mathrm{cm}^{-1}$. Therefore it has been estimated that the actual coupling coefficient will be approximately the average value of $1.78\,\mathrm{cm}^{-1}$ and $4.41\,\mathrm{cm}^{-1}$, thus $|\kappa| \sim 3\,\mathrm{cm}^{-1}$.

Using the new grating design and fabrication technology, in-situ etching times $t_{\mathrm{is}} = 150\,\mathrm{s}$ are preferred because this enables a reduction of the oxygen impurity density to $\rho_{peak} < 1 \cdot 10^{17}\,\mathrm{cm}^{-3}$, $\rho_{areal} \leq 3 \cdot 10^{11}\,\mathrm{cm}^{-2}$, starting from $\rho_{peak} > 1 \cdot 10^{19}\,\mathrm{cm}^{-3}$ without in-situ etching. The observed formation of aluminum rich and aluminum poor regions in the first $< 100\,\mathrm{nm}$ of the regrown AlGaAs increases the coupling coefficient. Nevertheless, this makes it more difficult to calculate and forecast the coupling coefficient and it would be therefore preferred if the influence of the inhomogeneous aluminum concentration on the coupling coefficient could be reduces.

Characterization of DFB-BA lasers

Wafers containing the newly developed grating structure in the p-waveguide, 230 nm below the p-cladding layer, were grown in a two step epitaxy process. An analysis of the cavity length dependence of the threshold current and slope efficiency has been used to determine the internal optical loss, internal quantum efficiency, transparency current density and modal gain coefficient from a wafer were the Bragg wavelength of the DFB grating was detuned to 1000 nm in order to run on FP modes at the gain peak at $\sim$ 975 nm. The measured internal optical loss, internal quantum efficiency transparency current density and modal gain coefficient have the same values as determined for the FP-BA laser reference material. This has been for the first time reported in a comparison of DFB-BA lasers (grating structured, two step epitaxy) with reference FP-BA (no grating layers, single stage epitaxy) from the same epitaxy design.

For the characterization, DFB-BA lasers ($L = 3000\,\mu\mathrm{m}$, $W = 90\,\mu\mathrm{m}$) with passivated and coated facets ($R_{\mathrm{f}} < 0.1\,\%$, $R_{\mathrm{f}} \approx 98\,\%$) were mounted on CuW heatsinks. Wafers were fabricated with three different in-situ etching times of $t_{\mathrm{is}} = 90$, 120 and 150 s. For each value of t_{is}, wafers with two different values for the spectral detuning between the gain peak wavelength ($\lambda_{\mathrm{gain}} = 968\,\mathrm{nm}$ targeted) and the Bragg wavelength of the DFB grating ($\lambda_{\mathrm{DFB}} = 973.7$ and $974.6\,\mathrm{nm}$ targeted) were realized.

Investigated under CW current injection at 25 °C heatsink temperature,

DFB-BA lasers have threshold currents of $I_{\mathrm{th}} = 645 - 821\,\mathrm{mA}$, a slope efficiency of $S = 0.906 - 1.026\,\mathrm{W\,A^{-1}}$, achieve a power conversion efficiency of $\eta_{\mathrm{PCE}} \approx 54 - 59\,\%$ (peak), $\approx 49 - 58\,\%$ at $P_{\mathrm{opt}} = 7\,\mathrm{W}$ and $> 43 - 52\,\%$ at $P_{\mathrm{opt}} = 10\,\mathrm{W}$. A comparison of DFB-BA lasers with the different values of the spectral detuning indicates that larger detuning improves the optical output power and efficiency (approximately +3 %) due to an increased slope efficiency, even though the threshold current is increased simultaneously.

Thus, the threshold current of the DFB-BA lasers is increased by $\sim 150\,\mathrm{mA}$ while the slope efficiency is decreased by $\sim 0.1\,\mathrm{W\,A^{-1}}$ in comparison to the reference devices. Additionally, the voltage of the DFB-BA lasers from all wafers is increased due to an additional series resistance of $\approx 5\,\mathrm{m\Omega}$ compared to the reference FP-BA lasers. Together with a stronger roll over of the optical output power, this results in a reduction in power conversion efficiency characteristics of $\sim 10\,\%$. On the one hand, this is of course an undesirable effect but on the other hand, this is the smallest difference in electro optical properties which has been reported for DFB-BA lasers an reference devices.

Except devices from one wafer with $t_{\mathrm{is}} = 90\,\mathrm{s}$ (lowest coupling coefficient), the spectra of all DFB-BA lasers are wavelength stabilized from threshold to 15 A. The wavelength of the fundamental mode is DFB stabilized at $976\,\mathrm{nm} \pm 3\,\mathrm{nm}$ as targeted. Unfortunately, wavelength stabilized side modes appear on the short wavelength side of the fundamental DFB mode which to some extent increase the spectral width with 95 % power content. These modes have been identified as higher-order vertical modes of the waveguide which can exceed threshold in contrast to the reference FP-BA lasers because the coupling coefficient of the DFB grating increases significantly for the higher mode orders which reduces their threshold current. Lasing on additional higher-order modes occurs predominantly for DFB-BA lasers with the larger spectral detuning. The DFB-BA lasers have, at currents where these side modes disappear, typical spectral width of $\Delta\lambda \approx 0.4\,\mathrm{nm}$ at $P_{\mathrm{opt}} = 7\,\mathrm{W}$ and $\Delta\lambda \approx 1.0\,\mathrm{nm}$ at $P_{\mathrm{opt}} = 10\,\mathrm{W}$. The vertical far field of the DFB-BA lasers fulfills the requirements, with typical divergence angles of 44 ° with 95 % power content. Nevertheless, at low currents where higher-order vertical modes appear, the vertical far field broadens up to 48 °.

Based on the developed epitaxy design and grating technology, DFB-BA lasers can be fabricated which, for the first time, achieve the same internal optical loss and internal quantum efficiency as efficient high power FP-BA reference lasers. The DFB-BA lasers achieve optical output power in the 10 W-class and their power conversion efficiency (up to 59 %) is only reduced by $\sim 10\,\%$ compared to the reference devices. Such performance level – com-

parable to state of the art FP-BA lasers – is reported for the first time for monolithic wavelength stabilized BA diode lasers.

The power conversion efficiency of the DFB-BA lasers is, compared to the reference devices, degraded due to a lower slope efficiency, higher threshold current and a higher voltage (series resistance). The slope efficiency can be further increased to $S \approx 1.03\,\mathrm{W\,A^{-1}}$ by reducing the coupling coefficient to approximately $|\kappa| \leq 1\,\mathrm{cm^{-1}}$ (from the numerical calculation) and this will more than compensate the simultaneous increase of the threshold current.

The used grating design and fabrication technology does not enable to achieve identical voltage as for the FP-BA reference lasers because of an additional series resistance of $\approx 5\,\mathrm{m\Omega}$. One possibility to improve the current flow through the grating layer is to completely etch through the $In_{0.49}Ga_{0.51}P$ grating layer (no residual $In_{0.49}Ga_{0.51}P$ layer left). This would enable to grow $Al_{0.15}Ga_{0.85}As$ on $Al_{0.15}Ga_{0.85}As$ and open a current path which is free of hetero-interfaces between the grating stripes (75 % of the area for $c_\mathrm{d} = 1/4$). Such gratings may be called floating DFB gratings [Lee97].

Furthermore, the spectral properties of the DFB-BA lasers must be improved in order to achieve the desired targets. Firstly, lasing on side modes in the optical spectrum must be eliminated. While lasing on FP-like modes can be suppressed with a better AR coating (lower reflectivity) of the front facet, suppression of higher-order waveguide modes would require to modify the waveguide design (at least the position of the DFB grating). Secondly, the spectral width $\Delta\lambda$ (95 % power content) in the fundamental DFB mode must be reduced to achieve the 0.3 nm target also at optical powers between 7 and 10 W. The spectral width has bee shown to depend approximately linear on the generated heat. Thus, improvement is expected for DFB-BA lasers with a higher power conversion efficiency.

Further investigations on DFB-BA lasers

An experimental determination of the DFB coupling coefficient based on parameter extraction by fitting ASE spectra ([Wen03]) lead to an average value of $|\kappa| = 1.15\,\mathrm{cm^{-1}}$ which is presumably underestimated. Sub-threshold ASE spectra of the DFB stopband have been measured, using DFB-RW lasers with a ridge width of $W \approx 10\,\mu\mathrm{m}$ and lateral index guiding by $\Delta n_\mathrm{eff} \approx 1 \cdot 10^{-3}$ (simplified test layout). The experimental determination of the coupling coefficient turned out too be challenging due to the low value of κ, because of optical feedback from the tapered fiber which has been used to couple the emitted light into a spectrometer, and because of the resolution limit of the spectrometer which was presumably too low to resolve the intensity modu-

lation in the stopband.

Knowledge of the actual coupling coefficient is essential for an optimization of the resonator loss in order to achieve a high slope efficiency. Several improvements are required to enhance the precision of the experimental determination of the coupling coefficient. Firstly, a measurement setup is required which significantly reduces the optical feedback into the diode lasers. Secondly, DFB-RW lasers with narrower ridge width $W \approx 5\,\mu$m, slightly higher lateral index guiding of $\Delta n_{\text{eff}} \geq 3 \cdot 10^{-3}$ and a better AR coating of the front facet are preferred.

The applicability of the DFB-BA lasers for possible applications where the injection current and heatsink temperature may be varied, has been investigated by determination of the DFB locking range in current and temperature for a typical DFB-BA laser. The experimental results show that a narrow spectrum with $\Delta\lambda \leq 1.5\,\text{nm}$ (95 % power content) can be achieved between $I = 0$ and 15 A and $T = 15$ and 50 °C within a band of $\sim 30\,\text{K}$ that shifts with approximately $-2.7\,\text{K}\,\text{A}^{-1}$ to lower temperatures with increasing temperature. The locking range (spectral width) is limited by lasing on higher-order waveguide modes (at low currents $\leq 8\,\text{A}$ *and* low temperatures $\leq 35\,°\text{C}$) and FP-like modes (at high currents $\geq 10\,\text{A}$ *and* high temperatures $\geq 35\,°\text{C}$).

The usable DFB locking range can be broadened to higher currents and heatsink temperatures by using a lower reflectivity front facet. This should be especially considered in the second part of this work, where the coupling coefficient (and $\kappa \cdot L$) of the DFB-BA lasers will be presumably further reduced. Of course, increasing the coupling coefficient would help to avoid lasing on FP-like modes but this option is not compatible with high efficiency lasers. Broadening the locking range to low powers and temperatures requires a better suppression of higher-order waveguide modes and will require changes in the waveguide design as mentioned above, for example changes regarding the thickness of the waveguide, the cladding layers, doping profile or the position of the grating. This might be in conflict with other development targets of this work.

Spectrally resolved lateral near fields and far fields have been measured in order to analyze the lateral and longitudinal modes in DFB-BA lasers. These lasers show roughly hermite-gaussian like lateral modes which are spectrally and spatially stable over hours. Lateral modes with mode orders $l = 1, \ldots 8$

were identified. A second longitudinal mode was observed at $P_{\mathrm{opt}} = 5.2\mathrm{W}$. The overall spectral width seems to be determined by the number of lateral modes which exceeds threshold. Furthermore, the dependence of the spatial and spectral properties of lateral modes on the lateral design of the BA lasers has been demonstrated by measurements of a second device without index guiding by etched trenches.

Because of being mostly determined by the high lateral mode orders which have a significant lower wavelength (lower effective index) than the fundamental mode, suppression of high-order lateral modes may be one option to reduce the spectral width of DFB-BA lasers. This could be probably achieved by influencing the lateral profile of the refractive index. Nevertheless, the most easiest way to do this is a reduction of thermal lensing via a higher power conversion efficiency or better cooling. Furthermore, lasing on multiple longitudinal modes should be avoided. Adjusting the DFB coupling strength to $\kappa \cdot L \approx 1$ is predicted to suppress lasing on multiple longitudinal modes because of reducing longitudinal spatial hole burning [Ear98] but this is in conflict with the goal to increase the slope efficiency to $> 1.0\,\mathrm{W\,A^{-1}}$ with the utilized epitaxy design (requires $\kappa \cdot L < 1$ because of the internal optical loss). In addition to a better understanding of the optical modes in DFB-BA lasers from a spectral point of view, the findings from the spectrally resolved lateral near fields and far fields also opens opportunities to improve the lateral far field width.

Finally, the measured and calculated threshold currents and slope efficiencies have been compared as functions of the DFB coupling coefficient. Therefore, the coupling coefficient of wafers with in-situ etching times of $t_{\mathrm{is}} = 90$, 120 and 150 s has been estimated as $|\kappa| = 1.3$, 2.4 and $3.6\,\mathrm{cm^{-1}}$, respectively. The measured threshold currents are $\approx 250\,\mathrm{mA}$ higher than the calculated threshold current, where no spectral detuning has been considered. The difference is assumed to be a consequence of both, an increased transparency current density j_{tr} and a reduced modal gain coefficient Γg_0. In contrast to the measured threshold currents, the experimentally determined slope efficiencies coincide with the calculated curve.

An optimization of the DFB resonator loss for a maximum slope efficiency requires a detailed comparison of the gained results for the threshold current and especially for the slope efficiency with the theoretical curve progressions. Therefore, the coupling coefficient should be determined more precisely than it has been possible in iteration I of this work. Nevertheless, a comparison

of the measurement results with the results from numerical calculations indicate that the coupling coefficient should be reduced in order to obtain a higher slope efficiency and thus, a higher power conversion efficiency.

Chapter 4

Experimental and theoretical results from iteration II

The aim of this chapter is to demonstrate how DFB-BA lasers can be further improved for high power conversion efficiency, based on the experimental results and findings from chapter 3 and theoretical fundamentals derived in chapter 1.

Firstly, the slope efficiency is expected to increase to $S > 1.0\,\mathrm{W\,A^{-1}}$ if the DFB coupling strength is further reduced to $\kappa \cdot L < 0.5$ and this will more than compensate for the simultaneous increase of the threshold current – leading to a higher power conversion efficiency. Secondly, the power conversion efficiency can be increased if the additional series resistance of $\approx 5\,\mathrm{m\Omega}$ which was observed compared FP-BA reference devices is eliminated. Both targets mentioned above can be achieved by exclusively optimizing the DFB grating, without changing the basic epitaxy design of the active region, waveguide and cladding layers. Thus, only the DFB grating will be modified in this second iteration, even though optimization of the basic epitaxy structure would also increasing the overall power conversion efficiency and potentially eliminate higher-order vertical modes in the optical spectrum. Nevertheless, this approach has important advantages. On the one hand, the goal for the DFB coupling strength $\kappa \cdot L$ is likely to be achievable with good precision. On the other hand, it allows the use of FP-BA lasers from the wafers, grown in a single stage epitaxy without the aluminum-free grating layers, to be used as reference devices for both, the DFB-BA lasers from iteration I and II and enables the fundamental physical impact of the DFB grating on the efficiency of DFB-BA lasers independent from the basic epitaxy design to be assessed.

A concept for the further enhancement of the electro-optical properties of DFB-BA lasers is presented and promising changes are introduced in the design and fabrication technology of the DFB grating. Subsequently, improved DFB-BA lasers are fabricated, experimentally characterized and compared to the DFB-

BA lasers and reference FP-BA lasers from iteration I with higher performance confirmed empirically. A preliminary reliability test at 10 W optical output power is performed in order to demonstrate the material quality of the developed devices and their relevance for possible applications.

4.1 A concept for the further enhancement of the electro-optical properties of DFB-BA lasers

As described in chapter 3, the development of DFB-BA lasers on the basis of a waveguide structure, suitable for high power and high efficiency FP-BA lasers, was quite successful in comparison with earlier published electro-optical, spectral and spatial emission properties of DFB-BA lasers. Nevertheless, a residual reduction in the power and efficiency characteristics is observed between the FP-BA lasers and DFB-BA lasers with the DFB grating technology from iteration I. Generally, the integration of an epitaxial overgrown DFB grating into a laser waveguide may lead to minor degradations of the electro-optical properties, due to at least marginal contamination with oxygen, impurities and other epitaxial imperfections. The DFB-BA lasers developed during iteration I of this work have been shown to be basically degraded because of slightly too high coupling coefficients which lead to a reduced slope efficiency as well as due to an additional series resistance which increases the voltage drop. Also the principle of DFB itself is understood to limit the CW electro-optical properties due to differences in the temperature dependence of gain peak and Bragg wavelength (increases roll over of the power characteristics), as well as due to radiation loss from second-order DFB gratings (estimated to be approximately negligible), discussed in chapter 3.

From chapter 3, one can derive three concepts, how the electro-optical properties of DFB-BA lasers could be further improved. Firstly, the influence of the DFB grating onto the voltage characteristics could in principle be reduced. Secondly, the resonator loss α_{DFB} could be reduced to the value of the FP-BA reference devices $\alpha_{\mathrm{m}} = 1/2L \cdot \ln(1/(R_{\mathrm{f}} \cdot R_{\mathrm{f}})) \approx 6.6\,\mathrm{cm}^{-1}$ or even lower, to enhance the output power from the front facet. This correlates to a coupling coefficient $|\kappa| \approx 1.4\,\mathrm{cm}^{-1}$. Thirdly, using a waveguide structure and active region with lower internal loss and higher internal quantum efficiency could improve the electro-optical properties. In chapter 4, concepts one and two will be studied in parallel. This allows for an experimental analysis of the physical and technological limits in comparison to the FP-BA reference

lasers from iteration I. This means, that an enhancement of the charge carrier transport through the grating region for a reduced series resistance will be one focus in the present chapter. The second focus, the reduction of the DFB coupling coefficient, must be executed with respect to a further modified grating layer design. The third concept, optimizing the waveguide structure and active region is not specifically a question of the limitations of high power and efficiency DFB and will be left for later work.

4.2 Development of a further optimized DFB grating

4.2.1 Changes of the properties of the DFB grating

The idea behind optimizing the DFB grating layers itself is to eliminate the voltage penalty from the grating. This means to avoid any supplementary series resistance in the voltage characteristics of the DFB-BA lasers, which occurs due to hindering the charge carriers, passing through the grating region. Furthermore it has to be considered that the coupling coefficient of the DFB grating has to be reduced. This can be done by tuning the vertical position of the grating in the *p*-waveguide to a position with a lower confinement factor with the optical field or by a reduction of the contrast of the effective index of refraction. Thus, the thickness of the $In_{0.49}Ga_{0.51}P$ layer which is basically responsible for the index contrast can be decreased but should not be increased.

The important question for the elimination of the voltage penalty is how the grating causes the voltage to increase. From the characteristics of the valence band along the epitaxial growth direction directly through a grating ridge and in between the grating ridges, shown in Fig. 3.21 (a) (undoped case), one can see that the $In_{0.49}Ga_{0.51}P$ layer forms a barrier for the holes, while the GaAs cap forms a shallow well. Nevertheless, this volume band discontinuities must be considered to be leveled out because of the *p*-doping level which is $2 \cdot 10^{18}\,cm^{-3}$ in the grating layers and $1 \cdot 10^{18}\,cm^{-3}$in the regrown $Al_{0.15}Ga_{0.85}As$ on top of the grating.

Charge carrier transport may be therefore assumed to be hindered due to potential barriers that are formed at the hetero-interfaces between the $Al_{0.15}Ga_{0.85}As$ / $In_{0.49}Ga_{0.51}P$ from the first epitaxy and the interfaces between the $In_{0.49}Ga_{0.51}P$ and GaAs with the regrown $Al_{0.15}Ga_{0.85}As$.

Semiconductor hetero-interfaces are known to induce additional voltage due to an increased series resistance, especially in the presence of defects. This has been studied especially for vertical cavity surface emitting lasers

(VCSEL's) and concepts have been developed to reduce the series resistance by using graded interfaces [Cha93], [Pet93], [Kha95], [Zho95], [Die08]. These VCSEL's have n-type and p-type Bragg mirrors, both bordering the cavity and active region. The Bragg mirrors consist of a sequence of semiconductor layers with refractive index contrast such as GaAs and $Al_xGa_{1-x}As$ and therefore build an ideal system to analyze the influence of hetero-interfaces on the voltage drop. In the case of the VCSEL's, the series resistance was reduced by replacing the digital material transitions with graded profiles, because the number of the quarter wavelength layers has to be maintained in order to maintain the desired reflectivity.

For the DFB gratings, a reduction of the series resistance is possible on the basis of the following two concepts. Firstly, the number of the layers and hetero-interfaces can be reduced. This has been already considered during the development of the two-layer grating design, reported in iteration I of this work. Nevertheless, two hetero-interfaces remain between the grating stripes because of the residual $In_{0.49}Ga_{0.51}P$ layer in the grating design of iteration I. Secondly, the presence of hetero-interfaces can be limited to $\approx 1/4$ of the area by the utilization of floating gratings whose grating ridges are completely embedded in the $Al_xGa_{1-x}As$ waveguide material. This means to eliminate the residual $In_{0.49}Ga_{0.51}P$ layer with the corresponding hetero-interfaces and is supposed to enhance the carrier (hole) transport through the grating, without changing the DFB coupling coefficient.

The idea behind this sensible approach is to transfer the vertical hight modulation of the ex-situ pre-structure GaAs cap stripes, lying on top of a thin continuous $In_{0.49}Ga_{0.51}P$ layer, into a hight modulation between the $In_{0.49}Ga_{0.51}P$ grating ridges (possibly with thin remaining GaAs caps) and the $Al_{0.15}Ga_{0.85}As$ waveguide via in-situ etching. Therefore, the $In_{0.49}Ga_{0.51}P$ layer has to be very thin. Otherwise, a loss in the surface corrugation during the in-situ etching and small differences in the vertical and in-plane etching rates could cause a annihilation of the grating corrugation and refractive index contrast.

From an investigation of the etching rates of GaAs ($\approx 200\,\mathrm{nm\,h^{-1}}$), $Al_{0.15}Ga_{0.85}As$ ($\approx 190\,\mathrm{nm\,h^{-1}}$) and $In_{0.49}Ga_{0.51}P$ ($\approx 360\,\mathrm{nm\,h^{-1}}$), assuming an in-situ etching time of 150 s being necessary to remove oxygen impurities, suitable layer thicknesses of 25 nm for the GaAs cap and 10 nm for the $In_{0.51}Ga_{0.49}P$ grating layer have been derived. Therefore it has been considered that the original 25 nm thick GaAs cap layer will be reduced to approximately $15 - 20$ nm during the ex-situ structuring and cleaning with oxygen plasma and oxide removal with sulfuric acid. The utilization of a 10 nm thin $In_{0.51}Ga_{0.49}P$ layer enables that the grating is etched through this layer after $t_{is} = 100$ s and allows for a moderate over-etching of 50 s to ensure

reproducibility. Figure 4.1 shows the chronological sequence of the thickness of the calculated residual $In_{0.49}Ga_{0.51}P$ layer, the GaAs cap and the overall corrugation depth (between the grating ridges and grooves) over an in-situ etching time off $t_{is} = 200\,s$. At $t_{is} = 100\,s$, the residual $In_{0.49}Ga_{0.51}P$ layer is removed and the grooves are further etched into the underlying $Al_{0.15}Ga_{0.85}As$ with a drastically decreased etching rate. This causes the overall corrugation depth to decrease slowly for $t_{is} > 100\,s$ because of the small differences in the etching rates of GaAs (cap) and $Al_{0.15}Ga_{0.85}As$ (in the grooves). A 6.7 nm thin GaAs cap is left after $t_{is} = 150\,s$ left in the calculation example which starts with 15 nm at $t_{is} = 0\,s$.

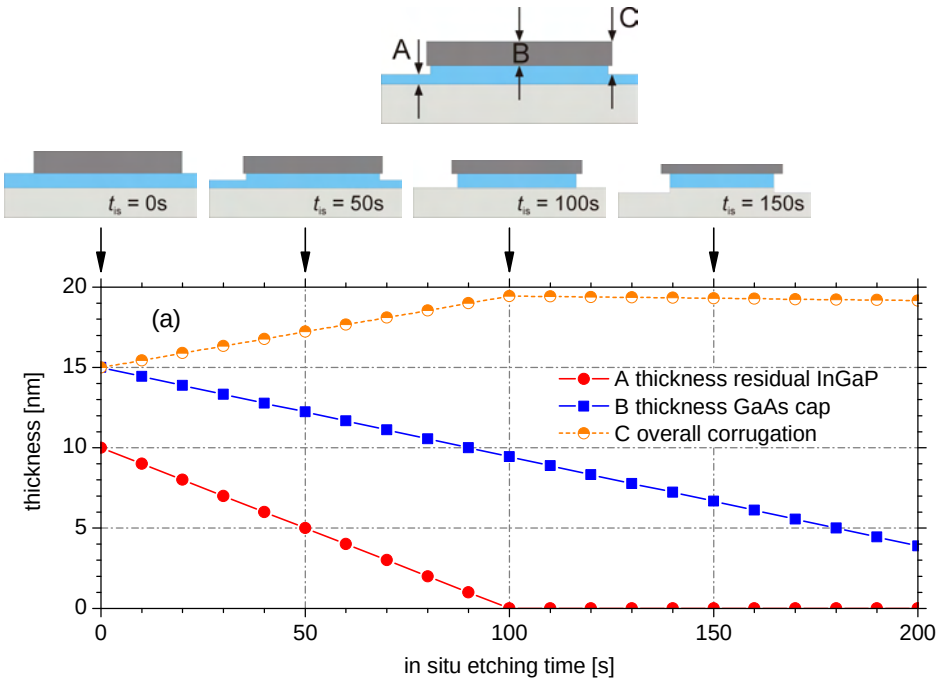

Figure 4.1: Sequence of the thickness of the calculated residual $In_{0.49}Ga_{0.51}P$ layer "A", the GaAs cap "B" and the overall corrugation depth "C" (between the grating ridges and grooves) over an in-situ etching time of $t_{is} = 200\,s$. Schemes of the corresponding grating shape are depicted on top of the diagram.

Investigations with SEM and STEM have shown that it is essential to ensure that a thin GaAs cap remains on top of the $In_{0.49}Ga_{0.51}P$ grating ridges during the in-situ etching and epitaxial regrowth with $Al_{0.15}Ga_{0.85}As$, because this prevents that the $In_{0.49}Ga_{0.51}P$ grating ridges diffluence because of the low binding energy of indium atoms.

In Fig. 4.2, a scheme of the grating after the in-situ etching and the

resulting overgrown grating is depicted for the DFB grating from iteration I ((a) and (b)) and the further optimized grating from iteration II ((c) and (d)).

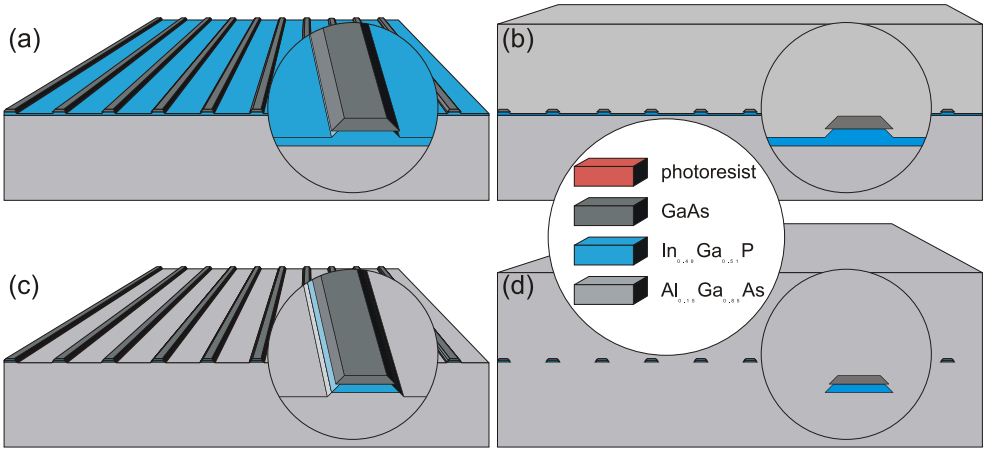

Figure 4.2: Manufacturing principle of the further optimized DFB grating in comparison to the DFB grating from iteration I. (a) DFB grating from iteration I after in-situ etching, before epitaxial overgrowth with a residual $In_{0.49}Ga_{0.51}P$ layer. (b) After epitaxial overgrowth of (a). (c) Further optimized DFB grating after in-situ etching, before epitaxial overgrowth without a residual $In_{0.49}Ga_{0.51}P$ layer. (d) After epitaxial overgrowth of (c), the grating ridges are completely buried in $Al_{0.15}Ga_{0.85}As$.

Firstly, the most important difference between the two types of DFB gratings is, that the residual $In_{0.51}Ga_{0.49}P$ layer, visible in Fig. 4.2 (a), is now completely removed in (c), when the in-situ etching is finished. Secondly, the $In_{0.51}Ga_{0.49}P$ layer is only 10 nm thick ((c) and (d)), instead of 20 nm in the grating from iteration I ((a) and (b)). Thirdly, the in-situ etching time of $t_{is} = 150\,s$ and small changes in the cleaning treatment after ex-situ pre-structuring will lead to a reduction of the thickness of the GaAs cap compared to the gratings in iteration I, where also shorter in-situ etching times of $t_{is} = 90$ and 120 s have been used. The thickness of the GaAs cap is estimated in table 3.14 for the different in-situ etching times used in iteration I. From the etching rates and Fig. 4.1 one can derive that $\approx 8.3\,nm$ of the GaAs cap will be removed during the 150 s of in-situ etching. Based on experimental experiences, presented in sections 3.3.2 and 3.4.1, this is sufficient to eliminate oxygen impurity density to $\rho_{peak} < 1 \cdot 10^{17}\,cm^{-3}$ or $\rho_{areal} = 3 \cdot 10^{11}\,cm^{-2}$ (at $t_{is} = 150\,s$) and enable low internal optical loss of $\alpha_i \approx 0.85\,cm^{-1}$ (determined at $t_{is} = 120\,s$).

Finally, Fig. 4.3 (a) and (b) shows the electronic band-structure (undoped case) and refractive index profile of the further optimized floating DFB grating design from iteration II in analogy to Fig. 3.21 (a) for iteration I. In Fig. 4.3, the thickness of the GaAs cap (region III) is chosen as 15 nm after overgrowth. In the undoped case depicted in Fig. 4.3 (a), the $In_{0.49}Ga_{0.51}P$ (region II) forms a barrier to the transport of holes and the GaAs cap forms a quantum well like structure inside the grating ridges (red dashed line). Nevertheless, the volume band discontinuities are leveled out due to the high doping level of $2 \cdot 10^{18}\,cm^{-3}$ which will be applied in the grating layers like in iteration I but hetero-interface band discontinuities will be left over inside the grating ridges. For the reduction of the series resistance of the DFB-BA lasers it is therefore essential that in the region between the grating ridges (blue solid line) which covers 3/4 of the area, the hetero-interfaces are removed and cannot form barriers to the transport of holes.

The averaged grating stripes, formed by 10 nm $In_{0.49}Ga_{0.51}P$ grating ridges and 15 nm GaAs caps (in this example), result in a negative contrast in the index of refraction $\Delta n \approx -0.022$, compared to the surrounding $Al_{0.15}Ga_{0.85}As$ p-waveguide. This is shown in Fig. 4.3 (b). The negative index contrast arises from the fact that (at 975 nm) the refractive index of $In_{0.49}Ga_{0.51}P$ (≈ 3.211) dominates the index of the averaged grating ridges (≈ 3.400), which is lower than the index of $Al_{0.15}Ga_{0.85}As$ (≈ 3.426) and GaAs (≈ 3.526). Therefore, the thickness of the GaAs cap must be below 21.3 nm in order to maintain the desired index contrast and achieve distributed feedback. In Fig. 4.3 (c), the refractive index of the averaged grating ridges is depicted as a function of the thickness of the GaAs cap d_{GaAs}, together with the index of $Al_{0.15}Ga_{0.85}As$. For $d_{GaAs} = 21.3\,nm$, the refractive index contrast between the averaged grating ridges and the surrounding waveguide cancels. On the one hand, d_{GaAs} should be $\leq 15\,nm$ in order to ensure a sufficient index contrast for the coupling coefficient. On the other hand, d_{GaAs} should be $> 5\,nm$ to ensure that a GaAs cap remains on the $In_{0.49}Ga_{0.51}P$ grating ridges and protects them during in-situ etching and overgrowth.

4.2.2 Manufacturing of the DFB grating

The manufacturing of the further optimized DFB grating is based on the same technology, as described in iteration I in section 3.3.2. The most important fact is the usage of an in-situ etching technique, executed within the MOVPE reactor. For some of the processed wafers in iteration II, the photoresist which is used to form an etch mask for the ex-situ pre-structuring of the GaAs cap layer has been changed.

In iteration I of this work, a positive photoresist has been used. After

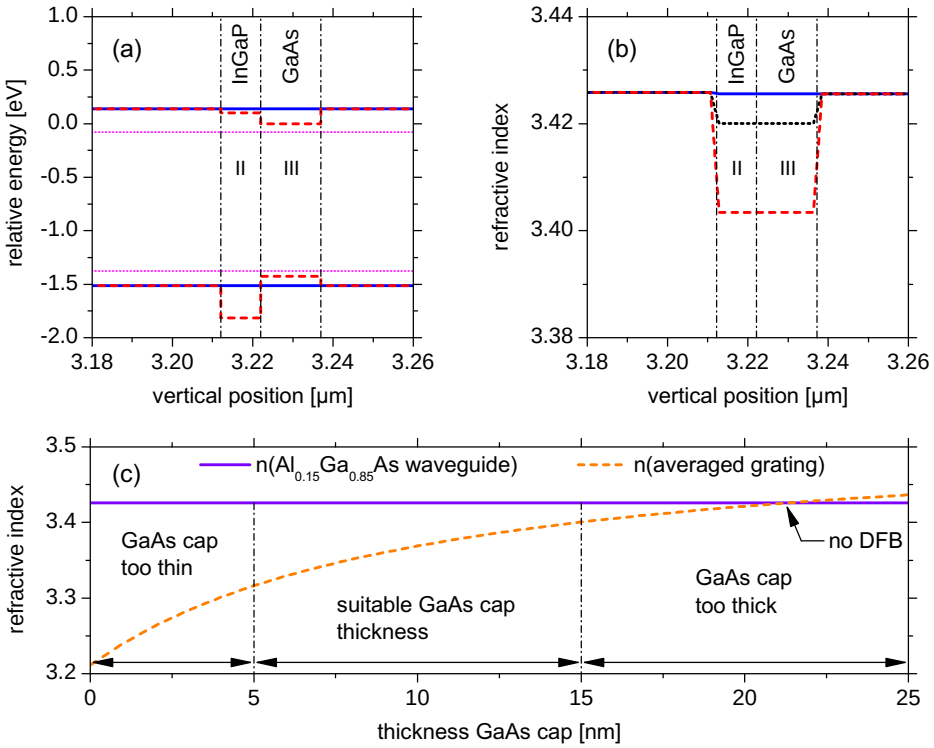

Figure 4.3: Electronic band-structure and refractive index profile of the further optimized DFB grating. (a) Minimum of the conduction band edges at the Γ- and X-point (in the grating ridge: upper red dashed line, between the grating ridges: blue solid line) and the heavy hole valence band edge (in the grating ridge: lower red dashed line, between the grating ridges: blue solid line). The corresponding first electron and first heavy hole energy levels are depicted as magenta dotted lines respectively. (b) Characteristics of the refractive index in the grating region within an grating ridge (GaAs and InGaP averaged, red dashed line), between two grating ridges (blue solid line) and the averaged characteristics for a duty-cycle of 1/4 (black dotted line). (c) Refractive index of the averaged DFB grating and waveguide as a function of the GaAs cap thickness.

developing of the photoresist and etching the ≈ 290 nm-period line pattern into the GaAs cap, the undeveloped photoresist mask was removed with a suitable photoresist remover (solvent). Followed by rinsing with water, this led to a clean grating surface, sufficient to transfer the wafer back into the epitaxy reactor for in-situ etching.

Some of the wafers in iteration II were spin coated with a negative photoresist, because this allows a better adjustment of the high duty cycle pho-

toresist stripes ($c_d > 1/2$) which are required to achieve the targeted low duty cycle ($c_d < 1/4$) regrown DFB gratings because of in plane etching of the line patterns. In addition, the line pattern from negative photoresist was found to have smoother edges and lower variations of the duty cycle, compared with ridges from positive photoresist. Certainly, the developed negative photoresist which is left on top of the GaAs cap stripes after in-situ pre-structuring cannot be completely removed with a photoresist remover. Therefore, a low DC-voltage oxygen plasma has been used to remove the deposits from the grating surface. Afterwards, the surface oxides which have been build on the semiconductor grating surface are selectively removed with H_2SO_4. Note, that by removing the photoresist and surface oxides, an approximately $10-15$ nm thin layer of the GaAs cap is removed as well, because the plasma treatment and H_2SO_4 etching are abrasive techniques. This effect increases the refractive index contrast of the double layer grating.

Figure 4.4 shows a scheme of the manufacturing of the DFB grating. In Fig. 4.4 (a), the photoresist stripes are depicted schematically. The GaAs cap layer is patterned by a selective wet etching process that stops on the $In_{0.49}Ga_{0.51}P$ layer. The remaining GaAs line pattern on top of the $In_{0.49}Ga_{0.51}P$ surface is shown in Fig. 4.4 (b).

After cleaning as mentioned above, the wafer is inserted back into the MOVPE reactor where the final in-situ etching step is applied. The in-situ etching over 150 s transfers the surface corrugation of the GaAs line pattern into the $In_{0.49}Ga_{0.51}P$ layer as depicted in Fig. 4.4 (c). The aim is to etch completely through the $In_{0.49}Ga_{0.51}P$ layer at positions between the GaAs stripes. Only at the positions of the GaAs stripes, a line pattern, consisting of a thin GaAs cap and $In_{0.49}Ga_{0.51}P$ grating stripes, remains. The fact, that a thin GaAs cap is left over on top of each $In_{0.49}Ga_{0.51}P$ stripe is slightly disadvantageous for the refractive index contrast of the overgrown DFB grating, but it helps to stabilize the $In_{0.49}Ga_{0.51}P$ stripes during the epitaxial overgrowth. The $In_{0.49}Ga_{0.51}P$ stripes were found to diffluence during the regrowth, if the GaAs cap is removed [Bug11], [Cru12b]. When starting the second epitaxy, $Al_{0.15}Ga_{0.85}As$ is grown on $Al_{0.15}Ga_{0.85}As$ from the first epitaxy at $\approx 3/4$ of the whole area, while only $\approx 1/4$ of the surface is covered with GaAs / $In_{0.49}Ga_{0.51}P$ grating stripes. The width of the photoresist stripes at the beginning of the lithographic etching process must be chosen carefully to achieve a duty cycle of 1/4 in the final grating.

In Fig. 4.5, three STEM overview images of the DFB grating are depicted. The material was taken from a test wafer D1878-4 which has not been processed after its growth. The preparation of samples and the STEM and energy dispersive X-ray spectroscopy (EDXS) investigations were done by A. Mogilantenko at the Humboldt-University, Berlin. The contrast in

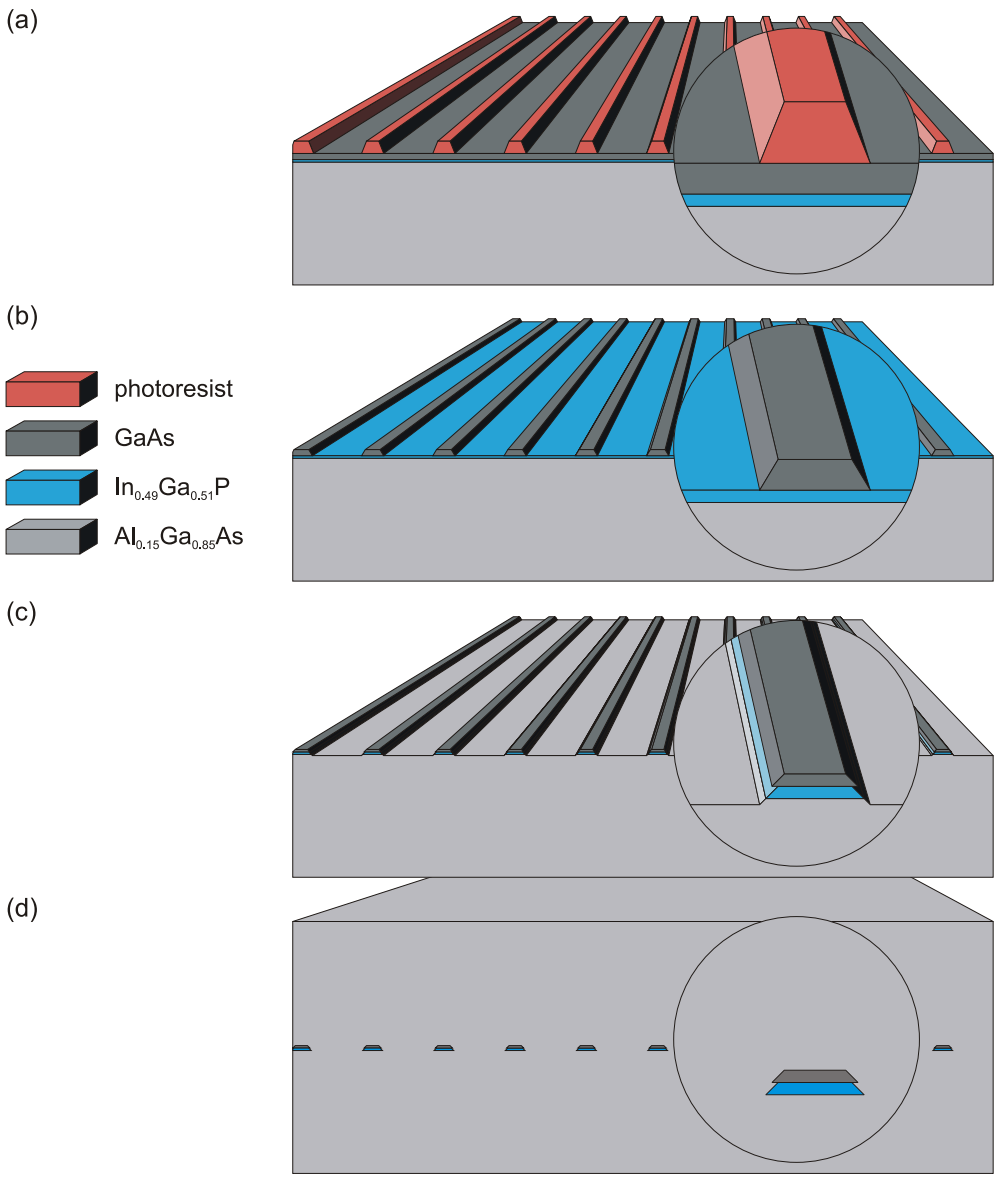

Figure 4.4: Schematic illustration of the processing of the DFB grating. (a) A mask of photoresist is structured on top of the grating layers. (b) The mask is transferred via selective etching into the GaAs cap layer. (c) The GaAs grating is transferred with a non selective in-situ etching through the $In_{0.49}Ga_{0.51}P$ layer. (d) The waveguide structure is finished with a second epitaxy step.

the STEM images in Fig. 4.5 (a) - (c) corresponds to the atomic number Z (dark: low atomic number, bright: high atomic number). With

$Z(\mathrm{Ga}) = 31$, $Z(\mathrm{As}) = 33$, $Z(\mathrm{Al}) = 13$, $Z(\mathrm{In}) = 49$ and $Z(\mathrm{P}) = 15$, the effective atomic numbers are $Z(\mathrm{Al_{0.15}Ga_{0.85}As}) = 30.65$, $Z(\mathrm{GaAs}) = 32$, $Z(\mathrm{In_{0.49}Ga_{0.51}P}) = 27.59$ and $Z(\mathrm{AlAs}) = 23$. Theoretically, the cross sections of four grating ridges should be visible in each Figure (a) - (c). In fact, Figures (b) and (c) show only three grating ridges with number three and four missing, respectively. Weak contrasts at the positions were the missing grating ridges would be expected indicate, that absence might be limited to short distances along the ridges. The local missing of single grating ridges may occur due to local deviations in the thickness of the GaAs cap layer before the beginning of the in-situ etching.

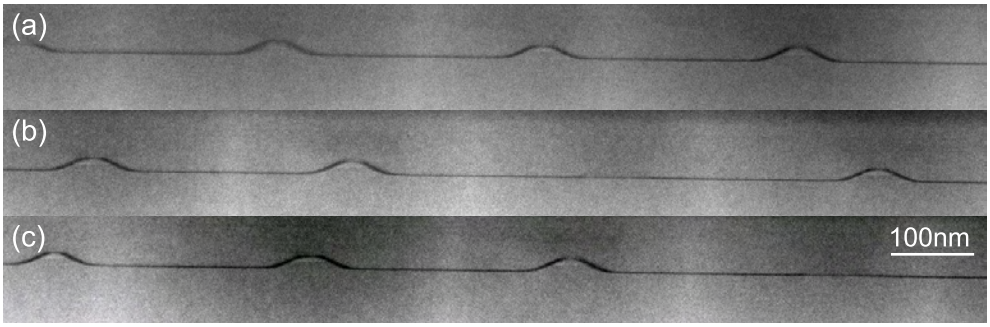

Figure 4.5: STEM investigation of the optimized DFB grating (z-contrast) with theoretically four grating ridges visible. (a) Four grating ridges visible. (b), (c) Only three of four grating ridges visible.

The contrast between $\mathrm{Al_{0.15}Ga_{0.85}As}$, GaAs and $\mathrm{In_{0.51}Ga_{0.49}P}$ is weak. In detail, the GaAs cap occurs slightly brighter than the $\mathrm{Al_{0.15}Ga_{0.85}As}$ and the $\mathrm{In_{0.49}Ga_{0.49}P}$ is slightly darker than $\mathrm{Al_{0.15}Ga_{0.85}As}$, what can be understood by comparing the effective atomic numbers, given above. A thin dark layer which is extended over the grating surface of this wafer, visible in Fig. 4.5, is not typical and was not observed in other wafers. This dark layer can be interpreted as $\mathrm{Al_xGa_{1-x}As}$ with an aluminum content considerably above $x = 0.15$.

Figure 4.6 shows a detailed STEM and EDXS analysis of typical grating ridges from wafer D1560-2, which has been processed in a simplified process without thick plated gold layers. The analysis of this material is of high importance, because DFB lasers from this wafer were used to determine the DFB coupling coefficient, and record high efficiency was obtained with mounted DFB-BA lasers from this wafer.

In Fig. 4.6 (a), an overview STEM micrograph is depicted showing two grating stripes. The grating period, the dimensions of the grating stripes

and hence, the duty cycle, is in good agreement with findings from wafer D1878-4, as can be seen by comparing Fig. 4.6 (a) to Fig. 4.5 (a), (b) and (c).

A Z-contrast image of a single grating stripe is depicted in Fig. 4.6 (b). The $In_{0.49}Ga_{0.51}P$ grating stripe is clearly visible and no residual $In_{0.49}Ga_{0.51}P$ layer is observed next to the grating stripe. On top of the dark $In_{0.49}Ga_{0.51}P$ ridge, the GaAs cap appears as a bright region with comparable intensity as the surrounding $Al_xGa_{1-x}As$.

On top of the GaAs cap, one can see a dark area, whose thickness decreases with increasing distance from the grating stripe. This is the aluminum rich region of the overgrown $Al_xGa_{1-x}As$. A bright region on both sides next to the grating stripe indicates the aluminum poor region of the overgrown $Al_xGa_{1-x}As$. Note that the aluminum rich region is extended only $\sim 10\,nm$ above the GaAs cap. Thus, the inhomogeneous distribution of aluminum in the regrown $Al_xGa_{1-x}As$ is limited to a hight of $\sim 30\,nm$ above the grooves of the etched grating. For the DFB gratings in iteration I, the inhomogeneous aluminum distribution has been extended over $\sim 50\,nm$ as can be estimated from Fig. 3.18.

Figure 4.6 (c) shows a single grating stripe, measured with atomic resolution. No crystal defects are found, demonstrating the technological improvement in buried index grating fabrication in comparison with standard buried DFB gratings as discussed in [Bug11]. The thickness of the $In_{0.51}Ga_{0.49}P$ grating stripe is measured as 10 - 12 nm and the thickness of the GaAs caplayer has been determined as 6 - 9 nm, from counting the atomic layers.

Finally, Fig. 4.6 (d) -(i) show the results from an EDXS scan. In Fig. 4.6 (d), a Z-contrast STEM micrograph of the region, used for the EDXS analysis is depicted. Figures 4.6 (e) -(i) show the aluminum, gallium, arsenic, indium and phosphite specific signals from the EDXS. The aluminum specific signal (Fig. 4.6 (e)) is less significant, because the aluminum content is relatively low even in the waveguide, and close to the noise level. Nevertheless, a minimum in the aluminum content is located at the position of the grating stripe and a local maximum is observed on top of it, which is associated with the inhomogeneous aluminum distribution in the overgrown $Al_xGa_{1-x}As$. The gallium specific signal (Fig. 4.6 (f)) is dominated by a missing of gallium in the $In_{0.49}Ga_{0.51}P$ grating stripe. Comparable to the gallium specific signal but much more pronounced, arsenic (Fig. 4.6 (g)) is missing in the $In_{0.49}Ga_{0.51}P$ grating stripe. In contrast, the concentration of indium (Fig. 4.6 (h)) and phosphite (Fig. 4.6 (i)) is clearly limited to the $In_{0.49}Ga_{0.51}P$ grating stripe and no residual layer from $In_{0.49}Ga_{0.51}P$ is observed next to the grating stripe. This is a clear evidence, that the fabrication of a floating DFB grating was successful and advantages are expected

for the series resistance, compared to the DFB gratings from iteration I of this work which had a residual $In_{0.49}Ga_{0.51}P$ layer and the corresponding additional hetero-interfaces.

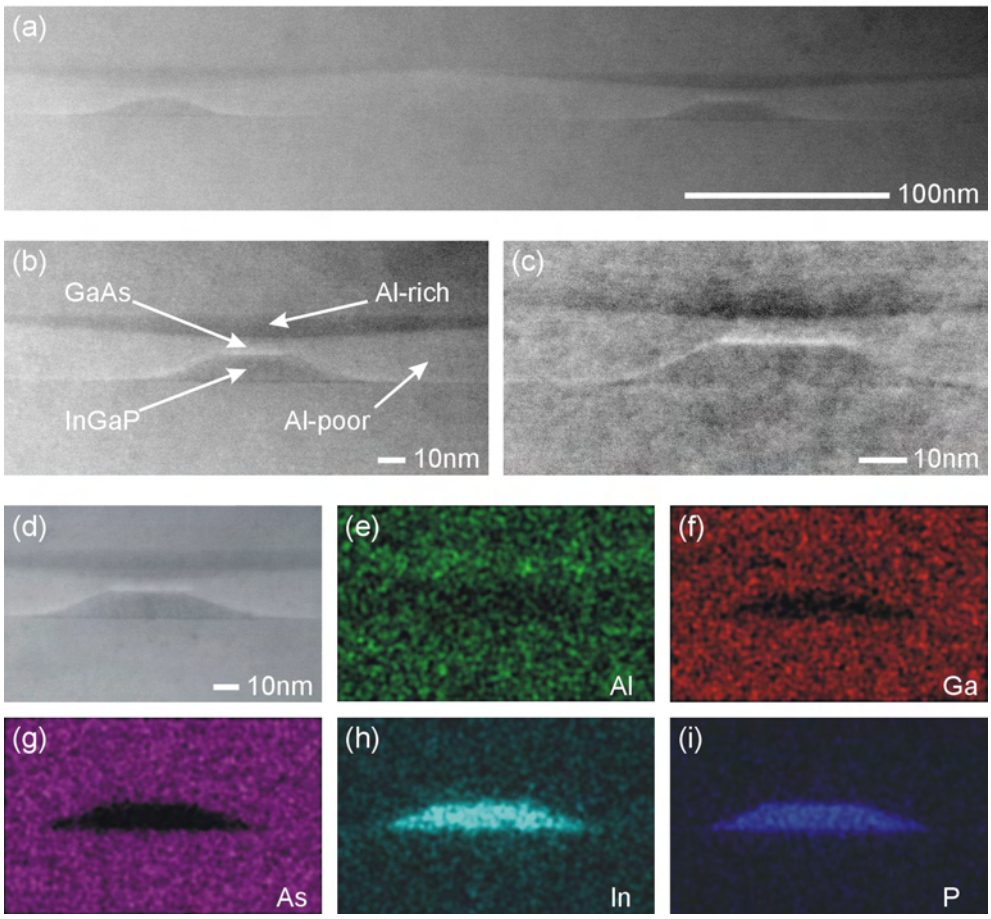

Figure 4.6: STEM images of the optimized DFB grating and EDXS mapping. (a) Overview of the grating region with two grating stripes. (b) Z-contrast image of a single grating stripe with inhomogeneous aluminum distribution, visible. (c) Image of a single grating stripe with atomic resolution. (d) STEM image of a single grating stripe with atomic resolution. (e) Surrounding of a single grating stripe for EDXS analysis. (f) - (i) Spatial distribution of elements Al, Ga, As, In and P from EDXS mapping.

4.2.3 Coupling coefficient of the DFB grating

In iteration I of this work, a DFB coupling coefficient of $\approx 3\,\mathrm{cm}^{-1}$ has been targeted. This was supposed to lead to a sufficient spectral stabilization in a DFB-BA laser with a 3000 μm long cavity and a low reflection front facet coating. Furthermore, the longitudinal optical field intensity of a DFB-BA laser was expected to be homogeneous, because $\kappa \cdot L \approx 1$ (see figure 1.24 for $\kappa = 3.3\,\mathrm{cm}^{-1}$).

As mentioned in section 4.1, one aim of iteration II is to increase the slope efficiency of the DFB-BA lasers by increasing the ratio of the optical power, coupled out of the cavity through the front facet. With fixed facet reflectivities, this is analogous to increasing the resonator loss of the laser cavity and analogous to decreasing the coupling coefficient. The new target value for the coupling coefficient is $\approx 0.5\,\mathrm{cm}^{-1}$. Based on the calculated and experimentally determined dependence of the slope efficiency on the coupling coefficient, $\kappa \approx 0.5\,\mathrm{cm}^{-1}$ is expected to be suitable to obtain a slope efficiency of $> 1.0\,\mathrm{W\,A}^{-1}$ from the DFB-BA lasers as targeted. This choice for the coupling coefficient would lead to $\kappa \cdot L = 0.15$.

In Fig. 1.24, the dependence of the longitudinal optical field profile on the facet phase section at the rear facet is depicted for different values of the coupling coefficient. The longitudinal optical field profiles were calculated with coupled mode theory as explained in section 1.2.4. Figure 1.24 (a) shows the longitudinal optical field profiles with $\kappa = 3.3\,\mathrm{cm}^{-1}$. In Fig. 1.24 (b) and (c), the longitudinal optical field profiles are depicted for $\kappa = 1.0\,\mathrm{cm}^{-1}$ and $\kappa = 0.5\,\mathrm{cm}^{-1}$, respectively. Two major changes are observed. Firstly, the dependence of the intensity at the rear facet (position 0 cm) on the facet phase section is drastically decreased. Secondly, the phase averaged field profiles (red solid lines) are no more constant, but increase from the rear facet to the front facet (position 0.3 cm) like for a asymmetrically facet coated FP-BA laser. Thus, for DFB-BA lasers with $\kappa \cdot L \approx 0.15$ as targeted, non uniform longitudinal intensity profiles of the optical field might lead to longitudinal spatial hole burning, increase the width of the optical spectrum due to multiple longitudinal mode lasing and degrade the power characteristics.

Again, the coupling coefficient is adjusted by gradually shifting the vertical position of the grating in the p-side waveguide relative to the optical field profile in simulations with QIP, following equation 1.60. The critical question is therefore, if it is possible to achieve the targeted value of κ in this way. This depends on the contrast of the effective index of refraction and on the shape of the vertical optical field. In order to avoid additional optical loss of relevant magnitude due to the thin but highly doped grating layers ($2 \cdot 10^{18}\,\mathrm{cm}^{-3}$), the grating should not be placed too close ($< 200\,\mathrm{nm}$)

to the active region. The simulation starts with a grating position, 200 nm above the DQW and 670 nm below the p-side cladding layer. In the following, the DFB grating is stepwise moved away from the DQW up to a distances of 770 nm from the DQWS. In Fig. 4.7 (a) the profiles of the refractive index and the intensity profiles for the fundamental vertical mode are depicted. The inset shows a magnified section of the refractive index, showing the small dips due to the DFB grating. For this simulation it has been assumed, that the grating consists of 10 nm thick $In_{0.49}Ga_{0.51}P$ ridges, each with a 15 nm GaAs cap and a duty cycle of $c_d = 1/4$. The further optimized DFB grating acts only as a very weak perturbation, so that the shifting of the position causes no significant changes in the vertical mode profile.

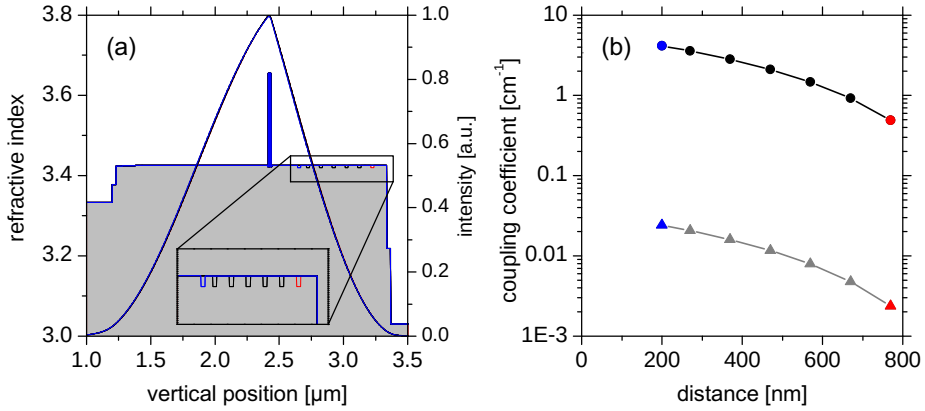

Figure 4.7: Characteristics of the refractive index with various positions of the DFB grating and its influence on the coupling coefficient. (a) Refractive index profile and the simulated near field intensity profiles of the fundamental waveguide mode for (200 (blue), 270, 370, ..., 770 nm (red)) distance between the DFB grating and the active region. (b) Real and imaginary part of the coupling coefficient as a function of the distance between the DFB grating and the active region.

The real and imaginary part of the coupling coefficient was determined for each vertical position of the grating and is depicted in Fig. 4.7 (b). The real part of the coupling coefficient decreases from 4.14 to 0.49 cm^{-1}, while the imaginary part of the coupling coefficient decreases from 0.024 to 0.002 cm^{-1}. Accordingly, the DFB grating must be positioned 770 nm above the DQW and only 100 nm below the p-side cladding layer to achieve $\kappa \approx 0.5\,\mathrm{cm}^{-1}$. A waveguide thickness of 100 nm is also assumed to be the lower limit which is necessary for the planarization of the surface corrugation from the grating ridges during regrowth, before the p-side cladding layer is grown. Otherwise, a hight modulated interface between the waveguide and the high aluminum

content cladding layer might act as an additional index grating. Because of the $Al_{0.85}Ga_{0.15}As$ material which is used for the *p*-cladding layer, the formation of additional aluminum rich and aluminum poor regions may further influence the coupling coefficient and make its value less controllable. Nevertheless, placing the DFB grating at the hetero-interface between the waveguide and *p*-cladding layer has been successfully realized as for example reported in [Ear98], [Cha00], [Kan06], [He09].

Diagrams of the conduction and valence band profiles, the refractive index profile and the vertical optical field intensity in the near field and far field are given in Fig. 4.8, equivalent to Fig. 3.20 in iteration I.

Figure 4.8 (a) shows the profiles of the minimum of the conduction band edge at the Γ- and X-point (blue solid line) and the corresponding first electron energy level (blue dashed line), the heavy hole valence band edge (red solid line) with the corresponding first heavy hole energy level (red dashed line). The vertical position of the DFB grating is indicated. In Fig. 4.8 (b), a section of (a) is reproduced in the grating region. The steps indicate the 10 nm thin $In_{0.49}Ga_{0.51}P$ grating ridge and the 15 nm GaAs cap. Because of identical scaling with Fig. 3.20 (b), the position of the grating is shifted to the right hand side at $\approx 3.22\,\mu$m.

Figure 4.8 (c) shows the profile of the refractive index and the normalized profiles of the four guided vertical waveguide modes (solid lines), as well as the near field mode profiles for the FP epitaxy structure (dashed lines). Significant differences between the mode profiles of the DFB and FP epitaxy structure occur only for the highest-order mode. Note that the first and second higher-order waveguide mode have significant intensity (close the their individual maximum) at the position of the DFB grating. Therefore, lasing on these higher-order modes must be expected at CW currents close to threshold where the gain peak wavelength must be detuned to shorter wavelengths than the Bragg wavelength of the fundamental DFB mode in order to achieve high slope efficiency and high power conversion efficiency in the desired 10 W range. As already mentioned, a better suppression of lasing on higher-order modes would have required to modify the basic epitaxy structure. This has not been targeted in the second iteration of this work in order to ensure comparability with the FP-BA reference lasers and DFB-BA lasers from iteration I.

In Fig. 4.8 (d), the normalized vertical far field profiles, corresponding to the near field profiles from (c), are depicted. As indicated, the fundamental mode is predominately emitting its power in a 45 ° vertical divergence angle.

Two problems concerning the coupling coefficient need to be discussed. Firstly, it will be discussed how much the coupling coefficient might deviate from the targeted value of $|\kappa| \approx 0.5\,\mathrm{cm}^{-1}$ in the experimental realization.

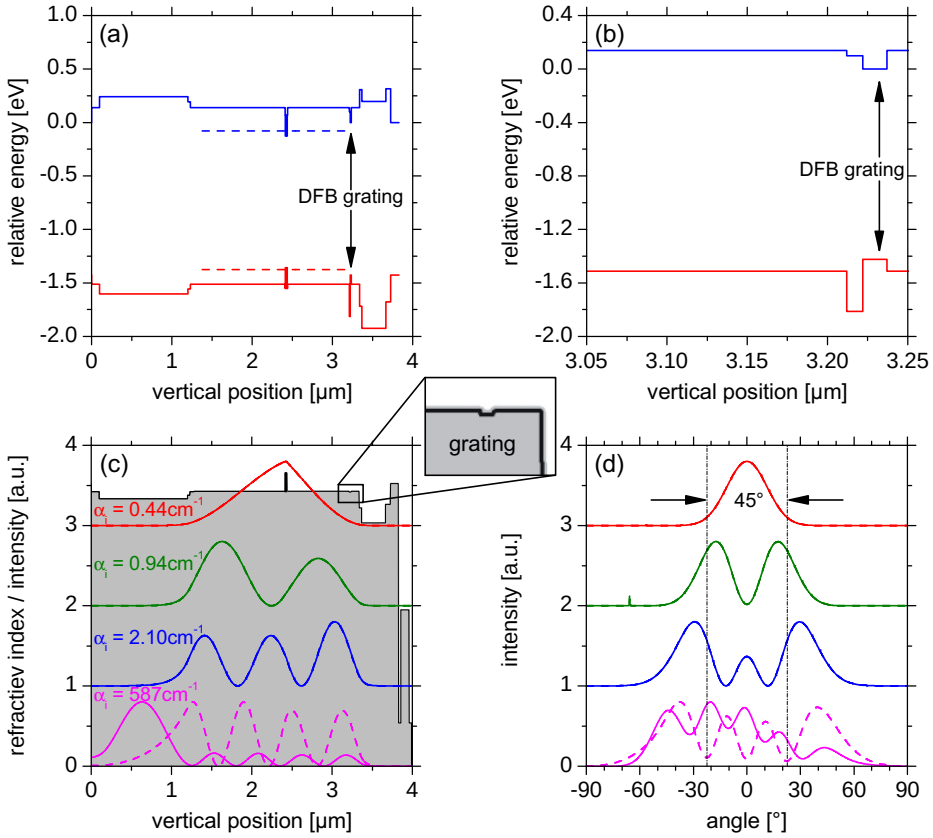

Figure 4.8: Electronic band structure, refractive index profile and vertical mode profiles of the further optimized DFB lasers. (a) Minimum of the conduction band edges at the Γ- and X-point (blue solid line) and the heavy hole valence band edge (red solid line). The corresponding first electron energy level and first heavy hole energy level are depicted as blue and red dashed lines respectively. (b) Magnified section of (a) in the DFB grating region. (c) Refractive index profile and the simulated near field profiles of the waveguide modes with the corresponding internal losses indicated (modes of FP-BA laser: dashed lines). (b) Simulated far field angular distribution of the waveguide modes (modes of FP-BA laser: dashed lines).

Secondly, the coupling coefficients of the higher-order waveguide modes and the corresponding threshold currents will be estimated in analogy to section 3.4.9 in order to assess if these modes can exceed threshold.

The coupling coefficient of the DFB grating in the fundamental vertical mode has been determined with QIP simulations for different thicknesses of the GaAs cap. Therefore, a rectangular DFB grating with an optimized

duty cycle of $c_d = 1/4$ has been considered. The thickness of the GaAs cap is expected to be subject to experimental variations and is therefore assumed to be an important factor for possible deviations of the coupling coefficient. Figure 4.9 (a) shows the simulation results of the real part $\Re|\kappa|$ and imaginary part $\Im|\kappa|$ of the coupling coefficient. Note, that in Fig. 4.9 (a), the imaginary part $\Im|\kappa|$ is multiplied with a factor of 100 for better visibility.

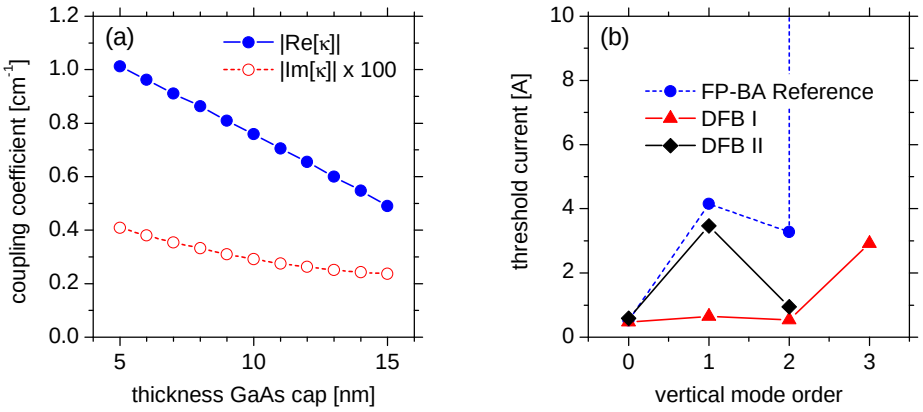

Figure 4.9: (a) Coupling coefficient of the DFB grating for variations of the GaAs cap thickness. (b) Calculated threshold currents for the fundamental and higher-order waveguide modes.

Between GaAs cap thicknesses of 5 and 15 nm, a decrease of $\Re|\kappa|$ from ≈ 1.0 to $\approx 0.5\,\mathrm{cm}^{-1}$ is observed. Even though the coupling coefficient at 5 nm is twice as high as the targeted value of $|\kappa| \approx 0.5\,\mathrm{cm}^{-1}$, this is is expected to be low enough to obtain a slope efficiency of $> 1.0\,\mathrm{W\,A}^{-1}$ as can be derived from Fig. 3.58 (b).

Three further effects must be expected to influence the coupling coefficient. Firstly, the formation of aluminum rich and aluminum poor regions might increase the coupling coefficient. Unfortunately, no values for the aluminum content x in the $Al_xGa_{1-x}As$ of the aluminum rich and aluminum poor regions which also occur in iteration II, visible in the STEM micrographs in Fig. 4.6, were available. Because of the lower corrugation of the DFB grating and the lower thickness of the region with an inhomogeneous aluminum distribution (~ 30 nm instead of ~ 50 nm in iteration I), the effect is presumed to be less important than in iteration I. Thus, the corresponding increase of $|\kappa|$ is expected to be significantly lower than $+1\,\mathrm{cm}^{-1}$. Secondly, the deviation of the real grating shape, which is more trapezoidal shaped, from the rectangular model used in the simulation will lead to a slightly lower coupling

coefficient. Thirdly, deviations from the optimal duty cycle can also decrease the coupling coefficient. Nevertheless, the adjustment of the duty cycle can be done precisely based on experiences with the required duty cycles of the photoresist line pattern and GaAs cap stripes before in-situ etching. Because of the sinusoidal characteristics as a function of the duty cycle, the coupling coefficient is not very sensitive to changes in the duty cycle of 0.1 around the optimal value $c_\mathrm{d} = 0.25$ ($|\kappa(c_\mathrm{d} = 0.25 \pm 0.10)| > 0.81|\kappa(c_\mathrm{d} = 0.25)|$) as can be estimated from Fig. 1.14.

Finally, the coupling coefficients of the fundamental and higher-order waveguide modes were calculated with QIP (15 nm GaAs cap) and the corresponding threshold currents were calculated as explained in section 3.4.9. The resulting threshold currents are depicted in Fig. 4.9 (b) and compared to the threshold currents of the DFB-BA lasers from iteration I and the reference FP-BA lasers. The parameters which have been used for the calculation are summarized in table 4.1, ins the same way as this has been already done for the values for the DFB-BA lasers and reference FP-BA lasers from iteration I, given in table 3.12.

Table 4.1: Parameters, used for the calculation of the threshold current for the vertical waveguide modes in DFB-BA lasers.

mode	R_f [%]	κ [cm^{-1}]	Γ [%]	α_i [cm^{-1}]	α_DFB [cm^{-1}]	I_th [A]
0	0.09	0.5	1.40	0.80	9.60	0.58
1	0.09	1.5	0.25	1.30	6.32	3.47
2	0.09	3.8	0.58	2.46	3.16	0.99
3	0.09	3.0	$8 \cdot 10^{-5}$	587	3.91	–

While the fundamental mode an the second higher-order mode of the DFB-BA lasers from iteration I and II have approximately comparable threshold currents, the threshold current of the first higher-order mode of the DFB-BA lasers from iteration II is increased nearly to the value for the reference devices. Therefore, the second higher-order mode is expected to exceed threshold (if the gain peak wavelength is close to its Bragg wavelength) in addition to the fundamental mode but the first higher-order mode is presumably sufficiently suppressed.

The high threshold current of $I = 3.47\,\mathrm{A}$ for the first higher-order mode can be explained with their low coupling coefficient $\kappa = 1.5\mathrm{cm}^{-1}$ and confinement factor $\Gamma = 0.25\,\%$. In contrast, the threshold current of the first higher-order mode is only $I = 0.99\,\mathrm{A}$ because of the higher $\kappa = 3.8\mathrm{cm}^{-1}$ and confinement factor $\Gamma = 0.58\,\%$ in combination with moderate internal optical loss $\alpha_\mathrm{i} = 2.46\,\mathrm{cm}^{-1}$. Because of the extremely low confinement factor and very high internal optical loss, no threshold current was calculated for the simulated third higher-order mode which couples to the substrate as can be seen in Fig. 4.8 (c).

4.3 Characterization of DFB-BA lasers

4.3.1 Overview of DFB wafers

For the second iteration, four wafers have been fabricated with small changes in the Bragg wavelength $\lambda_\mathrm{DFB}^\mathrm{tar}$ of the DFB grating and different types of photoresist were used for the lithographic structuring of the DFB grating. The epitaxy design, gain peak wavelength at threshold $\lambda_\mathrm{gain}^\mathrm{tar}$, in-situ etching time t_is and processing are identical for all these wafers.

As already done in iteration I, two different values for $\lambda_\mathrm{DFB}^\mathrm{tar}$ were chosen to find an ideal option for the DFB wavelength $\lambda_\mathrm{DFB}(I)$ and gain peak wavelength $\lambda_\mathrm{gain}(I)$ to coincide at a current I, that corresponds to an optical output power of $\approx 10\,\mathrm{W}$. For the specification of the suitable Bragg wavelengths $\lambda_\mathrm{DFB}^\mathrm{tar}$, it has been assumed that the power-voltage-current characteristics of the further optimized DFB-BA lasers will be improved compared to the power-voltage-current characteristics of DFB-BA lasers from iteration I and may therefore be comparable with the characteristics from reference FP-BA laser from wafer D1423-1. Typical power-voltage-current characteristics for a FP-BA reference device from wafer D1423-1 were used for the estimation of optimal $\lambda_\mathrm{DFB}^\mathrm{tar}$ and are depicted in Fig. 4.10 (a).

Based on a thermal resistance of $R_\mathrm{th} = 4\,\mathrm{K\,W}^{-1}$, the heat from dissipated power $P_\mathrm{d} = U(I)\cdot I - P_\mathrm{opt}$, shown in Fig. 4.10 (a) and temperature coefficients of $\mathrm{d}\lambda_\mathrm{gain}/\mathrm{d}T = 0.34\,\mathrm{nm\,K}^{-1}$ and $\mathrm{d}\lambda_\mathrm{DFB}/\mathrm{d}T = 0.077\,\mathrm{nm\,K}^{-1}$, the temperature shift of the gain peak and Bragg wavelengths was calculated. With $\lambda_\mathrm{gain}^\mathrm{tar} = 968\,\mathrm{nm}$ (at $I \approx 0\,\mathrm{A}$), target wavelength for the Bragg wavelength of the DFB grating (also at $I \approx 0\,\mathrm{A}$) of $\lambda_\mathrm{DFB}^\mathrm{tar1} = 971.74\,\mathrm{nm}$ and $\lambda_\mathrm{DFB}^\mathrm{tar2} = 973.55\,\mathrm{nm}$ were defined. This is shown in Fig. 4.10 (b). Note that $\lambda_\mathrm{DFB}^\mathrm{tar2}$ was chosen for the Bragg wavelength of the DFB grating and the gain peak wavelength to coincide at $I \approx 10.6\,\mathrm{A}$, $P_\mathrm{opt} \approx 10\,\mathrm{W}$, while $\lambda_\mathrm{DFB}^\mathrm{tar1}$ is more conservative – suitable for $I \approx 8.4\,\mathrm{A}$ and $P_\mathrm{opt} \approx 8\,\mathrm{W}$. The experimentally realized periods

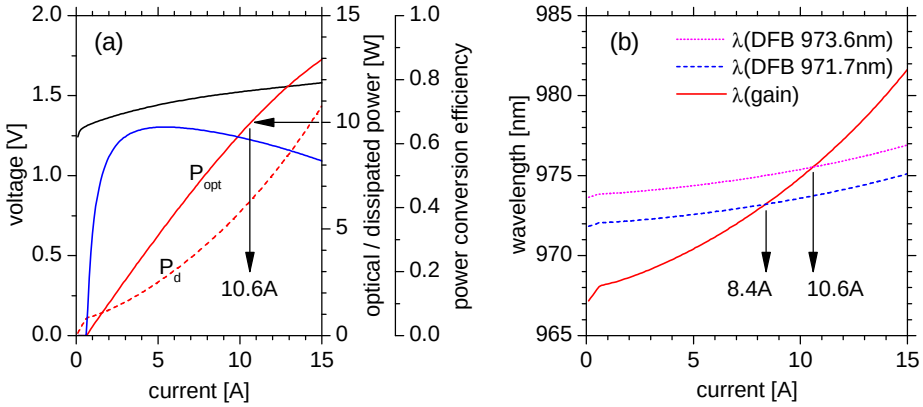

Figure 4.10: Power-voltage-current characteristics and calculated wavelengths of the gain peak an Bragg wavelength of the DFB grating. (a) Typical power-voltage-current characteristics of a FP-BA reference lasers from wafer D1423-1 and calculated dissipated power (heat). (b) Calculated wavelengths of the gain peak with $\lambda_{\text{gain}}^{\text{tar}} = 968\,\text{nm}$ and Bragg wavelengths of the DFB grating with $\lambda_{\text{DFB}}^{\text{tar1}} = 971.7\,\text{nm}$ / $\lambda_{\text{DFB}}^{\text{tar2}} = 973.6\,\text{nm}$.

of the DFB gratings are $\Lambda_{\text{tar1}} = 283.389\,\text{nm}$ and $\Lambda_{\text{tar2}} = 283.917\,\text{nm}$.

To achieve a minimal oxygen content in the overgrown grating region [Sch12], the in-situ etching time t_{is} was set to 150 s. This enables etching completely through the $In_{0.49}Ga_{0.51}P$ layer between the grating ridges. Thus, when starting the second epitaxy, $Al_{0.15}Ga_{0.85}As$ is grown on $Al_{0.15}Ga_{0.85}As$ at approximately 75 % of the surface without developing a hetero-interface. An overview of the different DFB wafers from iteration II is given in Tab. 4.2.

4.3.2 Facet coating for DFB-BA lasers

In iteration II of this work, DFB-BA lasers from completely processed wafers D1567-1, D1567-3, D1567-4 and D1567-5 were facet passivated, facet coated and mounted (mounting process described in section A.4).

In addition an identical test wafer D1560-2 (negative photoresist) was grown earlier and processed with a process layout for narrow stripe DFB-RW lasers which also contained a small amount of DFB-BA lasers. This wafer is of particular importance because of two reasons. Firstly, DFB-RW lasers from this wafer have been used for the experimental determination of the DFB coupling coefficient, presented in section 4.3.8. Secondly, a DFB-BA laser from this wafer achieved the highest reported power conversion efficiency

Table 4.2: Overview of wafers from DFB iteration II.

process	wafer	$\lambda_{\mathrm{tar}}^{\mathrm{DFB}}$ [nm]	$\lambda_{\mathrm{tar}}^{\mathrm{gain}}$ [nm]	in-situ etching [s]	photo resist
test	D1560-2	≈ 970	968.0	150	negative
5213	D1567-1	971.74	968.0	150	positive
	D1567-3	973.55	968.0	150	negative
	D1567-4	971.74	968.0	150	negative
	D1567-5	973.55	968.0	150	positive

and optical output power which has been to date reported for a DFB-BA laser [Cru11c], [Sch11], [Sch12]. In contrast to the completely processed wafers, the lasers on the test wafer have a stronger index guiding with $\Delta n_{\mathrm{eff}} \approx 3 \cdot 10^{-3}$ instead of $\approx 1 \cdot 10^{-3}$, optimized for DFB-RW lasers. The n-side and p-side contact metallization is thinner and has no thick galvanically deposited gold layer. Thus, soldering of lasers from the test wafer will have a lower yield and the devices are supposed do be more sensitive to strain from the soldering process. From the test wafer, four DFB-BA lasers with a contact stripe width of 100 μm and a cavity length of 3000 μm were mounted on the same type of heatsinks as the DFB-BA lasers from the completely processed wafers.

A difference between the test wafer and the completely processed wafers also occurs in the facet coating. Reflectivity spectra of the front and rear facet are depicted in Fig. 4.11 (a) and (b), respectively. The reflectivity was measured on GaAs-dummies. Afterwards, the reflectivity on the laser facet has been calculated with respect to the effective index of the waveguide mode. The test wafer has a facet coating (5229) which is optimized for a very low reflectivity of the front facet ($R_{\mathrm{f}} = 0.020\,\%$ at 976 nm), with a small penalty in high power reliability expected from the used material system. In contrast, the facet coating of the completely processed wafers (5315) is optimized for high power reliability with a small penalty in the front facet reflectivity ($R_{\mathrm{f}} = 0.065\,\%$ at 976 nm). Both facet coatings fulfill the targeted reflectivity $R_{\mathrm{f}} < 0.1\,\%$ at 976 nm.

From the reflectivity spectra of the front facet coatings, a better suppression of FP-like modes is expected for the lasers from the test wafer. In contrast to the targeted reflectivity spectra, the front facet reflectivity

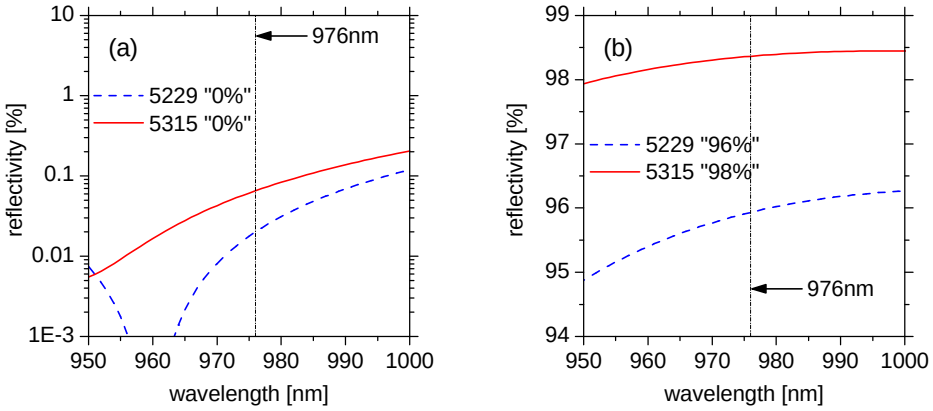

Figure 4.11: Reflectivity spectra of DFB-BA laser facets in iteration II. (a) Anti reflection coated front facet. (b) High reflection coated rear facet.

increases in the range between 976 and 985 nm, where lasing on FP-like modes has been observed for lasers from wafer D1366-4 in iteration I of this work, up to values of $R_\mathrm{f} = 0.048\,\%$ (5229) and $R_\mathrm{f} = 0.109\,\%$ (5315). For a strong suppression of FP-like modes, reflectivity spectra were preferred, having their minimum at the targeted DFB wavelength of 976 nm or even at longer wavelength between 976 and 985 nm instead of ≤ 960 nm as achieved. For $\lambda \geq 984$ nm, the reflectivity of the front facet for coating 5315 exceeds the targeted limit of $R_\mathrm{f} = 0.1\,\%$.

A very high rear facet reflectivity $R_\mathrm{r} = 98\,\%$ was achieved with coating 5315, while the reflectivity for coating 5229 is lower ($R_\mathrm{r} = 96\,\%$ at 976 nm) because of a lower number of used $\lambda/4$ layers.

4.3.3 Material parameters of DFB-BA wafers

In iteration II of this work, parameters such as the internal optical loss α_i, internal quantum efficiency η_i, transparency current density j_tr and modal gain coefficient Γg_0 have not been determined again from the cavity length dependence of the slope efficiency and threshold current using un-coated lasers with a de-tuned Bragg wavelength as shown in section 3.4.1.

The reduction of the thickness of the $In_{0.49}Ga_{0.51}P$ grating layer from 20 to 10 nm and the shift of the grating position from 230 to 100 nm below the *p*-cladding layer is expected to cause no significant changes in the parameters mentioned above. Shifting the highly doped grating layers ($2 \cdot 10^{18}\,\mathrm{cm}^{-3}$) by 130 nm away from the active region (to lower confinement region), etching through the $In_{0.49}Ga_{0.51}P$ layer (this reduces the fraction of the area which is

covered with highly doped grating material) and reducing the highly doped fraction of the p-waveguide ($1 \cdot 10^{18}\,\mathrm{cm}^{-3}$) from 230 to 100 nm may result in a reduction of the internal optical loss.

Simulations with QIP show that the internal optical loss of the fundamental waveguide mode reduces from $\alpha_\mathrm{i} = 0.59\,\mathrm{cm}^{-1}$ for the design from iteration I to $\alpha_\mathrm{i} = 0.44\,\mathrm{cm}^{-1}$ for the design from iteration II. Note that both values are lower than the experimentally determined $\alpha_\mathrm{i} \approx 0.85\,\mathrm{cm}^{-1}$ from iteration I. The obtained difference of $\Delta\alpha_\mathrm{i} = -0.15\,\mathrm{cm}^{-1}$ is roughly in the range of the resolution limit for the experimental determination of α_i. Thus, the internal loss, internal quantum efficiency, transparency current density and modal gain coefficient are supposed to be approximately the same as in iteration I, given in section 3.4.1.

4.3.4 Power-voltage-current characteristics of DFB-BA lasers

In the following section, power-voltage-current characteristics of DFB-BA lasers from iteration II will be presented and discussed. In contrast to iteration I, section 3.4.4, some devices were also measured at 15 °C that can lead to substantial enhancement in the power characteristics above 10 A. A reduction of the submount temperature was used to achieve an ideal tradeoff between the gain-peak and Bragg wavelength of the fundamental mode and the spectral dependence of the front facet reflectivity.

Two different periods of $\Lambda_\mathrm{tar1} = 283.389\,\mathrm{nm}$ and $\Lambda_\mathrm{tar2} = 283.917\,\mathrm{nm}$ were used for the DFB gratings, as discussed in section 4.3.1. This leads to different wavelengths of the both types of DFB lasers. For lasers with $\Lambda_\mathrm{tar1} = 283.389\,\mathrm{nm}$ / $\Lambda_\mathrm{tar2} = 283.917\,\mathrm{nm}$, an optical output power of 8 W is estimated to be achieved with wavelengths of 973.2 nm / 975.0 nm and 10 W at 973.7 nm / 975.6 nm.

In Fig. 4.12, the power-voltage-current characteristics of a sample device DFB-BA laser D1560-2 040925 (test wafer) at 25 and 15 °C heatsink temperature are depicted. The yield of these lasers from soldering on the CuW submounts was low because of the missing thick gold plating. These devices have a broader contact stripe width of 100 μm, compared to DFB-BA lasers from the completely processed wafers (90 μm). As a result of the larger pumped area, the current density at a certain injection current is slightly lower and the series resistance is slightly reduced as well. The threshold current and slope efficiency have been determined from a linear fit of the power-current characteristics to 2 A above threshold, identical to section 3.4.4.

The characteristics have been measured at 15 °C additionally to 25 °C

because of the smaller spectral detuning between the gain peak wavelength and the Bragg wavelength of the DFB grating (see table 4.2). The smaller spectral detuning ($\sim 2\,\mathrm{nm}$) has been chosen to make DFB-RW lasers from this wafer suitable to measure sub-threshold ASE spectra of the stopband for the experimental determination of the coupling coefficient. Nevertheless, by reducing the heatsink temperature from 25 °C to 15 °C, the spectral detuning can be increased to $\sim 4.6\,\mathrm{nm}$, making the DFB-BA lasers even more suitable to operate in the 10 W-range.

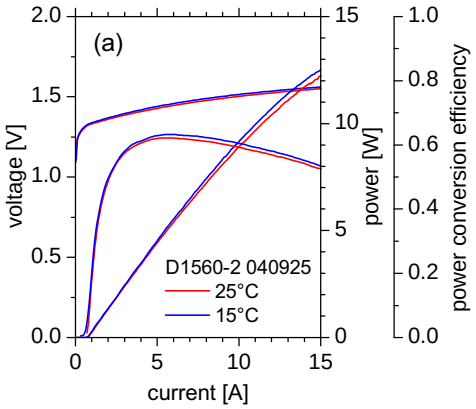

Figure 4.12: Power-voltage-current characteristics of laser 040925 from test wafer D1560-2 at 25 and 15 °C, process 5149, $t_{is} = 150\,\mathrm{s}$.

The laser has a threshold current of 765 mA at 25 °C and 724 mA at 15 °C, respectively. The slope efficiency is $1.073\,\mathrm{WA}^{-1}$ at 25 °C and $1.066\,\mathrm{WA}^{-1}$ at 15 °C. Thus, the slope efficiency is considerably enhanced, compared to DFB-BA lasers from iteration I, as can be extracted from table 3.7. The slight reduction of the slope efficiency at 15 °C in the region 2 A above threshold can be presumably explained with onset of lasing on a higher-order waveguide mode as will be seen later in section 4.3.6. A slope efficiency above $1.05\,\mathrm{WA}^{-1}$ is typical for efficient high power FP-BA laser but this was the first time to achieve this with a DFB-BA laser of the > 10 W-class. The highest published slope efficiencies are (in chronologically order) $0.9\,\mathrm{W\,A}^{-1}$ for 100 μm stripe 1000 μm long 975 nm DFB-BA lasers [Kan06], $\approx 1.1\,\mathrm{W\,A}^{-1}$ for 100 μm stripe 2000 μm long 808 nm DFB-BA lasers [He09] and $1.0\,\mathrm{W\,A}^{-1}$ for 90 μm stripe 3000 μm long 976 nm DFB-BA lasers [Sch10a].

Compared to the power-voltage-current characteristics of the DFB-BA lasers from iteration I (Fig. 3.26), the voltage characteristic is improved, due to a successful reduction in series resistance. Such a reduction has been

targeted with the floating grating design which is used for the DFB-BA lasers in iteration II as discussed above. This is an important achievement and the results will be discussed in section 4.3.5 in more detail. There it is also shown, that the reduction in series resistance is not only a consequence of the larger pumped area (100 instead of 90 μm).

A record high power conversion efficiency is achieved because of significant improvement in slope efficiency and series resistance. A peak power conversion efficiency of 0.633 (0.622) is achieved at 15 °C (25 °C). The power conversion efficiency drops to 0.627 (0.612) at 7 W, 0.592 (0.576) at 10 W and 0.552 (0.531) at 12 W for 15 °C (25 °C), respectively. This means, that for the first time, a DFB laser achieves a power conversion efficiency above 60 %. In detail, the power conversion efficiency is $\geq$ 60 % between 2.99 and 9.50 W (3.15 and 8.32 W) for 15 °C (25 °C), respectively. Combined with a good spectral stabilization (see section 4.3.6), such DFB-BA devices would be advantageous for various possible applications. In table 4.3, the results for the threshold current, slope efficiency and power conversion efficiency are denoted.

After the initial design test, the fabrication of DFB-BA lasers has been repeated as volume manufacture. Figure 4.13 shows the 25 °C power-voltage-current characteristics of DFB-BA lasers from completely processed wafers D1567-1, D1567-3, D1567-4 and D1567-5. These devices have the standard stripe width of 90 μm as for example needed to couple to 100 μm-core optical fibers.

The results for the threshold current, slope efficiency and power conversion efficiency of these lasers are given in table 4.3. Overall, an improvement of the electro-optical properties of the 90 μm stripe, 3000 μm long DFB-BA lasers is observed in comparison with the DFB-BA lasers from iteration I (Fig. 3.26). The diode voltage is reduced due to a decreased series resistance. An elimination of any excess series resistance of DFB-BA lasers, in comparison to FP-BA reference lasers, was a major target in iteration II. Details of the voltage characteristics are discussed later in section 4.3.5. The second major target of was to increase the slope efficiency of DFB-BA lasers, compared to the results from iteration I. It has been predicted, that the slope efficiency can be increased by use of a lower coupling coefficient. The results for the slope efficiency, noted in table 4.3 show, that this target is also achieved. The average slope efficiency at 25 °C is 1.02 W A^{-1}.

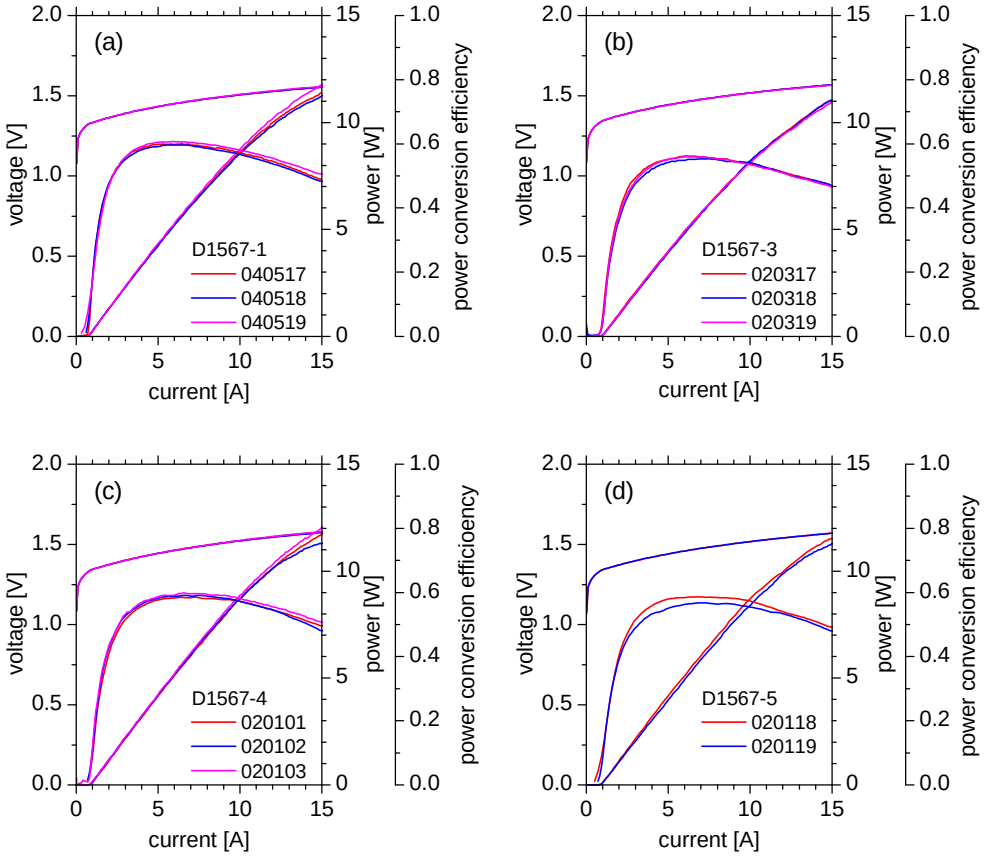

Figure 4.13: Power-voltage-current characteristics of lasers from four different wafers in iteration II at 25 °C, process 5213, t_{is} = 150 s. The characteristics of lasers from a specific wafer are differentiated by different colored lines. (a) Wafer D1567-1. (b) Wafer D1567-3. (c) Wafer D1567-4. (d) Wafer D1567-5.

4.3.5 Comparison of the power-voltage-current characteristics with FP-BA reference lasers and DFB-BA lasers from iteration I

In this section, power-voltage-current characteristics of DFB-BA lasers are compared to characteristics of FP-BA reference lasers and DFB-BA lasers from iteration I, in order to clarify the remaining differences after the optimizations in iteration II. FP-BA lasers from iteration I are also adequate reference devices for DFB-BA lasers from iteration II because the epitaxy design has been unchanged besides the position and design of the thin DFB grating. The first part of the section concerns the comparison of the power-

Table 4.3: Overview of the threshold gain, slope efficiency and power conversion efficiency from DFB lasers from DFB iteration II.

wafer	laser	I_{th} [mA]	$S_{2\,\mathrm{A}}$ [WA^{-1}]	$\eta_{\mathrm{PCE}}^{\mathrm{max}}$	$\eta_{\mathrm{PCE}}^{7\,\mathrm{W}}$	$\eta_{\mathrm{PCE}}^{10\,\mathrm{W}}$	$\eta_{\mathrm{PCE}}^{12\,\mathrm{W}}$
D1560-2	040925	765	1.073	0.622	0.612	0.576	0.531
	(15 °C)	724	1.066	0.633	0.627	0.592	0.552
D1567-1	040517	756	1.038	0.600	0.591	0.546	
	040518	736	1.023	0.597	0.586	0.535	
	040519	759	1.044	0.608	0.601	0.562	
D1567-3	020317	936	1.009	0.562	0.552	0.500	
	020318	976	0.986	0.554	0.545	0.496	
	020319	960	0.996	0.559	0.552	0.492	
D1567-4	020101	896	1.030	0.586	0.581	0.549	
	020102	865	1.040	0.591	0.589	0.549	
	020103	843	1.029	0.599	0.595	0.562	
D1567-5	020118	902	1.032	0.587	0.584	0.538	
	020119	890	0.982	0.567	0.565	0.531	

voltage-current characteristics of DFB-BA lasers from iteration II to FP-BA reference lasers. In the second part of the section, power-voltage-current characteristics of DFB-BA lasers from iteration II are compared to DFB-BA lasers from iteration I.

Firstly, the power-voltage-current characteristics of the 100 μm stripe DFB-BA laser D1560-2 040925 from the test wafer are compared to FP-BA reference lasers (90 μm contact stripe width). Of course, this is not a comparison between devices with identical contact stripe width. Thus, the larger electrically pumped area will for example lead to a reduction of the series resistance and an increase of the threshold current. Nevertheless, the electro-optical properties of this laser are compared to the FP-BA reference devices because it is the most powerful and efficient DFB-BA lasers which has been realized during iteration II of this work. Note that the width of the optical near field of nominal 90 μm stripe DFB-BA (FP-BA) lasers has been measured to be as broad as 98 μm (102 μm) for some devices as can be seen from tables 3.10, 3.11 and 3.3, respectively.

In Fig. 4.14 (a), the power-voltage-current characteristics of the DFB-BA laser, mentioned above, are compared to characteristics of 90 μm stripe FP-BA reference lasers F1850-4 071006 and D1423-1 040203 at 25 °C heatsink temperature. By comparing the power-voltage-current characteristics, the differences in the overall pumped area must be considered. The threshold current of the DFB-BA laser is 150 mA (141 mA) higher, compared to F1850-4 071006 (D1423-1 040203). The threshold current densities of lasers F1850-4 071006, D1423-1 040203 and D1560-2 040925 are 222 A cm^{-2}, 243 A cm^{-2} and 255 A cm^{-2}, respectively. The slope efficiency is reduced by only 0.017 W A^{-1} (0.019 W A^{-1}).

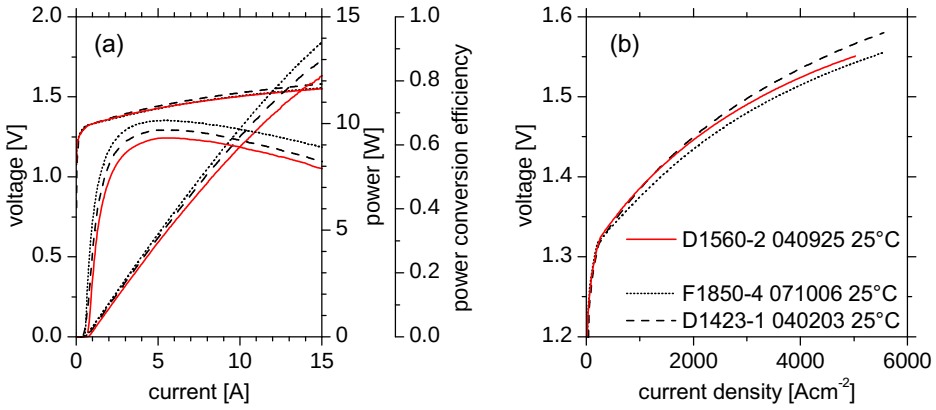

Figure 4.14: Comparison of the 25 °C power-voltage-current characteristics of DFB-BA D1560-2 040925 with sample characteristics of FP-BA reference lasers F1850-4 071006 and D1423-1 051303.

Scaling the voltage as a function of the current density allows to compare the voltage characteristics of the lasers with different stripe width. This is shown in Fig. 4.14 (b). Nearly identical voltage as a function of the current density with the FP-BA reference devices is observed for the DFB-BA laser for the first time. Thus, the additional series resistance lasers which has been found for DFB-BA lasers in iteration I of this work has been successfully eliminated with the floating grating design as targeted, which is a very important result. This was the first published buried overgrown DFB-BA laser with a voltage characteristic, identical to a BA laser without the grating layer, grown in a single epitaxy [Cru11b], [Sch11], [Cru11c], [Sch12]. The resulting reductions in power conversion efficiency for the DFB-BA laser are 0.047 (0.028) at the peak and 0.059 (0.033) at at 10 W.

Secondly, the voltage-current characteristics from the DFB-BA with 90 μm contact stripe width are compared to the sample voltage-current character-

istics from FP-BA reference lasers F1850-4 071006 and D1423-1 040203 at 25 °C heatsink temperature. The 14 different DFB-BA devices which have been used are specified in table 4.3. This comparison is shown in Fig. 4.15 (a) and (b). Even though small wafer-specific differences can be observed between the voltage-current characteristics of DFB-BA lasers from the four different wafers, the deviations are within the deviations between the voltage-current characteristics of the two reference FP-BA lasers. The small differences in the voltage-current characteristics mainly arise from different threshold currents as can be seen from Fig. 4.15 (b) and with the help of table 4.3. Thus, the observation of quasi identical voltage drop for the DFB-BA lasers and reference FP-BA lasers which was firstly observed for the laser from the test wafer (D1560-2 040925, shown in Fig. 4.14 (b)) is true for all DFB-BA lasers in the second iteration.

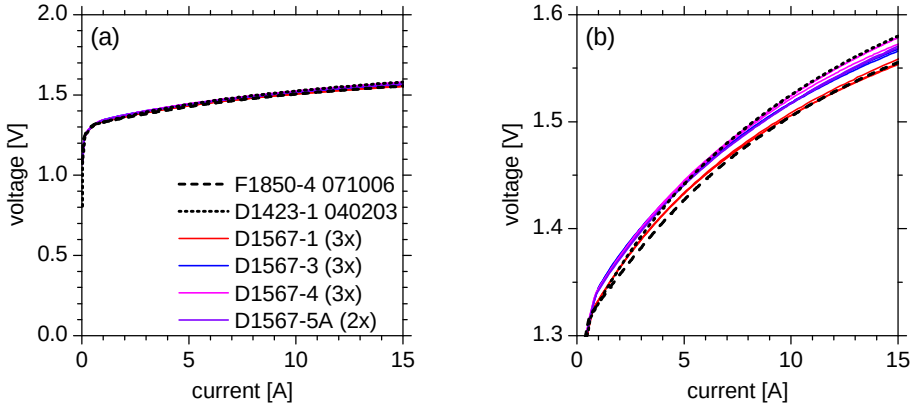

Figure 4.15: Comparison of the 25 °C voltage-current characteristics of DFB-BA lasers from iteration II with sample characteristics of FP-BA reference lasers F1850-4 071006 and D1423-1 051303 (all devices have 90 μm contact stripe width).

Figure 4.16 shows the power-voltage-current characteristics of standard 90 μm stripe DFB-BA laser from Fig. 4.13, also compared to sample characteristics of FP-BA reference lasers F1850-4 071006 and D1423-1 040203 from Fig. 3.5. In Fig. 4.16 (a), the characteristics of DFB-BA lasers from wafer D1567-1 are compared to reference FP-BA lasers. In average, the threshold current of the DFB-BA lasers is about 125 mA higher for the DFB-BA lasers. The slope efficiency is reduced by $\approx 0.06\,\mathrm{W\,A^{-1}}$. An average reduction between 0.06 (at the peak) and 0.07 (at 10 W) is found for the power conversion efficiency. The roll-over of the power characteristics is higher for the DFB-BA lasers than for the FP-BA lasers, as already discussed in section 3.4.5.

This fact can be attributed to a strong decrease of the available gain at the Bragg wavelength, when the gain peak is shifted onto the long-wavelength side of the Bragg wavelength of the DFB grating. The stronger roll-over can be presumably compensated (at least in part) by using an even stronger spectral detuning which is optimized for a coincidence of the gain peak and Bragg wavelength at $> 12\,\mathrm{A}$.

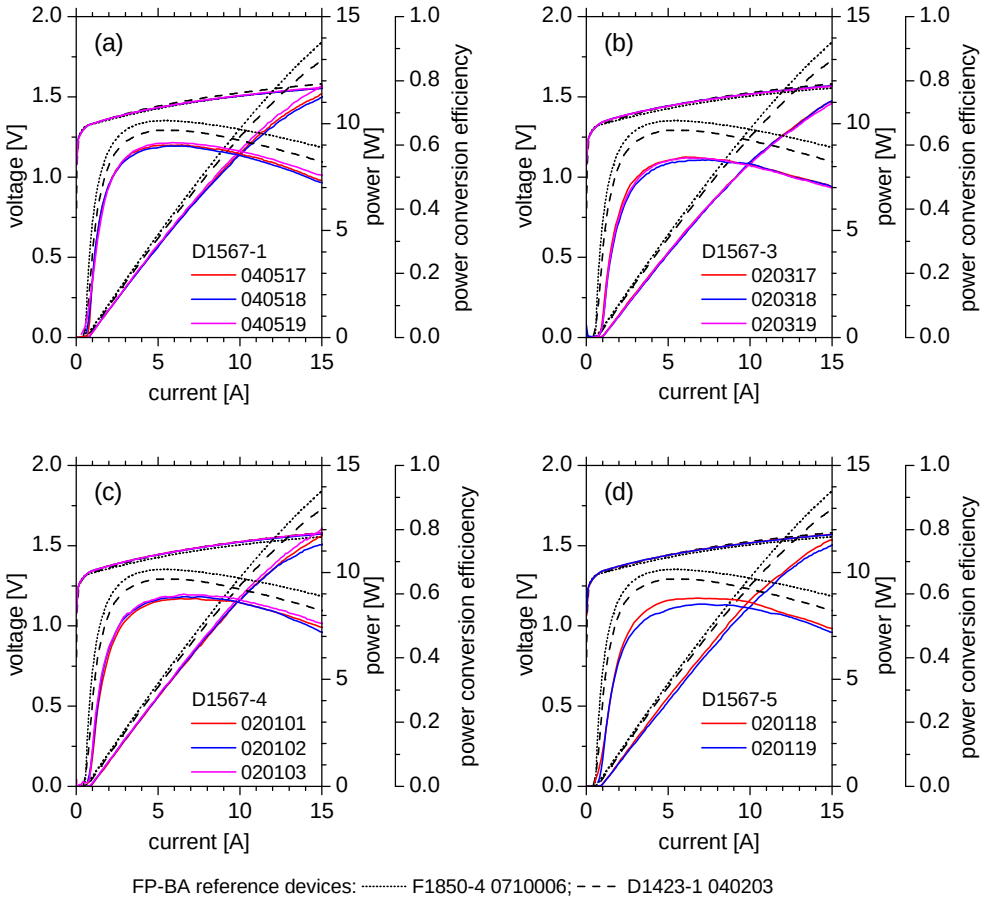

Figure 4.16: Comparison of the 25 °C power-voltage-current characteristics of DFB-BA lasers from Fig. 4.13 with sample characteristics of FP-BA reference lasers F1850-4 071006 and D1423-1 051303. (a) DFB-BA lasers from wafer D1567-1. (b) DFB-BA lasers from wafer D1567-3. (c) DFB-BA lasers from wafer D1567-4. (d) DFB-BA lasers from wafer D1567-5.

Fig. 4.16 (b) compares the power-voltage-current characteristics of DFB-BA lasers from wafer D1567-3 to the reference FP-BA lasers. In contrast to DFB-BA lasers from wafer D1567-1, the differences in threshold current,

slope efficiency and power conversion efficiency between the DFB-BA and FP-BA reference lasers are higher. The average threshold current is about 350 mA higher for the DFB-BA lasers. The slope efficiency is reduced by $\approx 0.09\,\mathrm{WA}^{-1}$. The simultaneous increase of the threshold current and decrease of the slope efficiency compared to lasers from wafer D1567-1 cannot be explained with changes in the coupling coefficient but may be caused by a higher internal optical loss. An average reduction between 0.10 (at the peak) and 0.13 (at 10 W) is found for the power conversion efficiency. Compared to the lasers from wafer D1567-1, no changes in the power-voltage-current characteristics are observed which can be clearly explained with the larger spectral detuning (5.6 nm instead of 3.7 nm, see table 4.3). In iteration I of this work, an increase of the slope efficiency and threshold current, as well as a reduction of the roll-over was observed for DFB-BA lasers with larger spectral detuning as can be seen from Fig. 3.26 and table 3.7, mostly resulting in a higher power conversion efficiency.

A comparsion between the power-voltage-current characteristics characteristics of DFB-BA lasers from wafer D1567-4 to the reference FP-BA lasers, is presented in Fig. 4.16 (c). The average threshold current of the DFB-BA lasers is about 240 mA higher. A reduction in slope efficiency of $\approx 0.06\,\mathrm{W\,A}^{-1}$ is found. The average power conversion efficiency is reduced by 0.08 (at peak) and 0.07 (at 10 W). Again, the roll-over of the DFB-BA lasers above 10 A is more distinct, but differs between the individual devices.

Finally, the power-voltage-current characteristics of DFB-BA lasers from wafer D1567-5 are compared to the reference FP-BA lasers in Fig. 4.16 (d). The DFB-BA lasers have an average excess threshold current of about 270 mA. The average slope efficiency is reduced by $\approx 0.08\,\mathrm{W\,A}^{-1}$ and a reduction of the average power conversion efficiency of 0.08 (at peak) and 0.09 (at 10 W) is observed.

To summarize, degradations in the electro-optical properties of the DFB-BA lasers relative to the FP-BA refernce devices were reduced from iteration I to iteration II for the 90 μm stripe devices. The slope efficiency (linear range 2 A above threshold) is now reduced by $0.06 - 0.09\,\mathrm{W\,A}^{-1}$ instead of $0.11 - 0.14\,\mathrm{W\,A}^{-1}$ in iteration I. Unfortunately, the slope efficiency ($1.02\,\mathrm{W\,A}^{-1}$ in average at 25 °C heatsink temperature) is still lower than expected from the numerical calculations, shown in Fig. 3.58 together with measurement results which indicates that the slope efficiency might increase from ≈ 0.96 (iteration I) to $\approx 1.05\,\mathrm{W\,A}^{-1}$ because of the targeted reduction of the DFB coupling coefficient.

The elimination of any excess series resistance compared to reference FP-BA devices which do not contain the grating layers and were grown in a single stage epitaxy is a break through in the field of buried overgrown DFB

gratings. Overall, DFB-BA lasers from iteration II show the smallest reported differences in power conversion efficiency (typically $< 10\,\%$) between DFB-BA and reference FP-BA lasers. No significant impact of the spectral detuning onto the threshold current, slope efficiency and roll-over is observed like in section 3.4.4.

The second part of the section concerns the comparison of the power-voltage-current characteristics of DFB-BA lasers from iteration II to sample characteristics of especially efficient DFB-BA lasers ($90\,\mu$m stripe) D1425-2 040102 and D1425-5 020104 from iteration I. These two DFB-BA lasers have been chosen as sample devices for the comparison, representing the two most powerful and efficient DFB-BA lasers from iteration I.

In Fig. 4.17, the 25 °C power-voltage-current characteristics of DFB-BA laser D1560-2 040925 ($100\,\mu$m stripe, from test wafer) are compared to sample characteristics of especially efficient DFB-BA lasers ($90\,\mu$m stripe) from iteration I as mentioned above. The characteristics of DFB-BA laser D1560-2 040925 are considerably improved due to an increased slope efficiency and a reduction in series resistance. Compared to laser D1425-2 040102 (D1425-5 020104), the threshold current is about 6 (84 mA) higher. The slope efficiency is enhanced by 0.08 ($0.13\,\mathrm{W\,A^{-1}}$). The power conversion efficiency increases by 0.03 (0.05) (at peak) and 0.05 (0.08) (at 10 W). The rollover of the optical power above 10 A is considerably reduced for D1560-2 040925, which is in part, attributed to the larger pumped area.

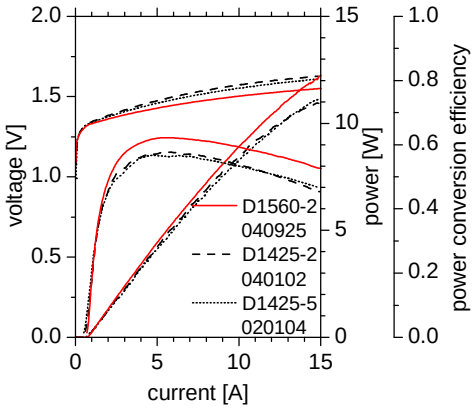

Figure 4.17: Comparison of the 25 °C P-U-I characteristics of DFB-BA laser D1560-2 040925 with sample P-U-I characteristics of DFB-BA lasers D1425-2 040102 and D1425-5 020104 from iteration I.

Figure. 4.18 shows the 25 °C power-voltage-current characteristics of DFB-BA lasers from Fig. 4.13, compared to sample characteristics of DFB-BA

lasers D1425-2 040102 and D1425-5 020104 from iteration I (90 μm stripe each). In a general overview one finds, that the power-voltage-current characteristics are improved for the further optimized DFB-BA lasers from iteration II, in terms of the optical output power, voltage and power conversion efficiency. Only DFB-BA lasers from wafer D1567-3 show characteristics, which have only a lower voltage in comparison to DFB-BA lasers D1425-2 040102 and D1425-5 020104 from iteration I. Note that the two DFB-BA lasers, chosen for this comparison, are the most efficient and powerful devices from iteration I.

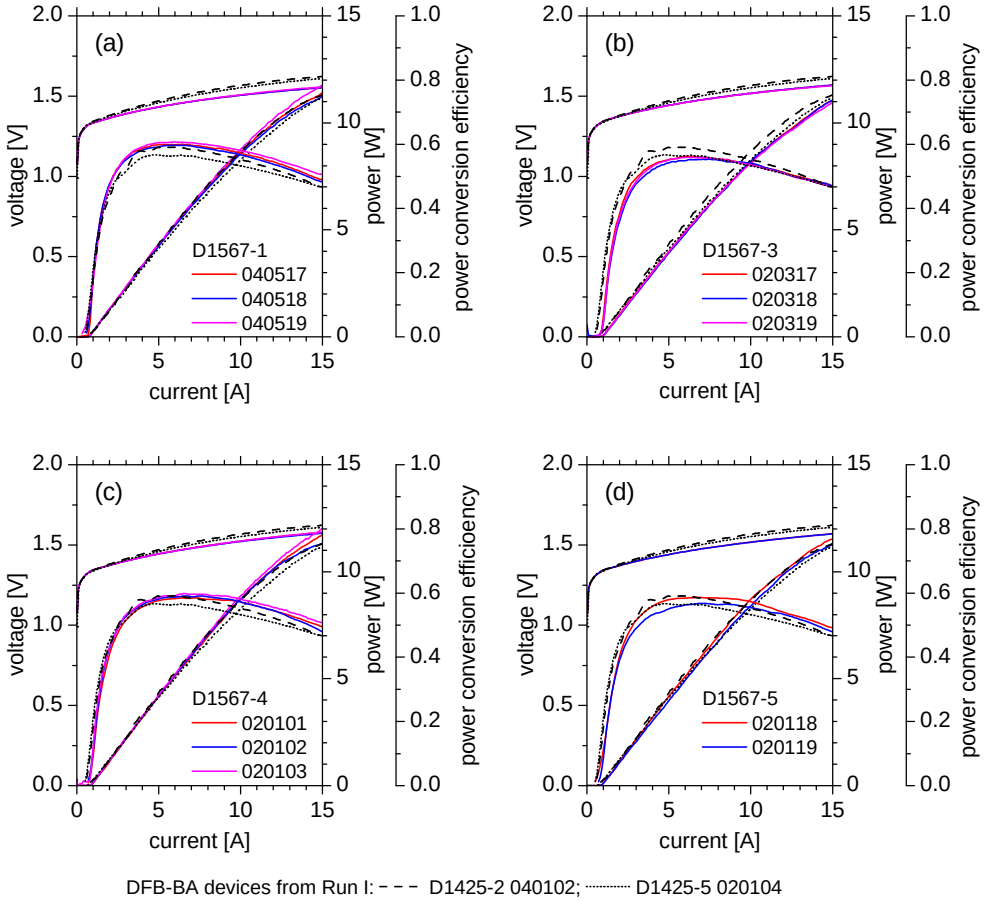

Figure 4.18: Comparison of the 25 °C power-voltage-current characteristics of DFB-BA lasers from Fig. 4.13 with sample characteristics of DFB-BA lasers D1425-2 040102 and D1425-5 020104 from iteration I.

In detail, the threshold current of the DFB-BA lasers from iteration II is enhanced by only $\approx$ 30 mA for wafer D1567-1 and remarkable $\approx$ 255 mA

for wafer D1567-3. The slope efficiency is increased by $0.04 - 0.07\,\mathrm{W\,A^{-1}}$ for most DFB-BA lasers from iteration II besides lasers from wafer D1567-3. All DFB-BA lasers from iteration II have in common that the voltage is increased due to a reduction in series resistance by $\approx 5\mathrm{m}\Omega$ compared to the DFB-BA lasers from iteration I and therefore the voltage characteristics coincide with the voltage from the FP-BA reference devices. The differences in the voltage between different wafers from iteration II is small and approximately in the same range as the voltage reproducibility for FP-BA lasers grown in a single stage epitaxy. As result of this improvements, the power conversion efficiency (besides wafer D1567-3) is increased by $2 - 4\,\%$.

4.3.6 Spectral properties of DFB-BA lasers

The following section concerns the spectral properties of DFB-BA lasers from iteration II. Spectral maps are presented for representative lasers from each of the five wafers. Afterwards, the spectral width is analyzed.

In Fig. 4.19 and 4.20, spectral maps over a wide spectral range from $950 - 1000\,\mathrm{nm}$ are depicted to give an overview of the spectral properties. The spectra were measured with a low resolution spectrometer with a wide spectral inspection range as described in chapter B.1.2, in order to capture the whole spectrum which may contain optical side modes at shorter or longer wavelength than the targeted DFB Bragg wavelength, in one measurement. An analysis of high resolution spectra will be presented subsequently. The spectral density is logarithmic scaled as illustrated in the intensity scale. In this scale, 100 % corresponds to the highest peak in each individual spectral map.

Figure 4.19 shows logarithmic scaled spectral maps of the DFB-BA laser D1560-2 040925 (from the test wafer) at 25 °C (a) and 15 °C (b). The spectral map measured at 15 °C is shown additionally because this laser has a lower spectral detuning between the gain peak wavelength and the Bragg wavelength of the DFB grating of only $\approx 2\,\mathrm{nm}$. Using a lower temperature than the targeted operating temperature of 25 °C allows to enlarge the spectral detuning ($\approx 4.6\,\mathrm{nm}$ at 15 °C). At 25 °C, the optical power is emitted only in the sharp DFB spectrum of the fundamental vertical waveguide mode. At threshold, the DFB wavelength is 969.6 nm and shifts to 972.7 nm at 15 A. Higher-order vertical waveguide modes at lower wavelengths and FP-like modes at longer wavelengths do not occur. In contrast to the spectrum at 25 °C, one higher-order vertical waveguide mode is observed in the spectral map at 15 °C at 962.3 nm but with low power content ($\sim 10\,\%$ for $I \leq 5.5\,\mathrm{A}$, $\sim 5\,\%$ for $5.5\,\mathrm{A} < I \leq 7.5\,\mathrm{A}$). The DFB wavelength of the fundamental mode shifts from 968.8 nm at threshold to 972.4 nm at 15 A. Again,

no FP-like modes can be found on the long wavelength side of the optical spectrum.

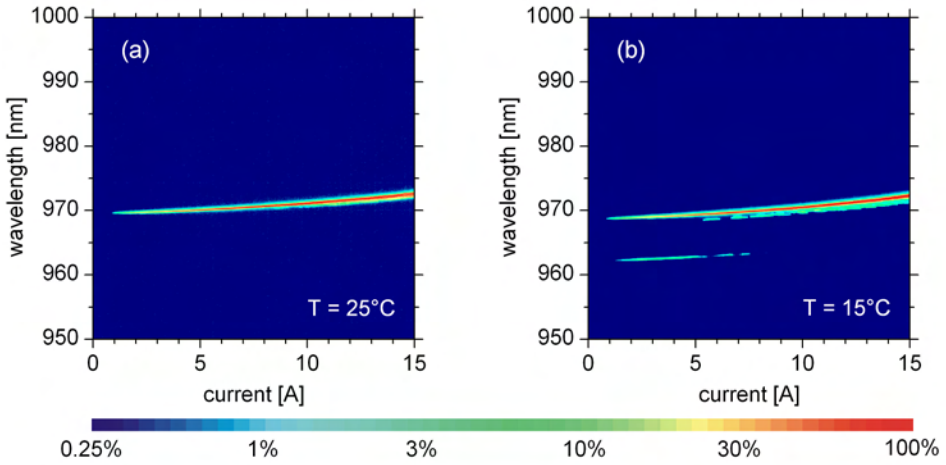

Figure 4.19: Logarithmic scaled spectral map over a wide spectral range for laser 040925 from test wafer D1560-2 ($\lambda_{\mathrm{DFB}}^{\mathrm{tar}} = 970\,\mathrm{nm}$): (a) At 25 °C. (b) At 15 °C.

The absence of FP-like modes at the long wavelength side of the DFB Bragg wavelength is a consequence of the low reflectivity front facet coating 5229, shown in Fig. 4.11 (a). For a high power DFB laser it would be preferred that the reflectivity drops down to even lower values on both, the short and long wavelength side of the Bragg wavelength on the fundamental waveguide mode. This would help to suppress FP-like modes on the long wavelength side of the Bragg wavelength at high powers, but also increase the threshold current for higher-order vertical waveguide modes at the short wavelength side. Unfortunately, the currently achievable reflectivity spectra for reliable facet coatings typically have one distinct local minimum that can either be positioned directly at the Bragg wavelength of the fundamental mode or optionally on the short or long wavelength side.

In practice, the spectral position of the local reflectivity minimum of such facet coatings cannot be designed with a precision better than $\approx \pm 10\,\mathrm{nm}$. In the case of facet coating 5229, the local minimum of the front facet reflectivity is located at 960 nm. In principle, locating the local minimum of the front facet reflectivity between 975 and 980 nm would be the best design to suppress FP-like modes in laser D1560-2 040925 because FP-like modes tend to onset at roughly +5 nm on the long wavelength side of the Bragg wavelength, as can be determined from measurement results obtained in iteration I, presented in Fig. 3.30 (a) and (d). Nevertheless, the front facet reflectivity of D1560-

2 040925 is low enough to avoid lasing on FP-like modes. This allows to determine that $R_f = 0.048\%$ (measured at 985 nm) is an acceptable front facet reflectivity in the spectral region, ≈ 5 nm above the Bragg wavelength (≈ 973 nm) at $I = 15$ A.

Fig. 4.19 also shows, that the reduction in spectral distance between the Bragg wavelength and the gain peak wavelength at threshold (2.0 nm for D1560-2, see table 4.2), compared to iteration I ($5.7 - 6.6$ nm, see table 3.6), leads to a sufficient suppression of higher-order vertical waveguide modes at 25 °C. At 15 °C, were the spectral distance is increased to approximately 4.6 nm, the suppression of higher-order waveguide modes is slightly too low as visible in Fig. 4.19 (b). For DFB-BA lasers in iteration I with a higher coupling coefficient $\kappa \approx 3\,\mathrm{cm}^{-1}$ it was shown, that a spectral detuning of 5.7 nm enables sufficient suppression of higher-order waveguide modes (in three of four cases: Fig. 3.30 (c), Fig. 3.31 (a), Fig. 3.31 (c) / Fig. 3.30 (c)), while 6.6 nm is too much (in three of four cases: Fig. 3.30 (d), Fig. 3.31 (b), Fig. 3.31 (d) / Fig. 3.30 (b)). Thus, for $\kappa \approx 0.5\,\mathrm{cm}^{-1}$, a spectral detuning between the Bragg wavelength and the gain peak below threshold of 2.0 nm enables suppression of higher-order waveguide modes, while 4.6 nm is slightly too much. For $\kappa \approx 3\,\mathrm{cm}^{-1}$, 5.7 nm enables suppression of higher-order waveguide modes, but 6.6 nm is too much. Differences occur not only because of the dependence on the coupling coefficient of the fundamental mode, but also because the threshold current (internal optical, confinement factor, coupling coefficient) of higher-order waveguide modes changes from iteration I to iteration II. Nevertheless, the calculated threshold currents for the second higher-order vertical waveguide modes are approximately comparable in iteration I and iteration II as can bee seen from tables 3.4.9 and 4.1 and Fig. 4.9 (b).

Spectral maps at 25 °C of representative DFB-BA lasers from completely processed wafers D1567-1, D1567-3, D1567-4 and D1567-5 are depicted in Fig. 4.20. In contrast to DFB-BA laser D1560-2 040925 whose spectral properties were presented in Fig. 4.19, these lasers have another facet coating, 5315 (see Fig. 4.11). The most important difference between the facet coatings 5315 and 5229 is, that the front facet reflectivity of 5315 is higher, namely 0.065 % at 976 nm for 5315 compared to 0.008 % at 970 nm for 5229. The differences in the rear facet reflectivity (5315: 98.4 % at 976 nm, 5229: 95.8 % at 970 nm) play a minor role for the spectral and power characteristics.

Figure 4.20 (a) shows the logarithmic scaled spectral map of DFB-BA laser D1567-1 040519. The spectrum is dominated by the sharp DFB spectrum of the fundamental vertical waveguide mode. Lasing on higher-order vertical waveguide modes is suppressed. Unfortunately, lasing on FP-like modes is observed above 11.1 A in the wavelength range between 980.2 and

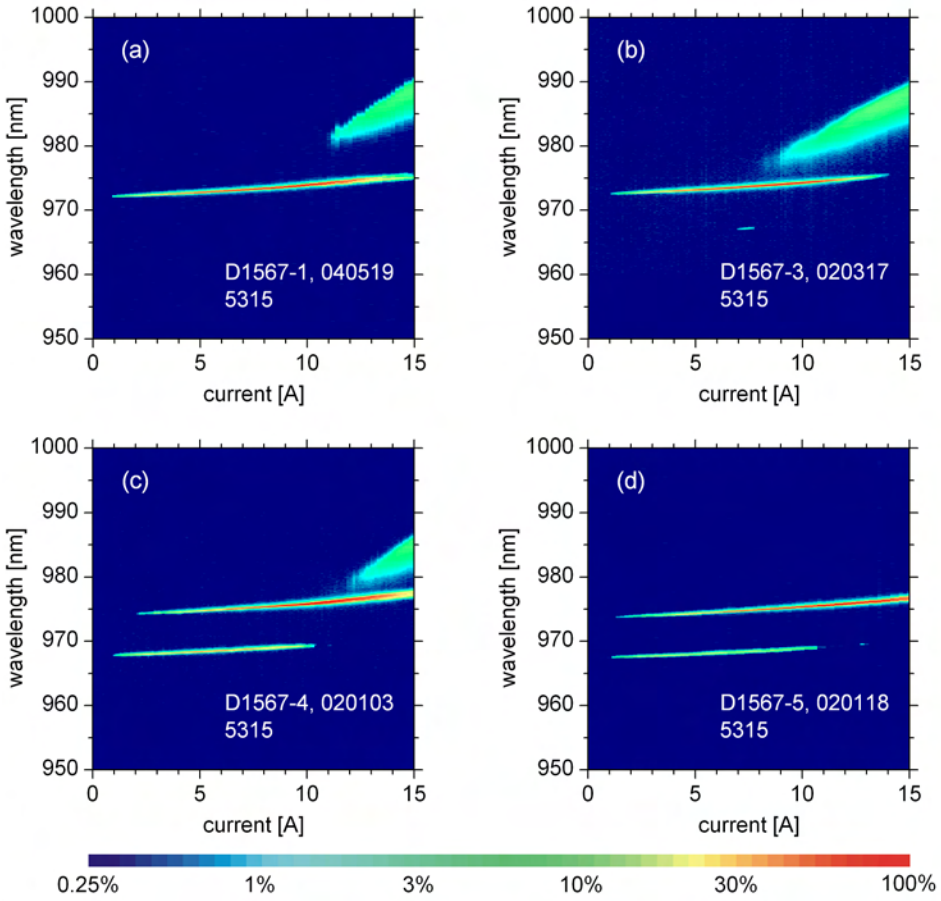

Figure 4.20: Logarithmic scaled spectral maps over a wide spectral range for the following lasers: (a) D1567-1 040519 ($\lambda_{\mathrm{tar}}^{\mathrm{DFB}} = 971.74\,\mathrm{nm}$), (b) D1567-3 020317 ($\lambda_{\mathrm{tar}}^{\mathrm{DFB}} = 974.55\,\mathrm{nm}$), (c) D1567-4 020103 ($\lambda_{\mathrm{tar}}^{\mathrm{DFB}} = 971.74\,\mathrm{nm}$), (d) D1567-5 020118 ($\lambda_{\mathrm{tar}}^{\mathrm{DFB}} = 974.55\,\mathrm{nm}$).

990.4 nm, where the intensity at the fundamental DFB wavelength decreases simultaneously. The DFB wavelength shifts from 972.6 nm at threshold to 975.6 nm at 15 A. The fact, that FP-like modes have a lasing threshold at 11.1 A, can be attributed to the increased front facet reflectivity (compared to laser D1560-2 040925) as well as to the decreased coupling coefficient of the fundamental mode, compared to DFB-BA lasers from iteration I.

Note that for DFB-Lasers from iteration I with facet coating 5128 (see Fig. 3.25 (a)), lasing on FP-like modes is suppressed (see Fig. 3.31 (a)) but for comparable facet coating 5315 in iteration II (see Fig. 4.11 (a)) FP-like modes can exceed threshold (see Fig. 4.20). In Detail, the front facet reflectivity of

coating 5128 (iteration I) at 980 nm is $R_f = 0.065\,\%$ and the reflectivity of coating 5315 (iteration II) at 980 nm is $R_f = 0.083\,\%$. Simultaneously, the coupling coefficients of the fundamental mode is reduced from $\kappa \approx 3\,\mathrm{cm}^{-1}$ in iteration I to $\kappa \approx 0.5\,\mathrm{cm}^{-1}$ in iteration II. Both, the decreased coupling coefficient and the slightly increased front facet reflectivity seems to reduce the FP mode suppression and this effect is not compensated by the small reduction of the spectra detuning (targeted values are 5.7−6.6 nm in iteration I and $3.7 - 5.6$ nm in iteration II).

In Fig. 4.20 (b), the spectral map of DFB-BA laser D1567-3 020317 is depicted. Again, the spectrum is dominated by the sharp DFB spectrum of the fundamental vertical waveguide mode. Lasing on FP-like modes starts already above ≈ 9.0 A and occurs in the wavelength range between 977.5 and 989.9 nm. Additionally, also very weak intensity of one higher-order vertical waveguide mode is observed at 967.1 nm between 7.0 and 7.7 A. The spectral distance between the fundamental DFB mode and the higher-order vertical waveguide DFB mode is ≈ 6.5 nm. At threshold, the fundamental DFB wavelength is 972.6 nm and shifts to 975.6 nm at 14.0 A, were lasing at the fundamental DFB wavelength vanishes for the benefit of lasing on FP-like modes at longer wavelengths, close to the wavelength were the gain peak is expected.

Figure 4.20 (c) shows the spectral map of DFB-BA laser D1567-4 020303. The spectrum consists of the fundamental vertical waveguide DFB mode, one comparatively strong higher-order vertical waveguide DFB mode at shorter wavelengths and FP-like modes at longer wavelengths and high currents. The fundamental DFB wavelength shifts from 974.3 nm at 2.1 A to 977.6 nm at 15 A. At the overall lasing threshold of 843 mA, only the higher-order DFB mode is involved with a center wavelength of 967.7 nm. The higher-order DFB mode vanishes at 10.4 A with a wavelength of 969.3 nm. The spectral distance between the fundamental DFB mode and the higher-order vertical waveguide DFB mode is ≈ 6.4 − 6.6 nm. Additional lasing on FP-like modes occurs above 12.1 A in the wavelength range between ≈ 978.9 and 986.5 nm, where the intensity at the fundamental DFB wavelength decreases rapidly. Shifting the target wavelength of the fundamental DFB mode from $\lambda_{\mathrm{tar}}^{\mathrm{DFB}} = 971.74$ nm (wafers D1567-1 and D1567-3) to $\lambda_{\mathrm{tar}}^{\mathrm{DFB}} = 974.55$ nm (wafers D1567-4 and D1567-5) has considerably reduced the suppression of the higher-order vertical waveguide DFB mode.

Finally, in Fig. 4.20 (d), the spectral map of DFB-BA laser D1567-5 020118 is depicted. The spectrum consists of the fundamental and one higher-order vertical waveguide DFB mode at shorter wavelengths, but in contrast to D1567-4 020103, no FP-like modes at longer wavelengths have been measured. The fundamental DFB wavelength starts lasing at 974.1 nm

at 1.2 A and shifts to 977.2 nm at 15 A. At threshold (902 mA), the higher-order DFB mode has a center wavelength of 967.7 nm. The higher-order DFB mode vanishes at 11.0 A with a wavelength of 969.4 nm and recurs around 12.7 A over ≈ 0.3 A. A spectral distance of $\approx 6.2 - 6.5$ nm between the fundamental DFB mode and the higher-order vertical waveguide DFB mode is observed. The relatively high intensity in the higher-order vertical waveguide DFB mode is typical for a target wavelength of the fundamental DFB mode of $\lambda_{\mathrm{tar}}^{\mathrm{DFB}} = 973.55$ nm and has been also observed for the lasers from wafer D1567-4.

The results for the wavelength of the fundamental and higher-order vertical waveguide DFB mode at its particular threshold $\lambda_{\mathrm{th}}^{0}$ and $\lambda_{\mathrm{th}}^{1}$, the particular threshold currents itself I_{th}^{0} and I_{th}^{1}, the threshold of FP-like modes $I_{\mathrm{th}}^{\mathrm{FP}}$ as well as the spectral distances between the higher-order waveguide mode and the FP-like modes relative to the fundamental mode $\Delta\lambda^{1-0}$ and $\Delta\lambda^{\mathrm{FP}-0}$ are summarized in table 4.4.

Table 4.4: Overview of spectral properties from DFB BA lasers from iteration II.

laser	$\lambda_{\mathrm{th}}^{0}$ [nm]	$\lambda_{\mathrm{th}}^{1}$ [nm]	I_{th}^{0} [A]	I_{th}^{1} [A]	$I_{\mathrm{th}}^{\mathrm{FP}}$ [A]	$\Delta\lambda^{1-0}$ [nm]	$\Delta\lambda^{\mathrm{FP}-0}$ [nm]
D1560-2							
040925, 25 °C	969.6	−−	0.77	–	–		–
040925, 15 °C	968.8	962.3	0.72	1.2	–	6.5	–
D1567-1							
040519, 25 °C	972.6	−−	2.1	0.80	12.1	6.5	≈ 6
D1567-3							
020317, 25 °C	972.6	967.7	0.94	6.9	8.9	6.5	≈ 3.5
D1567-4							
020103, 25 °C	974.3	967.7	2.1	0.84	12.1	6.5	≈ 2
D1567-5							
020118, 25 °C	974.1	967.7	1.20	0.90	–	6.2	–

The onset of FP-like modes and higher-order vertical waveguide DFB

modes limits the technically usable narrow wavelength current range for which the DFB-BA lasers from iteration II are running on the fundamental DFB mode. Only DFB-BA laser 040925 from test wafer D1560-2 is an exception, because of the lower front facet reflectivity and smaller spectral detuning. Lasing on FP-like modes below 15 A is a consequence of the too high front facet reflectivity and the low coupling coefficient which is required for a very high differential quantum efficiency. The onset of higher-order vertical waveguide DFB modes is attributed to the design of the waveguide structure and the position of the DFB grating. If one defines a usable narrow wavelength current range as the range between the threshold current of the fundamental mode or the current, where the higher-order mode vanishes and 15 A or the current, where FP-like modes start lasing, one obtains values between 2 and 10 nm for the DFB-BA lasers from iteration II.

The current range in which the spectrum is locked exclusively to the Bragg wavelength of the fundamental waveguide mode (or at least containing $\geq 95\,\%$ of the power content in this mode) is reduced for most of the DFB-BA lasers in iteration II, compared to iteration I. As mentioned above, this occurs on the one hand because the slightly higher front facet reflectivity and lower coupling coefficient decrease the suppression of FP-like modes and on the other hand, because the higher-order waveguide mode is extended to higher currents up to 11 A for the lasers with the larger spectral detuning.

Thus, the question arises how the spectral properties of the DFB-BA lasers can be improved towards a narrow spectral width emission at the Bragg wavelength of the DFB grating in the fundamental waveguide mode from threshold to currents of ~ 15 A which will ensure that optical output powers of minimum 10 W can be obtained. For this optimization it has to be considered that the power conversion efficiency of the DFB-BA lasers should not be reduced.

The measured power-voltage-current characteristics and spectral maps from DFB-BA laser 040925 from the test wafer D1560-2 indicate how such spectral improvement can be achieved based on the used epitaxy design with 3 mm long DFDB-BA lasers and a coupling coefficient of $\kappa \approx 0.5\,\mathrm{cm}^{-1}$. Firstly, the front facet reflectivity must be reduced to $R_\mathrm{f} \leq 0.025\,\%$ (coating 5229) in the region ~ 5 nm above the Bragg wavelength of the DFB grating in the fundamental waveguide mode for $I = 15$ A, instead of $R_\mathrm{f} \approx 0.1\,\%$ as realized with coating 5315. Secondly, the spectral detuning must be adjusted to ~ 2 nm (D1560-2) or ~ 3.7 nm (D1567-1, D1567-3) and less than 4.6 nm (D1560-2 at 15 °C) instead of up to 5.6 nm as realized for wafers D1567-4 and D1567-5. Nevertheless, both the low reflectivity front facet and the relatively low spectral detuning have disadvantages. The highly AR coating of the front facet makes the lasers more susceptible for external optical feedback

which is disadvantageous for applications of mirrors, filters, lenses or optical fibers in front of the diode lasers. The limitation of the spectral detuning to values of approximately $\leq 4\,\mathrm{nm}$ limits the achievable optical power and the power conversion efficiency at currents above the coincidence of the gain peak and Bragg wavelength.

In future work, the development of an improved epitaxy design is preferred to suppress lasing on higher-order waveguide modes. Therefore, a waveguide is required which guides only a fundamental mode. Such single vertical mode waveguides can be developed using a narrow waveguide width and a low step in refractive index between the n-waveguide and the n-cladding layer which suppresses higher-order modes by coupling to highly doped parts of the n-cladding layer and substrate. Nevertheless, due to the required thin waveguide, it is critical to achieve a narrow vertical divergence angle of $\leq 45\,^\circ$ (95 % power content) as targeted in this work.

For optimization work of the spectral properties it is essential that the targeted Bragg wavelength of the DFB grating (in the fundamental waveguide mode) and the gain peak wavelength can be experimentally realized with an accuracy better than $\sim 1\,\mathrm{nm}$. Furthermore, the evolution of the wavelength with increasing current must be predictable with appropriate assumptions for the power-voltage-current characteristics and thermal resistance of the DFB-BA lasers. This has been tested with selected DFB-BA lasers from iteration II. Therefore, the wavelength of the gain peak and the Bragg wavelength of the DFB gratin were calculated based on the targeted wavelengths, given in table 4.2. Furthermore, the temperature coefficients of the DFB grating $\mathrm{d}\lambda_{\mathrm{DFB}}/\mathrm{d}T \approx 0.077\,\mathrm{nm\,K^{-1}}$ and the gain peak $\mathrm{d}\lambda_{\mathrm{gain}}/\mathrm{d}T \approx 0.34\,\mathrm{nm\,K^{-1}}$ have been considered. The wavelength was then calculated from the dissipated power (generated heat) which was obtained from the power-voltage-current characteristics and from the thermal resistance which has been experimentally determined for each of the devices. The thermal resistances are $3.87\,\mathrm{K\,W^{-1}}$ for D1560-2 040925, $4.52\,\mathrm{K\,W^{-1}}$ for D1567-1 040519, $4.03\,\mathrm{K\,W^{-1}}$ for D1567-3 020317, $4.65\,\mathrm{K\,W^{-1}}$ for D1567-4 020103 and $3.59\,\mathrm{K\,W^{-1}}$ for D1567-5 020118. In Fig. 4.21, the calculated gain peak wavelength (red dashed line), the calculated DFB Bragg wavelength (red solid line) and the logarithmic scaled spectral maps are depicted.

A comparison of the calculated and measured wavelengths shows a good coincidence for the DFB Bragg wavelength of the fundamental waveguide mode, better than 1 nm. Furthermore, the evolution of the calculated gain peak wavelength relative to the DFB fundamental and second higher-order waveguide mode allow to understand the onset of lasing on the higher-order mode (if the gain peak is close enough) as well as on FP-like modes (which occur around the gain peak wavelength). Thus, the experimental realization

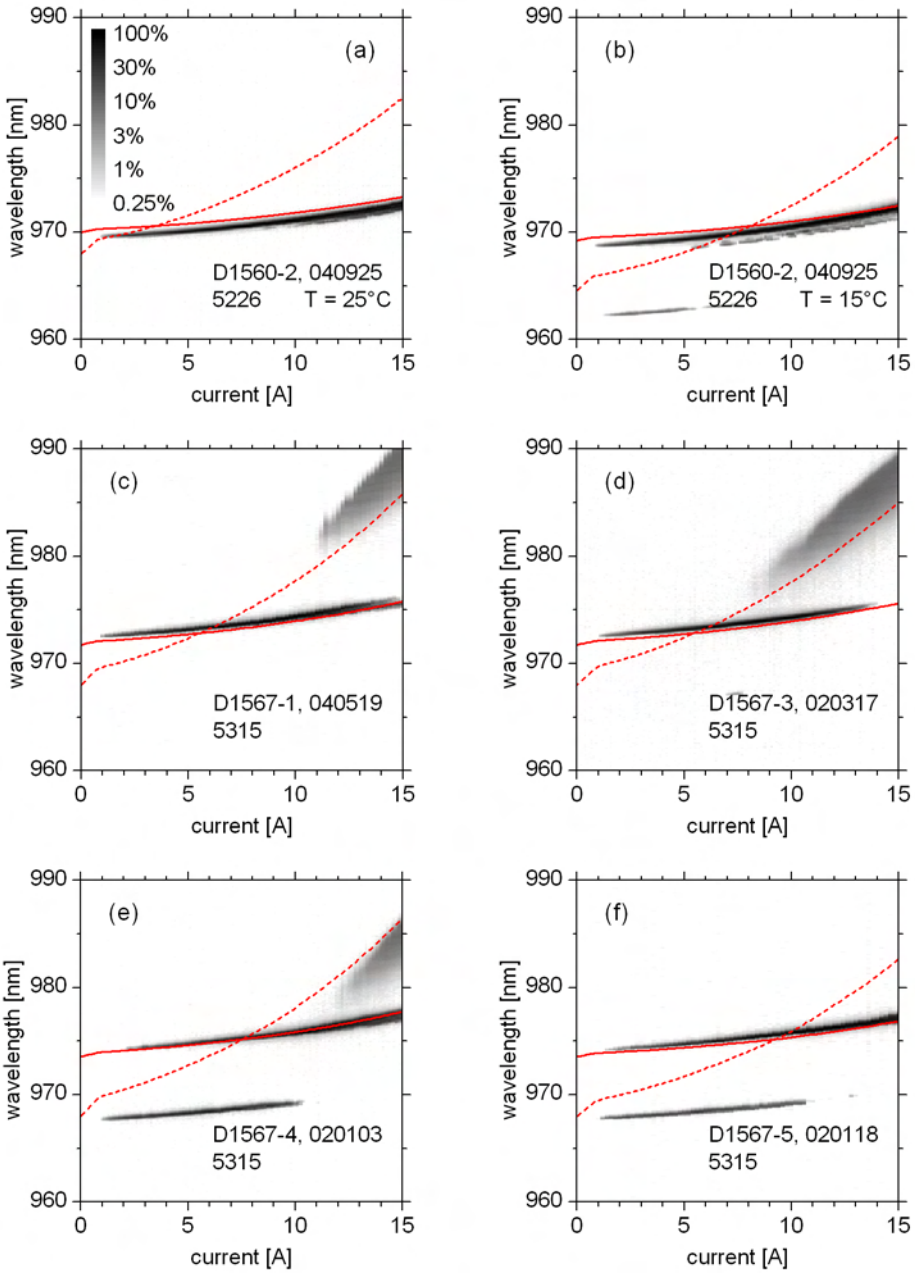

Figure 4.21: Calculated gain peak wavelength (red dashed line), the calculated DFB Bragg wavelength (red solid line) and logarithmic scaled spectral maps for selected DFB-BA lasers from iteration II. (a) Laser D1560-2 040925 at 25 °C. (b) Laser D1560-2 040925 at 15 °C. (c) Laser D1567-1 040519. (d) Laser D1567-3 020317. (e) Laser D1567-4 020103. (f) Laser D1567-5 020118.

of the targeted wavelength and their predictability is sufficiently precise to enable optimizations in the spectral detuning.

After discussion of the spectral properties in terms of suppression of lasing on FP-like modes and higher-order waveguide modes, the width of the optical spectrum when lasing exclusively on the Bragg wavelength of the DFB grating in the fundamental waveguide mode will be investigated. In section 3.4.6 it has been shown that the spectra width with 95 % power content was typically 1 nm in iteration I and thus, broader than the targeted spectral width of 0.3 nm. On the one hand, reducing $\kappa \cdot L \approx 1$ in iteration II to $\kappa \cdot L \approx 0.2$ in iteration II might broaden the spectral width via lasing on multiple longitudinal modes, caused by longitudinal spectral hole burning. On the other hand, the increase in power conversion efficiency might reduce the spectral width because the spectral width was found in section 3.4.6, Fig. 3.33 (e) and (f) to behave like a universal function of the dissipated power (generated heat).

In Fig. 4.22, high-resolution (0.15 pm) single spectra at optical output powers of 2.5, 5, 7 and 10 W are depicted for DFB-BA lasers D1560-2 040925 (a) and D1567-1 040519 (b). For laser D1560-2 040925, no FP-like modes or higher-order vertical waveguide modes appear at 25 °C heatsink temperature between threshold and 15 A as can be seen from Fig. 4.19 (a), so that the full lasing spectrum is visible in the shown wavelength range. Even the spectrum of laser D1567-1040519 is free of lasing on side modes in the optical spectrum at optical output powers of 2.5, 5 and 7 W but FP-like modes exceed threshold at $I \approx 11.2$ A and cover > 5 % power content while $P_{\mathrm{opt}} = 10$ W is achieved not until $I = 11.7$ A (see Fig. 4.20 (a)). Thus, ~ 5 % of the optical power is not shown in the $P_{\mathrm{opt}} = 10$ W spectrum in Fig. 4.22 (b) because it is contained in FP-like modes at ≈ 982 nm. The spectra are characterized by several sharp spectral lines, indicating, that a number of different modes are involved. It is assumed that lasing on a large number of different lateral modes occurs because this is typical for BA lasers and also for DFB-BA lasers as previously shown in section 3.4.12. As already mentioned, the question, if the measured sharp spectral lines consist to lateral modes ore even multiple longitudinal modes cannot be answered from the measured spectra for this lasers. For both lasers, the spectral width increases with the output power to ≤ 0.75 nm at 10 W, which is an improvement compared to DFB-BA lasers from iteration I.

Detailed analysis of the spectral width of the DFB stabilized fundamental waveguide mode was performed on the basis of measured high resolution (0.15 pm) spectral maps. Figure 4.23 (a) shows a high resolution spectral map with linearly scaled spectral density of DFB-BA laser D1560-2 040925 (from test wafer) at 25 °C. As shown in Fig. 4.19 (a) over a wide spectral

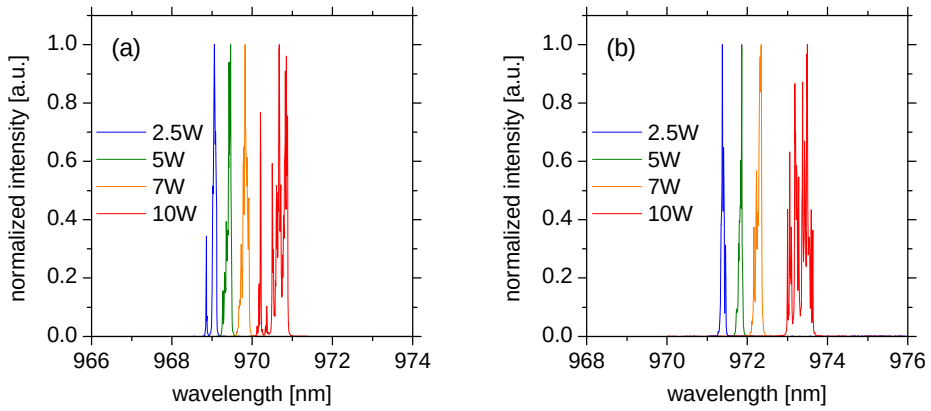

Figure 4.22: High-resolution single spectra at 2.5, 5, 7 and 10 W. (a) DFB-BA laser D1560-2 040925 (from the test wafer) (b) DFB-BA laser D1567-1 040519.

range, laser D1560-2 040925 has a spectrum that is free of FP-like modes and higher-order vertical waveguide DFB modes at 25 °C. In Fig. 4.23 (b), a high resolution spectrum map with linearly scaled spectral density of DFB-BA laser D1567-1 040519 is depicted. From Fig. 4.20 (a) and table 4.4 it can be deriveed that this DFB-BA laser starts lasing on FP-like modes at > 980 nm above ≈ 11.2 A at 25 °C. Thus, the spectrum map shown in Fig. 4.23 (b) is not spectrally completed for current values ≥ 11.2 A.

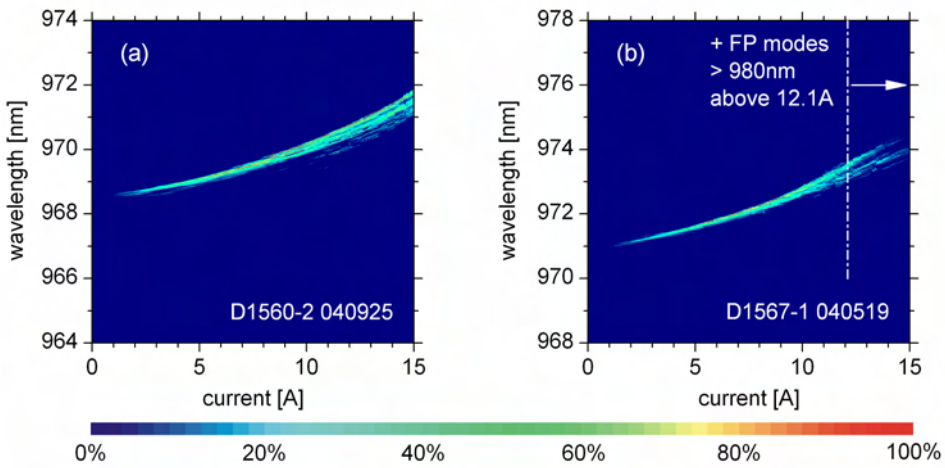

Figure 4.23: Linearly scaled high resolution spectral maps at 25 °C. (a) DFB-BA laser 040925 from test wafer D1560-2. (b) DFB-BA laser D1567-1 040519.

The spectral width with 95 % power content was calculated from the spectral maps shown in Fig. 4.23. The results are shown in Fig. 4.24 as (a) a function of the current, (b) a function of the output power and (c) a function of the dissipated power (generated heat). Note, that for laser D1567-1 040519 only values that correspond to currents of ≤ 11.2 A have been considered as mentioned above.

The spectral width of laser D1560-2 040925 is 0.26 nm at 7 W and remains below 0.68 nm at 10 W. For laser D1567-1 040519, the spectral width is also around 0.26 nm at 7 W and remains below 0.55 nm till 11.2 A, where FP-like modes exceed threshold and significantly broaden the spectral width with 95 % power content. These results are a significant reduction in the spectral width compared to the results from iteration I, were the spectral width at 7 W was $\approx 0.3 - 0.4$ nm and ≈ 1 nm at 10 W (see Fig. 3.33).

Thus, the reduction of the DFB coupling strength from $\kappa \cdot L \approx 3$ (iteration I) to $\kappa \cdot L \approx 0.2$ (iteration II) lead to a moderate reduction of the spectral width of the DFB spectrum when the laser is exclusively running at the Bragg wavelength of the fundamental waveguide mode. Unfortunately, this could only be achieved with laser D1560-2 040925 (from threshold to 15 A) and with laser D1567-1 040519 (from threshold to 11.2 A). The spectra of lasers from wafer D1567-3 were affected by lasing on FP-like modes already at $I \approx 9$ A and the spectra of lasers from D1567-4 and D1567-5 were affected by higher-order waveguide modes.

For future reduction of the spectral width the question arises, what determines the spectral width of DFB-BA lasers, running exclusively on the wavelength stabilized fundamental waveguide mode. As noted in [Ear98], devices with $0.5 \leq \kappa \cdot L \leq 1.0$ are expected to have the best discrimination against additional longitudinal modes because their optical field profile is appropriate to suppress longitudinal gain spectral hole burning. This is in good agreement with numerical results, depicted in Fig. 1.24. If longitudinal modes dominate the spectral width, devices with $\kappa \cdot L \sim 1$ should therefore have narrower spectra. Comparing the measured spectral width of DFB-BA lasers with $\kappa \cdot L \sim 1$, depicted in Fig. 3.33 and $\kappa \cdot L \approx 0.2$, depicted in Fig. 4.24 shows that the devices with $\kappa \cdot L \approx 0.2$ have narrower spectra. This indicates that lateral modes dominate the overall spectral width. The number of lateral modes in a BA lasers strongly depends on the current-induced heating, which leads to increased lateral waveguiding [Wen11], [Cru12a]. Thus, if lateral modes dominate the spectral width, it should scale with the dissipated power $P_{\mathrm{diss}}(I) \approx I \cdot U(I) - P_{\mathrm{opt}}(I)$ as observed in this work because the data points in Fig. 3.33 (e), (f) and Fig 4.24 (c) approximately converge to a single line. This finding can be interpreted as an indirect evidence that lateral modes are dominating the spectral width in DFB-BA lasers, with $\kappa \cdot L$

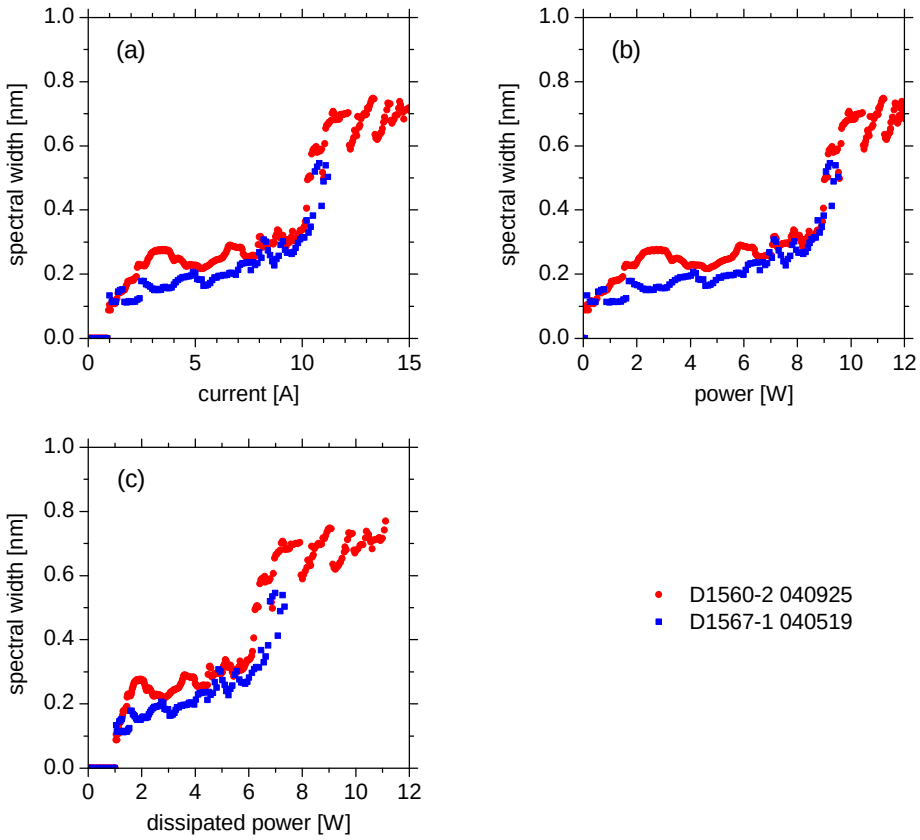

Figure 4.24: Spectral width with 95 % power content at 25 °C. (a) As a function of the current. (b) As a function of the output power. (c) As a function of the power conversion efficiency.

having mainly an indirect influence via power conversion efficiency and heat. Furthermore, the spectrally resolved lateral near fields and far fields shown in Figure 3.53 support this conclusion because two longitudinal modes, each with eight lateral modes, occur but the overall spectral width is mostly determined by lateral modes of one of these longitudinal modes because of the longitudinal spectral mode separation ($\approx 0.055\,\mathrm{nm}$) being much smaller than the spectral width of the lateral modes from one longitudinal mode ($\approx 0.189\,\mathrm{nm}$).

Finally, the precise overall width of the integrated optical spectrum with 95 % power content has been determined by combining the spectral width, determined from overview spectral maps (Fig. 4.19 and 4.20) and high resolution spectral maps (examples shown in Fig. 4.23) for the selected repre-

sentative DFB-Ba lasers. Therefore, the spectral width was determined from the high resolution (15 pm) spectral maps with 8 nm simultaneous inspection range, if the spectral width was narrow and determined only by one wavelength stabilized line (single fundamental or higher-order waveguide mode). For currents at which the spectrum was broad because of simultaneous lasing on multiple waveguide modes or on FP-like modes, the spectral width has been calculated from the low resolution ($\sim$ 1 nm) overview spectral maps with minimal 50 nm simultaneous inspection range. The resulting composed spectral width is shown in Fig. 4.25 as a function of the injection current.

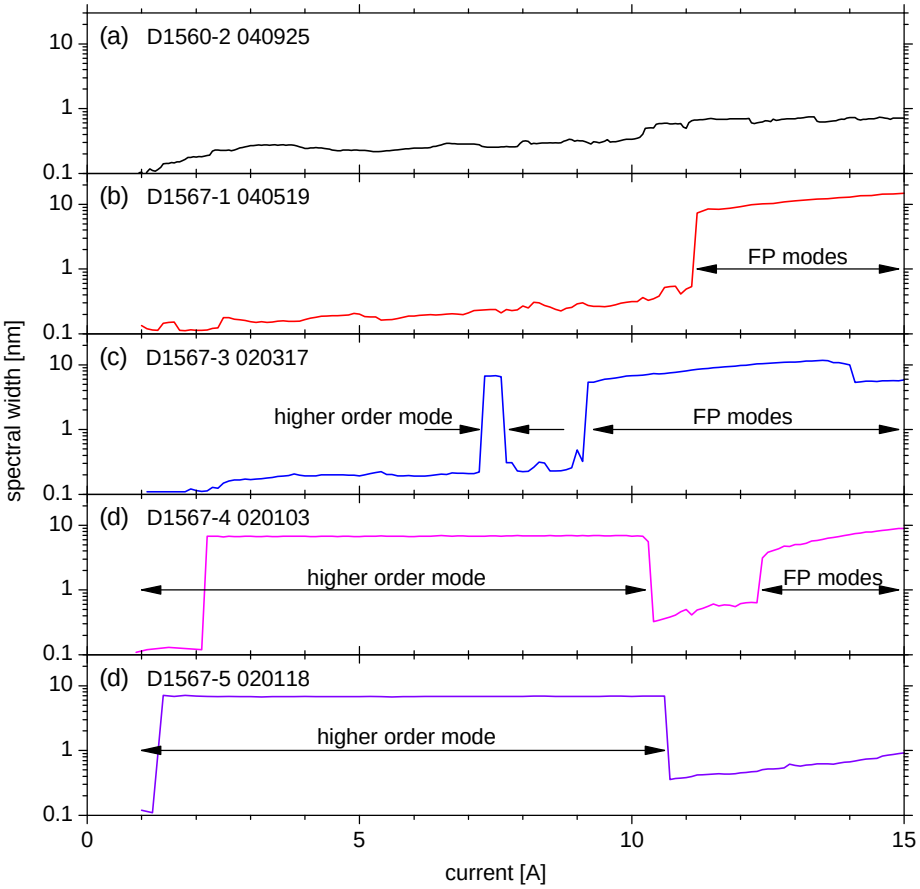

Figure 4.25: Spectral width of the integrated optical spectrum. (a) Laser D1560-2 040925, spectral detuning 2 nm, $R_{\mathrm{f}}^{\mathrm{FP}} \approx 0.025\,\%$. (b) Laser D1567-1 040519, spectral detuning 3.7 nm, $R_{\mathrm{f}}^{\mathrm{FP}} \approx 0.11\,\%$. (c) Laser D1567-3 020317, spectral detuning 3.7 nm, $R_{\mathrm{f}}^{\mathrm{FP}} \approx 0.11\,\%$. (d) Laser D1567-4 020103, spectral detuning 5.6 nm, $R_{\mathrm{f}}^{\mathrm{FP}} \approx 0.11\,\%$. (e) Laser D1567-5 020118, spectral detuning 5.6 nm, $R_{\mathrm{f}}^{\mathrm{FP}} \approx 0.11\,\%$.

With respect to the individual spectral detuning and the front facet reflectivity at the wavelength where FP-like modes exceed threshold (or might exceed threshold) $R_{\mathrm{f}}^{\mathrm{FP}}$, the characteristics of the spectral width for the five lasers shown in Fig. 4.25 can be understood qualitatively. Firstly, the spectrum of DFB-BA laser D1560-2 040925 is exclusively determined by lasing close to the Bragg wavelength of the DFB grating in the fundamental waveguide mode due to the low reflectivity front facet (suppresses FP modes) and the low spectral detuning (suppresses higher-order modes). Secondly, the spectra of DFB-BA lasers D1567-1 040915 and D1567-3 020317 are degraded by additionally lasing on FP-like modes because of the higher front facet reflectivity (reduces threshold of FP modes) but higher-order modes are predominantly suppressed due to the moderate spectral detuning. Thirdly, the spectra of DFB-BA lasers D1567-4 020103 and D1567-5 020118 are degraded by lasing on FP-like modes (D1567-47) and higher-order modes because of the higher front facet reflectivity and large spectral detuning, respectively.

In summary, the spectral properties of DFB-BA lasers were changed by the reduction of the DFB coupling coefficient from ≈ 3 to $\approx 0.5\,\mathrm{cm}^{-1}$ in three ways. Firstly, the spectral width of the fundamental DFB mode is reduced to $\approx 0.7\,\mathrm{nm}$ at 10 W, compared to $\approx 1\,\mathrm{nm}$ at 10 W in iteration I. Secondly, the suppression of FP-like modes is reduced. This must be attributed to the lower coupling coefficient as well as to the front facet reflectivity, which is too high for such a low coupling coefficient. Thirdly, even the suppression of higher-order vertical waveguide DFB modes is reduced. The threshold currents of the vertical waveguide modes were estimated at the end of section 4.2.3. Compared to the epitaxy design from iteration I, the threshold current of the first higher-order mode was found to be significantly increased to $\approx 3.5\,\mathrm{A}$. In fact, this mode did not exceed threshold as can be estimated from the spectral distance of the measured higher-order mode to the fundamental mode which was about 6.5 nm in iteration II, 6.2 nm in iteration I for the second higher-order mode and 2.2 nm for the first higher-order mode. Nevertheless, the threshold current of the second higher-order mode was calculated as $\approx 1\,\mathrm{A}$ for iteration II and this mode was found to exceed threshold at a wavelength $\approx 6.5\,\mathrm{nm}$ below the fundamental mode. As a consequence of lasing on these side modes in the optical spectrum, the current and power range in which narrow wavelength emission can be obtained at 25 °C heatsink temperature is reduced to a small window for some of the lasers. The spectral properties of DFB-BA laser 040925 from the test wafer D1560-2 show, that a sufficient suppression of FP-like modes and higher-order waveguide modes is possible for these DFB-BA lasers with $\kappa \approx 0.5\,\mathrm{cm}^{-1}$ by using a low front facet reflectivity $R_{\mathrm{f}} \leq 0.048\,\%$ and a low spectral detuning of $2 - 3.7\,\mathrm{nm}$.

4.3.7 Determination of the DFB locking range

The DFB locking range has been determined comparable to the locking range analysis in section 3.4.11 for iteration I. In iteration II, DFB-BA laser 040925 from the test wafer D1560-2 has been used for the measurements of power-voltage-current characteristics and spectral maps. This laser has a more preferable front facet coating (5229) compared to DFB-BA lasers from other wafers from iteration II (5315) as already discussed. A front facet reflectivity at the Bragg wavelength of $R_\mathrm{f} < 0.014\,\%$ was determined for coating 5229, but $R_\mathrm{f} < 0.070\,\%$ for coating 5315 which is applied to the completely processed wafers from iteration II. Therefore, the selected laser can be used to demonstrate that a broad locking range in current and heatsink temperature can be achieved with weakly coupled DFB-BA lasers ($\kappa \cdot L \approx 0.2$), using a low reflectivity front facet coating.

Locking is again defined with the criterium, that the measured spectral width with 95 % power content is limited to $\Delta\lambda \leq 1.5\,\mathrm{nm}$. This requires that the laser is neither running on higher-order vertical waveguide modes (the spectral distance for these modes is $\approx 6.5\,\mathrm{nm}$) nor running on FP-like modes.

The measurements were performed between CW currents of 0 and 15 A and between heatsink temperatures 15 and 50 °C. An increased measurement speed allowed to reduce the temperature step size from 5.0 to 2.5 K and the current step size was also reduced from 500 to 200 mA. Figure 4.26 (a) shows the measured power-voltage-current characteristics. The evolution with the heatsink temperature is indicated with an arrow, pointing towards higher temperatures. One observes a minor reduction of the diode voltage. The slope efficiency is reduced systematically and roll-over increases with temperature. The power conversion efficiency consequently decreases with temperature, the peak efficiency drops from $> 60\,\%$ to $\approx 45\,\%$.

In Fig. 4.26 (b), (c) and (d), the locked area (colored) is differentiated from unlocked regions (white). The locking range of this DFB-BA laser is only limited by the threshold current (white column on the left hand side) and a small structured area at low currents and temperatures, were the DFB BA laser is running on an additional higher-order waveguide modes. Lasing on FP-like modes is not observed in the investigated range of injection current and heatsink temperature. Figure 4.26 (b) shows the evolution of the center wavelength in the current-temperature matrix. For example, this knowledge allows one to increase the output power of the DFB-BA laser at an extremely precise emission wavelength by simultaneously changing current and temperature. In Fig. 4.26 (c), the locked output power is depicted at a linear intensity scale. Finally, the corresponding power conversion efficiency at every current-temperature pair is shown in a linear intensity scale.

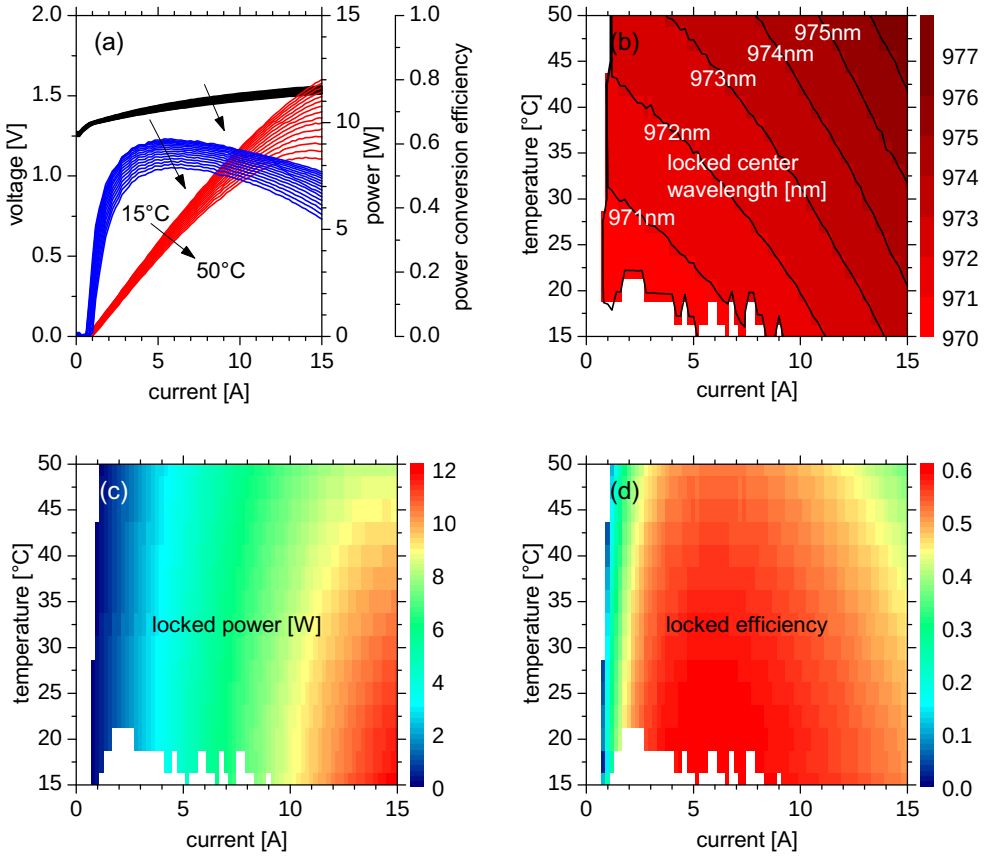

Figure 4.26: Locking range of DFB-BA laser D1560-2 040925 in the parameter range between 15.0 and 50.0 °C and between 0 and 15 A. (a) Power-voltage-current characteristics at 15.0, 17.5, ..., 50.0 °C). (b) Locking range with center wavelength, shown as a false color scale. (c) Locking range with output power, shown as a false color scale. (d) Locking range with power conversion efficiency, shown as a false color scale. False color scales to (b), (c) and (d) are indicated each at the right hand side.

The obtained DFB locking range is a remarkable result for a high power, high efficiency DFB-BA laser and a cear improvement compared to the locking range, obtained with the DFB-BA laser which has been tested in iteration I. This was enabled by the applied low reflectivity front facet coating against FP mode lasing which can easily occur in high efficiency DFB-BA lasers with $\kappa L < 1$ close to the gain peak at high currents and temperatures. For comparison, Kanskar *et al.* [Kan06] have shown a locking range of a 975 nm high efficiency DFB-BA laser. At 50 °C, locking is shown to vanish already

for an injection current of $\approx 2.5\,\mathrm{A}$. Also the suppression of higher-order waveguide modes is better than in iteration I (see Fig. 3.50 (c)). This must be attributed to the chosen low spectral detuning between the Bragg wavelength of the DFB grating in the fundamental waveguide mode and the gain peak wavelength (2 nm). Note that this value has been originally selected to improve DFB operation of DFB-RW lasers close to threshold for the measurement of sub-threshold ASE spectra. For a maximum power conversion efficiency at output powers in the 10 W-class, higher spectral detuning is preferred which enables coincidence of the gain peak and fundamental DFB wavelength at the current value which belongs to 10 W output power.

In summary, a broad DFB locking range in current and heatsink temperature nearly in the whole investigated range ($I = 0 - 15\,\mathrm{A}$, $T = 15 - 50\,^{\circ}\mathrm{C}$) can be obtained with a weakly coupled high efficiency, high power DFB-BA laser by using a low reflectivity front facet coating ($R_\mathrm{f} < 0.1\,\%$ even for the highest obtained gain peak wavelength which is estimated as $\approx 995\,\mathrm{nm}$) and an adequate spectral detuning (here 2 nm at 25 °C). Generally, the locking range must be expected to decrease with the coupling strength $\kappa \cdot L$ for a fixed front facet coating and a spectral detuning. Further improvement of the DFB locking range can be obtained with an optimized epitaxy design that enables an even better suppression of higher-order modes.

4.3.8 Experimental determination of the coupling coefficient

The coupling coefficient of the DFB lasers from iteration II is expected to be $\approx 0.5\,\mathrm{cm}^{-1}$ based on simulations, presented in section 4.2.3. This reduction in the coupling coefficient was necessary to increase the slope efficiency and thus, the power conversion efficiency. However, the reduction of the coupling coefficient is also expected to make the experimental determination of the coupling coefficient using parameter extraction even more complicated than in iteration I, because this will damp the modulation of the stopband structure in the sub-threshold ASE spectra.

For DFB-BA lasers from iteration I, the experimental determination of the coupling coefficient was challenging because of its low absolute value which lead to a very weak stopband structure at the Bragg wavelength. Furthermore, the measurement was also sensitive to optical feedback from the tip of the tapered fiber which was used to couple the emitted ASE to the spectrometer.

Therefore, several modifications were applied to advance the experimental determination of the coupling coefficient. Firstly, an AR coating with $R_\mathrm{facet} =$

0.01 % was applied to both facets to suppress FP-like modes. Secondly, single DFB-RW lasers with a stripe width W between 2.2 and 7 μm were mounted p-down on C-mount heatsinks. For an optimal lateral waveguiding (fundamental transversal mode) at the used stripe widths, index trenches that induce a step in the effective index of refraction of $\Delta n_{\text{eff}} \cong 3 \cdot 10^3$ were etched into the epitaxy layers. Thirdly, the measurement setup was modified. Instead of collecting the emitted ASE directly with a tapered optical fiber, a focussing optics was realized with two AR coated lenses of 3 mm focal length. An angled cleaved (FC/APC) optical fiber was used to collect the ASE at the imaging plane of the focussing optics. This setup was found to significantly reduce the optical feedback and allowed to measure ASE spectra with very good reproducibility of the stopband structure.

The coupling coefficient was determined by fitting calculated ASE spectra to the measured spectrum for parameter extraction with methods, described in [Wen03], [Wen04]. For the calculation of the DFB ASE spectra, the program FIT [Wen03] was used as already mentioned in section 3.4.10.

In Fig. 4.27 (a) - (f), six DFB ASE spectra from DFB-RW lasers from the test wafer D1560-2 are depicted as black dots, together with the calculated spectra, shown as red solid lines. For the measurement of the ASE spectra, the heatsink temperature and injection current were varied to shift the gain peak to the wavelength of the DFB stopband for sufficient intensity. The DFB-BA lasers in use did not exceed threshold in the applied current range $I \leq 500\,\text{mA}$ because of the low coupling strength ($\kappa \cdot L \approx 0.15$ for $L = 3.0\,\text{mm}$ cavity length and $\kappa \cdot L \approx 0.08$ for $L = 1.5\,\text{mm}$) and the AR coating ($R_{\text{facet}} = 0.01\,\%$) on both facets.

In each sub-figure of Fig. 4.27, the particular heatsink temperature, cavity length, stripe width and injection current is indicated. The calculated value for the coupling coefficient κ is given as a real number, even though the calculation also included the imaginary part, but the imaginary part was found to be typically two orders of magnitude lower than the real part.

The shape of the stopbands in the ASE spectra, shown in Fig. 4.27, deviates from typical stopbands in ASE spectra of DFB-RW lasers with a high coupling coefficient as for example shown in [Wen03], [Wen04]. Firstly, the width of the stopband approaches to the width of the neighboring longitudinal modes because of the low coupling coefficient. Secondly, the intensity decrease inside the stopband is much lower, also due to the low coupling coefficient. Because of the small spectral separation of longitudinal modes ($\Delta\lambda_{\text{lon}} \approx 0.08\,\text{nm}$ for $L = 1.5\,\text{mm}$ and $\Delta\lambda_{\text{lon}} \approx 0.04\,\text{nm}$ for $L = 3.0\,\text{mm}$), the intensity modulation of the longitudinal modes and the modulation depth inside the stopband is expected to be limited by the resolution of the spectrometer (10 pm). Figures 4.27 (a) - (c) show ASE spectra of DFB-RW lasers

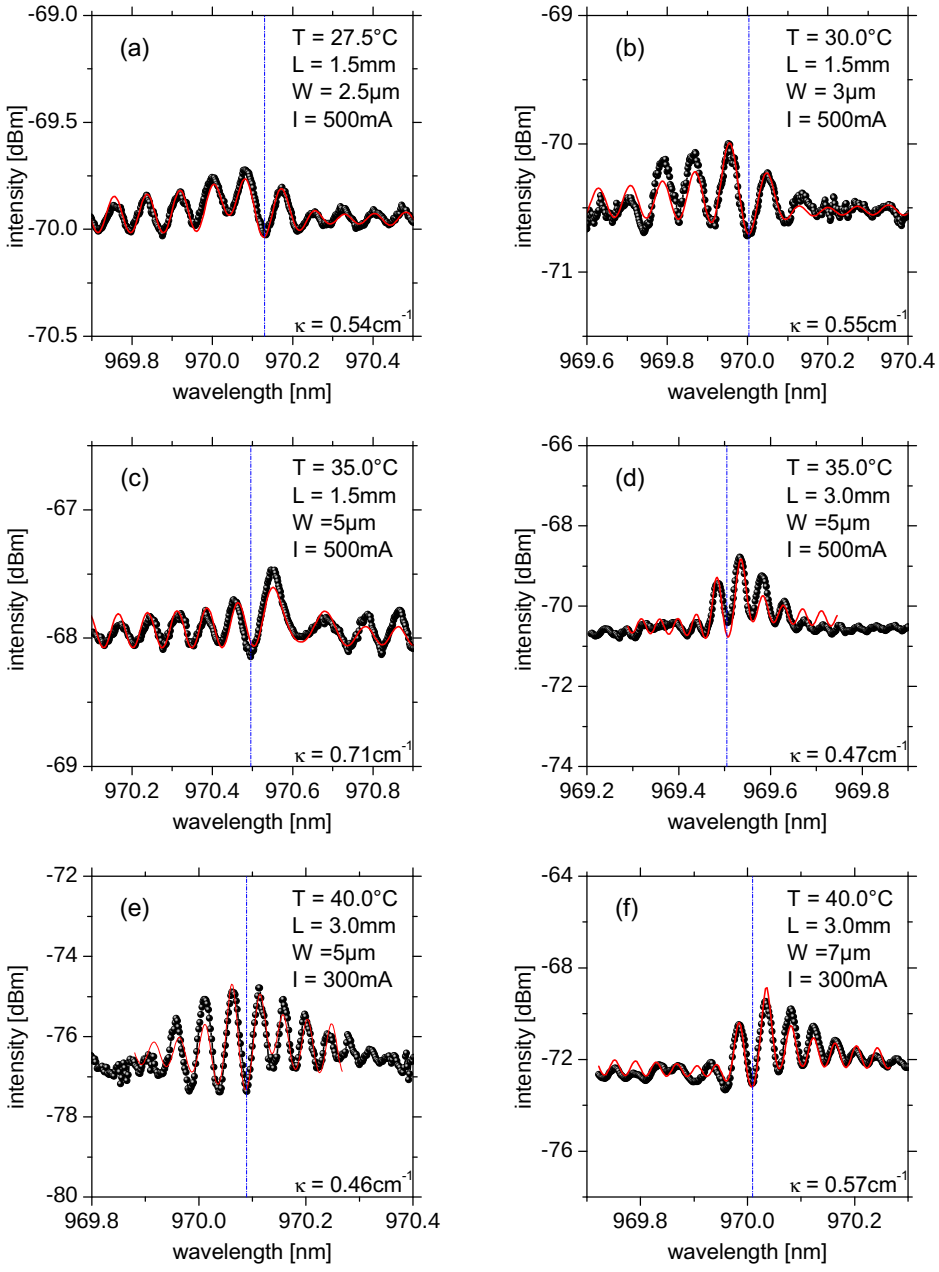

Figure 4.27: Measured (black dots) and simulated stopband spectra (red solid lines) for six DFB-RW lasers from wafer D1560-2. The center of the stopband is indicated with a blue dash-dotted line.

with a cavity length of $L = 1.5\,\mathrm{mm}$. In Fig. 4.27 (d) - (f), ASE spectra of $L = 3.0\,\mathrm{mm}$ long DFB-RW lasers are depicted.

The average value of the experimentally determined coupling coefficients of the fundamental waveguide mode is $\kappa = 0.55\,\mathrm{cm}^{-1}$. This is in good agreement with the coupling coefficients calculated with the simulation programm QIP [Wen90] from the vertical epitaxy design properties (see section 4.2.3. There, the coupling coefficient has been calculated for a rectangular DFB grating with a duty cycle of $c_\mathrm{d} = 1/4$, neglecting the effect of the inhomogeneous aluminum distribution in the regrown $\mathrm{Al}_x\mathrm{Ga}_{1-x}\mathrm{As}$ which was shown to increase κ in iteration I. Depending on the thickness of the remaining GaAs caps on top of the $\mathrm{In}_{0.49}\mathrm{Ga}_{0.51}\mathrm{P}$ grating stripes, κ increases from $\approx 0.5\,\mathrm{cm}^{-1}$ (15 nm GaAs) to $\approx 1.0\,\mathrm{cm}^{-1}$ (5 nm GaAs). Note that the thickness of the GaAs cap depends on the fabrication of the DFB gratings and might vary by up to 10 nm between different wafers. With the 6 nm thin GaAs cap which was found in the STEM micrograph from wafer D1560-2 (see Fig. 4.6), $\kappa = 0.96\,\mathrm{cm}^{-1}$ was calculated [Sch12].

One possible explanation for the good agreement is, that the effect of the spatially inhomogeneous aluminum distribution above the DFB grating layer (increases κ) plays a minor role for the DFB gratings in iteration II with their low corrugation depth ($15 - 25\,\mathrm{nm}$). Furthermore, additional effects such as deviations of the duty cycle and the non-rectangular grating shape which decrease κ may cancel out with the inhomogeneous aluminum distribution.

As already shown in section 3.4.10, Fig. 3.47, also the stopbands of higher-order vertical waveguide modes can be observed in overview spectra. Also in the spectra of DFB-RW lasers from iteration II, a stopband structure was visible at the wavelength of the higher-order waveguide mode ($\approx 6.5\,\mathrm{nm}$ shorter than the wavelength of the fundamental mode). As shown in section 4.2.3 (Fig. 4.9 (b) and table 4.1), QIP simulations lead to a coupling coefficient of $3.8\,\mathrm{cm}^{-1}$ for this second higher-order mode. Thus, the coupling coefficient of the second higher-order mode is much higher than the coupling coefficient of the fundamental waveguide mode. Therefore, it should be in principle easier to determine its coupling coefficient from fitting simulated ASE spectra to the measured ASE spectrum for parameter extraction. This lead to the idea, to determine the small coupling coefficient of the fundamental mode in an indirect way, based on the experimental determination of the coupling coefficient of the higher-order mode.

Firstly, ASE spectra of the higher-order mode at the stopband must be measured. Secondly, the coupling coefficient of the higher-order mode can be obtained with parameter extraction as described above for the fundamental mode. Thirdly, the confinement factors of the grating layers in the vertical intensity profile and the effective indices of refraction of the fundamental

and the higher-order mode must be determined from QIP simulations. Then it would be possible to determine the coupling coefficient of the fundamental mode from the coupling coefficient of the higher-order mode and the differences in the confinement factors and effective indices, regarding equation 1.60:

$$h_2 = \frac{-\omega^2 \Delta\varepsilon}{2K_0 c^2} \int \mathrm{d}x \quad \phi^2(x)\xi_2(x) \tag{4.1}$$

In Fig. 4.28, ASE spectra of the second higher-order mode are depicted for two 1.5 mm long DFB-RW lasers. The ASE spectra of the higher-order mode show a considerable increase of the intensity inside the stopband as expected for a higher coupling coefficient. Unfortunately, the calculated ASE spectra do not match on the short-wavelength side in Fig. 4.28 (a) and on the long-wavelength side in Fig. 4.28 (b) because of significant changes of the spectral separation between longitudinal modes on the short- and long-wavelength side of the stopband which cannot be reproduced with the simulation program FIT. Coupling coefficients of 3.35 and 1.97 cm^{-1} have been obtained from parameter extraction (average value 2.66 cm^{-1}). With the simulation programm QIP, a coupling coefficient of 3.8 cm^{-1} has been determined for the second higher-order mode. Thus, the agreement between the experimental determined and simulated coupling coefficient is relatively good, especially for the value obtained from the stopband in Fig. 4.28 (a).

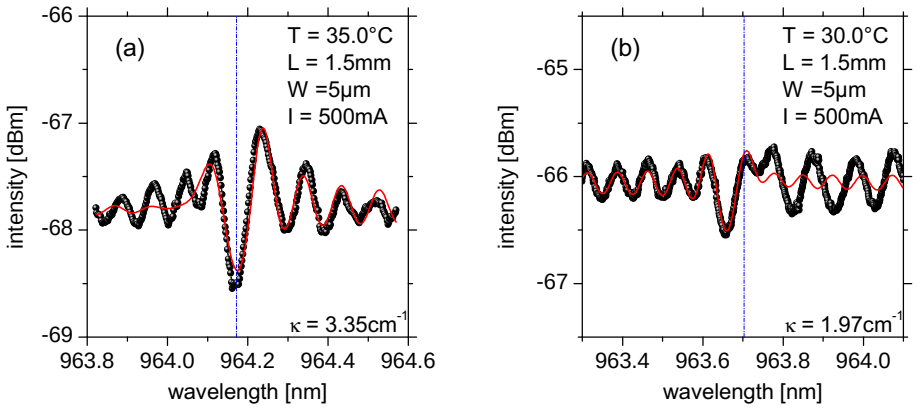

Figure 4.28: Stopband spectra of the higher-order vertical waveguide mode for two DFB-RW lasers from wafer D1560-2 (black dots). The temperature, stripe width, cavity length and current are each identified. The center of the stopband is indicated with a blue dashed dotted line. The simulated stopband spectra are shown as red solid lines and the result for the coupling coefficient is indicated.

The following confinement factors $\Gamma^{\mathrm{Mx}}_{\mathrm{grating}}$ were obtained for the DFB grat-

ing ($In_{0.49}Ga_{0.51}P$ grating ridges plus GaAs cap) for the four guided modes M0, M1, M2 and M3 in the waveguide structure with the DFB grating from iteration II:

$$\begin{aligned}\Gamma^{\mathrm{M0}}_{\mathrm{grating}} &= 0.158\,\% \\ \Gamma^{\mathrm{M1}}_{\mathrm{grating}} &= 0.486\,\% \\ \Gamma^{\mathrm{M2}}_{\mathrm{grating}} &= 1.283\,\% \\ \Gamma^{\mathrm{M3}}_{\mathrm{grating}} &= 0.001\,\%.\end{aligned}$$

In the simulation programm QIP, the dielectric function ε is averaged over the two grating layers, so that the confinement factor of the grating can be simply calculated by adding the confinement factors of both layers. Otherwise, one would have to consider the individual $\Delta\varepsilon$ for both layers in equation 1.60. From equation 4.1 (respectively equation 1.60), one can derive, that the coupling coefficient is proportional to Γ/n_{eff} as shown in equation 4.2 and 4.3. The coupling coefficient of the fundamental mode can be calculated from the coupling coefficient of the higher-order mode, the individual confinement factors and effective indices of refraction as denoted in equation 4.4.

$$\Re[\kappa] = \underbrace{\frac{-\omega^2}{2K_0c^2}}_{=\frac{\pi}{\lambda n_{\mathrm{eff}}}} \Delta\varepsilon \underbrace{\int \mathrm{d}x \quad \phi^2(x)\xi_2(x)}_{\propto\Gamma} \tag{4.2}$$

$$\Re[\kappa^{\mathrm{Mx}}] \propto \frac{\Gamma^{\mathrm{Mx}}}{n^{\mathrm{Mx}}_{\mathrm{eff}}} \tag{4.3}$$

$$\kappa^{\mathrm{M0}} \cong \kappa^{\mathrm{M2}} \cdot \frac{\Gamma^{\mathrm{M0}}}{\Gamma^{\mathrm{M2}}} \cdot \frac{n^{\mathrm{M2}}_{\mathrm{eff}}}{n^{\mathrm{M0}}_{\mathrm{eff}}} \tag{4.4}$$

With $n^{\mathrm{M0}}_{\mathrm{eff}} = 3.4227$, $n^{\mathrm{M2}}_{\mathrm{eff}} = 3.3747$ and the averaged experimentally determined coupling coefficients of the second higher-order mode one obtains $\kappa^{\mathrm{M0}} \cong 0.32\,\mathrm{cm}^{-1}$ ($\kappa^{\mathrm{M0}} \approx 0.41\,\mathrm{cm}^{-1}$ with $\kappa^{\mathrm{M2}} = 3.35\,\mathrm{cm}^{-1}$ and $\kappa^{\mathrm{M0}} \approx 0.24\,\mathrm{cm}^{-1}$ with $\kappa^{\mathrm{M2}} = 1.97\,\mathrm{cm}^{-1}$). These results are relatively close to the directly experimental result of $\kappa^{\mathrm{M0}} \approx 0.55\,\mathrm{cm}^{-1}$ and the result, determined with QIP simulations for the fundamental mode of $\kappa^{\mathrm{M0}} \approx 0.49\,\mathrm{cm}^{-1}$. Thus, it has been successfully demonstrated that the coupling coefficient of a fundamental mode of a DFB laser can be estimated by an experimental determination the coupling coefficient of a higher-order mode under consideration of the confinement factors and effective refractive indices. This indirect method can help to determine very low coupling coefficients, if a higher-order mode with a higher coupling coefficient exists in the waveguide.

To conclude, the experimental determination of the low DFB coupling coefficient has been successfully enabled by using DFB-RW lasers with an optimized lateral waveguiding and AR coating on both facets, as well as with a setup which reduces the problems with optical feedback which occurred for this type of measurements in iteration I. These improvements allowed to measure sub-threshold ASE spectra of the DFB stopband with good reproducibility. The coupling coefficients which have been obtained by fitting simulated ASE spectra to the measured spectra have minor variations around an average value of $\kappa = 0.55\,\mathrm{cm}^{-1}$ which is in good agreement with calculated values for the coupling coefficient ($0.5 - 1.0\,\mathrm{cm}^{-1}$). An additional method for the experimental estimation of the coupling coefficient of the fundamental mode (low $\kappa \approx 0.5\,\mathrm{cm}^{-1}$) which bases on the determination of the coupling coefficient for a higher-order waveguide mode (higher $\kappa \approx 3.8\,\mathrm{cm}^{-1}$) has been demonstrated successfully and reasonable agreement was obtained with the directly determined and simulated coupling coefficient.

4.3.9 Analysis of the reliability of DFB-BA lasers

The reliability of five DFB-BA lasers from iteration II was tested in a preliminary lifetime test, stabilized at an optical output power of 10 W. This power level has been chosen because the development of DFB-BA lasers for reliable wavelength stabilized, high efficiency operation at 10 W is a target of this work and 10 W output power is a typical operating point which can be achieved with $\sim 100\,\mu$m stripe, 3 mm long FP-BA lasers which serve as a benchmark for the newly developed DFB-BA lasers. Reliable operation of the reference FP-BA lasers at 7 and 10 W was reported in [Cru11c]. Six DFB-BA lasers from iteration I were tested in a 7 W reliability test over 4500 h without failure, the results have been reported in [Cru11c] for the first time.

Reliable operation of five DFB-BA lasers at 10 W optical output power over 5000 h was published for the first time in [Sch12]. Note that the DFB-BA lasers from iteration II have a more robust facet passivation and coating (5315) than the DFB-BA lasers from iteration I (coatings 5128, 4959 and 5055). The facet passivation and coating used for the DFB-BA lasers in iteration II is expected to be as robust as the facet passivation and coating for the reference FP-BA lasers. Thus, even though the front facet reflectivity of the DFB-BA lasers is much lower than for the FP-BA lasers ($R_\mathrm{f}^\mathrm{DFB} < 0.2\,\%$ instead of $R_\mathrm{f}^\mathrm{FP} \leq 3\,\%$), the power level for catastrophic optical mirror damage (COMD) should be the same (> 10 W) and do not limit the reliability in this test.

In the setup used for the lifetime test, the output power is measured and

stabilized at 10 W ± 0.1 W via corrections of the drive current, if necessary. Unfortunately, the stabilization of the heatsink temperature is not identical to that, used for measurements of the power-voltage-current characteristics and spectrum maps shown in this work. Because of technical reasons, the heatsink temperature could not be measured directly at the submount and stabilized to 25 °C. Instead, the temperature at the submount was ≈ 30 °C, lower temperatures were not achievable. As a consequence of the higher submount temperature, the threshold current of the lasers is higher, the slope efficiency lower and roll-over occurs at lower currents compared to 25 °C. Thus, the current which is necessary for 10 W optical output power is increased by ≈ 1 − 2 A. Furthermore, the ≈ 5 K higher heatsink temperature reduces the spectral detuning between the gain peak and Bragg wavelength at $I \approx 0$ A (2.4/4.2 nm instead of 3.7/5.6 nm). This will cause the gain peak wavelength to coincide with the Brag wavelength of the DFB grating at lower currents than at 25 °C and FP-like modes are supposed to exceed threshold at lower currents.

In Fig. 4.29 (a), the injection current, normalized to its individual start value for 10 W optical output power is depicted as a function of time for each of the devices. Figure 4.29 (b) shows the corresponding stabilized optical output power. The first part of the reliability test was performed over ≈ 5150 h (215 days). During the first 5000 h, the devices behave differently. For example, the current for laser D1567-1 040517 is extremely stable over 5000 h and drops only to 0.99. The highest drive current increase is observed for laser D1567-3 020319. Its current increase is roughly linear and occurs in many current steps, beginning at 866 h. In contrast, the current for DFB-BA laser D1567-4 020103, decreases to the range of 0.95 − 0.97 but sudden failure occurs at 4170 h, where the current increases drastically and the output power cannot be further stabilized to 10 W.

In table 4.5, the start value of the drive current $I_{\mathrm{start}}^{10\,\mathrm{W}}$ which is necessary to achieve 10 W output power, the resulting current value after 5000 h of the lifetime testing $I_{5000\,\mathrm{h}}^{10\,\mathrm{W}}$ and the current change $\Delta I_{5000\,\mathrm{h}}^{10\,\mathrm{W}}$. The estimated lifetime can be simply determined based on the a priori statement, that the devices may fail if the current which is necessary to achieve 10 W is increased by 20 %. For laser D1567-3 020319, which is the one with the highest current increase after 8424 h, one obtains an estimated lifetime of 14200 h. Thus, a usable lifetime of $> 10 \cdot 10^3$ h seems to be realistic, making these high efficiency, high power, spectrally stabilized diode lasers interesting candidates for possible applications.

From the application point of view it is critical to know exactly, if changes occur in the power-voltage-current characteristics and in the spectrum of the DFB-BA lasers after 5000 h reliability test. Therefore, power-voltage-

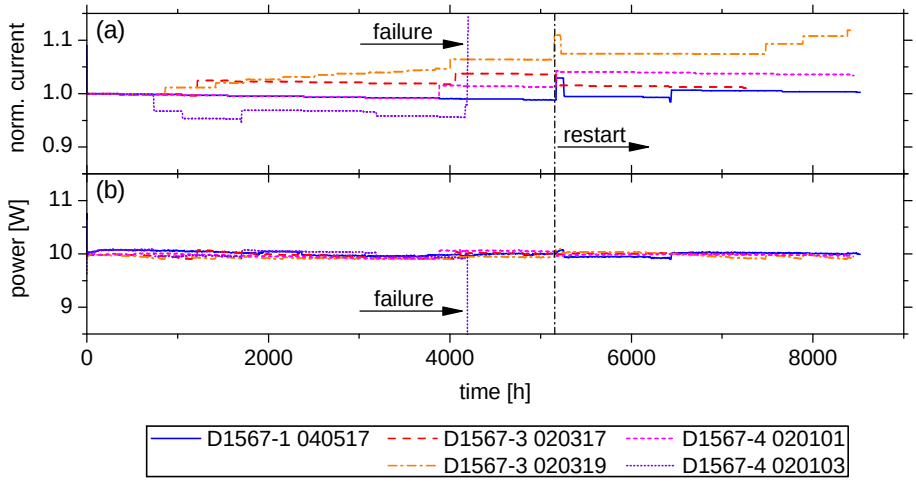

Figure 4.29: Preliminary reliability test of five DFB-BA lasers from three different wafers at 10 W CW optical output power, ≈ 30 °C heatsink temperature over 5000 h. (a) Normalized injection current. (b) Optical output power.

Table 4.5: Overview of the changes in drive current during 5000 h lifetime testing.

wafer	laser	$I^{10\,\mathrm{W}}_{\mathrm{start}}$ [A]	$I^{10\,\mathrm{W}}_{5000\,\mathrm{h}}$ [A]	$\Delta I^{10\,\mathrm{W}}_{5000\,\mathrm{h}}$ [%]
D1567-1	040517	12.83	12.68	−1.2
D1567-3	020317	13.51	14.00	+3.6
	020319	14.32	15.24	+6.4
D1567-4	020101	12.50	12.66	+1.3
	020103	13.09	–	–

current characteristics and spectral maps have been measured after the first ≈ 5150 h. Note, that the measurements were performed exactly under the same conditions as used for the initial measurement of power-voltage-current characteristics and spectral maps, discussed in sections 4.3.4 and 4.3.6, respectively. Note also, that the temperature stabilization for all these measurements differs from the temperature stabilization during the reliability

test. In Fig. 4.30, power-voltage-current characteristics of the five DFB-BA lasers after 5000 h reliability test are compared to the characteristics, measured before. One further DFB-BA laser (D1567-3 020318) which has not been reliability tested was also measured again after the reliability test was finished. This measurement was performed for reference, to determine changes in the power calibration, for example.

Only minor changes are observed between the power-voltage-current characteristics, measured before and after the reliability test. The most obvious changes appear in the roll-over behavior of the output power at currents above 10 A, which is more pronounced after the reliability test for three of the devices (D1567-1040517, D1567-3 020317 and D1567-3 020319). Changes in the roll-over behavior can occur due to different reasons. Firstly, internal degradations could be the reason for the stronger roll-over after the reliability test. Secondly, a slightly worse thermal contact between the submount and the fitting-mount, in which the submount is clamped, could be an explanation for this effect.

The power-voltage-current characteristics of DFB-BA laser D1567-3 020318, which has not been in the reliability test, have not changed significantly during the ≈ 5150 h, while the device was stored in a chamber under nitrogen atmosphere. Threshold currents and slope efficiencies of all the lasers before and after the reliability test were determined from linear fits over 3 A above threshold and are summarized in table 4.6. Both, the changes in threshold current and slope efficiency are moderate. Even reductions in the threshold current (D1567-1 040517 and D1567-3 020317) and an increases in the slope efficiency are observed (D1567-1 040517 and D1567-4 020101), but very close to the measurement accuracy. The most distinct changes occur with the increase of the threshold current for the devices D1567-3 020319, D1567-4 020101 and even for D1567-3 020318, which has not been in the reliability test.

In addition to the power-voltage-current characteristics, spectral maps have been measured in order to analyze possible changes in the spectral properties of the DFB-BA lasers, which could appear for the following reasons: Firstly, the coated facets could degrade due to the long time of facet load ($\approx 5.3 \cdot 10^6, \mathrm{W\,cm^{-2}}$) and change the front facet reflectivity. Secondly, if the power-voltage-current characteristics of the DFB-BA lasers are considerably degraded after the reliability test (higher threshold current, lower slope efficiency), the wavelength of both, the gain peak and the Bragg wavelength of the DFB grating would be shifted to longer wavelengths at a certain injection current because of higher heat generation. Thirdly, the DFB grating structure itself may degrade due to defects in the semiconductor crystal. Figures 4.31, 4.32 and 4.33 show linear intensity scaled spectral maps for the

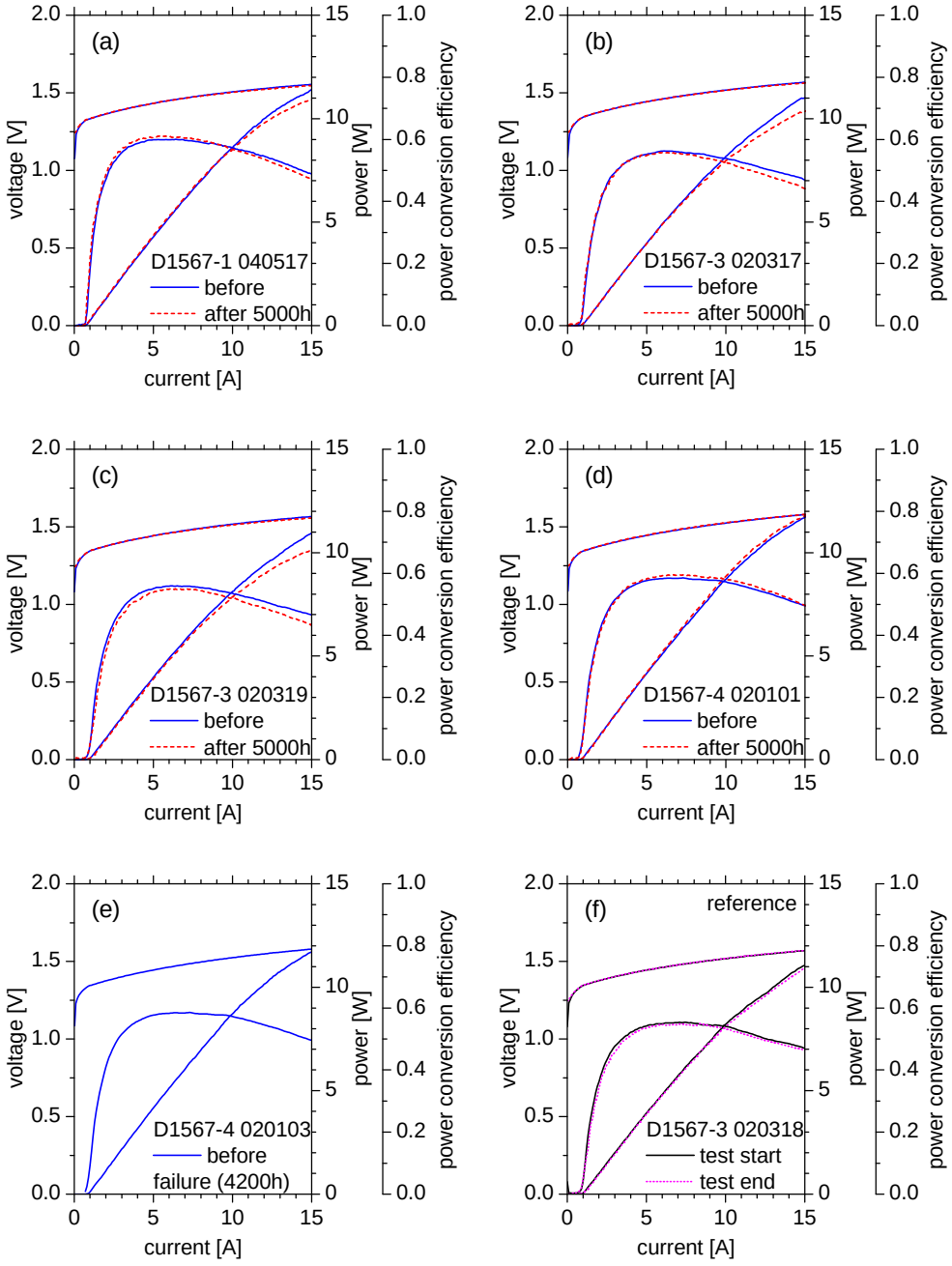

Figure 4.30: Power-voltage-current characteristics of DFB-BA lasers before and after the first $\approx 5150\,\mathrm{h}$ of the reliability test, measured at $25\,^{\circ}\mathrm{C}$ heatsink temperature.

Table 4.6: Changes in threshold current and slope efficiency before and after $\approx 5150\,\mathrm{h}$ lifetime testing. The device, marked with $*$, has not been in the reliability test and was measured together with the other lasers for reference.

wafer	laser	$I_{\mathrm{th}}^{\mathrm{start}}$ [mA]	$I_{\mathrm{th}}^{5000\,\mathrm{h}}$ [mA]	S^{start} [WA^{-1}]	$S^{5000\,\mathrm{h}}$ [WA^{-1}]
D1567-1	040517	749	715	1.030	1.035
D1567-3	020317	926	909	0.998	0.987
	020319	959	1022	0.996	0.986
D1567-4	020101	890	942	1.024	1.047
	020103	841	–	1.027	–
D1567-3	020318*	971	1033	0.981	0.981

DFB-BA lasers which have been in the reliability test and additionally, for laser D1567-3 020318, each before and after the $\approx 5150,\mathrm{h}$ lasting experiment. To enable a better comparability of the spectral position of the Bragg wavelength, a gray dash-dotted line is depicted in the figures at 975.0 nm. The spectral density is linearly scaled between zero counts (0 %) and the highest number of counts which has been detected on the CCD-chip in the spectrometer during the measurement of a certain spectral map (100 %). The spectral maps shown, are dominated by the fundamental DFB mode at $\sim 975\,\mathrm{nm}$. Furthermore, the spectra of the DFB-BA lasers are characterized by the onset of lasing on FP-like modes at high currents ($I > 9\,\mathrm{A}$) and at longer wavelengths ($\lambda > 978\,\mathrm{nm}$). Some of the devices are also lasing on the higher-order waveguide mode at $< 970\,\mathrm{nm}$ (D1567-4 020101 and D1567-4 020103). The spectral properties of the DFB-BA lasers are not significantly changed after the reliability test, compared to the measurements before the reliability test. In detail, the spectral position of the fundamental Bragg wavelength and its wavelength shift with the injection current is nearly unchanged for all devices. Even lasing on FP-like modes is nearly unchanged with respect to the current values, at which FP-like modes occur, with respect to the wavelength range and the spectral density distribution, relative to the DFB stabilized part of the spectrum. The current range, wavelength and spectral

density distribution of the higher-order modes which appear in the spectrum of laser D1567-4 020101 is also not changed after the reliability test. As one might have expected in particular, the spectral properties of the refernce device D1567-3 020318 which was not included in the reliability test, have not changed significantly as well.

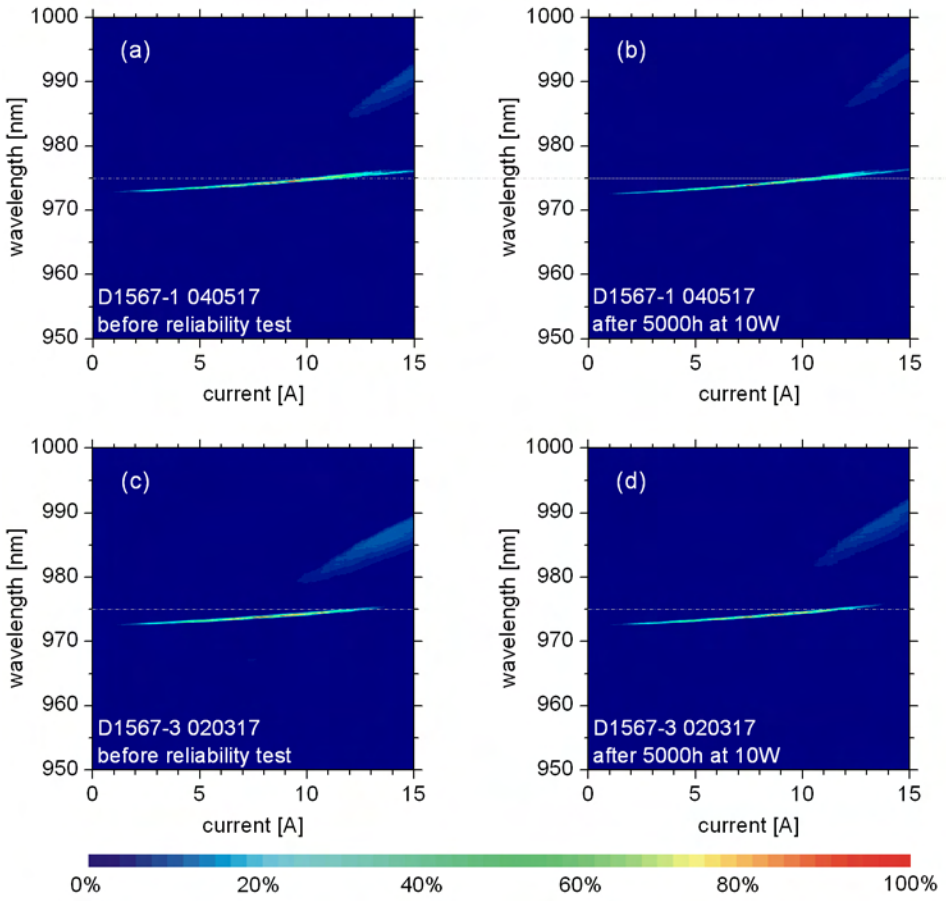

Figure 4.31: Spectral maps of DFB-BA lasers before and after the 5000 h reliability test, measured at 25 °C. (a) Laser D1567-1 040517 before the reliability test. (b) Laser D1567-1 040517 after the reliability test. (c) Laser D1567-3 020317 before the reliability test. (d) Laser D1567-3 020317 after the reliability test.

Finally, the reason for the failure of DFB-BA laser D1567-4 020103 after $\approx$ 4200 h has been studied. No damage was observed at the facets using a light microscope and even no evidence for COMD could be found in the electroluminescence from both facets. Therefore, the device has been prepared for investigation of internal defects with cathodoluminescence (CL).

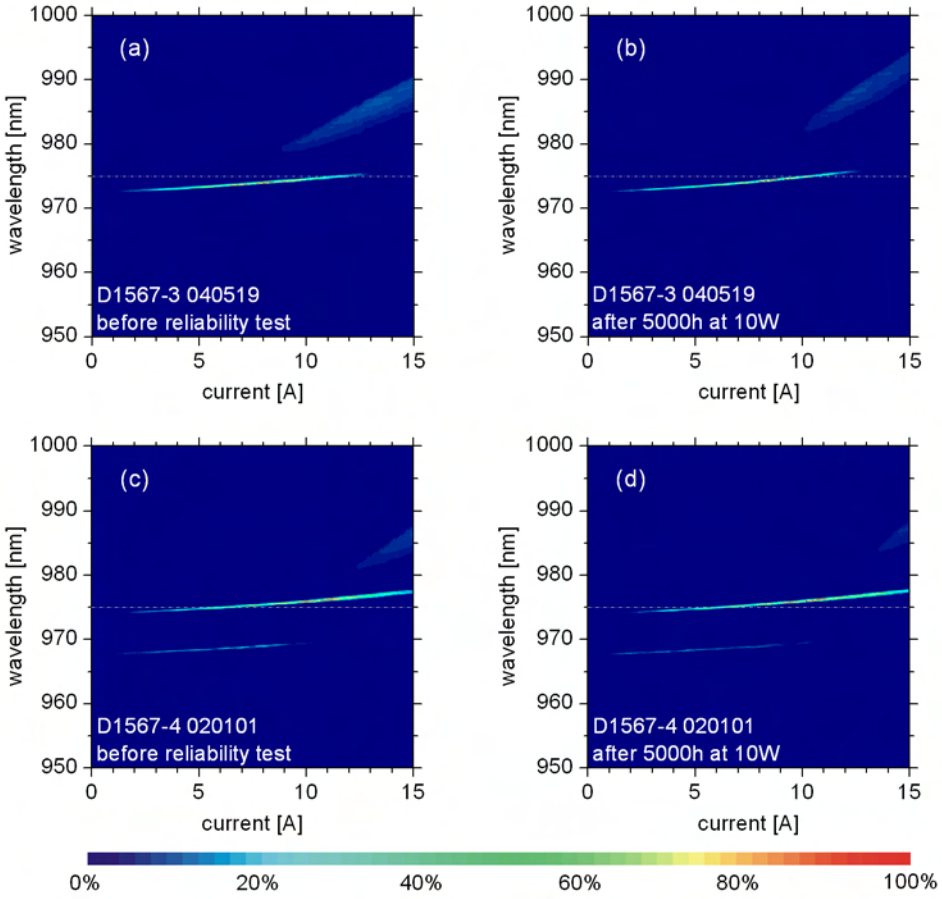

Figure 4.32: Spectral maps of DFB-BA lasers before and after the 5000 h reliability test, measured at 25 °C. (a) Laser D1567-3 020319 before the reliability test. (b) Laser D1567-3 020319 after the reliability test. (c) Laser D1567-4 020101 before the reliability test. (d) Laser D1567-4 020101 after the reliability test.

The $\sim 150\,\mu$m thick GaAs substrate was removed from the n-side with selective etching in a stripe around the electrically pumped area of the DFB-BA laser. Then, CL at 30 kV accelerating voltage and a temperature of 80 K was used to analyze internal defects. The spectrally integrated signal was detected, showing a typical internal defect which is clearly separated from both facets. This is depicted in Fig. 4.34.

In summary, reliable operation of DFB-BA lasers at a CW optical output power of 10 W over > 8000 h has been demonstrated for the first time in a preliminary reliability test. Lifetimes of more than 10000 h can be derived, assuming that $\leq 20\,\%$ current increase are acceptable for reliable operation.

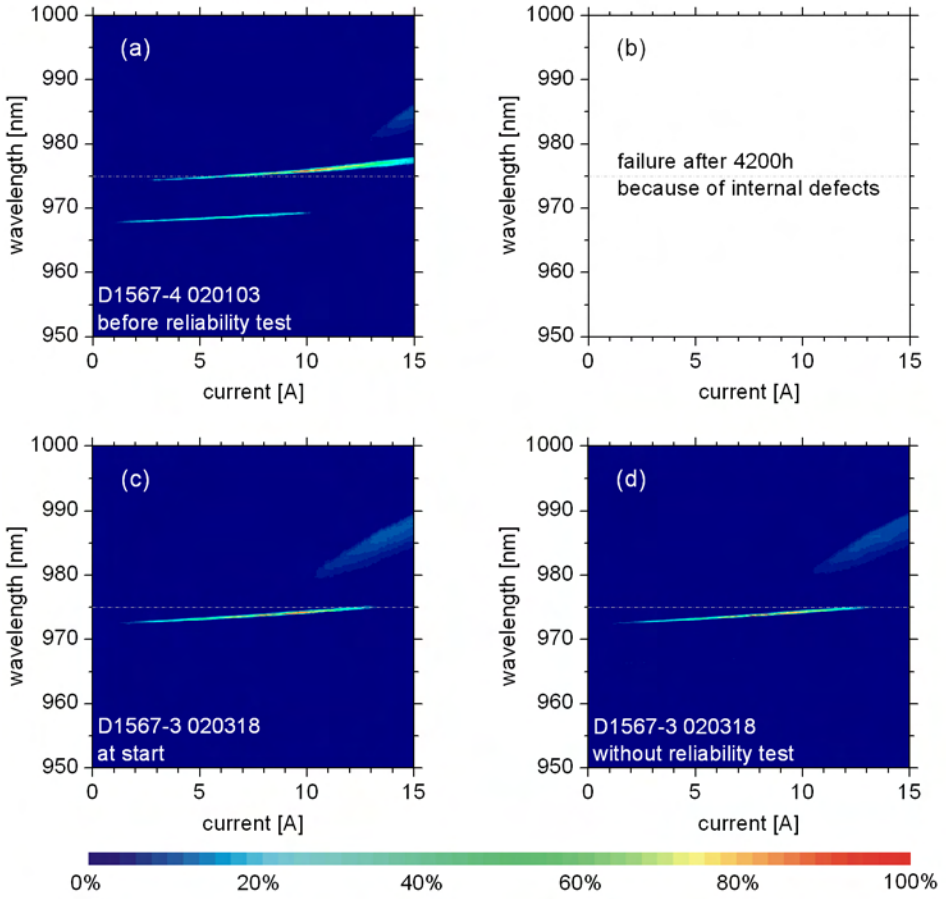

Figure 4.33: Spectral maps of DFB-BA lasers before and after the 5000 h reliability test, measured at 25 °C. (a) Laser D1567-4 020103 before the reliability test. (b) Laser D1567-4 020103 failed during the reliability test after ≈ 4200 h. (c) Laser D1567-3 020318 (not included in the reliability test) at the start of the reliability test. (d) Laser D1567-3 020318 (not included in the reliability test) after the reliability test.

A comparison of the power-voltage-current characteristics and spectral maps before and after the first 5150 h shows only minor degradations. The most significant change is an increase in the roll-over of the power characteristics at currents above 10 A. The reliability test is continued for four of the five devices which have already achieved up to 8515 h without failure. One device failed after ≈ 4200 h because of an internal defect.

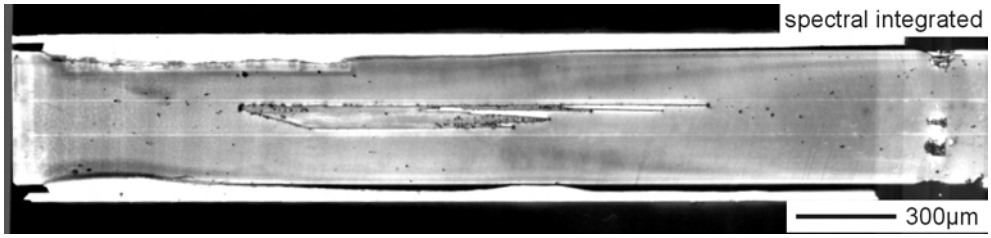

Figure 4.34: Spectrally integrated cathodoluminescence investigation of the internal defect in DFB-BA laser D1465-4 020103 which occurred after $\approx 4200\,\mathrm{h}$.

4.4 Comparison of experimental and theoretical results for threshold current and slope efficiency

In the following section, measured threshold currents and slope efficiencies are compared to values, determined from the numerical calculation of the threshold gain and differential quantum efficiency as described in chapter 1.2.4. In table 4.7, the parameters used for the numerical calculation are summarized. Note that in contrast to section 3.5 in iteration I, threshold currents were calculated for a stripe width of 90 and 100 μm and slope efficiencies for lasing wavelength of 975 and 970 nm, so that the results can be compared to both, measurement results from wafers D1567-1, D1567-3, D1567-4, D1567-5 and to the most efficient DFB-BA laser in iteration II, D1560-2 040925 from the test wafer.

In principle, threshold currents and slope efficiencies were calculated in the same way as presented in section 3.5. From the threshold gain and differential quantum efficiency, the threshold current and slope efficiency were calculated with equations 3.9 and 3.10 and are here shown in Fig. 4.35. Additionally, the measured values for the lasers, given in table 4.3, are depicted. Furthermore, the results from iteration I (table 3.7) are shown to demonstrate the agreements and disagreements of the experimental results with the calculations.

The measured values for the threshold current and slope efficiency are plotted at $\kappa = 0.55\,\mathrm{cm}^{-1}$, because this coupling coefficient was determined from parameter extraction of the stopband in ASE spectra below threshold as discussed in section 4.3.8. A very good agreement, both in threshold current and slope efficiency, is found between the calculated curve (red dashed line: $W = 100\,\mu$m, $\lambda = 970\,$nm) and the measured values from laser D1560-2 040925. A good overall agreement between the calculated and measured

Table 4.7: The fixed physical variables, their notations and values, used in the numerical simulation.

Variable	Notation	Value
Cavity length	L	$3000\,\mu$m
Contact stripe width	W	90 and $100\,\mu$m
Reflectivity, rear facet	R_r	96.00 %
Reflectivity, front facet	R_f	0.09 %
Effective index	n_eff	3.434308
Grating period	Λ	283.9 and 282.4 nm
Coupling coefficient	κ	$(0.0, 0.1, ..., 10.0)\,\mathrm{cm}^{-1}$
Rear facet phase sections	d_a	$(0.00, 0.02, ..., 0.48)\Lambda$
Internal loss	α_i	$0.80\,\mathrm{cm}^{-1}$
Internal quantum efficiency	η_i	0.90
Transparency current density	j_th	$151\,\mathrm{Acm}^{-2}$

slope efficiencies was already found for the DFB-BA lasers from iteration I. Nevertheless, the values of the coupling coefficients were uncertain in iteration I. Thus, the very good agreement between the measured slope efficiency from DFB-BA laser D1560-2 040925 and the corresponding calculated slope efficiency (Fig. 4.35 (b)) is an important verification that the numerical calculation describes the slope efficiency quite well, because DFB-RW lasers from wafer D1560-2 were used for the experimental determination of the DFB coupling coefficient. This experimental parameter extraction of the coupling coefficient (see section 4.3.8) was more reliable than in iteration I (see section 3.4.10).

Also the good agreement between the measured and calculated slope efficiency for this special DFB-BA laser is of particular importance (Fig. 4.35 (a)). For the DFB-BA lasers from iteration I, the measured threshold currents were $\sim 250\,\mathrm{mA}$ higher than the calculated values. This has been attributed to the spectral detuning between the gain peak and Bragg wavelength of the fundamental mode which is not included in the calculation, as well as to lasing on higher-order waveguide modes (also not considered in the calculation). For laser D1560-2 040925, the spectral detuning is significantly

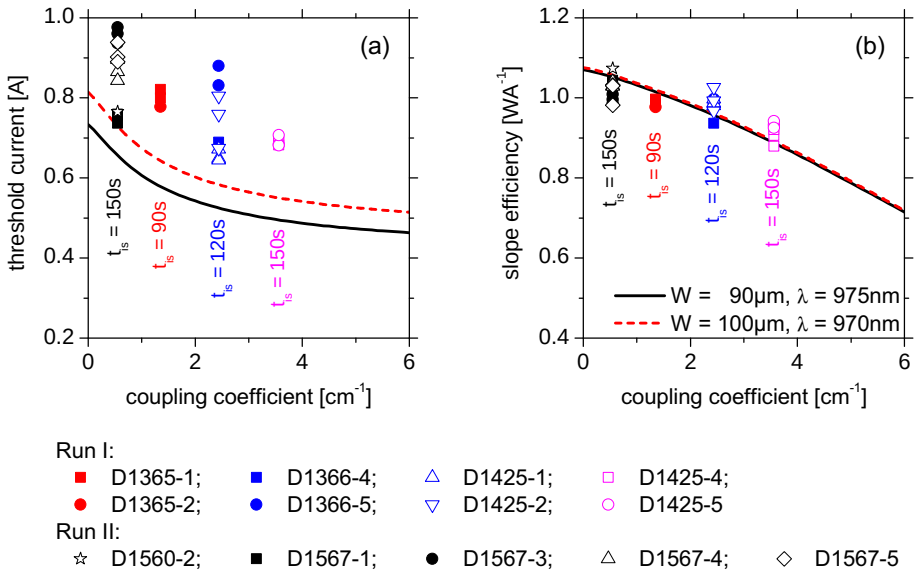

Figure 4.35: Calculated and measured threshold current and slope efficiency. (a) Calculated threshold current (black solid line ($W = 90\,\mu$m) and red dashed line ($W = 100\,\mu$m)) and measured values (symbols) from table 4.3. (b) Calculated slope efficiency (black solid line ($\lambda = 975\,$nm) and red dashed line ($\lambda = 970\,$nm)) and measured values (symbols) from table 4.3.

lower ($\approx 2\,$nm) than for the lasers from iteration I ($5.7 - 6.6\,$nm) and the other DFB-BA lasers from iteration II ($3.74 - 5.55\,$nm). Furthermore, the spectrum of this laser is free of any higher-order modes at a heatsink temperature of 25°C (see Fig. 4.19 (a)). Thus, the measured threshold current must be close to the calculated value (and this is the case indeed) if the arguments mentioned above are valid.

Even though the spectral detuning for the lasers from wafer D1567-1 is higher ($3.74\,$nm) than for laser D1560-2 ($2\,$nm) a very good agreement is observed between the measured and calculated threshold current (black line: $W = 90\,\mu$m, $\lambda = 975\,$nm). This good agreement can be presumably attributed to the fact that close to threshold, lasers from this wafer are exclusively lasing on the fundamental waveguide mode (see example spectral map in Fig. 4.20 (a)). Also the slope efficiency coincides with the calculation.

For the lasers from wafers D1567-3, D1567-4 and D1567-5, systematic deviations between the calculated and measured threshold currents and slope efficiencies are observed. On the one hand, the measured threshold currents are $190 - 320\,$mA higher than calculated (without consideration of spectra detuning and higher-order modes). On the other hand, the slope efficiencies

are up to $0.07\,\mathrm{W\,A^{-1}}$ lower than calculated. The deviations, depicted in Fig. 4.35 are expected to be a reason of the spectral offset between the gain peak wavelength and Bragg wavelength of the DFB grating at threshold, lasing on higher-order vertical waveguide DFB modes and possible small differences in the coupling coefficient.

Calculated power-voltage characteristics for coupling coefficients of 0.0 (FP laser), 0.5 and $2.0\,\mathrm{cm^{-1}}$ are compared to the measured power-voltage-current characteristics of DFB-BA laser D1560-2 040925 in Fig. 4.36. The calculated and measured threshold currents and slope efficiencies are noted aside. The calculated threshold current decreases from 815 mA at $\kappa = 0.0\,\mathrm{cm^{-1}}$ to 603 mA at $\kappa = 2.0\,\mathrm{cm^{-1}}$. Simultaneously, the calculated slope efficiency decreases from 1.073 to $0.986\,\mathrm{W\,A^{-1}}$.

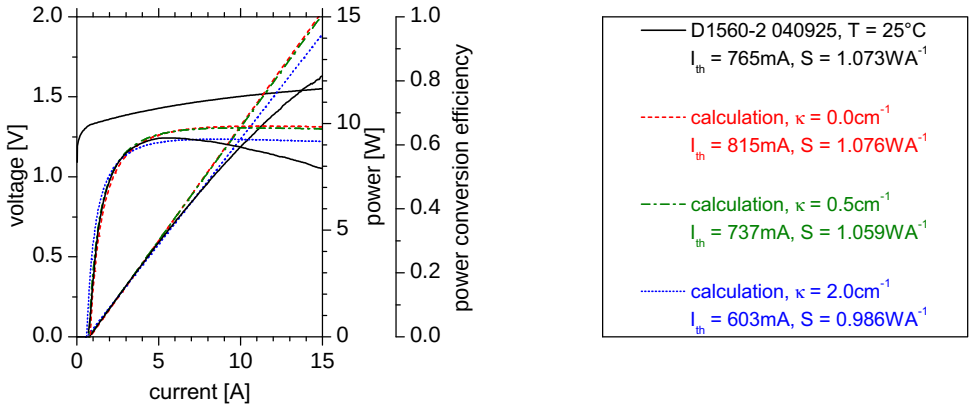

Figure 4.36: Comparison of the P-U-I characteristics for the numerical calculation and the measured characteristics for the laser D1560-2 040925. For the calculated characteristics, the threshold current and slope efficiency, gained for $\kappa = 0.0$, 0.5 and $1.5\,\mathrm{cm^{-1}}$, have been used.

The best overall agreement is observed between the measured power characteristics and the calculated characteristics for $\kappa = 0.5\,\mathrm{cm^{-1}}$. This agreement is a further verification that the experimentally determined coupling coefficient of this lasers (average value $\kappa = 0.55\,\mathrm{cm^{-1}}$) is determined precisely. Differences between the measured and calculated power characteristics for $\kappa = 0.5\,\mathrm{cm^{-1}}$ occur at currents above $\approx 5\,\mathrm{A}$ where a very weak roll-over of the measured power begins. This is even better visible in the resulting efficiency characteristics which decreases above 5.74 A (measured). A further increase of the power characteristics could have been presumably achieve by using a larger spectral detuning but this requires a better suppression of the higher-order modes to sustain a narrow spectrum.

To conclude, a very good agreement between the measured and calculated threshold currents and slope efficiencies is found for a DFB-BA laser with a small spectral detuning between the gain peak and Bragg wavelength which is exclusively lasing on the fundamental waveguide mode. This shows that the calculation of the threshold current and slope efficiency, based on the approach described in section 1.2.4, is applicable to predetermine the power characteristics of DFB-BA lasers (spectral detuning and higher-order modes are not considered in the calculation). For DFB-BA lasers from wafers with a larger spectral detuning, the measured threshold currents are $190-320\,\mathrm{mA}$ higher than calculated. Compared to DFB-BA lasers from iteration I, the average slope efficiency of DFB-BA lasers from iteration II is increased as predetermined from the calculations. Nevertheless, only two devices achieve slope efficiencies of $\geq 1.05\,\mathrm{W\,A^{-1}}$ as targeted.

Chapter 5

Evaluation of the electro-optical properties: Comparison to other publications

In this chapter, selected publications on wavelength stabilized BA lasers lasers are compared to experimental and theoretical results which have been obtained for DFB-BA lasers during *this work* (here always *emphasized* for clarity). Thereby the selected III/V semiconductor compounds and design properties of the DFB grating are discussed, as well as the technical progress in fabrication of the gratings which has enabled to improve the optical output power, voltage and power conversion efficiency close to the values for reference BA devices. For this comparison, published experimental results from DFB-BA lasers were taken into account and in addition one publication about high power DBR-BA lasers as an alternative way to realize spectrally stabilized high power BA lasers, having their own specific difficulties in design optimization and fabrication.

By comparing other published results to the results from *this work*, the importance of a low DFB coupling strength ($\kappa \cdot L$), optimized spectral detuning (between the Bragg wavelength of the DFB grating and gain peak wavelength) and AR front facet coating which are essential to achieve high power conversion efficiency and high output power from a DFB-BA lasers with sufficient wavelength stabilization, becomes even more clear.

Publication 1 T. Earles *et al.*: "1.1 W continuous-wave, narrow spectral width (< 1) emission from broad-stripe, distributed-feedback diode lasers ($\lambda = 0.893\mu$m)", Applied Physics Letters, Vol. **73**, 2072–2074 (1998)

In 1998, Earles *et al.* [Ear98] report on the development of DFB-BA lasers

based on a two step epitaxy process using MOCVD. A second-order, 50 nm deep DFB grating is wet etched into the surface of the completed $In_{0.47}Ga_{0.53}P$ waveguide after the first epitaxy step (holographically patterned). The 650 nm thick symmetric waveguide is embedded between $In_{0.5}(Ga_{0.5}Al_{0.5})_{0.5}P$ cladding layers. The active region consists of an $In_{0.03}Ga_{0.97}As$ DQW with 20 nm thick InGaAsP barriers. Thus, the fundamental fabrication methods are comparable to *this work*. The authors report they target good regrowth quality and low interface loss by etching the grating into the aluminum-free waveguide which is less susceptible for oxidization than aluminum-containing material. Nevertheless, they overgrow the grating corrugation with the aluminum-containing cladding material ($In_{0.5}(Ga_{0.5}Al_{0.5})_{0.5}P$). The usage of aluminum in the cladding layers instead of aluminum-free materials is motivated by a better carrier confinement due to the higher band-gap which increases the internal quantum efficiency and decreases the temperature sensitivity. A scheme of the laser structure is shown in Fig. 5.1, reproduced from [Ear98].

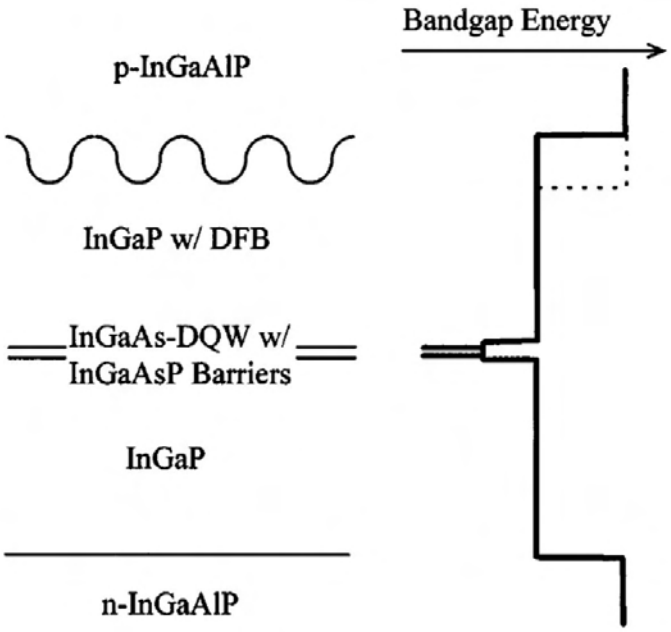

FIG. 1. Schematic cross section of DFB 0.893 μm emitting laser structure. The active region consists of two 55 Å wide $In_{0.03}Ga_{0.97}As$ quantum wells surrounded by 200 Å thick InGaAsP (E_g=1.62 eV) barriers and 0.3 μm thick InGaP confinement layers. The grating has a period of 2740 Å and a depth of ~500 Å.

Figure 5.1: Reprinted with permission from Earles *et al.* [Ear98]. Copyright 1998, American Institute of Physics.

The authors say, they have designed the waveguide structure (thickness) to prevent lasing on the second higher-order transverse mode, while lasing on the first higher-order mode is argued to be suppressed by its poor optical confinement factor. Indeed, in this work, lasing on higher-order vertical modes was observed for DFB BA lasers from iteration I and II and identified to limit the applicable (narrow single spectral peak) range in drive current and temperature. In addition it is shown in this work, that lasing on higher-order vertical modes in DFB-BA lasers can be much less suppressed compared to FP-BA lasers, if the DFB coupling coefficient increases with the vertical mode order. Thus, the suppression of higher-order modes cannot be estimated only from the optical confinement factor with the active region (low values increase the threshold current) and internal optical loss (high values increase the threshold current) but must be evaluated with respect to the individual coupling coefficient (high values decrease the threshold current).

A coupling coefficient of $\kappa = 7\,\mathrm{cm}^{-1}$ has been determined for the DFB grating from sub-threshold ASE spectra as shown in Fig. 5.2, reproduced from [Ear98]. The shape of the grating is reported to be nearly sinusoidal shaped. The authors have calculated the coupling coefficient of the DFB grating as $\kappa = 9.5\,\mathrm{cm}^{-1}$.

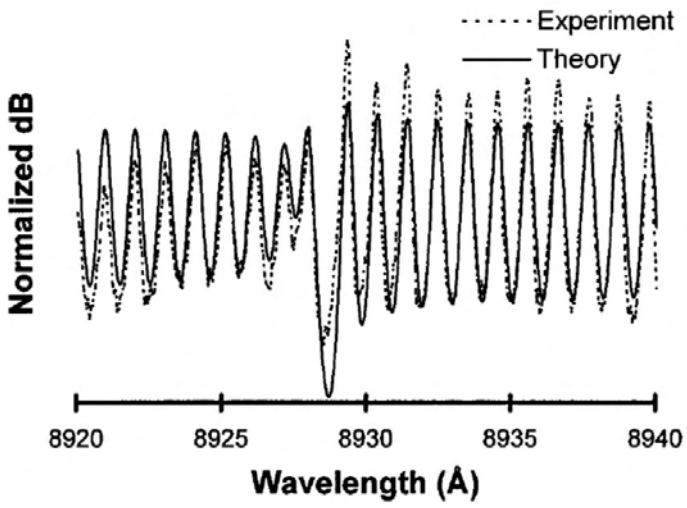

FIG. 4. Comparison of theoretical and experimental amplified spontaneous emission spectra. The modeled spectrum has a κL value of 0.7.

Figure 5.2: Reprinted with permission from Earles *et al.* [Ear98]. Copyright 1998, American Institute of Physics.

DFB-BA laser bars are facet coated to obtain front and rear facet reflec-

tivity of $R_f = 5\,\%$ and $R_r = 95\,\%$, respectively. Single emitters with a stripe width of 100μm and a cavity length of 1000μm have been used measure power-voltage-current characteristics and spectra at 10°C. The characteristics obtained are reproduced here in Fig. 5.3 from [Ear98]. A threshold current of 240 m A ($j_{th} = 240\,\mathrm{A\,cm^2}$) and a slope efficiency of $\cong 0.708\,\mathrm{W\,A^{-1}}$ ($\eta_d = 51\,\%$) can be determined from the power-voltage-current characteristics. A peak power conversion efficiency of 32 % is reached at 1.1 W output power and is approximately constant till the measured maximum power, slightly above 1.2 W. Since 1998, the maximum optical output power obtained with a DFB-BA laser has been increased by a factor of ≈ 10 in *this work* and simultaneously, the peak power conversion efficiency is nearly doubled.

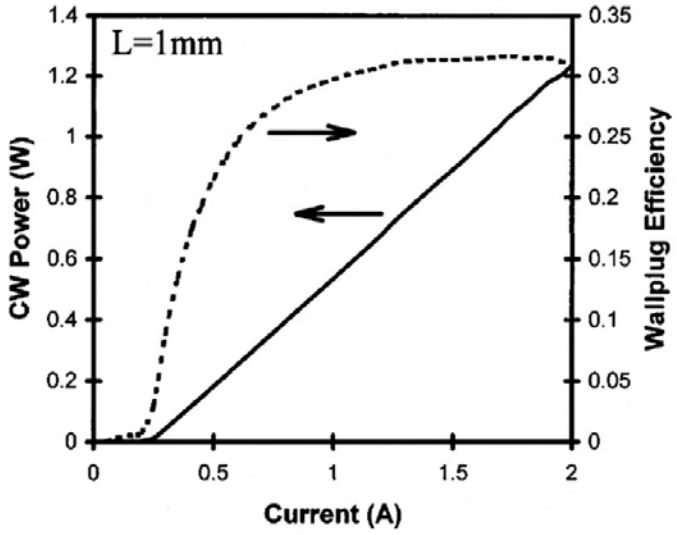

FIG. 2. Cw light current and wallplug efficiency η_p, characteristics for a 100 μm×1 mm contact area, 5%/95% facet-coated DFB laser (λ =0.893 μm) at 10 °C heatsink temperature. The differential quantum efficiency is 51% and the η_p reaches a maximum of 32% at 1.1 W.

Figure 5.3: Reprinted with permission from Earles *et al.* [Ear98]. Copyright 1998, American Institute of Physics.

Earles *et al.* also compare their results for DFB-BA lasers to FP-BA refernce lasers (at 20°C) from the same vertical design but without a grating, where they measure a threshold current density of $j_{th} = 225\,\mathrm{A\,cm^2}$ and a differential quantum efficiency of $\eta_d = 62\,\%$. Unfortunately, the comparability is hindered because of the different temperatures which have been used for the characterization of the devices. Possibly, the lower temperature was

used for the DFB-BA lasers to align the gain spectrum with the Bragg wavelength of the DFB grating. The differential quantum efficiency is reduced from 62 % (FP-BA reference lasers) to 51 % (DFB-BA lasers), which is 82 % of the value for the reference devices. In *this work*, the decrease in the differential quantum efficiency has been successfully reduced from ≈ 86 % (FP-BA reference lasers) up to ≈ 84 % (best DFB-BA laser D1560-2 040925), 98 % of the value for the reference devices. Earles *et al.* also provide the characteristic temperatures for threshold current and slope efficiency of $T_0 = 200\,\mathrm{K}$ and $T_1 = 480\,\mathrm{K}$, respectively. FP-BA reference lasers in *this work* have characteristic temperatures for threshold current and slope efficiency of $T_0 = 145\,\mathrm{K}$ and $T_1 = 422\,\mathrm{K}$.

Earles *et al.* distinguish, that the relatively small coupling strength of $\kappa \cdot L = 0.7$ provides for efficient operation of the DFB-BA lasers. This fact is in good agreement with what has been discovered in *this work* experimentally and theoretically. Nevertheless, a slope efficiency of only $\cong 0.708\,\mathrm{W\,A^{-1}}$ ($\eta_\mathrm{d} = 51\,\%$) is determined for the DFB-BA lasers, but $\eta_\mathrm{d} = 62\,\%$ for FP reference lasers. The authors analyze what causes the reduction in differential quantum efficiency by ≈ 18 % when the DFB grating is introduced into the laser structure. The authors determine the internal loss α_i of FP reference lasers to be $6.6\,\mathrm{cm^{-1}}$ and $\approx 7\,\mathrm{cm^{-1}}$ for DFB lasers (detuned from Bragg wavelength). Thus, the grating does not significantly increase the internal loss. This confirms that the grating fabrication on the aluminum-free waveguide material and regrowth with the aluminum-containing cladding layer causes no strong contamination with oxygen and other impurities. Therefore, the reason for the degradation in differential quantum efficiency can be identified as the difference in resonator loss which is $\alpha_\mathrm{DFB} \sim 6\,\mathrm{cm^{-1}}$ and $\alpha_\mathrm{m} \approx 15\,\mathrm{cm^{-1}}$.

A Figure with CW spectra at 0.5 and 1.1 W is shown in Fig. 5.4, reproduced from [Ear98]. At 0.5 W, the spectrum is dominated by a single peak (0.05 nm FWHM and ≈ 0.2 nm with 95 % power content) but at 1.1 W, three peaks can be observed (0.09 nm FWHM and ≈ 0.3 nm with 95 % power content). In *this work* spectral width of 0.2 to ≈ 0.3 nm with 95 % power content has been obtained for higher output powers of 1 to 9 W as depicted in Fig. 3.32, 3.33 , 4.22, 4.23 and 4.24.

A further figure with calculated longitudinal field profiles of DFB lasers for $\kappa \cdot L = 0.5$, 1.0 and 2.0 is presented in the publication but not reproduced here. Earles *et al.* say that $0.5 \leq \kappa \cdot L \leq 1.0$ provides relatively uniform longitudinal field profiles and good suppression of multiple longitudinal mode operation due to longitudinal gain spatial hole burning. Unfortunately, the phase relations at the facets have not been considered in a clearly comprehensible way ("assume no phase shifts at the facets" [Ear98]). In Fig. 1.24 in this work it is shown, that at $\kappa \cdot L \approx 1$, field profiles can be uniform or not,

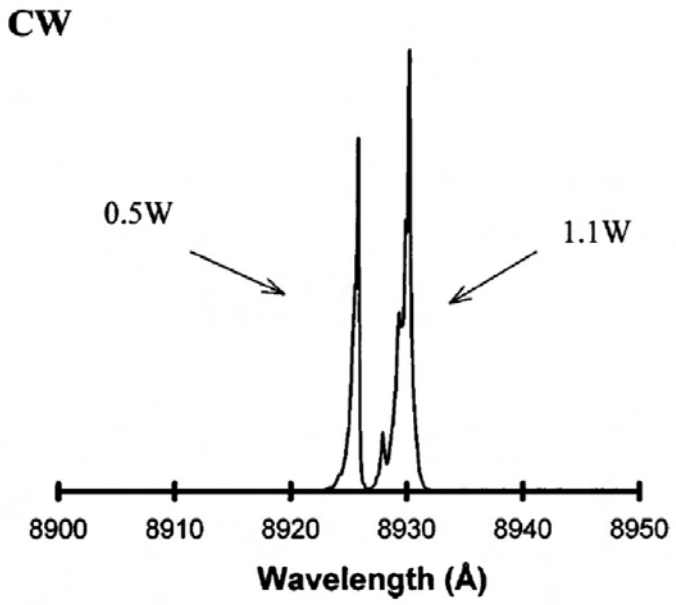

FIG. 3. High-power cw spectra for 100 μm stripe DFB laser operation at 10 °C heatsink temperature. The spectra have a temperature dependence of 0.6 Å/°C.

Figure 5.4: Reprinted with permission from Earles *et al.* [Ear98]. Copyright 1998, American Institute of Physics.

depending on the exact phase relation, but the averaged longitudinal field profile is indeed relatively uniform. Such averaging can be motivated with the fact that the phase relations will change along the facts of a BA laser (in lateral direction) due to limited accuracy in the alignment between the DFB grating ridges (holography) and the crystal (important for cleaved facets).

Publication 2 C.H. Chang *et al.*: "High CW power narrow-spectral width (< 1.5) 980 nm broad-stripe distributed feedback diode lasers", Electronics Letters, Vol. **36**, 954–955 (2000)

In 2000, Chang *et al.* [Cha00] have published experimental results obtained with 980 nm DFB-BA lasers. Obviously, the authors have adapted the fabrication methods and epitaxy design from [Ear98] to the new wavelength. As a motivation, they say that "High-power spatially incoherent diode lasers with narrow spectral width in the 940 - 980 nm wavelength range are desirable for pumping solid state lasers and instrumentation applications" [Cha00].

The epitaxy structure consists of a 1 μm thick InGaAsP waveguide, em-

bedded between 1 μm thick InGaP cladding layers. An $In_{0.2}Ga_{0.8}As$ DQW is located symmetrically in the waveguide and separated by 20 nm thick InGaAsP barriers. Details are shown in Fig 5.5, reproduced from Chang *et al.* [Cha00]. In contrast to [Ear98], the DFB grating is now placed in an completely aluminum-free epitaxy design, regrown with the aluminum-free cladding layer compound. This may help to avoid the formation of aluminum oxide during the grating fabrication.

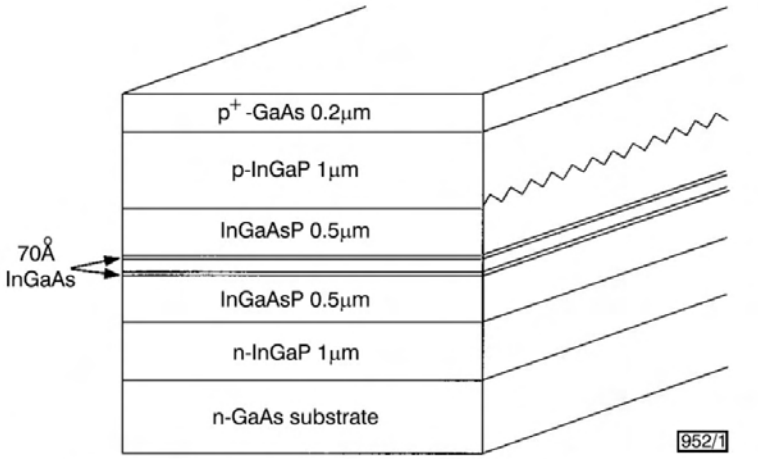

Fig. 1 *Schematic view of layered structure for Al-free, broad-waveguide 0.98 µm-emitting DFB laser*

Figure 5.5: Reprinted with permission from Chang *et al.* [Cha00]. Copyright 2000, The Institution of Engineering and Technology.

Chang *et al.* report, they have calculated the DFB coupling coefficient to be $\kappa_{\text{calc}} = 1.5\,\text{cm}^{-1}$ and $\kappa_{\text{meas}} < 2\,\text{cm}^{-1}$ has been determined by fitting ASE spectra to theory. Thus, $\kappa \cdot L \approx 0.3$ with $L = 2000\,\mu$m cavity length. The DFB-BA lasers are weakly coupled, approximately to the coupling strength of the DFB grating used in iteration II of t*his work*.

Single emitter devices with a stripe width if $W = 100\,\mu$m and a cavity length of $L = 2000\,\mu$m and facet reflectivity of $R_{\text{f}} = 5\,\%$ and $R_{\text{r}} = 95\,\%$ were investigated at 23 °C under CW conditions. Figure 5.6, reproduced from Chang *et al.* [Cha00], shows the power-voltage-current characteristics, from which a threshold current density of $j_{\text{th}} = 250\,\text{A}\,\text{cm}^2$ ($I_{\text{th}} \approx 500\,\text{mA}$ threshold current) and a differential quantum efficiency of $\eta_{\text{d}} = 52\,\%$ ($S \approx 0.658\,\text{W}\,\text{A}^{-1}$ slope efficiency) can be determined. At the highest current of $I = 2\,\text{A}$, the power conversion efficiency reaches 33 % at $P = 1\,\text{W}$ output power.

Experimental results for reference 970 nm FP-BA lasers with the same epitaxy design, stripe width, cavity length and facet coating have been pre-

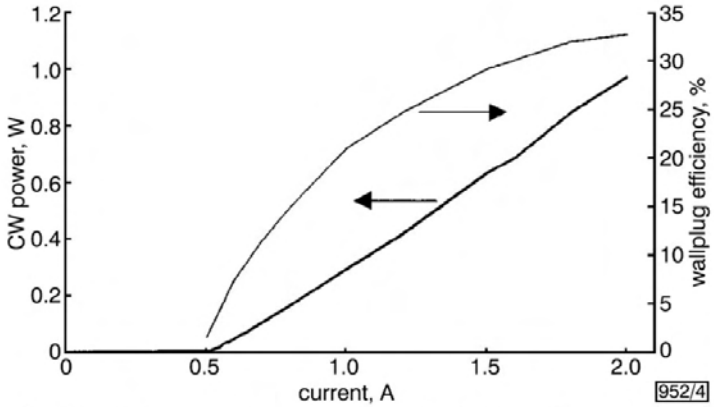

Fig. 2 *CW light-current characteristics and wallplug efficiency for 100 µm × 2 mm contact area, 5/95% facet-coated DFB laser (λ = 976 nm)*

Figure 5.6: Reprinted with permission from Chang *et al.* [Cha00]. Copyright 2000, The Institution of Engineering and Technology.

sented by part of the authors from [Cha00] in [AM98], but characterized at 10 °C. This reference lasers have approximately the same threshold current ($I_{\mathrm{th}} \approx 500\,\mathrm{mA}$) but a significantly higher differential quantum efficiency of $\eta_{\mathrm{d}} = 85\,\%$ ($S \approx 1.09\,\mathrm{W\,A^{-1}}$ slope efficiency).

The differences can be understood with respect to the following physical properties. Firstly, the DFB-BA lasers have an internal optical loss of $\alpha_{\mathrm{i}}^{\mathrm{DFB}} \sim 6\,\mathrm{cm^{-1}}$ at 23 °C [Cha00]. In contrast, the internal optical loss of the reference devices is only $\alpha_{\mathrm{i}}^{\mathrm{FP}} = 1\,\mathrm{cm^{-1}}$ at 10 °C [AM98]. Thus, the integration of the DFB grating has caused the internal optical loss to increase by $\sim 5\,\mathrm{cm^{-1}}$. The authors speculate that the increase in internal optical loss occurs because of high radiation loss from the second-order DFB grating. This seems comprehensible because the gratings are reported to be sinusoidal shaped which implicates that they have a duty cycle close to 1/2. The results are in contrast to what has been reported for 893 nm DFB-BA lasers in [Ear98] where the increase in the internal optical loss was only $\sim 0.4\,\mathrm{cm^{-1}}$. DFB-BA lasers and FP-BA reference devices in *this work* have comparable internal optical loss of $\alpha_{\mathrm{i}} \approx 0.9\,\mathrm{cm^{-1}}$ and radiation loss is assumed to be negligible do to an optimized duty cycle of $\approx 1/4$.

Secondly, the DFB-BA lasers have the same facet coating as the FP-BA reference lasers. For a weakly coupled DFB-BA lasers with $\kappa \cdot L \approx 0.3$, $R_{\mathrm{f}} = 5\,\%$ is a very high front facet reflectivity which on the one hand decreases the threshold current and slope efficiency and on the other hand, reduces the suppression of lasing on FP like modes at the maximum of the gain spectrum.

In *this work*, lasing on FP-like modes has been observed for DFB-BA lasers with a not sufficient AR coating of the front facet and the importance of the front facet coating for a broad DFB locking range in current and heatsink temperature is studied.

Reference 970 nm FP-BA lasers [AM98] were driven at $T = 10\,^{\circ}\mathrm{C}$ up to CW injection currents of 13 A where they achieve an optical output power of $P_{\mathrm{opt}} = 10.6\,\mathrm{W}$ with $\approx 41\,\%$ power conversion efficiency and have a peak power conversion efficiency of $\approx 58\,\%$. Thus, the question arises why DFB-BA lasers have not been also investigated at comparable high currents as done in *this work*. Chang *et al.* also do not show current characteristics and compare them to the current characteristics from the reference devices. Nevertheless, from the power and efficiency characteristics depicted in [Cha00] and [AM98] one can derive that at $I = 2\,\mathrm{A}$, the voltage of the DFB-BA lasers is $U_{\mathrm{DFB}} \approx 1.52\,\mathrm{V}$ (23 °C) and the voltage of the reference FP-BA devices is $U_{\mathrm{FP}} \approx 1.48\,\mathrm{V}$ (10 °C), respectively. Considering that the voltage drop increases with decreasing temperature, this indicates that the voltage of the DFB-BA lasers is increased. The elimination of any excess voltage for DFB-BA lasers (in iteration II) compared to reference BA lasers by using an optimized floating grating design is one important achievement in *this work* towards highly efficient DFB-BA lasers.

Possibly, the question why the power-voltage-current characteristics have not been measured up to higher currents than 2 A can be answered with respect to the CW optical spectrum at $P = 0.5$ and 1.0 W, shown in Fig. 5.7, reproduced from Chang *et al.* [Cha00]. Chang *et al.* denote that the CW spectral width of 2000 μm long devices is 0.05 nm FWHM at 0.5 W and 0.13 nm FWHM at 1.0 W. However, relatively broad spectral side peaks around $\approx$ 975.0 nm and $\approx$ 977.5 nm (the Bragg wavelength is close to $\approx$ 976 nm) seems to broaden the spectral width with 95 % power content significantly. In the publication, the origin for this spectral broadening is not explained. One could assume that lasing on FP-modes is the reason for the occurrence of the spectral side peaks. This assumption can be confirmed with respect to the DFB resonator loss of $\alpha_{\mathrm{DFB}} = 6.2\,\mathrm{cm}^{-1}$ [Cha00] and the mirror loss $\alpha_{\mathrm{m}} = 7.6\,\mathrm{cm}^{-1}$, which is only slightly smaller.

The authors furthermore say that "Beyond $\sim$ 0.5 W CW, oscillation at a second longitudinal resonance occurs" [Cha00]. Even though multiple longitudinal mode lasing is probable for the devices and has been observed in *this work* (from spectrally resolved near field and far field measurements), no evidence is given for this predication.

The importance of the publication from Chang *et al.* [Cha00] is that they have adapted the DFB-BA laser technology and fabrication from 893 nm [Ear98] to 980 nm and achieved comparable output powers and power con-

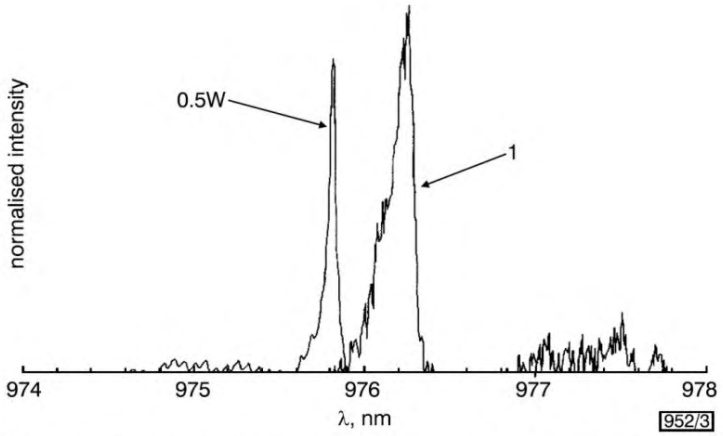

Fig. 3 *CW spectra for 100 µm stripe, 2 mm-long DFB laser operating at 0.5 W and 1 W output power*

Figure 5.7: Reprinted with permission from Chang *et al.* [Cha00]. Copyright 2000, The Institution of Engineering and Technology.

version efficiency with some disadvantages in the spectral stabilization. Nevertheless, the power, voltage and efficiency (−25 %) degradation compared to reference FP-BA devices is large. Therefore one can reason that optimizing the duty cycle of the DFB grating and using a better AR coated front facet could have significantly improved the performance of the DFB-BA lasers from Chang *et al.*

Publication 3 M. Kanskar *et al.*: "53 % wallplug efficiency 975 nm distributed feedback broad area laser", Electronics Letters, Vol. **42**, 1455–1457 (2006)

Kanskar *et al.* report on very efficient high power DFB-BA lasers at 975 nm [Kan06]. The authors have used a 1.1 μm thick waveguide and an InGaAs single quantum well (SQW). A second-order DFB grating is positioned at the p-side cladding layer as shown in Fig. 5.8 (reproduced from [Kan06]). The DFB grating is introduced into the layer structure with a two step epitaxy process, using holographically exposed photoresist patterning and etched 100 nm deep with reactive ion etching. Thus, the basic fabrication principles of the manufacturing process are the same as used in this work.

While the DFB grating in [Kan06] is etched 100 nm deep into a 200 nm thick single material grating layer from $In_{\approx 0.75}Ga_{\approx 0.25}P$ (the material composition was derived from the given refractive index of 3.21), DFB gratings

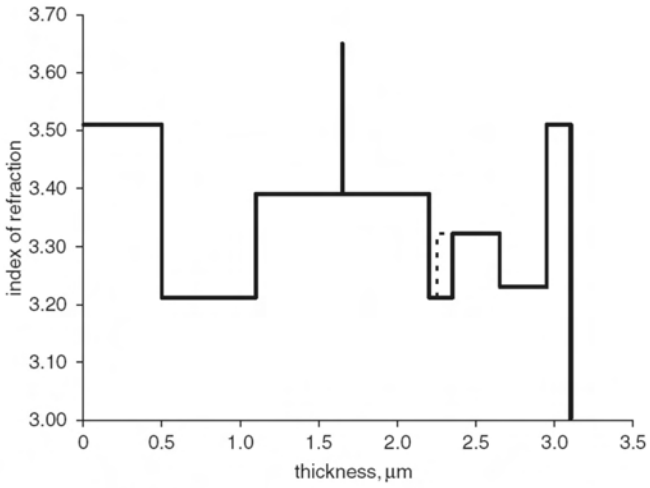

Fig. 1 *Index of refraction profile of DFB laser through low-index portion of grating along with high-index portion of grating shown by dotted line*

Figure 5.8: Reprinted with permission from Kanskar *et al.* [Kan06]. Copyright 2006, The Institution of Engineering and Technology.

in *this work* have a shallow etch depth of only $\approx 35\,\text{nm}$ (iteration I) and $\approx 20\,\text{nm}$ (iteration II). Shallow gratings have been used in *this work* because they are expected to lead to a higher quality of the semiconductor crystal in the compound grown on top of the DFB grating surface and a faster planarization of the corrugation during regrowth. In addition, the DFB gratings in *this work* consist of an aluminum-free two layer system which allows to use selective etching of the GaAs cap to precisely adjust the duty cycle of the final regrown grating. This is advantageous to achieve the maximum coupling coefficient from the thin second arder grating and to minimize radiation loss.

Kanskar *et al.* say, they have designed the grating and its position to keep $\kappa L \approx 1$. Thus, with $L = 1\,\text{mm}$, κ must be $\approx 10\,\text{cm}^{-1}$. The authors use a kind of an thin competing waveguide for the DFB grating as can be seen in Fig. 5.8. The DFB lasers in *this work* also have $\kappa L \approx 1$ in iteration I but $\kappa L \approx 0.15$ in iteration II because $\kappa L \approx 1$ was identified to limit the slope efficiency of high power DFB-BA lasers in comparison to BA lasers without a DFB grating and efficiency optimized facet coatings.

In contrast to epitaxy design in *this work*, the waveguide used by Kanskar *et al.* is $1\,\mu\text{m}$ thinner. The thinner waveguide epitaxy design results in a broader vertical divergence angle of 38° FWHM. Narrow vertical divergence angles of 26° FWHM and 45° with 95 % power content as reported in *this work* are more advantageous for a efficient coupling of the emitted power into

optical fibers and collimation with lenses. Nevertheless, thinner waveguides makes it easier to achieve a low threshold current and a low series resistance.

Broad are devices with 100 μm stripe width and with two different cavity lengths of 1 and 2 mm were investigated by Kanskar *et al.* under CW conditions at 25 °C heatsink temperature. With the shorter cavity length of $L = 1$ mm, Kanskar *et al.* obtain a maximum power conversion efficiency of 53 % at 2.0 W. At the time of publication (2006), this was the highest power conversion efficiency reported for edge emitting DFB diode lasers. The maximum power shown for these devices is 4.0 W, which was also a record high value at the time of publication. The corresponding power conversion efficiency is 43 %. A threshold current of 230 mA and a slope efficiency of 0.9 W A^{-1} is denoted. Power, voltage and power conversion efficiency are depicted in Fig. 5.9, reproduced from [Kan06].

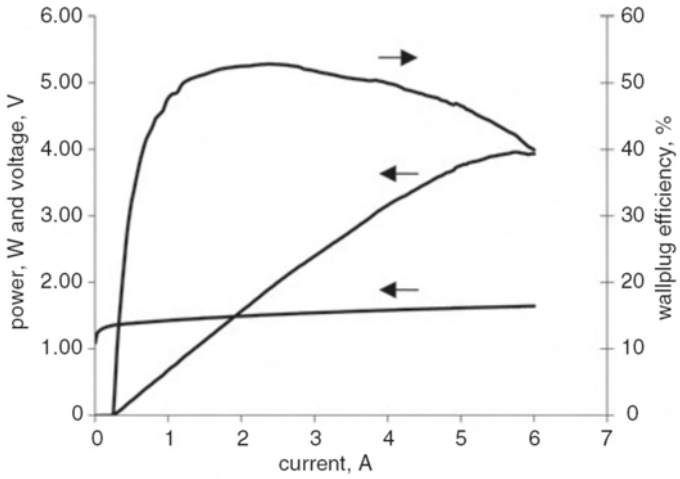

Fig. 2 *CW L–I–V and peak wallplug efficiency of 53% for 1 mm-long cavity 100 μm-stripe DFB laser*

Figure 5.9: Reprinted with permission from Kanskar *et al.* [Kan06]. Copyright 2006, The Institution of Engineering and Technology.

Devices with 2 mm cavity length reach a maximum power conversion efficiency of 49 % at 2.4 W and the highest output power published before [Sch10a] is 5.5 W with 41 % power conversion efficiency. In contrast to the device with 1 mm cavity length, no strong roll-over is observed at 8.0 A, 5.5 W. Therefore, it seems possible to further increase the output power if the facets are able to withstand power densities above 5 MW cm^{-2}, as approximately reached at 8.0 A, 5.5 W. Power, voltage and power conversion efficiency are depicted in Fig. 5.10, reproduced from [Kan06].

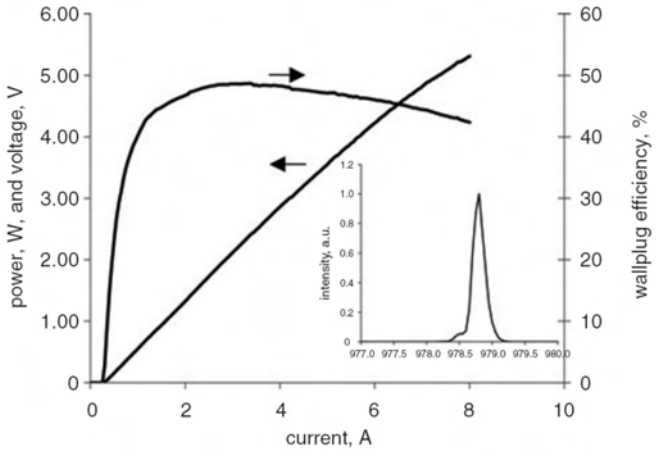

Fig. 3 *CW L–I–V of 2 mm-long cavity 100 μm-stripe DFB laser, and spectrum at 5 W*

Figure 5.10: Reprinted with permission from Kanskar *et al.* [Kan06]. Copyright 2006, The Institution of Engineering and Technology.

The spectral width of the device with 2 mm cavity length is denoted with 0.18 nm FWHM at the peak efficiency and 0.23 nm FWHM at 5 W. The spectrum at 5 W is shown in the inset to Fig. 5.10, a spectral width of ≈ 0.5 nm with 95 % power content can be read of the inset figure. Thus, the spectral width is slightly broader than the spectral width of DFB-BA lasers from iteration I of *this work*, as depicted in Fig. 3.32 and 3.33 as well as of iteration II of *this work* as shown in Fig. 4.22, 4.23 and 4.24.

The devices have a facet coating with front and rear facet reflectivity of $R_\mathrm{f} = 4\,\%$ and $R_\mathrm{r} = 95\,\%$, respectively. Thus, the feedback from the facets is relatively high, especially for the 2 mm long DFB-BA lasers. Using a SQW active region as gain medium is known to require a higher front facet reflectivity than a DQW to keep the threshold current density per quantum well low. The mirror loss caused by the facet coating is $\alpha_\mathrm{m} = 16.35\,\mathrm{cm}^{-1}$ for 1 mm cavity length and $\alpha_\mathrm{m} = 8.18\,\mathrm{cm}^{-1}$ for 2 mm cavity length. Spectral stabilization is enabled due to DFB coupling strength of $\kappa \cdot L \sim 1$ for but the authors do not quote if this is obtained for a cavity length of $L = 1$ mm or $L = 2$ mm.

In *this work*, DFB BA lasers (DQW) with a cavity length of 3 mm have a mirror loss caused by the facet coatings between $\alpha_\mathrm{m} = 12.1\,\mathrm{cm}^{-1}$ and $\alpha_\mathrm{m} = 13.6\,\mathrm{cm}^{-1}$ and a DFB coupling strength of $\kappa L \approx 1$ (iteration I) and $\kappa L \approx 0.15$ (iteration II).

Kanskar *et al.* have investigated the DFB locking range by measuring the

spectra of a DFB BA laser at 2 A CW drive current and temperatures of 10, 20, ..., 50 °C as shown in Fig. 5.11. Unfortunately, the cavity length of the laser used for this investigation is not indicated. The shown spectra have a spectral width between approximately 0.2 and 0.3 nm with 95 % power content. Presumably, a locking to higher temperatures and at higher currents could be achieved with the lasers from Kanskar *et al.* by using a lower front facet reflectivity.

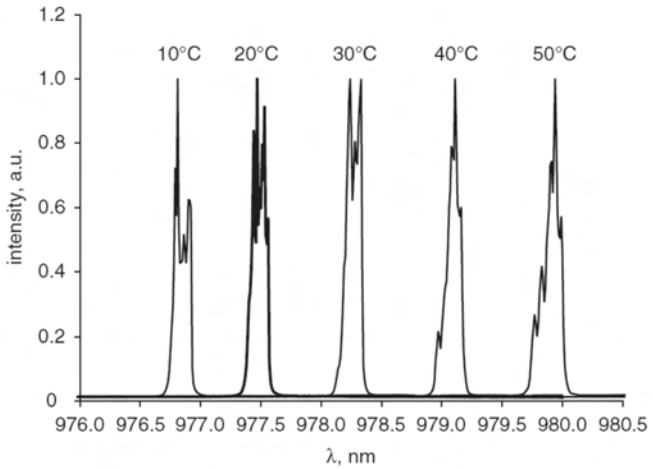

Fig. 4 *Spectra of 100 μm-stripe DFB laser for heatsink temperatures from 10 to 50°C at 2 A CW drive current*

Figure 5.11: Reprinted with permission from Kanskar *et al.* [Kan06]. Copyright 2006, The Institution of Engineering and Technology.

The devices are interpreted from the spectrum measurements to operate in multiple lateral modes but single longitudinal mode at low powers, but at several longitudinal modes at high powers. From the spectra shown in Fig. 5.11, this predication cannot be derived securely. Obviously, the spectra have several sub-peaks with a spectral distance in the range of ≤ 0.05 nm. Indeed, the lateral and longitudinal mode spacing cannot be separated securely. Nevertheless, it is obvious to assume lasing on multiple lateral modes even slightly above threshold. Spectrally resolved near field and far field measurements on DFB-BA lasers from iteration I of *this work* (see section 3.4.12) show, that lasing on more than one longitudinal mode can occur at output powers of > 5 W.

Publication 4 Y. He *et al.*: "808 nm broad area DFB laser for solid-state laser pumping application", Electronics Letters, Vol. **45**, 163–164 (2009)

In 2009, He *et al.* [He09] published results, obtained with 808 nm DFB BA lasers. These 808 nm DFB BA lasers were obviously developed on the basis of the knowledge and manufacturing skills, the group has gained with the 975 nm DFB-BA lasers reported in [Kan06]. Therefore and because of a very high power conversion efficiency, these lasers are interesting for a comparison with the 975 nm DFB BA lasers from *this work*. The design of the waveguide and SQW active region from [Kan06] has been adapted to a semiconductor material system that allows efficient waveguiding at 808 nm but no material details are given. The refractive index profile is depicted in Fig. 5.12, reproduced from [Kan06].

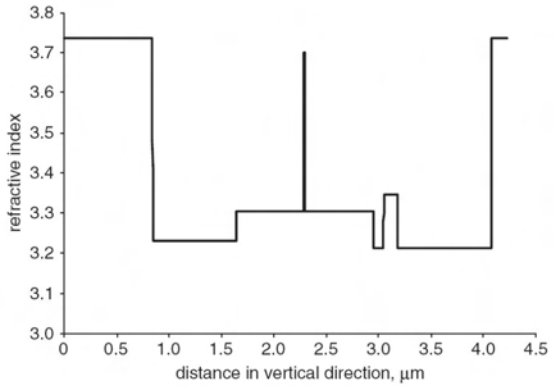

Fig. 1 *Refractive index profile of 808 nm wavelength stabilised laser*

Figure 5.12: Reprinted with permission from He *et al.* [He09]. Copyright 2009, The Institution of Engineering and Technology.

A second-order DFB grating is fabricated with lithographic techniques and reactive ion etching, then overgrown in a second epitaxy process. The fabrication is very similar to [Kan06]. DFB-BA diode lasers with 2 mm cavity length and a stripe width of 100 μm are fabricated and facet coating is applied to obtain $R_\mathrm{f} = 4\,\%$ and $R_\mathrm{r} = 95\,\%$. A DFB coupling strength of $\kappa L \sim 1$ and a vertical divergence angle of 38.6° FWHM is denoted by the authors. Thus, the coupling coefficient of the DFB grating must be $\approx 5\,\mathrm{cm}^{-1}$ which is presumably only 50 % of the coupling coefficient of the DFB grating in [Kan06] while the coupling coefficient in iteration I of *this work* is $\approx 3\,\mathrm{cm}^{-1}$ and $\approx 0.5\,\mathrm{cm}^{-1}$ in iteration II.

Figure 5.13, reproduced from [He09], shows the voltage, power and efficiency characteristics at 25 °C heat sink temperature. A threshold current of 450 mA and a slope efficiency of $> 1\,\mathrm{W\,A}^{-1}$ is denoted. From the graphic,

one can measure the slope efficiency as $S \cong 1.15\,\mathrm{W\,A^{-1}}$. At the time of publication, this is the highest slope efficiency for a DFB-BA laser. With $\eta_\mathrm{d} = (-q\lambda/hc) \cdot S$ (with the Planck constant h, the vacuum speed of light c, the electron charge q and the vacuum wavelength λ), the corresponding slope efficiency can be calculated as $\eta_\mathrm{d} \approx 0.749$. DFB-BA lasers from this work have slope efficiencies between 0.879 and $1.073\,\mathrm{W\,A^{-1}}$ (see tables 3.7 and 4.3). Thus, differential quantum efficiencies between $\eta_\mathrm{d} = 0.691$ and $\eta_\mathrm{d} = 0.839$ have been achieved, considering wavelengths of $\lambda = 975\,\mathrm{nm}$ and $\lambda = 970\,\mathrm{nm}$, respectively. The 808 nm DFB BA lasers from Y. He at al. obtain remarkable 4 W optical output power (without any roll-over being observed) at a peak power conversion efficiency of 57 %, a record high value at the time of publication.

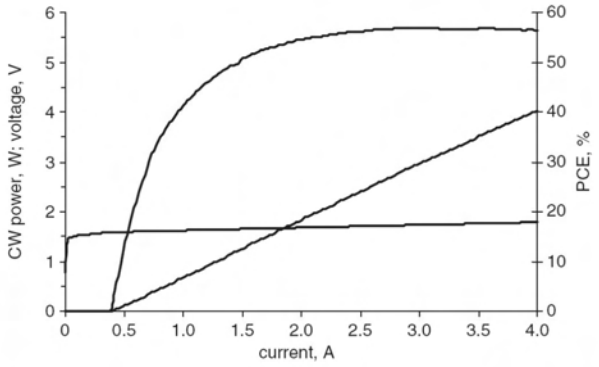

Fig. 2 *Light-current-voltage and wall-plug efficiency curves of 2 mm cavity length 808 nm wavelength stabilised laser at 25°C heatsink temperature*

Figure 5.13: Reprinted with permission from He *et al.* [He09]. Copyright 2009, The Institution of Engineering and Technology.

Optical spectra were measured in [He09] and found to have a spectral width of 0.3 nm FWHM at 2.5 W output power and temperatures of 15, 25, ... 45 °C. A width of ≈ 0.5 nm with 95 % power content can be estimated from figure 3 in [He09]. For DFB BA lasers from this work, the spectral width with 95 % power content is slightly more narrow at comparable output powers (see Fig. 3.32 and 3.33 for iteration I and Fig. 4.22, 4.23 and 4.24 for iteration II).

Figure 5.14, reproduced from [He09], shows a mapping of the locked output with "100 % of the power in the Bragg emission bandwidth" [He09], as a function of the heatsink temperature and operating current. The emission wavelength is reported to remain stabilized at the Bragg condition over ∼ 30 K in heatsink temperature. Such a broad DFB locking range could be

important for possible applications of DFB BA lasers, for example as pump source for spectrally narrow absorption lines. In *this work*, the DFB locking range was determined for DFB-BA lasers from iteration I (section 3.4.11) and II (section 4.3.7).

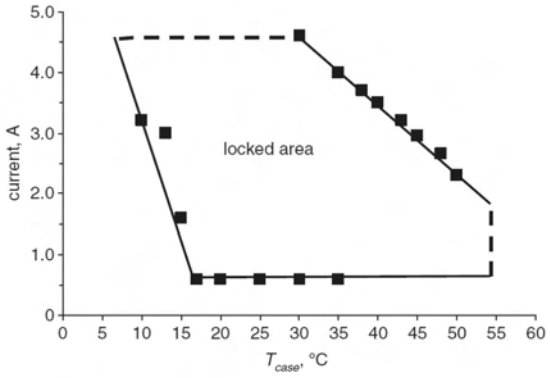

Fig. 4 *Locking range of wavelength stabilised 808 nm diode laser against heatsink temperature and operating current*

Figure 5.14: Reprinted with permission from He *et al.* [He09]. Copyright 2009, The Institution of Engineering and Technology.

With respect to changing the role of the x- and y-axis between Fig, 5.14 from [He09] and Fig. 3.50 (c) which shows the locking range from DFB-BA lasers from this work, the shape of the locking range is very similar. He *et al.* do not explain in detail, what exactly happens outside the indicated locking range. Because of the high front facet reflectivity of 4 %, one might assume that lasing on FP-like modes starts, if the gain peak is too much detuned from the Bragg wavelength of the DFB grating on the fundamental waveguide mode (detuned to longer wavelength at high currents and temperatures).

He *et al.* denote the important fact that "The temperature range of effective locking is limited by detuning between the optical gain peak wavelength and the Bragg wavelength, which is a function of the junction temperature at a given operating current." [He09]. This spectral detuning has been observed in *this work* to be essential for the properties of the optical spectrum because it determines the onset of lasing on FP-like modes and higher-order modes and influences the roll-over of the power characteristics. In the case of DFB-BA lasers from this work, also lasing on higher-order vertical waveguide DFB modes limits (narrow) single peak lasing. Presumably, this also occurs with the DFB-BA lasers reported in [He09] at heatsink temperatures $\leq 17\,^{\circ}\mathrm{C}$ where the locking range is limited (see Fig, 5.14).

Publication 5 J. Fricke *et al.*: "High-Power 980nm Broad-Area Lasers Spectrally Stabilized by Surface Bragg Gratings", Photonics Technology Letters, Vol. **22**, 284–286 (2009)

In 2009, Fricke *et al.* [Fri09] from the FBH have published experimental results, obtained with high power and high efficiency DBR-BA lasers. They also report on how high reflectivity Bragg reflector gratings can be fabricated at the rear facet of the device. Fricke *et al.* argue, that "employing a higher-order surface grating is a cost-effective standard fabrication technology" [Fri09] and could be possibly a more cost effective technology approach for the spectral stabilization of BA lasers compared to a two step epitaxy process for the fabrication of buried DFB gratings.

The epitaxy structure, grown by MOVPE on a GasAs wafer, consists of a 2.4 μm thick AlGaAs waveguide with AlGaAs cladding layers. The active region consists of a strain compensated InGaAs/GaAsP DQW and is placed asymmetrically into the waveguide with a *n*-waveguide thickness of 1.6 μm and a *p*-waveguide thickness of 0.8 μm, respectively. Thus, the epitaxy structure is roughly comparable to the one, used in *this work* during iteration I and II.

Internal loss of $\alpha_\mathrm{i} = 0.76\,\mathrm{cm}^{-1}$ and an internal quantum efficiency of $\eta_\mathrm{i} = 0.93$ has been determined from the cavity length dependence of the differential quantum efficiency of BA lasers from this material. In *this work*, $0.84\,\mathrm{cm}^{-1} \leq \alpha_\mathrm{i} \leq 1.05\,\mathrm{cm}^{-1}$ and $0.92 \leq \eta_\mathrm{i} \leq 0.96$ (see table 3.5) has been determined in iteration I for FP-BA reference lasers and DFB-BA lasers with a Bragg wavelength, detuned outside the gain spectrum. These values are, with respect to the measurement precision, comparable to what Fricke *et al.* have determined for their devices. Fricke et al also quote the threshold current characteristic temperature for their epitaxy design as $T_0 = 163\,\mathrm{K}$ which is higher than the value for the FP-BA reference lasers from *this work* ($T_0 = 132\,\mathrm{K}$).

The design of the DFB grating was optimized by calculating the peak reflectivity of a 500 μm long sixths-order Bragg grating section as a function of the duty cycle c_d (ratio between the un-etched part of the grating and the grating period Λ) and residual layer thickness d_res (thickness of layers remaining above the active region). Sufficient peak reflectivity of $> 65\,\%$ has been determined for very high $c_\mathrm{d} > 0.9$ (challenging for fabrication) and $d_\mathrm{res} < 550\,\mathrm{nm}$. For $0.88 \leq c_\mathrm{d} \leq 0.92$ and $d_\mathrm{res} = 350\,\mathrm{nm}$, the peak reflectivity is found to saturate for 500 μm grating length. The effective reflectivity of the DBR grating has been determined experimentally from the fraction of the output power from the rear and front facet $P_\mathrm{r}/P_\mathrm{f} = \sqrt{(R_\mathrm{f}/R_\mathrm{r})(1-R_\mathrm{r})}/(1-R_\mathrm{f})$. For 500 μm long sixths-order Bragg gratings, an effective reflectivity up

to $R_{\mathrm{r}}^{\mathrm{eff}} = 80\,\%$ was achieved. From the fabrication and functionality point of view, the Bragg gratings used in *this work* are quite different compared to the Bragg gratings for DFB-BA lasers as used by Fricke *et al.* Firstly, sixth-order Bragg gratings have very large grating periods what allows them to be fabricated with wafer i-line stepper lithography. For example, for $\lambda_{\mathrm{Bragg}} = 976.0\,\mathrm{nm}$ and $n_{\mathrm{eff}} = 3.4$, the grating period of a first-order Bragg grating is $\Lambda_{1\mathrm{st\,order}} = 143.5\,\mathrm{nm}$, $\Lambda_{2\mathrm{nd\,order}} = 287.1\,\mathrm{nm}$ for a second-order grating and $\Lambda_{6\mathrm{th\,order}} = 861.2\,\mathrm{nm}$ for a sixth-order grating. Secondly, sixth-order high reflectivity DBR gratings require duty cycles close to 1.0 and etching these high aspect ratio gratings (narrow, deep trenches) is challenging. In contrast, second-order DFB gratings in *this work* are preferably fabricated as very thin gratings with a duty cycle of 0.25 (narrow stripes oft the grating layer are left between broad and very shallow trenches) and require different fabrication techniques.

For the measurement of power-voltage-current characteristics and spectral properties, facet passivation and facet coating for front an rear facet reflectivities of $R_{\mathrm{f}} = 0.5\,\%$ and $R_{\mathrm{r}} < 0.1\,\%$ was applied to laser bars with a cavity length of $4000\,\mu\mathrm{m}$, containing a $500\,\mu\mathrm{m}$ long sixths-order DBR grating section as a rear-side reflector. Single emitters with $90\,\mu\mathrm{m}$ stripe (and DBR grating) width were mounted *p*-side down on CuW submounts and soldered on CCP-mounts. In contrast to the DBR-BA lasers which have an effective rear facet reflectivity of $R_{\mathrm{r}}^{\mathrm{eff}} \leq 80\,\%$, DFB-BA lasers in *this work* have very high reflectivity rear facet coatings with $R_{\mathrm{r}} \geq 96\,\%$. Therefore one must reason, that the fraction of the optical output power which is coupled out through the rear facet of a laser is higher for the DBR-BA lasers and reduces the differential quantum efficiency (and slope efficiency) from the front facet.

In Fig. 5.15, reproduced from Fricke *et al.* [Fri09], power-voltage-current characteristics measured at 25 °C under CW conditions, are depicted. The DBR laser has a threshold current of $I_{\mathrm{th}} \approx 1.4\,\mathrm{A}$ and an excellent slope efficiency of $S \approx 1\,\mathrm{W\,A^{-1}}$ (from threshold up to 4 A). A peak power conversion efficiency of 50 % is denoted for an optical output power of 7 W. Considerable roll-over starts at $\approx 17.5\,\mathrm{A}$ and the output power peaks at remarkable $\approx 14.5\,\mathrm{W}$, $\approx 20\,\mathrm{A}$, with $\approx 40\,\%$ power conversion efficiency. The divergence angle of the vertical far field is denoted as 24 ° FWHM.

A quantitative comparison of the power-voltage-current characteristics between the DBR-BA lasers from Fricke *et al.* and DFB-BA lasers from *this work* is difficult, because the DBR-BA lasers must be understood as $90\,\mu\mathrm{m}$ stripe BA lasers with a $3500\,\mu\mathrm{m}$ long pumped area and a passive section (not electrically pumped) whose length is defined by the effective penetration length of the optical field into the DBR grating section $l_{\mathrm{eff}} < 500\,\mu\mathrm{m}$. In contrast, DFB-BA lasers from *this work* consist of a single $3000\,\mu\mathrm{m}$ long

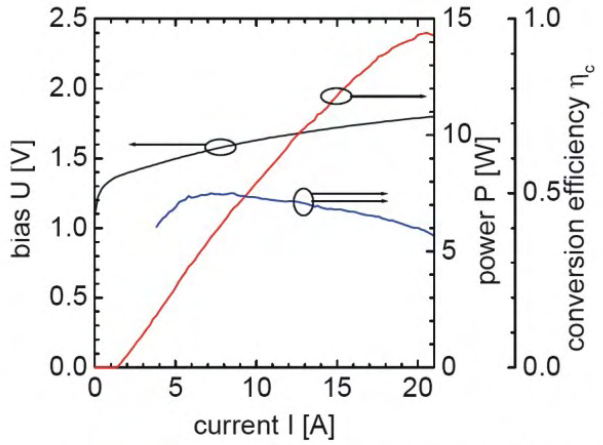

Fig. 6: PUI-characteristic under cw-condition of a 4mm DBR laser with 6th order grating at 25°C.

Figure 5.15: Reprinted with permission from Fricke *et al.* [Fri09]. Copyright 2009, IEEE.

actively pumped section. Nevertheless it is an important result that Fricke *et al.* [Fri09] have achieved a slope efficiency of $1\,\mathrm{W\,A^{-1}}$. Roll-over at $\approx$ 14.3 W, 20 A is also a remarkable result for a 90 μm stripe, 4000 μm long DBR-BA laser, including a 500 μm long DBR grating section. An output power of nearly 12 W at 15 A, achieved with the 4000 μm long DBR-BA laser is close to the best results with 3000 μm long DFB-BA lasers at 15 A in this work (see Fig. 3.26 for iteration I and Fig. 4.13 for iteration II). An advantage of the DFB-BA lasers from *this work* is, that their power conversion efficiency is up to 10 % higher at the same output powers as for the DBR-BA lasers from Fricke *et al.*, which achieve higher output powers.

A mapping of the CW spectra at 25 °C is shown in Fig. 5.16, reproduced from Fricke *et al.* [Fri09]. Single narrow spectral peak emission is observed between threshold and 21 A, indicating that the emission wavelength is locked to the Bragg condition over the whole current range. A total wavelength shift of 3.4 nm has been determined. The spectral width with 95 % power content remains $\leq$ 1 nm. Probably with respect to possible applications, the authors denote that "Up to 10 W power the spectral shift and width remain below 1.1 nm and 0.6 nm, respectively" [Fri09].

With regard to the spectral properties, DBR-BA lasers can be advantageous, compared to DFB-BA lasers, because of the following to three reasons. Firstly, the wavelength shift of the DBR spectrum to longer wavelength with increasing current is lower, because the DBR grating is not electrically

pumped (passive) and therefore, it is less heated, compared to a DFB grating which is a part of the electrically pumped active part of the laser diode. The differences in the current-induced wavelength shift between a DBR-BA laser and a DFB-BA laser reduces when QCW or short pulsed mode current injection is used instead of CW and it is expected to vanish at very short current pulses with low duty cycle. Secondly, the spectral width is basically determined by the reflection bandwidth of the Bragg grating and can be smaller than the spectral width of a DFB-BA laser, if the reflection bandwidth of the Bragg grating is very narrow. In a DBR-BA laser, optical modes (longitudinal and lateral) whose corresponding wavelength is outside the reflection bandwidth, are suppressed against modes within the reflection bandwidth of the DBR grating due to increased mirror losses. In contrast, each lateral mode has its own effective refractive index and consequently, its own stopband wavelength in a DFB-BA laser. The suppression of additional longitudinal modes which are considerably detuned from the stopband is typically small in weakly coupled ($\kappa L < 1$) DFB-BA lasers. Thirdly, the sensibility to external feedback is potentially much higher for DFB-BA lasers, because of the highly anti-reflection coated front facet, which is not required for DBR-BA lasers.

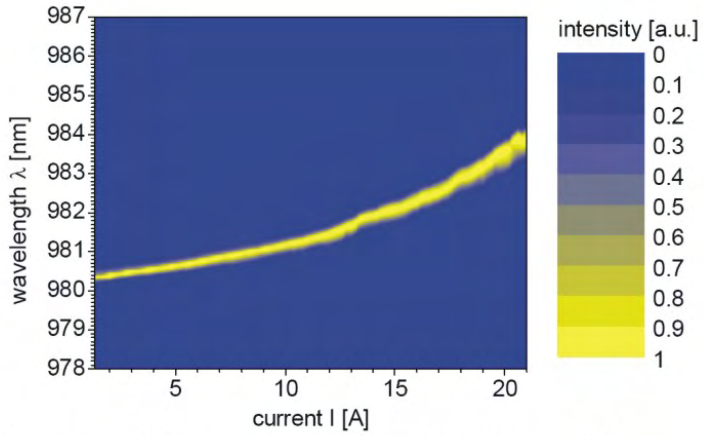

Fig. 7: CW color-scale mapping of the optical spectrum versus injection current..

Figure 5.16: Reprinted with permission from Fricke *et al.* [Fri09]. Copyright 2009, IEEE.

In summary, high power DBR-BA lasers are promising devices to achieve very high optical output powers, combined with narrow spectral width, wavelength stabilization and also high power conversion efficiency. Compared to DFB-BA lasers, devices reported in [Fri09] are advantageous compared to

DFB-BA lasers from *this work* with regard to the maximum achievable output powers and wavelength stability. To date, DFB-BA lasers achieve higher power conversion efficiency and are the first diode lasers with monolithic integrated wavelength stabilization, for which reliable operation at 10 W CW is reported for 7800 h. The fabrication of DBR-BA lasers, reported in Fricke *et al.* [Fri09] (single epitaxy, surface grating), is very different from the fabrication of DFB-BA lasers in this work (two-step epitaxy, buried grating). For the DBR-BA lasers, the etching of a high duty-cycle grating, to achieve a high reflectivity, is the most critical fabrication step. The most critical fabrication step for the DFB-BA lasers is the epitaxial regrowth of the etched grating corrugation and to achieve a clean, oxygen-free surface before the second epitaxy begins. If it is necessary to achieve the maximum output power from a minimum of wafer surface, DFB-BA laser could be advantageous, because in contrast to DBR-BA lasers, they do not need extra space for a passive grating reflector.

To conclude, substantial improvement has been achieved in the output power and power conversion efficiency of DFB-BA lasers since 1998. The ability to fabricate low optical loss, low series resistance DFB gratings and the usage of low coupling strength ($\kappa \cdot L < 1$) DFB gratings have been the most important factors to increase the power conversion efficiency.

The spectral detuning between the Bragg wavelength of the DFB grating on the fundamental waveguide mode and the gain peak wavelength has been identified as a crucial factor for wavelength stabilization on the fundamental waveguide mode and high power conversion efficiency at high optical output powers. This is of exceedingly importance while the maximal used CW injection currents have been increased to 15 A in order to achieve high output powers > 12 W. The spectral detuning es expected to become even more important in future DFB-BA lasers where longer cavity lengths ≥ 4 mm are supposed to be used. Using longer cavity length is an upcoming development in the field of high power BA lasers, motivated by low internal optical loss $\alpha_\mathrm{i} \sim 0.5\,\mathrm{cm}^{-1}$ which can be achieved with optimized SQW epitaxy designs. This will in future enable even higher injection currents, for example $I = 20$ A for $L = 4$ mm with the same current density as for $I = 15$ A for $L = 3$ mm.

DBR-BA lasers, with high reflection DBR gratings, used as a rear reflector, based on a epitaxy structure optimized for high power and high efficiency BA lasers, are promising devices to achieve comparable output power and power conversion efficiency with wavelength stabilization, having a small drawback in power conversion efficiency. Also reliable operation in the ~ 10 W range over > 5000 h has not been reported for DBR-BA lasers to date.

Chapter 6

Summary

In this chapter, the main aspects of the work are summarized, subdivided into the following paragraphs. The summary begins with a reiteration of the subject and goal of this work, the motivation and possible promising applications of high efficiency, high power, wavelength stabilized broad area (BA) lasers. The initial situation which gave several indications on the limitations of the efficiency of DFB-BA lasers is shortly explained subsequently. Afterwards, theoretical findings on the factors limiting the efficiency of DFB-BA lasers are summarized. The technological realization of the high efficiency, high power DFB-BA lasers which were developed during this work is summarized with respect to the design and fabrication technology. Experimental results obtained in iterations I and II are presented afterwards. The following section concerns selected findings and problems of high efficiency, high power DFB-BA lasers which have been identified during this work. In the second to last section, the significance of the present work for further research and development as well as potential applications is evaluated. Finally, an outlook is given on present unpublished and future work on DFB-BA lasers at the FBH, about a competing fabrication technology for DFB gratings and recently published considerations on the industrial high volume manufacturing of buried overgrown DFB gratings, using technologies which are comparable to the ones used in this work.

Subject and goal of the work, motivation and applications The aim of this work was to identify the factors which limit the efficiency of DFB-BA lasers compared to efficiency-optimized FP-BA lasers. A further aim was to develop and fabricate high efficiency, high power $\sim 100\,\mu$m stripe DFB-BA lasers based on the findings, which achieve high power conversion efficiency in the $\sim 60\,\%$ range at 10 W optical output power – an efficiency and power level which is typical for state of the art Fabry-Pérot (FP) BA lasers. Finally, it was essential to analyze the properties of these newly developed DFB-BA

lasers experimentally, to compare them to reference lasers and to gain a deep understanding of their physical properties as a basis for further research and development work.

This work was motivated by the consideration that additional wavelength stabilization and a narrow spectral width would make high efficiency, high power BA lasers more suitable for some kinds of possible applications. Such applications are pumping narrow absorption bands in gain media of solid state lasers, fiber lasers and amplifiers [Pas97], [Oso07], [Sch07], [Hu09], [Köh09], [Pat09], as well as dense incoherent spectral beam combination for direct diode lasers systems [Sch07], [Gra12], [Hei12]. Based on estimated technical requirements for possible applications mentioned above, goals for the optical output power, power conversion efficiency, spectral width and vertical beam divergence have been defined. These goals were to achieve a continuous wave optical output power of $\geq 10\,\mathrm{W}$ with a power conversion efficiency of $\geq 60\,\%$, a spectral width of $\leq 0.3\,\mathrm{nm}$ (95 % power content) and a vertical beam divergence of $\leq 45\,^{\circ}$, (95 % power content).

Initial situation Before the beginning this work, DFB-BA lasers were for example optimized for temperature-stable locking with low efficiency and power [Sch09a]. First efficiency optimized DFB-BA lasers [Kan06], [He09] were limited to relatively low output powers ($\leq 5.5\,\mathrm{W}$) which is only 50 % of the typical reliable output power from a $\sim 100\,\mu\mathrm{m}$ stripe state of the art BA lasers. The fabrication of DFB gratings using buried overgrowth technology was already well established but these gratings typically caused additional internal optical loss [Yor92], [Cha00], [Sch09a], [Sch09b] and series resistance [Lee97], [Cha00], [AM98], [Sch09a], [Sch09b] in DFB-BA lasers.

Theoretical findings The factors which limit the power conversion efficiency of DFB-BA laser have been studied theoretically and based on earlier publications. These factors are the choice of a too high DFB coupling strength $\kappa \cdot L$ [Che98], [Sch09a], [Sch09b], an excess internal optical loss from the DFB grating region [Yor92], [Cha00], [Sch09a], [Sch09b] and radiation loss from higher-order DFB gratings [Cha00] and an excess voltage drop due to the DFB grating [Cha00], [AM98], [Sch09a], [Sch09b].

Thus, increasing the efficiency of DFB-BA lasers firstly required the DFB coupling strength to reduced to an adequate value. Because of the typical stripe width of BA lasers of $\sim 100\,\mu\mathrm{m}$ and unavoidable marginal angular misalignment between the cleaved facets and the DFB grating, the phase relation between the facets and the last grating ridge is reasoned to be not well defined in BA lasers like in narrow stripe $\sim 3\,\mu\mathrm{m}$ RW lasers. Threshold gain

and differential quantum efficiencies were calculated for facet phase sections between 0 and 1/2 grating periods (second-order DFB grating) with a small step size using coupled mode theory numerical calculations and averaging over the facet phase section was therefore used to produce results relevant for BA lasers. These calculations show that for low DFB coupling strength $\kappa \cdot L \leq 1$, DFB-BA lasers and FP-BA lasers have nearly identical dependence of the differential quantum efficiency and threshold gain on the resonator loss, provided they have the same internal optical loss and internal quantum efficiency. Therefore, by decreasing the DFB coupling strength, the increase in threshold gain will be more than compensated by the increase in slope efficiency and the peak power conversion efficiency and corresponding optical output power increases with decreasing coupling strength.

Secondly, the internal optical loss of DFB-BA lasers had to be reduced to the value for reference FP-BA lasers from the same epitaxy design, grown in a single stage epitaxy without the grating layers. Because the grating region requires a high doping level for low electrical resistance, thin grating layers are preferred which are placed far enough from the active region at a position with a low confinement factor with the vertical optical field. Furthermore, contamination with oxygen which might occur during the two step epitaxy in the grating region must be minimized or prevented because oxygen contamination can cause deep level trap states within the band gap of AlGaAs [Goo91], [Kan97].

Radiation loss from higher-order DFB gratings can be minimized by using a second-order DFB grating with 25 % duty cycle and a low coupling coefficient $\kappa < 5\,\mathrm{cm}^{-1}$. Calculations show that in this case, the radiation loss will be two orders of magnitude smaller than the coupling coefficient and also more than one order of magnitude smaller than the typical doping level dependent internal optical loss $\alpha_\mathrm{i} \sim 1\ \mathrm{cm}^{-1}$ and thus, approximately negligible.

The appearance of an excess voltage drop because of an increased series resistance must be reduced or eliminated by using an adequate grating design, including material choice, layer thickness, geometry and doping level, as well as a suitable fabrication technology.

Technological realization The findings on the factors, limiting the efficiency of DFB-BA lasers have been considered in the basic epitaxy design development, in the design, position and coupling coefficient of the DFB grating and grating fabrication technology.

An AlGaAs-based epitaxy design was developed which was optimized for high efficiency, high power BA lasers and suitable for the integration of a DFB

grating in the p-waveguide [Sch10a], 230 nm (iteration I) or 100 nm (iteration II, [Sch11], [Cru12b], [Sch12]) below the p-cladding layer. The confinement factors in the DFB grating were only 0.46 % and 0.16 % in iteration I and II, respectively. The DFB grating basically consists of two aluminum-free layers, p-doped at $2 \cdot 10^{18}\,\mathrm{cm}^{-3}$. In iteration I, the DFB grating is formed by a ≈ 7 nm thick $In_{0.49}Ga_{0.51}P$ layer which extends over the whole wafer and grating ridges from ≈ 13 nm $In_{0.49}Ga_{0.51}P$ and $15 - 20$ nm GaAs (in growth direction). In contrast, no residual $In_{0.49}Ga_{0.51}P$ layer is left over in iteration II, where grating ridges from ≈ 10 nm $In_{0.49}Ga_{0.51}P$ and $5 - 15$ nm GaAs are completely isolated, floating in the AlGaAs p-waveguide [Sch12]. This floating grating design enables any hetero-interfaces between the grating ridges to be eliminated on 75 % of the grating area. From vertical cavity surface emitting lasers, hetero-interfaces are well known to increase the series resistance [Cha93], [Pet93], [Kha95], [Zho95], [Die08] and therefore, the floating grating design was presumed to enable even lower voltage and series resistance than the grating design from iteration I with a residual $In_{0.49}Ga_{0.51}P$ layer. The DFB gratings longitudinal index contrast, duty cycle and vertical position was chosen to obtain a coupling coefficient of $\kappa \sim 3\,\mathrm{cm}^{-1}$ in iteration I and was further reduced to $\kappa \approx 0.5\,\mathrm{cm}^{-1}$ in iteration II. Thus, with a cavity length of $L = 0.3$ cm, the achieved DFB coupling strength in iterations I and II were $\kappa \cdot L \approx 1$ and $\kappa \cdot L \approx 0.2$, respectively [Sch10a], [Sch12].

As mentioned above, the duty cycle of the DFB grating must be adjusted precisely in order to achieve a maximum coupling coefficient and to minimize the ratio between the coupling coefficient and the radiation loss from the DFB grating. This has been considered during the fabrication, beginning with an adequate duty cycle for the photoresist line pattern which was used as an etch mask for the first structuring. During the following etching and cleaning steps, the duty cycle of the corrugation is reduced stepwise until a duty cycle of ≈ 25 % is achieved in the final regrown DFB grating [Sch12].

Ex-situ pre-structuring with selective wet etching of GaAs was therefore used to obtain a GaAs line pattern with a precision duty cycle on top of the $In_{0.49}Ga_{0.51}P$ layer, while the wafer surface remains covered with an aluminum-free layer. After cleaning stages, in-situ etching was applied inside the epitaxy reactor with carbon tetrabromide (CBr_4) [Sch12]. This allows the grating corrugation from the GaAs line pattern to be transferred into the $In_{0.49}Ga_{0.51}P$ layer. Meanwhile, the oxides on the GaAs and $In_{0.49}Ga_{0.51}P$ are removed. In the first iteration, the in-situ etching was stopped within the 20 nm thick $In_{0.49}Ga_{0.51}P$ layer before the underlying $Al_{0.15}Ga_{0.85}As$ was uncovered, then regrown with $Al_{0.15}Ga_{0.85}As$. Usage of in-situ etching times of $t_{is} = 90$, 120 and 150 s was used to achieve DFB gratings with slightly

varying coupling coefficients.

In contrast, in-situ etching was applied in iteration II over $t_{is} = 150\,s$, using only 10 nm thick $In_{0.49}Ga_{0.51}P$ layers. This enables to uncover the underlying $Al_{0.15}Ga_{0.85}As$ under the nearly oxygen-free conditions in the MOVPE reactor without oxidization [Sch12]. Then, $Al_{0.15}Ga_{0.85}As$ can be grown on $Al_{0.15}Ga_{0.85}As$ over 75 % of the area between the grating ridges. For in-situ etching times of $t_{is} \geq 150\,s$, the oxygen contamination was found to peak at $< 1 \cdot 10^{17}\,cm^{-3}$ in the grating region [Sch12].

Experimental results in iterations I and II The evaluation of experimental results is based on a comparison with reference FP-BA devices, published results on wavelength stabilized BA lasers and the application-related goals which have been defined in the introduction.

The cavity length dependence of the slope efficiency and threshold current of uncoated 100 μm stripe DFB-BA lasers and reference FP-BA lasers was used for the experimental determination of parameters such as the internal optical loss α_i, internal quantum efficiency η_i, transparency current density j_{tr} and modal gain coefficient Γg_0. Comparable results of $\alpha_i \approx 0.9\,cm^{-1}$, $\eta_i \approx 0.95$, $j_{tr} \approx 140\,A\,cm^{-2}$ and $\Gamma g_0 \approx 21\,cm^{-1}$ have been achieved both for the DFB-BA and reference FP-BA lasers. This was an important achievement towards DFB-BA lasers with efficiency and power characteristics comparable to the reference devices [Sch10a], [Sch10b], [Sch12].

For the further characterization, the lasers were HR/AR facet coated and single emitters with $W = 90\,\mu m$ contact stripe width and $L = 3000\,\mu m$ cavity length were mounted on CuW submounts with a thermal resistance of $R_{th} \approx 4\,K\,W^{-1}$.

A comparison between the voltage-current characteristics of DFB-BA lasers from iteration I and reference FP-BA devices shows that the DFB lasers have a slightly increased voltage due to a $\approx 5\,m\Omega$ higher series resistance [Sch10a], [Sch10b]. This excess series resistance was attributed to the presence of the residual $In_{0.49}Ga_{0.51}P$ layer in the grating region and their corresponding hetero-interfaces. In contrast, DFB-BA lasers from iteration II have voltage-current characteristics identical to the reference devices [Sch12]. In order to achieve this important result, the residual $In_{0.49}Ga_{0.51}P$ layer was removed, resulting in isolated grating stripes which are floating in AlGaAs.

The DFB-BA which have been developed during this work are the first published 10 W-class DFB-BA lasers [Sch10a], [Sch10b], [Cru10]. DFB-BA lasers from iteration I achieve up to 11 W at 15 A, have a peak power conversion efficiency up to 59 % and up to 52 % at 10 W. Reference FP-BA lasers achieve up to 13.5 W at 15 A, have a peak power conversion efficiency

of $\approx 65-68\,\%$ and $\approx 61-65\,\%$ at 10 W. The reduction in power conversion efficiency compared to the reference devices is $\sim 10\,\%$. The threshold current of the DFB-BA lasers is increased to $\approx 0.7-0.8$ A compared to ≈ 0.6 A for the reference devices. In addition, the slope efficiency is reduced to $\approx 1.0\,\mathrm{W\,A^{-1}}$ while the reference devices have a slope efficiency of $\approx 1.1\,\mathrm{W\,A^{-1}}$.

In iteration II, the slope efficiency of the DFB-BA lasers was successfully increased to $\approx 1.05\,\mathrm{W\,A^{-1}}$ by using a lower DFB coupling strength of $\kappa \cdot L \approx 0.2$. The threshold current is slightly increased to $\approx 0.75-0.9$ A. Together with the reduction in series resistance, this leads to peak power conversion efficiencies up to 62 % and up to 58 % at 10 W. Thus, the reduction in power conversion efficiency compared to the reference devices is only $\sim 5\,\%$ [Cru11c], [Cru12b], [Sch12].

The developed DFB-BA lasers fulfill and even exceed the goal to achieve 10 W optical output power and have a power conversion efficiency up to 58 % at 10 W, close to the targeted value of 60 %.

Wavelength stabilization can be obtained with this DFB-BA lasers over the whole investigated current range from threshold to 15 A with a spectral width below 0.8 nm with 95 % power content [Sch12]. Unfortunately, lasing on wavelength stabilized modes at the short wavelength side of the Bragg wavelength of the DFB grating in the fundamental waveguide mode occurs for many of the studied devices [Sch10a]. The side modes limit the current range where a narrow spectral emission (single peak) can be achieved to currents above $\sim 5-10$ A for the affected devices. These additional side modes in the optical spectrum were identified as higher-order vertical modes of the waveguide [Cru11a]. Such higher-order modes are sufficiently suppressed in the reference FP-BA lasers because of their higher internal optical loss and lower confinement factors in the active region, compared to the fundamental mode. In contrast, these modes can exceed threshold in the DFB-BA lasers due to their higher DFB coupling coefficients which reduce the individual threshold currents. Furthermore, lasing on FP-like modes around the peak of the gain spectrum also limits the narrow spectral width emission for some of the devices, depending on the reflectivity of the AR coated front facet. For the best DFB-BA lasers from iteration II, the spectral width remains ≤ 0.3 nm with 95 % power content up to optical output powers of ≈ 8 W. The typical spectral width of these lasers at 10 W is ≤ 0.7 nm. The spectral width of the DFB spectrum is observed to decrease with higher power conversion efficiency at the same optical output power and broadens significantly when the roll-over of the power-current characteristics begins.

The spatial emission properties of the DFB-BA lasers were studied in iteration I at 2.5, 5.0, 7.0 and 10 W optical output power and compared to the reference FP-BA devices. Both, DFB-BA lasers and reference lasers

have comparable vertical far field profiles and divergence angles with 95 % power content of $\approx 44\,^\circ$ [Sch10b]. As targeted in the epitaxy design of the waveguide, the vertical far field divergence angle with 95 % power content was $\leq 45\,^\circ$. Higher-order waveguide modes which additionally occur for some of the DFB-BA devices increase the vertical far field with 95 % power content from $\approx 44\,^\circ$ to $\approx 48\,^\circ$. The lateral far field is also comparable for the DFB-BA lasers and reference lasers. Only at 10 W optical output power, the lateral far field of the DFB-BA lasers was observed to be broader - presumably because of the lower power conversion efficiency which m may lead to stronger thermal lensing and broadening of the far field [Cru12a].

Lateral near fields and far fields were measured with additional high spectral resolution in order to investigate the lateral and longitudinal modes in the DFB-BA lasers. These measurements provide evidence that the DFB-BA lasers are running on single or multiple (at least two) longitudinal modes, depending on the injected current level. The lateral modes are found to be stable over hours and reproducible in their spectral and spatial distribution. The lateral modes are approximately hermite-gaussian shaped and their highest mode order increases with increasing injection current. Because of their longitudinal mode selection, DFB-BA lasers are promising devices to study the lateral modes in BA lasers, even at optical output powers in the relevant 10 W range.

With DFB-BA lasers from iteration II, reliability over > 8000 h at 10 W optical output power was demonstrated with a monolithically wavelength stabilized BA laser for the first time [Sch12]. This is an indirect verification of the low defect density, high crystal quality of the regrown grating region, *p*-waveguide and *p*-cladding layer.

Findings and problems During the experimental investigation, the following factors were found to be critical for the performance of efficiency-optimized high power DFB-BA lasers.

Firstly, the spectral detuning between the Bragg wavelength of the DFB grating (in the fundamental waveguide mode) and the wavelength of the peak of the gain spectrum was observed to influence the properties of DFB-BA lasers. In order to achieve a high power conversion efficiency at the targeted operation powers at $\sim 5 - 10$ W, the Bragg wavelength of the DFB grating and the gain peak wavelength were designed to coincide at the desired power level. Considering the heat generation in the diode laser $P_{\mathrm{diss}} \approx U \cdot I - P_{\mathrm{opt}}$ and the temperature coefficients $\mathrm{d}\lambda_{\mathrm{gain}}/\mathrm{d}T \approx 0.34\,\mathrm{nm\,K^{-1}}$ and $\mathrm{d}\lambda_{\mathrm{DFB}}/\mathrm{d}T \approx 0.077\,\mathrm{nm\,K^{-1}}$, this implicates that close to $I = 0$ A, the gain peak wavelength must be several nanometers shorter than the Bragg

wavelength of the DFB grating. Different values for the spectral detuning between ≈ 2 and 6.6 nm have been utilized. Generally, with increasing spectral detuning, it has been observed that the threshold current, slope efficiency, optical output power and power conversion efficiency increase. Simultaneously, increasing spectral detuning was observed to favor the onset of lasing on (short wavelength) higher-order waveguide modes close to the gain peak wavelength at low injection currents [Sch10a], [Sch12] and to reduce lasing on FP-like modes at the gain peak which may occur at high injection currents. Both, lasing on higher-order waveguide modes and FP-like modes limits the usable range of the spectral detuning due to appearance of undesirable side modes in the optical spectrum.

Thus, better suppression of higher-order waveguide modes would enable to use larger spectral detuning and therefore enable to achieve even higher optical output powers (> 12 W) at reasonable power conversion efficiency and with a narrow spectral width. Additionally, elimination of higher-order modes would enable to achieve a narrow wavelength stabilized spectrum at lower heatsink temperatures and therefore increase the usable locking range in current and heatsink temperature [Sch12]. Higher-order waveguide modes could be suppressed using an optimized epitaxy design for the waveguide. For example, the thickness of the waveguide layer can be reduced until the cutoff condition for the higher-order modes is fulfilled. However, this might be in conflict with the target to achieve a narrow vertical far field of $\leq 45\,^\circ$ with 95 % power content. Furthermore, the suppression of higher-order modes can be increased by optimizing the vertical position of the active region and the DFB grating in order to reduce their modal gain and decrease their coupling coefficient by a reduction of the confinement factors of the active region and grating layers with the vertical optical field profile. Finally, the internal optical loss of higher-order modes can be increased when the refractive index contrast between the waveguide and cladding layers is optimized to enable coupling of the higher-order modes to the n- and p-type cladding layers and highly absorbing n-type substrate and p-type contact layer.

A better suppression of lasing on FP-like modes which were observed for some devices when the gain peak was significantly detuned to the long wavelength side of the Bragg wavelength of the DFB grating, would be advantageous. This would enable higher optical output powers and increase the usable locking range to higher currents and heatsink temperatures. Intuitively, one might tend to position the minimum of the reflectivity spectrum of the AR front facet coating at the Bragg wavelength of the DFB grating, for example at ≈ 975 nm. Instead, it can be advantageous to shift the minimum of the reflectivity spectrum to the wavelength range where FP-like modes were observed to occur at high current levels, for example at ≈ 980 nm.

Significance for further research and development work and potential applications Finally the question about the significance of the achieved results for the further research and development work on high efficiency DFB-BA lasers and for possible applications arises.

The developed DFB-BA lasers have approximately the same efficiency, power, spatial emission properties and reliability as state of the art FP-BA lasers which are used in industrial applications. Thus, their additional wavelength stabilization and narrow spectral width makes them promising for possible applications such as pumping narrow $\approx 976\,\mathrm{nm}$ absorption bands in Yb-doped and Er-Yb co-doped gain media of solid state lasers, fiber lasers and amplifiers.

The results which have been obtained in this work indicate that concerning several aspects such as the spectral properties, vertical mode content and slope efficiency of the power characteristics, the performance of the DFB-BA lasers can be even further improved in future work.

Firstly, higher-order vertical modes of the waveguide should be eliminated. This requires the development of an improved epitaxy design for the waveguide and active region. Also improvements targeting higher power conversion efficiency and optical output power such as even lower internal optical loss, higher internal quantum efficiency and an optimized gain per unit length could be considered during this development. Secondly, a better suppression of FP-like modes at the gain peak wavelength under high current injection ($> 12\,\mathrm{A}$) should be targeted. Thirdly, a better suppression of high lateral mode orders with techniques such as lateral anti-guiding [Sho08], could be advantageous for both, the target to achieve a smaller lateral far filed divergence [Cru12a] as well as a lower spectral width. Fourthly, the physical reasons for the roll-over of the power characteristics of the DFB-BA lasers should be analyzed. A quantitative model for the impact of the spectral detuning between the peak wavelength of the gain spectrum and the Bragg wavelength of the DFB grating on the properties of the laser such as the threshold current and slope efficiency would be advantageous. Even the influence of the inhomogeneous aluminum distribution on the DFB coupling coefficient and radiation loss, as well as its mitigation or functionalization should be further analyzed. As mentioned in [Sch12], long in-situ etching times could be used to completely remove the aluminum-free grating layers, with a final nanostructure being selfassembled purely in $\mathrm{Al}_x\mathrm{Ga}_{1-x}\mathrm{As}$ due to variations in the aluminum content x.

In order to verify the applicability, reliable operation of the DFB-BA lasers in typical $10 - 19$ emitter $1\,\mathrm{cm}$ laser bars without degradation of the laser properties and without inhomogeneity of the laser properties within the laser bar must be demonstrated. Also a detailed study on the homogeneity

of the laser properties over a single wafer and between different nominal identical wafers is required. Finally, the fabrication of the DFB gratings must be demonstrated to be reproducible.

Outlook This outlook gives a short overview about present and future work on the research and development of efficiency optimized high power DFB-BA lasers, a recently developed competing grating fabrication technology and a recent publication about considerations on the high volume fabrication of buried overgrown DFB gratings, using in-situ etching or cleaning technology.

Based on the results which are reported in this work, further initial unpublished work was performed at the FBH on the development of high efficiency, high power DFB-BA lasers. Firstly, an optimized epitaxy design was developed, using a SQW active region, a waveguide with refractive index and doping profile for even lower internal optical loss than used in this work [Sch10a], [Sch12], optimized for $L = 4\,\mathrm{mm}$ cavity length and even higher optical output power $> 12\,\mathrm{W}$. In addition, the epitaxy design was optimized to guide only a single fundamental vertical mode even with the integrated DFB grating. First fabricated DFB-BA lasers ($L = 4\,\mathrm{mm}$, $W = 90\,\mu\mathrm{m}$, HR/AR coated facets) from this material were investigated and found to operate in a fundamental wavelength stabilized mode without any higher-order waveguide modes and FP-like modes from threshold to 15 A.

The design of the DFB grating and the fabrication technology can be also transferred to other wavelength which are achievable with AlGaAs-based laser designs, such as $910 - 940\,\mathrm{nm}$ for pumping of Yb-doped gain media, $808\,\mathrm{nm}$ for pumping $\mathrm{Nd:YAG}$ crystals and $894\,\mathrm{nm}$ for generation of spin-polarized Xe gas via spin-polarization of Cs vapor [Kli96], [Ear98]. Additionally, the in-situ etching technique and floating line-pattern design can be advantageous for the manufacturing of various optical and electrical nanostructures, mainly in AlGaAs-based material systems, with high requirements for low oxygen-contamination and high quality epitaxial regrowth conditions [Sch12]. Furthermore, in-situ etching techniques could potentially be used in other applications such as for improved performance of GaAs/$\mathrm{In_{0.49}Ga_{0.51}P}$-based *nipi* photovoltaic devices [Slo12].

Colleagues from the FBH have recently adapted the fabrication technology used for surface etched DBR gratings [Fri05], [Fri09], [Fri12a] to surface etched DFB gratings in DFB-BA lasers [Fri12b]. In order to achieve a low coupling strength which is required for high efficiency, high power DFB-BA lasers, very high Bragg orders (80th 135th and 270th-order) have been used. In contrast to DBR gratings, current flows through the DFB grating which is typically extended over the whole cavity length. Surface etched grooves of a

DFB grating which are encapsulated with electrically isolating material may therefore hinder the current flow, increase the series resistance and might also increase the thermal resistance of a mounted laser. These drawbacks can be minimized or even eliminated by using very high Bragg order DFB gratings where the distance between the etched grooves is large. For example, a 100th-order Bragg grating for 976 nm with an effective index of refraction of $n_{\text{eff}} = 3.42$ for the laser mode requires a groove distance or grating period of $\approx 14.3\,\mu$m. This can be a promising technology for wavelength stabilized BA lasers in competition with buried overgrown DFB gratings. For technologies, the coupling strength must be optimized to $\kappa \cdot L \leq 1$, while radiation loss must be minimized.

Authors from JDSU Corporation have recently reported on AlGaAs-based 830 nm single mode DFB lasers with partial corrugated DFB gratings [Dou12]. This publication shows that in-situ etched, buried overgrown second-order DFB gratings might be attractive for industrial applications and therefore, confirms the industrial relevance of recent studies on in-situ etching for the manufacturing of buried overgrown DFB gratings [Maa08], [Sch12]. The authors report that they use "in-situ cleaning" of the wet etched AlGaAs grating surface in order to achieve high quality and manufacturing yield. The authors use a second-order holographic grating, placed in the p-side of the waveguide in order to achieve better quality of the active region [Dou12]. Furthermore, they report that an optimized cleaning process is used prior to in-situ cleaning (inside the epitaxy reactor). This is argued to result in significant improvement of interface quality and a reduction of the oxygen concentration at the regrowth interface from $\approx 1 \cdot 10^{19}\,\text{cm}^{-3}$ to $\approx 5 \cdot 10^{16}\,\text{cm}^{-3}$ is measured [Dou12]. Measured voltage-current characteristics of partially corrugated DFB lasers and reference FP lasers are presented to demonstrate that the regrown DFB grating causes no additional series resistance in the DFB devices [Dou12]. Nevertheless, the reference FP lasers seem to contain the uncorrugated grating layer which may already introduce an increase in the voltage drop. Finally, power characteristics from a 600 h reliability test of 114 devices are presented which demonstrate only one failure for the in-situ cleaned DFB lasers [Dou12].

Appendix A

Fabrication and mounting

In this chapter, the most important facts of the wafer fabrication, processing, facet coating and laser mounting will be mentioned. The aim of this chapter is to provide a basis for the evaluation of the properties and quality of the devices and their fabrication techniques in comparison to comparable stand of the art technology.

A.1 Wafer fabrication

The lasers, developed during this work, were grown with low pressure metal organic vapor phase epitaxy (MOVPE) on n-doped GaAs wafers. The wafer size was limited to three inch for DFB-BA lasers, because the laser holography setup (see section 3.3.2) for the fabrication of a photoresist etch-mask for the DFB grating was optimized to a diameter of three inch. For the fabrication of FP-BA lasers, three and four inch GaAs wafers were used.

Wafers for DFB-BA lasers were fabricated in a two-step epitaxy process, to achieve buried index gratings. The design development for such DFB gratings is one main aspect of this work and is described in sections 3.3 and 4.2 in more detail.

A.2 Wafer processing

After the epitaxial growth of the wafers is finished, the wafers are processed in order to achieve laser bars with single emitters, which can be cleaved, facet coated and soldered on sub-mounts. The processing is subdivided into the p-side and n-side processing.

The p-side process starts with defining contact windows for single emitters by helium-implantation of the complete surrounding wafer surface. The

implantation causes mid-band defects, leading to electrically insulating character of the high doped GaAs contact layer and makes it isolating outside the contact windows. Afterwards, reactive ion etching (RIE) is applied to form shallow index trenches in parallel to the contact windows of each single emitter in a distance of several micrometers which provide weak lateral index guiding. Deep trenches are additionally etched in parallel to each contact window for electrical and optical isolation. A 100 μm thick SiN_x isolator layer is deposited by plasma-enhanced chemical vapor deposition (PECVD) on the whole wafer surface and subsequently removed by RIE on the contact windows. Finally, the *p*-side is metallized with multiple layers of Ti , Pt and Au and plated with Au for heat spreading.

During the *n*-side process, at first, the *n*-side substrate of the wafers is thinned to a thickness of $\sim 150\,\mu$m and a further 20 μm relaxation etch is applied to remove the damages on the surface. Afterwards, an ohmic $Ni - Au - Ge$ layer is deposited as back side metal. To get the back side suitable for wire bonding, a second backside metallization of Ti , Pt and Au is evaporated to the surface.

A.3 Facet coating

After epitaxial growth and processing, the wafers were cleaved into 1 cm laser bars with 10 to 19 single emitters. The cleaved facets of these laser bars were passivated and coated with dielectric layers. The facet passivation [Res05] material ZnSe is deposited on the facets in a molecular beam epitaxy (MBE) reactor, after cleaning with atomic hydrogen. Facet passivation is applied in order to make the facets robust, so that catastrophic optical mirror damage (COMD) is suppressed. The passivated facets are coated with dielectric layers from materials, such as Al_2O_3 and TiO_2 by ion beam sputtering, in order to achieve the required reflectivity at the front and rear facet [Var84]. Un-coated cleaved facets have a reflectivity of $R \approx 32\,\%$, as it can be calculated from the refractive indices from GaAs ($n_1 \approx 3.6$) or AlGaAs to air ($n_2 \cong 1.0$), $R = [(n_1 - n_2)/(n_1 + n_2)]^2 = 0.319$.

In addition to the laser bars, GaAs dummies were also introduced into the process and afterwards, used to measure the reflectivity R_{GaAs} of the coating on GaAs as a function of the wavelength λ. Taking into account the effective refractive index of the fundamental mode in the laser waveguide, the reflectivity $R(\lambda)$ for the laser mode has been calculated.

A.4 Mounting of single emitters

For the characterization, single emitters were hard soldered junction-side down (p-down) with AuSn [Pit01] on CuW screening sub-mounts (SCS-mounts). These sub-mounts consist of 10 %, Cu and 90 %, W), resulting in a thermal expansion coefficient of $6.4\,10^{-6}\mathrm{K}^{-1}$, approximately matched to the thermal expansion coefficient of GaAs at a temperature of 300 K, which is $\approx 6\,10^{-6}\mathrm{K}^{-1}$ [Bro96], [Ada93]. Broad area diode lasers with 3 mm cavity length were found to have a thermal resistance of 3 to $4\,\mathrm{K\,W}^{-1}$ on 4 mm SCS-mounts. The n-contact is connected to two bond-bases, each one at the left and right hand side of the SCS-mount. The number of Au wire bonds per side was ≈ 38.

For some experiments, as the measurement of sub-threshold (stopband) spectra of DFB lasers, for example, single emitters were mounted on C-mounts. The p-side down mounting on C-Mounts is technically comparable to mounting on SCS-mounts, the lasers are hard soldered with AuSn on CuW sub-mounts, then soldered on C-mounts. For mounting p-up, the lasers are directly soldered with PbSn on the Cu C-mount. The n-contact is connected to one or two bond-bases with Au wire bonds.

Appendix B

Measurement methods

The aim of the following chapter is to give the reader the possibility to understand, on which methods, measurements were based on and what the general limitations and limitations in the measurement accuracy are. Its not the aim of the chapter to describe the particular used measurement setups in detail and to define the components. If possible, references are given, in which the measurement methods and setups are discussed, in order to keep the descriptions as short as possible.

B.1 Measurements under CW conditions

High power BA diode lasers, developed during this work, are optimized to function under CW current injection, temperature-stabilized to 15 – 25 °C. Consequently, the power-voltage-current characteristics, spectra and spatial emission characteristics of the devices were measured under CW conditions.

B.1.1 Measurement of power-voltage-current characteristics

The measurement of the optical output power and diode voltage as a function of the injected current is the basis for the experimental analysis of a diode laser. The laser diode, mounted on CuW screening sub-mount (SCS-mount) was clamped in a measurement holder. This measurement holder has the footprint of a CCP-mount and is screwed onto a heatsink plate. The temperature of the device is measured by a 100 Ω resistance temperature detector (Pt 100), directly positioned at the rear-side of the SCS-mount. Temperature stabilization is realized by adjusting the temperature, measured at the resistance temperature detector, with a Peltier-element and a temperature

controller. The Peltier-element is placed between the heatsink-plate and a water through flow cooler beneath. Current is injected from a laser current driver, which enables continuous wave (CW) and quasi continuous wave (QCW) operation with an accuracy of $\approx 10\,\mathrm{mA}$. The current is measured internally and current accuracy is regularly tested with a load resistor. The diode voltage is measured current-less in a four-terminal configuration with a high accuracy voltmeter at one side of the wire bond base, while the current is injected over the other side. The CW optical output power is detected directly with a thermopile power detector (gentec UP19K-15S-W5) with a maximum load capacity of 15 W, a responsivity of 1 mW and an absolute calibration uncertainty of $\pm 2.5\,\%$. It has been controlled, that almost 100 % of the laser beam is directed onto the detector surface. The thermopile power detector is annually referenced to national standards, the power measurements are in accordance with international standard ISO 11554 [ISO06].

B.1.2 Measurement of optical spectra

Optical spectra of mounted diode lasers were measured under the same conditions as the power-voltage-current characteristics, described in section B.1.1. The mounting, temperature stabilization and current injections is identical. Optical spectra were usually measured with the same current steps as the power-voltage-current characteristics characteristics, which makes it easier to analyze the properties of the device, for example to determine the thermal resistance. The optical output of the diode laser was collected with a four inch integrating sphere and coupled into the spectrometers via an optical fiber. Different types of spectrometers have been used. For wide spectral range measurements with moderate requirements to the spectral resolution and dynamic range, a spectrometer with $\approx 0.15\,\mathrm{nm}$ spectral resolution (FWHM, if the available dynamic range is complete exploited) was used (OceanOptics HR2000). Typically, the resolution limit was $\approx 0.5\,\mathrm{nm}$. The dynamic range of the spectrometer is $\approx 4 \cdot 10^3$ and the spectral range extends from 780 to 1030 nm. For measurements with higher requirements to the spectral resolution, an Echelle spectrometer with a pre-monochromator and $\approx 15\,\mathrm{pm}$ resolution at $\sim 975\,\mathrm{nm}$ and a dynamic range of $\approx 6 \cdot 10^4$ has been used (LTB Lasertechnik Berlin GmbH, Demon). The spectrometer covers a spectral range between 175 and 1100 nm, but the simultaneous inspection range at $\sim 975\,\mathrm{nm}$ is only $\approx 8\,\mathrm{nm}$ without moving the Echelle grating. The measurements of optical spectra are in accordance with international standard ISO 13695 [ISO04b]

B.1.3 Measurement of vertical and lateral near fields and far fields

Two different setups have been used to measure the spatial emission properties of the diode lasers. Firstly, the vertical far field was measured with a 4.5 cm-radius goniometer setup. As a detector, a large area photo diode with adynamic range of $\sim 1 \cdot 10^3$ has been used. In front of the photo diode, an optical slit was mounted, to enable a narrow vertical angle resolution of $< 0.1\,^\circ$. This moving slit method is configured according to international standards IEC 60747-5-4 [IEC06] and ISO 11146-3 [ISO04a]. At optical output powers above 1 W, only quasi-continuous wave (QCW) current injection (500 μs pulse duration, 20 kHz repetition rate) has been used with the goniometer setup to avoid damage of the detector.

Secondly, a linear moving slit method was applied for the measurement of the lateral near field and far field. Also vertical near fields could be measured with this method, but the maximum achievable spatial resolution of $\approx 1\,\mu$m is not sufficient to clearly resolve the near field of the lasers with vertical mode sizes in the range of $\approx 2\,\mu$m. The method in use is described in [Hod05] in more detail, it is based on an optical telescope setup, a further cylindrical lens for the measurement of far fields and a photodiode with an optical slit, mounted on a motorized linear stage. The mentioned setup is also described in [Sah02] and [Fro07]. The spatial resolution in the lateral near field is $\approx 1\,\mu$m and the angular resolution in the lateral far field is $\sim 0.1\,^\circ$. Mounting, temperature stabilization and current injection is similar to the one, described in section B.1.1. By using a photo diode as an optical detector, a wide dynamic range of $\sim 1 \cdot 10^4$ was achieved. The optical slit in front of the photo diode is used to increase the spatial resolution of the measured field component, while the other field component is completely integrated. The measurements of lateral near fields and far fields are in accordance with international standards IEC 60747-5-4 [IEC06] and ISO 11146-1 [ISO05].

B.1.4 Spectrum measurements with fiber coupling

The DFB coupling coefficient can be derived from sub-threshold ASE spectra by fitting the measured spectrum to theory [Wen03], [Wen04]. To measure these sub-threshold spectra, a high sensitive (up to -87 dBm), high resolution (up to 10 pm) fiber coupled optical spectrum analyzer has been used (Advantest Q8384, $600 - 1700$ nm, up to 60 dB dynamic range). Laser diodes were either measured as un-mounted single emitters on laser bars or soldered as single emitters on C-mount heatsinks. The laser bars were connected to the measurement holder by suctioning them with vacuum and contacted with

two or three metal tips, to ensure homogenous pumping scheme. Current was injected from a 1 mA precision current source with a maximum current of $\leq$ 2 A. The temperature of the laser mount was stabilized by use of a resistance temperature detector, Peltier-element and temperature controller. The emitted power from one facet was coupled into a tapered conical lensed single mode optical fiber, which was connected to the spectrum analyzer. Thus, only a spatially filtered part of the spectrum is analyzed.

In Run II during this work, the coupling scheme has been changed to reduce optical feedback from the tip of the tapered fiber back into the laser which. Therefore, the optical field at the front facet of the laser was imaged onto the angled facet of an optical fiber with a telescope setup, constructed from two AR-coated lenses with 6 mm focal length. With this setup, measured sub-threshold ASE spectra of the DFB stopband were found to be much better reproducible.

B.2 Measurements under short pulse conditions

Measuring the diode lasers under short pulse ($<$ 1000 ns pulse duration, typical 1 kHz repetition rate) current injection has been applied, because it allows to determine the temperature dependence of the laser wavelength, the threshold current characteristic temperature and the slope efficiency characteristic temperature, as well as the pre-characterization of single diode lasers on un-mounted laser bars without seriously heating of the active region.

B.2.1 Power-voltage-current characteristics and spectra of mounted single emitters

A measurement setup for the characterization of diode lasers under short pulsed current injection has been developed during this work. The aim was to drive the laser diodes with current pulses, shorter than 800 ns, so that one can assume that the temperature inside the diode and especially, in the active region, is identical with the ambient temperature at the submount. This enables one to determine the dependence of the laser wavelength on the temperature $\mathrm{d}\lambda/\mathrm{d}T$, as well as the threshold current characteristic temperature T_0 and the slope efficiency characteristic temperature T_1, for example. In addition, power-voltage-current characteristics up to very high currents of 100 A can be measured with this setup, because the output power of the diode lasers is not limited by thermal induced roll-over under these conditions. The

setup is based on a short pulse laser voltage supply source AVTECH AVOZ-A3-B with $0-100\,\mathrm{A}$, $0-100\,\mathrm{V}$, $\leq 30\,\mathrm{ns}$ rise time, $50\,\mathrm{ns}-2\,\mu\mathrm{s}$ pulse width at a maximum duty cycle of $0.1\,\%$. The current is injected into the diode laser via a 60 cm, long ribbon cable wit a characteristic impedance of $Z_0 = 1.0\,\Omega$. The laser diode is build in a series connection with a $1.0\,\Omega$ measuring resistor into the electric circuit in order to to keep the load resistance at $\approx 1\,\Omega$ and sustain the rectangular current pulse shape. Otherwise, a mismatch between the transmission line and the load may introduce significant ringing of the current pulses. The laser is mounted on the heat-sink plate comparable as described in section B.1.1. The temperature is measured at the heatsink, very close to the measurement mount and stabilized by use of a Peltier-element, water cooler and a temperature controller. Current and voltage over the diode laser are measured as follows. Firstly, the voltage over the diode and the measuring resistor is measured with an oscilloscope in the plateau of the pulse. Secondly, the voltage over the $1\,\Omega$ measuring resistor is measured, which equals the current in A. Then, thirdly, the diode voltage is determined from the difference of the two measured voltages. Note, that in this setup, the determination of the diode voltage is not very precise (especially at high currents) because it is given by the small difference of two high-voltage signals. The optical output power is directed into an integrating sphere and detected with a photo diode, which is connected to it. The values for the voltages are determined in a time window within the plateau of the approximately rectangular current pulses. The output power in W is calibrated either, by fitting the slope efficiency close to the threshold to the slope efficiency of a calibrated CW or QCW measurement, or by measuring the time-averaged power with a μW-sensitive thermopile detector (gentec XLPF12-3S-H2) under consideration of the duty cycle. Spectra were measured by connecting a sensitive spectrometer (OceanOptics HR2000) to the fiber-port of the integrating sphere.

B.2.2 Power-voltage-current characteristics and spectra of un-mounted single emitters on laser bars

The measurement setup which is described here has been used for the pre-characterization of diode lasers after the epitaxial growth and processing. Therefore, the wafer is cleaved into laser bars with 10 or 19 single emitters, depending on the layout used. The laser bars were connected to the measurement holder by suctioning them with vacuum and contacted with two metal tips, to ensure homogenous pumping scheme. The setup also enables temperature stabilization. Current is applied with a short pulse current source

(typical 1000 ns pulse duration, 1 kHz repetition rate) to avoid current induced heating of the diode. Power was detected with a calibrated photo diode, spectra were measured with a low resolution ($\approx$ 1 nm) but sensitive spectrometer. For the standard characterization, power-voltage-current characteristics of BA lasers with cleaved facets, 100 and 200 μm stripe width and typically 1000 μm cavity length were measured at 20,° C up to 2 A and a single spectrum was taken at 2 A. Particularly, the cavity length dependence of the slope efficiency and threshold current was measured with this setup and was used to determine the internal optical loss α_i, internal quantum efficiency η_i, modal gain coefficient Γg_0 and transparency current density j_tr following the method described in section 3.1.

B.3 Measurement of spectrally resolved lateral near fields and far fields

Lateral near fields and far fields have been measured additionally with high spectral resolution in order to analyze the lateral and longitudinal modes in DFB-BA lasers. This measurement technique has been used in many different cases to enable a deep insight into the optical modes of broad area diode lasers [Ste06], [Ste09], [Cru12a], large mode area optical fibres [Nic09], [Nic10], [Lau11] and micro-resonators [Str07], [Str08b], [Str08a], [Str12]. However, no measurements were carried out at high output powers in the 5 to 10 W range, which is to date a typical reliable output power of high power $\approx$ 100μm stripe BA lasers. For the measurement of spectrally resolved lateral near fields and far fields, the setup, described in section B.1.3 has been used with modifications. Instead of the photo diode as a detector for the emitted optical power, the optical image of the near field or the far field was scanned with a multimode optical fiber, connected to a spectrometer. To achieve a high spatial resolution better than 2 μm, the fiber was mounted behind an optical slit with the possibility for adjustment in three transverse axes and tilting. The spectrometer used as a wavelength-sensitive detector, has to fulfill high demands on its spectral resolution, sensitivity and dynamic range. For this reasons, a custom made Echelle-spectrometer (ELIAS III from LTB Lasertechnik Berlin GmbH) with an extremely high spectral resolution capability was employed. This spectrometer allows to use the Echelle-grating either two- or for-times for the diffraction of light and uses a multitude of high interference orders. The measurements were carried out in double-pass configuration with a spectral resolution of $\approx$ 0.4 pm at 975 nm and a dynamic range of 10^4. Each spectrum consists of 2046 pixels, the si-

multaneous inspection range in the selected configuration is $\approx 174\,\mathrm{pm}$ (2048 pixel CCD detector, presumably two pixels damaged). The near field and far field profiles were scanned with 500 steps, so that each spectrally resolved field consists of 500×2046 data points.

Bibliography

[Ada93] S. Adachi, editor, *Properties of Aluminum Gallium Arsenide*, EMIS datareviews series, INSPEC (1993), ISBN 9780852968857.

[Afr74] M. A. Afromowitz, *Refractive index of Ga1-xAlxAs*, Solid state Communications **15**, 59 (1974).

[AM98] A. Al-Muhanna, L. J. Mawst, D. Botez, D. Z. Garbuzov, R. U. Martinelli, and J. C. Connolly, *High-power (>10 W) continuous-wave operation from 100-µm-aperture 0.97-µm-emitting Al-free diode lasers*, Applied Physics Letters **73**, 1182 (1998).

[And89] S. Ando and T. Fukui, *Facet growth of AlGaAs on GaAs with SiO2 gratings by MOCVD and applications to quantum well wires*, Journal of Crystal Growth **98**, 646 (1989), ISSN 0022-0248.

[And09] O. Andrusyak, V. Smirnov, V. Venus, G. Rotar, and L. Glebov, *Spectral Combining and Coherent Coupling of Lasers by Volume Bragg Gratings*, IEEE Journal of Selected Topics in Quantum Electronics **15**, 344 (2009).

[Bao11] L. Bao, P. Leisher, J. Wang, M. Devito, D. Xu, M. Grimshaw, W. Dong, X. Guan, S. Zhang, C. Bai, J. G. Bai, D. Wise, and R. Martinsen, *High reliability and high performance of 9xx-nm single emitter laser diodes*, volume 7918, page 791806, SPIE (2011).

[Baw09] A. Bawamia, B. Eppich, K. Paschke, H. Wenzel, F. Schnieder, G. Erbert, and G. Tränkle, *Experimental determination of the thermal lens parameters in a broad area semiconductor laser amplifier*, Applied Physics B: Lasers and Optics **97**, 95 (2009).

[Bef00] F. Beffa, H. Jäckel, M. Achtenhagen, C. Harder, and D. Erni, *High-temperature optical gain of 980 nm InGaAs/AlGaAs quantum-well lasers*, Applied Physics Letters **77**, 2301 (2000).

[Ber02] G. Berry, G. Burns, P. Charles, P. Crump, A. Davies, R. Ghin, M. Holm, C. Kompocholis, J. Massa, P. Ryder, A. Taylor, and M. Agrest, *100°C, 10 Gb/s directly modulated InGaAsP DFB lasers for uncooled Ethernet applications*, in *Optical Fiber Communications Conference*, page ThF1, Optical Society of America (2002).

[Bia99] G. Biasiol and E. Kapon, *Mechanism of self-limiting epitaxial growth on nonplanar substrates*, Journal of Crystal Growth **201 - 202**, 62 (1999).

[Bos96] D.J. Bossert and D. Gallant, *Gain, refractive index, and α-parameter in InGaAs-GaAs SQW broad-area lasers*, IEEE Photonics Technology Letters **8**, 322 (1996).

[Bot96] D. Botez, L.J. Mawst, A. Bhattacharya, J. Lopez, J. Li, T.F. Kuech, V.P. Iakovlev, G.I. Suruceanu, A. Caliman, and A.V. Syrbu, *66% CW wallplug efficiency from Al-free 0.98 μm-emitting diode lasers*, Electronics Letters **32**, 2012 (1996).

[Bot99] D. Botez, *Design considerations and analytical approximations for high continuous-wave power, broad-waveguide diode lasers*, Applied Physics Letters **74**, 3102 (1999).

[Bou89] D. P. Bour and A. Rosen, *Optimum cavity length for high conversion efficiency quantum well diode lasers*, Journal of Applied Physics **66**, 2813 (1989).

[Bro96] M.R. Brozel and G.E. Stillman, editors, *Properties of Gallium Arsenide*, EMIS datareviews series, INSPEC (1996), ISBN 9780852968857.

[Bug11] F. Bugge, A. Mogilatenko, U. Zeimer, O. Brox, W. Neumann, G. Erbert, and M. Weyers, *Characterization and optimization of 2-step MOVPE growth for single-mode DFB or DBR laser diodes*, Journal of Crystal Growth **315**, 74 (2011), 15th International Conference on Metalorganic Vapor Phase Epitaxy (ICMOVPE-XV).

[Bul07] K. A. Bulashevich, V. F. Mymrin, S. Yu Karpov, D. M. Demidov, and A. L. Ter-Martirosyan, *Effect of free-carrier absorption on performance of 808 nm AlGaAs-based high-power laser diodes*, Semiconductor Science and Technology **22**, 502 (2007).

[Buu79] J. Buus and M. J. Adams, *Phase and group indices for double heteroststructure lasers*, Solid-Stateand Electron Devices **3**, 189 (1979).

[Cam85] D. Campi and C. Papuzza, *Refractive index dispersion in group IV and binary III-V semiconductors: Comparison of calculated and experimental values*, Journal of Applied Physics **57**, 1305 (1985).

[Cas75] H. C. Casey, D. D. Sell, and K. W. Wecht, *Concentration dependence of the absorption coefficient for n- and p-type GaAs between 1.3 and 1.6 eV*, Journal of Applied Physics **46**, 250 (1975).

[Cha93] S. A. Chalmers, K. L. Lear, and K. P. Killeen, *Low resistance wavelength-reproducible p-type (Al,Ga)As distributed Bragg reflectors grown by molecular beam epitaxy*, Applied Physics Letters **62**, 1585 (1993).

[Cha00] C.H. Chang, T. Earles, and D. Botez, *High CW power narrow-spectral width (< 1.5 Å) 980 nm broad-stripe distributed-feedback diode lasers*, Electronics Letters **36**, 954 (2000).

[Che98] T. R. Chen, W. Hsin, and N. Bar-Chaim, *Very high power InGaAsP/InP distributed feedback lasers at 1550 nm wavelength*, Applied Physics Letters **72**, 1269 (1998).

[Chi88] S.R. Chinn, P.S. Zory, and A.R. Reisinger, *A model for GRIN-SCH-SQW diode lasers*, IEEE Journal of Quantum Electronics **24**, 2129 (1988).

[Cho77] A. Y. Cho, A. Yariv, and P. Yeh, *Observation of confined propagation in Bragg waveguides*, Applied Physics Letters **30**, 471 (1977).

[Coh09] Coherent, *An Introduction to Diode Lasers for Materials Processing*, Technical report, Choherent Inc., https://www.coherent.com/downloads/HPDDLBackground(2009).

[Col95] L. A. Coldren and S. W. Corzine, *Diode Lasers and Photonic Integrated Circuits*, John Wiley & Sons, Inc. (1995).

[Cru09] P. Crump, H. Wenzel, G. Erbert, and G. Tränkle, *Advances in spatial and spectral brightness in 800-1100 nm GaAs-based high power broad area lasers*, volume 7483, page 74830B, SPIE (2009).

[Cru10] P. Crump, C. M. Schultz, A. Pietrzak, S. Knigge, O. Brox, A. Maaßdorf, F. Bugge, H. Wenzel, and G. Erbert, *975-nm high-power broad area diode lasers optimized for narrow spectral linewidth applications*, volume 7583, page 75830N, SPIE (2010).

[Cru11a] P. Crump, C. M. Schultz, H. Ekhteraei, H. Wenzel, and G. Erbert, *The Modal Content of High Power Broad Area Diode Lasers with Integrated Distributed Feedback Gratings*, in *IEEE Photonics Conference (PHO)*, pages 581 – 582 (2011).

[Cru11b] P. Crump, C. M. Schultz, and P. Immerz, *Internal gratings create powerful, spectrally pure lasers with high efficiencies*, Compound Semiconductor **17**, 42 (2011).

[Cru11c] P. Crump, C. M. Schultz, H. Wenzel, S. Knigge, O. Brox, A. Maaßdorf, F. Bugge, and G. Erbert, *Reliable operation of 976nm high power DFB broad area diode lasers with over 60% power conversion efficiency*, volume 7953, page 79531G, SPIE (2011).

[Cru12a] P. Crump, S. Böldicke, C. M. Schultz, H. Ekhteraei, H. Wenzel, and G. Erbert, *Experimental and theoretical analysis of the dominant lateral waveguiding mechanism in 975 nm high power broad area diode lasers*, Semiconductor Science and Technology **27**, 045001 (2012).

[Cru12b] P. Crump, O. Brox, F. Bugge, J. Fricke, C. Schultz, M. Spreemann, B. Sumpf, H. Wenzel, and G. Erbert, *High Efficiency Monolithic Edge-Emitting GaAs-Based Laserswith Narrow Spectral Widths*, volume 86, chapter Advances in Semiconductor Lasers, pages 49–92, Academic Press, Semiconductors and Semimetals (2012).

[Cru12c] P. Crump, S. Hengesbach, U. Witte, H.D. Hoffmann, G. Erbert, and G. Tränkle, *High Power Diode Lasers Optimized for Low Loss Smile-insensitive External Spectral Stabilization*, IEEE Photonics Technology Letters **24**, 703 (2012).

[Die08] O. Dier, C. Reindl, A. Bachmann, C. Lauer, T. Lim, K. Kashani-Shirazi, and M.-C. Amann, *Reduction of hetero-interface resistivity in n-type AlAsSb/GaSb distributed Bragg reflectors*, Semiconductor Science and Technology **23**, 025018 (2008).

[Dou12] P. Doussiere, M. Tashima, H. Djie, K. W. Lee, V. Wong, D. Venables, V. Rossin, and E. Zucker, *830nm high power single mode DFB laser for high volume applications*, volume 8277, page 82770A, SPIE (2012).

[Dup78] R. D. Dupuis and P. D. Dapkus, *Room-temperature operation of distributed-Bragg-confinement Ga1-xAlxAs-GaAs lasers grown by*

metalorganic chemical vapor deposition, Applied Physics Letters **33**, 68 (1978).

[Ear98] T. Earles, L. J. Mawst, and D. Botez, *1.1 W continuous-wave, narrow spectral width (<1 Å) emission from broad-stripe, distributed-feedback diode lasers (lambda = 0.893 μm)*, Applied Physics Letters **73**, 2072 (1998).

[Ebe07] C. Ebert, J. Levkoff, J. Roberts, J. Seiler, C. Wanamaker, and T. Pinnington, *Selective area etching of InP with CBr4 in MOVPE*, Journal of Crystal Growth **298**, 94 (2007), 13th International Conference on Metal Organic Vapor Phase Epitaxy (ICMOVPE XIII).

[Eic04] J. Eichler, L. Dünkel, and B. Eppich, *Die Strahlqualität von Lasern – Wie bestimmt man Beugungsmaßzahl und Strahldurchmesser in der Praxis?*, Laser Technik Journal **1**, 63 (2004), ISSN 1863-9119.

[Erb00] G. Erbert, A. Bärwolff, J. Sebastian, and J. Tomm, *High-Power Diode Lasers – Fundamentals, Technology, Applications, High-Power Broad-Area Diode Lasers and Laser Bars*, volume 78 of *Topics in Applied Physics*, Springer-Verlag Berlin Heidelberg New York (2000).

[Erb07] G. Erbert and R. März, *High Power Diode Lasers – Technology and Applications, Principles of Diode Laser Operation*, Springer Series in Optical Sciences, Springer Science+Business Media, LLC (2007).

[Fri05] J. Fricke, H. Wenzel, M. Matalla, A. Klehr, and G. Erbert, *980-nm DBR lasers using higher order gratings defined by i-line lithography*, Semiconductor Science and Technology **20**, 1149 (2005).

[Fri09] J. Fricke, F. Bugge, A. Ginolas, W. John, A. Klehr, M. Matalla, P. Ressel, H. Wenzel, and G. Erbert, *High-Power 980nm Broad-Area Lasers Spectrally Stabilized by Surface Bragg Gratings*, IEEE Photonics Technology Letters **22**, 294 (2009).

[Fri12a] J. Fricke, W. John, A. Klehr, P. Ressel, L. Weixelbaum, H. Wenzel, and G. Erbert, *Properties and fabrication of high-order Bragg gratings for wavelength stabilization of diode lasers*, Semiconductor Science and Technology **27**, 055009 (2012).

[Fri12b] J. Fricke, H. Wenzel, F. Bugge, O. Brox, A. Ginolas, W. John, P. Ressel, L. Weixelbaum, and G. Erbert, *High-Power Distributed*

Feedback Lasers With Surface Gratings, IEEE Photonics Technology Letters **24**, 1443 (2012).

[Fro07] P. Froese, *Die Analyse der elektrischen und optischen Eigenschaften von GaInP/AlGaInP Trapezlasern im Wellenlängenbereich von 650 bis 670 nm*, Diplomarbeit, Fachhochschule Köln (2007).

[Fun04] M. Funabashi, H. Nasu, T. Mukaihara, T. Kimoto, T. Shinagawa, T. Kisea, K. Takaki, T. Takagi, M. Oike, T. Nomura, and A. Kasukawa, *Recent Advances in DFB Lasers for Ultradense WDM Applications*, IEEE Journal of Selected Topics in Quantum Electronics **10**, 312 (2004).

[Gal12] K. Gallup, W. Hu, R. Lammert, and J. Ungar, *High-Power Laser Diodes: Wavelength stabilization improves laser diode efficiency and brightness*, Laser Focus World **48** (2012).

[Goo91] M. S. Goorsky, T. F. Kuech, F. Cardone, P. M. Mooney, G. J. Scilla, and R. M. Potemski, *Characterization of epitaxial GaAs and AlxGa1-xAs layers doped with oxygen*, Applied Physics Letters **58**, 1979 (1991).

[Gra12] D. M. Grasso, N. Shou, H. Chen, R. Pathak, Pa. Liang, S. D. Roh, and D. Lee, *Wavelength-stabilized fiber-coupled diode laser with 500-W output and 20-mm mrad beam quality*, volume 8241, page 82410K, SPIE (2012).

[He09] Y. He, H. An, J. Cai, C. Galstad, S. Macomber, and M. Kanskar, *808nm broad area DFB laser for solid-state laser pumping application*, Electronics Letters **45**, 163 (2009).

[Hei12] S. Heinemann, B. Lewis, K. Michaelis, and T. Schmidt, *Very high brightness diode laser*, volume 8241, page 82410L, SPIE (2012).

[Hen85] C. Henry, R. Kazarinov, R. Logan, and R. Yen, *Observation of destructive interference in the radiation loss of second-order distributed feedback lasers*, IEEE Journal of Quantum Electronics **21**, 151 (1985).

[Hod05] N. Hodgson and H. Weber, *Laser Resonators and Beam Propagation*, Springer Science + Business Media, Inc. (2005).

[Hof01] L. Hofmann, D. Rudloff, I. Rechenberg, A. Knauer, J. Christen, and M. Weyers, *(AlGa)As composition profile analysis of trenches overgrown with MOVPE*, Journal of Crystal Growth **222**, 465 (2001).

[Hon99] J. Hong, C. Blaauw, R. Moore, S. Jatar, and S. Dzioba, *Strongly gain-coupled (SGC) coolerless (-40°C +85°C) MQW DFB lasers*, IEEE Journal of Selected Topics in Quantum Electronics pages 442–448 (1999).

[Hu09] W. Hu, F. D. Patel, M. L. Osowski, R. M. Lammert, S. W. Oh, C. Panja, V. C. Elarde, L. Vaissié, and J. E. Ungar, *High-spectral brightness pump sources for diode-pumped solid state lasers*, volume 7198, page 71981R, SPIE (2009).

[Hua11] R. K. Huang, B. Chann, and J. D. Glenn, *Ultra-high brightness wavelength-stabilized kW-class fiber coupled diode laser*, volume 7918, page 791810, SPIE (2011).

[IEC06] IEC-60747-5-4, *Semiconductor devices – Discrete devices – Part 5-4: Optoelectronic devices – Semiconductor lasers*, International Standard (2006).

[ISO04a] ISO-11146-3, *Lasers and laser-related equipment – Test methods for laser beam widths, divergence angles and beam propagation ratios – Part 3: Intrinsic and geometrical laser beam clasification, propagation and details of test methods*, International Standard (2004).

[ISO04b] ISO-13695, *Lasers and laser related equipment – Test methods for the spectral characteristics of lasers*, International Standard (2004).

[ISO05] ISO-11146-1, *Lasers and laser-related equipment – Test methods for laser beam widths, divergence angles and beam propagation ratios – Part 1: Stigmatic and simple astigmatic beams*, International Standard (2005).

[ISO06] ISO-11554, *Lasers and laser related equipment – Test methods for laser beam power, energy and temporal characteristics*, International Standard (2006).

[Kam01] M. Kamp, J. Hofmann, F. Schäfer, M. Reinhard, M. Fischer, T. Bleuel, J.P. Reithmaier, and A. Forchel, *Lateral coupling - a material independent way to complex coupled DFB lasers*, Optical Materials **17**, 19 (2001).

[Kan97] J. U. Kang, M. Y. Frankel, J.-W. Huang, and T. F. Kuech, *Ultrafast carrier trapping in oxygen-doped metal-organic vapor phase epitaxy GaAs*, Applied Physics Letters **70**, 1560 (1997).

[Kan05] M. Kanskar, T. Earles, T.J. Goodnough, E. Stiersa, D. Botez, and L.J. Mawst, *73% CW power conversion efficiency at 50W from 970nm diode laser bars*, Electronics Letters **41**, 245 (2005).

[Kan06] M. Kanskar, Y. He, J. Cai, C. Galstad, S.H. Macomber, E. Stiers, D. Botez, and L.J. Mawst, *53% wallplug efficiency 975nm distributed feedback broad area laser*, Electronics Letters **42**, 1455 (2006).

[Kan09] M. Kanskar and F. Brunet, *Novel grating boosts brightness*, Compound Semiconductor pages 21–23 (2009).

[Kaz85] R. F. Kazarinov and C. H. Henry, *Second-Order Distributed Feedback Lasers with Mode Selection Provided by First-Order Radiation Losses*, IEEE Journal of Quantum Electronics **21**, 144 (1985).

[Köh09] B. Köhler, T. Brand, M. Haag, and J. Biesenbach, *Wavelength stabilized high-power diode laser modules*, volume 7198, page 719810, SPIE (2009).

[Köh12] B. Köhler, S. Ahlert, A. Bayer, H. Kissel, H. Müntz, A. Noeske, K.n Rotter, A. Segref, M. Stoiber, A. Unger, P. Wolf, and J. Biesenbach, *Scalable high-power and high-brightness fiber coupled diode laser devices*, volume 8241, page 824108, SPIE (2012).

[Kha95] A. Khan, K. Woodbridge, M. Ghisoni, G. Parry, G. Beyer, J. Roberts, M. Pate, and G. Hill, *Application of intermixing to p-type GaAs/AlAs distributed Bragg reflectors for series resistance reduction in vertical cavity devices*, Journal of Applied Physics **77**, 4921 (1995).

[Kle06] A. Klehr, F. Bugge, G. Erbert, J. Fricke, A. Knauer, P. Ressel, H. Wenzel, and G. Tränkle, *High-power broad-area 808 nm DFB lasers for pumping solid state lasers*, volume 6133, page 61330F, SPIE (2006).

[Kle07] A. Klehr, H. Wenzel, O. Brox, F. Bugge, G. Erbert, T-P. Nguyen, and G. Tränkle, *High-power 894 nm monolithic distributed-feedback laser*, Optics Express **15**, 11364 (2007).

[Kli96] W. M. Klipstein, S. K. Lamoreaux, and E. N. Fortson, *Observation of Spontaneous Spin Polarization in an Optically Pumped Cesium Vapor*, Physical Revue Letters **76**, 2266 (1996).

[Kön10] H. König, G. Grönninger, C. Lauer, W. Reill, M. Arzberger, U. Strauß, H. Kissel, J. Biesenbach, Ar. Kösters, J. Malchus, and V. K. Krause, *Scaling brilliance of high power laser diodes*, volume 7583, page 75830T, SPIE (2010).

[Kni05] A. Knigge, G. Erbert, J. Jonsson, W. Pittroff, R. Staske, B. Sumpf, M. Weyers, and G. Tränkle, *Passively cooled 940nm laser bars with 73% wall-plug efficiency at 70W and 25°C*, Electronics Letters **41**, 250 (2005).

[Koe70] W. Koechner, *Thermal Lensing in a Nd:YAG Laser Rod*, Applied Optics **9**, 2548 (1970).

[Koe11] T. Koenning, K. Alegria, Z. Wang, A. Segref, D. Stapleton, W. Faßbender, M. Flament, K. Rotter, A. Noeske, and J. Biesenbach, *Macro-channel cooled high power fiber coupled diode lasers exceeding 1.2kW of output power*, volume 7918, page 79180E, SPIE (2011).

[Kog71] H. Kogelnik and C. V. Shank, *Stimulated emission in a periodic structure*, Applied Physics Letters **18**, 152 (1971).

[Kog72] H. Kogelnik and C. V. Shank, *Coupled-Wave Theory of Distributed Feedback Lasers*, Journal of Applied Physics **43**, 2327 (1972).

[Koo00] E. M. Koontz, G. S. Petrich, L. A. Kolodziejski, and M. S. Goorsky, *Overgrowth of submicron-patterned surfaces for buried index contrast devices*, Semiconductor Science and Technology **15**, R1 (2000).

[Kre77] H. Kressel and J.K. Butler, *Semiconductor lasers and heterojunction LEDs*, Quantum electronics–principles and applications, Academic Press (1977), ISBN 9780124262508.

[Lam98] R.M. Lammert, J.E. Ungar, S.W. Oh, H. Qi, and J.S. Chen, *High-power InGaAs-GaAs-AlGaAs distributed feedback lasers with non-absorbing mirrors*, Electronics Letters **34**, 886 (1998).

[Lau11] M. Laurila, T. T. Alkeskjold, J. Lægsgaard, and J. Broeng, *Modal analysis of a large-mode area photonic crystal fiber amplifier using spectral-resolved imaging*, Optical Engeneering **50**, 111604 (2011).

[Lee97] Y. K. Lee, Genlin Tan, G. Pakulski, Toshi Makino, and J. M. Xu, *Plasma and thermal effects on the performance of high power floating grating DFB laser*, volume 3038, pages 14–22, SPIE (1997).

[Li03] S. Li, G. Witjaksono, S. Macomber, and D. Botez, *Analysis of surface-emitting second-order distributed feedback lasers with central grating phaseshift*, IEEE Journal of Selected Topics in Quantum Electronics **9**, 1153 (2003).

[Lop99] J. Lopez, G. Witjaksono, and D. Botez, *Single-mode, single-lobe operation of surface-emitting, second-order distributed feedback lasers*, Applied Physics Letters **75**, 885 (1999).

[Luo90] Y. Luo, Y. Nakano, K. Tada, T. Inoue, H. Hosomatsu, and H. Iwaoka, *Purely gain-coupled distributed feedback semiconductor lasers*, Applied Physics Letters **56**, 1620 (1990).

[Maa08] A. Maaßdorf and M. Weyers, *In-situ etching of GaAs/AlxGa1-xAs by CBr4*, Journal of Crystal Growth **310**, 4754 (2008), 14th International conference on Metalorganic Vapor Phase Epitaxy.

[Mar09] T. Markurt, *Strukturelle Charakterisierung von distributed feedback (DFB) Laserdioden mit der Transmissionselektronenmikroskopie*, Diplomarbeit, Humboldt University, Berlin (2009).

[Maw96] L. J. Mawst, A. Bhattacharya, J. Lopez, D. Botez, D. Z. Garbuzov, L. DeMarco, J. C. Connolly, M. Jansen, F. Fang, and R. F. Nabiev, *8 W continuous wave front-facet power from broad-waveguide Al-free 980 nm diode lasers*, Applied Physics Letters **69**, 1532 (1996).

[Mor98] S. Morgott, P. Chazan, M. Mikulla, M. Walther, R. Kiefer, J. Braunstein, and G. Weimann, *High-power near-diffraction-limited external cavity laser, tunable from 1030 to 1085 nm*, Electronics Letters **34**, 558 (1998).

[Nak73] M. Nakamura, A. Yariv, H.W. Yen, S. Somekh, and H. L. Garvin, *Optically pumped GaAs surface laser with corrugation feedback*, Applied Physics Letters **22**, 515 (1973).

[Nak89] Y. Nakano, Y. Luo, and K. Tada, *Facet reflection independent, single longitudinal mode oscillation in a GaAlAs/GaAs distributed feedback laser equipped with a gain-coupling mechanism*, Applied Physics Letters **55**, 1606 (1989).

[Nic09] J.W. Nicholson, A.D. Yablon, J.M. Fini, and M.D. Mermelstein, *Measuring the Modal Content of Large-Mode-Area Fibers*, IEEE Journal of Selected Topics in Quantum Electronics **15**, 61 (2009).

[Nic10] J.W. Nicholson, J.M Fini, S. Ghalmi, J.C. Jasapara, A. DeSantolo, E. Monberg, and F. Dimarcello, *Measuring the modes of optical fibers using S2 imaging*, in *Conference on Lasers and Electro-Optics (CLEO) and Quantum Electronics and Laser Science Conference (QELS)*, volume CWL1, pages 1 – 2 (2010).

[Oso07] M. L. Osowski, W. Hu, R. M. Lammert, T. Liu, Y. Ma, S. W. Oh, C. Panja, P. T. Rudy, T. Stakelon, and J. E. Ungar, *High-brightness semiconductor lasers*, volume 6456, page 64560D, SPIE (2007).

[Pas97] R. Paschotta, J. Nilsson, A.C. Tropper, and D.C. Hanna, *Ytterbium-doped fiber amplifiers*, IEEE Journal of Quantum Electronics **33**, 1049 (1997).

[Pas10] K. Paschke, S. Spießberger, C. Kaspari, D. Feise, C. Fiebig, G. Blume, H. Wenzel, A. Wicht, and G. Erbert, *High-power distributed Bragg reflector ridge-waveguide diode laser with very small spectral linewidth*, Optics Letters **35**, 402 (2010).

[Pat09] R. Pathak, J. Minelly, J. Haapamaa, J. Watson, D. Schleuning, H. Winhold, E. Weiss, M. Toivonen, S. Lehkonen, D. Roh, N. Ostrom, D. Grasso, J. Pfaff, and T. C. Hasenberg, *915 nm laser bar-based high-performance sources for fiber laser pumping*, volume 7198, page 719808, SPIE (2009).

[Pet93] M. G. Peters, B. J. Thibeault, D. B. Young, J. W. Scott, F. H. Peters, A. C. Gossard, and L. A. Coldren, *Band-gap engineered digital alloy interfaces for lower resistance vertical-cavity surface-emitting lasers*, Applied Physics Letters **63**, 3411 (1993).

[Pet07] M. Peters, V. Rossin, M. Everett, and E. Zucker, *High-power, high-efficiency laser diodes at JDSU*, volume 6456, page 64560G, SPIE (2007).

[Pie11] A. Pietrzak, *Realization of High Power Diode Lasers with Extremely Narrow Vertical Divergence*, Dissertation, Technical University of Berlin (2011).

[Pit01] W. Pittroff, G. Erbert, G. Beister, F. Bugge, A. Klein, A. Knauer, J. Maege, P. Ressel, J. Sebastian, R. Staske, and G. Traenkle, *Mounting of high power laser diodes on boron nitride heat sinks using an optimized Au/Sn metallurgy*, IEEE Transactions on Advanced Packaging **21**, 434 (2001).

[PTI11] IOFFE Physico-Technical Institute, *Electronic archive , physical properties of semiconductors*, http://www.ioffe.ru/SVA/NSM/Semicond/index.html (2011).

[Puc00] R. Puchert, A. Bärwolff, M. Voss, U. Menzel, J.W. Tomm, and J. Luft, *Transient thermal behavior of high power diode laser arrays*, IEEE Transactions on Components and Packaging Technologies **23**, 95 (2000).

[Red11] U. Reddy, N. L. Dias, A. Garg, and J. J. Coleman, *A single spectral mode wide stripe laser with very narrow linewidth*, Applied Physics Letters **99**, 171109 (2011).

[Ren92] N. Reng and B. Eppich, *Definition and measurements of high-power laser beam parameters*, Optical and Quantum Electronics **24**, 973 (1992).

[Res05] P. Ressel, G. Erbert, U. Zeimer, K. Häusler, G. Beister, B. Sumpf, A. Klehr, and G. Tränkle, *Novel Passivation Process for the Mirror Facets of Al-Free Active-Region High-Power Semiconductor Diode Lasers*, IEEE Photonics Technology Letters **15**, 962 (2005).

[Rob97] J. Robadey, U. Marti, R.O. Miles, M. Glick, F. Filipowitz, M. Achtenhagen, D. Martin, F. Morier-Genoud, P.C. Silva, Y. Magnenat, P.-H. Jouneau, F. Bobard, and F.K. Reinhart, *Distributed feedback gain-coupled lasers based on InGaAs quantum-wire arrays*, IEEE Photonics Technology Letters **9**, 5 (1997).

[Roh09] S. D. Roh, D. M. Grasso, and J. A. Small, *Very high-brightness fiber-coupled diode lasers*, volume 7198, page 71980Y, SPIE (2009).

[Sah02] S. Sahre, *Untersuchungen an Hochleistungsdiodenlasern hoher Strahlqualität*, Diplomarbeit, Technische Fachhochschule Wildau (TFH) (2002).

[Sak92a] M. Sakamoto, J.G. Endriz, and D.R. Scifres, *120 W CW output power from monolithic AlGaAs (800 nm) laser diode array mounted on diamond heatsink*, Electronics Letters **28**, 197 (1992).

[Sak92b] M. Sakamoto, J.G. Endriz, and D.R. Scifres, *20 W CW monolithic AlGaAs (810 nm) laser diode arrays*, Electronics Letters **28**, 178 (1992).

[Sch94] R. Schatz, E. Berglind, and L. Gillner, *Parameter extraction from DFB lasers by means of a simple expression for the spontaneous emission spectrum*, IEEE Photonics Technology Letters **6**, 1182 (1994).

[Sch07] C. Schnitzler, S. Hambuecker, O. Ruebenach, V. Sinhoff, G. Steckman, L. West, C. Wessling, and D. Hoffmann, *Wavelength stabilization of HPDL array: fast-axis collimation optic with integrated VHG*, volume 6456, page 645612, SPIE (2007).

[Sch09a] C. M. Schultz, P. Crump, H. Wenzel, O. Brox, F. Bugge, and G. Erbert, *Narrow Vertical Far-Field 975-nm Broad-Area DFB Lasers for Wide Temperature Range Operation*, IEEE Photonics Technology Letters **21**, 593 (2009).

[Sch09b] C. M. Schultz, P. Crump, H. Wenzel, O. Brox, F. Bugge, and G. Erbert, *Wide Temperature Range High Power Broad Area 975nm DFB Lasers*, in *Conference on Lasers and Electro-Optics/International Quantum Electronics Conference*, page CWF6, Optical Society of America (2009).

[Sch10a] C. M. Schultz, P. Crump, H. Wenzel, O. Brox, A. Maaßdorf, G. Erbert, and G. Tränkle, *11W broad area 976nm DFB lasers with 58% power conversion efficiency*, Electronics Letters **46**, 580 (2010).

[Sch10b] C. M. Schultz, P. Crump, H. Wenzel, O. Brox, A. Maaßdorf, G. Erbert, and G. Tränkle, *11W Broad Area 976nm DFB Lasers with 58% Efficiency*, in *Conference on Lasers and Electro-Optics*, page CWE1, Optical Society of America (2010).

[Sch11] C. M. Schultz, P. Crump, H. Wenzel, S. Knigge, O. Brox, A. Maaßdorf, F. Bugge, and G. Erbert, *Efficiency-optimized 973nm high power broad area DFB lasers with overgrown aluminium-free gratings for peak power conversion of 63%*, in *CLEO/Europe and EQEC 2011 Conference Digest*, page CB7 3, Optical Society of America (2011).

[Sch12] C. M. Schultz, P. Crump, A. Maaßdorf, O. Brox, F. Bugge, A. Mogilatenko, H. Wenzel, S. Knigge, B. Sumpf, M. Weyers, G. Erbert, and G. Tränkle, *In situ etched gratings embedded in AlGaAs for efficient high power 970 nm distributed feedback broad-area lasers*, Applied Physics Letters **100**, 201115 (2012).

[Sci74] D. R. Scifres, R. D. Burnham, and W. Streifer, *Distributed-feedback single heterojunction GaAs diode laser*, Applied Physics Letters **25**, 203 (1974).

[Sci75] D. R. Scifres, R. D. Burnham, and W. Streifer, *Highly collimated laser beams from electrically pumped SH GaAs/GaAlAs distributed - feedback lasers*, Applied Physics Letters **26**, 48 (1975).

[Sev08] A. Sevian, O. Andrusyak, I. Ciapurin, V. Smirnov, G. Venus, and L. Glebov, *Efficient power scaling of laser radiation by spectral beam combining*, Optics Letters **33**, 384 (2008).

[Sho08] N. Shomura, M. Fujimoto, and T. Numai, *Fiber Pump Semiconductor Lasers With Optical Antiguiding Layers for Horizontal Transverse Modes*, IEEE Journal of Quantum Electronics **44**, 819 (2008).

[Sie98] A. E. Siegman, *How to (maybe) measure laser beam quality*, in *DPSS (Diode Pumped Solid State) Lasers: Applications and Issues*, page MQ1, Optical Society of America (1998).

[Sin93] Y.K. Sin and H. Horikawa, *High power 0.98 μm InGaAs-GaAs-InGaP distributed feedback buried heterostructure strained quantum well lasers*, Electronics Letters **29**, 920 (1993).

[Slo12] M. A. Slocum, D. V. Forbes, and S. M. Hubbard, *Interface quality enhancement of the epitaxial regrowth process for nipi photovoltaic devices*, volume 8256, page 82561B, SPIE (2012).

[Som73] H.S. Jr. Sommers, *Experimental properties of injection lasers: modal distribution of laser power*, Journal of Applied Physics **44**, 1263 (1973).

[Ste06] N. Stelmakh and M. Flowers, *Measurement of spatial modes of broad-area diode lasers with 1-GHz resolution grating spectrometer*, IEEE Photonics Technology Letters **18**, 1618 (2006).

[Ste09] N. Stelmakh, *External-to-cavity lateral-mode harnessing devices for high-brightness broad-area laser diodes: concept, realizations, and perspectives*, volume 7230, page 72301B, SPIE (2009).

[Str75] W. Streifer, R. D. Burnham, and D. R. Scifres, *Effect of external reflectors on longitudinal modes of distributed feedback lasers*, IEEE Journal of Quantum Electronics **11**, 154 (1975).

[Str76] W. Streifer, R. Burnham, and D. Scifres, *Radiation losses in distributed feedback lasers and longitudinal mode selection*, IEEE Journal of Quantum Electronics **12**, 737 (1976).

[Str77] W. Streifer, D. Scifres, and R. Burnham, *Coupled wave analysis of dfb and dbr lasers*, IEEE Journal of Quantum Electronics **13**, 134 (1977).

[Str07] Ch. Strelow, C. M. Schultz, H. Rehberg, H. Welsch, Ch. Heyn, D. Heitmann, and T. Kipp, *Three dimensionally confined optical modes in quantum-well microtube ring resonators*, Physical Review B **76**, 045303 (2007).

[Str08a] Ch. Strelow, H. Rehberg, C. M. Schultz, H. Welsch, Ch. Heyn, D. Heitmann, and T. Kipp, *Optical Microcavities Formed by Semiconductor Microtubes Using a Bottlelike Geometry*, Physical Review Letters **101**, 127403 (2008).

[Str08b] Ch. Strelow, H. Rehberg, C. M. Schultz, H. Welsch, Ch. Heyn, D. Heitmann, and T. Kipp, *Spatial emission characteristics of a semiconductor microtube ring resonator*, Physica E: Low-dimensional Systems and Nanostructures **40**, 1836 (2008), 13th International Conference on Modulated Semiconductor Structures.

[Str12] Ch. Strelow, C. M. Schultz, H. Rehberg, M. Sauer, H. Welsch, A. Stemmann, Ch. Heyn, D. Heitmann, and T. Kipp, *Light confinement and mode splitting in rolled-up semiconductor microtube bottle resonators*, Physical Review B **85**, 155329 (2012).

[Sum12] B. Sumpf, A. Klehr, G. Erbert, and G. Tränkle, *Application of 940 nm high-power DFB lasers for line-broadening measurements at normal pressure using a robust and compact setup*, Applied Physics B **106**, 357 (2012).

[SZA00] A.M. Shams-Zadeh-Amiri, Jin Hong, Xun Li, and Wei-Ping Huang, *Second- and higher-order resonant gratings with gain or loss-Part 1: Green's function analysis*, IEEE Journal of Quantum Electronics **36**, 1421 (2000).

[Tho80] G. H. B. Thompson, *Physics of Semiconductor Laser Devices*, Wiley, Chichester (1980).

[Tre00] H.-G. Treusch, A. Ovtchinnikov, X. He, M. Kanskar, J. Mott, and S. Yang, *High-Brightness Semiconductor Laser Sources for Materials Processing: Stacking, Beam Shaping, and Bars*, IEEE Journal of Selected Topics in Quantum Electronics **6**, 601 (2000).

[Vai08] L. Vaissie, T. Streele, and P. T. Rudy, *High-power diode lasers advance pumping applications*, Laser Focus World (2008).

[Vai10] L. Vaissie, *Brightlock pump diodes take the heat out of high power lasers*, Photonics Online (2010).

[Var84] M. Varasi, C. Misiano, and L. Lasaponara, *Deposition of optical thin films by ion beam sputtering*, Thin Solid Films **117**, 163 (1984).

[Vos96] M. Voss, C. Lier, U. Menzel, A. Bärwolff, and T. Elsaesser, *Time-resolved emission studies of GaAs/AlGaAs laser diode arrays on different heat sinks*, Journal of Applied Physics **79**, 1170 (1996).

[Wen90] H. Wenzel and H.-J. Wünsche, *A Model for the Calculation of the Threshold Current of SCH-MQW-SAS Lasers*, physica status solidi (a) **120**, 661 (1990).

[Wen03] H. Wenzel, *Green's function based simulation of the optical spectrum of multisection lasers*, IEEE Journal of Selected Topics in Quantum Electronics **9**, 865 (2003).

[Wen04] H. Wenzel, A. Klehr, M. Braun, F. Bugge, G. Erbert, J. Fricke, A. Knauer, P. Ressel, B. Sumpf, M. Weyers, and G. Traenkle, *Design and realization of high-power DFB lasers*, volume 5594, pages 110–123, SPIE (2004).

[Wen06] H. Wenzel, R. Güther, A. M. Shams-Zadeh-Amiri, and P. Bienstman, *A Comparative Study of Higher Order Bragg Gratings: Coupled-Mode Theory Versus Mode Expansion Modeling*, IEEE Journal of Quantum Electronics **42**, 64 (2006).

[Wen08] H. Wenzel, M. Dallmer, and G. Erbert, *Thermal lensing in high-power ridge-waveguide lasers*, Optical and Quantum Electronics **40**, 379 (2008).

[Wen11] H. Wenzel, P. Crump, H. Ekhteraei, C. Schultz, J. Pomplun, S. Burger, L. Zschiedrich, F. Schmidt, and G. Erbert, *Theoretical and experimental analysis of the lateral modes of high-power broad-area lasers*, in *11th International Conference on Numerical Simulation of Optoelectronic Devices (NUSOD)*, pages 143–144 (2011).

[Wen12] H. Wenzel, *Unpublished personal communication with H. Wenzel, FBH* (2012).

[Wol11] P. Wolf, B. Köhler, K. Rotter, S. Hertsch, H. Kissel, and J. Biesenbach, *High-power, high-brightness and low-weight fiber coupled diode laser device*, volume 7918, page 79180O, SPIE (2011).

[Yor92] P.K. York, J.C. Connolly, N.A. Hughes, T.J. Zamerowski, J.H. Abeles, J.B. Kirk, J.T. McGinn, and K.B. Murphy, *MOCVD regrowth over GaAs/AlGaAs gratings for high power long-lived InGaAs/AlGaAs lasers*, Journal of Crystal Growth **124**, 709 (1992).

[Zho95] P. Zhou, B. Lu, J. Cheng, K. J. Malloy, S. Z. Sun, S. D. Hersee, and J. C. Zolper, *Vertical-cavity surface-emitting lasers with thermally stable electrical characteristics*, Journal of Applied Physics **77**, 2264 (1995).

Publications, talks and patent

Publications

First author publications

C.M. Schultz, P. Crump, A. Maaßdorf, O. Brox, F. Bugge, A. Mogilatenko, H. Wenzel, S. Knigge, B. Sumpf, M. Weyers and G. Erbert, "Buried DFB gratings floating in AlGaAs with low oxygen contamination enable high power and efficiency DFB lasers", IEEE Summer Topical Meetings, 978-1-4577-1527-3/12, 59-60 (2012).

C.M. Schultz, P. Crump, A. Maaßdorf, O. Brox, F. Bugge, A. Mogilatenko, H. Wenzel, S. Knigge, B. Sumpf, M. Weyers, G. Erbert, and G. Tränkle, "In situ etched gratings embedded in AlGaAs for efficient high power 970nm distributed feedback broad-area lasers", Applied Physics Letters **100**, 201115 (2012).

C.M. Schultz, P. Crump, H. Wenzel, S. Knigge, O. Brox, A. Maassdorf, F. Bugge and G. Erbert, "Efficiency-optimized 973nm high power broad area DFB lasers with overgrown aluminium-free gratings for peak power conversion of 63%", in CLEO/Europe and EQEC 2011 Conference Digest, OSA Technical Digest, paper CB7_3 (2011).

C.M. Schultz, P. Crump, H. Wenzel, O. Brox, A. Maaßdorf, G. Erbert and G. Tränkle, "11W broad area 976nm DFB lasers with 58% power conversion efficiency", Electronics Letters **46**, 580-581 (2010).

C.M. Schultz, P. Crump, H. Wenzel, O. Brox, A. Maaßdorf, G. Erbert and G. Tränkle, "11W Broad Area 976nm DFB Lasers with 58% Efficiency", in Conference on Lasers and Electro-Optics, OSA Technical Digest, paper CWE1 (2010).

C.M. Schultz, P. Crump, H. Wenzel, O. Brox, F. Bugge and G. Erbert, "Wide Temperature Range High Power Broad Area 975nm DFB Lasers", in Conference on Lasers and Electro-Optics/International Quantum Electronics Conference, OSA Technical, paper CWF6 (2009).

C.M. Schultz, P. Crump, H. Wenzel, O. Brox, F. Bugge, and G. Erbert, "Narrow Vertical Far-Field 975-nm Broad-Area DFB Lasers for Wide Temperature Range Operation", IEEE Photonics Technology Letters **21**, 593-595 (2009).

Co-author publications

P. Crump, G. Erbert, H. Wenzel, C. Frevert, C.M. Schultz, K.-H. Hasler, R. Staske, B. Sumpf, A. Maassdorf, F. Bugge, S. Knigge, and G. Tränkle, "Efficient High-Power Laser Diodes", IEEE Journal of Selected Topics in Quantum Electronics **19**, 1501211-1501211 (2013).

P. Crump, C.M. Schultz, H. Wenzel, G. Erbert and G. Tränkle, "Efficiency-optimized monolithic frequency stabilization of high-power diode lasers", Journal of Physics D, **46**, 013001, (2013).

A. Maaßdorf, C.M. Schultz, O. Brox, H. Wenzel, P. Crump, F. Bugge, A. Mogilatenko, G. Erbert, M. Weyers, and G. Tränkle, "In-situ etching of patterned GaAs/InGaP surfaces for highly efficient 975nm DFB-BA diode lasers", Journal of Crystal Growth **370**, 226-229, (2013).

P. Crump, S. Böldicke, C.M. Schultz, H. Ekhteraei, H. Wenzel and G. Erbert, "Diagnosing and addressing the limitations to lateral far field angle in high power broad-area diode lasers", IEEE Summer Topical Meetings, 978-1-4577-1527-3/12, 63-64 (2012).

Ch. Strelow, C.M. Schultz, H. Rehberg, M. Sauer, H. Welsch, A. Stemmann, Ch. Heyn, D. Heitmann, and T. Kipp, "Light confinement and mode splitting in rolled-up semiconductor microtube bottle resonators", Physical Revue B **85**, 155329 (2012).

P. Crump, S. Böldicke, C. Schultz, H. Ekhteraei, H. Wenzel and G. Erbert, "Experimental and theoretical analysis of the dominant lateral waveguiding mechanism in 975nm high power broad area diode lasers", Semiconductor Science and Technology **27**, 045001 (2012).

P. Crump, O. Brox, F. Bugge, J. Fricke, C. Schultz, M. Spreemann, B. Sumpf, H. Wenzel and G. Erbert, "High power, high efficiency monolithic edge-emitting GaAs-based lasers with narrow spectral widths", Semiconductors and Semimetals **86**, 49-92 (2012).

P. Crump, C.M. Schultz, H. Wenzel, S. Knigge, O. Brox, A. Maaßdorf, F. Bugge and G. Erbert, "Reliable operation of 976nm High Power DFB Broad Area Diode Lasers with over 60% Power Conversion Efficiency", Proc. SPIE **7953**, 79531G (2011).

X. Wang, P. Crump, H. Wenzel, A. Liero, T. Hoffmann, A. Pietrzak, C.M. Schultz, A. Klehr, A. Ginolas, S. Einfeldt, F. Bugge, G. Erbert, and G. Tränkle, "Root-Cause Analysis of Peak Power Saturation in Pulse-Pumped 1100 nm Broad Area Single Emitter Diode Lasers", IEEE Journal of Quantum Electronics, **46**, 658-665 (2010).

P. Crump, C.M. Schultz, A. Pietrzak, S. Knigge, O. Brox, A. Maaßdorf, F. Bugge, H. Wenzel and G. Erbert, "975-nm high-power broad area diode lasers optimized for narrow spectral linewidth applications", Proc. SPIE **7583**, 75830N (2010).

X. Wang, P. Crump, A. Pietrzak, C. Schultz, A. Klehr, T. Hoffmann, A. Liero, A. Ginolas, S. Einfeldt, F. Bugge, G. Erbert and G. Tränkle, "Assessment of the Limits to Peak Power of 1100 nm Broad Area Single Emitter Diode Lasers under Short Pulse Conditions", Proc. SPIE **7198**, 7198G (2009).

Ch. Strelow, H. Rehberg, C.M. Schultz, H. Welsch, Ch. Heyn, D. Heitmann, and T. Kipp, "Optical Microcavities Formed by Semiconductor Microtubes Using a Bottlelike Geometry", Physical Revue Letters **101**, 127403 (2008).

Ch. Strelow, H. Rehberg, C.M. Schultz, H. Welsch, Ch. Heyn, D. Heitmann and T. Kipp, "Spatial emission characteristics of a semiconductor microtube ring resonator", Physica E **40** 1836-1839 (2008).

Ch. Strelow, C.M. Schultz, H. Rehberg, H. Welsch, Ch. Heyn, D. Heitmann, and T. Kipp, "Three dimensionally confined optical modes in quantum-well microtube ring resonators", Physical Revue B **76**, 045303 (2007).

Talks

C.M. Schultz, P. Crump, A. Maaßdorf, O. Brox, F. Bugge, A. Mogilatenko, H. Wenzel, S. Knigge, B. Sumpf, M. Weyers and G. Erbert, "Buried DFB Gratings Floating in AlGaAs with Low Oxygen Contamination Enable High Power and Efficiency DFB Lasers", IEEE Photonics Society Summer Topical Meeting on High Power Semiconductor Lasers, Seattle, WA4.1 (invited talk) (2012).

C.M Schultz, P. Crump, H. Wenzel, S. Knigge, O. Brox, A. Maassdorf, F. Bugge and G. Erbert, "Efficiency-optimized 973nm high power broad area DFB lasers with overgrown aluminium-free gratings for peak power conversion of 63%", CLEO/Europe-EQEC Conference, Munich, CB7, CB7.3 (2011).

C.M. Schultz, P. Crump, H. Wenzel, O. Brox, A. Maaßdorf, G. Erbert and G. Tränkle, "11W Broad Area 976nm DFB Lasers with 58% Efficiency", CLEO/QELS Conference, San Jose, CWE, CWE1 (2010).

C.M. Schultz, P. Crump, H. Wenzel, O. Brox, F. Bugge and G. Erbert, "Wide Temperature Range High Power Broad Area 975nm DFB Lasers", CLEO/ IQEC Conference, Baltimore, CWF, CWF6 (2009).

C.M. Schultz, "High Power 975nm Distributed Feedback Lasers", Seminar: Spezielle Fragen zur Halbleiterphysik, Institut für Angewandet Physik der Universität, Hamburg (2009).

Patent

O. Brox, F. Bugge, P. Crump, G. Erbert, A. Maaßdorf, C.M. Schultz, H. Wenzel and M. Weyers, "Diodenlaser und Verfahren zur Herstellung eines Diodenlasers mit hoher Effizienz", Deutsches Patent- und Markenamt, DE 10 2011 086 744 B3 (2013).

Abbreviations and Symbols

Abbreviation	Explanation
A	
α_{DFB}	DFB resonator loss
α_{i}	internal optical loss
α_{m}	mirror loss
Al	aluminum
AR	anti reflection
As	arsine
Au	gold
B	
BA	broad area
Br	bromine
C	
c	vacuum speed of light
C	carbon
CCD	charge-coupled device
CCP	conduction cooled package heat sink
CL	cathodoluminescence
C-mount	common copper heatsink

Abbreviation	Explanation
C	
CMT	coupled mode theory
COMD	catastrophic optical mirror damage
Cs	caesium
Cu	copper
CW	continuous wave
D	
DFB	distributed feedback
DQW	double quantum well
E	
EDXS	energy-dispersive X-ray spectroscopy
η_d	differential quantum efficiency
η_i	internal quantum efficiency
η_PCE	power conversion efficiency
Er	erbium

Abbreviation	Explanation

F	
FP	Fabry-Pérot
G	
Ga	gallium
Γ	confinement factor of a specific layer with the optical field
Γg_0	modal gain coefficient
H	
H	hydrogen
HR	high reflection
I	
In	indium
I_th	threshold current

Abbreviation	Explanation
J	
j_{th}	threshold current density
j_{tr}	transparency current density
K	
κ	DFB coupling coefficient
L	
L	cavity length
λ	wavelength
Λ	grating period
LFF	lateral far field
LNF	lateral near field
M	
MBE	molecular beam epitaxy
MOVPE	metal-organic vapor phase epitaxy
N	
n_{eff}	effective index of refraction
Nd : YAG	neodymium-doped yttrium aluminum garnet
O	
O	oxygen
P	
P	phosphore
PECVD	plasma-enhanced chemical vapor deposition
PL	photoluminescence
PUI	power (P), voltage (U) and current (I)
Q	
QCW	quasi continuous wave
QIP	quasi 2-dimensional semiconductor laser simulation program

Abbreviation	Explanation
R	
R_{f}	front facet reflectivity
R_{r}	rear facet reflectivity
RW	ridge waveguide
S	
S	slope efficiency
S	sulfur
SCS-mount	screening sub-mount
SEM	scanning electron microscopy
STEM	scanning tunneling electron microscopy
SIMS	secondary ion mass spectrometry
SMSR	side mode suppression ratio
Sn	tin
SQW	single quantum well
T	
TE	transverse electric (polarization)
TM	transverse magnetic (polarization)
V	
VFF	vertical far field
VBG	volume Bragg grating
v_{g}	group velocity
W	
W	contact stripe width
W	tungsten
X	
Xe	xenon
Y	
Yb	ytterbium
Z	
Z	atomic number

Eidesstattliche Versicherung

Hiermit versichere ich, Christoph Matthias Schultz, dass ich die Arbeit selbständig und unter ausschließlicher Verwendung der angegebenen Quellen und Hilfsmittel verfasst habe.

Berlin, 14. August 2012 Christoph M. Schultz

Danksagung

Mein Dank gilt all jenen, die zum Gelingen dieser Arbeit beigetragen haben.

Insbesondere bedanke ich mich bei:

- Prof. Dr. Günther Tränkle dafür, dass er mir die Anfertigung dieser Dissertation am Ferdinand-Braun-Institut in Berlin ermöglicht und diese durch regelmäßige fachliche Aussprachen intensiv begleitet hat, für seine Unterstützung, seinen Rat und seine Einschätzung.

- Prof. Dr. Klaus Petermann für die Übernahme des zweiten Gutachtens.

- Prof. Dr. Hartmut Hillmer für die Übernahme des dritten Gutachtens als externer Gutachter.

- Dr. Götz Erbert, der mit seinem Fachwissen und seiner Erfahrung durch viele richtungsweisende Empfehlungen und Ratschläge zum Gelingen dieser Arbeit maßgeblich beigetragen und als Leiter der Abteilung Optoelektronik die Leitung des Projekts HessLa übernommen hat.

- Dr. Paul Crump, für seine sehr umfangreiche Unterstützung während meiner Einarbeitungszeit am FBH und bei der gesamten Durchführung des Projektes HessLa, für viele fachliche Erläuterungen, Ratschläge und seine starke Motivation.

- Dr. Hans Wenzel für die Beantwortung sehr vieler Fragen zu DFB Lasern und Gittern und für zahlreiche intensive Diskussionen über die Berechnung der Eigenschaften von Moden in DFB-Lasern.

- Dr. Olaf Brox, unter dessen Verantwortung die DFB-Gitter ex-situ mittels holographischer und lithographischer Techniken strukturiert wurden, für viele hilfreiche Erläuterungen zu DFB-Gittern, zu deren Herstellung und für seine Hilfe bei der experimentellen Bestimmung der Koppelkoeffizienten.

- Dr. Andre Maaßdorf, der die im Projekt HessLa und während dieser Arbeit verwendeten Wafer gewachsen und in-situ geätzt hat, für seine Unterstützung, seine guten Ideen, für die Beantwortung meiner zahlreichen Fragen und für die Analyse der Proben.

- den Kolleginnen und Kollegen Dr. Gunnar Blume, Dr. Frank Bugge, Petra Brade, Dr. Bernd Eppich, Dr. Jörg Fricke, Armin Ginolas, Dr. Andreas Klehr, Dr. Martin Maiwald, Dr. Anna Mogilatenko, Dr. Steffen Knigge, Dr. Wolfgang Pittroff, Dr. Peter Ressel, Ralf Staske, Dr. Bernd Sumpf, Dr. Ute Zeimer danke ich für Ihre Unterstützung in Ihren jeweiligen Fachbereichen sowie für die Beantwortung vieler Fragen.

- den Doktoranden während meiner Zeit am FBH, Dr. Agnieszka Pietrzak, Martin Spreemann, Xiaozhuo Wang, Daniel Jedrzejczyk, Christian Fiebig, David Feise, Ahmad Bawamia, Stefan Spiessberger, Mirko Übernickel, Dr. Sven Schwertfeger und Carlo Frevert für Ihre Motivation und für viele wichtige Diskussionen.

- Hossein Ekhteraei für die Durchführung der Messungen spektral aufgelöster lateraler Nah- und Fernfelder von DFB-BA Lasern.

- Für Ihre unerschütterliche Unterstützung und für Ihren Zuspruch bedanke ich mich bei meinen Eltern Dr. med. Christa Schultz-Wernitz und Manfred Schultz.

- Ich danke Elisabeth und Rainer Thiemann für Ihre vielseitige Unterstützung.

- Meine große Dankbarkeit gilt meiner Verlobten Kirsten Thiemann, die mir immer wieder zu dem Mut verholfen hat der notwendig war, die lange Zeit der intensiven Arbeit in Berlin auch unter schwierigen gesundheitlichen Bedingungen durchzustehen, für Ihre Zuversicht, Ihr Vertrauen und Ihren Beistand.